tuNNel HY

Pre-normative research for safety of hydrogen driven vehicles and transport through tunnels and similar confined spaces

Clean Hydrogen Partnership
Grant Agreement Number 826193

Deliverable D4.4
Results of the deferred experimental programme and associated activities

Lead author: HSE (W. Rattigan, K. Lyons, S. Bergin, M. Pursell)
Contributing authors: UU (D. Makarov, V. Shentsov, S. Kashkarov, D. Cirrone)
                         NCSRD (S. Giannissi, A. Venetsanos, I. Tolias)
                         DTU (L. Giulani, F. Markert, L. Schiøtt Sørensen)
                         KIT (Z. Xu, M. Kuznetsov)
                         PS (J. Grune)
                         USN (A. Gaathaug, K. Vågsæther, J. Lundberg)

Clean Hydrogen Partnership

Deliverable administration					
Work Package	WP4. Explosion prevention and mitigation				
N. and title	D4.4 (D51) Results of the deferred experimental programme and associated activities				
Type	Report				
Status	Draft/Working/**Released**	Due	M41	Date	31-07-2022
Comments					
Development and revision					
Version No.	Date	Authors	Description		
220606	06-06-22		ToC		
220606	06-06-22	Z. Xu	Contribution from KIT		
220701	01-07-22	J. Grune	Contribution from PS		
220701	01-07-22	S. Bergin	Contribution from HSE		
220704	04-07-22	A. Venetsanos	Contribution from NCSRD		
220721	21-07-22	S. Giannissi	Contribution from NCSRD		
220722	22-07-22	F. Markert	Contribution from DTU		
220722	22-07-22	I. Tolias	Contribution from NCSRD		
220722	22-07-22	K. Lyons	Contribution from HSE		
220725	25-07-22	V. Shentsov	Contribution from UU (10.2)		
220725	25-07-22	S. Kashkarov	Contribution from UU (10.6.1)		
220728	28-07-22	D. Cirrone	Review		
220729	29-07-22	S. Giannissi	Review		
221221	21-12-22	W. Rattigan	Updated contribution from HSE		
221224	24-12-22	D. Cirrone	Review		
221227	27-12-22	D. Makarov	Review		
230103	03-01-23	S. Giannissi	Review		
230109	09-01-23	W. Rattigan	Document finalisation		
230227	03-03-23	W. Rattigan, D. Makarov	HSE update in Sub-task 4.4.6		

Disclaimer

Despite the care that was taken while preparing this document the following disclaimer applies: the information in this document is provided as is and no guarantee or warranty is given that the information is fit for any particular purpose. The user thereof employs the information at his/her sole risk and liability.

The document reflects only the authors' views. The Clean Hydrogen Joint Undertaking and the European Union are not liable for any use that may be made of the information contained therein.

Acknowledgments

The HyTunnel-CS project aims to conduct internationally leading pre-normative research (PNR) to close knowledge gaps and technological bottlenecks in the provision of safety and acceptable level of risk, in the use of hydrogen and fuel cell cars as well as hydrogen delivery transport in underground transportation systems.

The project was originally due for completion in February 2022 (M36) but due, in part, to the COVID-19 pandemic, some work was delayed. An extension (to July 2022 (M41)) to the project was granted to allow for the outstanding contributions to be reported within the project. It was agreed that all outstanding work from the three experimental work packages, WP2, WP3 and WP4, would be reported in a new deliverable (D4.4) and owned by HSE (WP4 leader). The work was completed in December 2022 (M46)

This document presents the deliverable (D4.4), which includes outstanding contribution from WP2 A*nalytical, numerical and experimental studies regarding unignited leaks in tunnels and underground parking*, WP3 *Analytical, numerical and experimental studies on fires regarding ignited leaks in tunnels and underground parking*, WP4 *Analytical, numerical and experimental studies regarding explosion prevention and mitigation in tunnels and underground parking*.

This report is organised by Work Package and identified by task (sub-task) number. This report should be read in conjunction with the Final report from each of the individual work packages: deliverables D2.3, D3.3 and D4.3.

Table of contents

1. Nomenclature and abbreviations

ACH   Air Change per Hour

ALARP   As Low As Reasonably Practicable

CFD   Computational Fluid Dynamics

CHSS   Compressed Hydrogen Storage System

CNG   Compressed Natural Gas

CS   Confined Spaces

EoS   Equation of State

FCEV   Fuel Cell Electric Vehicle

FCH JU   Fuel Cells and Hydrogen/ Clean Hydrogen Joint Undertaking

FED   Fractional Effective Dose

FRP   Fibre Reinforced Polymer

FRR   Fire Resistance Rating

HGV   Heavy Goods Vehicle

HPV   Hydrogen-Powered Vehicles

HRR   Heat Release Rate

HRR/A   Specific Heat Release Rate (HRR divided by fire source area, A)

ICE   Internal Combustion Engine

ISO   International Standardization Organization

LBG   Liquefied Bio Gas

LBT   Load-Bearing Thickness

LFL   Lower Flammability Limit

LH2   Liquid Hydrogen

LNB   Leak-No-Burst or Microleak-No-Burst

LNG   Liquefied Natural Gas

M   Milestone

MCP   Multi Cylinder Pack

NWP   Nominal Working Pressure

PNR   Pre-Normative Research

PP	Polypropylene
PPP	Pressure Peaking Phenomenon
QRA	Quantitative Risk Assessment
RCS	Regulations, Codes and Standards
RSET	Required Safe Egress Time
RID	Regulation concerning the International Carriage of Dangerous Goods by Rail
SAB	Stakeholders Advisory Board
SDO	Standards Developing Organization
SOP	Standard Operation Procedures
TPL	Thermal Protection Layer
TPRD	Thermally-activated Pressure Relief Device

2. List of figures

3. List of tables

4. Introduction

The HyTunnel-CS project aims to conduct internationally leading pre-normative research (PNR) to close knowledge gaps and technological bottlenecks, in the provision of safety and acceptable level of risk, in the use of hydrogen and fuel cell cars as well as hydrogen delivery transport in underground transportation systems.

This document presents the deliverable D4.4 "Results of the deferred experimental programme and associated activities", which reports the activities and works conducted during the period March to December 2022. The reported outstanding contributions involve the analytical, numerical and experimental campaigns performed within work packages WP2 "Effect of mitigation systems on hydrogen release and dispersion in confined spaces", WP3 "Thermal and pressure effects of hydrogen jet fires and structure integrity" and WP4 "Explosion prevention and mitigation". Therefore, the present deliverable D4.4 complements the work reported in final reports D2.3, D3.3 and D4.3 associated respectively to WP2, WP3 and WP4.

5. Effect of mitigation systems on hydrogen release and dispersion in confined spaces (WP2, NCSRD)

5.1 Analytical studies and development of engineering tools (Task 2.2, CEA)

5.1.1 Non-adiabatic tank blowdown (ST2.2, NCSRD)

5.1.1.1 Introduction

This contribution presents the extension of the DISCHA integral engineering tool to account for heat transfer through the storage tank walls during tank blowdown both for compressed gaseous and liquid storage.

The DISCHA integral engineering tool was first developed within Net-Tools EC project (partly based on pre-existing software, e.g. Venetsanos and Giannissi 2017) to run under the e-Lab web-platform interface in order to calculate: a) accurate physical properties of hydrogen and methane through Helmholtz Free Energy (HFE) based Equations of State (EoS), including two-phase conditions modelled using the Homogeneous Equilibrium Mixture (HEM) model, b) steady state release conditions (constant stagnation conditions) and c) transient release (blowdown) conditions. A standalone version sharing the same underlying Fortran dynamic library was developed in parallel to the web version, equipped with a separate more flexible Python interface. Details on some of the algorithms applied regarding physical properties can be found in (Venetsanos, 2020).

DISCHA standalone tool was later extended for non-equilibrium and discharge line effects (resistance, area change and heat transfer through piping walls) in the framework of the PRESLHY EC project (Venetsanos 2018, Venetsanos 2019, Venetsanos et al. 2021a, Venetsanos et al. 2021b) and its overall validation and capabilities were presented at the PRESLHY dissemination conference (Venetsanos, 2021).

5.1.1.2 Modelling

In the new model formulation, the energy equation is solved within the tank walls using either Cartesian or cylindrical coordinates, with the second option to account better for the curvature of the tank side walls in case of cylindrical tanks. The walls are assumed to be comprised of a number of consecutive material layers, each having its own physical properties (specific heat, density and conductivity). Heat flux continuity is imposed at the two interfaces (internal interface with tank interior and external interface with ambient atmosphere), permitting calculation of the interface temperatures. A given value and constant heat transfer coefficient is used at the external interface. Natural convection heat transfer coefficient correlations are used at the internal interfaces. These correlations may depend on wall orientation with respect to gravity (top wall, bottom wall, side wall). The internal heat transfer coefficient will also depend on the properties of the neighbouring fluid, whether it is liquid or vapour. The energy equation is discretized using a one-dimensional grid within each layer. The number of grid cells within each layer is a user defined option (default 1).

The new formulation also includes solving a transient tank integral energy equation (integrated over the entire tank internal volume) with source terms a) the energy rate released through the tank openings and b) the heat power transferred through the internal tank walls. Two options

are available for the type of energy equation to solve: a) entropy balance and b) internal energy balance.

5.1.1.2.1 Sensitivity and validation for compressed gaseous storage

The helium blowdown test of KIT, see Dadashzadeh et al, 2019 and Molkov et al., 2021 was selected for validation. The experiment considered helium blowdown through a 1 mm nozzle from a 19L type-IV tank at 70 MPa, 293.15K. The tank internal diameter was 180 mm and was equipped with an HDPE (High density poly-ethylene) liner of 7 mm thickness wrapped with 17 mm thick CFRP (Carbon fibber reinforced polymer). Physical properties for HDPE and CFRP were considered independent of temperature and were taken as given in Dadashzadeh et al, 2019. For the needs of the present work helium physical properties were implemented in the DISCHA standalone tool both with HFE formulation and Abel-Noble EoS. HFE coefficients were taken from CoolProp github. All the simulation results reported below were performed with the HFE EoS formulation. Heat transfer coefficients were taken as in Dadashzadeh et al, 2019 and Molkov et al., 2021, that includes the same correlation for heat transfer coefficient for all tank walls irrespective of their orientation compared to gravity.

Before the validation, a sensitivity analysis was performed to examine the effects of a) grid size within the tank walls, b) type of coordinates in the wall energy equation, c) tank energy equation type (entropy based or internal energy based), d) non-adiabatic effect and e) discharge coefficient (Cd). The default parameters were 1 cell within each wall layer, cylindrical coordinates, entropy-based tank energy and Cd = 1.0.

5.1.1.2.2 Grid effect

Three different grids were considered as shown in Table 1. Figure 1 shows the predicted conditions in the tank and Figure 2 the predicted conditions at the nozzle. It can be observed that the results converge quickly as the grid is refined. The temperature predictions for grid-1, composed of 1 cell in each layer, are quite close to the converged solution. The grid effect on the pressure and mass flow rate is insignificant. The simulation results presented in the sections below were obtained using grid-3.

Table 1: Grid cases considered and number of cells per layer.

Grid	HDPE (7mm)	CFRP (17mm)
1	1	1
2	7	17
3	14	34
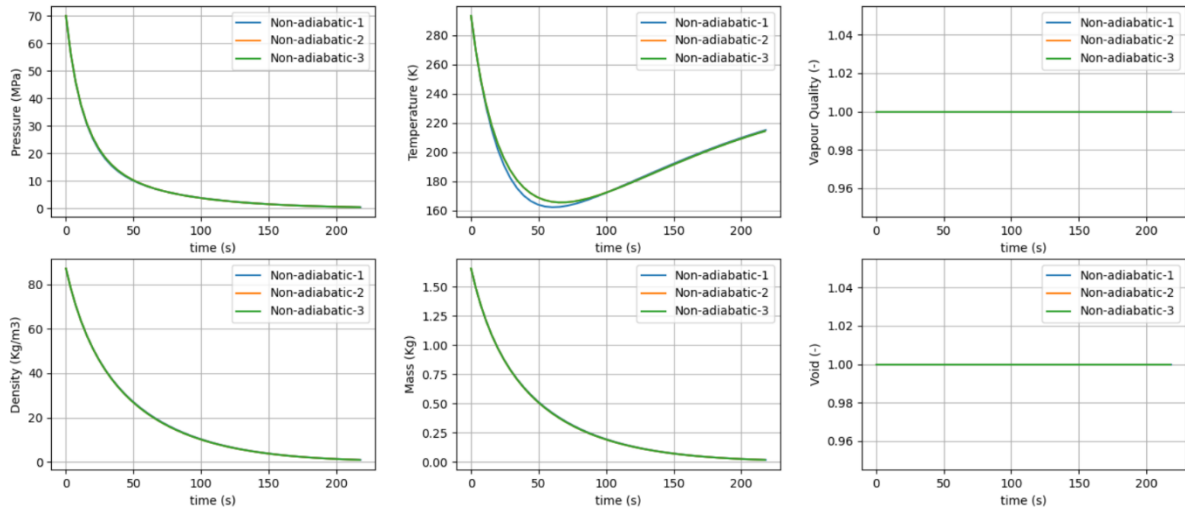
Figure 1: Grid sensitivity. Conditions in the tank.
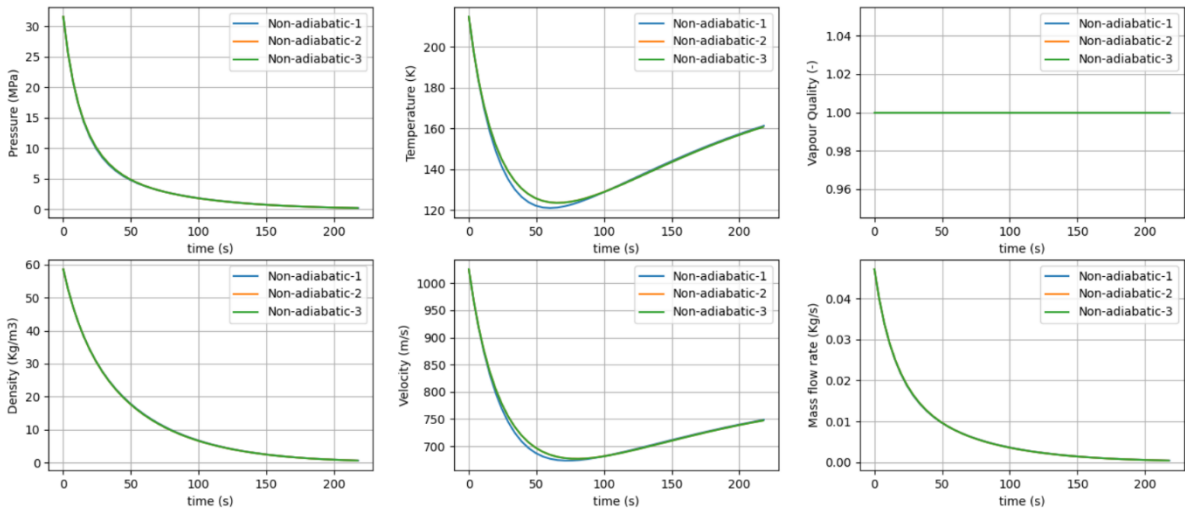
Figure 2: Grid sensitivity. Conditions at the nozzle.

5.1.1.2.3 Coordinates effect

The coordinates effect is shown in Figure 3 and Figure 4. The temperatures are affected but the effect on the pressure and mass flow rate is insignificant.
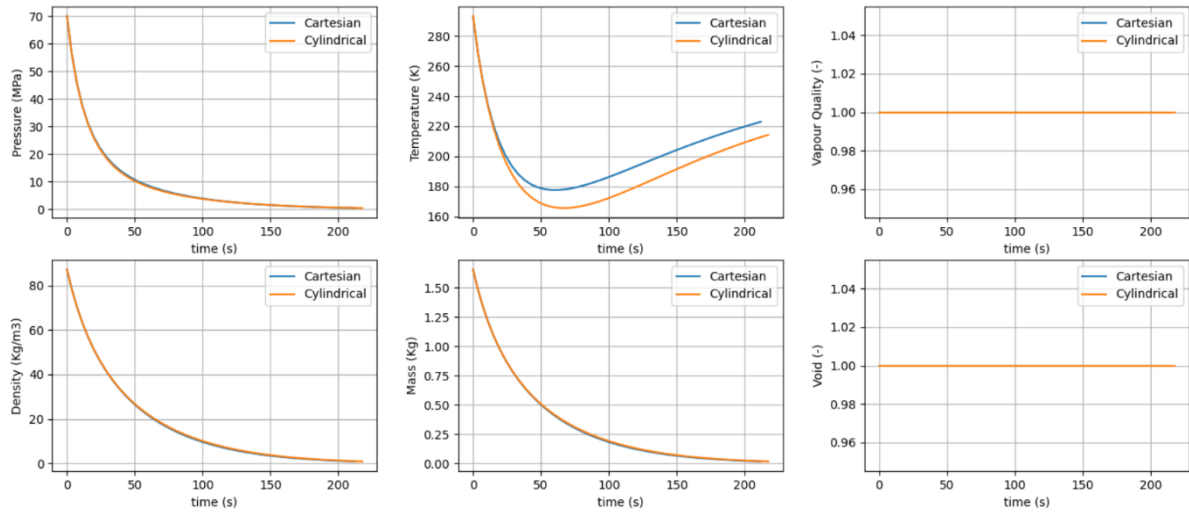
Figure 3: Coordinates effect. Conditions in the tank.
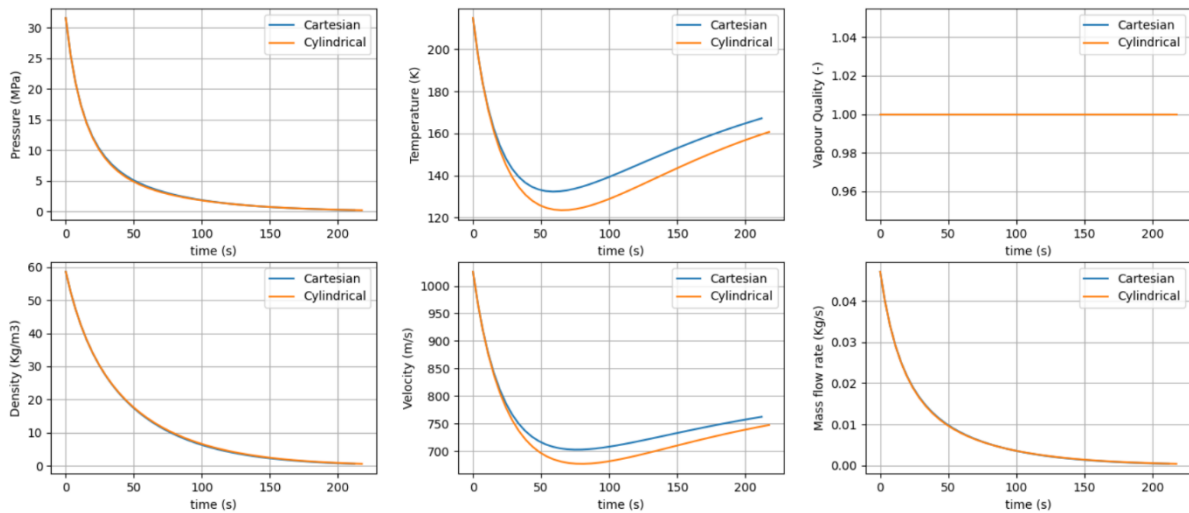
Figure 4: Coordinates effect. Conditions at the nozzle.

5.1.1.2.4 Tank energy equation effect

The tank energy equation effect is shown in Figure 5 and Figure 6. The effect on predicted temperatures is quite small. Pressure and mass flow rate are practically not affected.
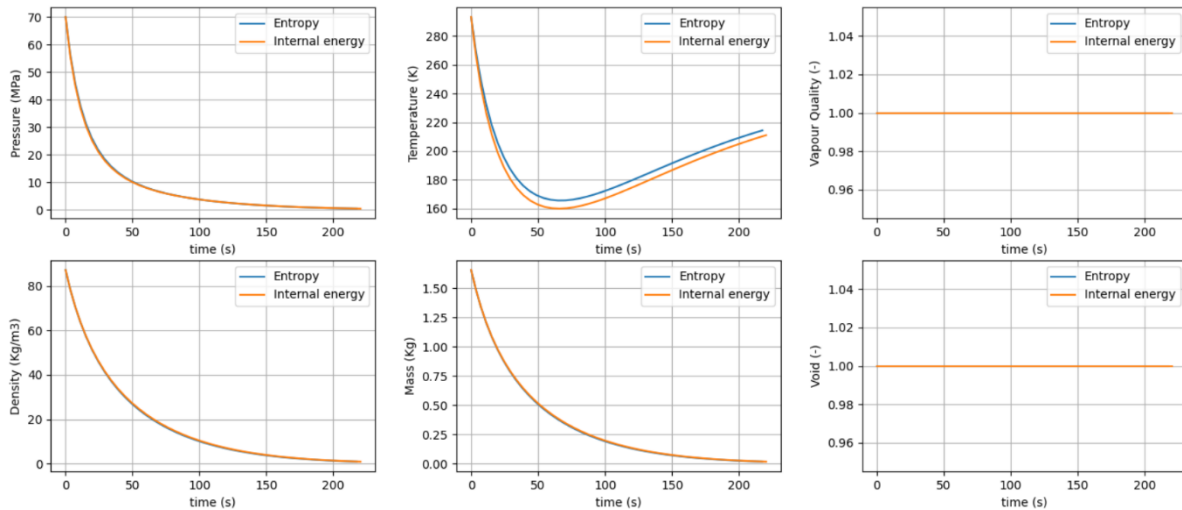
Figure 5: Tank energy equation effect. Conditions in the tank.
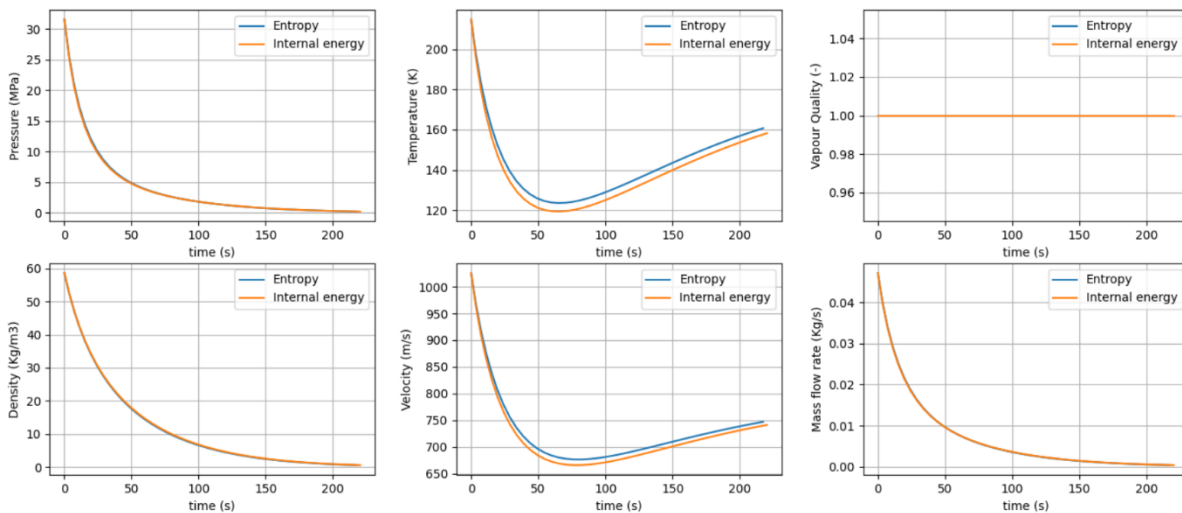
Figure 6: Tank energy equation effect. Conditions at the nozzle.

5.1.1.2.5 Non-adiabatic effect

The non-adiabatic tank effect is shown in Figure 7 and Figure 8. Comparison between the non-adiabatic tank and adiabatic tank simulation results shows that both pressure and temperature dynamics are significantly affected. It is impressive however to see that the predicted mass flow rate is not affected to such a big extent and certainly not during the first stages of the blowdown during which heat transfer has not had the necessary time to affect the blowdown dynamics.
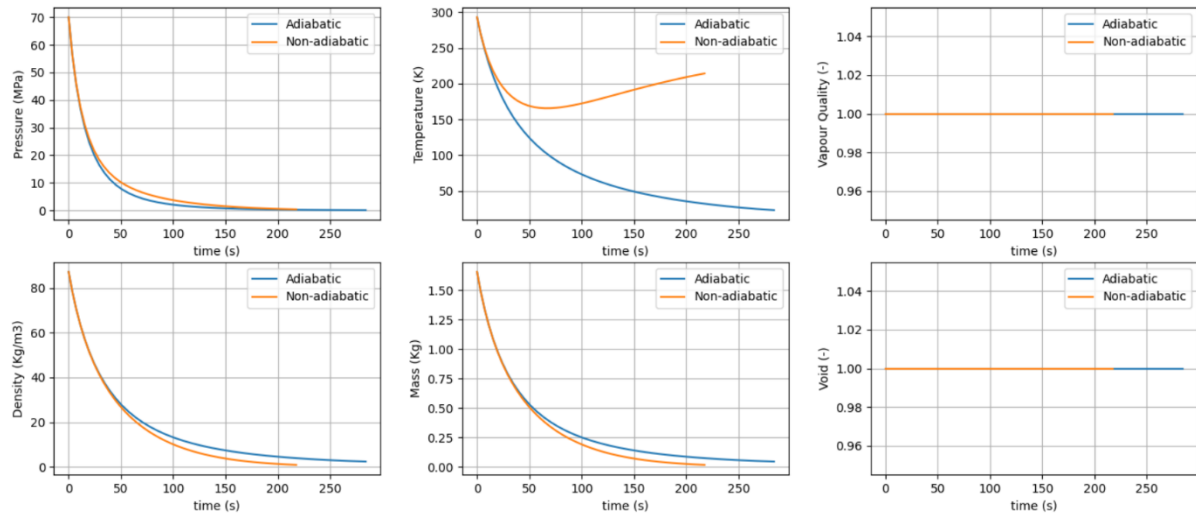
Figure 7: Non-adiabatic effect. Conditions in the tank.
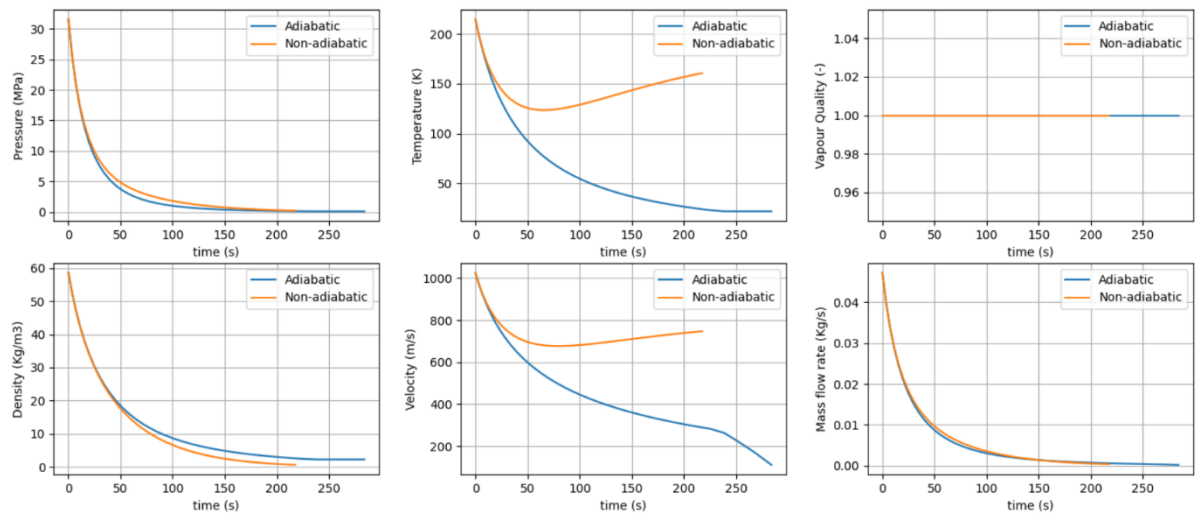
Figure 8: Non-adiabatic effect. Conditions at the nozzle.

5.1.1.2.6 Discharge coefficient effect

The discharge coefficient effect is shown in Figure 9 and Figure 10. The discharge coefficient represents the effect of the discharge line and is implemented here by introducing a reduced nozzle diameter, which is equal to the nominal one (1 mm) times the square root of Cd. Table 2 shows the discharge coefficients and corresponding nozzle diameters considered. It is clear that the discharge coefficient affects the temperature and pressure dynamics and also the mass flow rate. More precisely the initial mass flow rate is significantly affected by Cd.

Table 2: Discharge coefficients considered.

Cd	Nozzle diameter (mm)
1.0	1
0.9	0.9487
0.8	0.8944
0.7	0.8367
0.6	0.7746
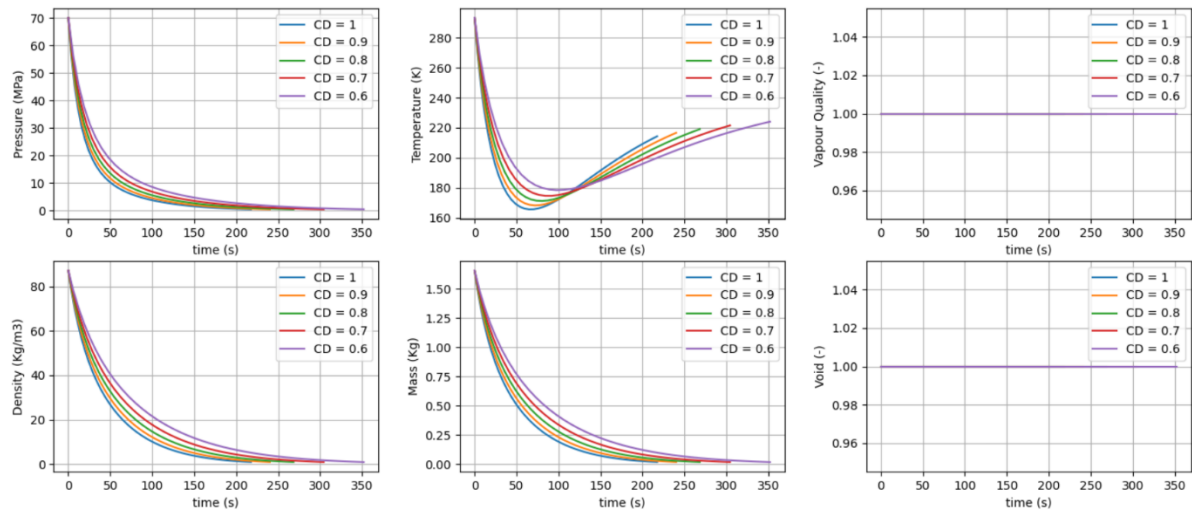
Figure 9: Discharge coefficient effect. Conditions in the tank.
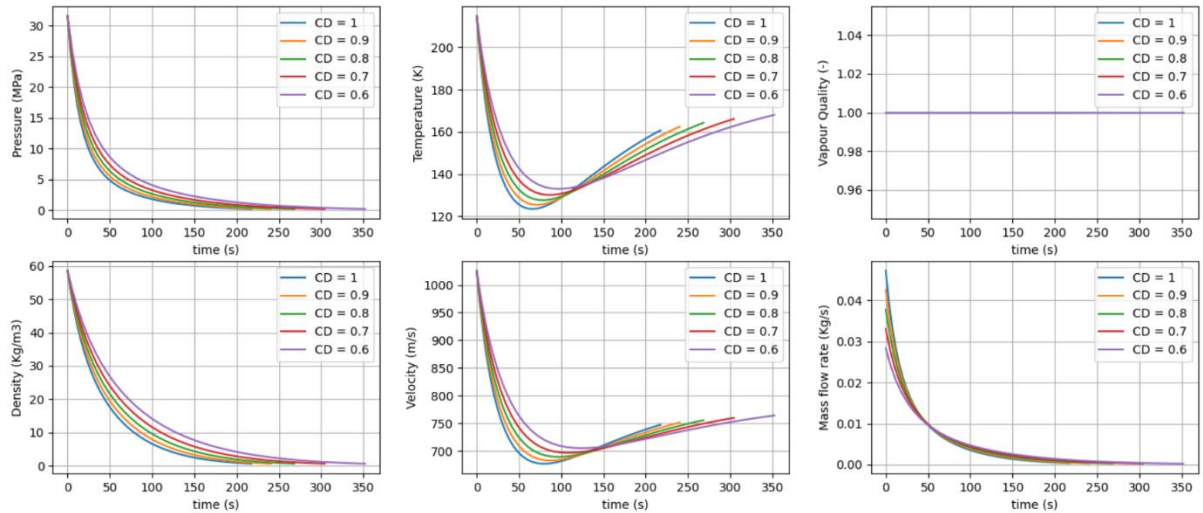
Figure 10: Discharge coefficient effect. Conditions at the nozzle.

5.1.1.3   Validation against KIT tests

Figure 11 presents a comparison between predictions and KIT experimental data for tank pressure and temperature dynamics during the blowdown. The simulation with Cd=0.8 reproduces almost exactly the pressure dynamics. The simulation with Cd=0.6 gives the best qualitative agreement with the experimental temperatures. Overall Cd = 0.7 could be suggested for this blowdown case (Cd was not determined experimentally). This is in contrast to Dadashzadeh et al, 2019 who applied Cd = 0.9.
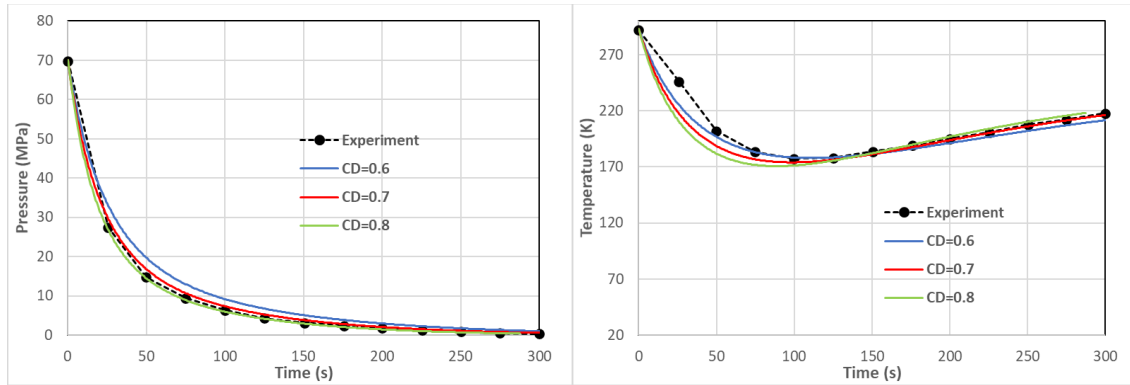
Figure 11: Predicted tank pressure and temperature against KIT experiments.

5.1.1.4 *Validation for gaseous release (boil-off) from LH2 storage*

For the validation the tank boil-off experiments performed at the Lawrence Livermore National Lab. (LLNL, US) as described in (Petitpas, 2018) and (Machalek et al., 2021) were used in the present work.

The tank was cylindrical upstanding with a diameter of 2 m and a height of 3.97 m resulting in 12.4721 m³ internal volume. Its wall consisted of 3 layers: an inner steel part with 11.1 mm thickness, MLI-vacuum insulation 50.8 mm in thickness and an external steel wall 3.8 mm thick. The tank was also equipped with a pressure relief valve (PRV) 5 mm in diameter, that opens at 3.1 bar and closes at 2.9 bar.

The tank was initially 80% filled with LH2 (20% initial void fraction). Using HFE EoS for normal hydrogen (Leachman et al., 2009) and ambient pressure (1 atm) as initial pressure this corresponds to an initial tank vapor quality of 0.0047 and 709.61 kg initial H2 stored mass at 20.369 K.

The wall energy equation was discretized using 1 cell within each wall layer. Cylindrical coordinates were used for the side wall and Cartesian coordinates for the top and bottom walls. External heat transfer coefficient was assumed equal to 6 W/m²/K. Internal heat transfer coefficients were modelled as in Machalek et al., 2021, i.e. using a different natural convection correlation depending on wall orientation. The transient simulation was performed with a constant time step of 60 s for a total simulation period of 120 days. A discharge coefficient of 1.0 was used in the simulation. Ambient temperature was assumed to be 25 °C.

Figure 11 presents the evolution of tank conditions and mass as function of time, while Figure 12 presents the path followed by the tank state on standard thermodynamic charts during the simulation. It can be observed that a period of approximately 10 days is required for the tank pressure to increase from ambient to 3.1 bars (PRV opening pressure) during which the tank void fraction decreases, i.e. the liquid level in the tank increases due to pressurization. It is interesting to see that the tank vapor quality increases during this period. After the 10 days period oscillations in tank pressure can be observed, due to the successive opening and closing of the PRV. Beyond approximately 108 days the tank does not contain liquid hydrogen and the tank void fraction equals to 1.0.

Figure 14 shows the predicted time evolution of tank liquid fraction compared to the experiments and the simulation of Machalek et al., 2021. The present results agree reasonably well with the simulation of Machalek et al., 2021. The disagreement against the experiments for large times is an issue that requires further investigations.
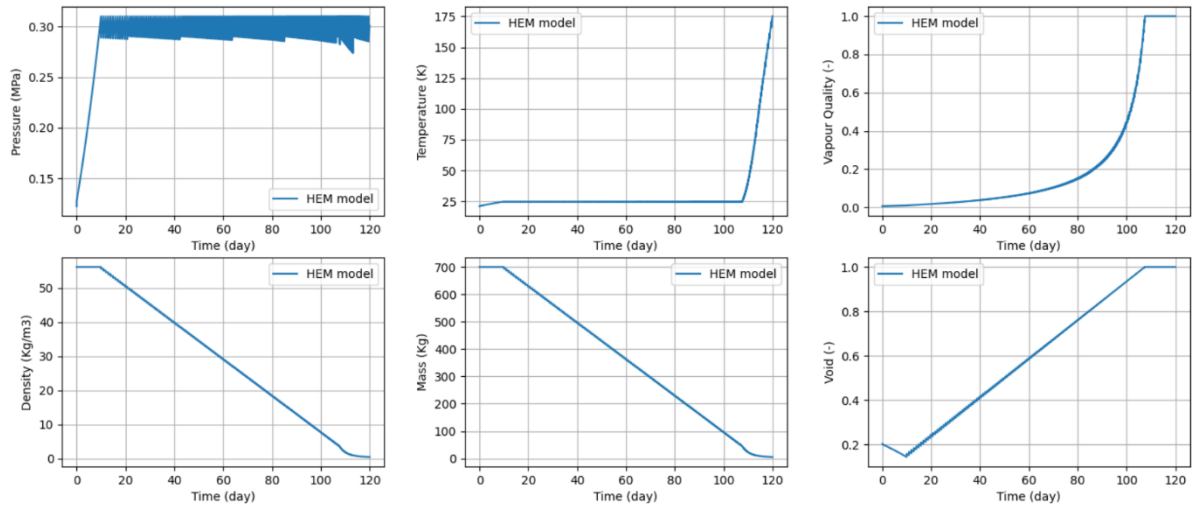
Figure 12: Predicted tank conditions and tank mass as function of time.
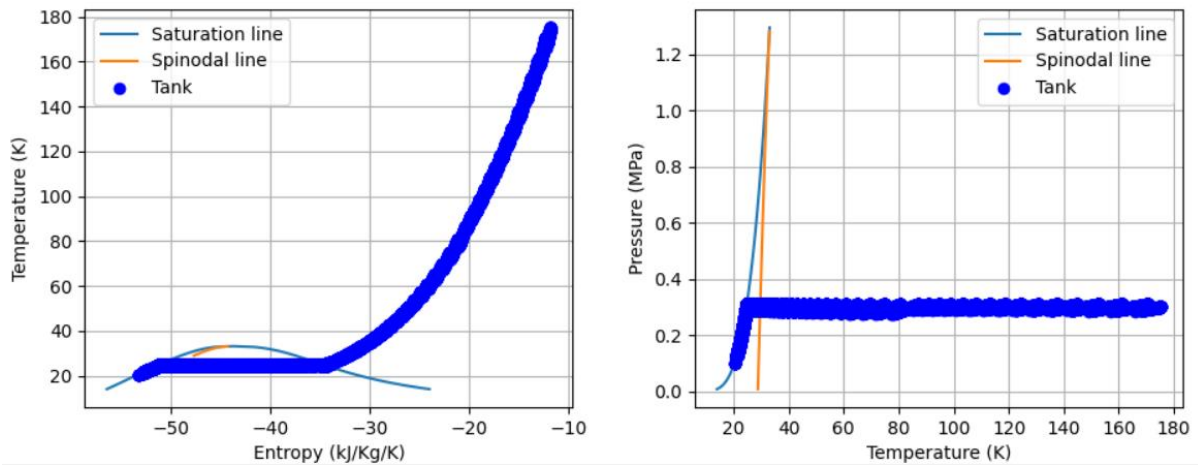
Figure 13: Predicted evolution of tank state in TS-chart (left) and PT-chart (right).
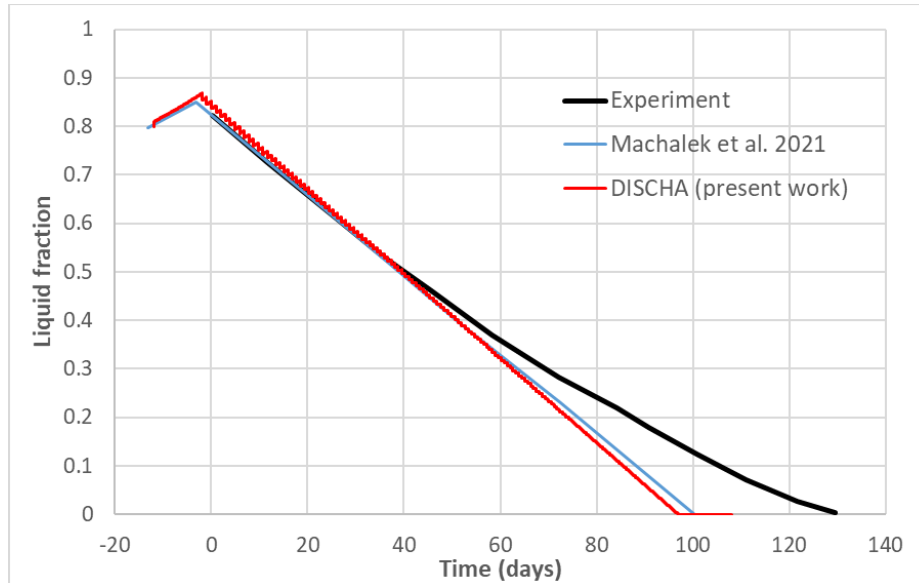
Figure 14: Predicted evolution of tank liquid fraction

5.1.1.5 Conclusions and future work

The DISCHA standalone tool was extended to account for tank wall heat transfer effects. The tool was validated against an experiment involving He release from gaseous storage at 700 bar (KIT tests) and gaseous cryogenic H2 release (boil-off) from LH2 storage (LLNL tests). The effect of the discharge coefficient was found to be predominant regarding mass flow rate prediction. Future development work will consist in extending DISCHA for tank-to-tank transfer simulations.

5.2 Numerical simulations (Task 2.3, NCSRD)

5.2.1 Dynamics of H2 release and dispersion in a tunnel - validation simulations (ST2.3.1, NCSRD)

The CFD code, ADREA-HF, is validated against experiments conducted by HSE that involve hydrogen release inside a tunnel. The aim of this task is to confirm the good predictive capabilities of the CFD tools on applications related to road mobility inside confined spaces. More specifically, it addresses hydrogen dispersion inside ventilated tunnel resulting from transient release through TPRD. After a successful code validation the CFD tools can be recommended as reliable tools for hydrogen safety engineering.

5.2.1.1 Experimental description

A series of experiments have been performed by HSE to investigate the behavior of both ignited and unignited high-pressure hydrogen jets resulting from a TPRD release from car, bus and train inside ventilated scaled tunnel. Different inventories, storage pressures and TPRD sizes have been examined based on each vehicle's (car, bus and train) characteristics. Proper scaling has been performed to assure that the same mass flow rate is introduced in the scaled tunnel and that the measured variables (e.g. concentration and over-pressure) will be similar in a real scale tunnel. More details can be found in the Section 5.3.1.

Several pre-test simulations were carried out by NCSRD based on the planned experimental matrix and are reported in (HyTunnel-CS D2.2, 2020) and (HyTunnel-CS D2.3, 2022). The pre-tests were performed before the experiments' commence. The scope was to assist with the experimental design and provide recommendations on sensors' positioning, ignition delay and location, etc.. After the experiments were performed one test, which was not simulated as pre-test, was chosen to conduct the validation. This test involved release from a train (TRAIN2) through *4.7* mm TPRD in an empty tunnel with ventilation speed 1.25 m/s. More details about the experimental conditions are presented in Table 3. In addition to the validation simulation, a comparison of one pre-test as blind-prediction simulation with its counterpart experiment was carried out. The conditions of this test are also shown in Table 3 (TRAIN1) and involve release from a train through *5.7* mm TPRD in an empty ventilated tunnel.

Table 3: Experimental conditions.

	Train1	Train2
Tank pressure (barg)	510	580
Tank Mass (kg)	5.07	5.55
Scaled nozzle (mm)	5.7	4.7
Scaled ventilation velocity (m/s)	1.25	1.25
Release direction	Upwards	Upwards
Car models	No vehicles	No vehicles

5.2.1.2 *Release modelling*

All simulations were performed using the ADREA-HF CFD code, which is an in-house code developed in NCSRD. The blowdown conditions of the blind-prediction (TRAIN1) were calculated using the in-house release code of NCSRD (Venetsanos et al., 2021a), (Venetsanos et al., 2021b). The release code performs isentropic expansion from tank conditions to nozzle conditions using the NIST EoS. The Birch 84 notional approach was employed to model the under-expanded jet and to estimate the conditions after the jet has expanded to ambient pressure. The notional conditions are set as hydrogen release conditions in the CFD simulation. Table 4 presents the notional nozzle conditions at the time zero. As time progresses temperature and velocity remain constant, while the notional diameter and the mass flow rate decrease.

Table 4: The conditions at the notional nozzle for the two simulations.

	Temperature (K)	Velocity (m/s)	Diameter (m)	Flow rate (kg/s)
TRAIN1-5.7 mm	288	1289.92	0.095	0.77
TRAIN2-4.7 mm	288	1293.52	0.1077	1

The results of the blowdown for TRAIN1 are shown in Figure 15 in comparison with the experimental release rate. The experimental tank pressure and tank mass are also shown in comparison with the predicted values. During the experiments the pressure upstream the nozzle was also measured. Due to pressure losses in the discharge line the nozzle pressure is lower than the tank pressure. For that reason, a slight higher tank pressure than the one originally planned was set to account for the pressure losses. Still the nozzle (stagnant) pressure is lower than the stagnant pressure that was used in the TRAIN1 simulation. In general, it is observed that there are some inconsistencies in the measured flow rate and the flow rate predicted by the

model. The predicted flow rate was under estimated by about 26% at the initial stage, while after approximately 6 sec the agreement was fairly good.
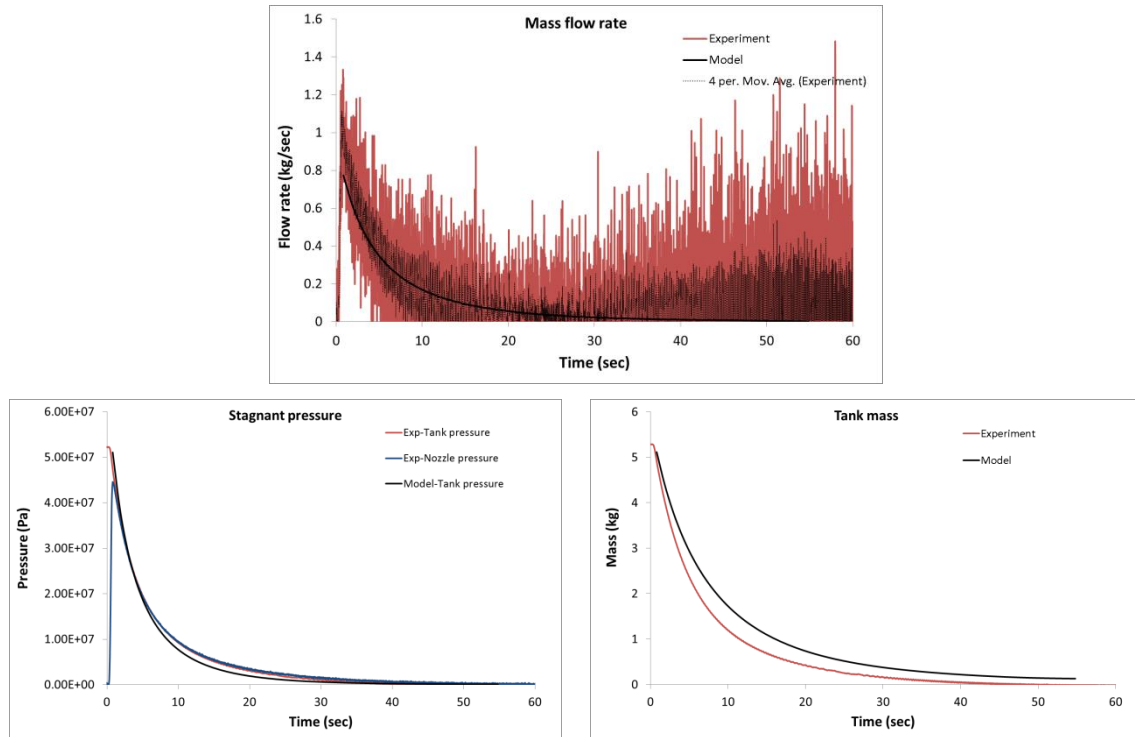
Figure 15: The blowdown results (top), the stagnant pressure and tank mass (bottom) using the in-house release code of NCSRD in comparison with the experiment for the TRAIN1. In the flow rate diagram the moving average trend line of the experimental rate is also shown.

For the validation simulation (TRAIN2) the experimental release rate (Figure 16) was used, since the measurements were available at the time when the simulation was designed. The experimental release rate was calculated by the measured tank conditions (tank temperature, pressure and volume). Figure 16 shows the blowdown experimental results. The moving average trend line is also shown. As input mass flow rate for the simulation a smooth curve was used (shown in Figure 16). The Birch 84 notional approach was applied to calculate the notional diameter evolution in time based on the smoothed flow rate (see Table 4).
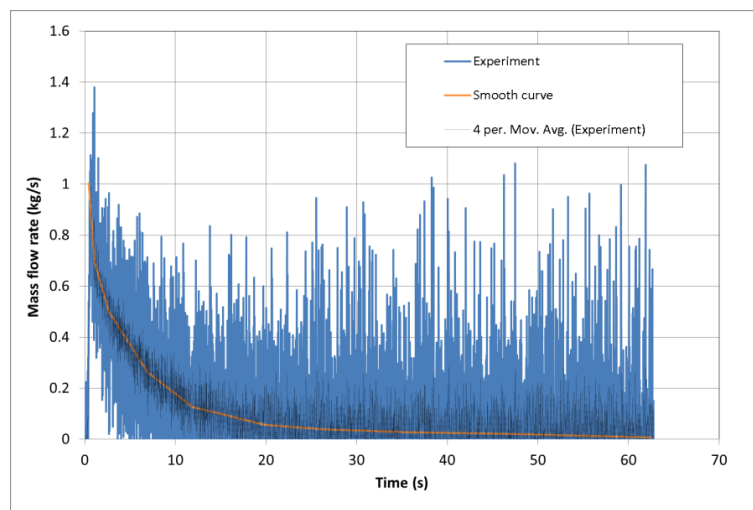
Figure 16: The blowdown experimental results and the smoothed curve used in the simulation for the TRAIN2.

5.2.1.3 Dispersion modelling

The numerical set-up followed the Best Practice Guidelines developed within the SUSANA project (2013-2016). The modeling strategy consists of the two following steps:

- 3D simulation without release to obtain the steady state of the ventilation. The ventilation velocity is imposed uniformly along the one opening of the tunnel and the established steady state velocity field is set as initial and inflow boundary condition in the CFD dispersion simulation (next step). Approximate values for k and epsilon on the inlet boundary were imposed based on the values that the CFD code predicts at the beginning of the simulation according to the applied inlet velocity. Given non-zero values at the inlet boundary are necessary, because if no turbulence is imposed the initially generated turbulence is dampened down. This leads to extremely low turbulence kinetic energy (almost zero) at steady state, which is unphysical. Furthermore, if the initial and inlet boundary conditions in the dispersion simulation (next step) have very small k and epsilon values the results exhibit instabilities and are highly susceptible to solvers' numerical errors (even if they are initially very small), which are "accumulated" as simulation progresses and result in taking different predictions if different number of CPUs is used.
- 3D dispersion simulation with time-dependent hydrogen release (based on the blowdown results).

Domain extension at all directions was imposed at the opening of the tunnel where there is no ventilation (see Figure 17) and constant pressure boundary condition was applied at open boundaries. The hydrogen release is discretized using 4 cells and low expansion ratios smaller than 1.12 were applied close to the release point. ADREA-HF uses the porosity method for the definition of the active (fluid) domain. To reduce the active cells and consequently the run time of the simulation, fully blocked cells were used around the tunnel in y- and z- direction. The number of the active cells for the TRAIN1 case is 430,718.
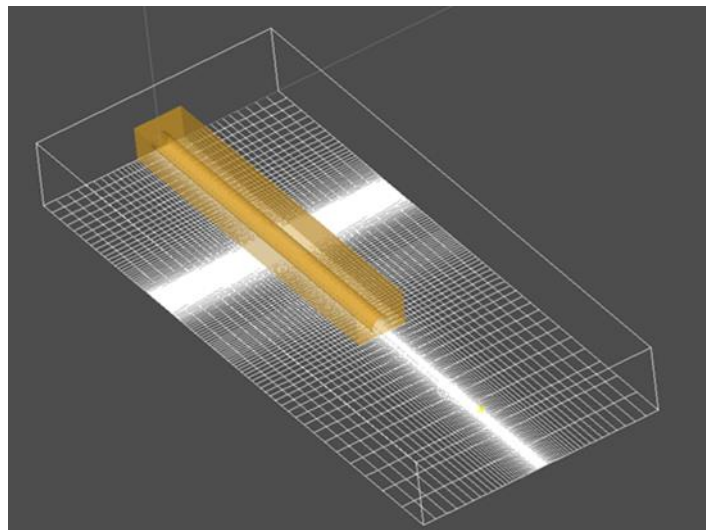
Figure 17: The problem geometry for TRAIN1 case. The fully blocked cells around the tunnel are hidden for better visualization.

For the validation simulations of TRAIN2 three grids were examined to obtain grid independent results. The grids were designed in such a manner to be used for the deflagration

validation simulations too presented in the following Section 5.2.1.4. Similar to TRAIN1, 4 cells were used to discretize the source in all grids. Downwind the source the cell size increases with expansion ratios which vary depending on the grid. Along x-direction the maximum cell size inside the tunnel is located at the entrance. Table 5 summarizes some key features of the grids. The cell size at two characteristic positions upwind and downwind the source, at x=30 and x=40 m respectively, are also presented in the Table. The maximum cell size in the y-direction is located at the tunnel wall which is further from the source, whereas the maximum cell size in z-direction inside the tunnel is at the bottom.

The main difference between Grid 1 and 2 was the larger number of cells that were used in Grid 2 downwind the x=40 m. Grid 2 is also more refined along y- and z-direction. In Grid 3, the number of cells was increased compared to Grid 2 in all directions. A significant refinement was also imposed upwind the release in the area between x=30 and x=35 m.

Table 5: Grid characteristics.

	Cells	Dx min	Dx at x=30 m	Dx at x=40 m	Dx max inside tunnel	Dy min	Dy max inside tunnel	Dz min	Dz max inside tunnel
Grid 1	398,288	0.0477	0.414	0.189	2.641	0.0477	0.201	0.04	0.118
Grid 2	1,025,854	0.0477	0.414	0.189	0.806	0.0477	0.077	0.04	0.079
Grid 3	1,783,137	0.0477	0.190	0.143	0.791	0.0477	0.051	0.04	0.05

For time integration the 1st order implicit scheme is used, while for the convective terms the MUSCL numerical scheme is used. The central differences are used to discretize the diffusive terms. A very small initial time step (=10^{-10} s) is applied, but soon it is increased with maximum CFL restriction equal to 10.

5.2.1.4 Computational results

5.2.1.4.1 TRAIN1 blind-predictions

Figure 18 - Figure 20 show blind-predictions for TRAIN1 case at all available experimental sensors. The results are in satisfactory agreement with the experiment with a tendency to underpredict the concentration. This behavior is attributed to the lower introduced mass flow rate in the simulations (see Section Release modelling). The highest underprediction is found on sensor 3 (almost half peak concentration is predicted), which is a bottom sensor close the release along x-axis. The reason for such high discrepancy only at this sensor needs further investigation. Small differences are also observed in terms of the arrival time of the peak concentration at the offset sensors (Figure 20), which reveal faster cloud spreading along y-direction.
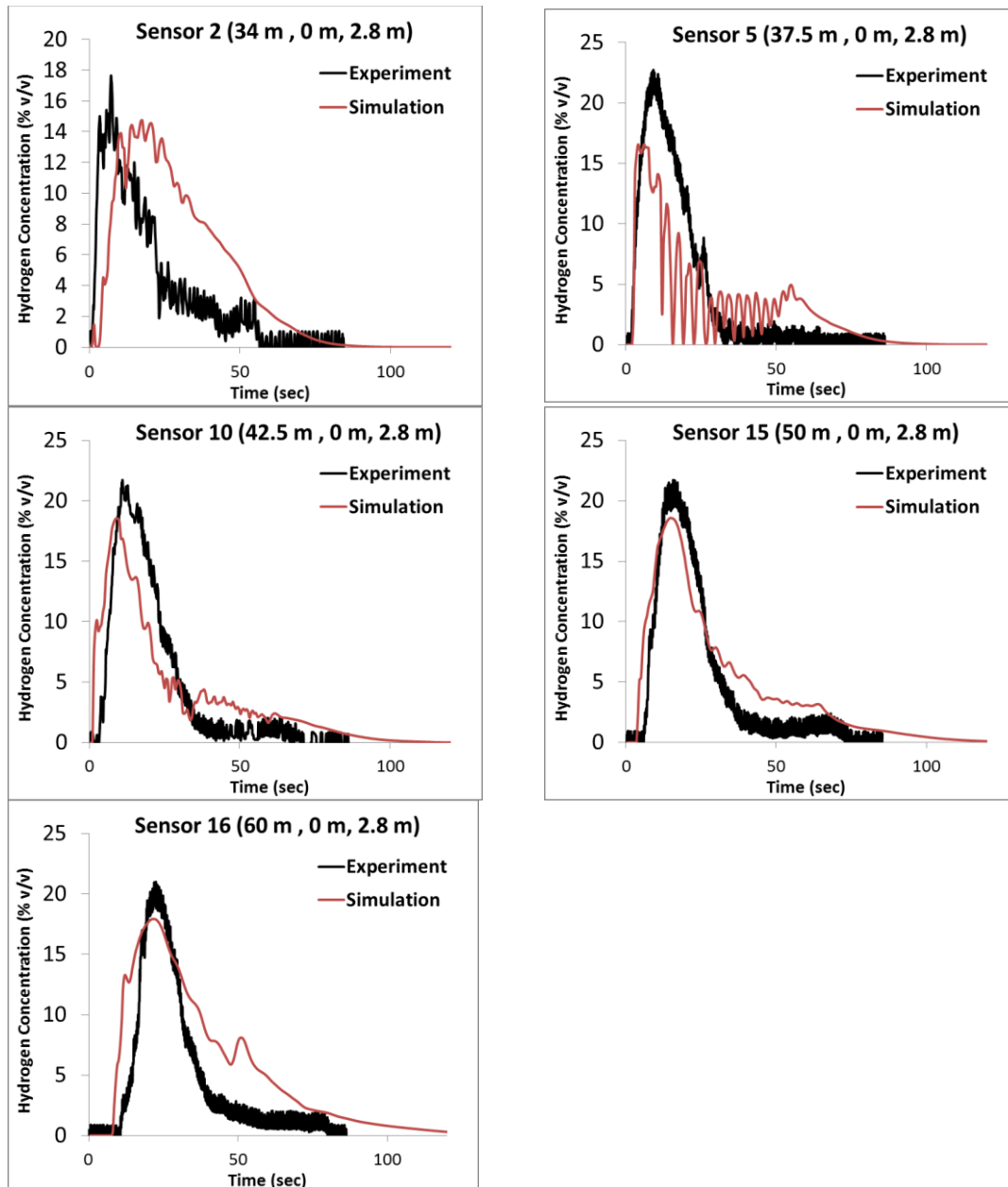
Figure 18: Concentration time series at the top sensors. The source is located at (35 m, 0.61 m, 1.54 m).
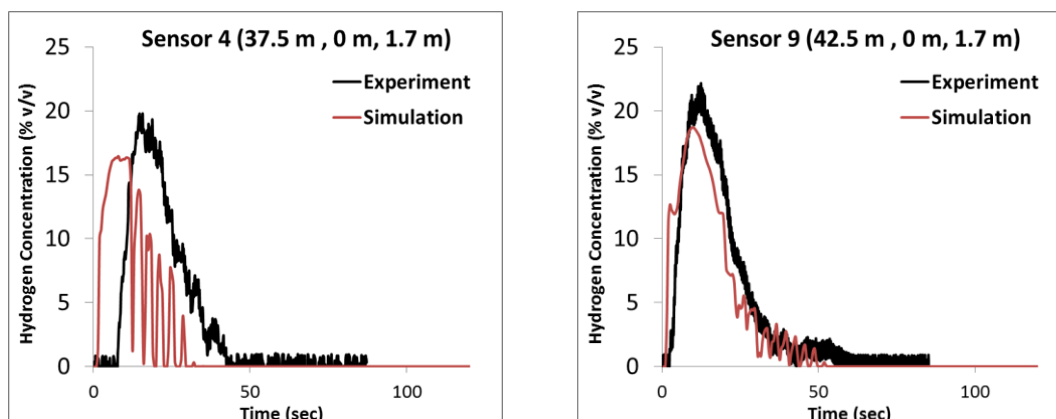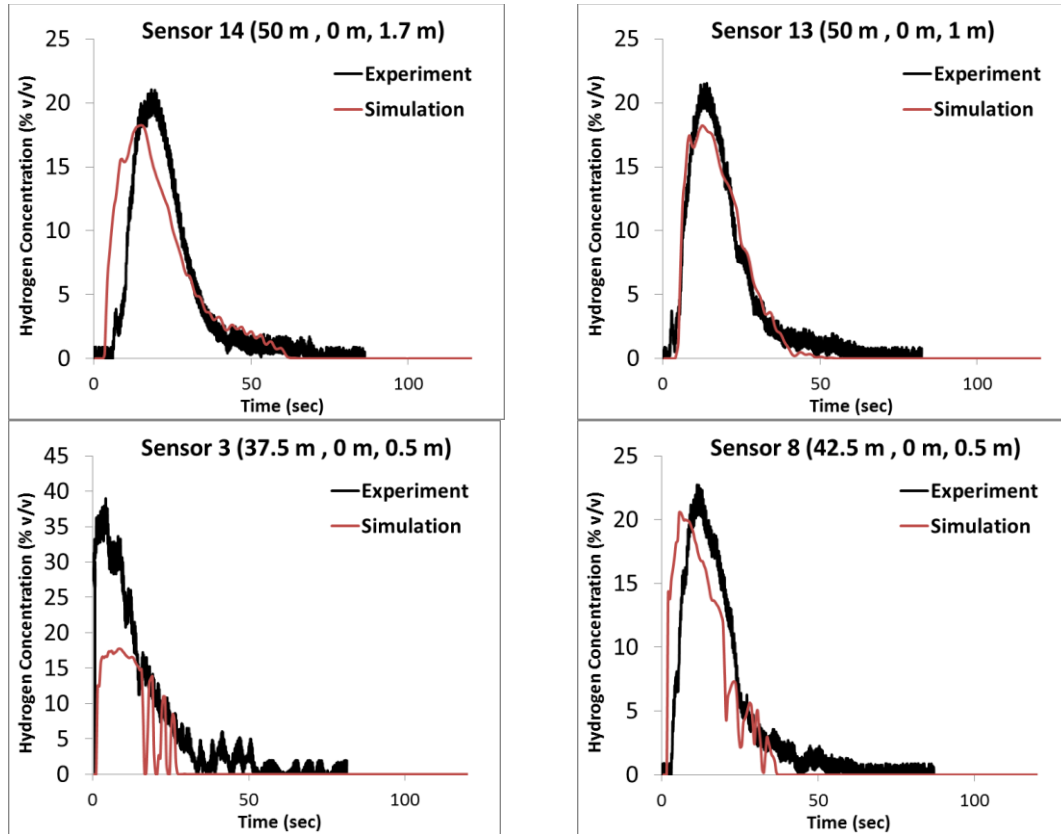
Figure 19: Concentration time series at the medium and bottom sensors. The source is located at (35 m, 0.61 m, 1.54 m).
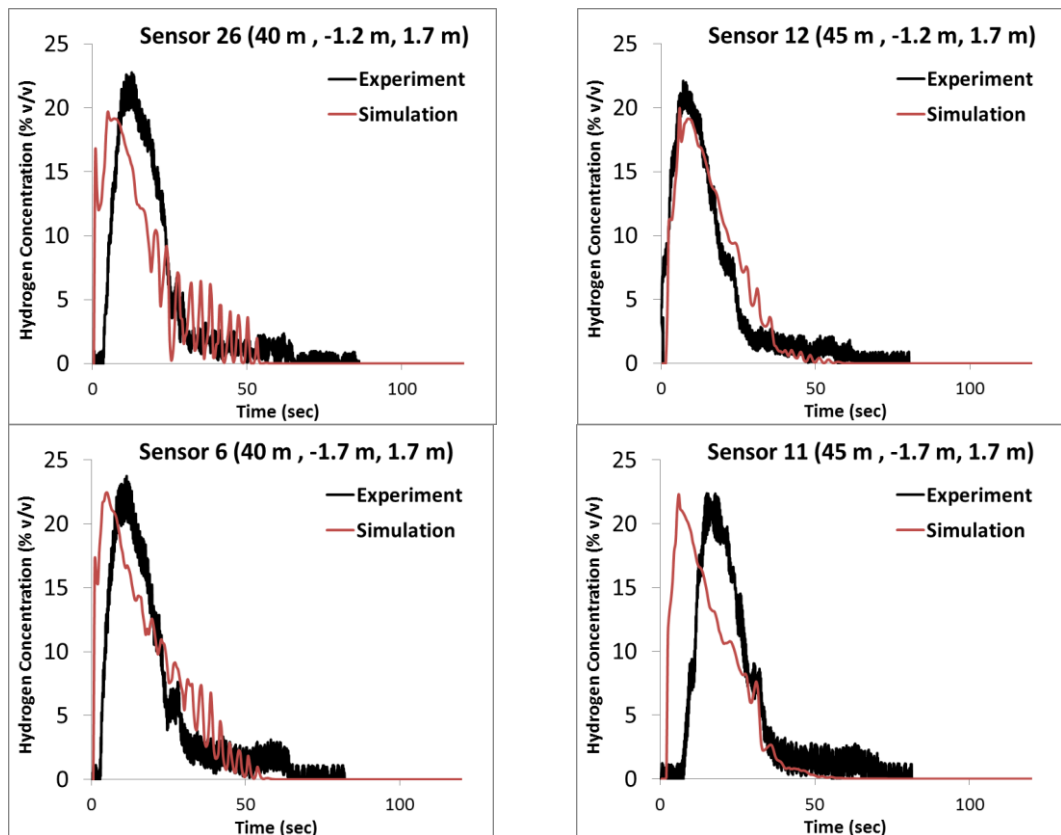
Figure 20: Concentration time series at the offset from the source sensors. The source is located at (35 m, 0.61 m, 1.54 m).

5.2.1.4.2 Train2 validation simulations

Figure 21 - Figure 23 show the predicted concentration time series versus the experiment at the available sensors for the three grids. Among the two finer grids small differences were observed in terms of peak concentration and mainly at the sensors closer to the release, as shown in Figure 21 - Figure 23. Larger differences were observed among Grid 1 and finer grids, but still the differences are limited to the sensors closer to the release (sensor 2, 3 and 4). At the remaining sensors the results are quite similar. The medium grid (Grid 2) can be considered as the independent grid and the discussion that follows concerns Grid 2 results.

Good agreement with the experiment is found at most of the sensors with a slight tendency to overpredict the peak concentrations. Similar to TRAIN1 case, serious underprediction occurs at sensor 3, the bottom sensor close to the release. Interestingly, it is observed that the measured concentration at this sensor is even higher that the concentrations at the top sensors. Further investigation is deemed necessary.

Small differences are also observed in terms of the arrival time of the peak concentration at the offset sensors (Figure 23), which reveal faster cloud spreading along y-direction.
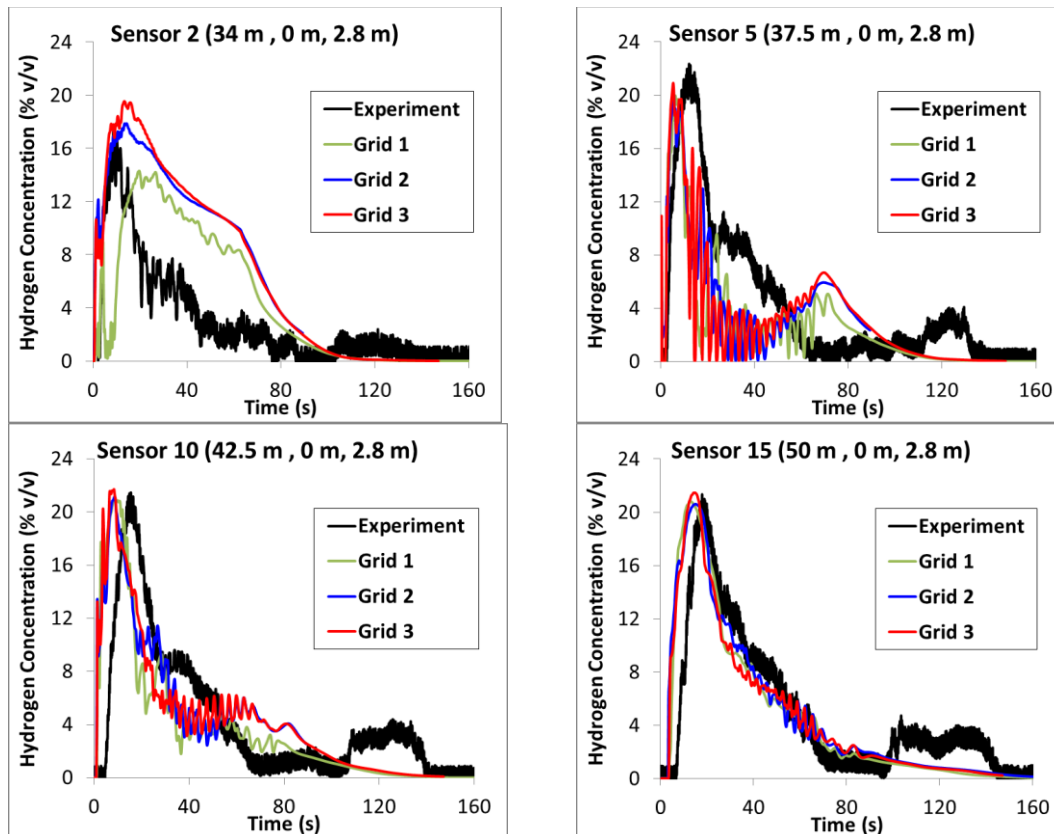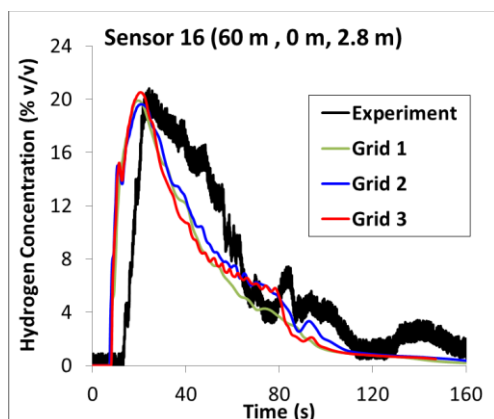
Figure 21: Concentration time series at the top sensors. The source is located at (35 m, 0.61 m, 1.54 m).
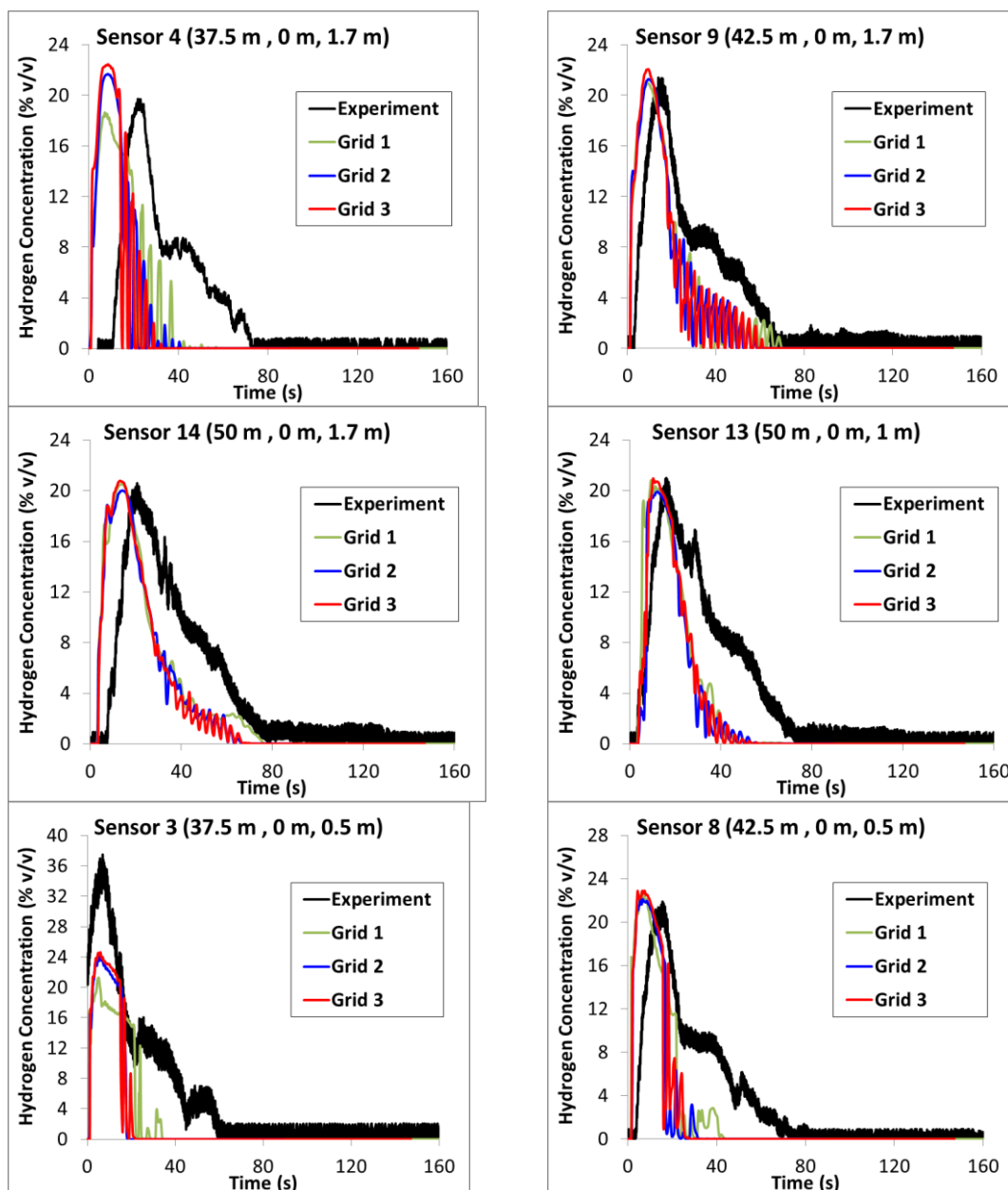
Figure 22: Concentration time series at the medium and bottom sensors. The source is located at (35 m, 0.61 m, 1.54 m).
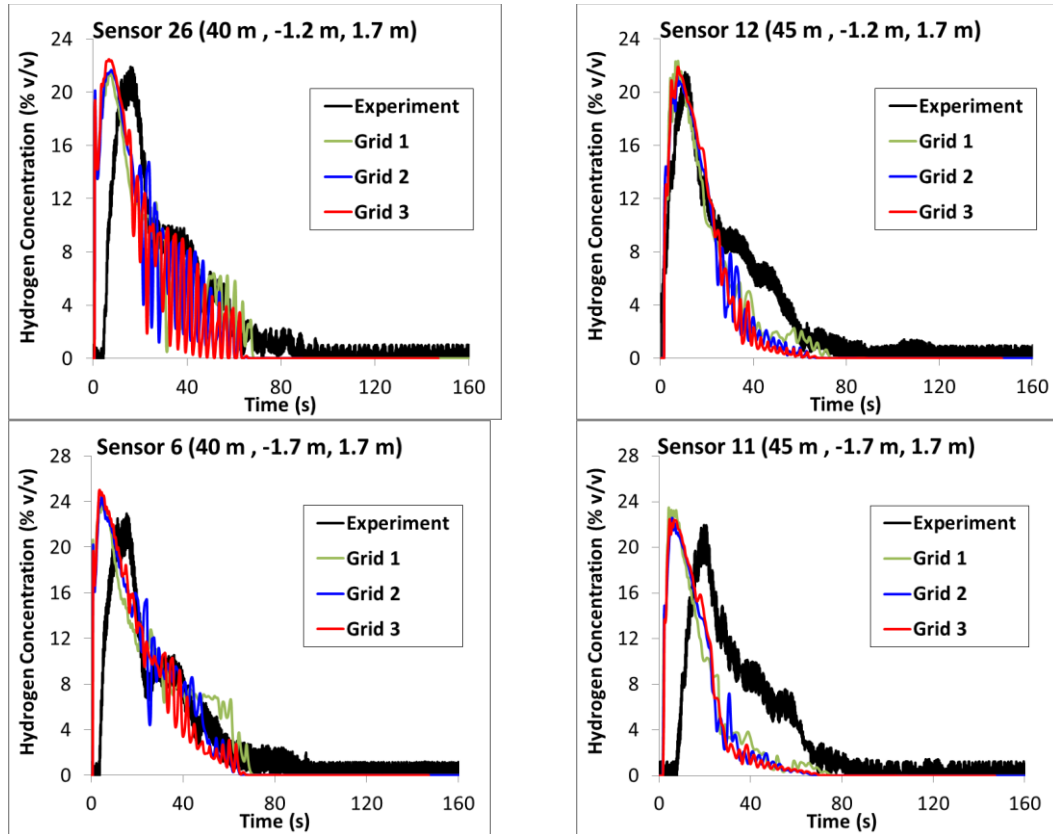
Figure 23: Concentration time series at the offset from the source sensors. The source is located at (35 m, 0.61 m, 1.54 m).

5.2.1.5   Conclusions

Comparison of a blind prediction and a validation simulation with two different HSE experiments involving hydrogen release from a train inside a ventilated tunnel are shown. In the blind prediction hydrogen was released through a TPRD size equal to 5.7 mm from a 510 barg tank, while in the test used for the validation hydrogen was released through a 4.7 mm diameter from a 580 barg tank.

In the blind predictions the flow rate was calculated using the DISCHA tool which performs isentropic expansion from tank conditions to the nozzle conditions using the NIST EoS. The tool under-predicted the mass flow rate (by about 26 %) at the initial stage of the release. After approximately 6 sec the agreement was fairly good. As far as the concentration is concerned overall satisfactory agreement has been found with a tendency to underpredict the concentrations, most likely due to the lower mass flow rate imposed.

In the validation simulations the experimental mass flow rate was used in the simulation too. Overall fairly good agreement has been found between simulation and experiment. Serious underprediction was found at one bottom sensor located close to the release. However, at this sensor the experimentally observed concentrations are even higher than the concentrations at the top sensors. Thus, further investigation is deemed necessary to explore the reasons for this behavior and explain the discrepancies among predictions and measurements.

Based on the successful validation of the CFD code it can be concluded that CFD codes are a reliable safety tool to simulate hydrogen dispersion inside tunnels.

5.3 Experiments (Task 2.4, HSE)

5.3.1 Dynamics of H_2 release and dispersion in a tunnel (ST2.4.3, HSE)

5.3.1.1 Background

This section outlines a series of experiments undertaken at the HSE Science and Research Centre investigating the release and dispersion properties of pressurised gaseous hydrogen in a tunnel. The experiments form part of Work Package 2 of the HyTunnel-CS project, which is focused on unignited hydrogen dispersion in confined spaces. This section can be taken as a stand-alone experimental report.

5.3.1.2 Experimental objectives

The main objective of this series of experiments was to generate hydrogen dispersion data for realistic (scaled) hydrogen releases in a tunnel. The releases for this section would simulate a thermally activated pressure relief device (TPRD) in operation on hydrogen vehicles. This required source term definition as well as hydrogen concentration measurements throughout the tunnel. Two levels of ventilation were used to explore the dispersion with various flow conditions. The data generated will be used to validate numerical models, which will then be used to predict the total flammable extent for realistic accident and release scenarios.

To meet this objective, a series of 19 experiments were carried out whereby hydrogen was pressurised through a series of booster pumps to the scaled pressure, then released through the corresponding nozzle. This scaling was based on equivalent initial mass flow rates for the defined scenarios and is described further in section 5.3.1.4. Four scaled scenarios were investigated: Car, Bus, Train 1, and Train 2. These were each tested with two ventilation rates. Since hydrogen is colourless, the video records do not contribute to the experimental data, so the output is limited to pipework measurements to define the hydrogen source, and concentration measurements down the tunnel to measure the dispersion.

5.3.1.3 Facility overview

The HyTunnel facility at the HSE Science and Research Centre has five main components: the large, steel tunnel; the gas delivery rig; the fan structure for providing the ventilation; the experimental delivery method; and the experimental sensors. Each of these are described in the following sections in suitable detail to interpret the raw data files, which are publicly available[1].

5.3.1.3.1 Tunnel description

The tunnel, shown in its full extent in Figure 24, has a nominal diameter of 3.7 m and comprises 5 sections totalling 70 m in length. The central section is 8 m long and has a wall thickness of 55 mm. The outer sections have a wall thickness of 25 mm and together are approximately 31 m in length each side of the central section. The sections are aligned with each other and the gaps between sections sealed to prevent any leakage of gas. This allows for the safe intentional release of hydrogen inside the tunnel and contributes to the integrity of the dispersion experiments.

---

[1] (HyTunnel CS | Zenodo) https://zenodo.org/communities/hytunnelcs/?page=1&size=20
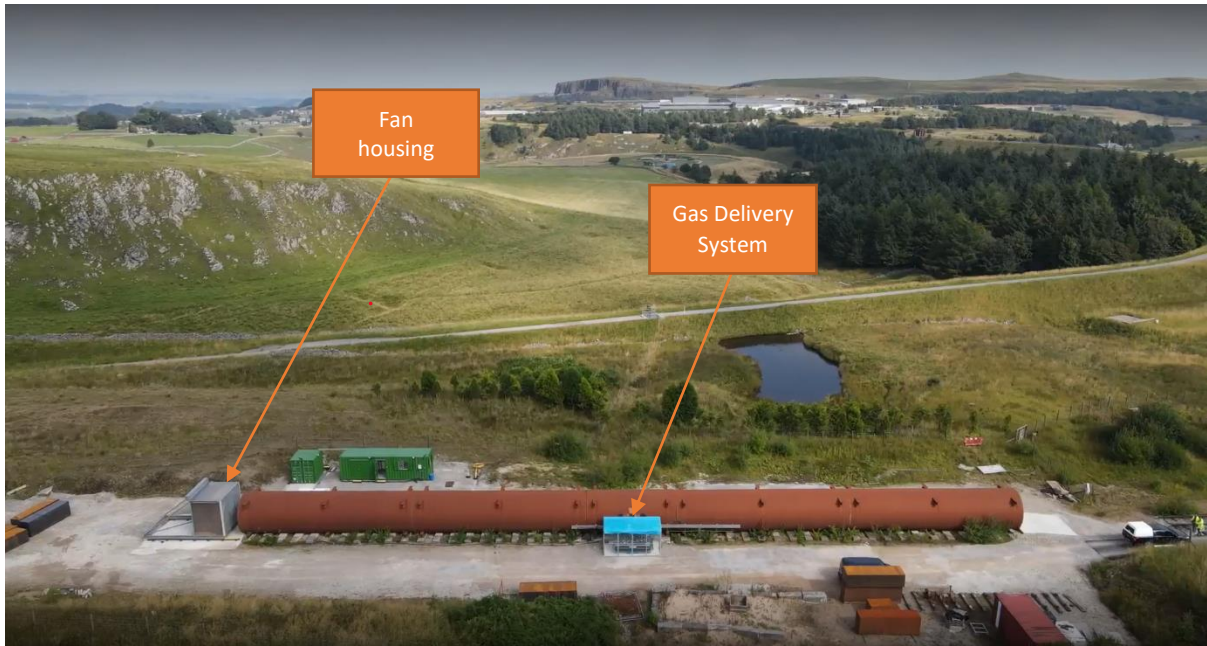
Figure 24: External view of HSE tunnel.

As shown in Figure 24, the tunnel has a large fan structure at one end (on the left of the tunnel in the image), and the gas delivery system is in the centre of the tunnel. This corresponds to the internal location that the hydrogen is released.

Inside the tunnel there is a concrete base with a 0.45 m depth, which supports a set of rails and the release structure. The rails extend along half the tunnel, downstream of the release point away from the fans, and are used to fasten the congestion models when they are used. Figure 25 shows a photograph of the inside of the tunnel. The temporary lighting seen in this image was removed prior to the series of experiments. Figure 26 shows a cross-sectional sketch of the centre of the tunnel with the internal dimensions and the release points.

Figure 25: Internal view of HSE tunnel.
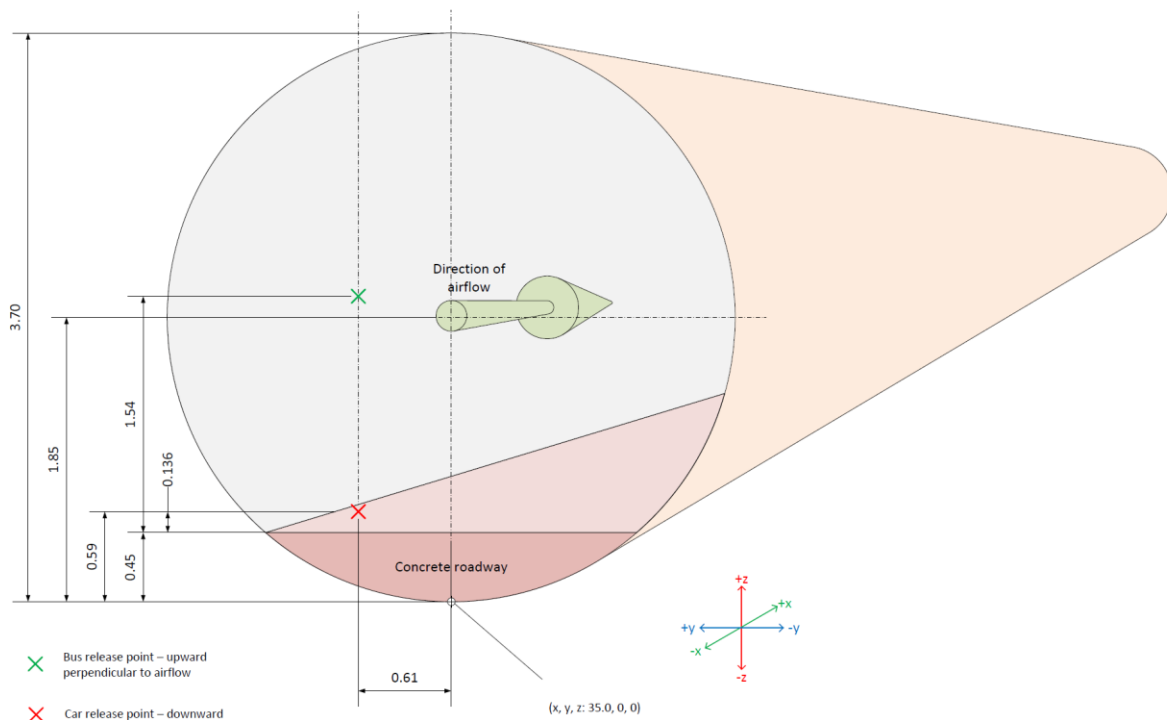
Figure 26: Cross-section sketch of the release point of the tunnel.

5.3.1.3.2   Gas delivery rig

The gas delivery rig, located externally at the centre of the tunnel and shown in Figure 27, is the system that is used to pressurise the hydrogen to the test pressure and to provide suitable volume to simulate the scaled scenarios. The functionality of the facility is to take hydrogen from standard bottle pressure (approximately 200 bar) and pressurise it to up to 700 bar. This is completed in two stages using a series of booster pumps and four type IV composite tanks. The first stage takes hydrogen from three standard manifolded cylinder packs (MCPs) and charges the hydrogen to pressures up to 350 bar using one Haskel 8AGD-30 booster pump, into a 320 l tank. The second stage takes the hydrogen from this first stage storage and charges to the final test pressure through a pair of twin Haskel AGD-75 booster pumps, shown in Figure 28, to a set of three type IV composite vessels – shown in Figure 29. The second stage can be used as either a single 53 L vessel, or all three with a volume of 159 L.

The P&ID for this facility is shown in Figure 30. In the P&ID there is a nitrogen MCP connected to the final release line, which is used to purge the final section of pipework immediately prior to a release to avoid the possibility of autoignition of the hydrogen following a high-pressure release. The instrumentation on the facility is not only used for operation, but also logged and used to define the source term of the experimental releases.

Figure 27: Gas delivery rig photograph.
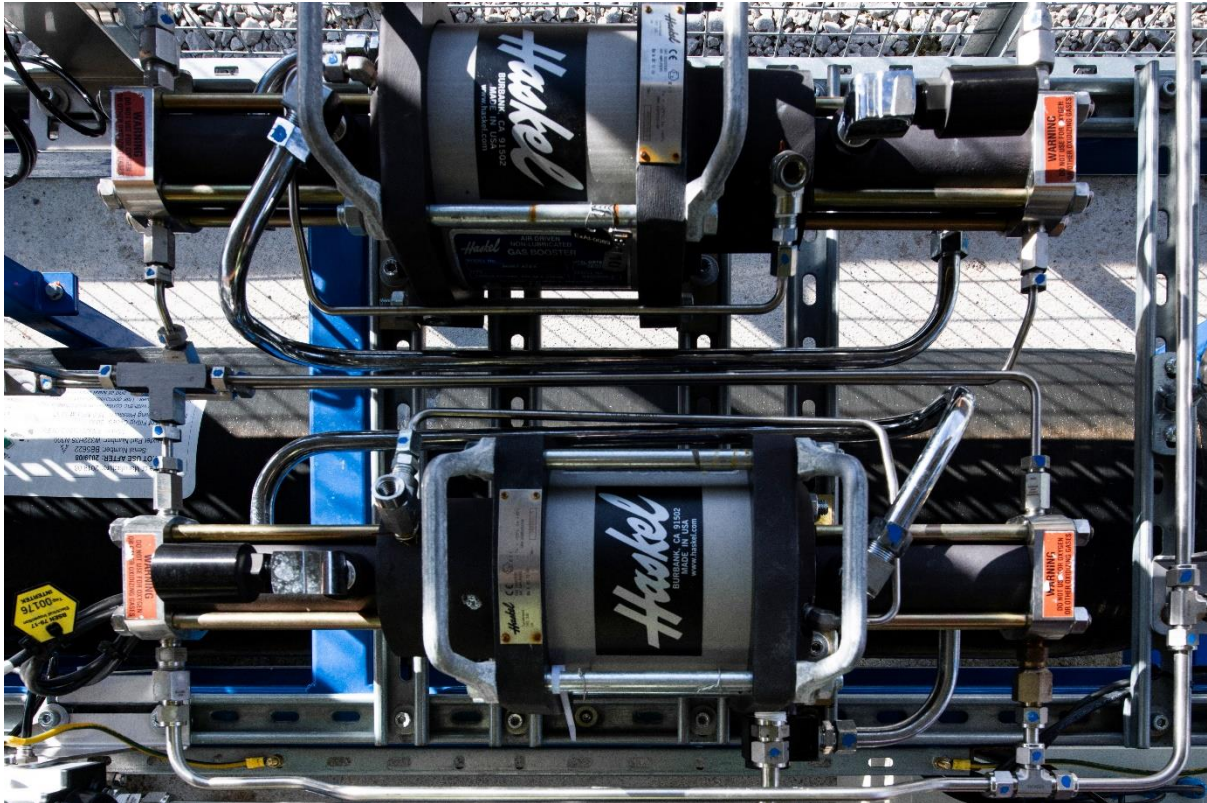
Figure 28: 2nd stage Haskel gas booster pumps photograph.

Figure 29: 2nd stage type IV composite storage vessels.
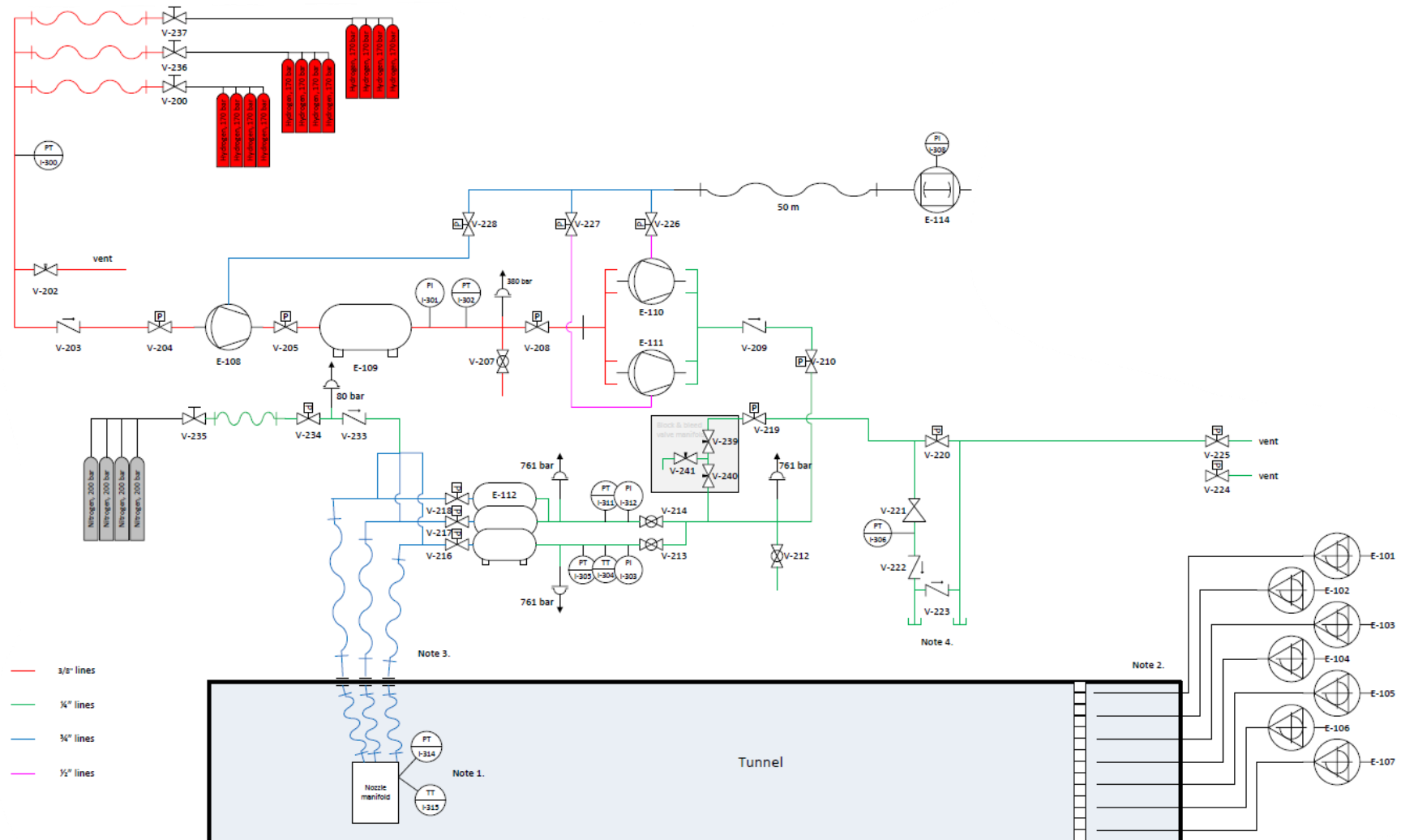
Figure 30: P&ID for gas delivery rig.

5.3.1.3.3 Ventilation fans

To mimic realistic hydrogen accident/release scenarios in tunnels, a set of seven Casals HCX71 T4 3-phase fans were installed at the end of the tunnel to provide ventilation and a semi-consistent wind speed. This set of fans was supported by a bespoke, retractable structure to allow access into the tunnel when required. The rear of the structure is shown in Figure 31. Aluminium honeycomb flow straighteners were also used to reduce the 'swirl' induced by the large axial fans. A sketch of this is shown in Figure 32. The front of the fan structure was completely covered by a 60 mm layer of this material, with a cell size of 9.5 mm.

Figure 31: Photograph of fan structure.
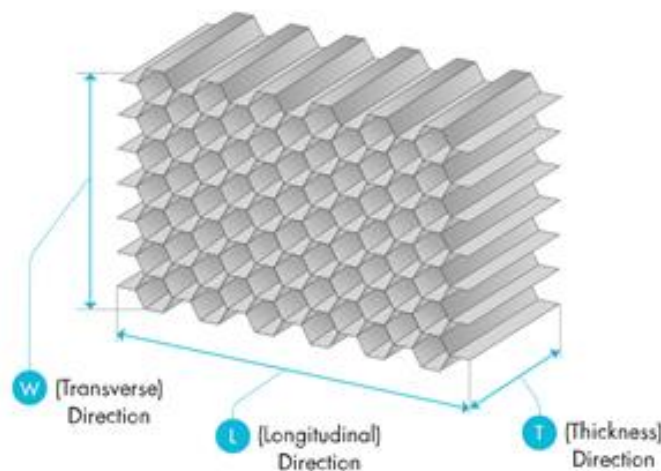
Figure 32: Sketch of honeycomb flow straightener.

With the fans drawn up to the tunnel face, the fans can achieve wind speeds between 0 m/s to approximately 5 m/s. While more stable than ambient conditions, the wind does have an impact on the measured wind speed inside the tunnel. In particular, strong counter and co-flows influence the flow regime inside the tunnel. The natural variation in the wind also influences the measured wind speed in the tunnel, resulting in the measured wind speed fluctuating within a range of the desired value. This range reduces as the fans speed increases, as the variation in ambient conditions is proportionally less dominant.

5.3.1.3.4 Release structure

The objective of this set of experiments is to investigate TPRD-style releases of hydrogen. As such, the delivery mechanism of the hydrogen into the tunnel takes to form of a configurable nozzle system through which blowdowns can occur. A set of flexible hoses connects the gas delivery rig to the tunnel and the release point inside. These hoses allow for the change in height and orientation of the release point. The steel support structure consists of a vertical steel beam with a moveable horizontal steel beam connected, holding the nozzle. The horizontal beam can be set at heights between 0 m to 1.4 m and can support the release point for upwards, downwards, or horizontal releases. The structure is securely mounted onto the concrete layer in the tunnel via a 150 mm high steel plate. This steel plate extends beyond the release point, which means that the height of the release is based upon the distance to this steel plate rather than the concrete surface. Figure 33 shows a photograph of this structure.

Figure 33: Nozzle support structure during commissioning.

The nozzle itself consists of a main body and a replaceable nozzle. The main body is stainless steel and contains internal manifolds for three flexible hoses and two instrumentation ports. The replaceable nozzle allows for various nozzle diameters to be used whose sizes were determined by the scaling methodology to fit four scenarios: Car, Bus, Train 1, and Train 2. This was a nominal 2.2 mm, 4.0 mm, 5.7 mm, and 4.7 mm respectively. Details on the scaling methodology are given in section 5.3.1.4. Table 6 shows the measured diameters of each nominal sized nozzle used for the duration of the experiments. Each of these nozzles has internal tapering to minimise the pressure losses in the nozzle, which is shown in Figure 34.

Table 6: Measured nozzle diameters.

Nominal Nozzle Diameter (mm)	Measured Nozzle Diameter (mm)
2.2	2.2487
4.0	4.0731
4.7	4.7662
5.7	5.7318
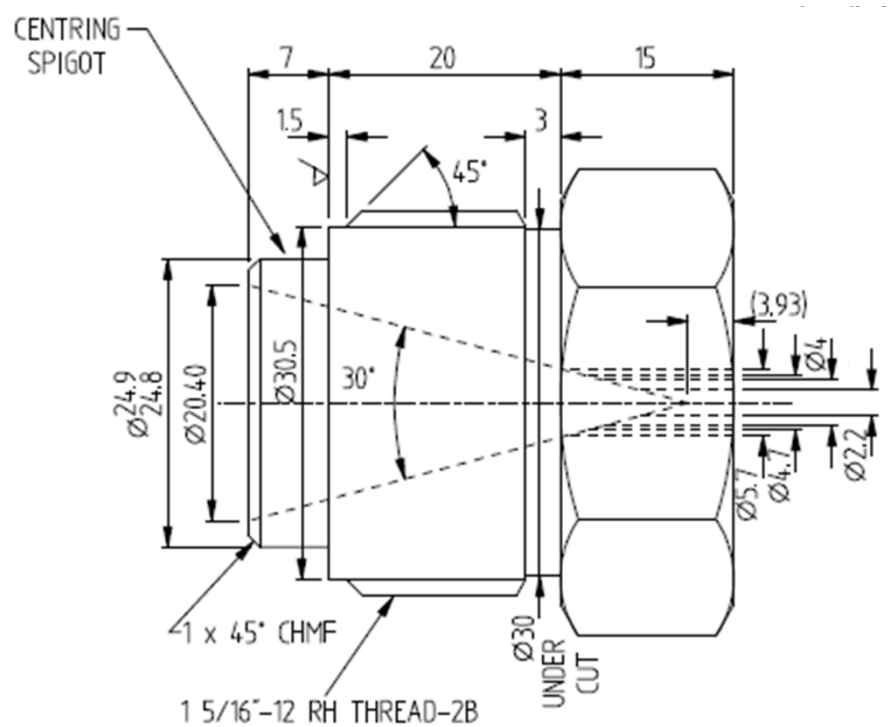
Figure 34: Schematic of replaceable nozzles.

5.3.1.3.5 Congestion

A set of steel structures was installed on a subset of the tests to simulate the effect of vehicles on the dispersion of hydrogen. The layout used, shown in Figure 193, is a total of 8 steel boxes, arranged in two lines of four. A steel wedge designed to limit the effects of blastwaves on the face of the nearest model was also installed for each line.

5.3.1.3.6 Instrumentation and Control

To generate valuable data from these experiments, both source term and dispersion measurements are required. As well as the sensors measuring the experimental parameters, i.e. pressure transducers, thermocouples and gas concentration monitors; various instruments were used in the operation of the facility. Some of these, such as the second stage pressure and temperature measurements, are used for both source term definition and facility control.

Throughout the gas delivery rig and at the release nozzle manifold, five Druck Unik 5800 pressure transducers were used. The pressure transducers were supplemented with four analogue pressure gauges to assist with the facility operation. Temperature measurements were made at two locations on the facility: on the inlet to the second stage vessels, and on the nozzle manifold. This was done with type K thermocouples placed within the gas flow. Table 7 displays the pressure transducer and thermocouple locations and details the meaning of the readings.

Table 7: Pressure transducer locations.

Sensor ID	Output title	Description
PT I-300	Cylinder Pressure I-300 [bar]	Pressure at the hydrogen MCPs.
PT I-302	LP Tank Pressure I-302 [bar]	Pressure in the 1st stage storage vessel.
PT I-305	HP Tank Pressure I-305 [bar]	Pressure in the 2nd stage, single tank.
PT I-309	Nozzle Pressure I-309 [bar]	Pressure in the nozzle manifold.
PT I-311	HP Tank Pressure I-311 [bar]	Pressure in the 2nd stage, double tank.
TT I-304	HP Tank Temperature I-304 [°C]	Temperature in the 2nd stage, single tank.
TT I-315	Nozzle Temperature I-315 [°C]	Temperature in the nozzle manifold

Mass flow rate was not measured directly, so requires calculation based on the other measured parameters. The reason for this was to avoid restrictions in the final section of pipework to achieve the required mass flow rates.

The wind speed was measured using a ThermoAir 64 hot wire anemometer placed 5 m from the entrance to the tunnel on the radial mid-line (x, y, z = 5, 0, 1.85). This was not logged throughout the test, however, due to the potential for unintended ignitions. To obtain the wind speed for the test, the wind speed was set, and the range of outputs noted prior to each test. This sensor is shown in Figure 35.

Figure 35: Photograph of the hot wire anemometer and stand.

The hydrogen concentration measurements were logged with a separate system. A set of 16 Xensor XEN-5320 USBs were used to measure the hydrogen concentration across the tunnel, each with an independent sampling line and pump. The sampling lines were polyurethane but were protected in the tunnel by steel pipe and had copper tips. The tips were each oriented to face the source of the hydrogen. The location of each sampling point is shown in Figure 36 and Table 8 contains the Cartesian coordinates of the sampling point correlating to the individual sensor. They were connected to a control and data acquisition PC via USB hubs and continuously logged at approximately 8 Hz in a LabVIEW program. Each sensor generates a separate txt file, which can be merged into one large data file. Figure 37 shows a photograph of the sensor housing cabinets and peripheral electronics. The sampling lines (the red tubes in Figure 37) were each 25 m to keep relative consistency in the draw-time for the samples. The sensors themselves have a t_{90} response time of less than 1 s, and the sampling delay is shown for each sensor in Table 8. The variation stems from individual pump performances.
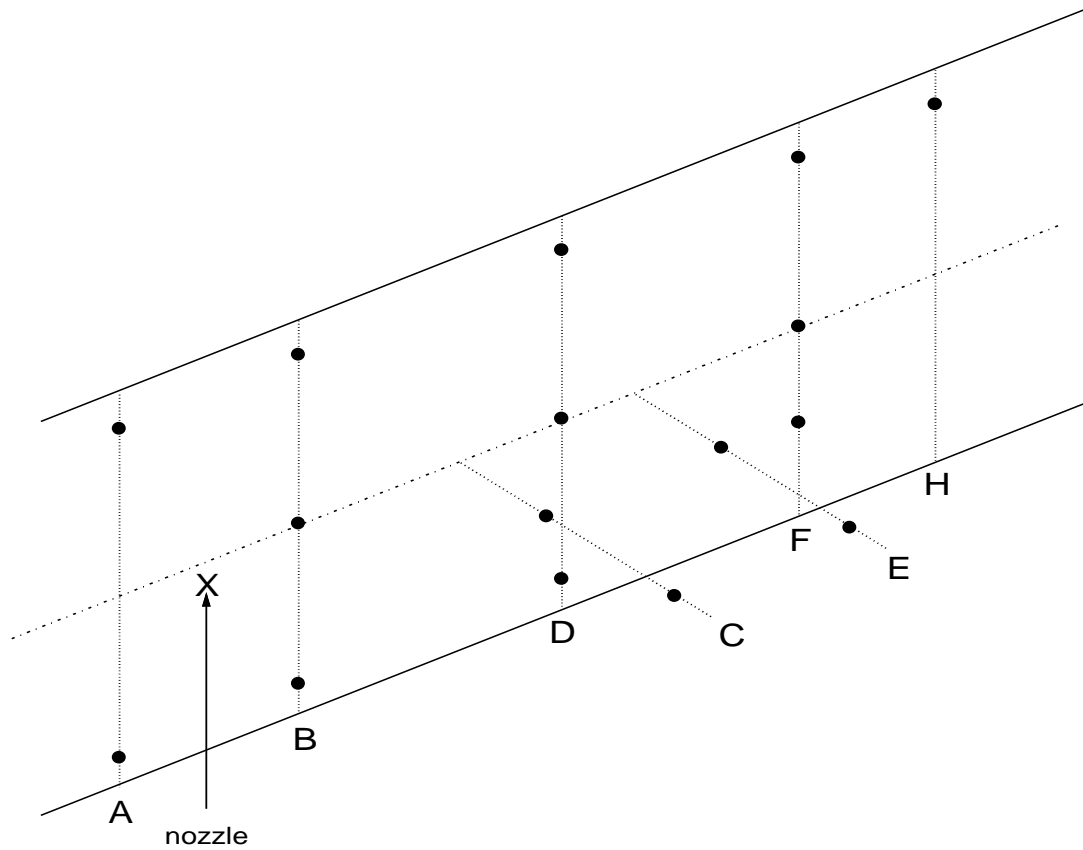
Figure 36: Sketch of the hydrogen sampling point array locations.

Table 8: Hydrogen gas sensor locations, serial numbers, and delay times.

ID	Position	x (m)	y (m)	z (m)	Delay (s)
02E002	A high	34.0	0.0	2.8	7.3
02E003	B low	37.5	0.0	0.5	11.7
02E004	B mid	37.5	0.0	1.7	5.7
02E005	B high	37.5	0.0	2.8	6.5
02E006	C far	40.0	-1.7*	1.7	10.1
02E026	C near	40.0	-1.2*	1.7	6.6
02E008	D low	42.5	0.0	0.5	5.8
02E009	D mid	42.5	0.0	1.7	7.0
02E010	D high	42.5	0.0	2.8	6.8
02E011	E far	45.0	-1.7*	1.7	11.7
02E012	E near	45.0	-1.2*	1.7	12.7
02E013	F low	50.0	0.0	1.0	10.0
02E014	F mid	50.0	0.0	1.7	6.2
02E015	F high	50.0	0.0	2.8	7.1
02E016	H high	60.0	0.0	2.8	6.7

Note: (0, 0, 0) is at the fan end of the tunnel, at the base, along the centreline. The car scenario release point is (35, 0.6, 0.6), for the other scenarios it is (35, 0.6, 2).

*For test B13 to B20 (*Table 17* gives full description of test matrix), -1.7 m becomes 1.7 m and -1.2 m becomes 1.4 m. This is due to the steel congestion structures blocking *the sensor support structures.*

Figure 37: Photograph of the hydrogen concentration sensors and electrical peripherals.

The pressure and temperature sensors were logged through the main control system, which is a bespoke LabVIEW program developed by Scitek Consultants Ltd. The logging rate was 72 Hz. The wind speed was controlled through a parallel system. The frequency of the fan speed was set between 0 Hz and 50 Hz, and then measured with the anemometer. Once a semi-stable state was reached, the range of the measured wind speed was noted.

5.3.1.4   Scaling methodology

Since the HSE tunnel has fixed dimensions but the range of scenarios under investigation is broad, scaling is required. This scaling is completed under the principle that the hydrogen dispersion in the HSE tunnel should be proportionally similar to the dispersion of a realistic vehicle in a representative tunnel. For instance, experiments relating to road vehicles should have equivalent hydrogen concentration distances (normalised based on the relative diameter of the tunnels) to a full-size accident or release. The upcoming sections describe the dimensions of the HSE tunnel, a summary of the scenarios, the methodology of the scaling, and the scaled parameters for each scenario.

5.3.1.4.1   HSE Tunnel dimensions

Relevant information on the geometry of the HSE Buxton test tunnel is given in Table 9 below.

Table 9: Geometry of the HSE Buxton test tunnel.

Radius	1.85 m
Depth of concrete base	0.45 m
Area of segment containing concrete base	0.75 m^2
Circular area of tunnel (full diameter)	10.75 m^2
Area through which vehicles travel	10.00 m^2
Equivalent diameter, D_{HSE}	3.57 m

5.3.1.4.2   Basis of scaling methodology

The objective of the scaled experiment is to match the concentration of hydrogen in the downstream flow and the proportion of the tunnel over which the flow is distributed. Scaling of the release scenarios therefore follows the scaling principles outlined in *Scaling rules for reduced-scale field releases of hydrogen fluoride* (Hall and Walker, 1997). Thus, the scaled volume released is the cube of the ratio of the length scales, where the length scale is the representative tunnel diameter. In respect of the time scales for a release, the scaling parameter is dimensionless time (UT/L, where U is flow, T is time and L is length) which must have the same values at full and model scales. Thus, it also scales as the square root of the length scale ratio. Thus, given the scaled volume (mass) release and the same tank initial pressure the diameter of the nozzle for the scaled release can be calculated to match the scaled volume (mass) flowrate versus the scaled time tank blowdown curve for the full-scale release.

The appropriate scaling relationships between the tunnel airflow *U*, the hydrogen volume or mass flow rate $\dot{V}$ and the tunnel scaling factor *H* (ratio of full-scale tunnel diameter D to HSE tunnel diameter D_{HSE}) for a *steady* release experiment in a model tunnel is: $U \propto H^{\frac{1}{2}}$ and $\dot{V} \propto H^{\frac{5}{2}}$. If U and V are chosen in this way, then the concentration in the flow developing around the source will be the same and the relationship between the buoyancy head associated with the release and the dynamic head of the flow will be the same. This means there will be a similar tendency for the gas to be blown down stream or flow backwards at high level. If the timescale of the blow down process is reasonably long compared with the characteristic time scale for the tunnel flow past the source U/H then this quasi-steady scaling will give reasonable results.

In summary for a blowdown release at any rate:

- Scaling factor (H) for tunnel diameter is D/D_{HSE}
- Scaling factor for mass of hydrogen stored is H^3
- Scaling factor for the mass flow rate is $H^{5/2}$.
- Scaling factor for the discharge time is $H^{1/2}$.
- Scaling factor for the airflow in the tunnel is $H^{1/2}$.

Based upon the accident scenario analysis carried out in HyTunnel-CS D1.3 (2019), we proposed a test programme for which the following assumptions are considered applicable:

1. In the case of normal TPRD operation in a fire, it is assumed that the total inventory is released through the TPRDs. All TPRDs open at roughly the same time.
2. In the case of a spurious TPRD operation it is assumed that at least one tank is involved.
3. Only one tank fails catastrophically in a fire due to single TPRD malfunction.
4. A tunnel cross-sectional area is represented by a circle of the equivalent area.

5.3.1.4.3 Scaled scenario definition

The hydrogen inventories carried by the three different types of vehicle, based on HyTunnel-CS D1.3 (2019), are as follows:

CAR: Five makes specified, all operating at 700 bar. Tank capacity varies between 115 and 156 litres, usually made up from two tanks each of similar capacity. Average capacity 135 litres, containing a mass of 5.4 kg hydrogen. Vent lines specified as between 2 mm to 4 mm diameter, although 4.2 mm diameter seems to be used in some cases. Vent line is downwards from underneath the vehicle at 135 degrees backward. The TPRD diameter is quoted as 2.0 mm, with one TPRD per tank.

BUS: Three makes specified, all operating at 350 bar. They use four and nine tanks, roof mounted, each with a capacity of 74 to 205 litres. Assume 210 litres per tank on a four-tank pack each containing 4.97 kg each of hydrogen, giving a total capacity of about 40 kg. Vent line is upwards from top of vehicle. The TPRD diameter is 3.3 mm and there are two fitted to each cylinder, giving a total of eight. Other buses may have a slightly larger capacity with either 11 or 12 TPRD's fitted. Recently Wrightbus have introduced a series of single decker buses with a hydrogen capacity of between 35-50 kg. In view of which we have used a 40 kg capacity (say five tanks) with ten TPRD's fitted as the basis for our modelling.

TRAIN: Only one make specified, manufactured by GE Alstom. They refer to a two-carriage unit each with 96 kg of hydrogen operating at 350 bar. Each unit has 24 cylinders each with a capacity of 175 litres containing 4.14 kg of hydrogen. Assume that only one carriage is involved in the fire. Each cylinder has two TPRD's, each with a diameter of 3.3 mm.

A three-carriage unit is also under consideration by GE Alstom for the UK market, known as "Breeze". This will have a mass of hydrogen of 417 kg at 350 bar pressure, contained in 72 cylinders each with a capacity of 245 litres. Each cylinder contains 5.8 kg of hydrogen and there are 36 cylinders in both the lead and trailing cars. Assume that only one car is involved

in the fire, consequently the total inventory per car will be 209 kg. The tanks are arranged in cassettes, comprising nine tanks each. There are four cassettes per car, contained in a unit behind the cab. There are two cassettes on either side of the storage bay, assumed separated by a partition. Each cylinder has two TPRDs, hence each cassette has 18 TPRDs of 3.3 mm diameter. We assume that for modelling purposes only two cassettes (one side) would be involved in a fire. The inventory involved in a fire is therefore 105 kg with 36 TPRDs able to vent the inventory.

Based on the foregoing average scaling factors for the various tunnel types can be obtained, then used to establish the scaled inventories for a car, bus, and train in the relevant tunnels for both continuous releases as shown in Table 10.

Table 10: Scaled hydrogen inventories for cars, buses, and trains.

	Total Inventory	Average Scaling Factor	Scaled Total Inventory
CAR 700 bar	5.4 kg	2.275	0.46 kg
BUS 350 bar	40.0 kg	2.275	3.40 kg
TRAIN 350 bar	96.0 kg 105.0 kg	2.665	5.07 kg 5.54 kg

Using a commercially available fixed volume off-the-shelf 53 litre tank (MWP 800 bar) or a combination of these, requires the desired inventory to be contained in them but at the relevant pressure. Consequently, the required pressures, scaled vessel inventories, capacities, orifice diameters and initial mass flow rates can be calculated using the suite of programmes given in: https://elab-prod.iket.kit.edu/. We therefore obtain the scaled values using 1 or 3 vessels shown in Table 11.

Table 11: Correlation of proposed hydrogen to actual tank inventories.

	Total Inventory (kg)	Pressure (bar)	Tank Volume (litres)
CAR	0.46	118	53
BUS	3.40	310	159
TRAIN 1	5.07	510	159
TRAIN 2	5.54	580	159

Calculation of orifice sizes for the total inventory contained on a car, bus and train, from the literature typical TPRD orifice sizes are 2.0 mm and 3.3 mm diameter, in addition a car has two tanks, buses four to twelve (assume five) tanks, and trains eighteen or twenty-four tanks. In a fire it is assumed that the total inventories are discharged with all TPRDs open at the same time. The equivalent orifice sizes are shown in Table 12.

Table 12: Equivalent orifice sizes for full-sized releases.

Orifice Dia. (mm) Single TPRD	Car: Two TPRD's Equivalent diameter	Bus: 10 TPRD's Equivalent diameter	Train: 48/36 TPRD's Equivalent diameter
2.0 mm	2.83 mm	-	-
3.3 mm	-	10.44 mm	22.86/19.80 mm

Using the above equivalent diameters, the initial mass flow rates, and discharge times (to choke point) are obtained for the actual full-size inventories using the actual storage pressures (700 or 350 bar) as shown in Table 13.

Table 13: Initial mass flow rates and discharge times for full size and for scaled inventories.

	^^Total Inventory (kg)	Initial mass flow rates (kg/s)	Discharge times (sec)	^^Scaled total inventory (kg)	Scaled initial mass flow rates (kg/s)	^Scaled discharge times (sec)	*Scaled orifice dia's used (mm)
CAR 700 bar	5.4 (135 l)	0.215	168	0.46 (12 l)	0.0275	120 (111)	1.0
BUS 350 bar	40.0 (1700 l)	1.638	134	3.40 (145 l)	0.21	86 (89)	3.8
TRAIN 1 350 bar	96.0 (4050 l)	7.85	67	5.07 (215 l)	0.677	41 (41)	6.7
TRAIN 2 350 bar	105.0 (4450 l)	5.89	97	5.55 (235 l)	0.508	60 (60)	5.8

These are the orifice diameters needed to give the correct scaled initial mass flow rates.
^The values in brackets are those obtained from scaling the values shown in column three.
^^Numbers in brackets are the volumes in litres required for the inventory at the pressures shown at the start of each row.

NB: The approach is equally valid for other orifice sizes than those used here.

If using standard 53 litre size cylinders, then we can model the foregoing using different pressures but fixed volumes (multiples of 53 litres) to give the same initial mass flow rates as shown in Table 14, giving nozzle diameters appropriate to the different pressures.

As an example, the jet from a car cylinder at 700 bar pressure with an orifice diameter of 1.0 mm is the equivalent of releasing at 118 bar through a 2.2 mm diameter nozzle, given the same initial mass flow rates. This is because the fully expanded jets in both cases have an initial fully expanded diameter of 16.8 mm at atmospheric pressure and thereafter, they both behave in the same manner, namely as a free turbulent jet, for which the decay characteristics are well documented in the literature.

Table 14: Scaled orifice size for experimental releases.

	Scaled total inventory (kg)	Scaled initial mass flow rates (kg/s)	Discharge times (s)	Scaled orifice diameters used (mm)
CAR 118 bar	0.46 (53)	0.0275	70	2.2
BUS 310 bar	3.40 (159)	0.21	83	4.0
TRAIN 1 510 bar	5.07 (159)	0.677	46	5.7
TRAIN 2 580 bar	5.55 (159)	0.508	69	4.7

5.3.1.5   Data file interpretation

The data for these tests was collected through two systems: the control and primary data acquisitions system, and the gas concentration system. The primary system generates a .csv file containing data from the facility sensors. Table 15 contains the units and a description of each of the columns. The gas concentration system generates a .txt file for each gas sensor, with the timestamp and the "Output (%)" being the relevant outputs for this measurement.

Table 15: Description of output from primary DAQ system.

Output title	Description
Timestamp [s]	Time in seconds from the last system restart.
Adjusted time (s)	Time in seconds from the opening of the primary release valves.
<title> Pressure I-3## [bar]	The pressure in bar for a sensor on the facility.
<title> Temp I-3## [°C]	The temperature in degrees Celsius for a sensor on the facility.
PILZ Relay Health	Boolean value showing the health of the electrical system.
Shop Air Pressure	Boolean value showing the presence of pressure for the pneumatic valves.
Key Enable	Boolean value showing the status of the enable switch.
Ignition Power	Boolean value showing electrical power to the ignition system.
V-2## LSO	Valve open signal.
V-2## LSC	Valve close signal.
V-2## Output	Valve feedback signal.
Raw *<title>* [V]	The output of a sensor measured as a voltage.
Blowdown Flowrate [m³/s]	NOT IN USE - software calculated mass flow rate.
Calculated Density (kg/m3)	Calculated density of hydrogen.
Calculated Mass (kg)	Calculated mass of hydrogen.
ln mass	Natural logarithm of the calculated mass.
Mass estimate (kg)	Exponential estimate of mass.
Mass flow (kg/s)	Derivative of estimated mass.

These two systems were independent and parallel. As well as this, the delay induced on the gas concentration outputs caused by the sample lines and individual pump performance creates a

difference in relative t_0 times for each sensor. Table 16 is a list of the sensors pump draw delay times.

Table 16: Hydrogen sensor delay times.

H2 sensor ID	Pump delay time (s)
02E002	7.3
02E003	11.7
02E004	5.7
02E005	6.5
02E006	10.1
02E026	6.6
02E008	5.8
02E009	7
02E010	6.8
02E011	11.7
02E012	12.7
02E013	10
02E014	6.2
02E015	7.1
02E016	6.7

5.3.1.6 Results

The results of interest for these unignited blowdown releases primarily relate to the source term of the hydrogen release, as well as the dispersion pattern down the tunnel. The measured pressure decay on the vessel, calculated mass decay, and estimated mass flow rates provide insight as to the source term for each scenario. These are consistent across tests of similar initial conditions. The dispersion varies based on additional factors, such as the ventilation rate and ambient conditions.

5.3.1.6.1 Test matrix

Table 17 shows the initial conditions for each test completed. Two wind speeds were used for each of the four scenarios, and multiple repeats were conducted. After test 12, an intentional ignition in the system resulted in catastrophic damage to the fan system, so natural ventilation was relied upon.

Table 17: Unignited blowdown initial conditions.

Test No.	Blowdown No.	Nozzle diameter (mm)	Orientation	Height (mm)	Inventory (l)	Nominal pressure (bar)	Congestion	Wind speed (m/s)
1	B1	2.2	Downwards	137	53	128	None	0.2 to 0.7
2	B2	2.2	Downwards	137	53	128	None	0.9 to 1.3
3	B3	2.2	Downwards	137	53	128	None	2.1 to 2.6
4	B4	4	Upwards	1407	159	320	None	0.8 to 1.5
5	B5	4	Upwards	1407	159	320	None	2.2 to 2.7
6	B6	4.7	Upwards	1407	159	592	None	0.8 to 1.5
7	B7	4.7	Upwards	1407	159	592	None	2.2 to 2.9
8	B8	5.7	Upwards	1407	159	521	None	1.0 to 1.7
9	B9	5.7	Upwards	1407	159	521	None	2.2 to 2.8
10	B10	5.7	Upwards	1407	159	521	None	0.6 to 1.7
11	B11	2.2	Downwards	140	53	127	None	0.9 to 1.7
12	B12	2.2	Downwards	140	53	127	None	1.1 to 1.8
47	B13	4.7	Upwards	1400	159	592	Yes	Natural*
48	B14	4.7	Upwards	1400	159	592	Yes	Natural*
49	B15	4	Upwards	1400	159	320	Yes	Natural*
50	B16	4	Upwards	1400	159	320	Yes	Natural*
52	B17	4.7	Upwards	1400	159	592	None	-1.3 to -1.7
53	B18	4.7	Upwards	1400	159	592	None	0.3 to 0.5
54	B19	4.7	Upwards	1400	159	592	None	0.1 to 0.3

*Weather reports from these two test days indicate a wind speed of approximately -3.6 m/s.

Note: The wind speed is taken as positive if originating from the 'fan' end of the tunnel. This translates to a northely wind direction. Southerly wind is denoted as negative.

5.3.1.6.2 Blowdown pressure curves

Since the pressurisation of the hydrogen gas was completed outside the tunnel, but the release point was inside, a section of flexible hosing was used to facilitate hydrogen dispensing to the desired location. This section of pipework was unpressurised during charging. As such, the pressure measured at the nozzle began the blowdown at atmospheric pressure, rapidly raised, and then followed the decay curve from the vessel. This can be seen in the red line in Figure 38. The blue colour line shows the pressure measured inside the pressurised vessel and has two corresponding decay modes: the initial pressurisation of the flexible lines, characterised by a steeper decline; then a standard pressure decay curve. Figure 38 to Figure 41 show the pressure decay curves for the car, bus, train 2 and train 1 scenarios respectively. The variation in pressure decay curves for each scenario was minimal so only one graph per scenario is shown.
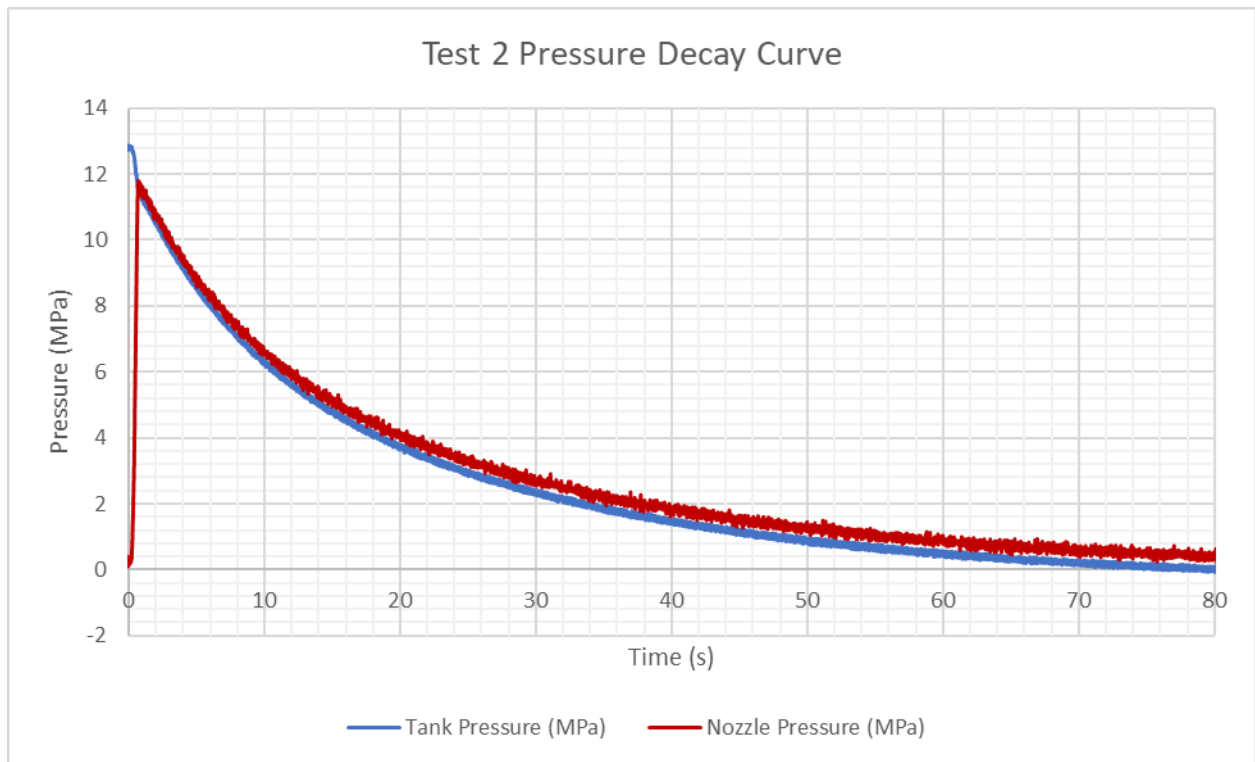
Figure 38: Test 2 pressure decay curve - car scenario.
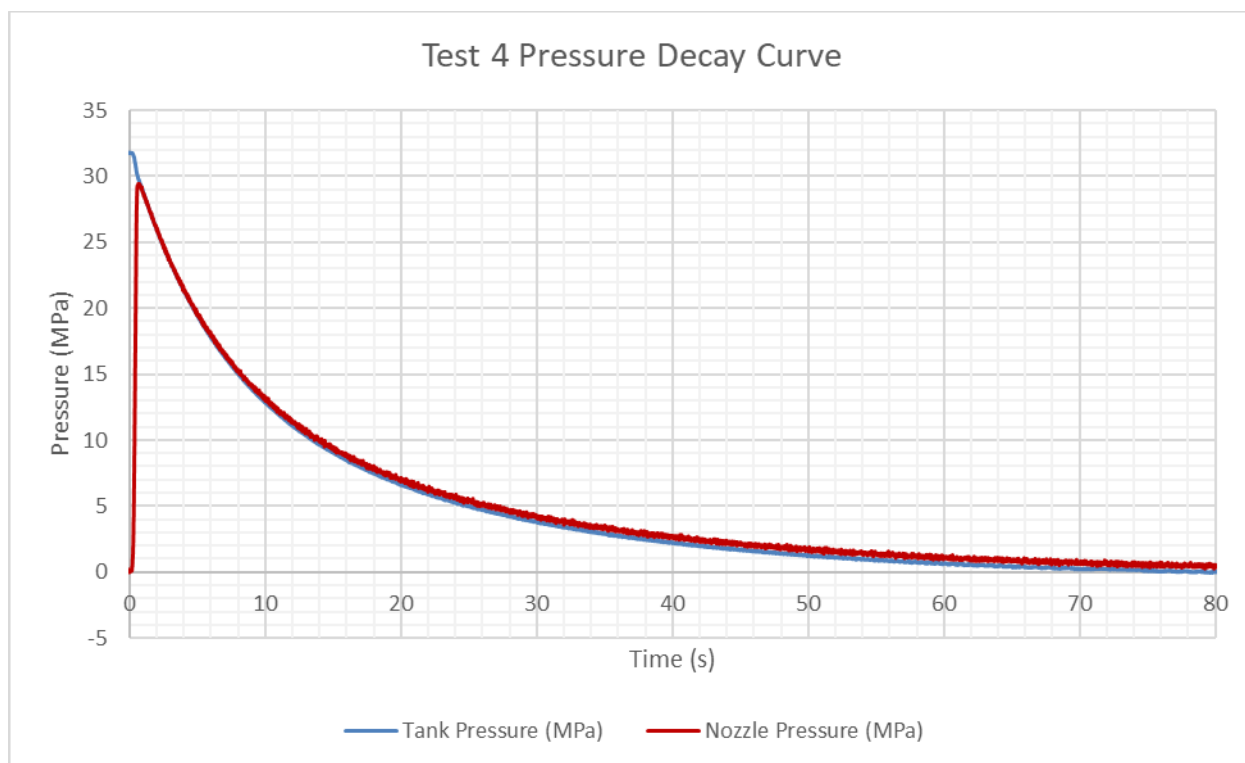
Figure 39: Test 4 pressure decay curve - bus scenario.
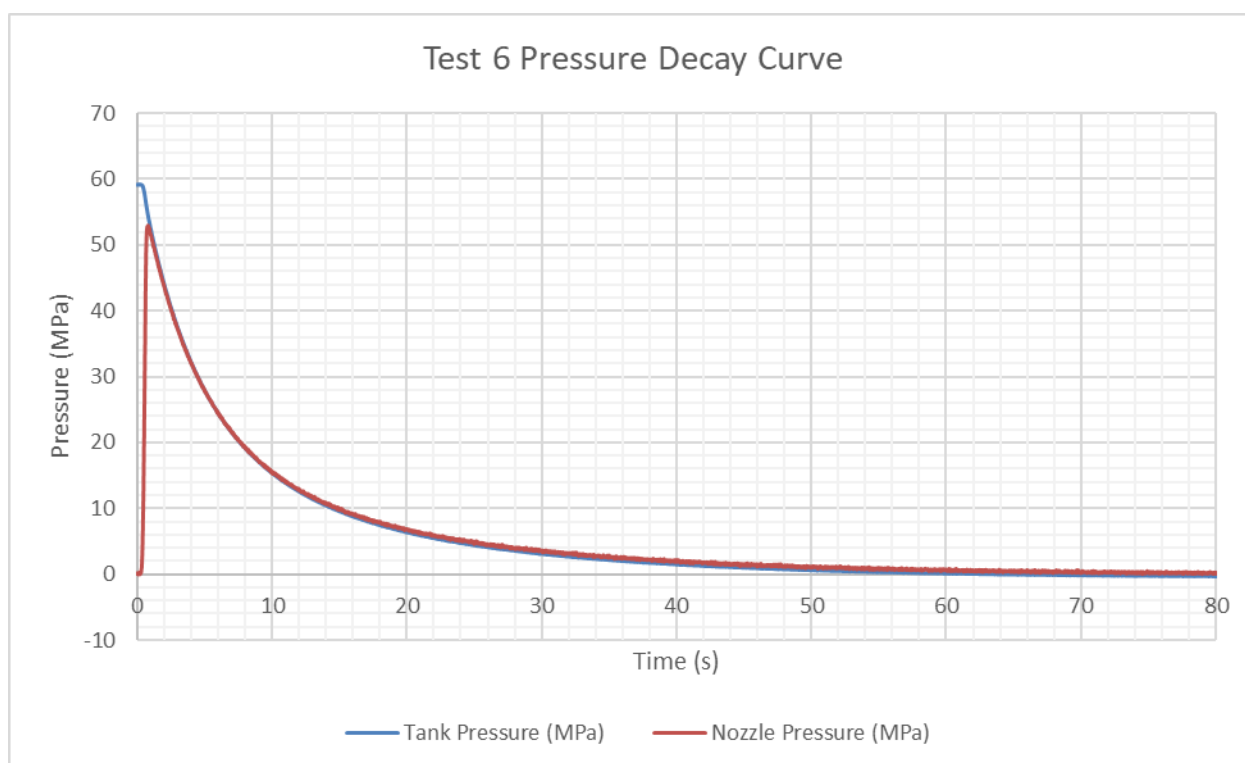
Figure 40: Test 6 pressure decay curve - train 2 scenario.
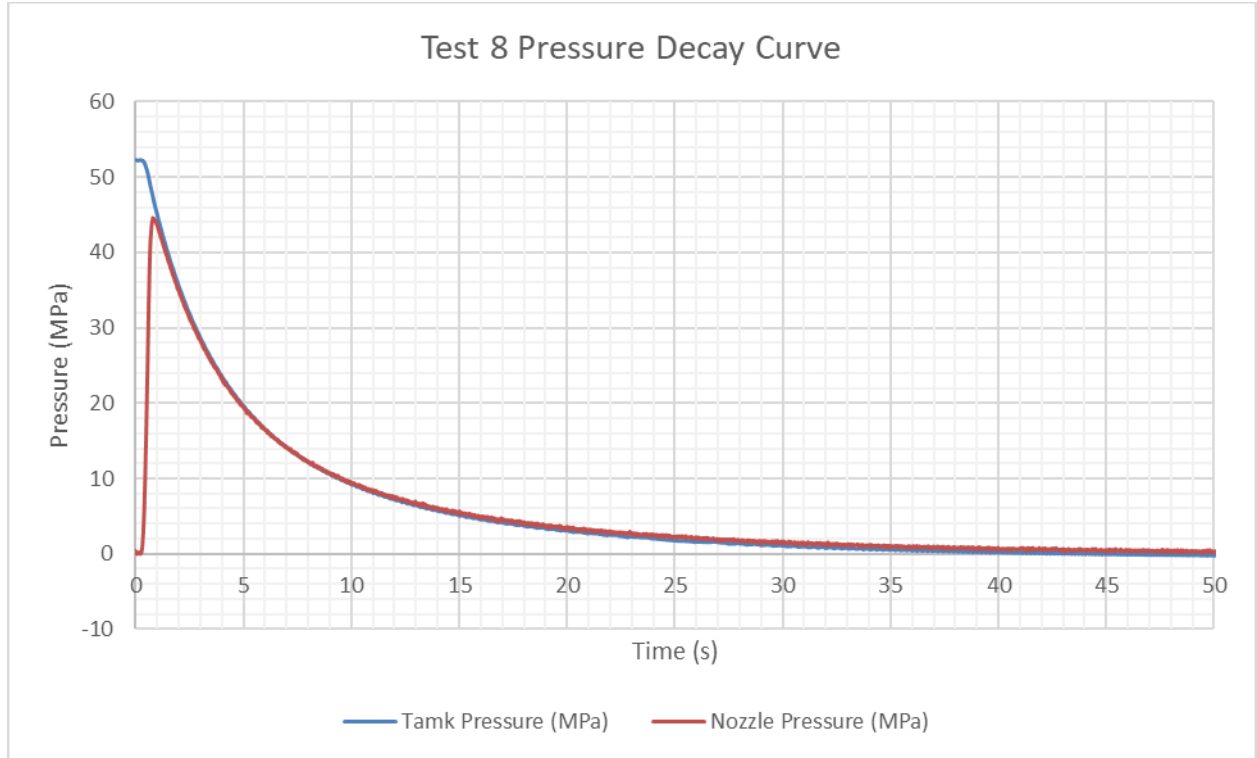
Figure 41: Test 8 pressure decay curve - train 1 scenario.

5.3.1.6.3 Calculated mass decay curves

Using the pressure and temperature measurements and the volume of the facility, the mass of hydrogen at each point can be calculated. This is completed by first using a rearrangement of the Abel-Noble equations of state, shown in Equation 1, to calculate the density of the gas in the facility. This calculated density is then multiplied by the volume of the facility to obtain the mass of hydrogen. Figure 42 shows the typical mass decay curves for each initial condition based on this equation.

Equation 1

$$\rho = \frac{P}{bP + R_{H2}T}$$

where ρ is the density of hydrogen at time t (kg/m^3), P is the measured pressure in the vessel at time t (Pa), b is the co-volume of hydrogen (m^3/kg), R_{H2} is the gas constant of hydrogen (J/kg K), and T is the measured temperature in the vessel at time t (K).

Equation 2

$$m = \rho V$$

where m is mass of hydrogen in the vessel at time t (kg), ρ is the density of hydrogen at time t (kg/m^3), and V is the volume of the vessel and intrinsic pipework (m^3).
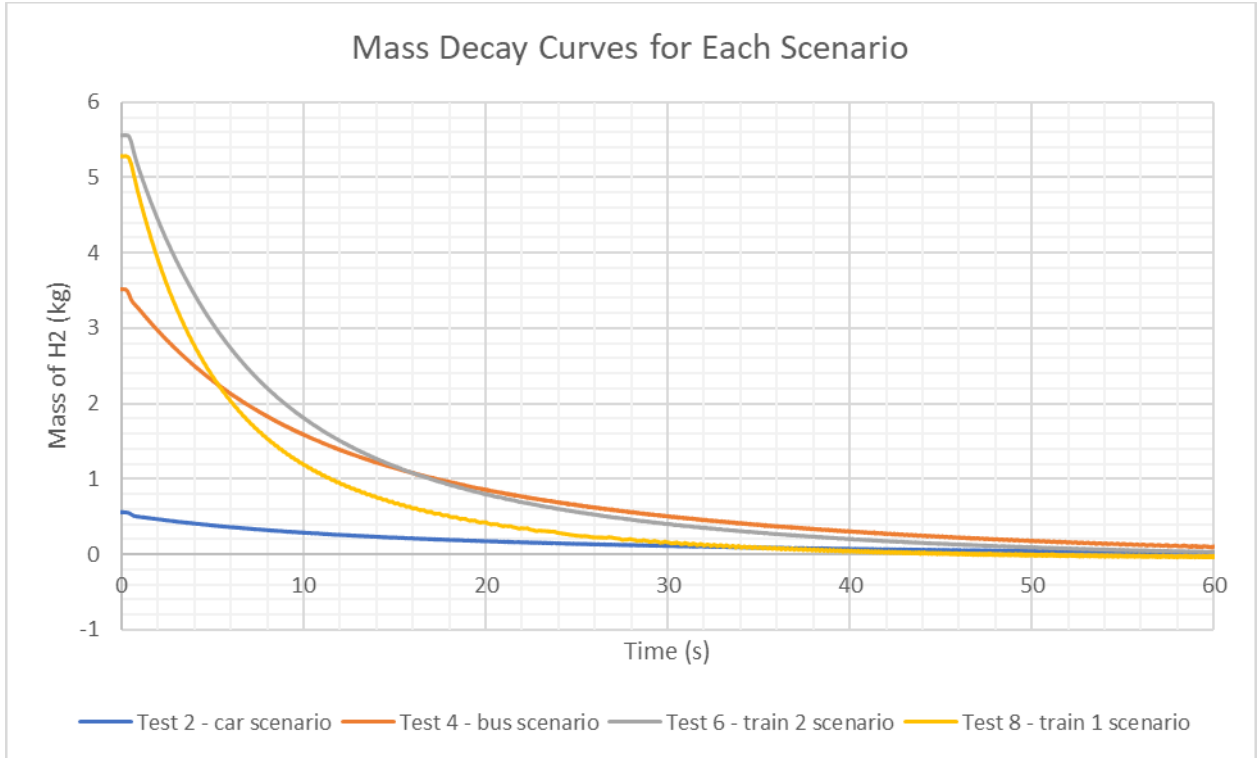
Figure 42: Tests 2, 4, 6, and 8 calculated mass decay curves.

5.3.1.6.4 Estimated mass flow rates

From the mass decay curves, the mass flow rates can be estimated. This has been completed by exponential regression of the initial 10 seconds of the mass decay curves; differentiation then gives an estimate for the mass flow rate. The regression for the mass decay curves was completed in the form shown in Equation 3. Figure 43 shows the calculated mass flow rate with the overlayed estimate using the exponential regression. The estimate for the mass flow rate is shown in Equation 4. To obtain the initial mass flow rate out of the release point, the section of the graph corresponding to the pressurisation of the release pipework has been removed. The estimated mass flow rate has also been multiplied by -1 to show a positive flow rate out of the pipework. Figure 44 to Figure 47 show the output of this method for each scenario.

Equation 3

$$f(m) \approx e^{at^2+bt+c}$$

where m is mass of hydrogen in the vessel at time t (kg), t is the time (s), and a b c are constants obtained through the regression method.

Equation 4

$$\frac{df(m)}{dt} \approx -(2at+b)e^{at^2+bt+c}$$

where m is mass of hydrogen in the vessel at time t (kg), t is the time (s), and a b c are constants obtained through the regression method.
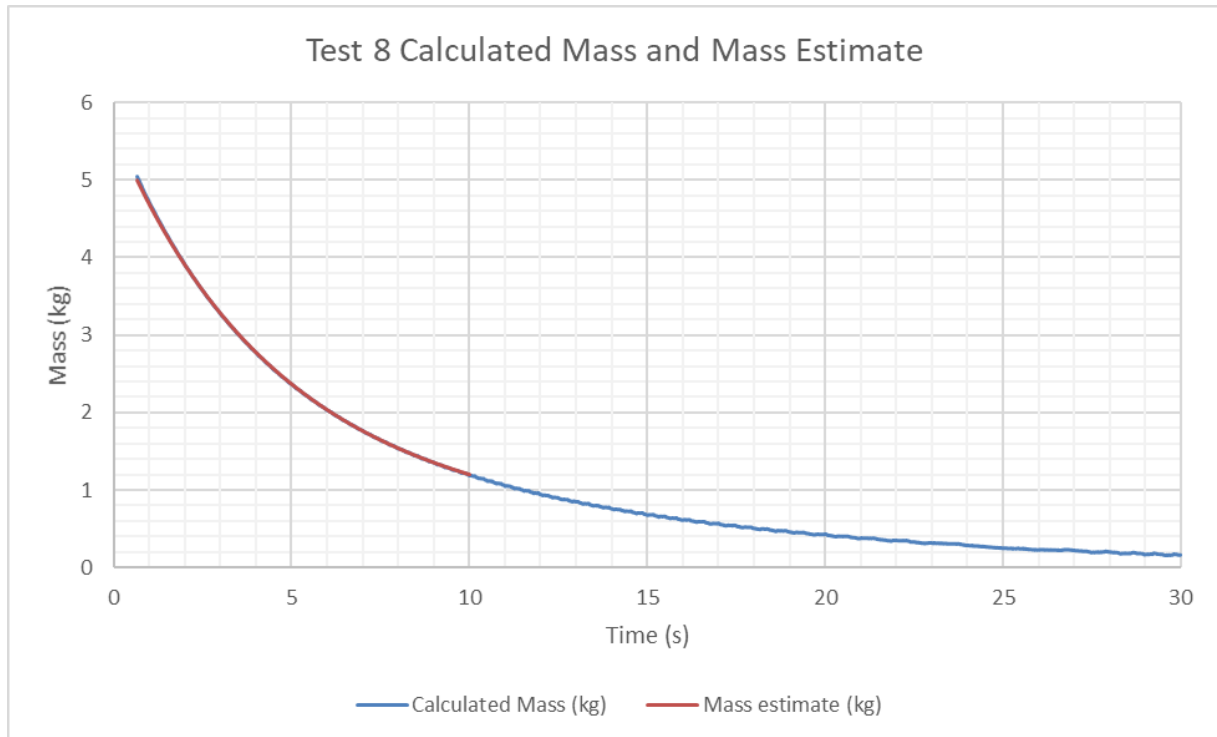
Figure 43: Mass estimate overlay on calculated mass for test 8.
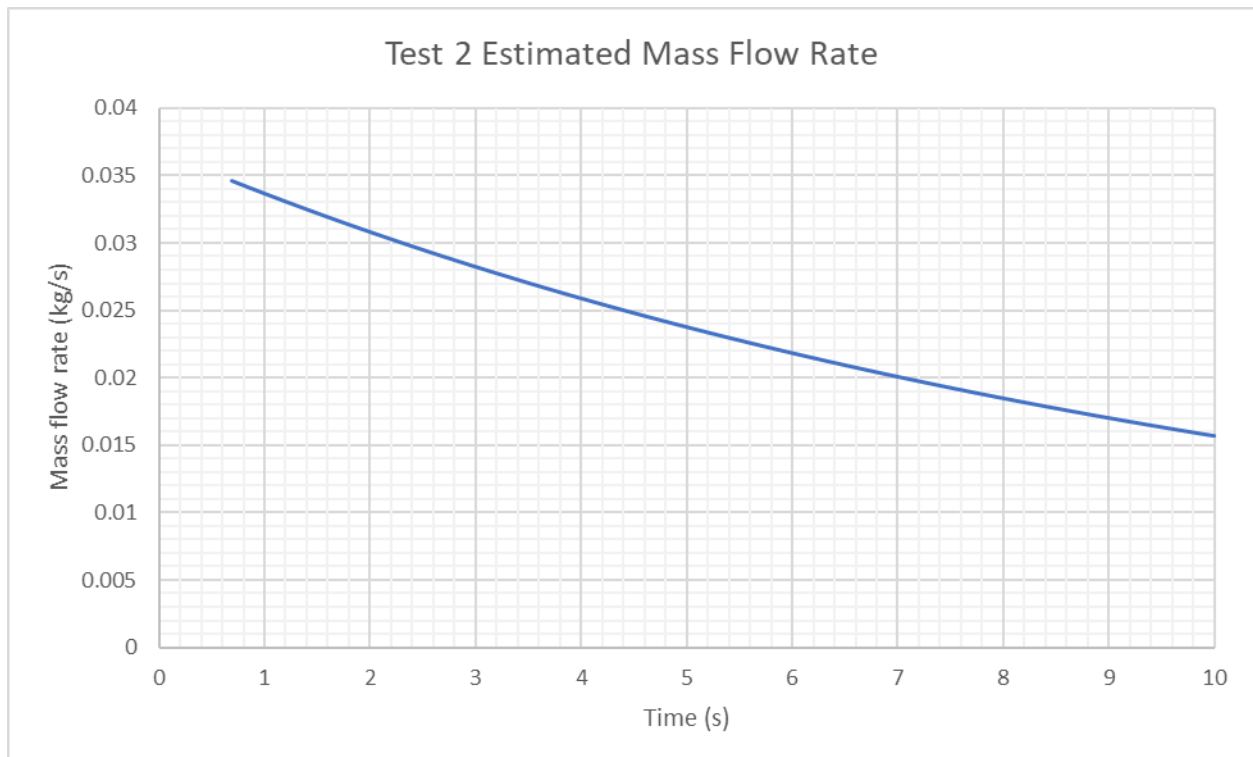
Figure 44: Test 2 estimated mass flow rate - car scenario.
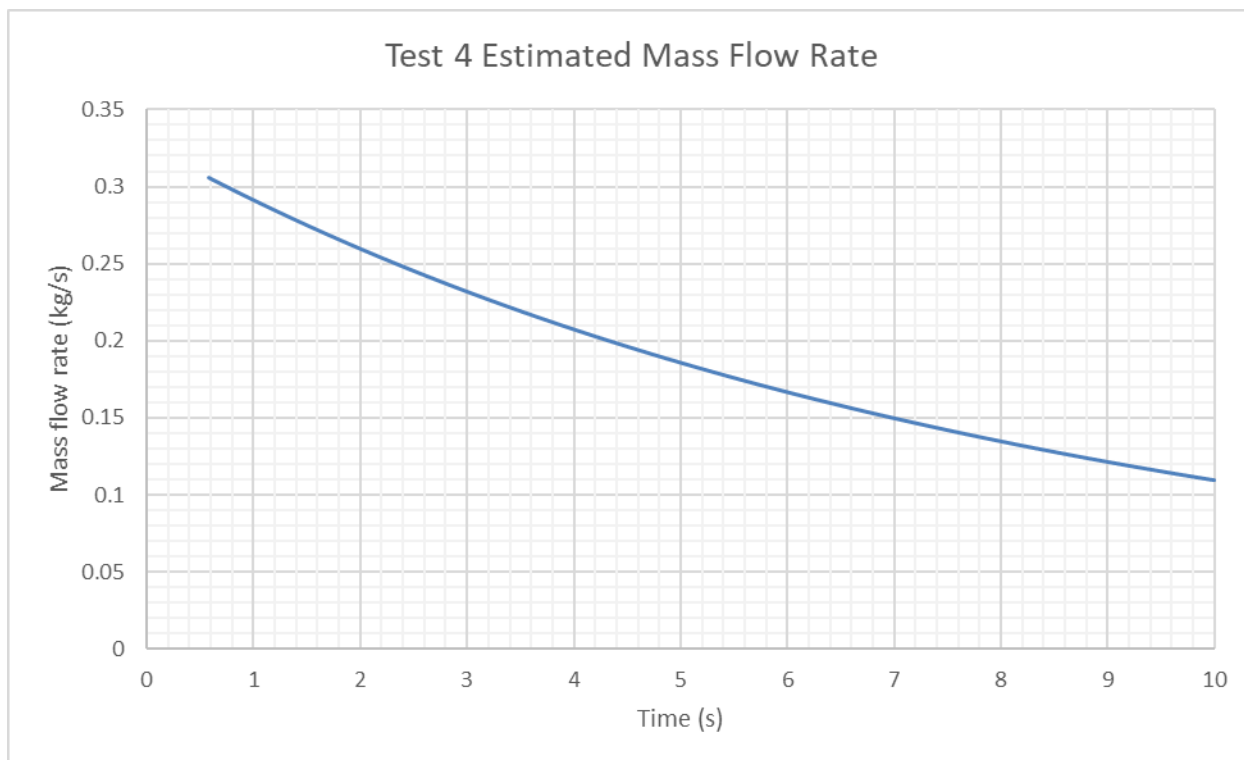
Figure 45: Test 4 estimated mass flow rate - bus scenario.
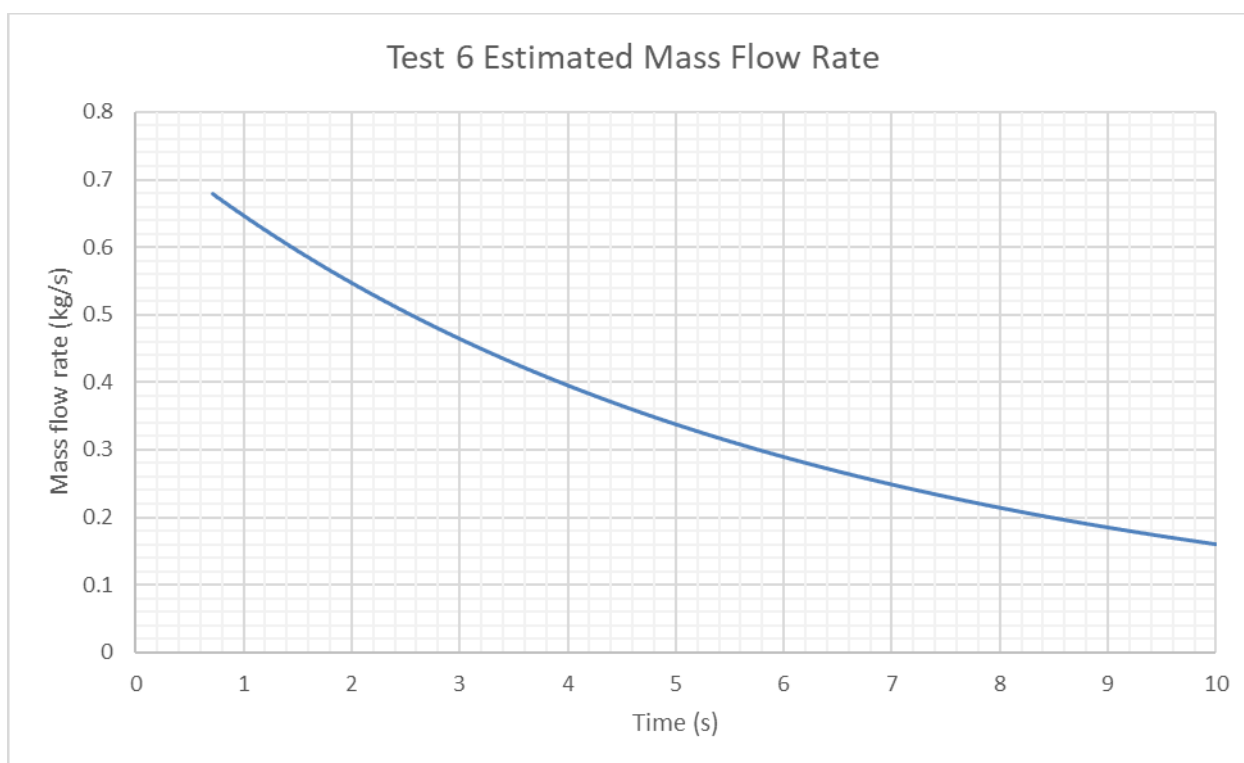
Figure 46: Estimated mass flow rate - train 2 scenario.
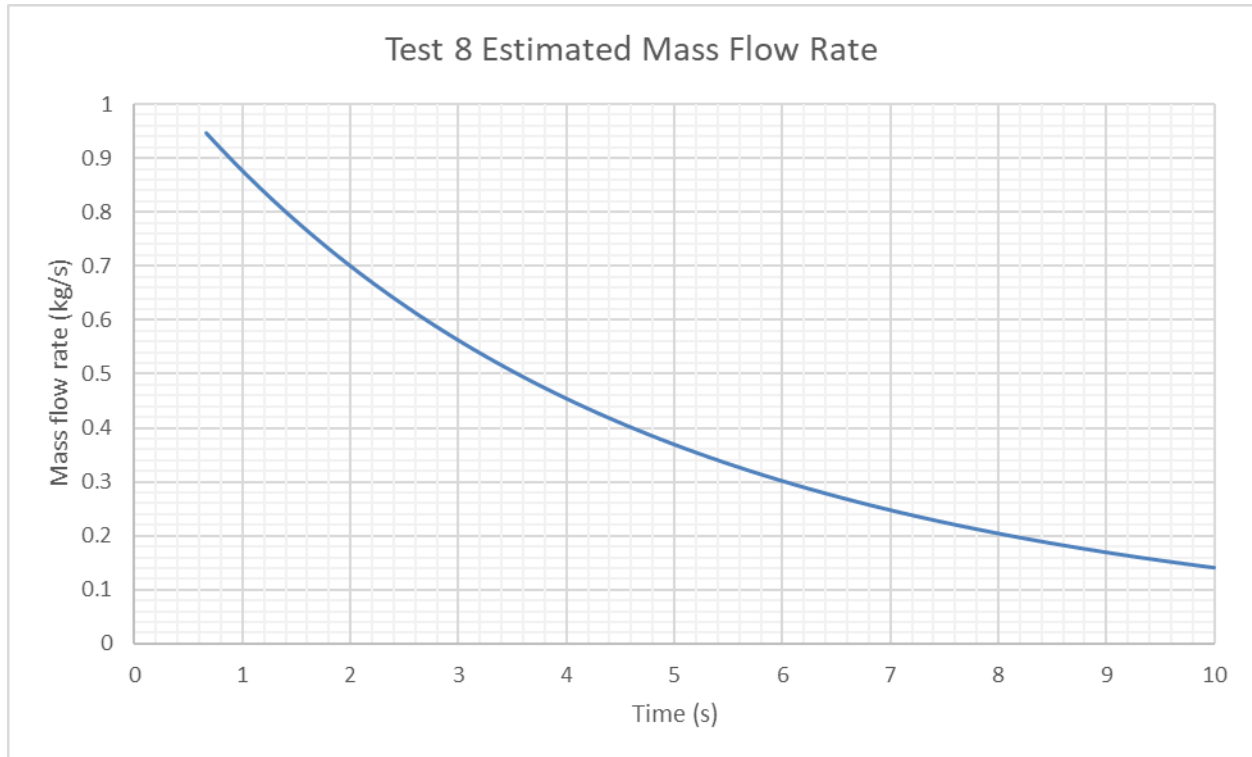
Figure 47: Test 8 estimated mass flow rate - train 1 scenario.

5.3.1.6.5 Hydrogen dispersion results

The output of the hydrogen sensors is a set of time series for each point in the tunnel for each test. Due to the multi-dimensional nature of this data, visualisation of the full set has not been completed. The maximum hydrogen concentration measured at each point per test is shown in Table 18. Table 19 shows the maximum difference in peak measured hydrogen and average maximum measurements across the vertical arrays. This shows the vertical variation in peak hydrogen at distances of 2.5 m (array B), 7.5 m (array D), and 15 m (array F) from the release point.

Table 18: Maximum measured H2 concentrations per sensor per test.

Test No:	B1	B2	B3	B4	B5	B6	B7	B8	B9	B10
02E002 Max (% H2)	5.2	1.1	1.1	10.3	8.4	17.3	12.1	17.7	15.2	19.3
02E003 Max (% H2)	n/a	6.9	8.0	21.0	16.1	37.5	25.5	39.0	32.3	42.9
02E004 Max (% H2)	4.7	3.4	1.1	10.6	7.3	19.7	11.3	19.8	15.3	22.7
02E005 Max (% H2)	5.1	5.0	1.0	12.1	9.0	22.4	15.9	22.7	17.3	24.3
02E006 Max (% H2)	5.8	3.8	1.4	11.3	8.4	23.0	14.2	23.8	17.0	24.9
02E026 Max (% H2)	4.7	3.7	1.4	9.9	6.9	21.9	11.7	22.8	14.4	24.0
02E008 Max (% H2)	3.8	2.8	4.0	9.9	7.2	21.9	12.9	22.7	15.1	23.5
02E009 Max (% H2)	4.5	2.8	1.0	9.9	8.0	21.4	13.1	22.2	15.2	23.3
02E010 Max (% H2)	0.0	3.6	2.6	10.6	9.3	21.4	15.4	21.7	16.5	23.2
02E011 Max (% H2)	5.3	4.1	1.9	10.8	9.0	22.0	15.7	22.4	16.5	24.0
02E012 Max (% H2)	4.8	3.7	1.7	10.6	8.7	21.5	15.0	22.1	16.4	23.5
02E013 Max (% H2)	3.8	2.7	1.9	9.5	8.3	21.0	14.0	21.5	16.0	22.5
02E014 Max (% H2)	4.6	3.8	2.1	9.5	8.3	20.6	13.3	21.0	15.4	22.1
02E015 Max (% H2)	4.7	3.2	2.3	9.8	8.0	21.3	13.5	21.7	15.4	23.1
02E016 Max (% H2)	4.5	3.0	1.9	9.6	8.1	20.8	13.4	21.0	15.4	22.2
Average Max (% H2)	4.4	3.6	2.2	11.0	8.7	22.2	14.5	22.8	16.9	24.4

Table18 (cont.): Maximum measured H2 concentrations per sensor per test.

Test No:	B11	B12	B13	B14	B15	B16	B17	B18	B19
02E002 Max (% H2)	1.1	2.0	21.8	18.1	17.2	17.1	13.7	30.6	21.0
02E003 Max (% H2)	7.9	7.3	1.5*	1.5*	33.3	26.8	3.0*	3.0*	3.0*
02E004 Max (% H2)	1.9	3.5	24.4	9.8	17.3	11.8	5.9	27.7	27.4
02E005 Max (% H2)	4.7	5.1	25.6	18.3	18.5	15.0	16.1	29.0	26.6
02E006 Max (% H2)	3.5	4.1	23.1	5.9	16.5	6.7	1.1	24.2	27.0
02E026 Max (% H2)	1.7	4.1	14.2	1.6	8.5	3.1	0.8	25.0	26.7
02E008 Max (% H2)	2.9	3.4	22.5	4.7	15.8	4.1	0.9	24.6	25.0
02E009 Max (% H2)	2.6	3.8	21.8	8.2	16.6	7.1	1.1	25.5	26.3
02E010 Max (% H2)	3.5	3.5	18.0	1.5	13.0	4.1	0.8	20.7	25.8
02E011 Max (% H2)	3.6	4.1	17.9	2.3	13.0	8.0	0.9	20.5	25.7
02E012 Max (% H2)	3.1	3.7	18.8	1.5	13.2	1.1	1.1	3.0	16.7
02E013 Max (% H2)	2.4	2.7	20.0	0.8	15.0	2.3	0.8	18.8	20.3
02E014 Max (% H2)	2.7	3.1	22.6	0.9	16.5	5.8	0.9	25.2	24.2
02E015 Max (% H2)	2.5	3.4	21.0	0.1	15.5	0.8	0.8	24.4	23.7
02E016 Max (% H2)	2.6	3.2	22.3	5.7	15.6	7.5	0.8	24.4	26.6
Average Max (% H2)	3.1	3.8	21.0	5.7	16.4	8.1	3.3	23.1	24.5

This sensor experienced a fault during these tests, showing an inverse response to the gas.

Table 19: Average maximum concentration and variation for each vertical array.

Test No	Array B average maximum (H2 Vol%)	Array B variation (H2 Vol%)	Array D average maximum (H2 Vol%)	Array D variation (H2 Vol%)	Array F average maximum (H2 Vol%)	Array F variation (H2 Vol%)
B1	4.9	0.4	2.8	4.4	4.4	0.9
B2	5.1	3.5	3.1	0.8	3.2	1.1
B3	3.4	7.1	2.5	3.0	2.1	0.4
B4	14.6	10.4	10.1	0.8	9.6	0.3
B5	10.8	8.8	8.2	2.1	8.2	0.2
B6	26.5	17.8	21.6	0.5	21.0	0.7
B7	17.6	14.3	13.8	2.5	13.6	0.6
B8	27.2	19.2	22.2	1.0	21.4	0.7
B9	21.7	17.0	15.6	1.4	15.6	0.6
B10	30.0	20.2	23.3	0.3	22.6	1.0
B11	4.8	6.0	3.0	0.9	2.6	0.3
B12	5.3	3.8	3.6	0.3	3.1	0.7
B13	25.0	1.2	20.8	4.4	21.2	2.6
B14	14.1	8.5	4.8	6.7	0.6	0.8
B15	23.0	15.9	15.1	3.6	15.7	1.5
B16	17.9	15.0	5.1	3.0	3.0	5.0
B17	11.0	10.2	0.9	0.3	0.8	0.0
B18	28.4	1.2	23.6	4.8	22.8	6.4
B19	27.0	0.8	25.9	0.7	22.7	3.8

As shown in Table 18 and Table 19 , the sensors close to the release point show higher concentrations that the rest of the tunnel. Beyond 2.5 m from the release point the concentrations are relatively constant along the length of the tunnel. The hydrogen concentration at 2.8 m height for each horizontal distance in the forced ventilation test are shown in Figure 48. This shows the dilution rate of the cloud as it moves down the tunnel.

The average maximum hydrogen concentrations measured throughout the tunnel for each scenario (car, bus, train 1 and train 2) was also assessed for both the low and high wind speed tests. The results are shown in Table 20. The effect of the ventilation is also shown through the reduction in average peak concentration throughout the tunnel both in terms of absolute hydrogen concentration reduction, and as a percentage of the low wind speed reading.
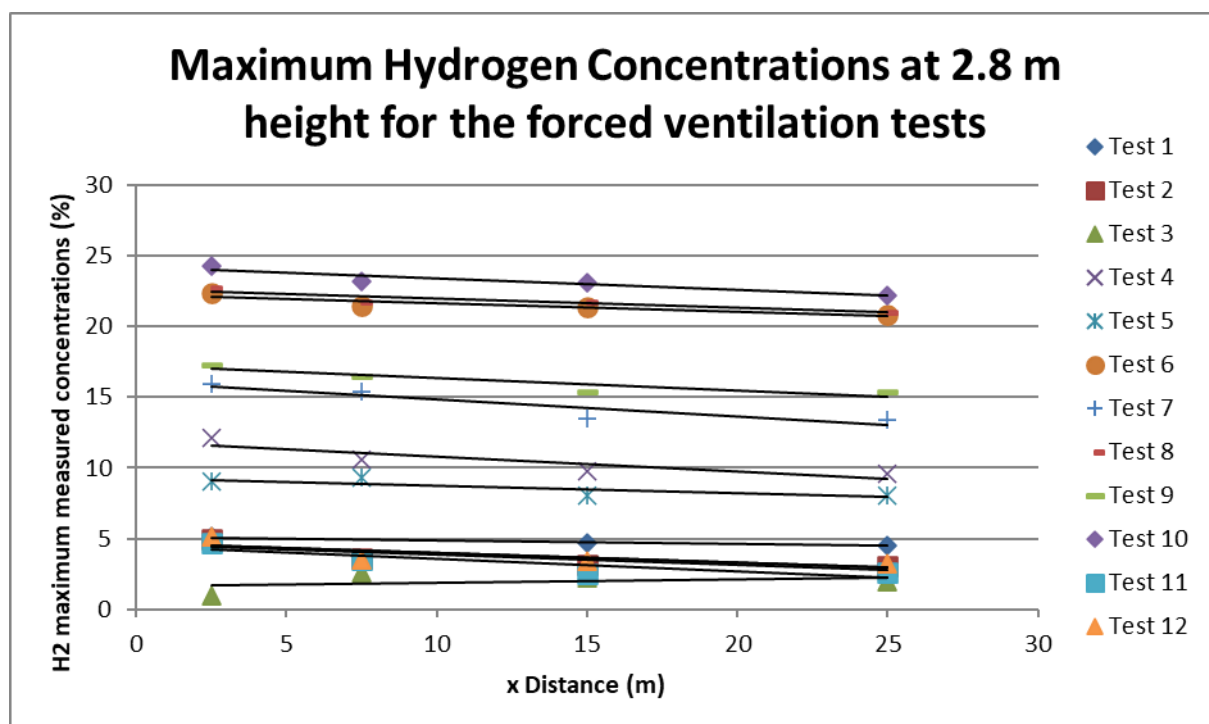
Figure 48: Maximum hydrogen concentrations at 2.8 m per test.

Table 20: Average maximum measured H2 concentrations for low and high wind speed cases.

Scenario	Average maximum measured concentration - Low wind speed (% H2)	Average maximum measured concentration - High wind speed (% H2)	Average absolute H2 reduction (% H2)	Average reduction in concentration (% rd.)
Car	3.5	2.2	1.3	37
Bus	11	8.7	2.3	21
Train 1	24.4	16.9	7.5	31
Train 2	22.2	14.5	7.7	35

Figure 49 is a representative graph showing the propagation of the hydrogen cloud down the tunnel for test 8, which is the train 1 scenario with low wind speed. Sensors 02E005, 02E010, 02E015 and 02E016 are shown, which are located 2.8 m from the tunnel floor at 2.5 m, 7.5 m, 15 m and 25 m from the release point respectively. Figure 50 is a repeated graph from test 9, which is the same scenario but with a high wind speed. The difference in hydrogen cloud propagation can be seen from the graphs as an average 2.5 m/s for the low wind speed, and 4.4 m/s for the high.

Figure 51, Figure 52, and Figure 53 show the output of the same sensors but for the train 2 scenario. Figure 51 shows the output for a test with natural ventilation, measured at 0.1 m/s to 0.3 m/s. The low and high wind speeds are shown after. Both the residence time in the tunnel and the progression of the cloud down the tunnel are impacted by the ventilation rate.

Following these graphs, Figure 54 and Figure 55 show results from the array at the furthest distance from the release point of the hydrogen. Test 8 and 9 are shown as demonstrative cases, with the aim of illustrating the effects of stratification of the gas layer.
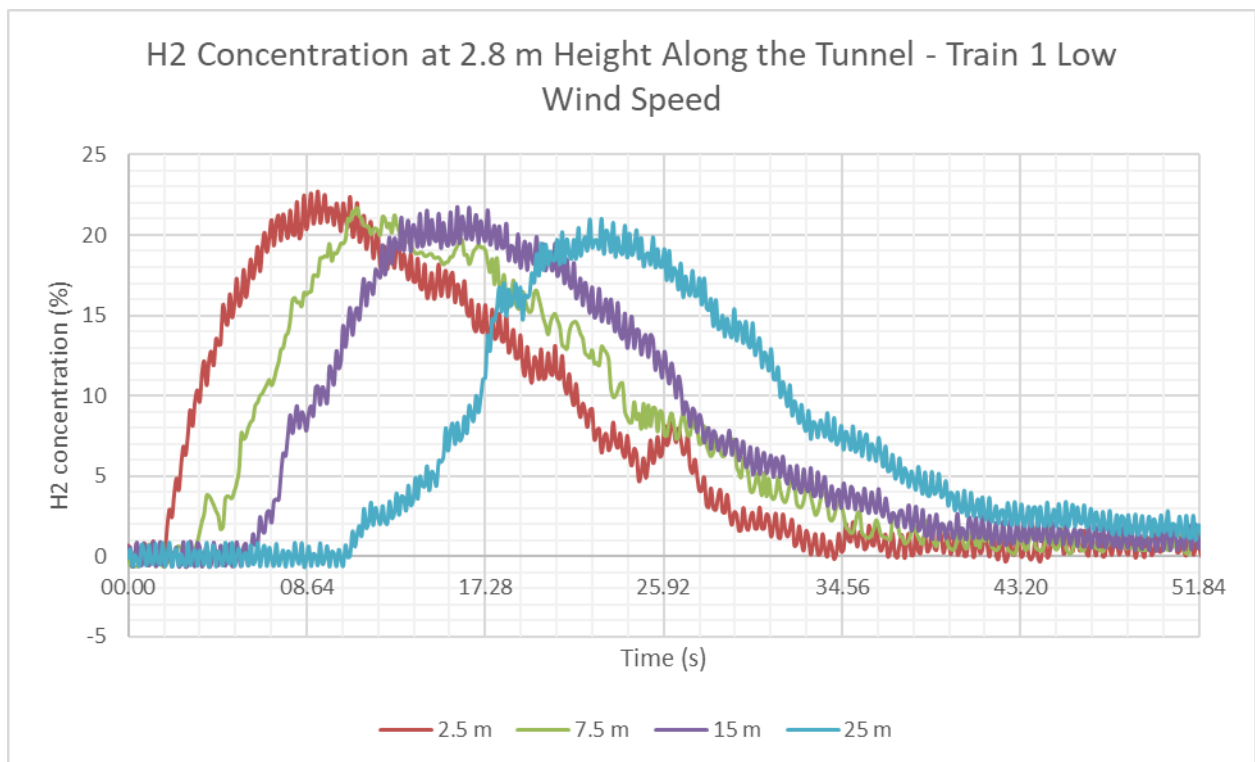
Figure 49: Test 8; H2 concentration measurements at 2.8 m height - train 1 low wind speed.
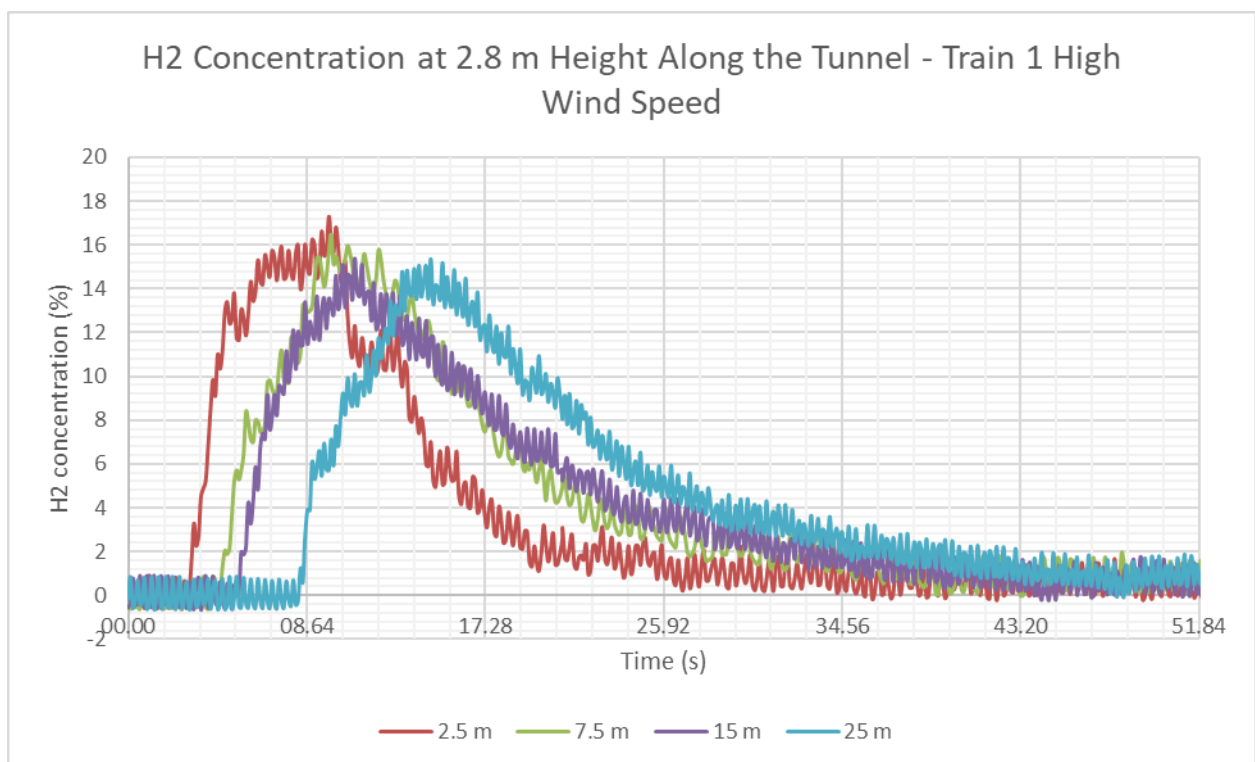
Figure 50: Test 8; H2 concentration measurements at 2.8 m height - train 1 high wind speed.
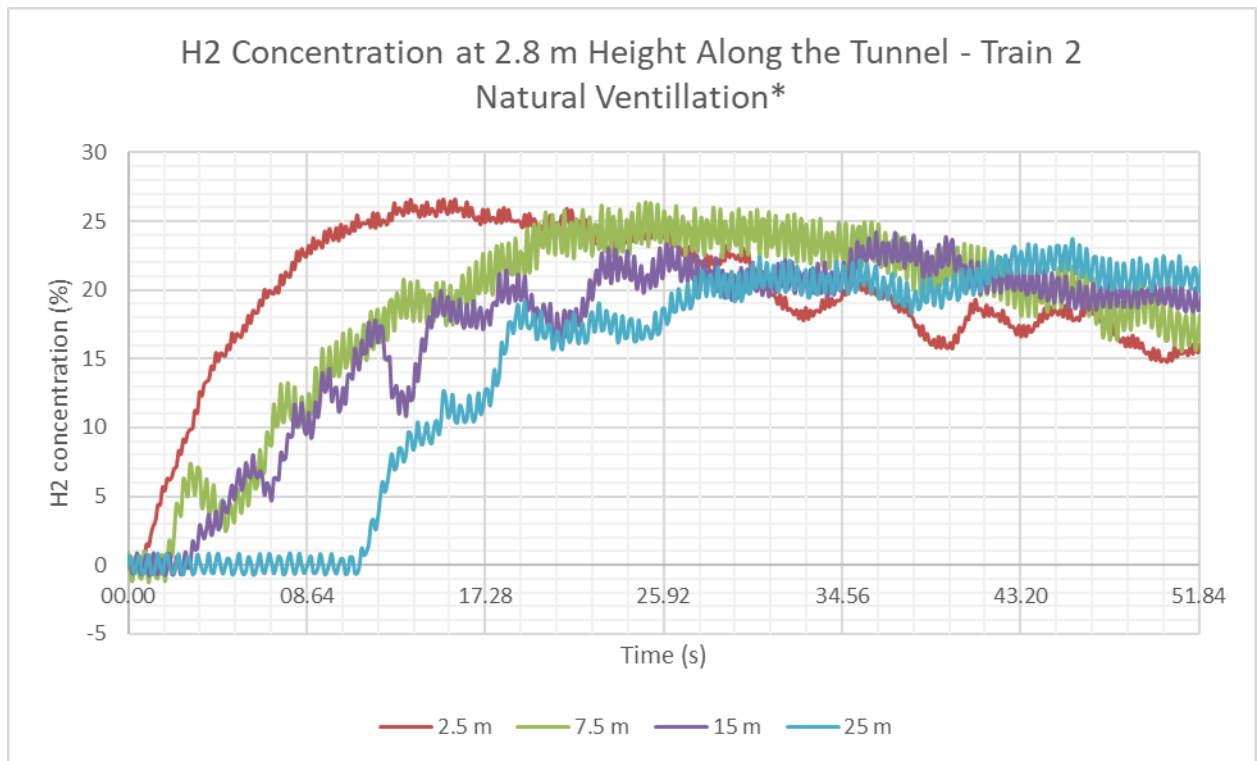
Figure 51: Test 19; H2 concentration measurements at 2.8 m height - train 2 natural ventilation.

There is greater uncertainty regarding the relative time series of the sensors for this test due to variations in operating conditions.
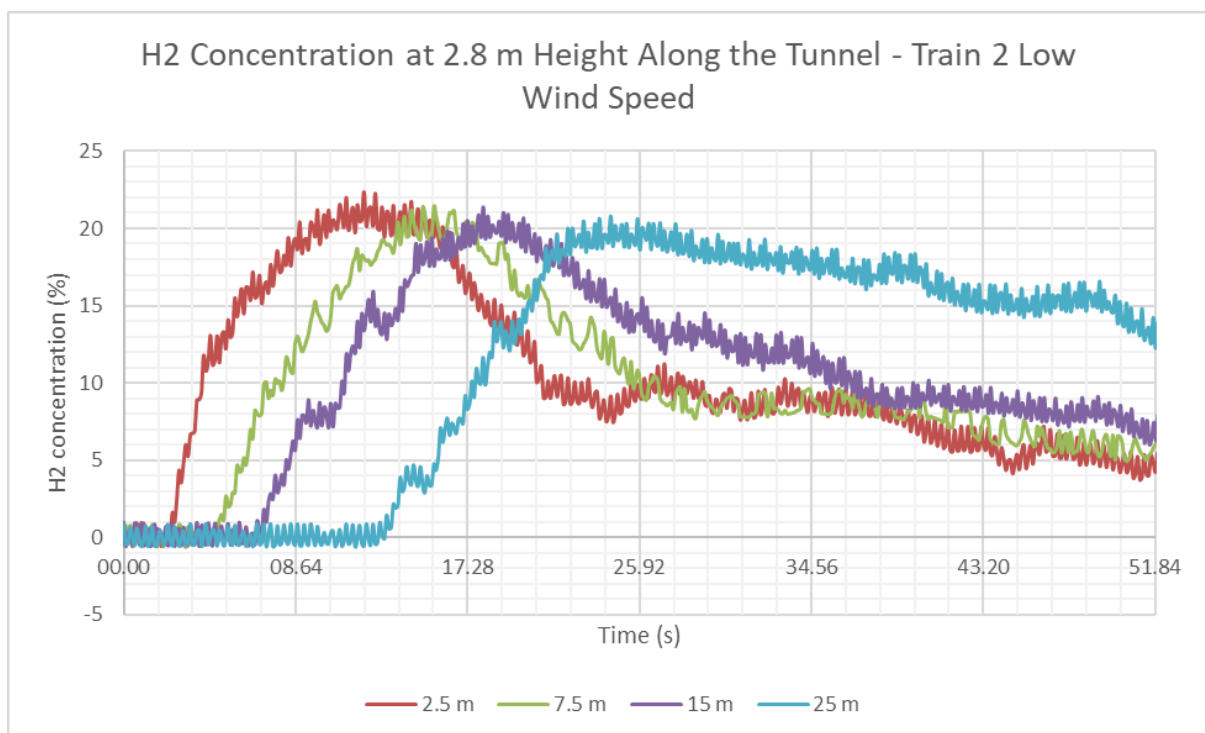
Figure 52: Test 6; H2 concentration measurements at 2.8 m height - train 2 low wind speed.
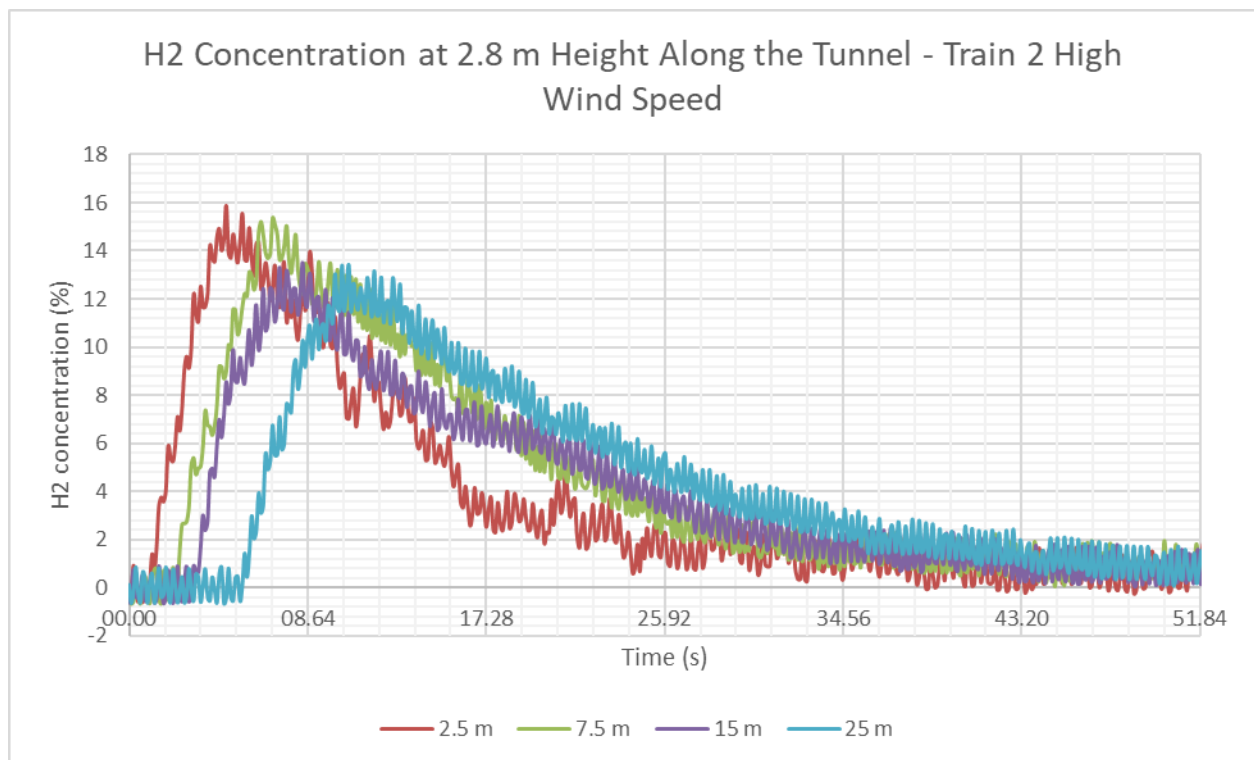
Figure 53: Test 7; H2 concentration measurements at 2.8 m height - train 2 high wind speed.
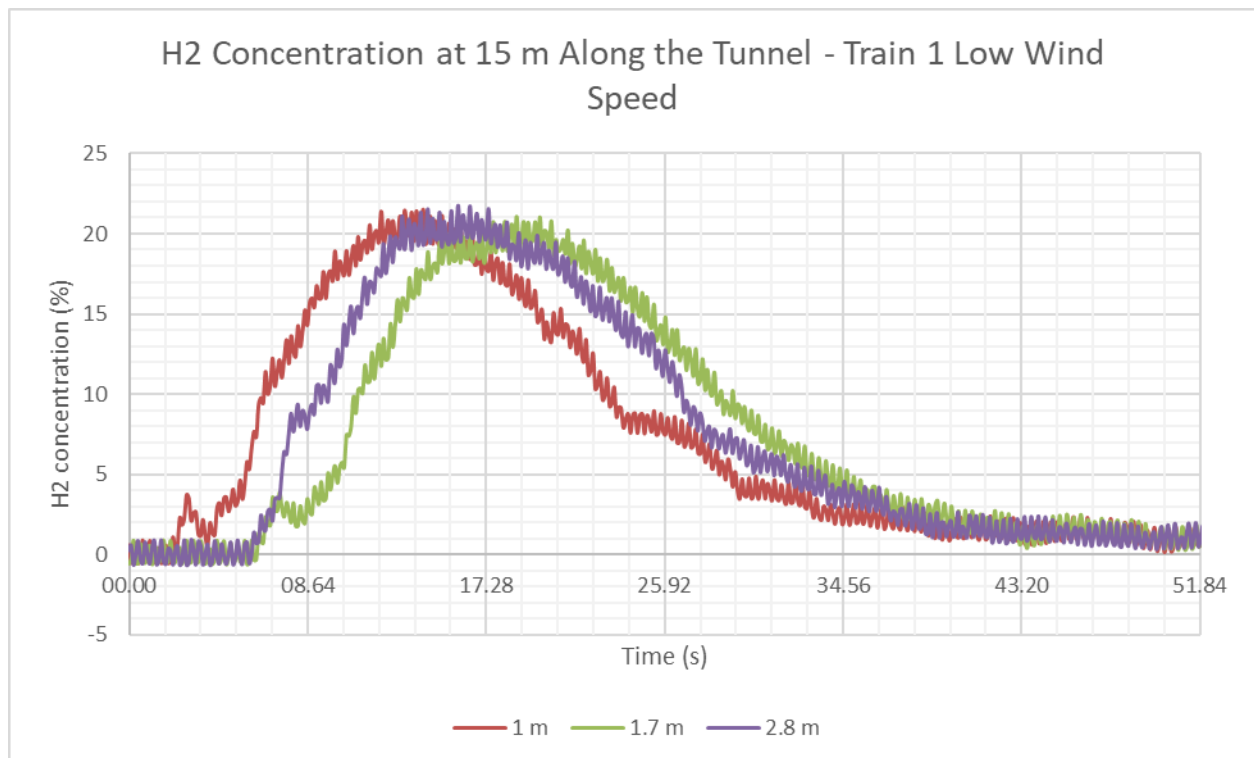
Figure 54: Test 8; Hydrogen concentration at final array.
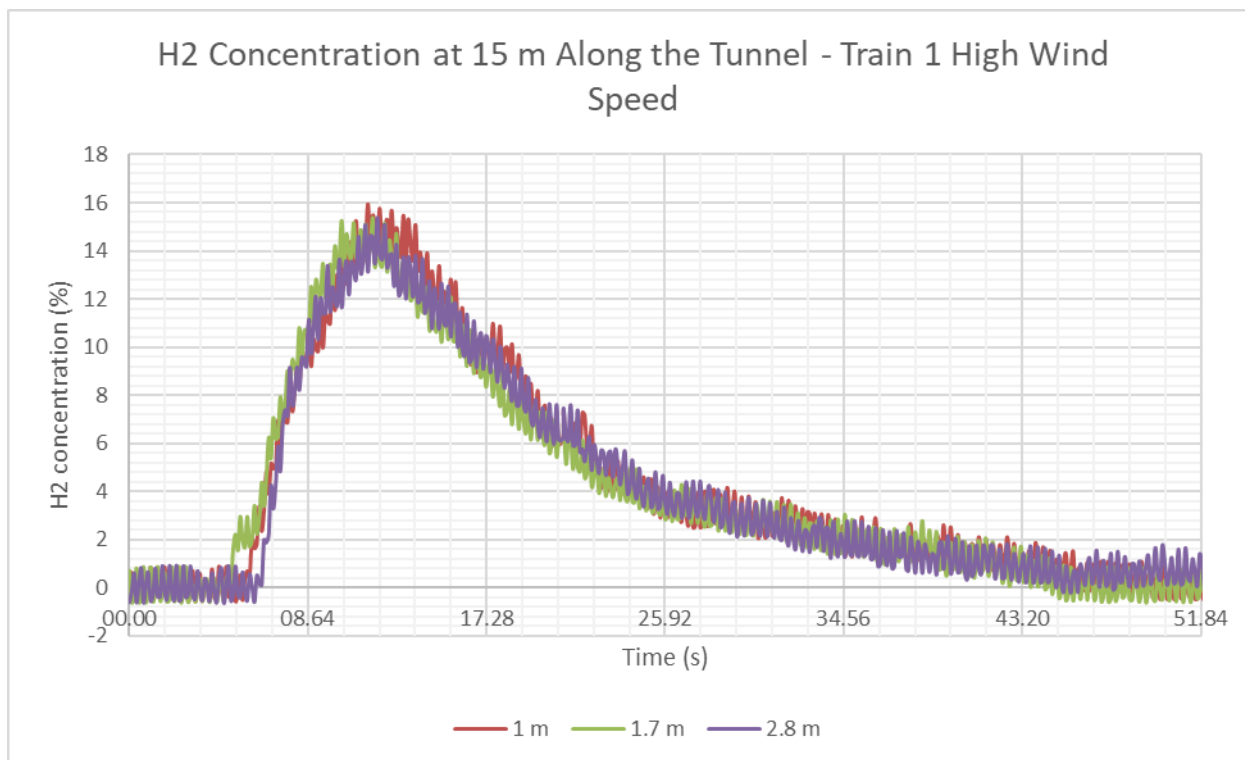
Figure 55: Test 9; Hydrogen concentration at final array.

5.3.1.7 Discussion

With the objective of carrying out scaled releases of hydrogen that represent realistic scenarios, 19 unignited tests were conducted. The source term of each test being characterised by measurements within the system, and the subsequent dispersion was captured by hydrogen concentration measurements throughout the tunnel in use.

With regards to the source term characterisation, the pressure measurements show the expected exponential decay that was predicted for pressurised vessel blowdowns. Noise is present on the outputs and is proportionally larger during the lower pressure experiments. Despite this, the measurements are suitable for source term characterisation, particularly for the bus and train scenarios. The temperature outputs also show noise, and potentially do not show the true temperature of the gas due to the physical location of the sensor in the system.

Due to the design of the system having a section of unpressurised pipework between the facility and the release point inside the tunnel, the initial pressure loss in the vessel is steeper than the 'steady-state' blowdown. This is due to the pressurisation of the pipework, which occurs through a different diameter than the release nozzle. As such, the initiation of the blowdown is considered to be after this pressurisation takes place, which is taken as when the measured nozzle pressure spikes. This means that the initial mass flow rate is taken a fraction of a second after the release valves have opened.

Using the pressure and temperature measurements in the facility after the pressurisation of the release pipework, the density, mass, and mass flow rate of the blowdowns were calculated. This was completed using the Abel-Noble equations of state. Some uncertainty does exist with this method, which derives from assumptions about the facility such as total volume. The measured temperatures did not go as low as predicted in the pre-trial simulations, suggesting

that the location of the temperature sensor was not ideal. This higher-than-expected temperature factors into these equations has a knock-on effect to the subsequent calculations, including an overprediction of the mass flow rates. Even with this overprediction, the mass flow rates displayed in Figure 44 to Figure 47 are of a similar magnitude to those predicted in Table 13.

The method of estimating the mass flow rate, which involves an exponential regression on the calculated mass, results in a good fit for the first 10 s of the mass decay. This was selected as the most important part of the source term. The closeness of fit suggests that the gradient of this curve, obtained through differentiation, is a reasonable prediction of the mass flow rate.

The dispersion along the tunnel was measured by 15 hydrogen sensors. By reviewing the outputs of these sensors, the general behaviour of the release can be surmised. It appears that, as the hydrogen is released, the turbulence of the release aids in mixing in the region close to the release point. By 2.5 m lengthwise along the tunnel, the hydrogen has formed a semi-uniform cloud. This is shown by the similar concentrations at various heights in the same lengthwise position. The difference between the measured concentrations at each array decreases further from the release point. This cloud then travels down the tunnel with limited dilution. This is shown in the near-linear reduction in hydrogen concentration down the tunnel shown in Figure 48. The rate of dilution, shown in the gradients in this graph, are similar.

For the car scenario, natural ventilation results in concentrations above the lower flammablility limit throughout the tunnel, however low ventilation pushes the majority of the cloud below the lower flammability limit. The high wind speed put the measurements consistently below flammable region. Both bus and train scenarios resulted in flammable concentrations throughout the tunnel across the range of ventilation rates.

The wind speed does appear to have an impact on both the speed of propagation of the semi-uniform cloud, and the dilution of the cloud. High wind speed increases the speed and reduces the maximum concentrations for the majority of sensor positions in the tunnel. The exception being very close to the release point, where some higher concentrations were measured with high wind speed. This is demonstrated in Figure 49 to Figure 53, which show longer residence time for the cloud with lower wind speeds.

In an attempt to observe stratification of the hydrogen cloud, Figure 54 and Figure 55 show the measured hydrogen concentrations at the furthest vertical array with three measurement points, located 15 m from the release point. The high wind speed case suggests that there is no stratification at that point. The low wind speed case shows slightly more difference in the response times of the sensors, however this is still within the uncertainty of the delay times of the pump systems. Stratification may still develop further from the release point.

Unfortunately, following the catastrophic damage to the fan system by an intentional ignition test, the blowdown tests with the congestion had an uncontrolled variable (ambient wind) that appears to have had a dominant effect on the dispersion down the tunnel. This means that the effect of the congestion on the dispersion is difficult to quantify.

Indicative results are that hydrogen cars in tunnels should be manageable with existing ventilation rates, vehicles with larger inventory and TPRD sizes i.e., buses and trains, would generate larger flammable clouds that would require further mitigation beyond current

ventilation strategies. These findings are based on a limited set of experiments and different initial conditions could result in different outcomes.

5.3.1.8   Conclusions

In total, 19 unignited blowdown tests were carried out in the HSE HyTunnel facility to simulate hydrogen releases through TPRDs in confined spaces. The objective of these releases was to generate dispersion data that can validate predictive hydrogen dispersion models. The scaling methodology used has resulted in a set of 4 initial conditions relating to a selection of hydrogen vehicle releases: car, bus, train 1 and train 2.

Due to the limited number of tests completed, these conclusions are indicative results of the specific releases conducted, and therefore may not be representative in other cases.

The tests conducted were fairly well representative of the intended scenarios:

- The pressure decay curves were similar to the pre-trial expectations.
- Despite some uncertainties, the concentration and mass calculations were close to those predicted by pre-trial simulations.
- The estimation of the mass flow rate through exponential regression gives similar values to those predicted by pre-trial blowdown calculations.

Several observations of hydrogen dispersion in tunnels were also made:

- The general behaviour of these releases was turbulent mixing close to the release point, followed by the formation of a semi-uniform cloud that then moves down the tunnel.
- There is limited dilution of the semi-uniform cloud as it progresses down the tunnel.
- No vertical stratification of the cloud was observed.
- For the car scenario, low wind speed diluted the cloud well, with most peak hydrogen concentrations below 4 %. The high wind speed diluted the hydrogen cloud even further.
- For the bus and train scenarios, large flammable cloud were formed that persisted to the end of the tunnel.
- For the train scenarios, peak measured hydrogen concentrations were above 20%, which could lead to severe consequences if ignited.
- High wind speeds increased the speed of progression of the hydrogen cloud, reducing potential hazard exposure.
- High wind speeds slightly increased dilution.
- Very low wind speeds greatly increased the residence time of hydrogen in the tunnel.

6. Thermal and pressure effects of hydrogen jet fires and structure integrity - experiments (WP3, DTU)

6.1 Effect of hydrogen jet fire on structure integrity and concrete spalling (ST3.4.3, DTU)

6.1.1 Introduction

In the following spalling experiments on different strengths concrete cylinders and walls are described. In order to investigate the potential differences in spalling due to the hydrogen jet flames, several concrete cylinders and wall elements are exposed to heat radiation, a low-pressure propane flame and a high-pressure hydrogen jet flame. The report describes the experiments and results of three sets of tests conducted to increase the knowledge of spalling of different types of concrete due to different impacts:

1) Heat radiation exposure of concrete cylinders using a furnace,

2) Impinging low-pressure propane gas flames on concrete walls,

3) Impinging high-pressure hydrogen jet flames on concrete walls.

The hydrogen experiments have been done in cooperation with USN. They kindly supported DTU with their high pressure hydrogen equipment and actively helped performing the experiments conducted in the period 28/02 to 04/03-2022 at North-Zealand's Fire School (Nordsjællands Brandskole) in Denmark.

6.1.2 Experimental setups

The first heat radiation exposure experiments are done in a furnace (see Figure 56). It consists of a furnace electrically heated, typically to 1000°C . Through an opening in the furnace the concrete is exposed to the heat radiation of about 45 kW/ m^2 (@ 1000 °C).

Figure 56: Furnace test setup including mantle for compression.

The concrete types to be tested are casted in form of cylinders with a diameter of 150 mm and a height of 300 mm. They are placed in a steel mantle for testing of the concrete under various compressive loads, e.g. typical for tunnel designs. A pressure-distributing layer of neoprene is placed between the concrete cylinder and the steel mantle to compensate for irregularities of the concrete surface. The steel mantle is constructed in such a way that it can resist the pressure from thermal expansion that could develop at the surface of a concrete wall in a fire situation. One end of the cylinder is exposed through a 100 mm diameter hole to heat radiation of about 45 kW/m^2 from an oven at 1000°C.

The second setup for the impinging low pressure LNG (propane/butane) flame is shown in Figure 57. In Figure 59 is shown the test setup using wall elements under a load (provided through tension on the green steel bars). The compression was chosen to be 1.2 MPa in all experiments. It also allows to control the gas flow rate by adjusting the gas burner valve and by continuously measuring the LNG containers mass loss flames using a weight. From that the Heat Release Rate (HRR) is calculated (see Figure 59).

Figure 57: Setup pre-test of propane impinging flame burner on a concrete cylinder.

Figure 58: Pre-test cracks observed after impinging propane flame on concrete cylinder. The surface shows large cracks.

The result of the propane flame exposure on a test concrete cylinder is showing deep cracks, but not a spalling of the surface concrete in Figure 58.

Figure 59: Low pressure impinging propane flame setup using a concrete wall 1000mm x 1000mm x 100mm. Compression 1.2MPa.

In Figure 60 a detailed drawing of the wall setup with the exposure areas is shown, which is used for the low- and high-pressure experiments. Thermocouples of type K are introduced from the site closest to the respective exposure areas to measure the surface temperature as well as the temperature profile into the concrete.
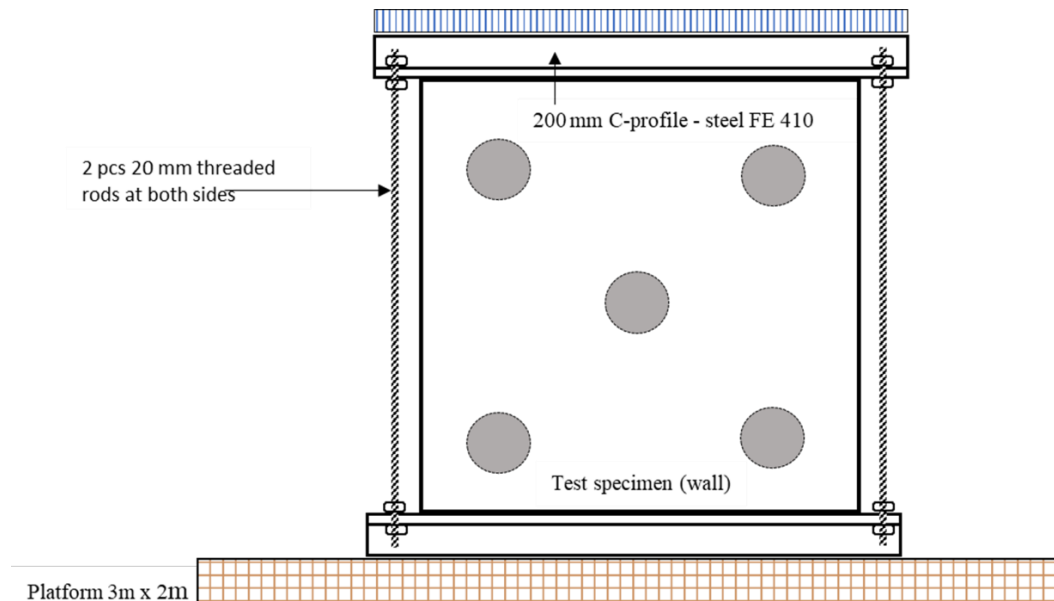
Figure 60: Test setup for tests of concrete wall elements in compression, with propane and hydrogen flame exposure.

The third setup for the high-pressure impinging hydrogen flame is shown in Figure 61. The setup uses the high-pressure hydrogen equipment from USN. The test setup is split into a "safe site" where the air compressor, the hydrogen battery pack and the high-pressure pump is placed. Separated by a container on the "dangerous site" the high-pressure hydrogen tank, a vent, mass flow controller, and the outlet nozzle as well as the concrete wall to be tested are placed.
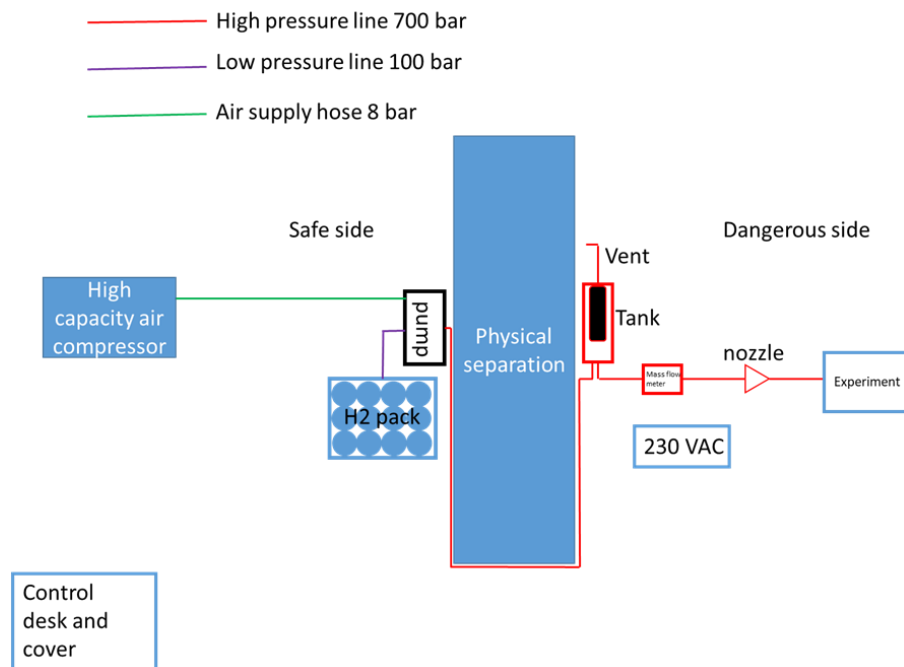
Figure 61: Setup of the high-pressure impinging hydrogen jet test rig.

In Figure 62 a P&ID diagram provides the basis components of the high-pressure setup and the respective connections. The following photos (Figure 63, Figure 64 and Figure 65) show the real layout of important components as installed and placed for this experimental campaign.
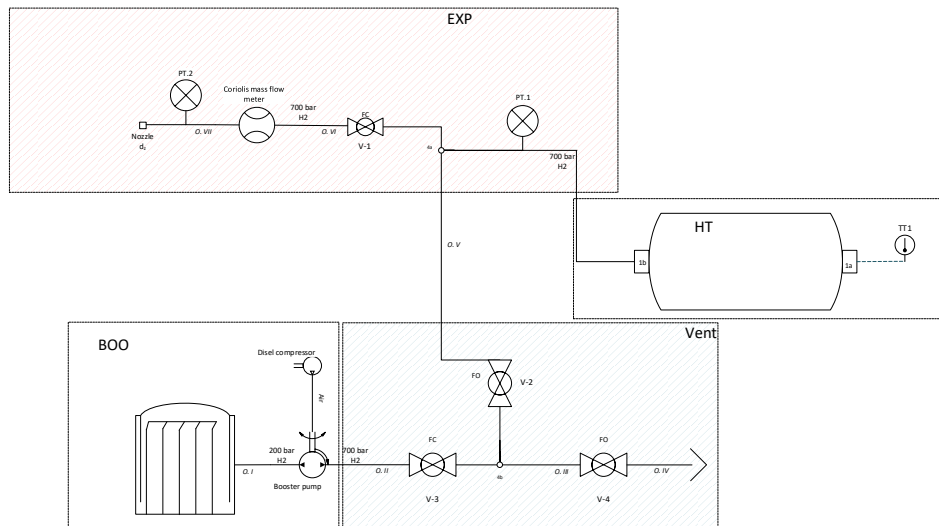
Figure 62: The experimental P&ID for the spalling tests. HT – 70MPa hydrogen tank; BOO – High pressure booster. Inlet to booster pump is the bottle pack; V-X – Valves to operate the systems; PT.X – Pressure transmitters; TT.X – Temperature transmitters; Coriolis mass flow meter; Diesel compressor; Nozzle is the spouting nozzle of the system.

The setup for the hydrogen exposure tests, consists of a frame made of a top and bottom C-profile and four threaded rods (two in each side). The frame is placed on a platform made of timber (see Figure 70 and Figure 71). The system is levelled in place and supported by wedges etc. for achieving a stable system. A concrete wall element for testing is placed in the frame, and adjusted horizontally and vertically to ensure the desired placement in the setup, see Figure 60. The threaded rods are tightened using a torque wrench. The applied tension is adjusted according to the size of the specimen, for instance the wall thickness, for reaching a desired compression in the concrete.

Figure 63: Hydrogen test setup for 700 bar hydrogen spalling experiment. Left: Hydraulic booster pump, hydrogen battery pack and high pressure pipe on top of container. Right: hydrogen vent arrangement.

Figure 64: Hydrogen test setup for 700 bar hydrogen spalling experiment. Coriolis flow meter and high pressure hydrogen tank.

Figure 65: Hydrogen test setup for 700 bar hydrogen spalling experiment. 3mm nozzle positioned for impinging hydrogen flames on concrete wall.

During the experiments the pressure outflow and mass flow rates were monitored as shown in Figure 66. As it can be seen the initial hydrogen pressures were about 700 bar and the initial mass flow rate was about 53 g/s with an outflow time of about 200 s.
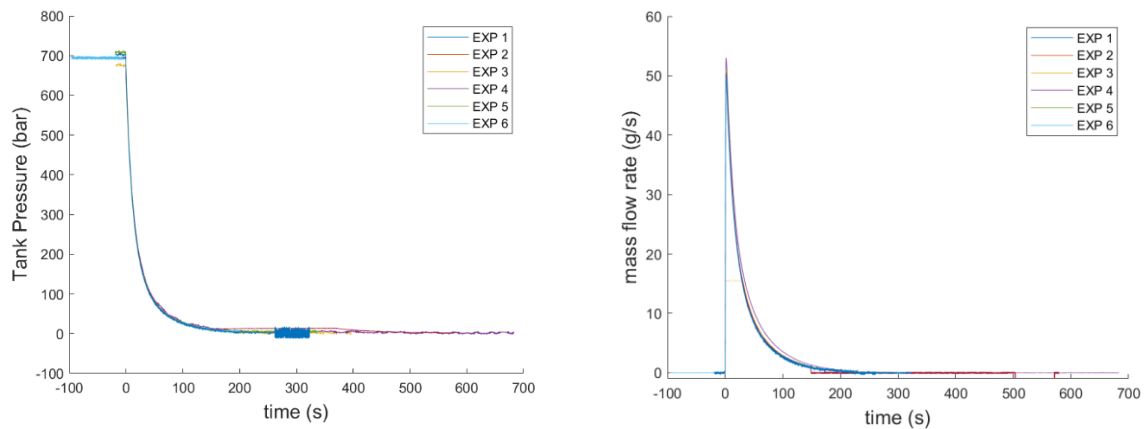
Figure 66: Tank pressure (left) and mass flow rate (right) histories for all experiments.

The corresponding heat release rate of the hydrogen jet flames are found in Figure 67. It shows a peak HRR of above 6 MW.
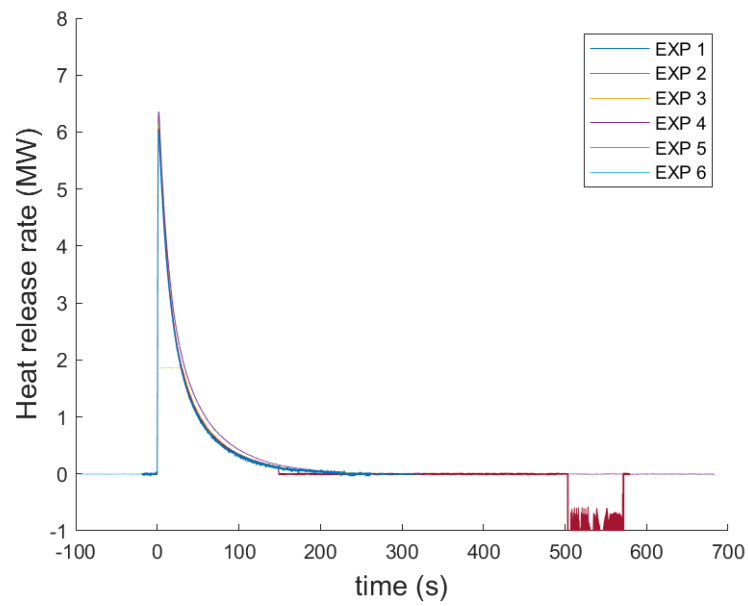
Figure 67: Heat release rate of hydrogen jet flame during the experiments.

The temperatures of the outflowing gas and the temperatures in the pressure vessel are shown in the following Figure 68 and Figure 69.
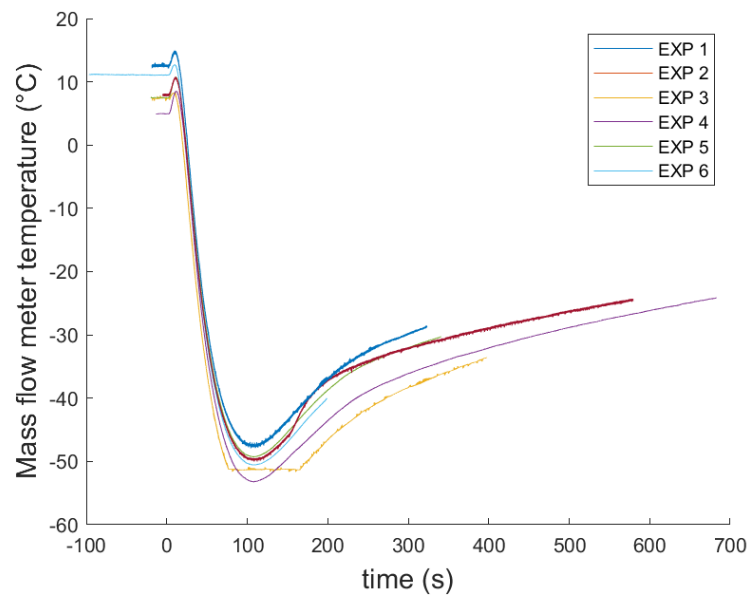
Figure 68: Mass flow meter temperatures during the experiments.
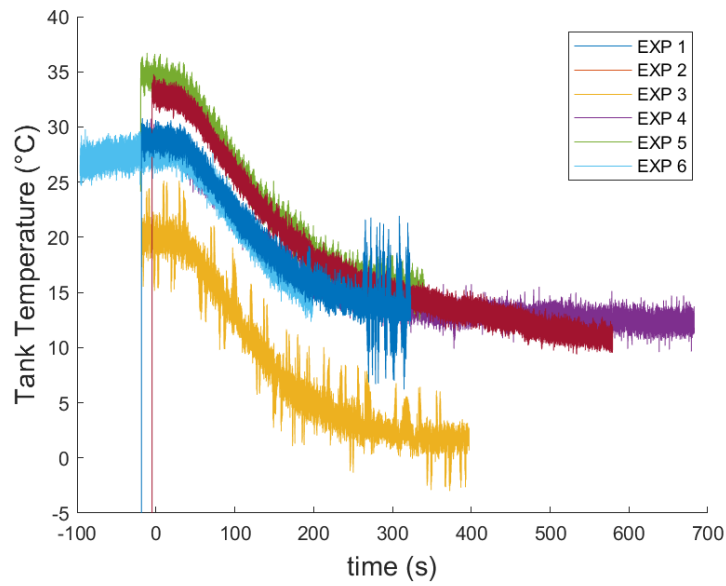
Figure 69: High-pressure tank temperatures during the experiments.

Figure 70: Check of exposure geometry for wall element for the spalling experiment.

Figure 71: Placement and protection of nozzle for hydrogen gas exposure of wall.

When the specimen is in place as shown in Figure 70, the gas burner is placed in front of the concrete surface, with the gas burner head at 50 mm distance to the concrete surface (see Figure 71).

6.1.3 Concrete types

Table 21: Characteristics of the concrete types.
W/C=water/cement ratio, MC=micro-silica, FA=fly ash, PL=plasticizer, PP=polypropylene, AG=aggregates, %=w/w%.

Concrete	Characteristics	W/C ratio	MC	FA	PL	PP	AG
A	Reference	0.45	0%	0%	-	0%	Sea
B	Dense	0.40	1%	0%	+	0 or 1%	Sea
C	Dense +	0.35	2%	2%	+	0 or 1%	Sea
D	Dense + High strength	0.30	4%	0%	+	0 or 1%	Sea

The casted concrete cylinders were placed in a 40 °C hot water bath, for curing, for about 6 weeks (see Figure 72). After the curing period, the cylinders are put in a climate chamber at 20 °C and RH = 60%.

Two different batches of 21 cylinders were casted and tested in the first setup (heat radiation exposure using the furnace setup) in two different periods, namely December 2019 and March 2020. In each batch, three cylinders were casted for each of the 7 concrete types: the reference type A without fibers and the types B to D of increasing concrete densities with and without fibers (indicated with N and F respectively, see Table 21). Thus in total, 6 cylinders were casted for each of the seven concrete types. One cylinder of each type from the second batch was dried out and used to assess the moisture of the other 2 cylinders at the time of testing. This was done because the moisture is known to affect the spalling significantly and, after analyzing the variability of the spalling results of the first batch, it was decided to investigate whether the moisture content of the cylinders of the second batch was within the expected limits and how well the moisture content could be assessed by means of literature formulas.

The first batch was tested in early May 2020, while the second batch was tested in July 2020. For detailed information about the curing time of each batch see Table 22 .

Figure 72: The concrete cylinders for spalling tests are placed in a water bath for curing.

Table 22: Details of casting, curing time and days in water of the first and second batch.

Date	Type	W/C	Fiber	Duration hot water curing (days)	Remark
03.12.2019	A-N	0.45	none	69	Batch 1
04.12.2019	B-N	0.40	None	68	Aggregates water content estimated to 0.1%
	C-N	0.35	None		
	D-N	0.30	None		
16.12.2019	C-F	0.35	Yes	56	
	D-F	0.30	Yes		
19.12.2019	B-F	0.40	Yes	53	
25.02.2020	A-N	0.45		98	Batch 2 Aggregates water content estimated to 0.1% for the first 3 types; measured for the remaining
26.02.2020	B-N	0.40	None	97	
27.02.2020	C-N	0.35	none	80	
02.03.2020	B-N	0.40	none	76	
	C-N	0.35	none		
	D-N	0.30	none		
	A-N	0.45	none		
03.03.2020	B-F	0.40	yes	75	
	C-F	0.35	yes		
	D-F	0.30	yes		

6.1.4 Spalling results of the tested cylinders

The concrete cylinders were tested in the mantle-oven for explosive spalling. The results are reported in Table 23 for the first and the second batch.

The reference concrete A) shows no sign of spalling in the first batch, as expected, while it had a minimum amount of spalling in the second batch. All cylinders casted with fibers in either the first or second batch did not show any type of spalling, also as expected.

Some of the cylinders of concrete types from B to D without fibers (N) showed spalling.

In the second batch, all cylinders of type B to D without fibers spalled except one (B-N-5) and the amount of spalling (measured by means of the weight of the debris) is increasing with the density of concrete (B to D). In the first batch, only one cylinder of type B and two cylinder of type D (both without fibers) showed spalling and the spalling of type B was quite significant (61 gr) and bigger than the type D, despite the lower density. Possible reasons of such results are currently being investigated. Figure 73 shows the spalling of this cylinder, indicated as B-N-1 in the result table.

Figure 73: Test of concrete cylinder B-N-1, including 1 % MC and no PP-fibres. This concrete type spalled during the test. The oven is 1000 °C.

Table 23: Spalling results for the concrete types.

Sample	Spalling	Time of spalling (min)	Spalling temperature (°C)	Debris (g)	Diameter of spalling area (mm)	Depth of spalling area (mm)	Remark
A-N-1							
A-N-2							
A-N-3							Top hat crack
A-N-7	Yes	1 - 2		0.5			Top-hat & middle crack
A-N-8	Yes	1 - 2		2.7			
B-N-1	Yes	3 - 4	440	60.9	115 - 135	7	
B-N-2							
B-N-3							
B-N-4	Yes	1 - 2		0.5			
B-N-5							
B-F-1							
B-F-2							Top-hat crack
B-F-3							
B-F-4							Top-hat crack
B-F-5							
C-N-1							
C-N-2							Top-hat crack
C-N-3							Middle crack
C-N-4	Yes	2 - 3		13.0			
C-N-5	Yes	1 - 3		27.6			Middle crack
C-F-1							
C-F-2							
C-F-3							
C-F-4							
C-F-5							
D-N-1							
D-N-2	Yes	2- 3	544	22.8	90 - 96	6	Top-hat & middle crack
D-N-3	Yes	2- 3	505	18.6	78 -112	3	
D-N-4	Yes	1 -3		16.5			Top-hat crack
D-N-5	Yes	1-2		30.5			
D-F-1							
D-F-2							
D-F-3							Top-hat crack
D-F-4							
D-F-5							

6.1.5   Spalling tests of concrete using low- and high-pressure impinging flame exposure

After the presented initial standard cylinder tests (Zaineb 2020) exposed to heat radiation from a furnace, three types of concretes containing PP fibres were selected. These types showed no damage during the furnace screening tests. Therefore, three wall elements (1 x 1 x 0.1 m) are casted containing an amount of micro silica of 1%, 2% and 4%, respectively. One of the concretes (Type C) was added 2% of fly ash as well (see Table 24).

Table 24: Characteristics of the concrete types casted as a 1 x 1 m walls.
W/C=water/cement ratio, MC=micro-silica, FA=fly ash, PL=plasticizer, PP=polypropylene, AG=aggregates, %=w/w%

Wall	Concrete	Characteristics	W/C ratio	MC %	FA %	PL	PP %	AG
1	B	Dense	0.40	1	0	+	1	Sea
2	C	Dense +	0.35	2	2	+	1	Sea
3	D	Dense + High strength	0.30	4	0	+	1	Sea

The selected concretes *with PP-fibres* (concrete B, C, D) are tested further using the low pressure LNG flame setup and the high pressure hydrogen jet flame setup. The intention is to test for differences in the spalling behaviour compared to the furnace results, where the three concretes did not showed signs of spalling using the standard cylinder furnace test.

For each of the three test items tested as wall elements in compression, in total four gas burning exposure tests were performed, two with low-pressure impinging propane gas flames, and two with high-pressure impinging hydrogen jet flames.
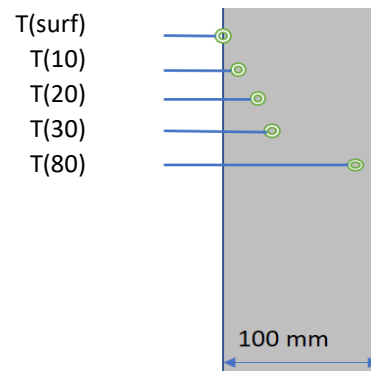
Figure 74: Test with a propane gas burner exposure on Wall Element 1 (WE1), w/c=0.40, concrete B, dense+. To the right shown placements of the thermocouples.

Below, in Figure 75 photos of the conducted propane gas exposure test are shown during and after the test.

Figure 75: Concrete wall elements for further gas exposure testing. To the right a first test setup. Wall 1 w/c=0.40 – concrete B – dense. Left: during test with propane. Right: After test.

6.1.6   Results for propane gas exposure

The respective wall elements were exposed to impinging LPG gas flames for a duration of about 1800s.

The temperatures are measured by thermocouples placed at different distances from the concrete surface, see the figure above. The measurements during the tests are presented on the next figures. It is seen that the concrete surface reaches temperatures of 950-1000 °C, whereas the temperature inside the concrete varies, depending on the depth, however with a quite steady temperature increase per time unit. The maximum temperature in 10 mm depth is about 450 °C for concrete type B (Figure 76), and that is above the critical temperature level where spalling often is seen for concretes susceptible for spalling. The maximum temperatures in 10 mm depth for types C and D is below 400 °C at 1800 seconds as seen in Figure 77, Figure 78, Figure 79, and Figure 80.
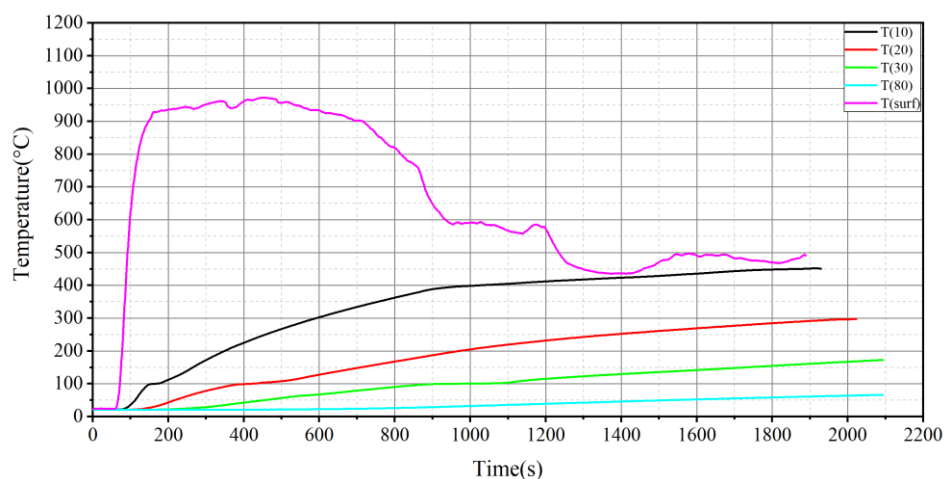
Figure 76: Temperature profiles for wall element 1- WE1 w/c=0.40, concrete B (test date 28-6-2021, start at 12:39). Propane flame. Depths 0mm, 10 mm, 20mm, 30 mm and 80 mm.
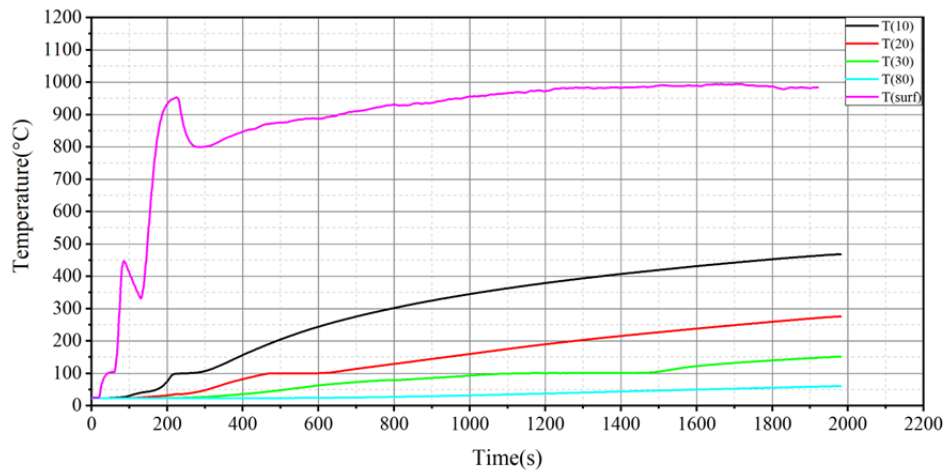
Figure 77: Temperature profiles for wall element 2 – WE2, w/c=0.35, concrete C (test date 29-6-2021, start at 11:29). Propane flame at depth 0mm, 10 mm, 20mm, 30 mm and 80 mm of the concrete, during propane gas flame exposure.
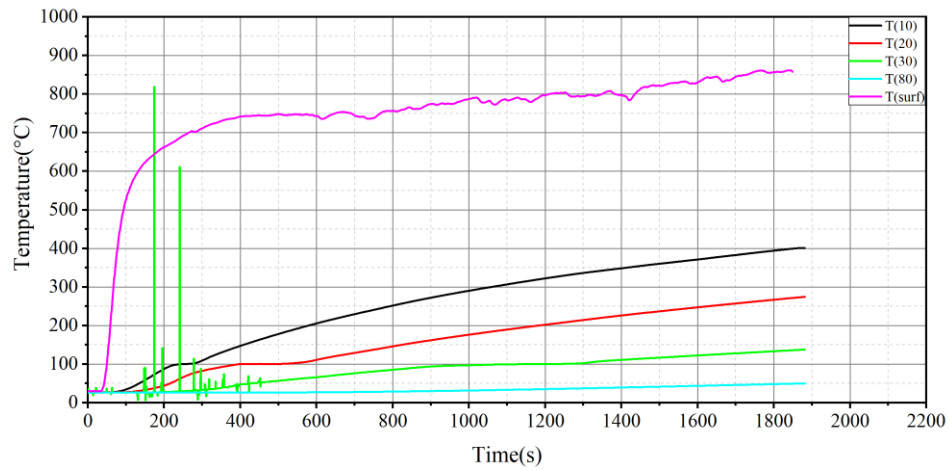
Figure 78: Temperature profiles for wall element 2 – WE2, w/c=0.35, concrete C (test date 29-6-2021, start at 13:28). Propane flame TC at 0mm, 10 mm, 20mm, 30 mm and 80 mm.
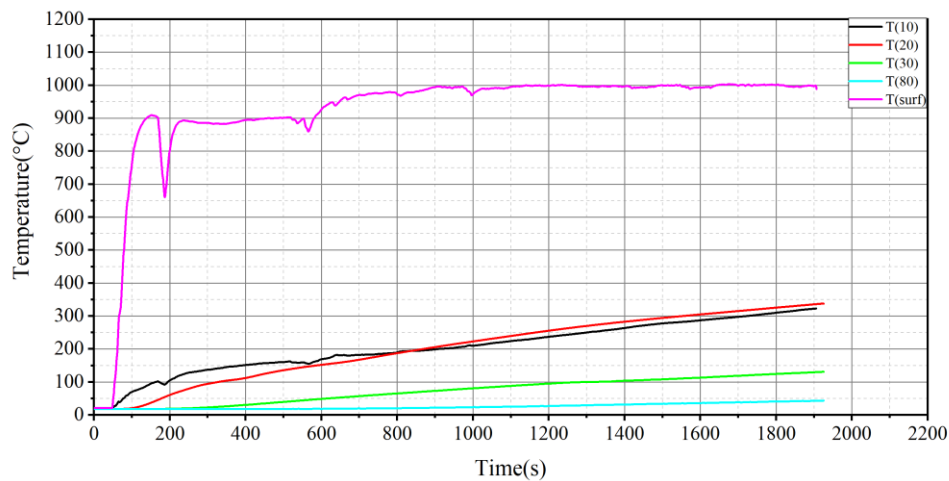
Figure 79: Temperature profiles for wall element 3 – WE3, w/c=0.30, concrete D (test date 1-7-2021, start at 11:03). Propane flame TC at 0mm, 10 mm, 20mm, 30 mm and 80 mm.
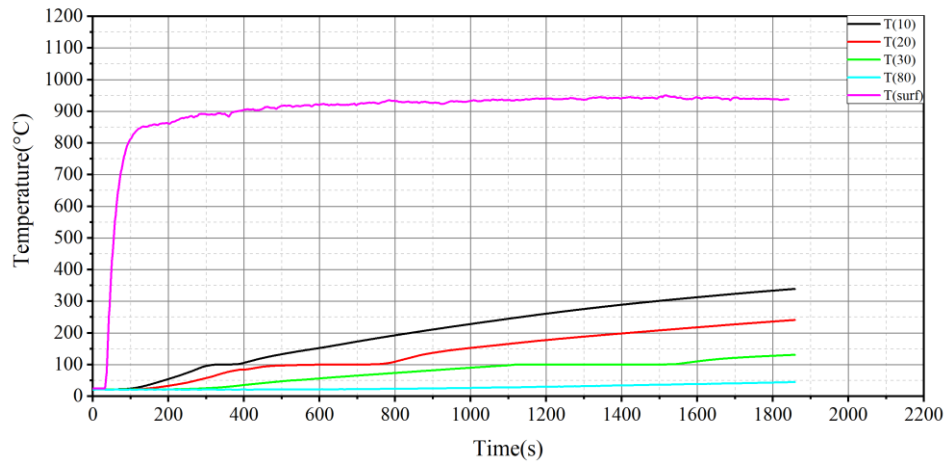
Figure 80: Temperature profiles for wall element 3 – WE3, w/c=0.30, concrete D (test date 1-7-2021, start at 12:52). Propane flame TC at 0mm, 10 mm, 20mm, 30 mm and 80 mm.

Table 25: Tests of wall elements with propane gas flame exposure. Average HRR of flame is 13.2 kW. No spalling occurred, just some fine cracks.

Wall element	W/C	Concrete type	PP-Fibers	Gas flow (g/min)	HRR flame (kW)	Spalling	Cracks
WE1	0.40	B	Yes	16.50	12.65	No	Fine
WE2	0.35	C	Yes	17.75	13.53	No	Fine
WE3	0.30	D	Yes	17.60	13.49	(No)[*]	Fine

6.1.6.1 Conclusions

No spalling occurred during the LPG (propane flame) tests as shown in Table 25. Therefore, there is no difference observed compared to the furnace setup tests.

6.1.7 Hydrogen tests on the wall elements

The above described reference experiments are made in order to predict in a more reliable way any effects that may arise from hydrogen jet flame impingements. The furnace test screened out a number of concrete types as described above. For the LPG and hydrogen tests 3 concrete types B, C and D with PP fibres have been selected as described in the previous chapter. The principal setup from these tests is shown in Figure 63. The placement of the thermocouples is shown in Figure 81 and Figure 82.

Figure 81: Placement of thermocouples in wall element (left) and first hydrogen test (right).
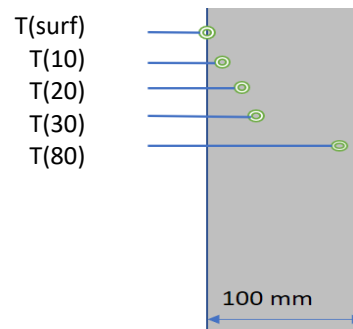
Figure 82: Placement of thermocouples to measure the temperature profiles in the concrete.

The experiments have been conducted within one working week, and the schedule for the different walls are as follows in Table 26.

Table 26: Hydrogen spalling experiments at North-Zealand's Fire School, Helsingør, Denmark.

Date	Experiment	Wall	Concrete type
02-03-2022 morning	1	3	w/c=0.30, concrete D with PP fibres
02-03-2022 afternoon	2	3	w/c=0.30, concrete D with PP fibres
03-03-2022 morning	3	2	w/c=0.35, concrete C with PP fibres
03-03-2022 - afternoon	4	2	w/c=0.35, concrete C with PP fibres
04-03-2022 - morning	5	1	w/c=0.40, concrete B with PP fibres
04-03-2022 - afternoon	6	1	w/c=0.40, concrete B with PP fibres

The first and second experiments used the high strength concrete D, the third and fourth experiments the concrete C and the fifths and sixths experiments concrete B. All concrete mixtures had added PP fibres.

The conduction of the experiment with a hydrogen jet flame is shown in the Figure 83 and Figure 84.

Figure 83: Photos during the hydrogen gas exposure test.

Figure 84: Photos during the hydrogen gas exposure test (left) and resulting spalling (right).

6.1.7.1   *Temperature measurements for spalling tests on concrete walls with hydrogen jet flames*

On the next six figures the measured temperatures are monitored during the hydrogen flame exposure tests. The temperatures are measured at the surface and in the depths of 10 mm, 20 mm, 30 mm and 80 mm. The holes are drilled from the side parallel to the concrete surface at the respective depths. Some validation has been done by measuring the depths for one of the tests.

The figures below (Figure 85, Figure 86, Figure 87, Figure 88, Figure 89, Figure 90) show the surface temperatures exceeding 1200 °C, while the temperature inside the concrete varies strongly, which is due to some thermocouples that got malfunctioning during the tests. The duration of the impinging flames is about 200s in all the experiments. The temperature profiles were followed over a much longer period. Nevertheless, the temperature rise inside the concrete reaches more than 200 °C in the experiments and presumably even above 400 °C close to the critical temperature for spalling.
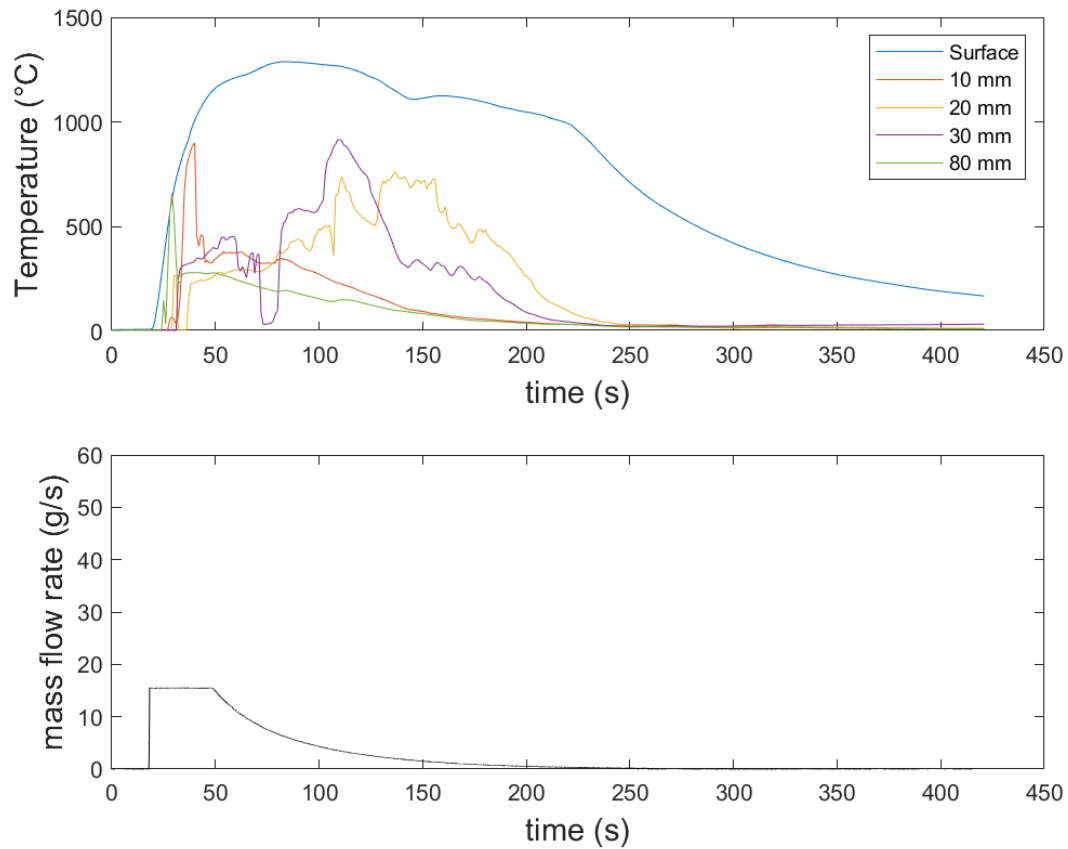
Figure 85: Temperature profile hydrogen flame for Wall Element 3 – WE3, w/c=0.30, concrete D (test date 2-3-2022, morning). Note: The mass flow rate is cut-off due to an error and not showing the maximum flow rate.
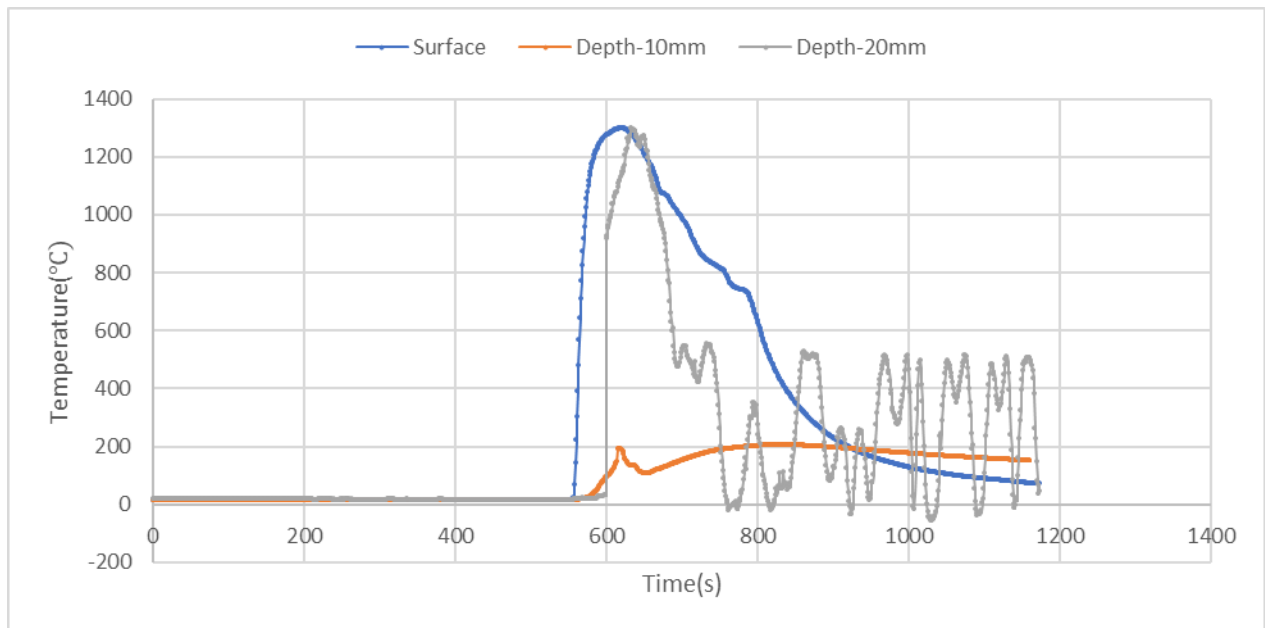
Figure 86: Temperature profile hydrogen flame for Wall Element 3 – WE3, w/c=0.30, concrete D (test date 2-3-2022, afternoon). Profile for 20mm depths is erroneous.
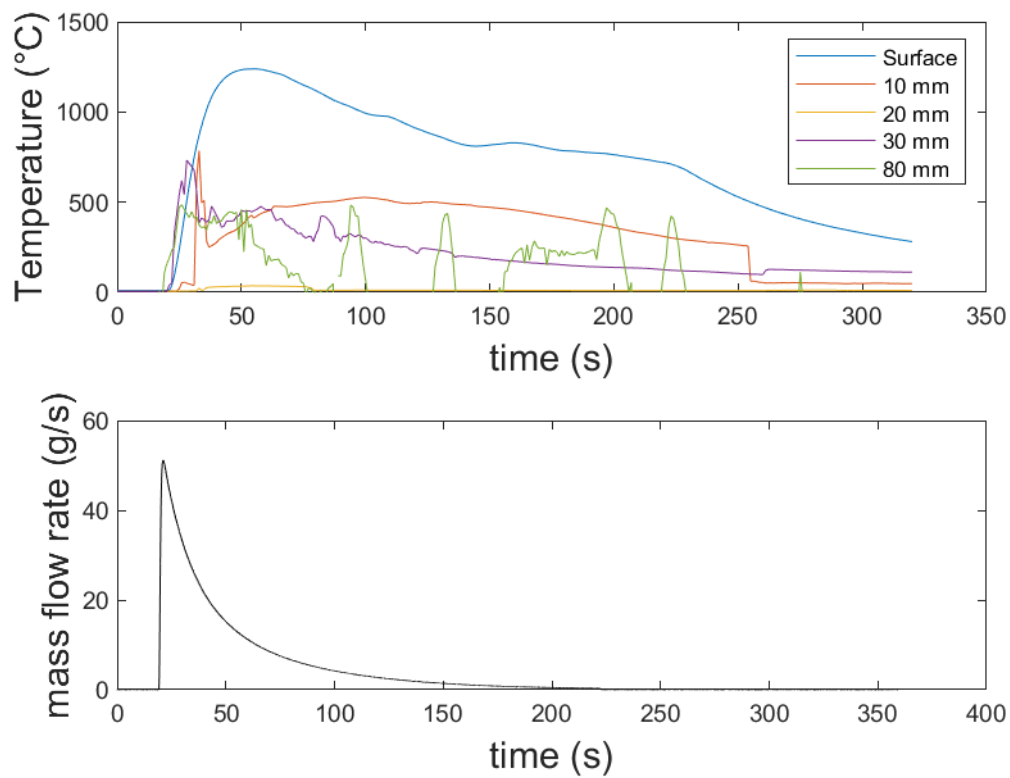
Figure 87: Temperature profile hydrogen flame for Wall Element 2 – WE2, w/c=0.35, concrete C (test date 3-3-2022, morning).
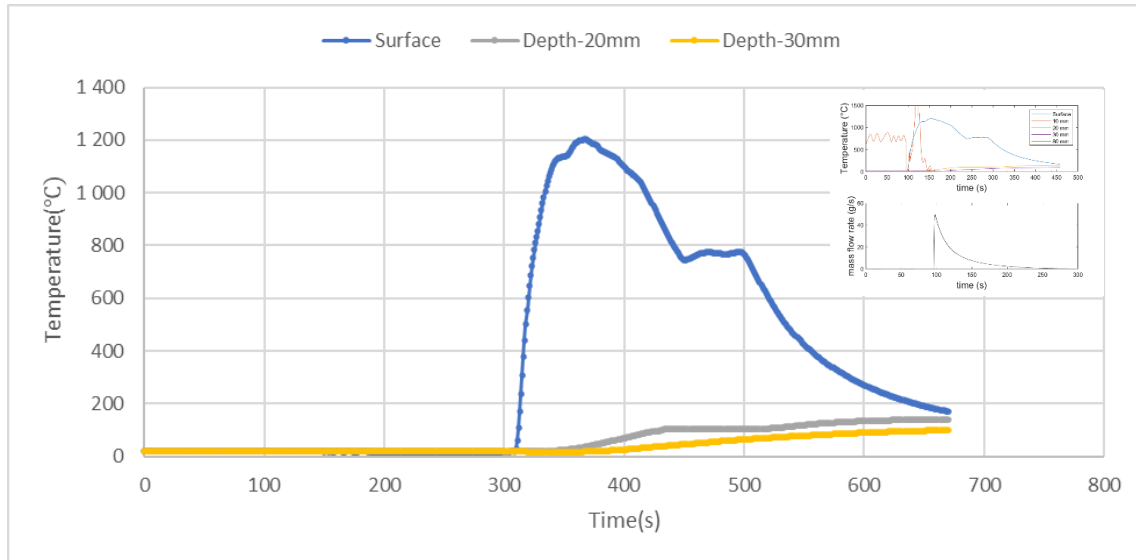
Figure 88: Temperature profile hydrogen flame for Wall Element 2 – WE2, w/c=0.35, concrete C (test date 3-3-2022, afternoon).
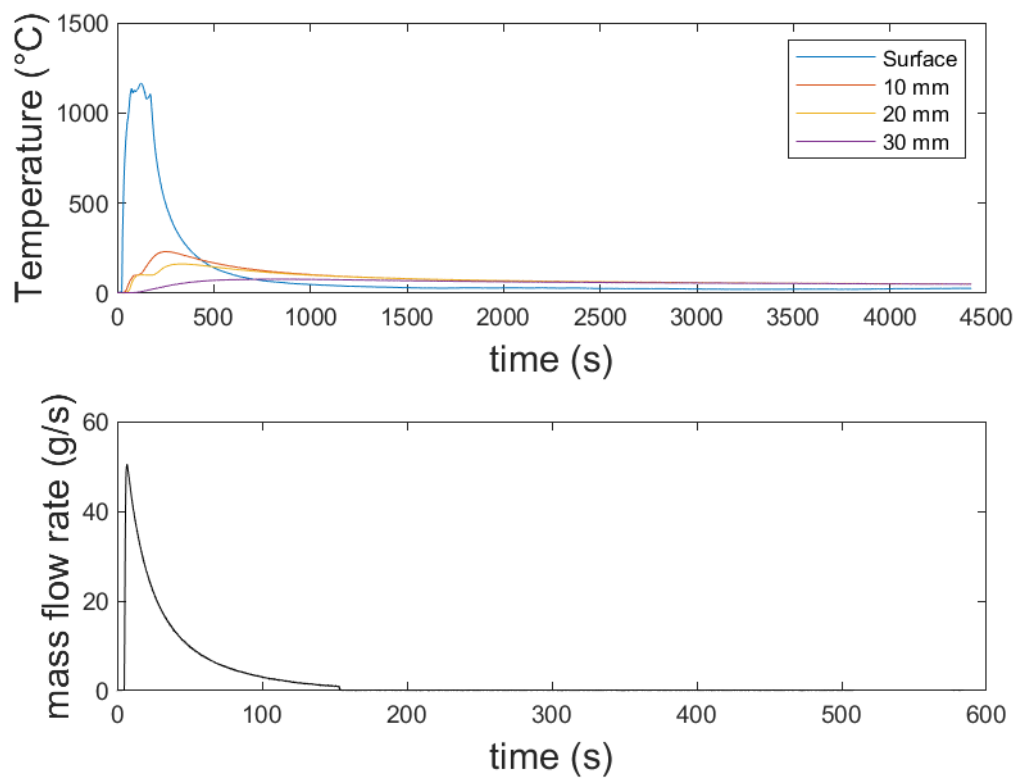
Figure 89: Temperature profile hydrogen flame for Wall Element 1 – WE1, w/c=0.40, concrete B (test date 4-3-2022, morning).
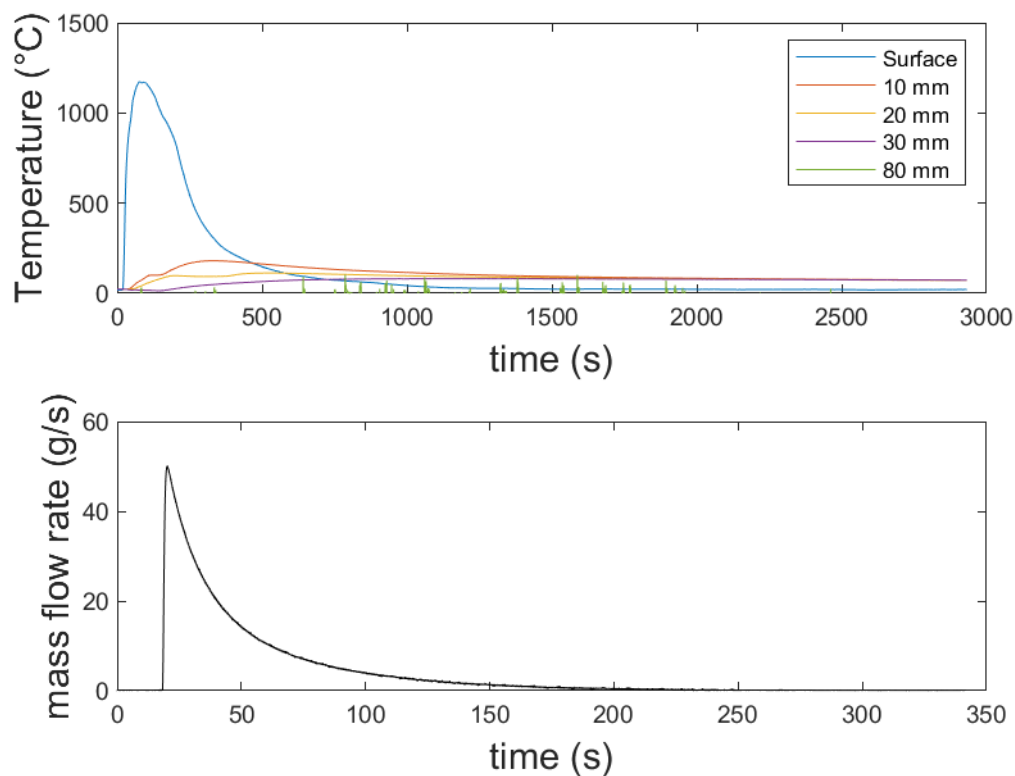
Figure 90: Temperature profile hydrogen flame for Wall Element 1 – WE1, w/c=0.40, concrete B (test date 4-3-2022, afternoon).

6.1.7.2 Conclusions

The experiments with the high pressure hydrogen jet flames show a very high temperature increase of the concretes surface to about 1200 °C and the surface showed some spalling behaviour even though the time of exposure is relatively short with about 200 s in the experiments with the limited amount of hydrogen.

The peak HRR of the hydrogen jet flame is calculated to about 8 MW, which is much higher than the propane flame with a constant HRR of 13.2 kW, as well as the HRR of about 45 kW/m² for the furnace. The maximum surface temperature is remarkable higher compared to the LPG tests with measured surface temperatures below 1000 °C using an exposure time of up to 1800 s.

6.1.8 Microstructural analysis of the concrete types exposed to a high pressure hydrogen jet flame

The exposed concrete parts in the hydrogen tests are further analysed. For each experiment the central area exposed by the jet flame are drilled out in form of a small cylinder. This was treated with alcohol and dried again and finally sealed in a plastic bag for transport. This procedure is chosen to prevent further concrete degradation after the heating period. Concretes chemistry after a heat exposure results in an additional loss of strength over a period of about a week (Hertz, 2019).

These cylinders are transferred to the Danish company Pelcon Materials & Testing ApS and in their laboratory treated with an epoxy containing fluorescence dye and cut into sections. The analysis for cracks and pores (see Figure 91) under a microscope is performed at DTU.

To analyse the microscopic fine structure of the hydrogen jet flame exposed concretes, nine fluorescence epoxy impregnated thin grinding sections of concrete were chosen. Each of the sample has a dimension of 45 x 30 mm, as shown in Figure 98. For each of the three different types of concrete core cylinders (wall 1 to 3) three thin grinded sections are chosen, i.e., two of the sections are taken starting at the surface, while one is chosen from the bottom. The latter one is assumed to be the reference sample, which structure has not been impacted to a substantial temperature increase. Two thin sections are very close to the concrete slab surface, and the height direction of these thin sections (about 0cm-4.5cm) is along with the depth direction of the concrete slab (10cm), such as sample 6-1 and 6-2. The 6-bottom section is extracted from the bottom part of the cylinder concrete which can ignore the influence of the hydrogen jet fire. It is therefore taken as the baseline for the investigations.
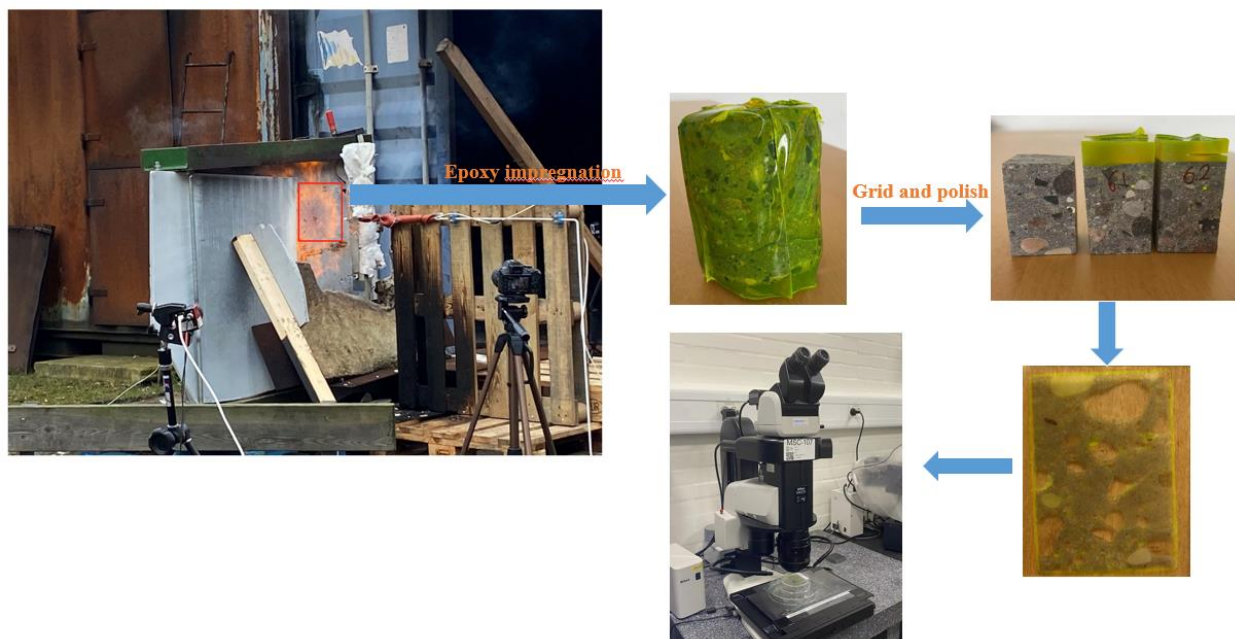
Figure 91: Testing procedure.

The samples are following the wall experiments 1 to 3.
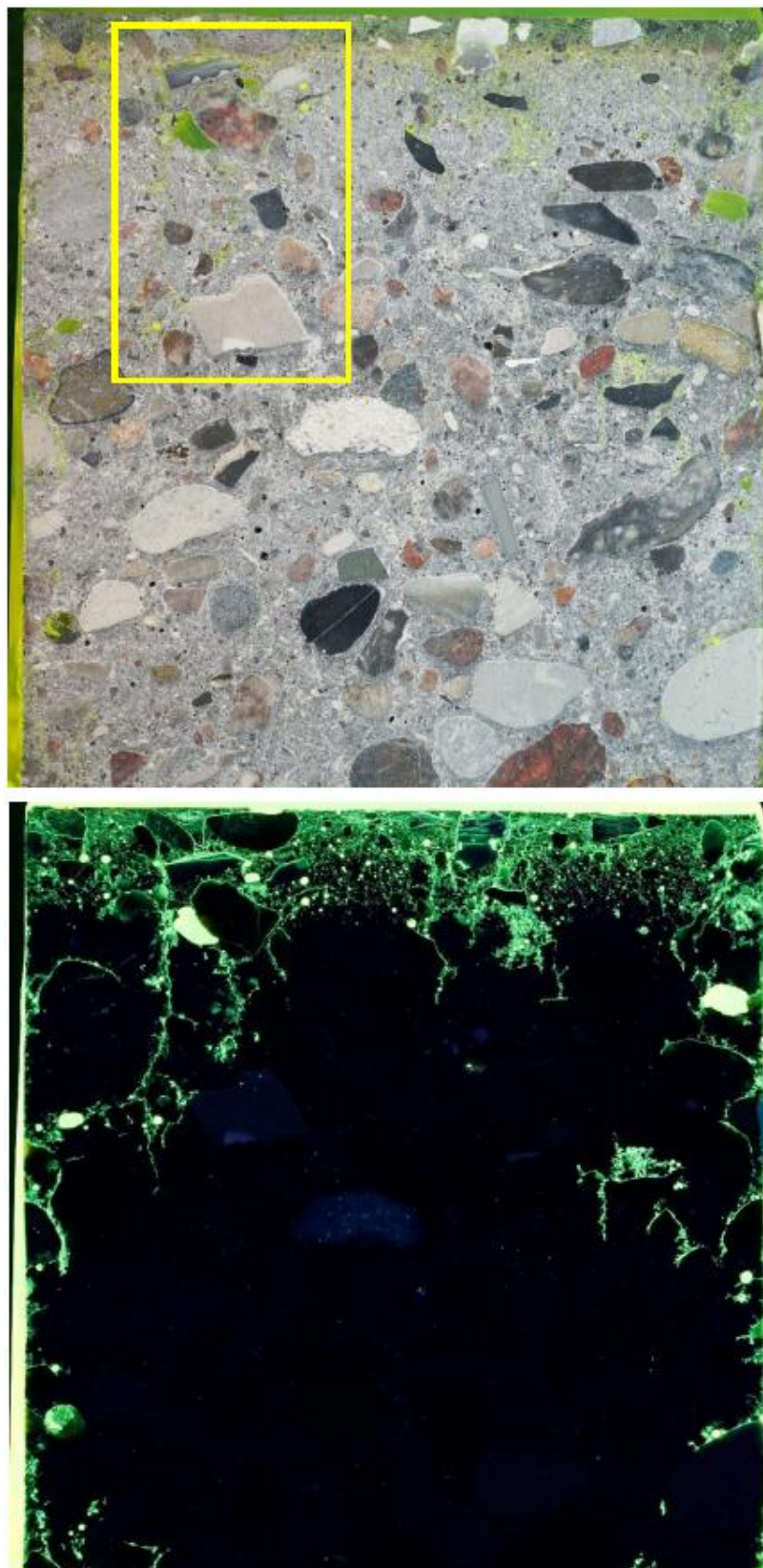
Figure 92: Wall 3 experiment 1: Core cylinder 1 after epoxy treatment and cutting in white light (top) and UV-light (bottom).
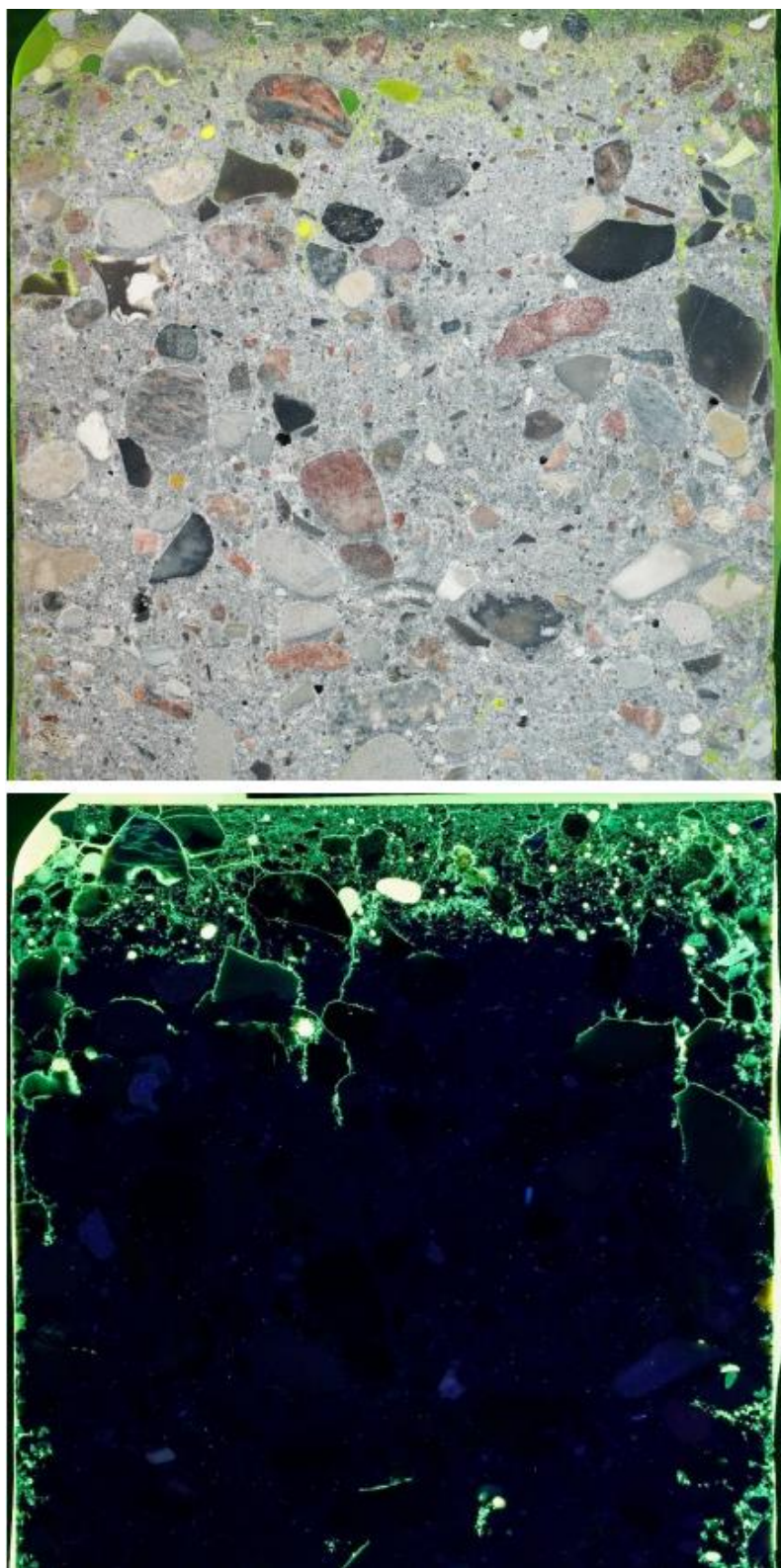
Figure 93: Wall 3 experiment 2: Core cylinder 2 after epoxy treatment and cutting in white light (top) and UV-light (bottom).
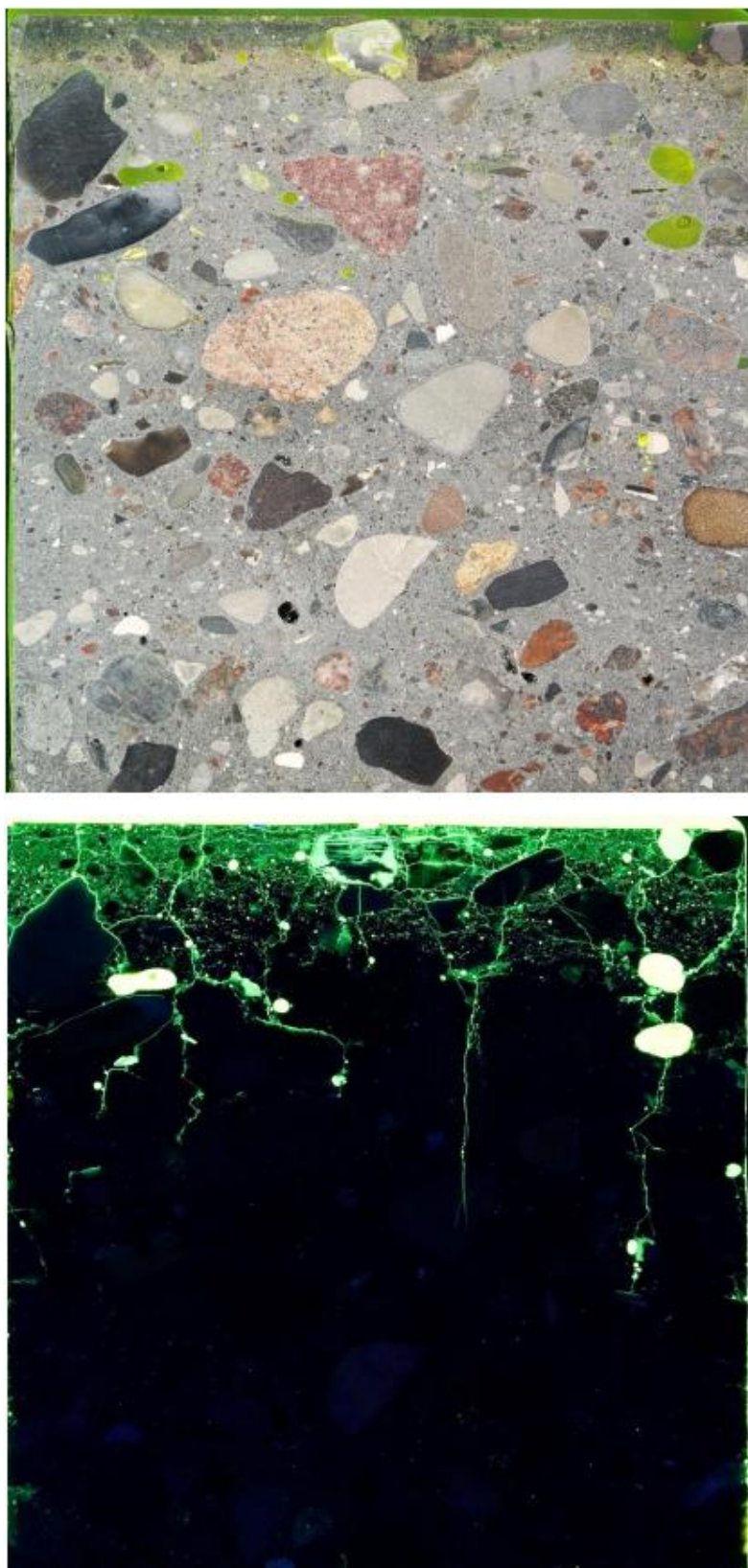
Figure 94: Wall 2 experiment 3: Core cylinder 3 after epoxy treatment and cutting in white light (top) and UV-light (bottom).
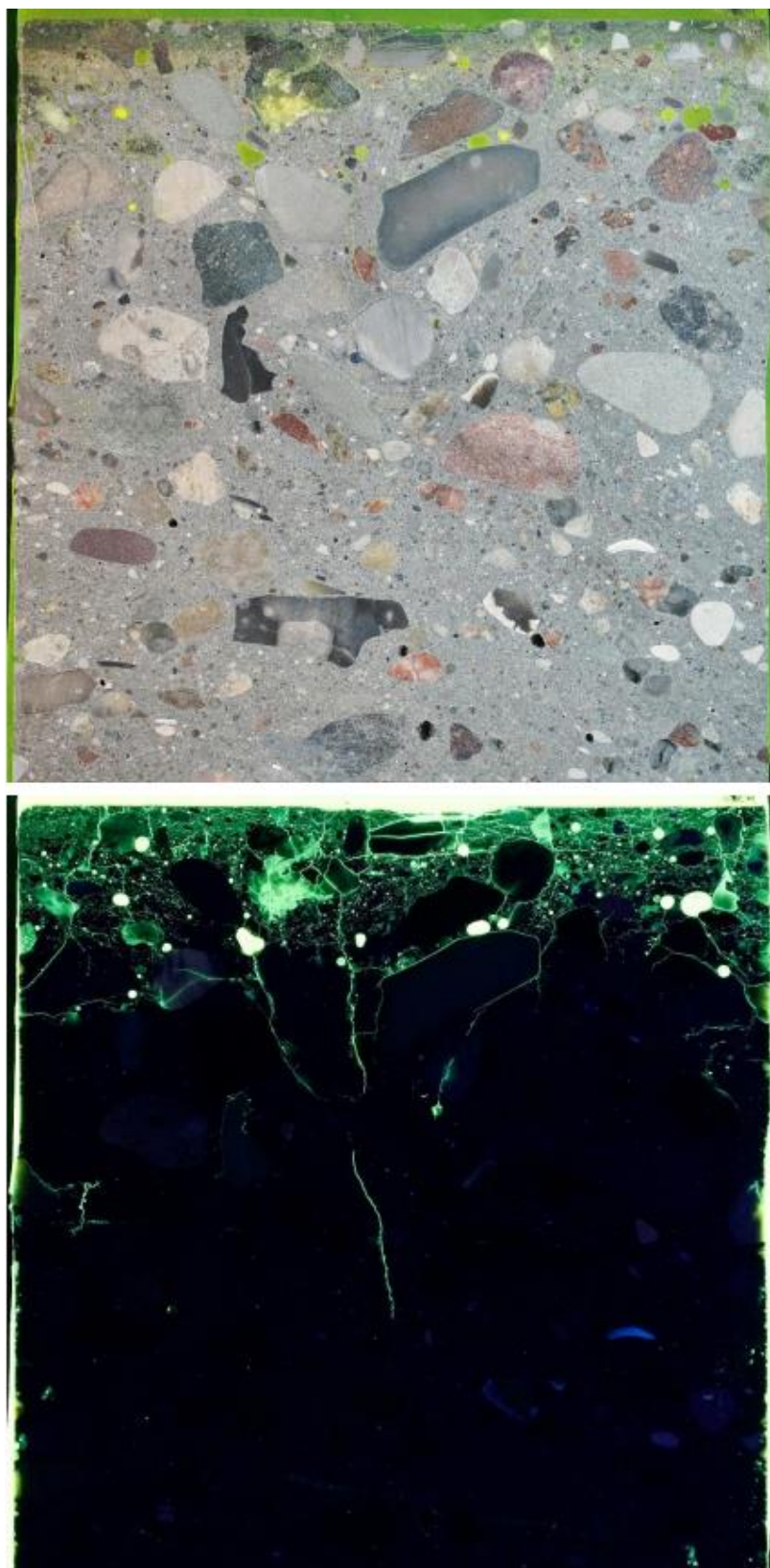
Figure 95: Wall 2 experiment 4: Core cylinder 4 after epoxy treatment and cutting in white light (top) and UV-light (bottom).
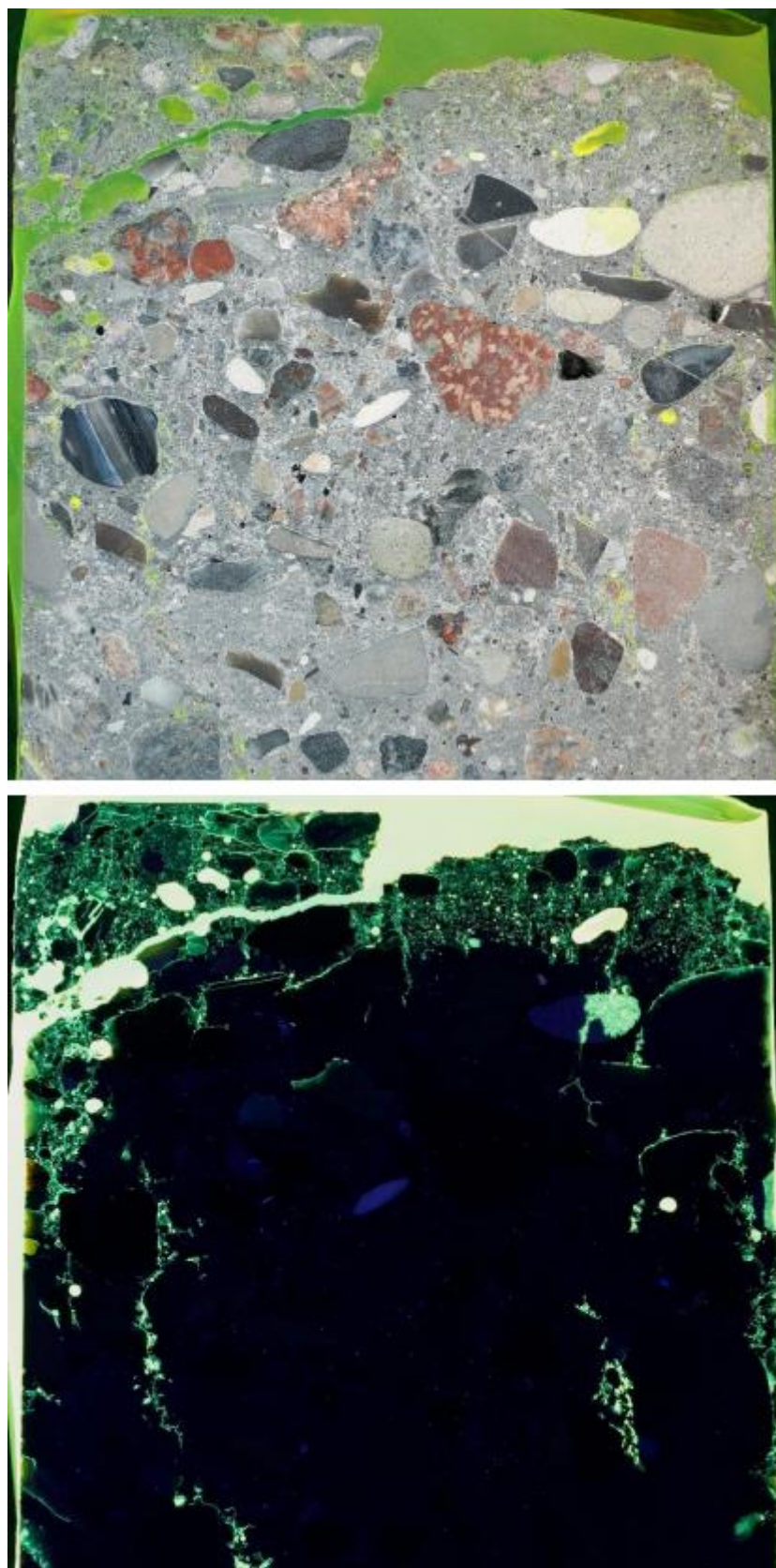
Figure 96: Wall 1 experiment 5: Core cylinder 5 after epoxy treatment and cutting in white light (top) and UV-light (bottom).
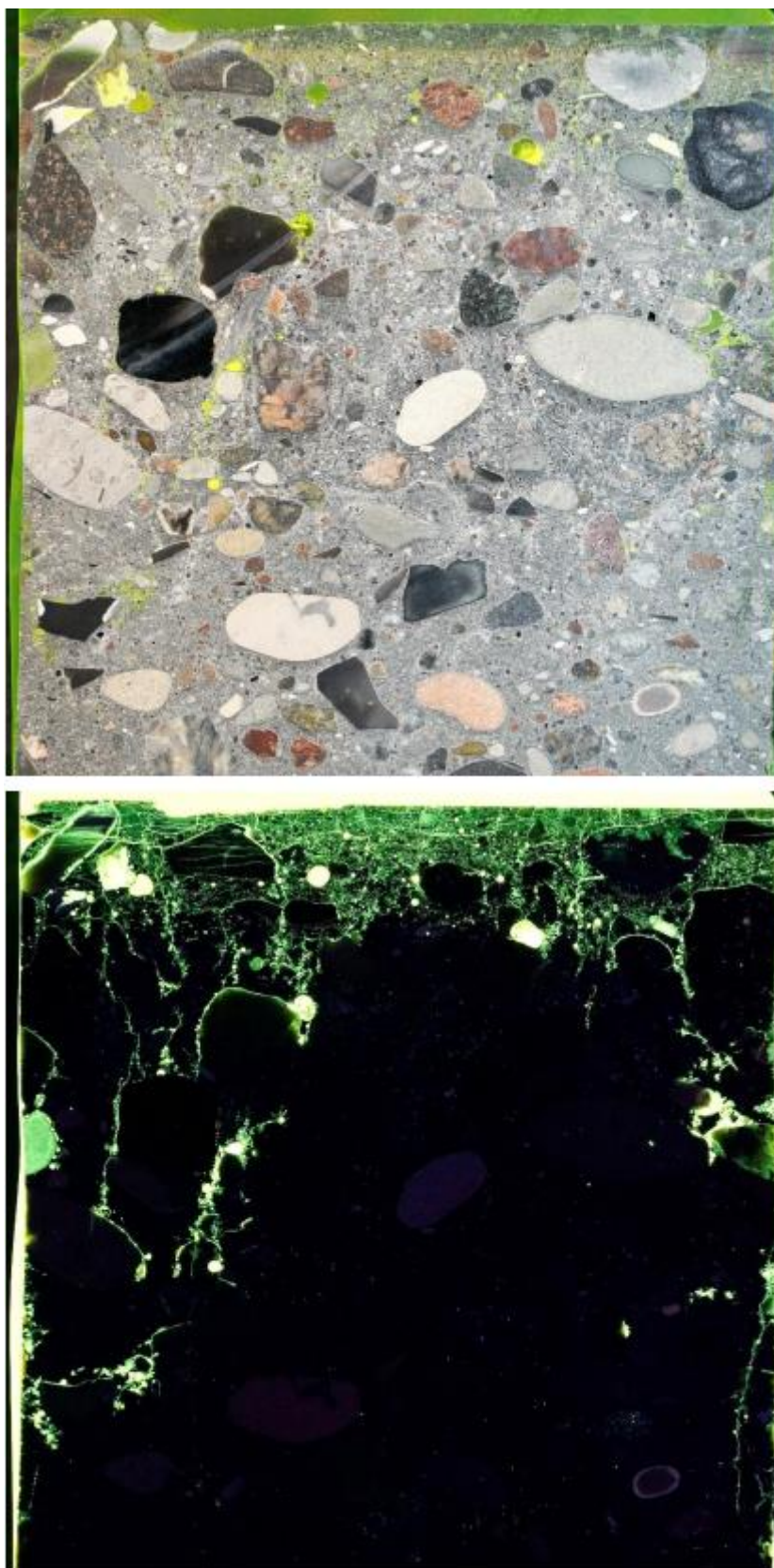
Figure 97: Wall 1 experiment 6: Core cylinder 6 after epoxy treatment and cutting in white light (top) and UV-light (bottom).

From the experiments 1 to 6 done pairwise on the some concrete walls 3 to 1, three samples covering the three wall concrete types D, C, B were chosen to establish a thin grinding samples for further analysis described in the following paragraphs.
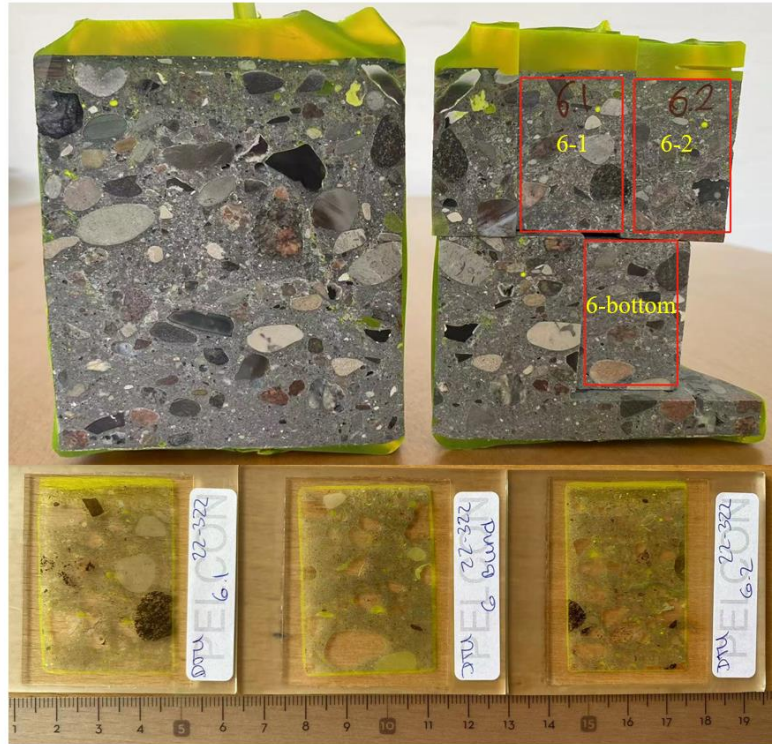
Figure 98: Fluorescence impregnated thin sections. Concrete type B.

6.1.9 Microstructural results and discussion

Below are reported the images obtained in the scanning microscope.

(a-1) Sample 6-bottom with grayscale processing	(b-1) Sample 6-1 with grayscale processing	(c-1) Sample 6-2 with grayscale processing
(a-2) Sample 6-bottom	(b-2) Sample 6-1	(c-2) Sample 6-2
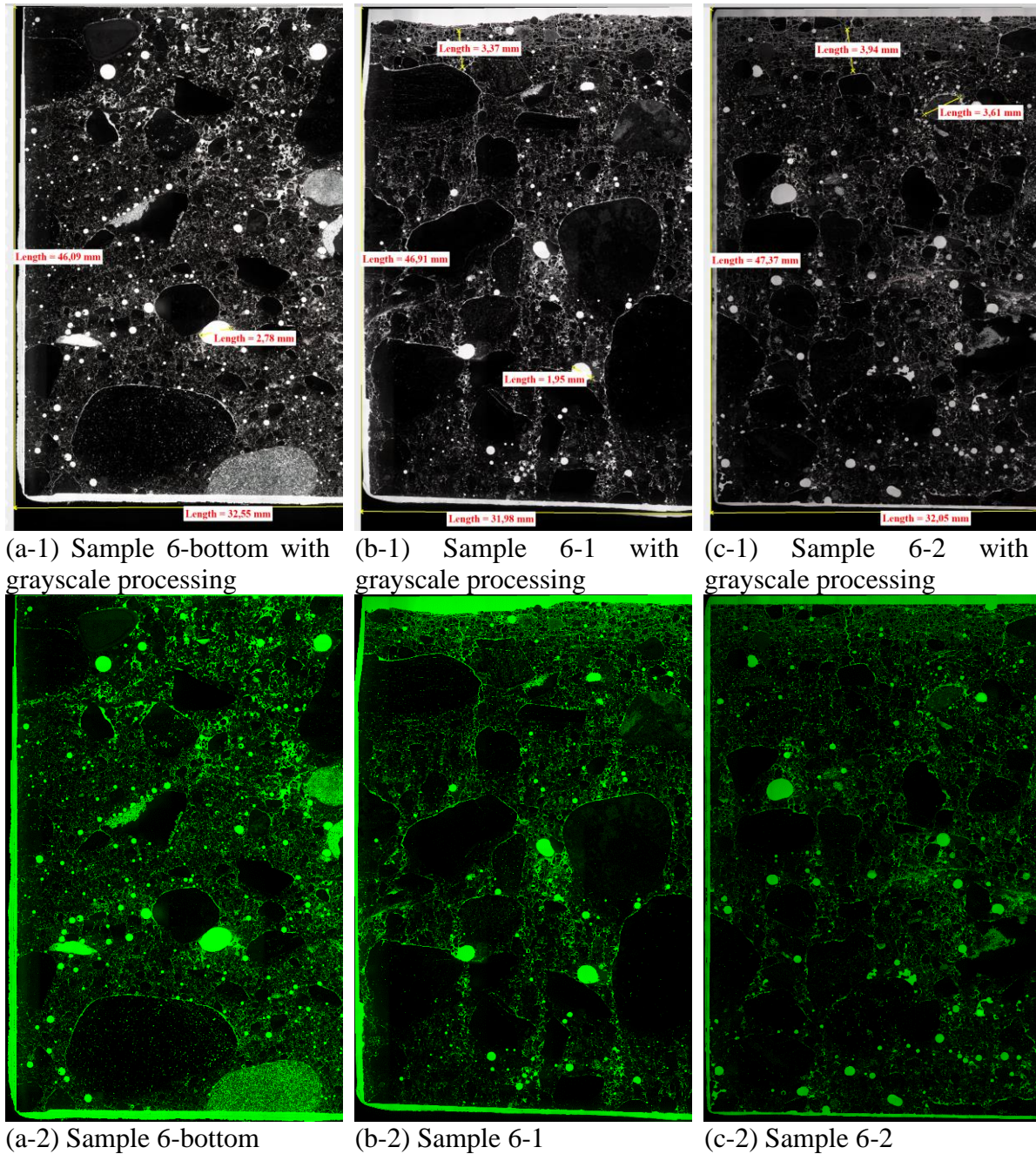
Figure 99: Sample 6 (experiment 6 with concrete type B) after scanning.

(a-1)2-bottom with grayscale processing

(b-1)2-1 with grayscale processing

(c-1)2-2 with grayscale processing

(a-2)2-bottom

(b-2)2-1

(c-2)2-2
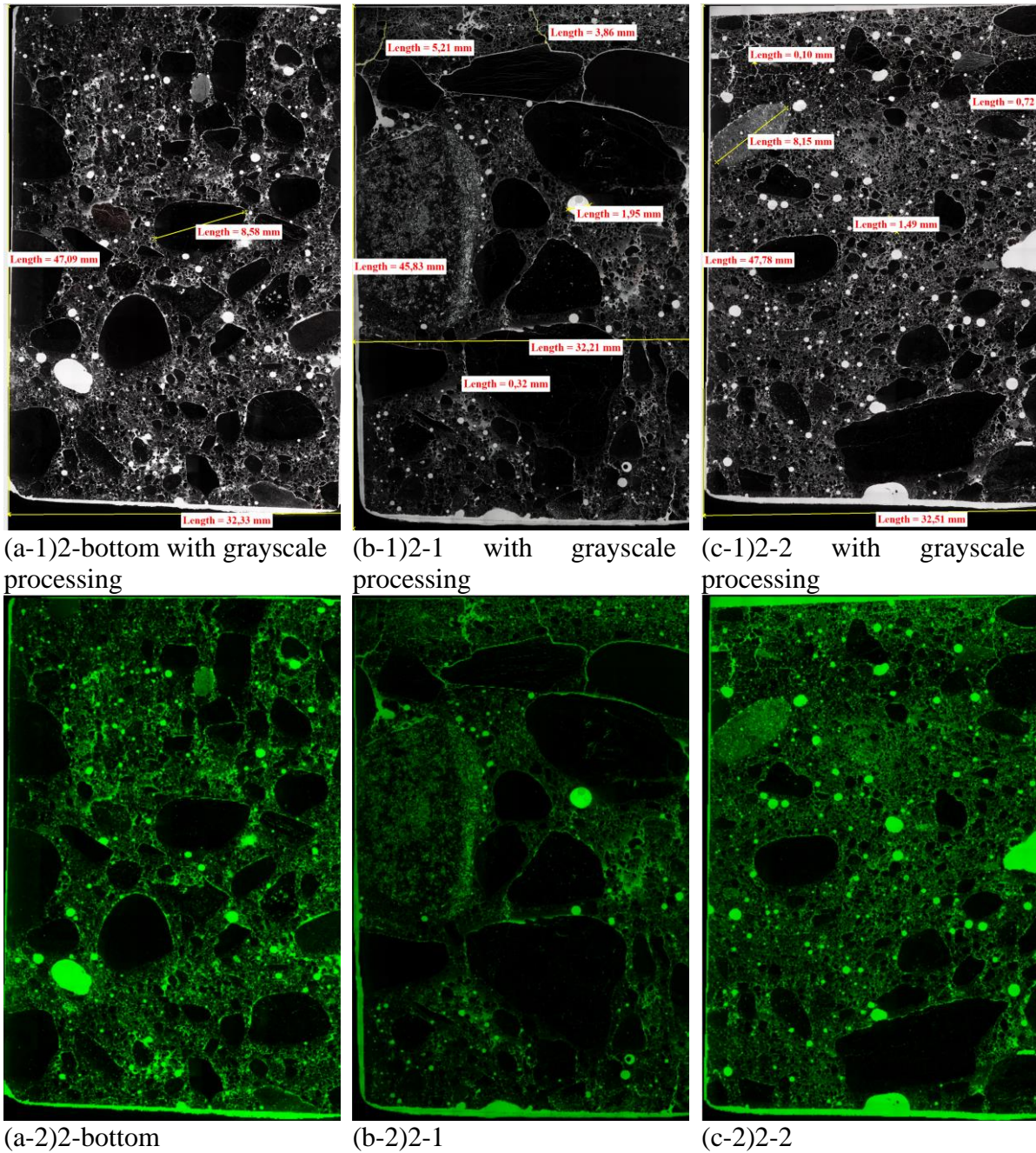
Figure 100: Sample 2 from experiment 2 with concrete type D after scanning.

(a-1)3-bottom with grayscale processing

(b-1)3-1 with grayscale processing

(c-1)3-2 with grayscale processing

(a-2)3-bottom

(b-2)3-1

(c-2)3-2
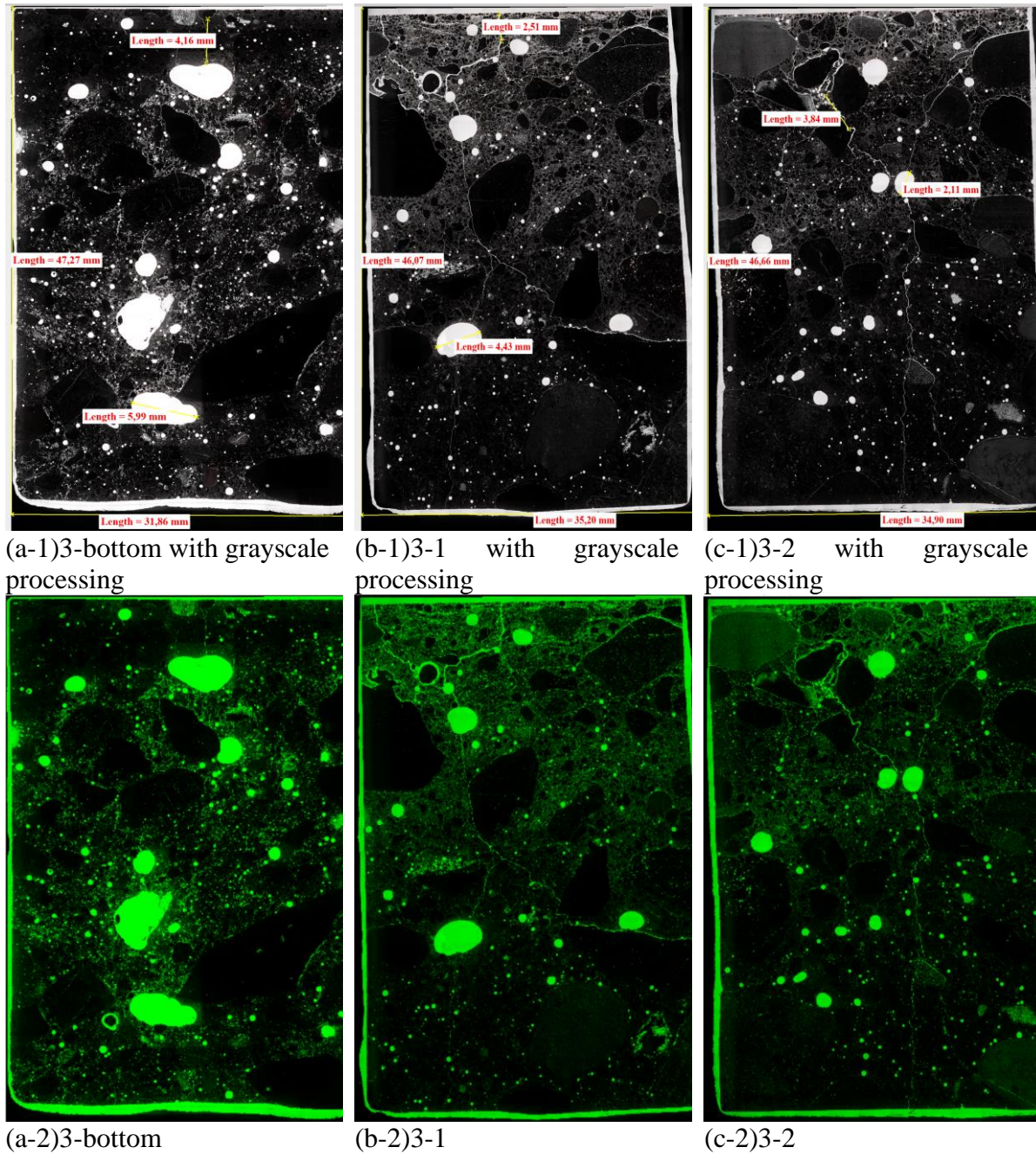
Figure 101: Sample 3 from experiment 3 with concrete type C after scanning.

6.1.10 Defect distribution of concrete sample-6 at different depth
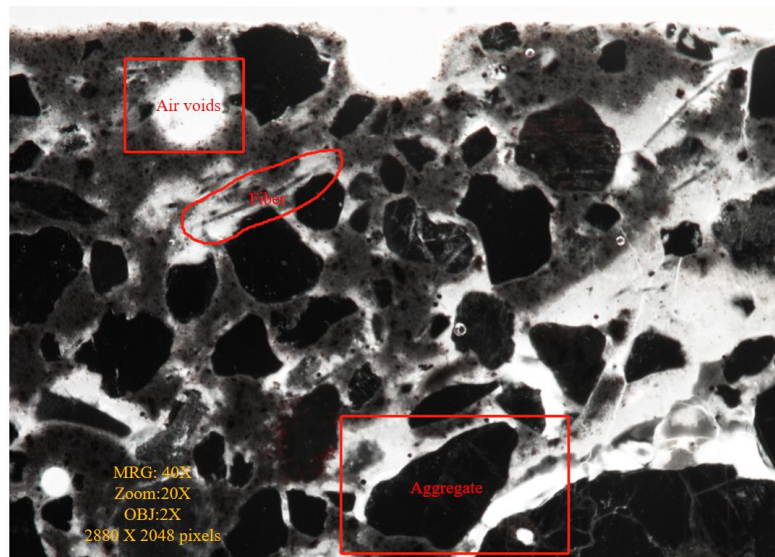
Figure 102: Sample 6-bottom image of sample 6 taken from wall 3 concrete type B.

The defects in concrete mainly include micro-cracks and pores. Hereunder, it is assumed that the micro-cracks are caused both by the concrete casting and the exposure to elevated temperatures. Based on the classification of pores suggested by Visser, three types of pores are usually observed in concrete, namely micro-pores (<10 nm), capillary pores (10-200 nm), and air voids(>200 nm). Due to the limitation of the SMZ25 optical microscope, capillary pores and micro-pores are difficult to observe.

Figure 102 is the scanning image obtained by the SMZ25 optical microscope with grayscale processing. This image is in the sample 6-bottom and the temperature of this position is approximate to the ambient temperature. Thus, air voids, fibres and aggregates can be seen in this image except for cracks.

Figure 103 and Figure 106 are the images shown that are analysed using an adaptive threshold. These images are chosen through the position of temperature measurement points in the concrete slab under hydrogen jet fire. According to Figure 103 and Figure 106 it can be seen that cracks are gradually disappearing with increasing concrete core cylinders depth. It is observed that the hydrogen jet fire exposure of 200 s has no influence on the crack development of the concrete core at depths larger than 1.8 cm.

(1) Sample 6-1   (2) Sample 6-2
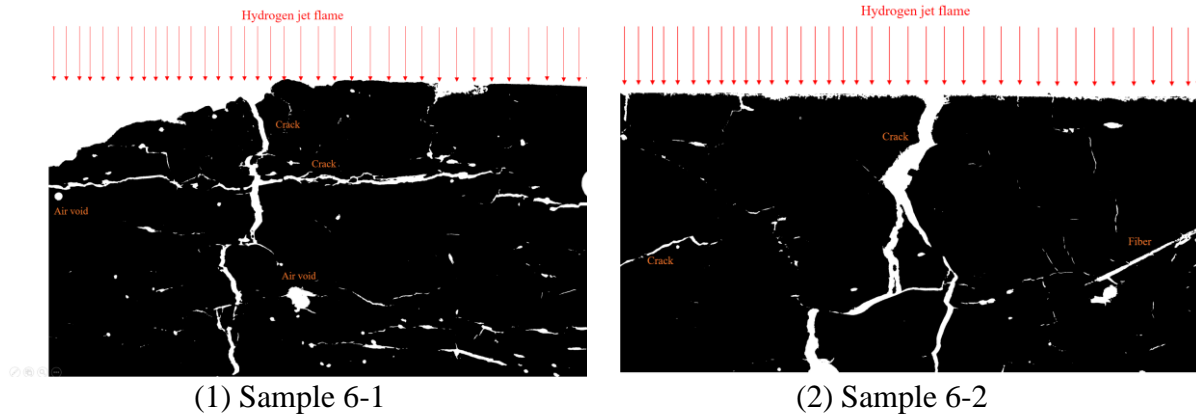
Figure 103: Sample images in the concrete slab depth from 0cm to 0.2cm (surface T>1200℃).

(1) Sample 6-1   (2) Sample 6-2
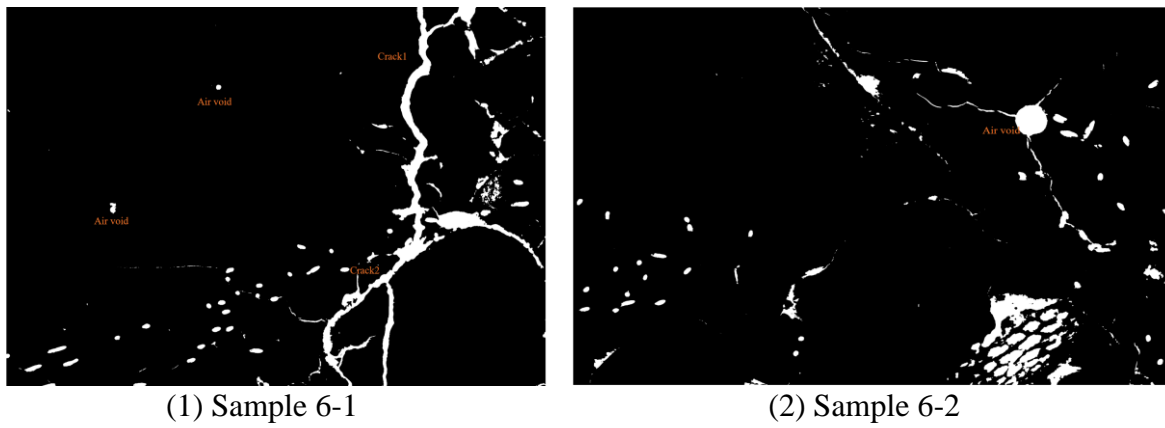
Figure 104: Sample images in the concrete slab depth from 0.8cm to 1cm (T=180℃).

(1) Sample 6-1   (2) Sample 6-2
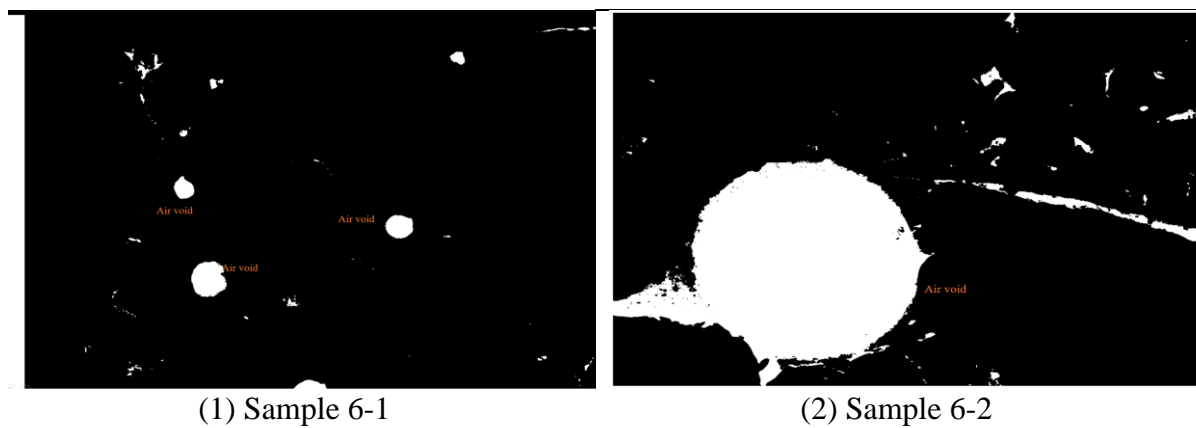
Figure 105: Sample images in the concrete slab depth from 1.8cm to 2cm (T=97℃)
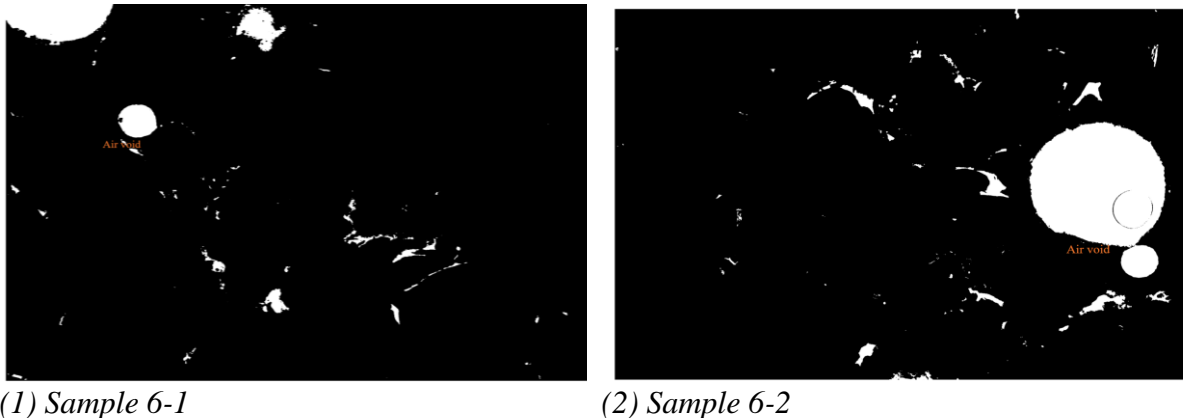
(1) Sample 6-1   *(2) Sample 6-2*

Figure 106: Sample images in the concrete slab depth from 2.8cm to 3cm (T=80℃).

6.1.10.1 Comparison of defects dimension in different samples

Table 27: Pores and cracks results.

Sample	Total area of pores (cm^2)	Number of pores	Pore area ratio (%)	Total area of major cracks (cm^2)	Major cracks area ratio (%)
3-bottom (ref.)	1.09224	253	8.09	0.003047	0.0226
3-1	0.4205567	334	3.12	0.02491783	0.184
3-2	2.723031	380	20.17	0.03761483	0.279
2-bottom (ref.)	0.184844	224	1.37	0	0
2-1	0.147362	175	1.09	0.013292	0.0985
2-2	0.3364267	293	2.49	0.01617883	0.12

Some defects' (closed to the concrete core cylinders surface in the different samples) dimensions are shown in the following pictures (Figure 107, Figure 108 and Figure 109). It can be seen that the pore diameter and crack width in sample-3 are larger than that in other samples. The macro-cracks always appear in the samples, which are closer to the concrete slab surface. This indicates that the test's hydrogen jet flame only can cause the concrete thermal damage for very short depth. The air voids not only can be seen in the bottom sample, but also can be found in the top sample. This is because the air voids are caused by the concrete curing and casting.

(a) Sample 6-bottom

(b) Sample 6-1
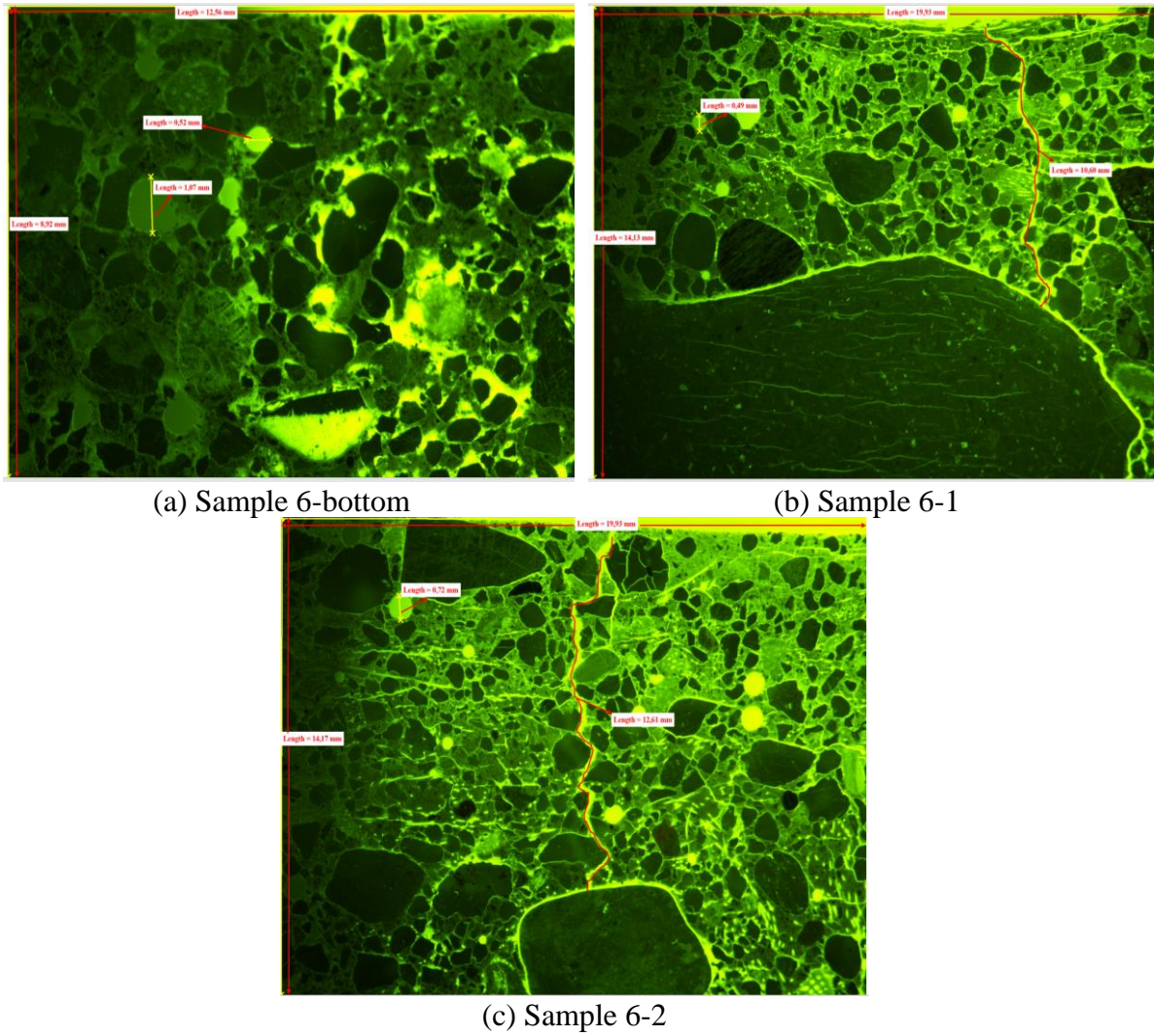
(c) Sample 6-2

Figure 107: Dimension of some defects close to the sample 6 surface.

(a) Sample 3-bottom

(b) Sample 3-1
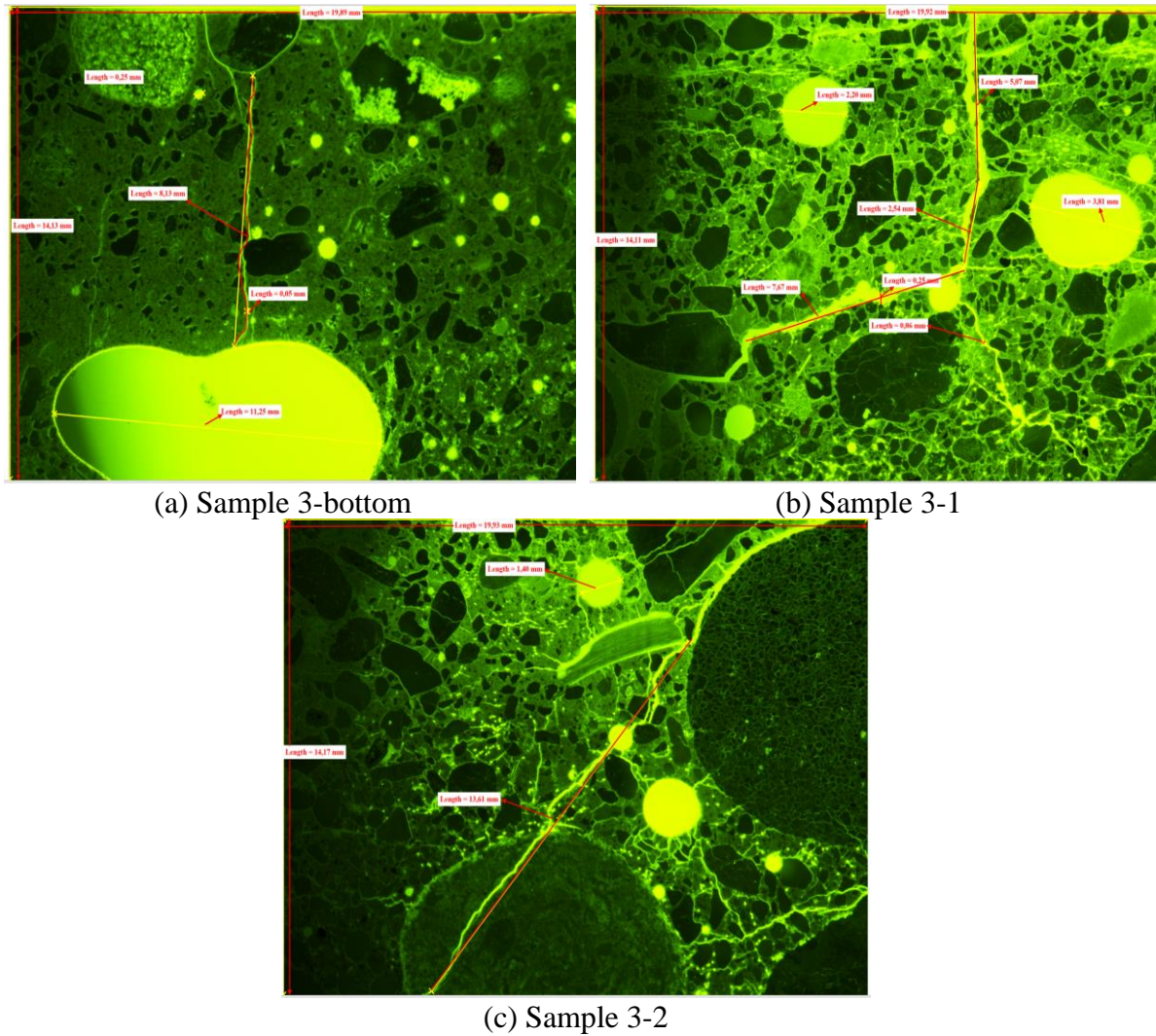
(c) Sample 3-2

Figure 108: Dimension of some defects close to the sample 3 surface.

(a) Sample 2-bottom

(b) Sample 2-1
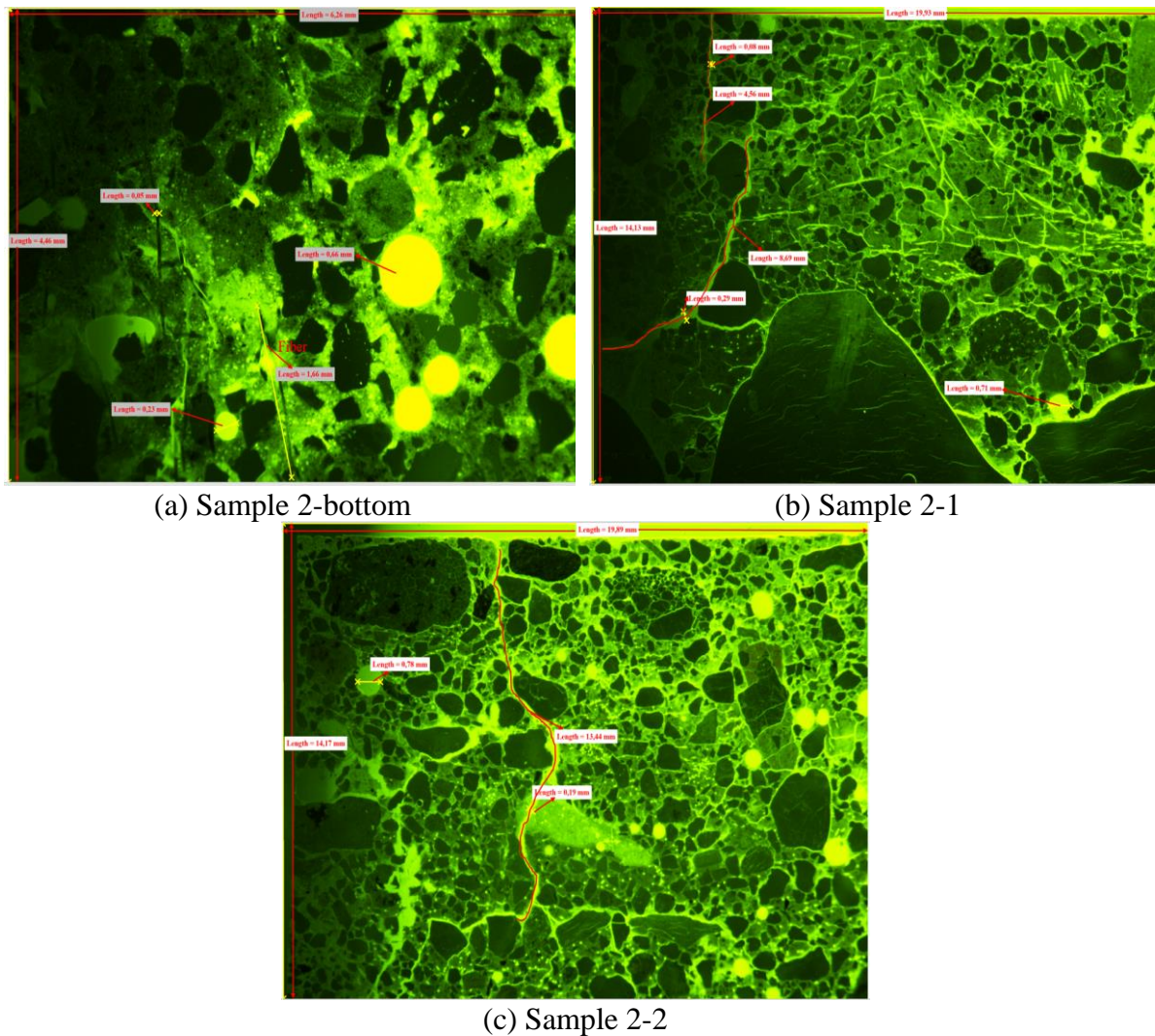
(c) Sample 2-2

Figure 109: Dimension of some defects close to the sample 2 surface.

6.1.11 Conclusions

The tests in the first standard cylinder tests (Hertz & Sørensen, 2005) found the types of concrete recipes showing spalling or not. The concretes without spalling were selected for the LPG and hydrogen flame experiments. None of these LPG (propane) gas flame tests showed sign of spalling. These 3 concrete types are also tested being exposed by an impinging high pressure hydrogen flame (700 bar initial pressure, 3 mm nozzle). For the hydrogen flame exposure tests, it was only the wall element 1 made of concrete B (dense, w/c=0.40, 1 % MC and 1% PP) that did not show severe sign of spalling. The denser higher strength concrete types C and D showed some spalling on the surface. Microscopic analysing revealed that heat related cracks are seen up to about 2 cm into the concrete under the test conditions described above.

For the microstructural analysis we can conclude that:

(1) In elevated temperature, the micro-cracks of concrete can grow and develop to form macro-cracks. Cracks disappeared gradually with the concrete slab depth increasing.
(2) When the concrete slab depth is more than 1.8 cm, the hydrogen jet fire has no influence on the development of concrete crack for the here described exposer of an impinging initial 8 MW hydrogen flame lasting for 200 s.

(3) Longer lasting hydrogen flames using a larger amount of hydrogen and/or smaller nozzle sizes may lead to an increased heating of the concretes raising the temperature at greater depth inside the concrete.

6.2 Effect of hydrogen jet fires on the erosion of tunnel road materials and lining materials (ST3.4.4, HSE)

6.2.1 Introduction and scope

It is envisaged that hydrogen as a fuel will play an essential role alongside battery technologies in the attempts to decarbonise transport. Fuel Cell Hydrogen (FCH) vehicles represent a valid alternative to replace current internal combustion engines. The use of FCH vehicles, and thus introduction of hydrogen gas in tunnels and other confined spaces such as underground car parks, maintenance shops, garages, etc. does however raise concerns in terms of safety of users, as well as impact for property and environment protection. There is a need to develop validated hazard and risk assessment tools for the behaviour of hydrogen in tunnels, as concluded by the internal HyTunnel project by European Network of Excellence HySafe (NoE HySafe) (HyTunnel-D111, 2009).

The HyTunnel-CS project has specifically examined the consequences of potential accidents associated with the onboard hydrogen storage system used in FCH transportation. The scope of the project is primarily limited to the high-pressure storage vessel and associated fittings that may operate at high pressure and release large quantities of hydrogen over a short timeframe. In assessing the consequence, the project will determine the extent and severity of an accident but will not determine the frequency of a particular accident pathway. The project aims to identify prevention and mitigation strategies and engineering solutions for inherently safer use of hydrogen, including tunnels and similar confined spaces.

HyTunnel-CS Work Package 3 assessed the thermal and pressure effects of hydrogen jet fires in tunnels and confined spaces. Five accident scenarios were identified in HyTunnel-CS D1.3 (Pursell & Garcia, 2019) that related to active jet fires and the consequences, these were:

1. Hydrogen jet fire in confined spaces with limited ventilation
2. Hydrogen jet fire and vehicle fire in a mechanically ventilated confined space (maintenance shop/ underground parking)
3. Hydrogen jet fire impingement on a tunnel
4. Hydrogen jet fire and vehicle fire in a tunnel
5. Fire spread in underground parking.

As part of the programme of work outlined in the HyTunnel-CS description of work, HSE has undertaken Sub-Task 3.4.4 and performed an experimental campaign into aspects of Scenario 3 - hydrogen jet fire impingement on a tunnel. The aim of Task 3.4.4 is to establish the effect of hydrogen jet fires on the integrity of construction materials found within tunnel structures.

6.2.2 Aims of testing

There were two main aspects that formed the focus of this experimental work.

The first aspect was to understand the nature of the jet release itself e.g., blowdown characteristics, magnitude of temperature and pressure, flame length. The second aspect was to investigate the effects of the jet flame impinging on concrete, e.g., spalling, thermal effects, potential structural degradation.

The overall aim for Sub-Task 3.4.4 was to begin to define elements that could form part of a standard materials test for protective materials from a representative burning hydrogen jet and to provide recommendations for relevant Regulations, Codes, and Standards (RCS).

6.2.3 Supporting literature

6.2.3.1 Structural integrity of tunnels

As part of the objectives for HyTunnel-CS D1.1 report (Xu et al., 2019), a review was carried out where the structural integrity of tunnels was considered, specifically looking at concrete lining degradation in high temperatures, applied counter measures and the test scenarios that form part of the standards for confirming efficacy of the counter measures. These features are discussed in more detail in deliverable D1.1 (Section 4. "Structural protection") and the main features from the report are represented here.

6.2.3.2 Concrete lining degradation in high temperatures

Structural material layers intended to offer functionality such as fire protection and waterproofing are usually incorporated into tunnel design, the specific features of which will be based on the conditions and intended usage of the tunnel, as illustrated in Figure 110, which relates to the tunnel design for the London Elizabeth east-west railway line (Coughlan et al., 2017).
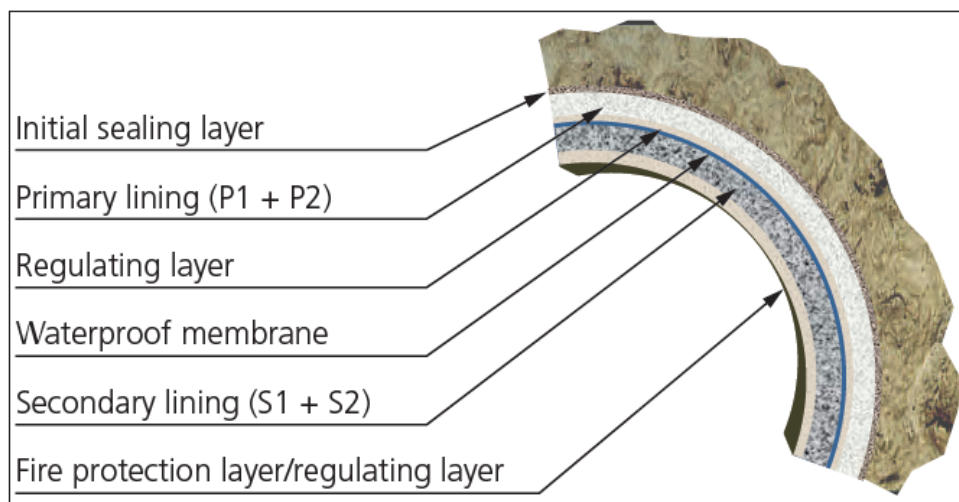
Figure 110: Tunnel design for the London Elizabeth east-west railway line (Coughlan et al., 2017). The primary and secondary linings have been constructed using sprayed concrete and applied to differing thicknesses. The secondary lining, as well as being designed to resist forces, such as long-term ground loadings and shrinkage, was also designed to have sufficient residual capacity to resist these forces after a tunnel fire, allowing for degradation of the lining due to the fire, up to 75mm depth.

When concrete is subjected to high temperatures i.e.,>300 °C, the aggregates and steel reinforcements (if present) begin to expand. At the same time shrinkage also occurs due to "burning off" of the water content, forming steam. These thermal effects, depending on the composition of the concrete, can result in formation of cracks or spalling.

Fire protection measures to mitigate for these effects are factored into tunnel design, as illustrated in Figure 110 and can include:

- Application of a secondary cementitious layer to the tunnel surface
- Application of fire-resistant cladding to the tunnel surface

- Incorporation of specific fibres e.g., polypropylene (PP) fibre, into the concrete mix to reduce internal stresses when subjected to fire.

6.2.3.3 Tests scenarios for fire protection measures

The nature and severity of a fire will differ from one event to the next, influenced by factors such as the fuel source and the available ventilation. Fires have been categorized into three scenarios: building fires, hydrocarbon fires, and tunnel fires. Corresponding standard fire scenarios have been established based on real fire experiments, for testing, modelling and design purposes.

The fire scenarios are typically represented as a time-temperature curve, where the materials of interest are exposed to an increasing temperature profile over a time period that is representative of the potential fire progression that may occur in that scenario. These time-temperature curves have been incorporated into standards, such as ISO834 (International Organization for Standardization, 1999), various Eurocodes, and have facilitated classification of building elements based on their durability in specified fire conditions. Figure 111 shows an illustration of the most popular fire curves, including those related to tunnel design e.g., the RWS (representing a severe hydrocarbon fire, such as from a petrol tanker, in a tunnel) and RABT-ZTV (a rapid initial temperature rise, with varying temperature drop-off duration depending on the selected vehicle scenario i.e., train or car).
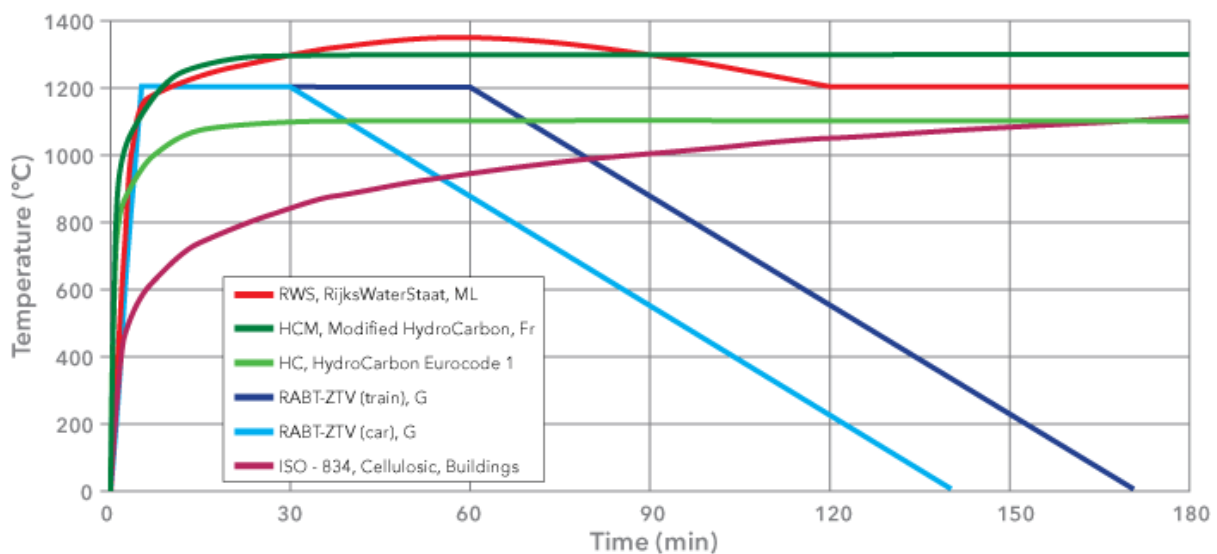
Figure 111: Illustration of the time/temperature curves for a series of fire scenarios (image taken from www.promat.com).

As seen in Figure 111, these fire scenarios are of long duration e.g., the RWS curve accounts for tunnels reaching 1200 °C in 10 minutes, 1370 °C in 1 hour and cooling to a steady state of 1200°C, over 2 hours. The structural elements will get significantly heated over this time duration, causing degradation of the mechanical properties and possible structural failure.

Hydrogen jet fires on the other hand, due to the limited inventory, would be expected to provide a short i.e., of the order of minutes, but very intense flame e.g., up to 2210 °C in adiabatic conditions. This mechanism of rapid local heating is known to negatively affect concrete and steel materials as discussed in HyTunnel-CS D1.2, Section 3.2 "Hydrogen jet fires" (Cirrone et al., 2019).

There have been numerous studies performed, aiming to identify factors that influence propensity of concrete to spall, such as the effect of external loading during testing, addition of polypropylene fibres, influence of sample size on stress release.

Unfortunately, the influence of specific spalling parameters is difficult to assess and compare with others due to differences in the testing procedures applied during these studies. Mohammed et. al. have attempted to summarise the main work that has been performed in the field of spalling, with a particular focus on the factors that are deemed to be highly influential (Mohammed et al., 2022), as shown in Figure 112.
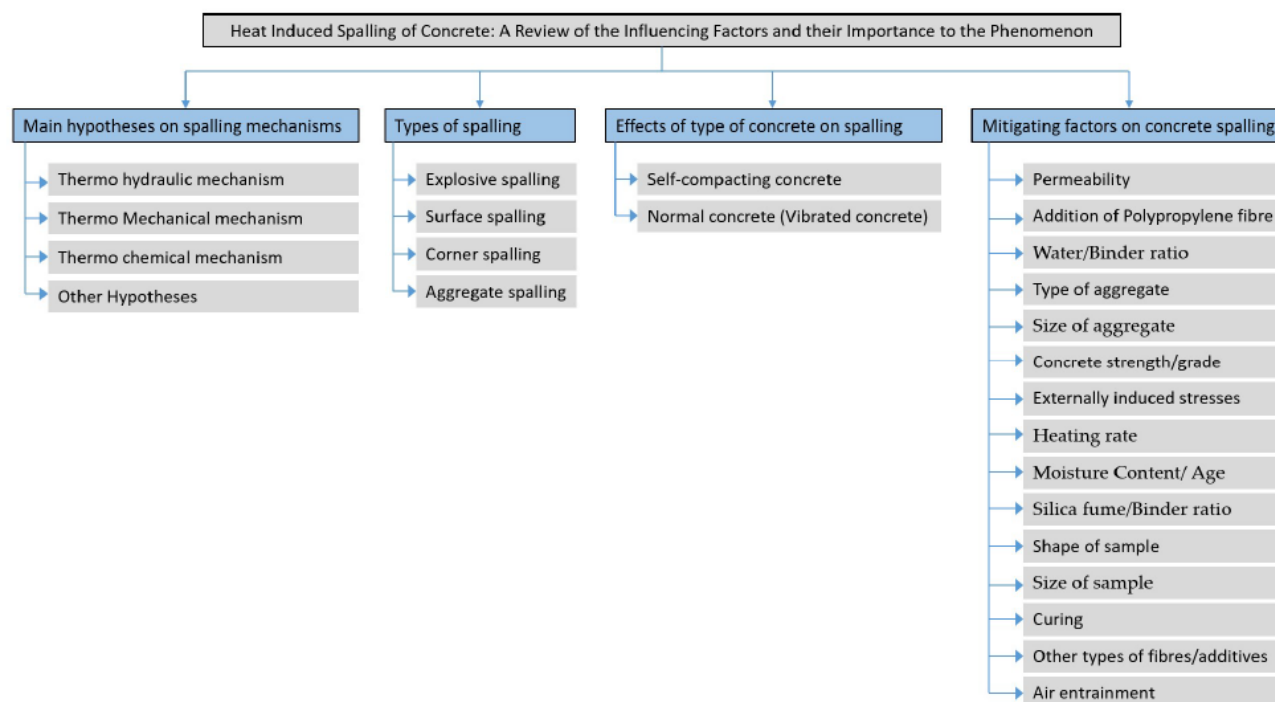
Figure 112: Summary of main factors that influence spalling, as summarised by (Mohammed et al., 2022).

In most cases, a furnace is placed in a loading ram along with a concrete specimen which is stressed during heating (Mróz, 2016). The high temperature conditions are provided mostly by propane or oil burners. During the test, temperature development is measured with the use of thermocouples moulded inside concrete specimens, as well as placed near the fire exposed surface. The sample can be unloaded or loaded i.e., subject to external compression.

6.2.4   High pressure hydrogen jets

A more detailed discussion about hydrogen properties that are relevant to hazards and safety provisions in tunnels and similar confined spaces is given in HyTunnel-CS D1.2, Section 2 "Hydrogen hazards". This section aims to outline the main characteristics of an ignited hydrogen jet, and underpinning equations that have informed on the experimental design for this test programme e.g., expected flame temperature, duration of release.

6.2.4.1   Free jet

When the TPRD activates, the contents of the fuel tank will be released through a short pipe length and of a diameter prescribed through a manufacturing standard.

Due to the pressure of the tank contents (700 bar for a car) most of the duration of the release will involve reservoir pressures which give rise to a choked flow condition at the discharge pipe exit, i.e., the reservoir pressure Po > 1.899 x Pa, where Pa is the external ambient pressure and where the gas is assumed to behave as an ideal gas.

At higher pressures i.e., greater than 100 bar, the non-ideal behaviour of hydrogen needs to be considered when understanding the expansion process, involving the use of a different equation of state than that for a perfect gas. The equation frequently used for hydrogen is the Abel-Noble equation, where a compressibility factor is included when relating pressure, density, and temperature.

The methodology (V. Molkov et al., 2009) that forms the basis for the e-Laboratory blowdown modelling tool used within this research programme employs the Abel-Noble equation of state. In this methodology, the flow at the actual nozzle is choked. It then undergoes an isentropic expansion to the notional nozzle, where at this point ambient pressure and uniform velocity equal to the local speed of sound are reached. The system of equations to evaluate the flow characteristics is closed by the conservation of mass and energy.

This model assumes an unignited release. The representation of the features of the burning hydrogen jet is less comprehensive than that of the unignited case due to the greater experimental challenge of internal jet measurement. Much of the investigation of these has centred on the main hazard evaluation, which is flame radiation. Figure 113 identifies the first of the main parameters in this description, i.e., flame length and width.
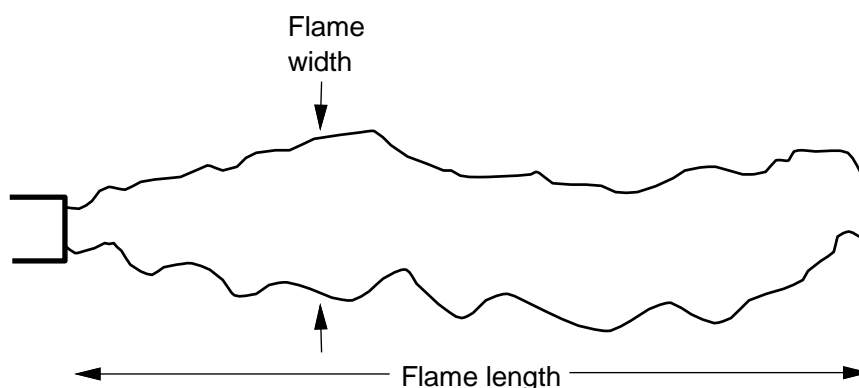
Figure 113: Simple parameters representing a burning jet.

Even these simple measures are not completely trivial to determine due to a) the fluctuating nature of the flame arising from turbulence and b) the difference in the radiation emission bands associated with different aspects of the flame evolution.

The relationship between flame width W and flame length L_{vis} has been described in simple terms of $W = 0.17 Lf_{vis}$ for a range of flame fuels and this has been confirmed in the reported results, as shown in Figure 114 (taken from (Schefer et al., 2006)). The width W refers to the widest part of the visible flame and this simple relation is used by most authors.
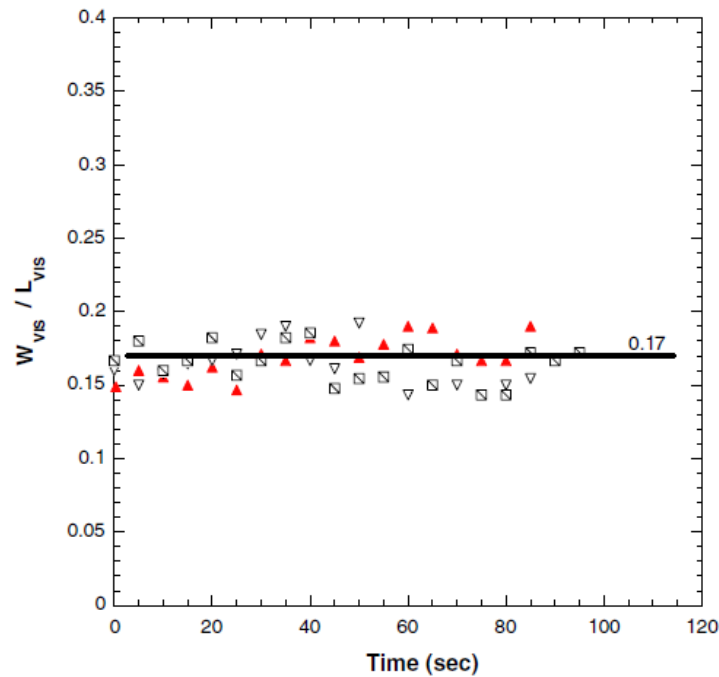
Figure 114: Flame width/length ratio during discharge of high-pressure hydrogen tests (Schefer et al., 2006).

The most robust determination of flame length has derived from the review work of Molkov et al (Vladimir Molkov & Saffers, 2013), where a non-dimensional group approach has been used to rationalise the data involving different nozzles, fuels and mass flow rates. Figure 115 shows that a good collapse of the data from a wide range of published material can be obtained using only the mass flow rate and the actual nozzle diameter.

The flame length then takes the form:

$$L_f = 76 \ (m \, D)^{0.347}$$

Where m is mass flow rate in kg/s and D is the nozzle diameter in m.
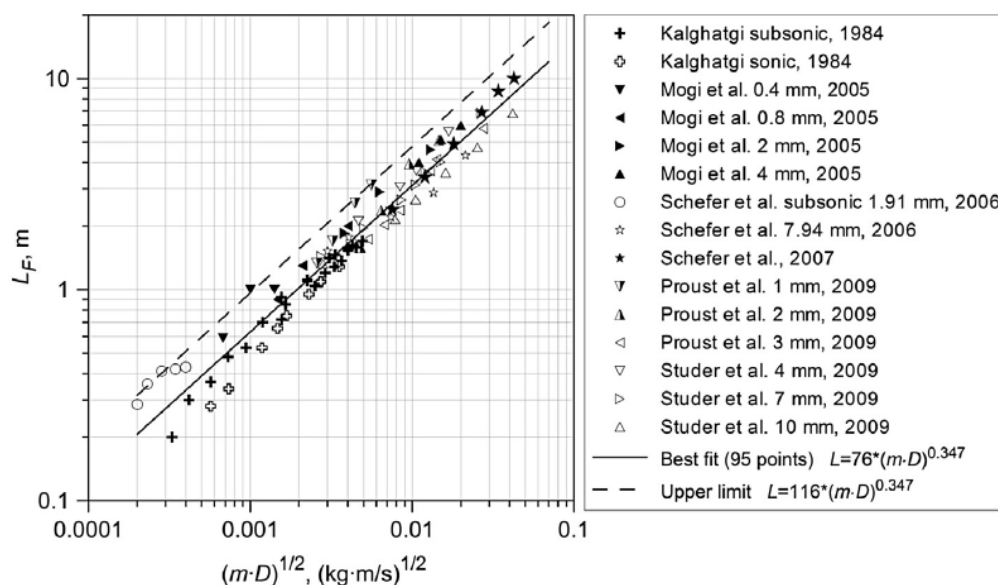
Figure 115: Review of jet flame data showing flame length as a function of only mass flow rate m, and actual nozzle diameter D (Vladimir Molkov & Saffers, 2013).

When a jet impinges on a surface, it is expected that there will be three distinct flow regions; free jet, stagnation, and wall jet, as illustrated in Figure 116 (Tolias & Venetsanos, 2016).
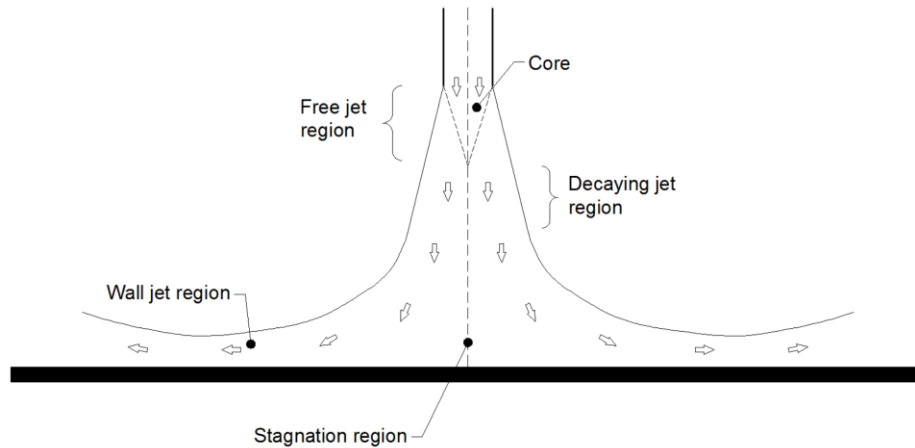
Figure 116: Main flow regions of impinging jet, taken from (Tolias & Venetsanos, 2016).

In the free jet region, entrainment of the surrounding fluid (air) occurs, causing a decrease in the jet velocity, the axial velocity decreases as a Gaussian distribution. As the jet approaches the structure, there will be a stagnation region where the axial velocity will rapidly decrease, creating an increasing static pressure at that impingement point, and turbulence. As the jet then moves along the wall, further entrainment of the surrounding air occurs, creating a larger turbulent cloud with the average velocity decreasing.

For the purposes of this experimental test programme, the equations as outlined above have been employed to inform on positioning of sensors, samples and expected blowdown times and pressures.

6.2.5   Experimental setup

Following a review of the characteristics of fuel cell and hydrogen (FCH) vehicles and potential accident scenarios that could occur (Pursell & Garcia, 2019), a set of experimental parameters were selected for the hydrogen jet fire testing, outlined in Table 28.

A typical FCH car has a thermal pressure relief device (TPRD) vent line diameter of 2 mm, therefore a release nozzle of the order of this diameter was used for most of the tests.

Other HyTunnel sub-tasks in WP 2 and 4 are assessing the effectiveness of reducing the TPRD diameter from 2 mm to 0.5 mm in terms of mitigating other hazards, such as pressure peaking phenomena (PPP) and the formation of flammable atmospheres in confined spaces. Therefore, some tests were carried out using an orifice diameter of approximately 0.5 mm.

Table 28: Expected release characteristics during venting of a FCH car.

Parameter	Value	Notes
Vessel Pressure	700 bar	700 bar is maximum fill pressure for storage vessel for a car
Hydrogen mass / Vessel volume	50 and 100 L	50 L is approx. size of a single vessel in a car. Typically, will have 2 vessels or up to 120 L / 4.5 kg of hydrogen
Release orifice	0.5 mm, 2 mm	Cars currently use a relief device with a 2 mm orifice, HyTunnel-CS proposal to reduce orifice size to 0.5 mm to mitigate pressure peaking phenomenon (PPP) hazard
Flame length, Lf / Sample stand off	Lf = 1.5 m – 2 m (d = 0.5 mm) Lf = 4.4 m - 6.6 m (d = 2 mm)	Correlations give range of flame lengths, Lf Hottest flame temperature at 0.7 Lf for free jet fire at initial stage of 700 bar jet blowdown Commissioning test to inform sample location
Jet flame width, Wf / Sample size	Wf ≈ 0.25 m (d = 0.5 mm) Wf ≈ 0.90 m (d = 2 mm)	Correlations relate flame width Wf (at end of flame) to length: Wf = 0.17Lfvis

6.2.6 High pressure hydrogen rig (HPHR)

The experimental programme was undertaken using the High-Pressure Hydrogen Rig (HPHR) facility at the HSE Science and Research Centre, as shown in Figure 117.
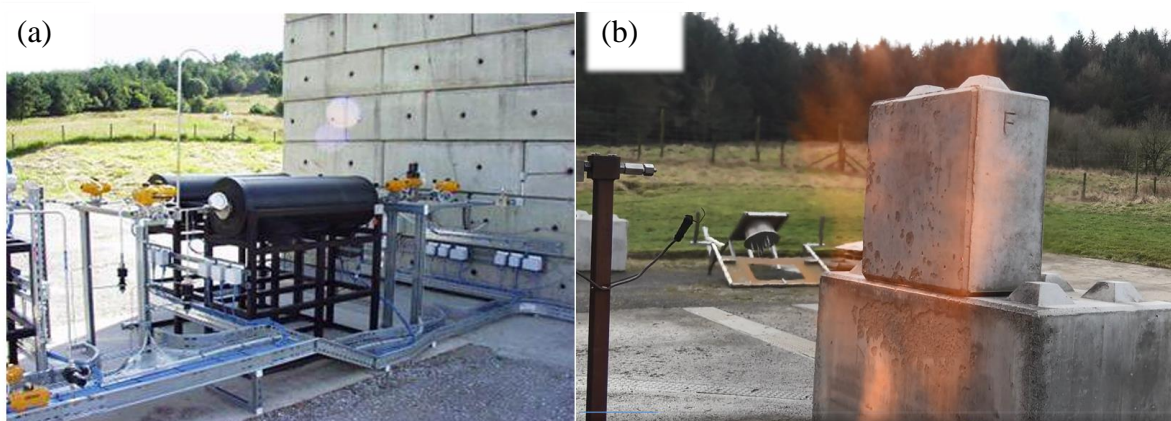
Figure 117: High pressure hydrogen rig (HPHR) a. pressure vessels and pipework, b. jet release onto concrete sample.

It comprises:

• Two 49 L storage vessels with 1000 bar working pressure which are suitable for hydrogen service; hydrogen is delivered through ½" bore pipework.

• A gas booster compressor to charge the vessels from a hydrogen delivery pack pressure of <175 bar up to 1000 bar.

• A remote operation, release timing and firing control system to perform, monitor and record test sequence data, including temperatures and pressures within the pipework and vessels during blowdown.

A diagram of the experimental setup is shown in Figure 118. Pressure release data from pressure sensors PS01 and PS02 (Wika IS-3 standard, 0-1000 bar range) has been included and overlayed onto the test sample data.
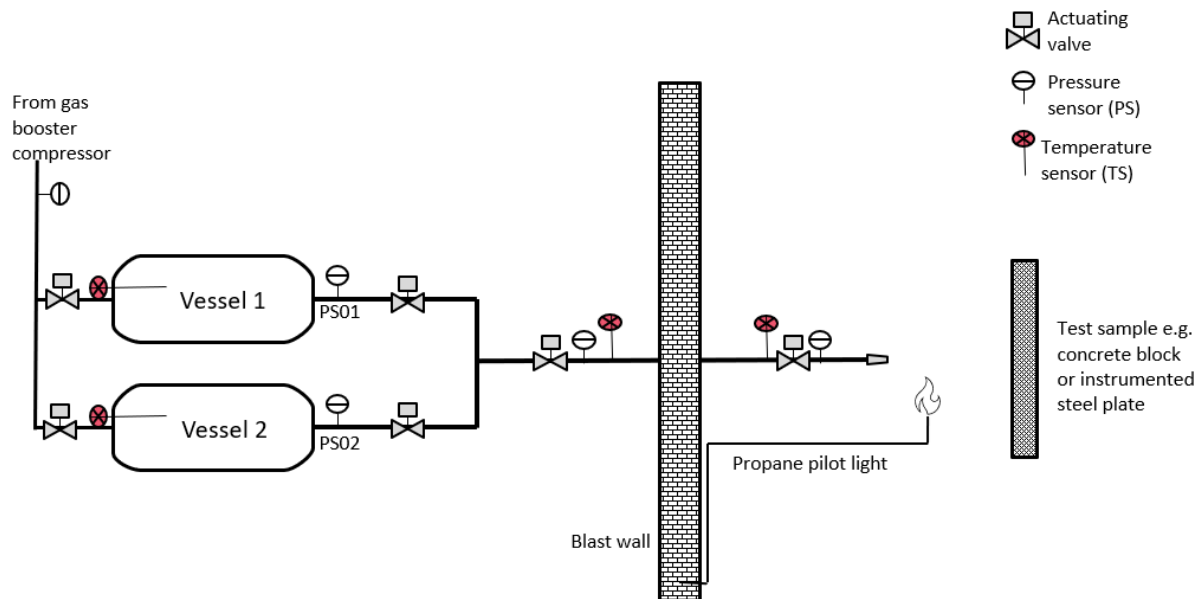
Figure 118: Experimental setup of release. Hydrogen is pressurised to 700 bar from gas booster compressor and stored in two storage vessels. Releases are initiated by activation of pneumatically controlled valves, with gas blowdown being directed through blast wall, where it is ignited using a propane pilot light. Gas pressure and temperature is monitored at stages along the pipework. Test sample is placed in front of release point.

A local weather station was installed adjacent to the test facility; wind speed and direction (Gill WindsonicM) and ambient temperature and humidity (Skye instruments SKH2065) were logged using a National Instruments (NI) data acquisition (DAQ) system for each release.

6.2.7   Release conditions

Experiments were conducted using two release orifice sizes, nominally referred to as 2 mm and 0.5 mm. The orifices were machined from high pressure fittings supplied by Fitok (AMH series adapter fitting) for the 2 mm nozzle and HiP (NPT 15000psi series fittings) for the 0.5 mm nozzle. Microscopic examination of the fittings showed that actual diameters were 2.1 mm and 0.57 mm, respectively. The cross-sectional design of the orifice fittings is shown in Figure 119.
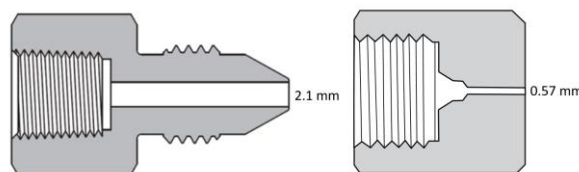
Figure 119: Schematic of 2.1 mm nozzle and 0.57 mm nozzle.

Based on the actual orifice dimensions, an initial flow rate was calculated using the adiabatic blowdown model for an unignited hydrogen jet (V Molkov & Saffers, 2012).

Using this model, the initial flow rate of a 700 bar hydrogen release was estimated to be 0.12 kg/s and 0.009 kg/s for nominally 2 mm and 0.5 mm orifices, respectively. Some deviation from these flow rates was expected as the experimental conditions were not adiabatic (heat transfer was expected between the vessels and gas); this will be discussed in more detail in the results section.

The release pipework and orifice were orientated horizontally such that a horizontal jet fire occurred. The orifice was located 1.125 m above ground for all experiments. An example of a typical free jet fire is shown in Figure 120; this image relates to a blowdown using the 0.5 mm nozzle. A thermal image of the jet itself has been overlayed to aid visualisation (the jet is not visible ordinarily).
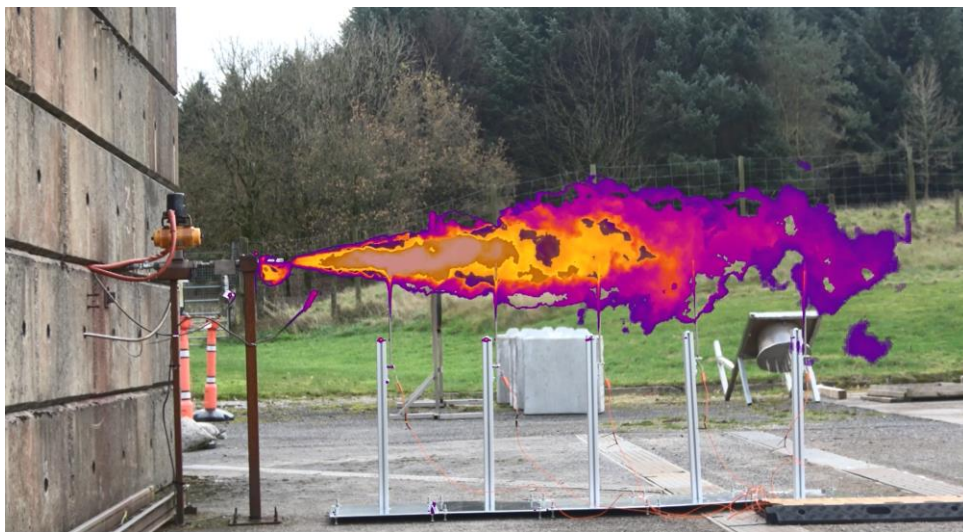
Figure 120: Free jet from 0.5 mm nozzle. Thermal imaging of the jet itself has been overlayed on a visible image.

6.2.8 Ignition mechanism

In order to ensure an ignition was consistently achieved without the build-up of a flammable cloud, a propane pilot light was used. This was positioned approximately 20 cm horizontally downstream from the release orifice. This location was selected in order to be beyond the lift off position of the jet i.e., at a distance where a turbulent premixed portion of the jet is expected. The pilot light was lit prior to the start of each test, and then extinguished a few seconds after the jet fire was established, by closing a valve on the propane gas supply line. The pilot light was extinguished as it was found for the 0.5 mm nozzle, when remaining lit, it was causing repeated "light-ups" of the releasing gas, thus interrupting the smooth blowdown of the jet.

6.2.9 Material samples

As this research considers fires originating from vehicles within the tunnel, the focus was on the materials that are used for the final layers of the tunnel structure i.e., the tunnel linings, as these are likely to suffer the most serious effects from hydrogen jet impingement.

Following consultation with an industrial provider of tunnel boring machinery, the following information was provided regarding typical tunnel segments.

"The size and thickness of (circular) tunnel segments are typically 1 m long axially, with typically 6 to 9 segments in a circle. Their thickness will be anywhere between 200 mm minimum on smaller tunnels (180 mm to 220 mm), although most new road tunnels are an absolute minimum of 350 mm to 400 mm thick.

Most precast concrete tunnel segments these days and for the imminent future are fibre reinforced, with steel fibres for strength and durability and polypropylene for fire. The design of the precast concrete tunnel segments incorporates a 50 – 100 mm sacrificial layer on the inside of the tunnel; so once explosive spalling is mitigated, fire cannot affect the structural concrete behind. Thus, a 500 mm thick concrete segment will have polypropylene fibres and steel fibres throughout the section, but only say a 400 mm thickness will be used in the structural design."

A set of smaller (than typical precast tunnel segments) concrete samples were cast as shown in Figure 121. The concrete composition aimed to replicate typical tunnel lining properties, in particular those that were likely to influence whether explosive spalling occurred.

Figure 121: Concrete test samples. Dimensions 800x800x400 mm, high strength concrete.

It was decided to focus on high strength concrete specifically. Concrete is known to be subject to explosive spalling where the design strength is greater than 60 MPa or greater than 3% moisture content (European Committee for Standardization, 1992). It has been shown that the addition of polypropylene (PP) fibres can mitigate the occurrence of spalling (Hertz, 2003; Shuttleworth, 2001).

Bespoke concrete test samples were manufactured by a local supplier (RT Mycock & Sons) based on the composition used by project partners, Danish Technical University, (DTU). Where possible, the DTU composition was replicated, however due to variations in locally available additives there were differences in the resulting concrete characteristics. Table 29 provides a summary of the concrete composition and compares the DTU specification with the specification used by HSE, together with an indication of the deviations. The samples were cured in open air (with no specific weather protection implemented) for 30 days before being moved to the test area. Testing took place on day 337 of sample age.

Table 29: DTU and HSE concrete specification, including explanation for deviations.

	DTU composition Dense + High strength	HSE composition High strength	Deviations due to manufacturer capability
Concrete Grade	C85 (85 MPa)	C40/50 (50 MPa)	Unable to cast to C85 strength. Compressive strength at time of test ≈ C55
Water/cement (w/c) ratio	0.30	0.45	Unable to achieve lower moisture content
Microsilica	Yes	No	Not licensed to use microsilica
Fly ash	No	No	Ground Granulated Blast-furnace Slag (GGBS) used instead, cement substitute to improve strength and reduce porosity
Plasticiser	Yes	Yes	Water reducing admixture used
PP fibres	Yes	Yes (12 mm)	Two samples with and two samples without
Aggregates	Sea (0-16 mm)	Land (0-20 mm)	Sea aggregates not available. Limestone used

In addition to the tunnel lining material, given that the orientation of the TPRD on a hydrogen fuelled car is angled downwards towards the road, it was decided to fabricate one sample that is typical of road covering material, namely tarmac.

The tarmac sample was asphalt based with hot cure bitumen, which was poured into a mould, giving a sample with dimensions 800x800x45 mm, as shown in Figure 122.

Figure 122: Tarmac sample, polymer modified asphalt (PMA).

In summary, the materials that were fabricated were:

1. High strength concrete (2 samples)

2. High strength concrete with PP fibres (2 samples)

3. Tarmac (1 sample)

6.2.10 Measurements

A National Instruments (NI) data acquisition (DAQ) system was used for data logging of the jet release temperature and pressure measurements. Pressure sensor readings were logged at a sampling rate of 100 Hz using an NI current input module (NI-9203). Thermocouple readings were logged at a sampling rate of 1 Hz using a dedicated NI thermocouple input module (NI-9213).

The parameters being measured for each release scenario are described in more detail in the subsequent sections.

6.2.10.1 Free jet releases - sensors and equipment

Two free jet releases i.e., with no samples placed in the jet path, were carried out, using the 2 mm nozzle and subsequently the 0.5 mm nozzle to gain some insight into the flame length and temperature when unimpeded and the variation as a result of differing nozzle sizes.

Five type 'R' sheathed Pt/Rh 3 mm diameter thermocouples were positioned axially along the centreline of the jet, spaced up to a range of just over 3 m, as shown in Figure 123. One vessel (49 L volume) was used for each release, giving a blowdown time of just over 100 seconds.

Thermal imaging was carried out, where the camera was placed side-on to the release.
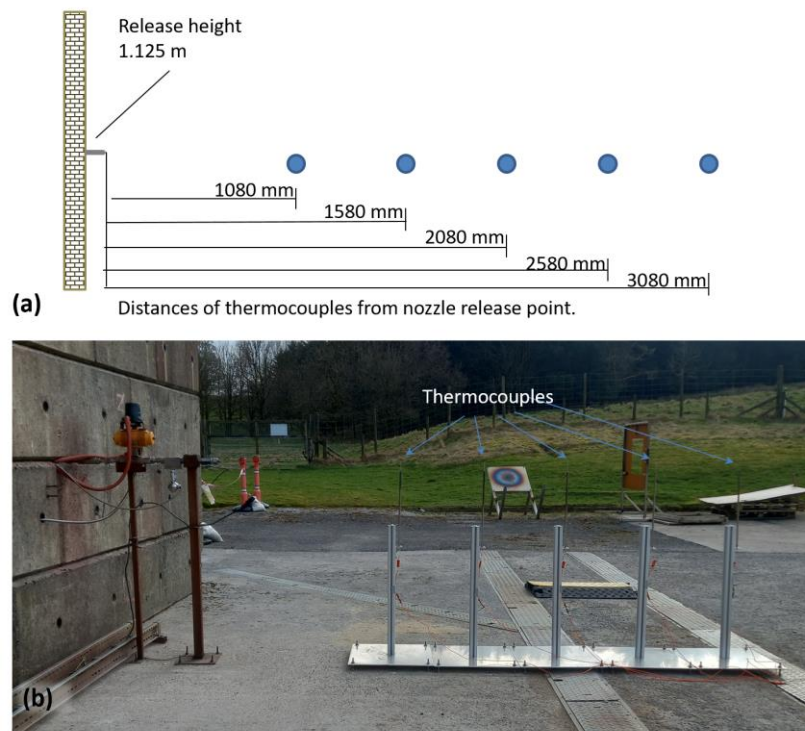
Figure 123: Unimpeded jet release; 2 mm nozzle, 700 bar, 49 L Graphic (a) and Image (b) showing spacing of thermocouples along the axial length.

6.2.10.2 Impeded jet releases – sensor plates

In order to understand the pressure and temperature distribution across the incident surface of the concrete samples as the jet blowdown occurred, two sensing plates were fabricated, with the same incident surface dimensions as the concrete samples, i.e., 800x800 mm. One

contained a spaced cross array of pressure sensors and the other contained the same spaced cross array of thermocouples, as illustrated in Figure 124.

The spacing of the sensors on the plates aimed to capture as much information across the span of the evolving jet flame, e.g., from a possible 0.7 m width flame at initial release at 700 bar, to the reducing span as the jet blows down e.g., a flame width of 0.35 m at 30 bar.
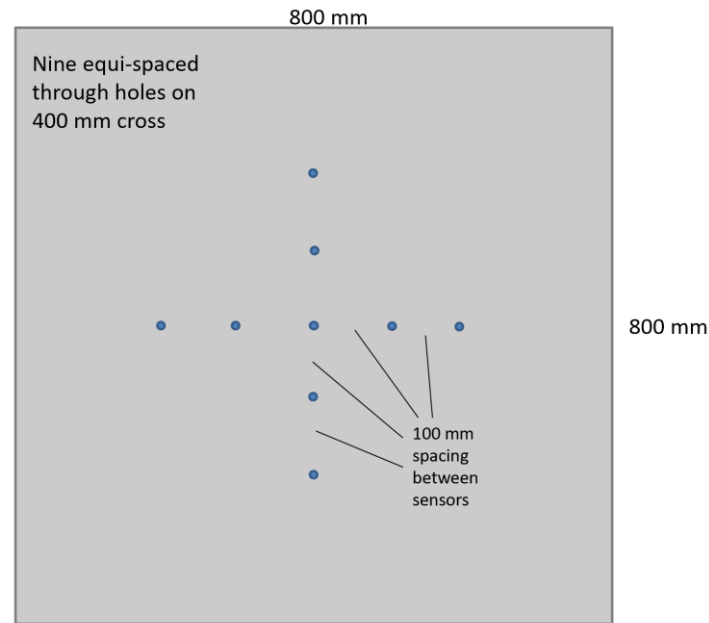
Figure 124: Graphic to illustrate spacing of sensors relative to overall plate dimensions.

A stainless-steel stand was built, onto which the two sensing plates could be bolted at the release height of 1.125m and such that their positioning mimics that of the "interlocked" concrete test sample, as shown in Figure 125.
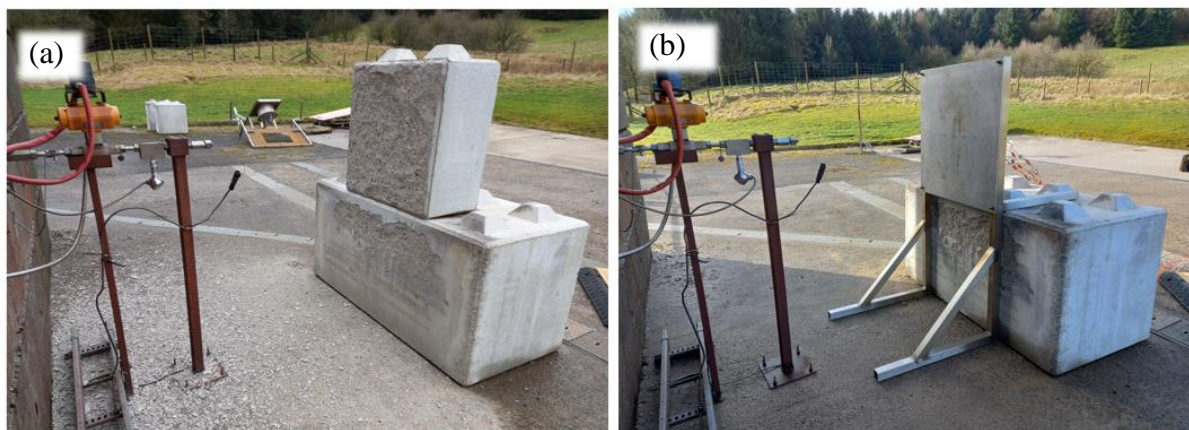
Figure 125: Experimental setup of (a) concrete test sample and (b) sensing plate.

6.2.10.2.1 Temperature sensing plate

The temperature plate consisted of an 8 mm thick, 800 x 800 mm, stainless steel plate. The plate was constructed from 304L standard dull finish stainless steel (emissivity ≈ 0.85).

There was a centred 'cross' array of nine 1.5/3 mm diameter tapped holes, equi-spaced on a 400 mm cross. Four type 'N' Inconel sheathed, 1.5 mm thermocouples were placed at the

outermost (relative to the plate centre) positions and five platinum/rhodium sheathed type 'R' 3mm thermocouples were placed in the more central holes; all thermocouples were inserted such that the sensing end protruded through the plate and directly into the jet flame. Whilst this plate was in situ, the thermal imaging camera was setup at the end face of the plate, approximately 10 m behind, to attempt to obtain a heat map of the plate during the release. The standoff distance of the plate from the 2 mm nozzle was 0.95 m and 1 m from the 0.5 mm nozzle. One vessel (49 L volume) was used for each release, giving a blowdown time of just over 100 seconds.

6.2.10.2.2 Pressure sensing plate

The pressure sensing plate consisted of an 8 mm thick, 800 x 800 mm 304L, mill finish stainless steel plate as shown in Figure 126. There was a centred 'cross' array of nine 3 mm diameter tapped holes, equi-spaced on a 400 mm cross, to which were attached stainless steel tubes, length 500 mm with inner diameter of 12.05 mm, each terminated by an Omega PXM319-001GI 4-20mA pressure transducer. These tubes were cooled by use of a water jacket surrounding the tubes.

The standoff distance of the plate from the 2 mm nozzle was 0.972 m and 1.02 m for the 0.5 mm nozzle.
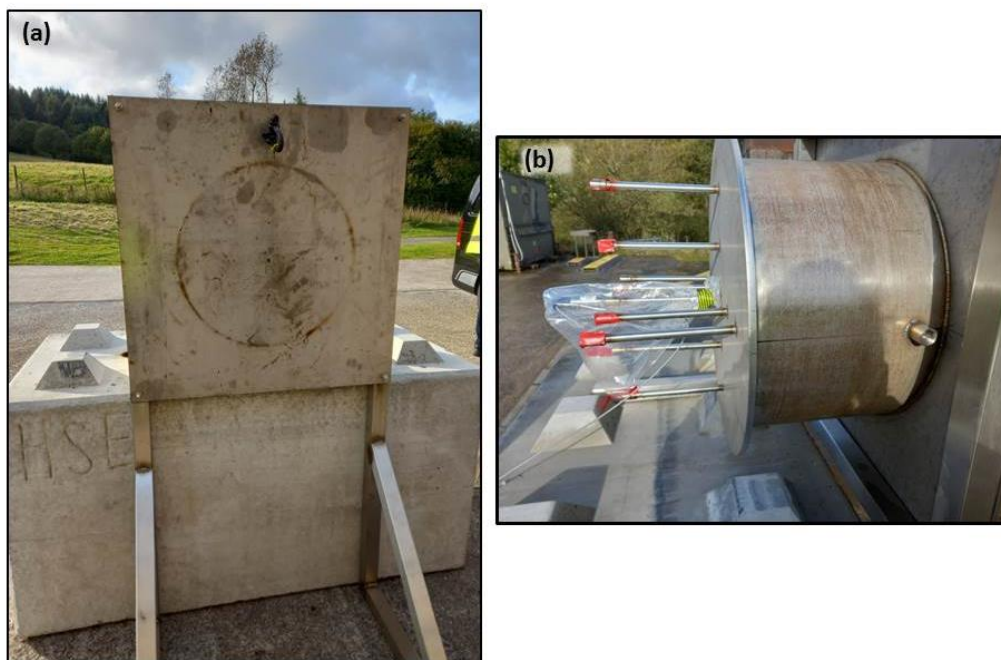
Figure 126: Close-up image of pressure sensing plate (a) front face and (b) back face with water jacket and steel tubes to which pressure sensors were attached.

6.2.10.3 Concrete samples - material analysis

The four concrete samples were cast using commercially available "interlocking concrete block" moulds, with dividers put in the mould during casting to achieve test samples of dimensions 400x800x800 mm. These smaller test samples were then placed on a base block (dimensions 1600x800x800 mm) in order to achieve the desired height i.e., centred around the jet release height, as shown in Figure 127.

Figure 127: Smaller concrete test sample on top of base block.

No additional load or external compression was applied to the samples during testing. With these moulds, as there are no reinforcing bars it was not possible to cure samples with sensors in situ.

Thus, a series of post-test material analyses were carried out as described in the subsections below.

6.2.10.3.1 Concrete test sample – post-test analysis

Each sample was impinged upon by the full available volume i.e., both vessels with combined volume of 98 L and at a pressure of 700 bar. The stand-off distance and nozzle size were varied depending on what aspects were being tested. For example, two standoff distances were selected for the 2 mm nozzle, using the two non-fibre containing samples to understand the effect of standoff distance on likelihood of occurrence of spalling.

The test matrix is summarised in section 6.2.11.

When each blowdown test was completed, a visual assessment of the incident surface was made. Where visible damage occurred on the incident surface, the sample surface was 3D laser scanned to provide more detailed information as to the depth and extent of the damage. Cores (150 mm diameter, 400mm depth) were then extracted from the impinged upon samples to be sent away for analysis.

Three test methods were applied to the extracted cores. The three tests and their related standards are listed in the bulleted list:

- Compressive strength – crush test carried out according to BS EN 12390 standard (BS EN 12390-1:2021 British Standards Institution, 2021) - Testing hardened concrete. The tested cores were clipped to a depth of 300mm.
- Thermal conductivity – The cores were clipped to a depth of 45mm such that both ends i.e. impinged and un-impinged face, could be analysed in the same way, as a comparison. A thermal resistance measurement was made as per BS EN12664 standard

(BS EN 12664:2001 British Standards Institution, 2001) – testing thermal resistance using guarded hot plate method.

- Ultrasonic testing – Pulse velocity measurements were made, where each core was clipped to a depth of 150 mm in order to investigate presence of cracks or voids, changes in uniformity of the concrete. As with the thermal conductivity measurements, the unimpinged and impinged ends were analysed for both concrete sample types i.e. with PP fibres and without. The test was carried out according to BS EN 12504 standard (BS EN 12504‑4:2021 British Standards Institution, 2021)– determination of ultrasonic pulse velocity.

6.2.10.3.2 Concrete core – heat transfer measurement

In order to gain some understanding of the heat transfer through the concrete in real time, one of the extracted cores, i.e., the high strength concrete containing no fibres, was trimmed such that it had dimensions 150 mm diameter and 45 mm depth. Four holes were then drilled into the back face of this shallower core and four Type R thermocouples were placed into the holes. The holes were drilled to a 3mm diameter and to different depths, the thermocouple ends were coated in thermal grease to encourage heat transfer between the concrete and the thermocouple end, and inserted into the holes, as shown in Figure 128. The core was reinserted into the original block and secured in place using wire. One vessel (49 L volume) and the 2 mm nozzle were used for the release, giving a blowdown time of just over 100 seconds release. The sample was placed at a standoff distance of 1.09 m

Figure 128: Back face of concrete sample showing inserted thermocouples in drilled core (core depth 45 mm).

6.2.10.4 Impeded jet release – tarmac sample

A section of pipework with a 90° bend was added for the release onto the tarmac sample, the aim being to extend and orient the release downwards onto the tarmac sample. The stand-off distance between the nozzle and tarmac surface was 100 mm, approximately. The ignition light was placed adjacent to the jet incident location. The setup is shown in Figure 129. The 2 mm nozzle was used and both vessels (98 L volume) were pressurised to 700 bar. During the release, two cameras were setup, one on the test pad adjacent to the release, and the other was attached to a drone to give a more elevated overview.

Stills were taken from the drone footage and the ground level camera to demonstrate the progression of the jet.

Figure 129: Release onto tarmac sample; Illustration of nozzle orientation. Nozzle was set 100 mm approximately from the sample.

6.2.11 Summary of test matrix

A series of release scenarios were designed, where different parameters were measured:

•   Free jet release – temperature measurements along free jet;

•   Impeded jet release – impinging on temperature sensing plate and subsequently, pressure sensing plate;

•   Impeded jet release – impinging on concrete samples.

Thirteen jet fire experiments were conducted in total; the test matrix is summarised in Table 30.

Each concrete sample was impinged upon by the full available volume i.e., both vessels with combined volume of 98 L and at a pressure of 700 bar. The stand-off distance and nozzle size were varied depending on what aspects were being tested e.g. one distance aimed to achieve maximum flame impingement over the full duration of the release thus imparting as much heat as possible. In most cases, the experiments were carried out with a standoff distance of approximately 1 m.

Table 30: Summary of test matrix, including selected nozzle sizes, standoff distances of the test pieces and visualisation and analytical techniques used.

Test ID	Notes	Conditions			Measurement
		Volume (L)	Orifice Size (mm)	Sample stand-off (m)	
1	Free jet	49	2.1	n/a	Axial temperature VIS/IR camera
2	Free jet	49	0.57	n/a	Axial temperature
3	Impeded jet – temperature plate	49	2.1	0.95	Radial temperature IR imaging (end on) Vis imaging (side on)
4	Impeded jet – temperature plate	49	0.57	1	Radial temperature Vis imaging (side on)
5	Impeded jet – pressure plate	49	2.1	0.972	Radial Pressure Vis imaging (side on) camera
6	Impeded jet – pressure plate	49	0.57	1.02	Radial pressure
7	High strength concrete (no fibres)	98	2.1	1.06	3D laser scan/ Vis imaging (side on), material analysis
8	High strength concrete (no fibres)	98	2.1	2.236	Vis imaging (side on)
9	High strength concrete with PP fibres	98	2.1	1.06	3D laser scan/ Vis imaging (side on), material analysis
10	High strength concrete with PP fibres	98	0.57	1.11	
11	Reinstated concrete core with thermocouples	49	2.1	1.09	Heat transfer through sample
12	Impeded jet – temperature plate	49	5	3.3	Radial temperature Vis imaging (side on)
13	Tarmac	98	2.1	1.08	Vis imaging (drone and side on)

Test no. 12 i.e., the impeded jet using the 5mm nozzle was carried out to provide experimental data to support model validation for another subtask and so does not form part of the discussion in this subtask. The results for the 5 mm nozzle are shown in Appendix A1.1.

6.2.12 Results

The results are shown for both the 2 mm and 0.5 mm nozzle.

6.2.12.1 Blowdown parameters

A modelling toolkit was used to inform on expected blowdown duration (Molkov et al., 2009; Dadashzadeh et al., 2019).

Figure 130 below shows a comparison of the experimental release vs a modelled release for a 2 mm nozzle. The modelled release describes an adiabatic non-steady state under-expanded jet release using the Elabs toolkit (E-laboratory, 2020). This model is derived from the Abel-Noble equation of state for hydrogen and the conservation equations for mass and energy, The discharge coefficient using this model is assumed to be 0.9; this is based on correlation with an experimental setup used for a different test campaign (Kuznetsov et al., 2015), where a conical nozzle was used. It is expected that the discharge coefficient in that test programme was higher than would be expected for this experimental scheme.

The experimental data relates to the pressure readings in the vessels on the HPHR, for a 700 bar, 98 L release through a 2 mm nozzle i.e., the releases for Samples 1, 2 and 4. The average starting pressure for these three experimental releases was 675 bar±7 bar, and it took 3mins 45secs for the vessels to depressurise to 3.8 bar (modelled data assuming adiabatic conditions achieved this after 3mins 6secs).

It is seen in Figure 130 that the modelled release is in good agreement with the experimental releases at the beginning of the blowdown, when there is not much heat transfer through the wall. As the release progresses, the blowdown model predicts a faster pressure decrease than that of the experimental releases. This is not unexpected as in reality there will be some heat transfer from the pressure reservoirs due to their thermal mass (Dadashzadeh et al., 2017), with the effect becoming more pronounced as the relative gas temperature increases. The nozzle is likely experiencing greater headloss than is being assumed in the model.

Using the modelled data, and the theory as described in 6.2.4.1, the maximum flame length and width were predicted to be 4.05 m and 0.69 m respectively for a release through a 2 mm nozzle.
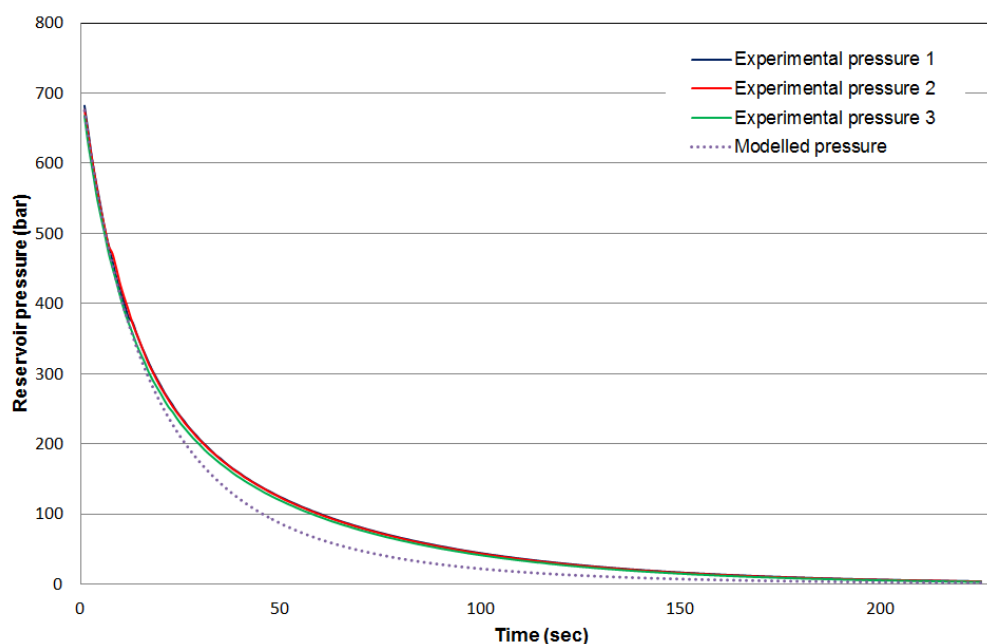
Figure 130: Comparison of experimental blowdown with modelled (adiabatic) blowdown. Assume starting pressure of 700 bar, Volume of 98 L, nozzle of 2 mm.

6.2.12.2 Unimpeded jet release – jet axial temperature

The test parameters (Test 1 in Table 30) were as follows; 700 bar, 2 mm nozzle, one 49 L vessel. Five type 'R' thermocouples were positioned along the axial length of the unimpeded jet release, at a height of 1.125 m, spaced as outlined in Figure 123 and centred in the flame.

Figure 131 (a), shows a still thermal image of the release at 25seconds into release approx. and the measurements from the five thermocouples are plotted in Figure 131 (b), including the pressure measurements from the vessel as the release progressed.

R1 represents the thermocouple closest to the nozzle/release point. From the results shown in Figure 131 (b), R1 does not reach its highest temperatures until almost 70 seconds into the release. It is expected that this is the case, as, at the beginning of the release, R1 is in a fuel-rich portion of the jet and thus, does not experience a stoichiometric mix.

The camera thermal range was set from 0 to 300 °C to facilitate better visualisation of the jet relative to ambient background temperature, and so the imaging does not represent the actual jet temperature. On a general note, the emissivity coefficient of a hydrogen flame is relatively small i.e. less than 0.1 (Mogi, T.; Nishida, H.; Horiguchi, et al., 2005). As a consequence, it is expected that the thermal imaging in this test programme will be capturing the reflected temperatures from surrounding objects rather than faithfully representing the temperature of the jet itself. It should also be noted that the radiation from the jet will also have a thermal effect on its surroundings, which in turn, will also affect the thermal image readout.
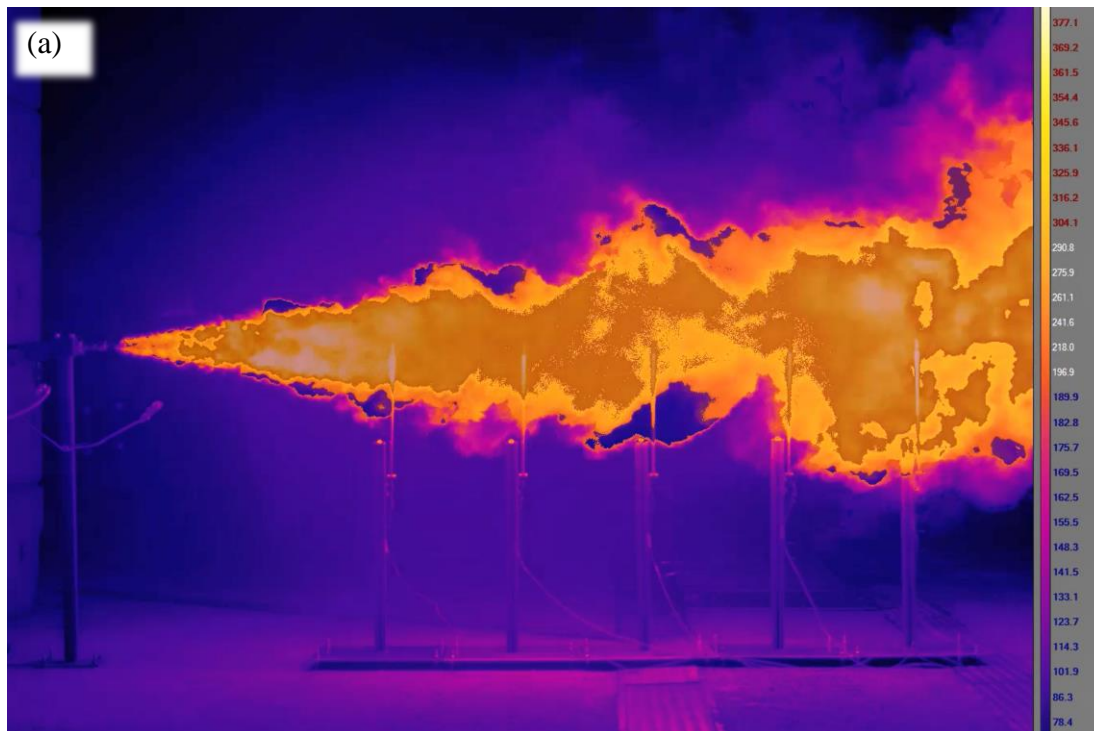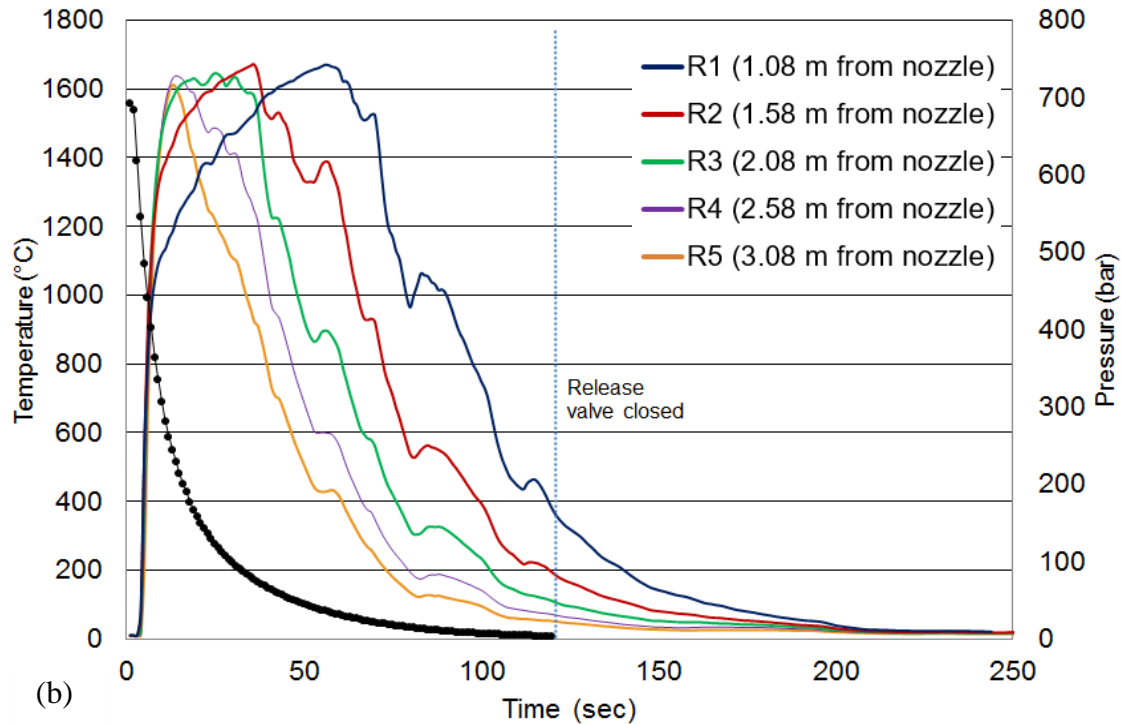
Figure 131: 700 bar blowdown, 49 L volume, 2 mm nozzle ignited release. Type 'R' thermocouple placed along the axial direction of the jet (a) Thermal image of release i.e., at 25 seconds into release approx. Camera field of view was not wide enough to capture full extent of jet. (b) plot of temperature readings from each thermocouple and pressure data from vessel.

The time values at which the jet was at its maximum temperature at each thermocouple location are plotted in Figure 132. The flame decay rate trends in a similar way to the vessel blowdown i.e., rate of pressure decay slows as overall pressure in the vessel is reduced. Over the distance of 0.5 m from R4 to R3 where maximum temperature was achieved, the time period equated to 9 seconds, or 0.055 m/s. Over the distance of 0.5 m from R2 to R1 where maximum temperature was achieved at a later stage of the release, the time period equated to 20 seconds, or 0.025 m/s. The expected visible flame length at these maximum temperatures, as calculated using the Elabs tools is listed in the table in Figure 132.

Time (sec)	Distance at max temp (m)	Vessel pressure (bar)	Calculated visible flame length (m)
13	3.08	244	5.13
14	2.58	228	4.30
25	2.08	123	3.47
36	1.58	76	2.63
56	1.08	36	1.80
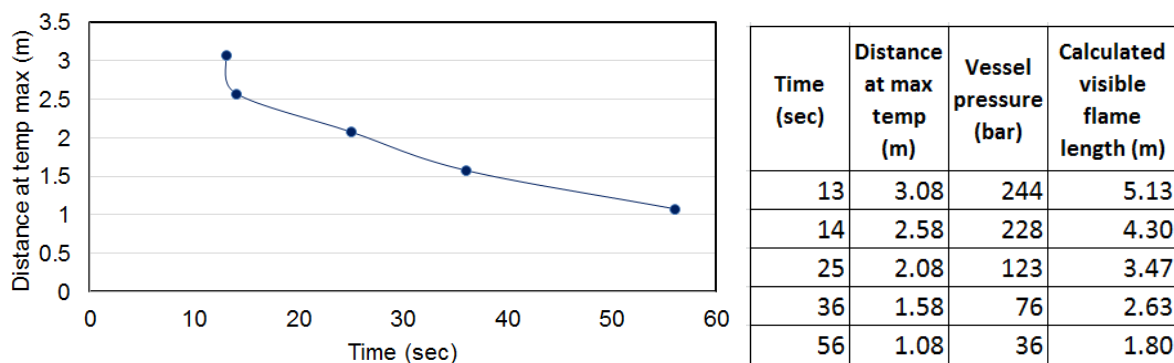
Figure 132: Plot on left; Distance at maximum recorded temperature vs. time. Table on right; Temperature and thermocouple distance locations with corresponding vessel pressure and calculated (Elabs) visible flame length at that time.

For the 0.5 mm nozzle (Test 2 in Table 30), one vessel was used and released from 700 bar down to 42 bar, lasting just over 1000 seconds (16.5 mins), as seen inFigure 133. The five R-Type thermocouples were again placed along the axial distance of the jet.

The Type R thermocouples have a maximum temperature range of 1700 °C. It is thought that the temperature at R1 during the early stage of the blowdown would likely have reached 1800 °C (Molkov & Saffers, 2013), however this couldn't be measured due to the limitations of the thermocouple.

Both unimpeded jets i.e., from the 2 mm and 0.5 mm nozzle, were momentum driven, however the 0.5 mm jet flame had a narrower width and shorter length and thus, excepting the closest thermocouple, the thermocouples did not experience sustained impingement at the higher temperatures. In addition, the 0.5 mm jet was more affected by ambient conditions e.g., gusting wind, leading to further fluctuation in the temperatures than the thermocouples would experience. This is evident in the plotted data in Figure 131 and Figure 133 , where the temperature readings appear to fluctuate more for the 0.5 mm nozzle. Using the visualisation from the thermal and visible imaging, it was estimated that the jet lengths at their longest were up to 6 m for the 2 mm nozzle and up to 3 m for the 0.5 mm nozzle.
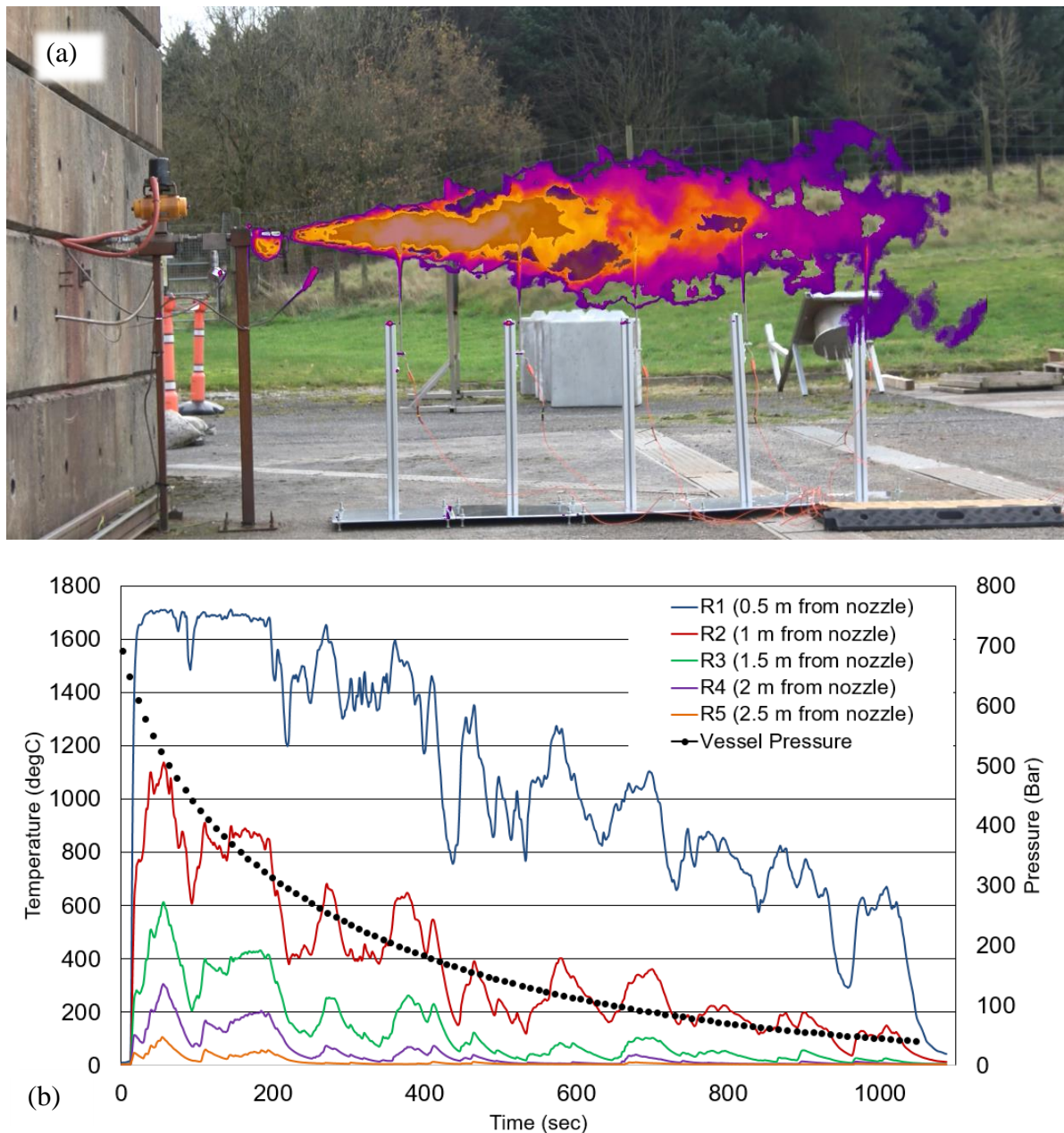
Figure 133: 700 bar blowdown, 49 L volume, 0.5 mm nozzle ignited release. Type 'R' thermocouple placed along the axial direction of the jet (a) Thermal overlay onto visible image of release. Jet was not visible otherwise, (b) plot of temperature readings from each thermocouple and pressure data from vessel.

There were notable differences between the two releases. For a release from one vessel, i.e., 49 L, the duration of the release from 700 bar to 40 bar was 53 seconds for the 2 mm nozzle and 1048 seconds for the 0.5 mm nozzle. The maximum flame temperature i.e., of 1700 °C, was recorded at all thermocouple distances for the 2 mm nozzle i.e., at up to 3 m from the nozzle whereas the maximum temperature was recorded at the closest thermocouple only for the 0.5 mm nozzle i.e. at a distance of 0.5 m.

6.2.12.3 Impeded jet releases – sensor plates

Impeded jet releases onto the two sensor plates were carried out for both the 2 mm and 0.5 mm nozzles. The first section outlines the results from the temperature plate reading and the second section outlines the results from the pressure plate readings.

6.2.12.3.1 Temperature plate impingement

One vessel (49 L) was used each time for the 2 mm (Test 3 in Table 30) and 0.5 mm (Test 4 in Table 30) nozzle, pressurised up to 700 bar. Figure 134 shows the results from the 2 mm nozzle impingement, where the plate was at a standoff distance of 0.95 m. Unlike the unimpeded jet releases, where temperatures of up to 1700 °C were measured, the maximum temperatures measured were 1400 °C; these were measured at outer thermocouple locations i.e., not at the incident surface of the jet impingement.

It is expected that the central thermocouples would initially be in the stagnation and decaying jet region of the impinging jet (as described in section 6.2.4), where there is not much entrainment of air and thus the temperature at these locations does not reach its maximum until later on in the release, when the magnitude of the jet impinging on that area will have decreased, thus allowing for a better fuel/air mixture, through entrainment of air.
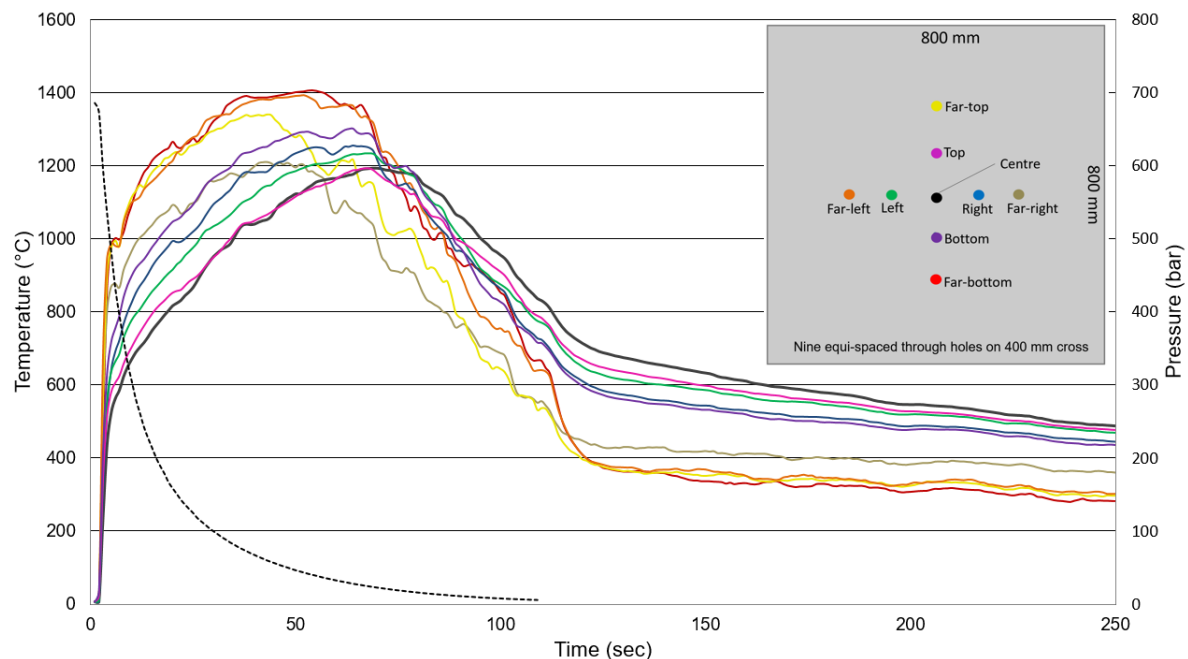
Figure 134: Impeded jet release; 2 mm nozzle, 49 L, 700 bar, 0.95 m standoff. Temperature readings taken equi-spaced across a 400 mm cross, centred in the plate. (Black dashed line represents pressure decay in cylinder during blowdown).

The test was repeated, using the 0.5 mm nozzle; the temperature progression over time for each thermocouple is plotted in Figure 135.

In the case of the 0.5 mm nozzle, comparing the temperature progression, the jet appeared to have been tending towards the left side of the plate; the wind was tending towards that direction at the time of testing and wind speed was approximately 4 m/s as measured by the local weather station. The jet, in this case, with its smaller profile i.e., width and length, upon impingement, appeared to have sufficient air entrainment such that maximum temperatures were reached along the surface adjacent to the incident surface almost immediately, beginning to decrease as the jet receded. The central thermocouples did still experience the stagnation region of the jet,

where maximum temperatures were not reached until approximately 110 seconds into the release. After 15 minutes (vessel pressure 50 bar approximately), the jet was no longer impinging on the plate and so the thermocouple data logging was stopped.
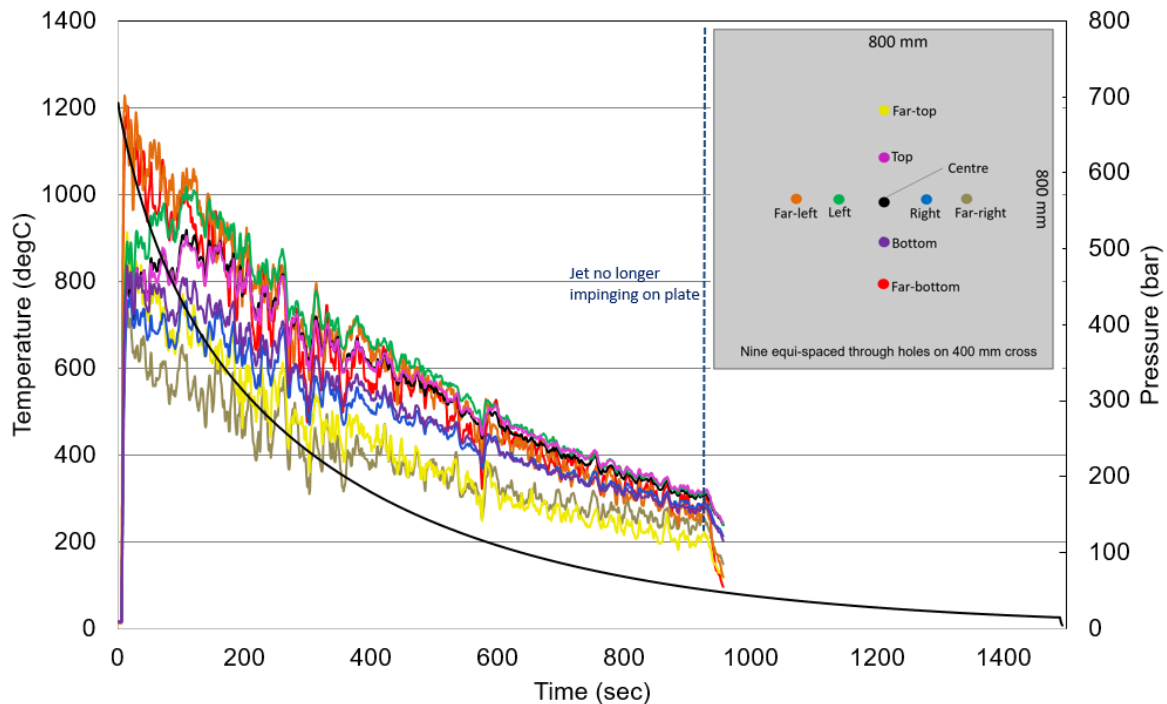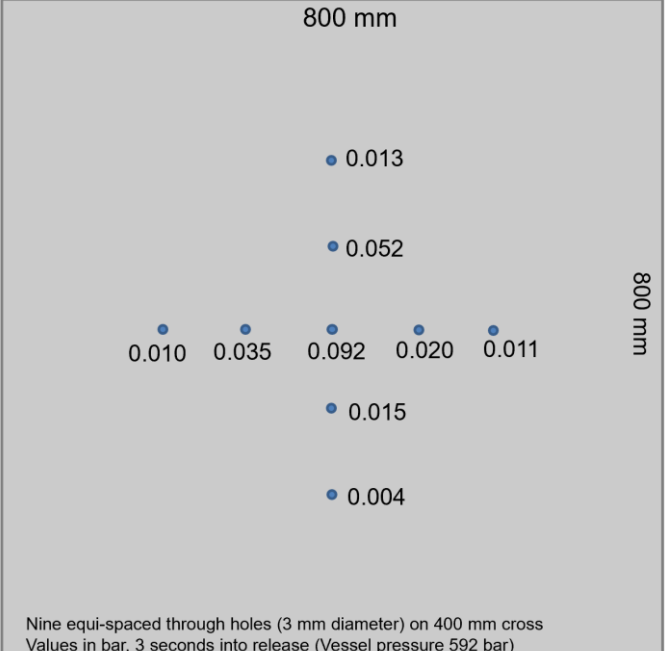
Figure 135: Impeded jet release; 0.5 mm nozzle, 49 L, 700 bar, 1 m standoff. Temperature readings taken, equi-spaced across a 400 mm cross, centred in the plate. Positions are relative to the front face of the plate. (Black solid line represents pressure decay in cylinder during blowdown).

6.2.12.3.2 Pressure plate impingement

One vessel (49 L) was used for each release, resulting in a blowdown time of just over 100 seconds. The pressure plate was at a standoff distance of 0.972 m. A moving average over 10 points has been applied to the data to align the 100 Hz sampling rate more closely with the vessel pressure blowdown. For the 2 mm nozzle (Test 5 in Table 30), the maximum pressure readings were recorded 3 seconds into the release, when vessel pressure reading was 592 bar. The values are listed in Table 31.

The sensor plate pressures decreased, trending in the same way as the vessel pressure i.e., decreasing over time, with the rate of decrease slowing as the vessels emptied. The pressure measurement from the central sensor is overlayed onto the vessel pressure reading in Figure 136 as an example.

Table 31: 2 mm nozzle pressure release data for the nine pressure sensors at maximum pressure, 3 seconds into the release, vessel pressure was 592 bar.

Location (distance relative to plate centre, mm)	Sensor Pressure at 3 seconds into release (bar)
Far right (200)	0.011
Right (100)	0.020
Centre (0)	0.092
Left (100)	0.035
Far left (200)	0.010
Far top (200)	0.013
Top (100)	0.052
Bottom (100)	0.015
Far bottom (200)	0.004

800 mm

• 0.013

• 0.052

0.010   0.035   0.092   0.020   0.011

• 0.015

• 0.004

800 mm

Nine equi-spaced through holes (3 mm diameter) on 400 mm cross
Values in bar, 3 seconds into release (Vessel pressure 592 bar)

Figure 136: Plot of the magnitude of the pressure at the central sensor on the sensing plate. The secondary axis contains an overlay of the simultaneous vessel pressure readings.

The test was repeated using the 0.5 mm nozzle (Test 6 in Table 30); the plate was at a standoff distance of 1.02 m. It was found that no pressure readings above background were measured using this nozzle at this standoff distance.

6.2.12.4 Concrete sample impingements

Four concrete samples were tested (Tests 7-10 in Table 30), two containing polypropylene (PP) fibres, and two without fibres. The impingement time varied depending on the nozzle size and standoff distance, ranging from 1.5 minutes for the 2 mm nozzle with greater standoff distance (2.24 m) to 40 minutes for the 0.5 mm nozzle at the closer standoff distance (1.06 m).

Table 32 summarises the test conditions of the releases for each concrete sample and the visual result following impingement from the jet.

Table 32: Jet impingement onto concrete samples; test parameters and visual results following test. PP = polypropylene.

	Nozzle diameter (mm)	Standoff distance (m)	Result
Sample 1 High strength concrete – No PP fibres	2	1.06 (3.5 mins impingement approx.)	Spalling across entire surface, deepest spall occurred at centre of sample.
Sample 2 High strength concrete – With PP fibres	2	1.06 (3.5 mins impingement approx.)	Minimal spalling occurred, scorch mark resulted
Sample 3 High strength concrete – With PP fibres	0.5	1.11 (40 mins impingement approx.)	No spalling occurred, larger scorch mark than that of Sample 2
Sample 4 High strength concrete – No PP fibres	2	2.24 (1.5 mins impingement approx. – due to greater standoff distance)	Spalling evident across the majority of the sample surface. Depth and extent of spall not as severe as Sample 1, which was closer to the release nozzle.

6.2.12.4.1 Laser scanning of surface

The surfaces of Sample 1 (no fibres) and Sample 2 (with PP fibres) were laser scanned in order to understand the depth of spall on each and is shown in Figure 137. The single lines, visible along the left and uppermost edge of the laser scans show a 1D representation of the depth profile across the centre lines of the samples (there is a faint cross visible on the scan itself to show the location that those depth lines relate to).

The sample containing no fibres, Sample 1, Figure 137a, spalled extensively across the entire surface of the sample, up to a depth of 30 mm in the centre of the sample. In contrast, the sample containing PP fibres, Sample 2, Figure 137b, appeared to scorch at the incident surface of the jet impingement but exhibited minimal ejection of concrete pieces. The same lack of spalling was observed when the other fibre containing sample, Sample 3, was impinged upon using the 0.5 mm nozzle. This had a much longer impingement time than the sample with the 2 mm nozzle i.e. up to 40 minutes instead of 3.5 minutes. In the case of the longer impingement time, a larger and more pronounced scorch mark resulted (diameter of the scorch mark was approximately 650 mm), however no spalling was observed. The final sample, Sample 4, which

had no fibres, was placed at a further standoff distance to see if the proximity of the jet had an effect on the propensity for spalling. This non-fibre containing sample spalled in a similar way to the first sample, however to a lesser depth. This is not surprising, given the shorter impingement time.
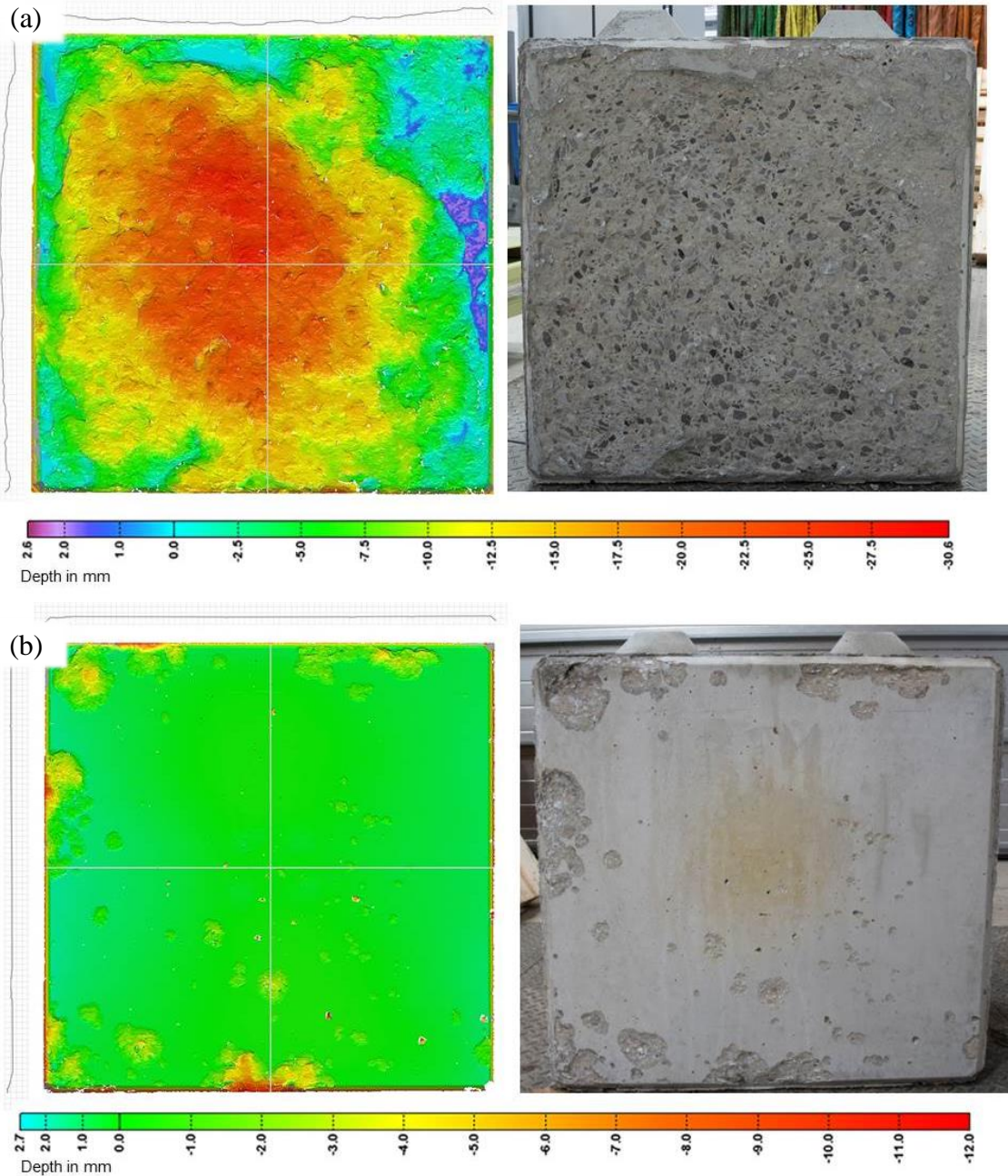
Figure 137: Laser scan and visual image of surface of (a) Sample 1, containing no PP fibres, and (b) Sample 2, containing PP fibres. Release conditions for both, 700 bar, 98 L, 1.06 m standoff, 2 mm nozzle. PP= polypropylene.

6.2.12.4.2 Post-test material analysis

Two cores each were extracted from Samples 1 and 2, post jet fire impingement, for further materials analysis. The results are presented in the sub-sections below.

6.2.12.4.2.1 Compressive strength

The compressive strength measurements for the two post jet fire samples are shown in Table 33. Also assessed was an additional core from Sample 4, extracted prior to the jet fire test. This sample was taken so that a comparative non fire impinged compressive strength measurement could be made for the sample containing no PP fibres i.e. the sample that exhibited spalling.

The results (Table 33), show that the compressive strength of the non-fibre containing samples does not appear to have been affected as a result of the fire impingement. A value of 55.3 N/mm^2 was recorded for the non-fire impinged sample vs. 54.9 N/mm^2 for the fire impinged sample. The compressive strength of Sample 2, the fibre containing sample is marginally lower than the non-fibre containing sample. However, this is not unexpected as polypropylene fibres would not contribute to the compressive strength in the same way as cement or aggregate. The lower (relative to the non-fibre containing sample) compressive strength value for the PP fibre containing samples was also observed during the curing process, when strength measurements were made.

Table 33: Compressive strength measurements as at time of testing.

	Sample 4 (pre jet fire)	Sample 1 (post jet fire)	Sample 2 (post jet fire)
Test parameter	None	2 mm nozzle, no PP fibres	2 mm nozzle, with PP fibres
Age at test (days)	337	337	337
Apparent density (kg/m^3)	2410	2420	2380
Core compressive strength (N/mm^2)	55.3	54.9	50.1

6.2.12.4.2.2 Thermal conductivity

Four thermal conductivity measurements were made, where sample cores were clipped to a depth of 45 mm and measured as per the standards described in 6.2.10.3.1. The first two clipped cores were taken from Sample 1, the non-fibre containing sample, where the front, fire impinged face and back, non-fire impinged face of the same full-length core were used. Likewise with the fibre containing sample, Sample 2, the front and back face cores were clipped and analysed in the same way.

Average temperature difference across the specimen was measured with thin thermocouples on the specimen surfaces and compressible foamed silicon rubber contact sheets either side, as described in BS EN 12664 : 2001 (BS EN 12664:2001 British Standards Institution, 2001). The measured properties for each core are listed in Table 34.

When concrete is subjected to heating, it has been found that the thermal conductivity declines with increasing temperature due to the moisture loss and the change of permeability at elevated temperature (Mohammed et al., 2022). During this process it is expected that there will be a migration of the moisture and a pore pressure increase i.e., pressure in the voids of the concrete, generated by water evaporation. This may ultimately result in a mass loss due to loss of moisture.

Considering the effects of jet fire impingement, the results as shown in Table 34 suggest a slightly lower thermal conductivity on the front, fire impinged, face of Sample 1 (non PP fibre containing) relative to the back face. This result is in line with the theory of having a lower thermal conductivity with declining moisture content (Saleheen et al., 2022). Sample 2 (PP fibre containing) on the other hand, displayed the opposite behaviour with the front, fire impinged, face having a higher thermal conductivity than the back face. This may be the result of the solid to liquid phase change that will occur when the polypropylene fibres are heated during the jet fire. Upon cooling, these may have left heat conduction channels in the melted fibres that would increase the thermal conductivity of the sample overall.

On a general note, at ambient temperature it is expected that the presence of PP fibres would, by their nature, provide increased thermal resistance, which would translate as a lower thermal conductivity than the non PP fibre containing sample.

Table 34: Thermal conductivity and resistance measurements for Sample 1 (no PP fibres) and Sample 2 (with PP fibres) for the front fire impinged faces and back non fire impinged faces.

	Sample 1 (front face)	Sample 1 (back face)	Sample 2 (front face)	Sample 2 (back face)
Thermal conductivity ($W·m^{-1}·K^{-1}$)	$0.649 \pm 2.5\%$	$0.792 \pm 2.5\%$	$0.933 \pm 2.5\%$	$0.614 \pm 2.5\%$
Thermal resistance ($m^2·K·W^{-1}$)	$0.0610 \pm 2.5\%$	$0.0500 \pm 2.5\%$	$0.0440 \pm 2.5\%$	$0.0680 \pm 2.5\%$
Density ($kg.m^{-3}$)	2198	2160	2161	2015
Mean temperature (°C)	10.7	11.0	10.9	10.8

6.2.12.4.2.3 Ultrasonic scanning

The method consists of measuring the time of travel of an ultrasonic pulse passing through the concrete being tested, in accordance with BS EN 12504-4:2004 (BS EN 12504‑4:2021 British Standards Institution, 2021). Comparatively higher velocity is obtained when the concrete quality is good in terms of density, uniformity, homogeneity, etc.

Three pulse velocity measurements were made for each sample, i.e., front and back face of Samples 1 and 2. The average of the three measurements for each sample is shown in Table 35.

All the measurements have velocities of greater than 4 km/s, which, according to the terms of the testing standard, would indicate very good to excellent quality concrete. The cores from the front face had slightly higher pulse velocity readings than their corresponding, non-jet impinged back face, but the differences are minimal.

The results indicate that the jet impingement and resultant spalling has had little effect on the uniformity of the concrete i.e., had not introduced structural deformities such as cracks or voids. It should be noted that this technique is better at picking up deformities of the order of

100 mm, and relatively small defects have little effect on transmission. Thus, the observed depth of spall i.e., up to 30 mm could possibly have been a surface only, relatively small defect, that would have little or no effect on transmission times. From a structural point of view, it is thought that defects of this magnitude are probably of minor engineering importance (BS EN 12504‑4:2021 British Standards Institution, 2021).

Table 35: Result from pulse velocity tests (average of 3 tests). All values were over 4km/s indicating good quality concrete with good structural uniformity.

Test	Pulse time (µs)	Path length (mm)	Pulse velocity (km/s)
Sample 1 (front face)	39.9	191	4.79
Sample 1 (back face)	39.8	185	4.65
Sample 2 (front face)	35.0	175	5.00
Sample 2 (back face)	42.2	195	4.62

6.2.12.4.3 Heat transfer through concrete core sample

Figure 138 shows the temperature readings measured by four thermocouples that were inserted into drilled holes in a clipped core from a sample containing no polypropylene fibres. This sample was then subjected to a jet fire impingement where the test conditions were one vessel (49 L), 2 mm nozzle, and a standoff distance of 1.09 m (Test 11 in Table 30).

The thermocouple temperatures readings (Figure 138) show that higher temperatures were recorded at locations closer to the surface. However, the central thermocouple, Temp 2 did not trend in the same way as the other three readings; this may have occurred due to poor thermal contact being made with the concrete surface. The other three thermocouples reached their maximum temperatures after the hydrogen reservoir had depleted and the jet fire was no longer impinging on the sample; thus, it is possible that the temperature readings may have continued to increase if the jet impingement time was longer. This release used only one vessel (49 L), lasting just over two minute; thus it's possible that the temperatures may have exceeded 100 °C (the vaporization temperature of water) had both vessels been used (the releases onto the concrete samples, as described in the preceding sections used two vessels and lasted 3 mins 45 secs).

In general, it is suggested that this data should be treated as indication only as there were uncertainties as to the effectiveness of thermal contact between thermocouples and concrete. Ideally, this test would be repeated where thermocouples would be inserted during the curing of the sample.
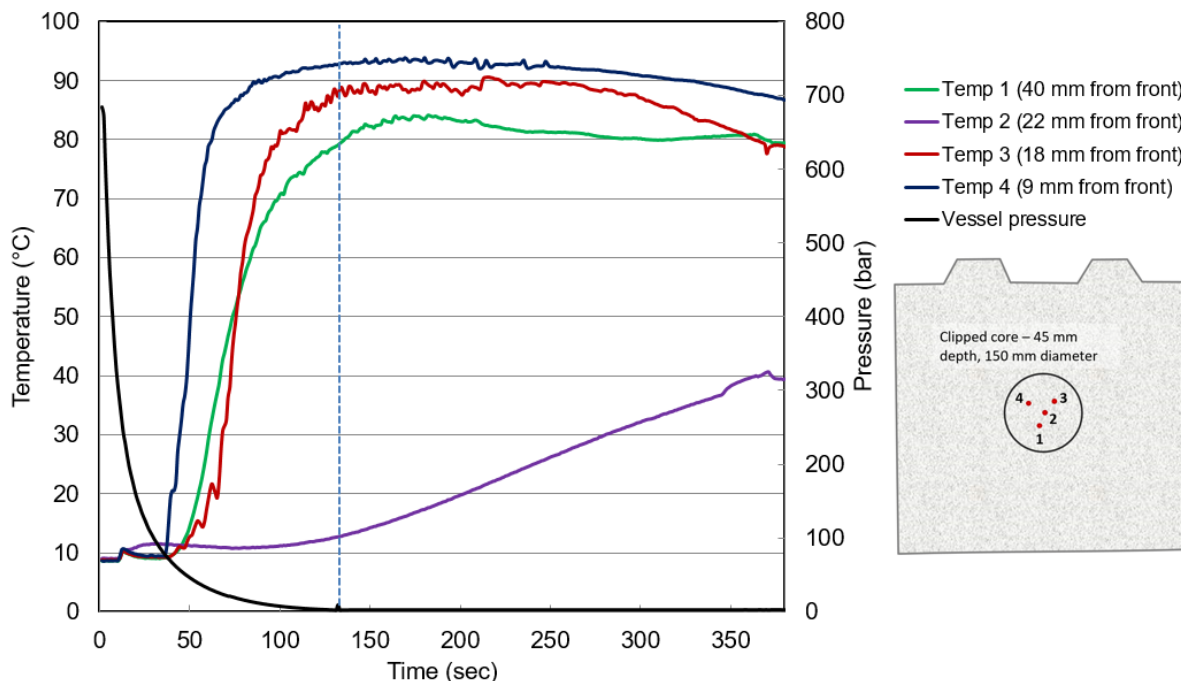
Figure 138: Heat transfer through concrete core sample. Temperature readings for thermocouples inserted into holes drilled to different depths within the reinstated concrete core sample.

6.2.12.5 Impeded jet release – tarmac sample

The thermally activated pressure relief device (TPRD) on a hydrogen fuelled car is typically oriented downwards onto the road surface, rather than towards the roof of the tunnel as with trains and buses, and so one release was carried out where the nozzle was directed downwards onto a typical road surface material i.e., tarmac. The stand-off distance between the nozzle and tarmac surface was 100 mm, approximately. The wider objective of this test was to provide a training visual reference for emergency service responders to identify whether vessel blowdown and jet fire had occurred.

The duration of the jet release onto the tarmac sample, was approximately 40 seconds, from 700 bar down to 212 bar (Test 13 from Table 30). The blowdown was stopped at 212 bar because nearby sensors and the release valve itself were at risk of becoming severely damaged (this was due to the protective fireboard falling over during the release, thus exposing the sensors and valve to the jet flames).

Figure 140 shows still images taken from video recording above the test site (via a drone) and at ground level. The images demonstrate the jet progression at ten second intervals over the 40 second period. The 0 second image shows the setup before the hydrogen jet was introduced, the 40 second image shows the setup immediately after the jet release valve had been closed.

The resultant flames (Figure 139) do not appear to contain partially combusted carbon products i.e., often evident as black smoke, as may be expected during combustion of a bituminous sample, suggesting that it is only the hydrogen providing the fuel source during the blowdown. The flames are visible; visible orange-ish flames were also observed during the horizontal impeded jets i.e., onto the concrete samples.

At the 40 second period, once the jet was quenched, black smoke was observed emanating from the tarmac sample, however the sample did not progress to sustained combustion. Figure 139

below shows the appearance of the sample once the black smoke was no longer emanating from the sample. In the central location of the sample, a well had been generated at the location where the jet directly impinged onto the sample. Parts of the sample were forcibly ejected during the release. It was also observed, immediately after the jet was quenched that there was a pool of molten tarmac of approximately half a metre diameter in the centre of the sample. The melting point of tarmac will vary depending on the grade of bitumen binder used but will typically soften between 50 and 80 °C.

Figure 139: Images of the tarmac sample, taken once the black smoke had receded. Note the molten pool in the left-hand image. Pieces of ejected tarmac are visible in the right hand image.
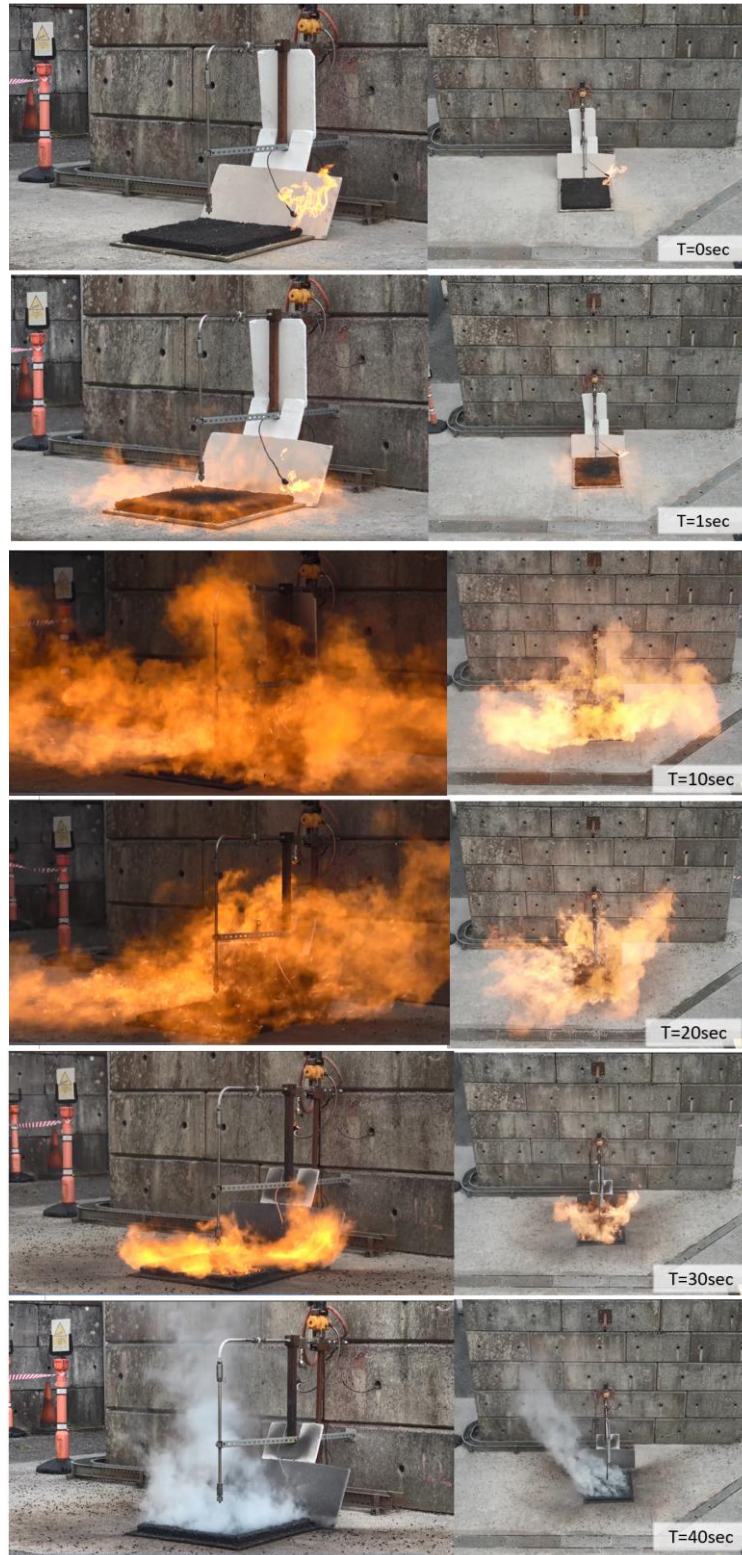
Figure 140: Still images from recording of jet release onto tarmac sample. Images show jet progression over the 40 second blowdown.

6.2.13 Discussion

6.2.13.1 Jet release characteristics

The axial temperature readings from the unimpeded jet releases for both nozzles show that the highest recorded flame temperatures were 1650 °C, and more likely to be 1800 °C. However,

the maximum range of the thermocouples is 1700 °C, therefore it is feasible that higher temperatures occurred. For the 0.5 mm nozzle, this maximum temperature was recorded by the closest thermocouple at 0.5 m from the nozzle, whereas for jet fires where the 2 mm nozzle was used, the maximum temperature was recorded 3 m downstream.

When the jet fire was impinging upon the temperature plate, the maximum temperature reading, for a standoff distance of approximately 1 m, was found to be 1200 °C at the jet centre, rising to 1400 °C at the surfaces adjacent to the first strike spot of the jet. When the jet fire using the 2 mm nozzle was impinged onto the pressure plate the maximum pressures were measured at the initial stage of the release. The maximum pressure reading was recorded by the most central pressure sensor where the jet was incident, giving a value of 92 mbar. The pressure readings from the adjacent surfaces gave a range of readings from 15-52 mbar at approximately 100 mm from the centre of the plate. The pressure readings over the duration of the release appeared to decay in the same way as the vessel pressure decay with blowdown.

The duration of a hydrogen release would be limited by the inventory of the vehicle, and the development/duration of a representative fire curve for a hydrogen jet fire would be of the order of a few minutes rather than 1-2 hours as is typical of the standard fire curves. Figure 141 shows an overlay of the free jet test results from the axial measurement of the 2 mm nozzle, 49 L, 700 bar release (Test 1 in Table 30) with the RABT-ZTV car fire curve.
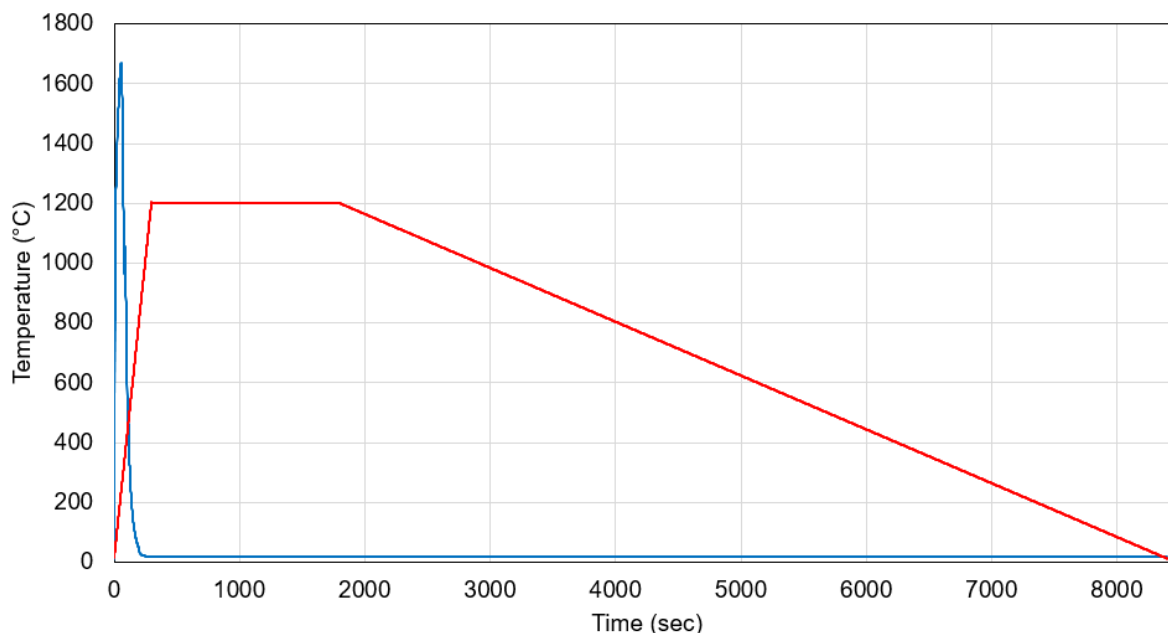
Figure 141: Plot showing comparison of temperature progression of 2 mm nozzle, 700 bar release vs. RABT-ZTV fire curve (car). Both are characterised by rapid initial temperature rises i.e., hydrogen jet temperature increases to a maximum of 1650 °C after 70 seconds approximately, whereas the fire curve, which assumes a hydrocarbon fuel reaches a maximum temperature of 1200 °C after 30 minutes.

The test data that has been used in Figure 141 illustrates a free jet and represents the highest temperature readings measured during this test programme. It was observed when the temperature plate was placed in the jet path, at a standoff distance of 0.95 m (Test 3 in Table 30), that the maximum temperatures achieved when the jet is impinging on a surface was 1400 °C, and tended to be along the adjacent surfaces to where the jet was incident on the surface i.e. where better fuel/air mixing occurred. The duration of the releases when considering the full inventory (98 L at 700 bar) for a 2 mm nozzle was approximately 3 minutes 45 seconds. Thus, a representative fire test curve for a hydrogen jet release from a car would be characterised by a rapid and intense temperature increase, up to potentially 1650 °C, lasting in the order of 3 - 5 minutes.

This test programme was undertaken outdoors and so these jets will likely have had better ventilation and quicker gas dispersion than would be expected in a tunnel. This may also facilitate better air/fuel mixture and thus higher temperatures. A similar study (Proust et al., 2011), was carried out where Type C thermocouples were placed along the axial path of a 900 bar jet, 25 L inventory with 3 mm nozzle and the maximum temperature reached was 1400 °C. This study was carried out in an enclosed facility, which may have reduced air/fuel mixing, however it is more likely that shorter blowdown duration i.e. up to 70 seconds, and differing response times, radiative losses (Roberts et al., 2011) from the two thermocouple types would be a larger contributory factor to explain differences between this study and the test programme covered in this report.

The work presented here has considered hydrogen jet releases to be the sole fuel source in the fire scenario, whereas in reality it is possible that other hydrocarbon fuelled vehicles may be involved. To account for this scenario, the fire curves could be designed to include this progression; it is expected that this portion of the scenario would then be accounted for using the typical fire curves profiles.

In terms of the jet light up, it was also noted that ventilation affected the ignition source i.e., gusting could move the ignition flame out of the jet path temporarily, resulting in a delayed ignition; this had consequences in terms of how mixed the jet was at the time of ignition and thus the resultant light up pressure and noise. A more informed fire curve could be developed by looking at results from WP4 tunnel experiments. In the WP4 programme, temperature and pressure readings have been recorded along the length of the tunnel and for different scenarios, including overpressures generated when a delayed ignition occurs.

6.2.13.2 Jet effects on structural material

It was observed that spalling occurred in both of the non-PP fibre containing concrete samples, even at the differing stand-off distances i.e., 1.06 m vs. 2.24 m. The samples containing the polypropylene fibres on the other hand, whilst sustaining a scorch mark in each case, did not appear to spall, even when using the 0.5 mm nozzle, which gave a longer impingement time than the 2 mm nozzle (40 minutes vs 3.5 minutes). For the most severely spalled sample, the maximum depth of the spalling was approximately 30 mm and the spalling appeared deepest in the central region of the sample. This is not unexpected given that the centre of the sample would be the area interacting for the longest with the jet flame and would have less opportunity to relieve stresses from thermal expansion compared to the edges.

Post-test analysis i.e., pulse velocity measurements looking for defect formation and compressive strength measurements looking at sample strength suggested that the damage sustained by the samples was mostly superficial and would probably not contribute serious engineering repercussions as result of an impingement of this type and duration. The heat transfer measurements suggested that the temperatures at increasing depth into the sample did not appear to approach those temperatures at which pore pressure increases, and spalling is likely to occur i.e., 200-300 °C.

It is worth commenting that these test methods and results are specific to this setup only. Previous research (Mcnamee & Jansson, 2015) has concluded that a multitude of factors, including the chosen test method, will influence whether spalling will occur, not one property in isolation. For example, it was found that larger samples with the same concrete composition as smaller samples were found to be more likely to spall due to the added load generated by the sample bulk itself (Mcnamee & Jansson, 2015). Previous research has noted that the severity of spalling appears to be greater when the sample is exposed to slower heating rate rather than faster heating (Mindeguia et al., 2009; Phan, 2008). Thus, it is possible that though hydrogen has the potential to reach greater temperatures and faster than that of a hydrocarbon fire, the resultant fire by itself, may not contribute additional risk in terms of erosion of structural materials.

6.2.13.3 Recommendations for regulations, codes, and standards

As mentioned in 6.2.13.2, and commonly noted when researching this area, it is difficult to conclude a definitive test method for spalling due to the multitude of factors that can affect the resultant behaviour of a structural material when fire impinged. In the case of an unobstructed hydrogen jet, with the limited inventory e.g. 2-4 kg hydrogen, temperature rather than pressure appeared to be the most influencing factor.

It is envisaged that other factors such as delayed ignition, and further obstruction by presence of vehicles could contribute to a different fuel/air mixing scenario situation, which may

contribute additional pressure effects that were not seen in this test programme. Work package 4 investigates this in more detail and so measured overpressures in this work could be used to inform on representative pressure tests to be considered for structural material.

The key findings and recommendations from this work are:

1. The materials testing results indicate that polypropylene fibres do provide effective fire resistance in concrete samples when impinged upon with a hydrogen burning jet. It was found that the impinging hydrogen jet, over the short duration of venting of a typical vehicle inventory, would be unlikely to cause more severe damage than that of a hydrocarbon fuelled fire.
2. The present test results will be specific to both the jet fire setup used and the composition of the sample itself and the results are not necessarily directly transferable to any arbitrary sample. For example, ventilation will affect the magnitude of the resultant temperature of the burning hydrogen jet, compression/external load on the sample will affect its propensity to spall. Therefore, it is recommended that a wider range of test conditions and material properties are investigated.
3. A representative materials test, similar to existing fire curve scenarios should be developed e.g., a standard test where a sample is exposed to a temperature profile over a defined time period. In contrast to existing fire curves, a burning hydrogen jet from a vehicle would be characterised as a short duration event with a rapid temperature increase, which then decays with the decreasing jet pressure.
4. The use of the smaller nozzle diameter did result in shorter hazard distances when considering the extent of the temperatures reached. Thus, the use of smaller TPRD sizes will limit the size of the affected zone around a vehicle accident/jet fire.
5. The hydrogen free jet itself is not visible, however when impinging upon a surface, a bright yellow-orange flame was observed. In addition, the noise generated by the momentum driven jet could be heard easily, whether ignited or not. Therefore, it is expected that there would be visual and audible indicator to inform emergency service responders that there is a depressurising vessel and hydrogen jet fire.

6.2.14 Conclusions and suggested further research

6.2.14.1 Conclusions

A series of high-pressure hydrogen jet tests were carried out, aiming to understand the jet characteristics of an ignited hydrogen jet, and the erosive effects of this jet on structural materials with an overall aim of using these observations to provide recommendations for relevant Regulations, Codes, and Standards.

It was shown that the hydrogen jet can produce temperatures up to 1650 °C when unimpinged, with temperatures of up to 1400 °C when impinging on a surface. It was noted that the location of the maximum measured temperatures and thus hazard distances were greatly reduced when the release nozzle diameter was reduced e.g., maximum temperature of 1650 °C at 0.5 m distance for a 0.5 mm nozzle vs. over 3 m distance for a 2 mm nozzle.

In terms of the erosive effects, the testing and analysis indicated that a short duration hydrogen jet impingement i.e., 4 kg hydrogen inventory, 700 bar release through a 2 mm nozzle lasting for 3 mins 45 secs approximately, appeared to generate surface spalling only (to a depth of 30 mm at its worst). The post-test material analysis indicated that the jet impingement did not

appear to have weakened the concrete or introduce appreciable pore deformation or defects into the concrete itself. The presence of polypropylene fibres in some samples, a known mitigation strategy for spalling, proved effective for a hydrogen jet also, with no spalling observed on those samples.

6.2.14.2 Further research

As mentioned in the discussion section, it is difficult to use the conclusions drawn from this one test programme as a definitive guide for behaviour of other structural materials as there are a multitude of factors, including the chosen test method, which will influence whether spalling will occur, not one property in isolation.

Further hydrogen testing should be undertaken where factors such as external loading are implemented, or where reinforcement materials have been included. Pore deformation due to pore pressure is cited as one of the major influencing factors for spalling. Real-time measurements of strain, temperature and pressure within the concrete structure should be performed, potentially considering smaller embedded sensors where their presence would not disrupt the bonding of the material during curing e.g., distributed fibre optic sensors.

Little is understood as to the mechanism of concrete degradation when exposed to rapid temperature change. This factor should be further investigated in order to understand if there are additional risks that a hydrogen jet, which by its nature produces a rapid temperature increase, may contribute that would not be identified during regular fire resistance testing.

7. Explosion prevention and mitigation (WP4, HSE)

7.1 Analytical studies, development, and validation of engineering correlations (Task 4.2, UU)

7.1.1 Engineering models for assessment of blast wave and fireball of hydrogen tank rupture (UU)

7.1.1.1 Universal correlation of blast wave decay in a tunnel with presence of vehicle

7.1.1.1.1 Background

State-of-the-art research done on high-pressure hydrogen tank rupture and the attenuation of blast waves in tunnels is very limited. Several parameters such as, the energy of the hydrogen stored based on volume and pressure, and the tunnel dimensions, all have a significant influence on peak overpressure and its attenuation in a tunnel. The condensed material used for explosive sources for the generation of blast wave in tunnels is mostly TNT, or its equivalent mass in form of another explosive charge. The initial form of the blast wave decay law, as shown in equation (1), below, indicates the dependence of the peak overpressure, P, on the ratio of charge weight, m, to volume of enclosure or tunnel, V, taking the general form:

$$P \propto A\left(\frac{m}{V}\right)^{b},$$

where A and b are derived empirically from best curve fits, and therefore mostly defined within specific parameters, such as distance or overpressure (Curran, 1966; Fang et al., 2019; Smith and Sapko, 2005). However, this method limits the fitted values of A and b to one -tunnel-case applicability. Furthermore, the constraint in the power law method suffers from the omission of other factors, such as the geometrical shape of the tunnel (i.e., aspect ratio), the percentage of energy of tank that becomes blast wave and minor and friction losses along the tunnel distance. With the aim of developing a universally applicable model across various tunnel sizes, these additional parameters are all considered in the novel methodology developed for blast wave decay in tunnel in this study.

7.1.1.1.2 Problem formulation

A CFD model was used in this study, to analyse the effect of high-pressure hydrogen tank rupture in a tunnel with presence of vehicle. This model development and the related validation processes are described elsewhere (Molkov and Dery, 2020; Molkov and Kashkarov, 2015). Within this project, building on the previous CFD model for tunnel without vehicle conditions, a parametric numerical study is conducted with the aim of developing a correlation between blast wave decay and tunnel confinements to include the vehicle. This includes tunnels with cross-sections 24, 40 and 139 m^2 (corresponding to tunnels with 1, 2 and 5 traffic lanes) and tank masses of hydrogen ranging from 0.58 kg to 6.96 kg with pressure before burst values of 95 MPa. The dimensions and parameter of the tunnels and tanks used in the simulations are summarised in Table 36 below.

Table 36: Tunnel dimensions and hydrogen tank parameters used in rupture simulation.

Tunnel cross section, m^2	Tunnel length, m	Tank volume, L	Tank mass, kg	Tank pressure, MPa
24, 40, 139	750 m	10	0.58	95
		30	1.7	
		60	3.5	
		120	6.9	

7.1.1.1.3 Dimensionless variables

To determine a decay law for blast wave overpressure in a tunnel, the main impact parameters of influence are required. There are various interpretations of these parameters, but the most commonly ascertained are the following: atmospheric pressure, P_0, energy of the blast, E, the cross-section area of the tunnel, A, and the distance of the wave from the energy release point, L. To find the relationships between these four physical quantities, dimensional analysis is firstly performed, identifying the three basic dimensions as mass, $M = kg$, length, $L = m$, time, $T = s$. Table 37 shows the variables for the parameters mentioned together with their dimensions.

Table 37: Variables of the problem together with the corresponding symbols and dimensions.

Variable	Symbol	Basic dimensions
Atmospheric pressure	P_0	$M^1 L^{-1} T^{-2}$
Energy	E	$M^1 L^2 T^{-2}$
Tunnel cross-section area	A	$M^0 L^2 T^0$
Distance from release	L	$M^0 L^1 T^0$

Using the Buckingham π theorem, a relationship between the variables can be represented as follows; with four physical quantities presented and three dimensions, there is one $(4 - 3 = 1)$ independent dimensionless π parameter. Choosing three parameters (i.e., P, L, E) to be repeating variables, the one dimensionless quantity is derived as $\pi_1 = \frac{(P_0 L A)}{E}$. This derived quantity may be considered as a dimensionless distance based on storage tank energy and tunnel dimensions and represented as:

$$\overline{L} = \frac{P_0 L A}{E}$$

To convert overpressure, ΔP, from dimensional to dimensionless form it is divided by the surrounding (atmospheric) pressure:

$$\overline{P} = \frac{\Delta P}{P_0}$$

7.1.1.1.4 Contribution of energies

The total energy released on tank rupture in a car fire accident includes not only the instantaneously released mechanical energy of compressed hydrogen (i.e., "physical explosion"), but also the energy of chemically reacting hydrogen (i.e., combustion energy). In calculations, the total released energy is defined as:

$$E = \alpha \cdot E_m + \beta \cdot E_{ch}$$

with E_m and E_{ch} being the total mechanical compression and chemical energies of hydrogen in the vessel respectively; α is a mechanical energy coefficient; β is a chemical energy coefficient. For high-pressure tank rupture, close to the ground surface, the shock wave is reflected back in its entirety, and therefore, the energy associated with the generated blast wave will be twice as large. However, due to energy lost to partial reflections and ground cratering, a factor of $\alpha = 1.8$ is used. The chemical energy coefficient, β, indicates the fraction of the total hydrogen chemical energy gradually released during complete combustion contributing to the blast wave. This is determined either by the inverse problem method based on experimental values (found to be 5 % for the open atmosphere tank rupture and described by (Molkov and Kashkarov, 2015)), or by identifying, through simulation, when the primary (or leading) shock leaves the combustion zone. The contribution from combustion energy occurs only when the leading shock is still within the combustion zone. Once propagated away from the combustion zone, the secondary wave inhibits the energy feedback, by acoustic waves overcoming the positive temperature gradient generated spatially ahead, towards the leading front. In the absence of detailed experimental data on hydrogen tank rupture in tunnels, the second method to determine the chemical energy coefficient β is used in this study. The determined fractions of α and β, together with the calculated energies are listed in Table 38 below.

Table 38: Determined energies contributing to the leading shock, based on total energy, including coefficients α and β.

Tank mass, kg	Tank pressure, MPa	α	β	$\alpha \cdot E_m$, MJ	$\beta \cdot E_{ch}$, MJ
0.6	95 MPa	1.8	0.12	6.3	8.2
1.7			0.11	18.9	22.9
3.5			0.11	37.8	45.9
6.9			0.095	75.6	79.2
5.2	70 MPa		0.10	51.5	61.8
2.6	35 MPa		0.11	12.5	30.9

7.1.1.1.5 Numerical details for tank rupture simulation

Simulations are performed using ANSYS Fluent V2021R2 as a CFD engine. The density-based solver is coupled with LES for turbulence with the Smagorinsky-Lilly model for simulation of sub-grid scale turbulence and the Finite rate Eddy Dissipation combustion employing one-step reaction. The governing equations are based on the filtered conservation equations for mass, momentum, and energy in their compressible form with Redlich-Kwong real gas EoS. The tunnel walls and floor are specified as non-adiabatic to allow heat transfer from the combustion no-slip wall conditions applied. The external non-reflecting boundary is defined as a pressure outlet with zero-gauge pressure. The Least Square Cell-Based and second-order upwind scheme were used for convective terms. The time step adapting technique was employed to maintain a constant Courant-Friedrichs-Lewy (CFL) number at the value of 0.2 until the blast wave left the tunnel at 1 s and gradually increased up to the value of 2 during 100 time seps to speed up the simulation of a fireball.

The computational grid is shown in Figure 142 with refinement zone around the vehicle.
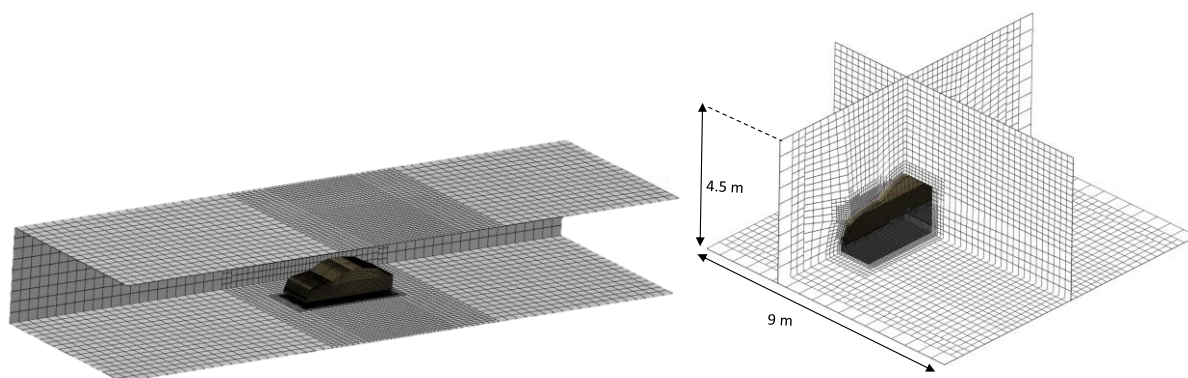
Figure 142. Example of computational grid for 2 lane tunnel: middle segment 3D (left), cross-sections (right).

Altogether there were 12 simulations performed that include tunnels with cross-sections 24, 40 and 139 m^2 (corresponding to tunnels with 1, 2 and 5 traffic lanes) and 4 different inventories as shown in Table 39. A single lane of a minimum width of 3.5 m was considered to treat the worst-case scenario. Following the lane width, a standard 1 m is extended on each side referring to the area outside the marked driving lane, totalling a singlelane tunnel width as 5.5 m. For the second tunnel geometry chosen, road traffic is mostly constructed using two lanes, and in some countries, e.g. Germany, they constitute up to 90% of all rural roads. This was actualised by extending the single-lane tunnel geometry by another 3.5 m lane, totalling the width to 9 m. The height was kept the same at 4.5 m.

A third tunnel geometry chosen as a part of the parametric study to accommodate the road tunnel with the largest cross-section area currently constructed. The Yerba Buena tunnel, part of the San Franciscoe Oakland Bay Bridge, was selected as an example of a tunnel with a large cross-section area. This tunnel features a double-decked design, each five-lanes, the larger upper deck with a total cross-section area of around 140m^2. In extending the number of lanes to 5, the height was also correspondingly increased to meet the required cross-section area target. The calculated height was 7.2 m. Parameters of the tunnels and respective tank inventories are given in Table 39.

Table 39: Tank inventories and energies stored.

Hydrogen volume, L	Hydrogen pressure, MPa	E_m, MJ		E_{ch}, MJ		E_{tot}, MJ
		E_m	αE_m	E_{ch}	βE_m	$\alpha E_{m+} \beta E_m$
15	95	73.45	4.38	73.45	8.81	13.19
30		146.94	8.75	146.90	17.63	26.38
60		293.81	17.50	293.81	35.26	52.76
120		587.62	35.01	587.62	70.51	105.52

7.1.1.1.6 Blast wave propagation

Figure 143 shows the maximum blast wave overpressure measured across the entire cross-section at each distance over the entire duration of the process. Capturing the maximum overpressure, including those from reflections, is a conservative approach that somewhat acts irrespective of the two zones. The general trend of all the curves is similar to those been obtained in the previous study with a stand alone tank in a tunnel (Molkov and Dery, 2020). In the beginning, pressure peak is observed to decay quite significantly with very slight oscillations due to initial reflections of the tunnel structure and Mach stem formation and

disappearance at different locations of the tunnel surface. Once the transition from initial 3D to 1D (planar) blast wave front propagation is established, the pressure attenuation rate is significantly reduced.
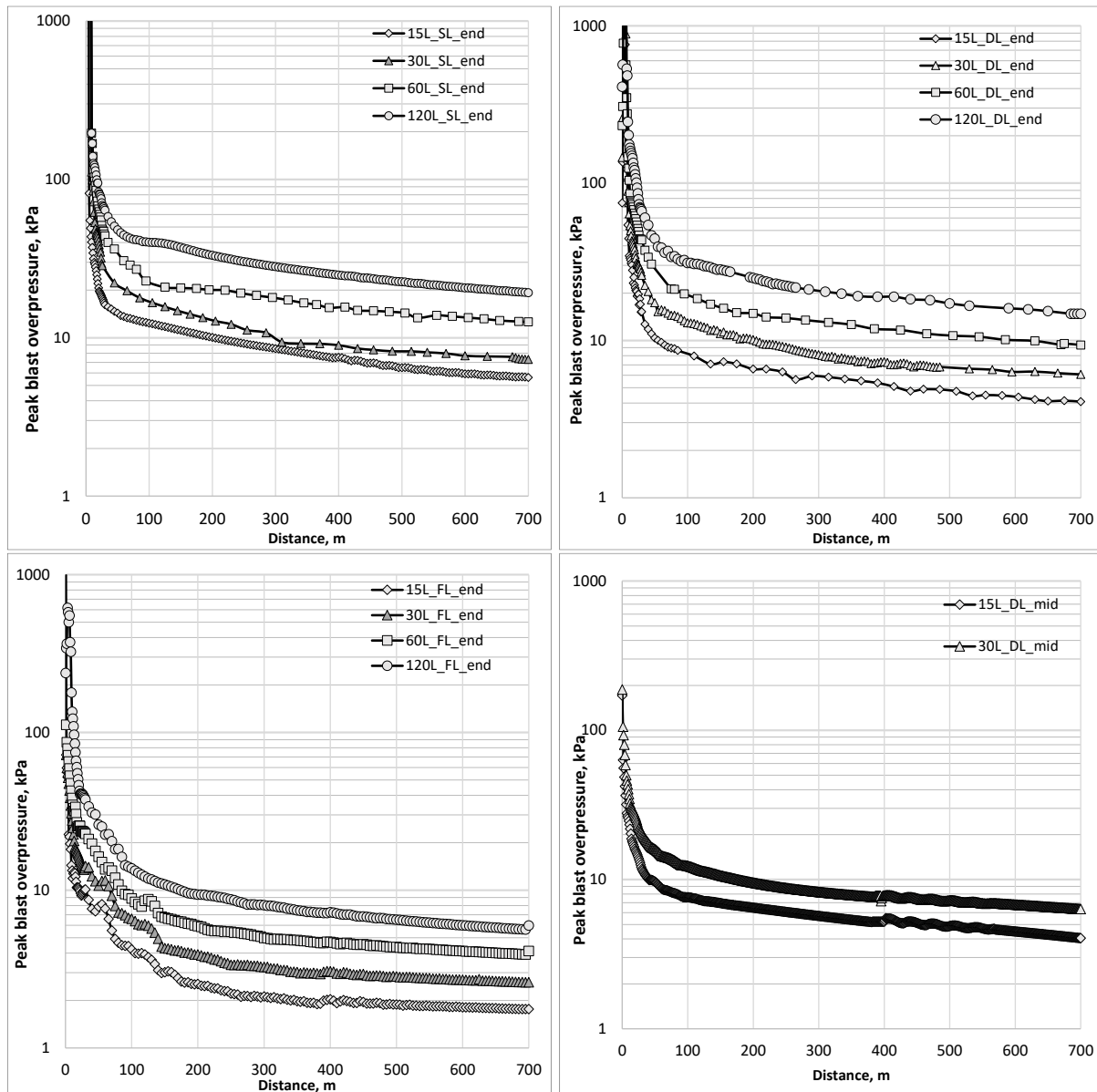
Figure 143: Maximum blast wave overpressure as a function of distance for different tunnels and hydrogen inventories at tank, single lane (top left), double lane (top right), five lane (bottom centre).

7.1.1.1.7 Correlation for blast decay in the tunnel

Following the logic outlined in the previous study (Molkov and Dery, 2020) and having new simulation data shown in Figure 143 above with the presence of vehicle the adjusted correlation for the best-fit and conservative estimate have been derived which is shown in Figure 144.

The scatter of correlation points around the best fit curve was checked around different powers of the friction parameter fL=DT: m = 0.5, m = 1 and m = 2. Furthermore, with the introduction of friction parameter, the determined power of AR was re-tested.
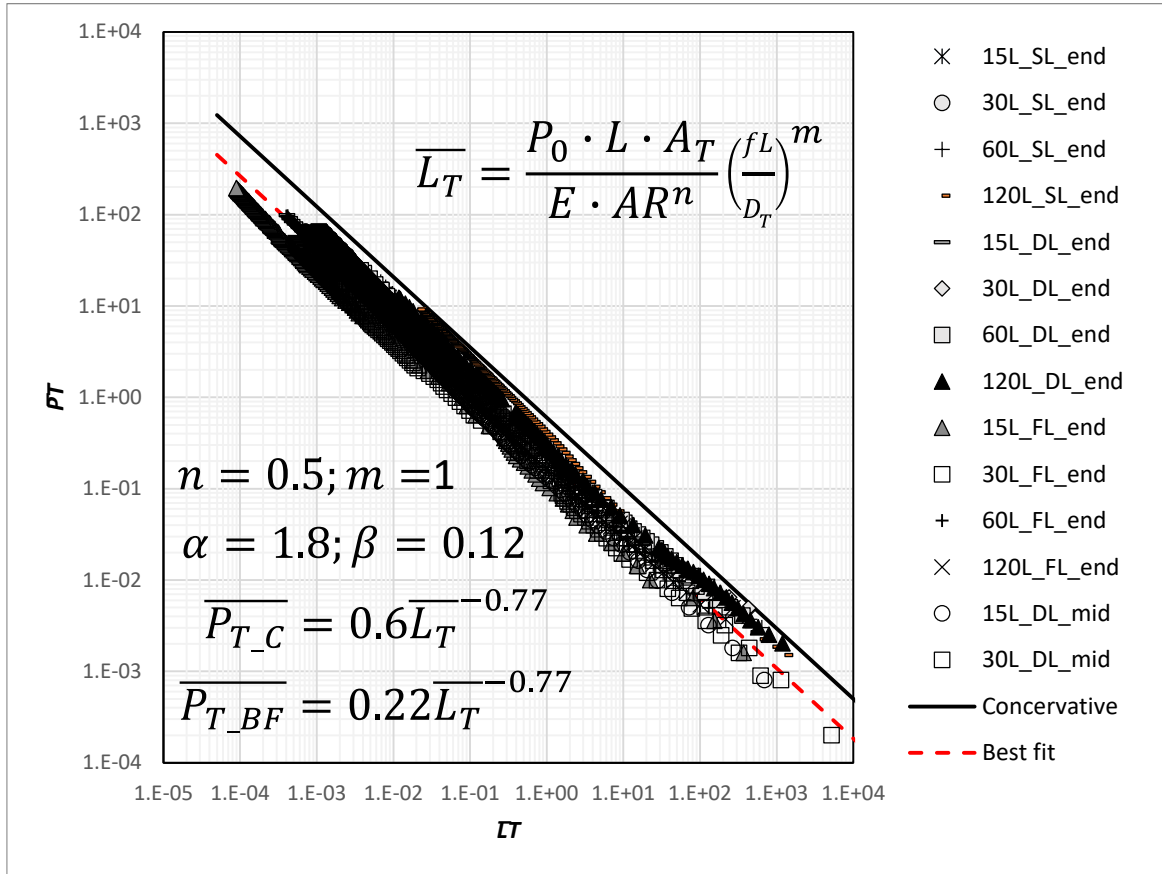
Figure 144: The universal correlation for the blast wave decay after a hydrogen tank rupture in a tunnel fire.

7.1.1.1.8 Example of application

The application of the universal correlation for the blast wave decay in a tunnel requires the following calculation steps:

1. Hydrogen mass in the tank
$$m = \rho V = \left(\frac{P_G}{P_G b + RT/M}\right) V$$

2. Mechanical energy
$$E_m = \frac{(P_g - P_0)(V - mb)}{\gamma - 1}$$

3. Chemical energy
$$E_{ch} = m \cdot H_C$$

4. Total energy
$$E = \alpha \cdot E_m + \beta \cdot E_{ch} \quad \alpha = 1.8, \ \beta = 0.12$$

5. Tunnel hydraulic diameter
$$D_T = 4A_T/P$$

6. Dimensionless tunnel length
$$\overline{L}_T = \frac{P_0 L A_T}{E \cdot AR^n}\left(\frac{fL}{D_T}\right)^m$$

7. Dimensionless pressure
$$\overline{P_{T\_C}} = 0.6\overline{L_T}^{-0.77}, \ \overline{P_{T\_BF}} = 0.22\overline{L_T}^{-0.77}$$

8. Dimensional overpressure
$$\Delta P = \overline{P} \cdot P_0$$

7.1.1.1.9 Conclusions

The study of blast wave after under-vehicle tank rupture in a fire in a tunnel was performed. The CFD model was validated against experiment. The correlations to assess the blast wave decay after high-pressure hydrogen tank rupture in a tunnel are proposed on compressed hydrogen tank rupture in a fire. The correlations have been compared with the numerical simulation to assess the dynamics of blast wave. It could be stated that none of simple correlations can be applied for the blast wave hazard distance in a tunnel due to dynamics of its propagation.

7.1.1.2 Fireball model

The work focuses on the assessment of hazard distances arising from the fireball following the high-pressure hydrogen tank rupture in a fire in a tunnel. The semi-empirical correlation to assess the fireball size in a tunnel proposed in previous deliverable shown not sufficient performance compared to the CFD results achieved, therefore additional numerical study was required to close this knowledge gap and propose a new correlation for the assessment of fireball distance propagation in different tunnels and various inventories.

7.1.1.2.1 Temperature and hazard distance distribution in a tunnel

Following the blast wave the simulation continued to study the fireball and all simulations with the dynamics of the fireball is presented in Figure 145 to Figure 147. Each figure shows the dynamics of the hazard distances defined by the temperature "fatality" (red, 309 °C), "pain" (yellow, 115 °C), "no-harm" (green, 70 °C). As can be seen from all cases the fireball behaves in a similar manner. The tank rupture happens 50 m from the tunnel entrance and first after rupture the fireball occupies all tunnel cross-section and rises up to the ceiling; after that extends to both sides, but after a while it propagates to the longer side being dragged by the blast wave extending the hazard distance inside the tunnel.

All simulations were kept as long as reasonably possible since some of them took more than a month. They were stopped at the moment when the layer was about 50 cm thick and temperature below the fatality threshold.
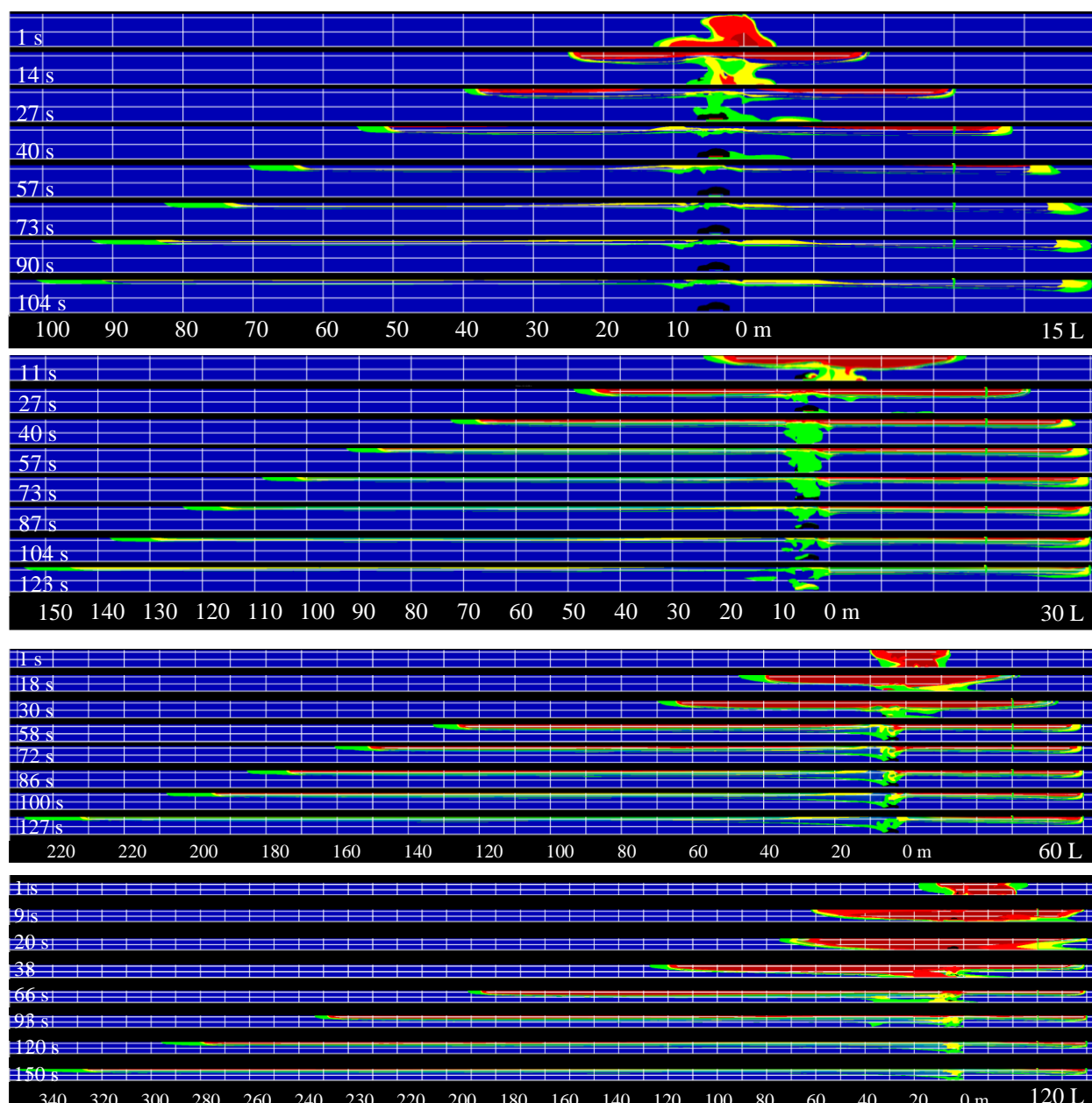
Figure 145: Snapshots of hazard distance defined by temperature distribution in a single lane tunnel.
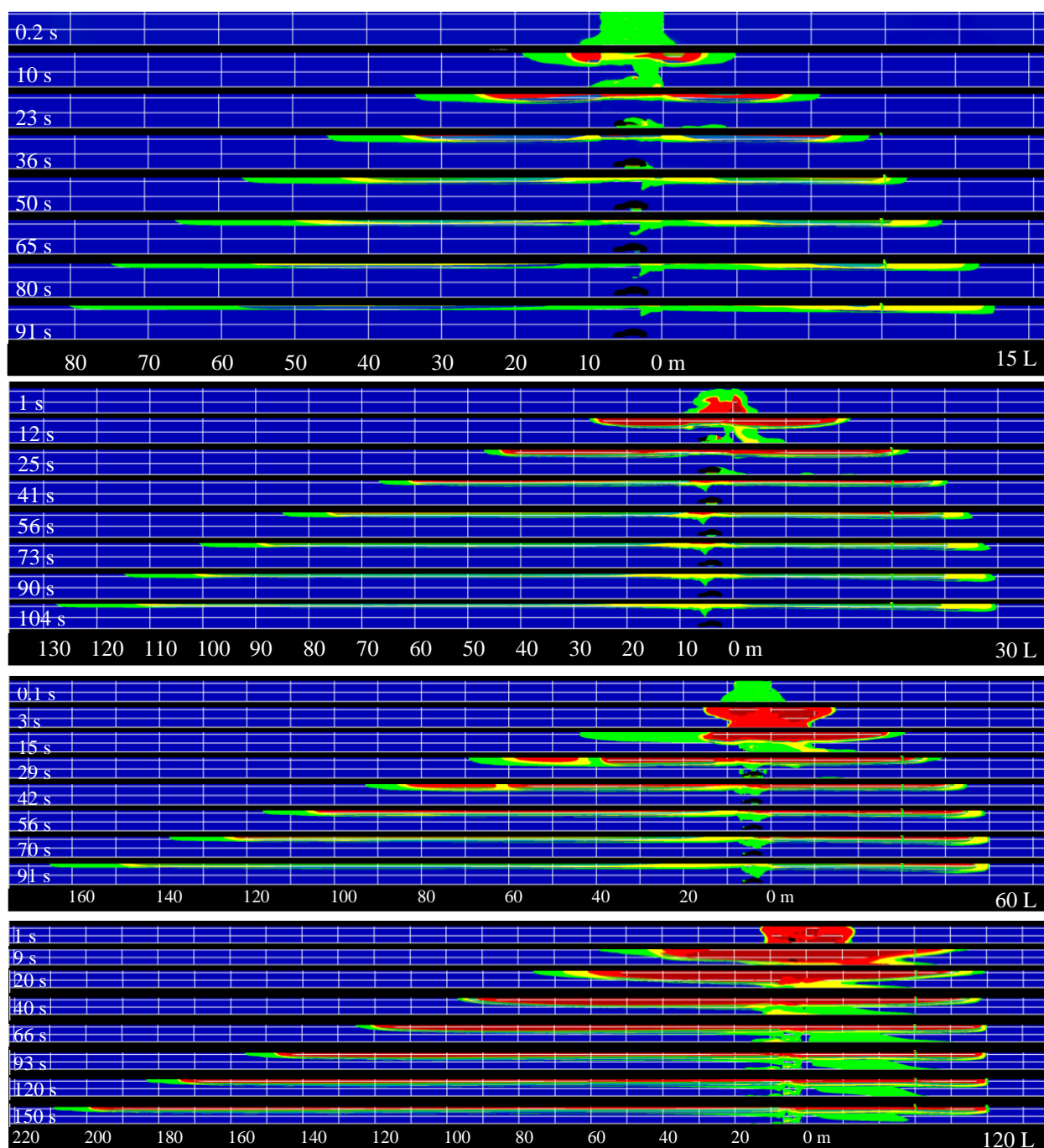
Figure 146: Snapshots of hazard distance defined by temperature distribution in a double lane tunnel.
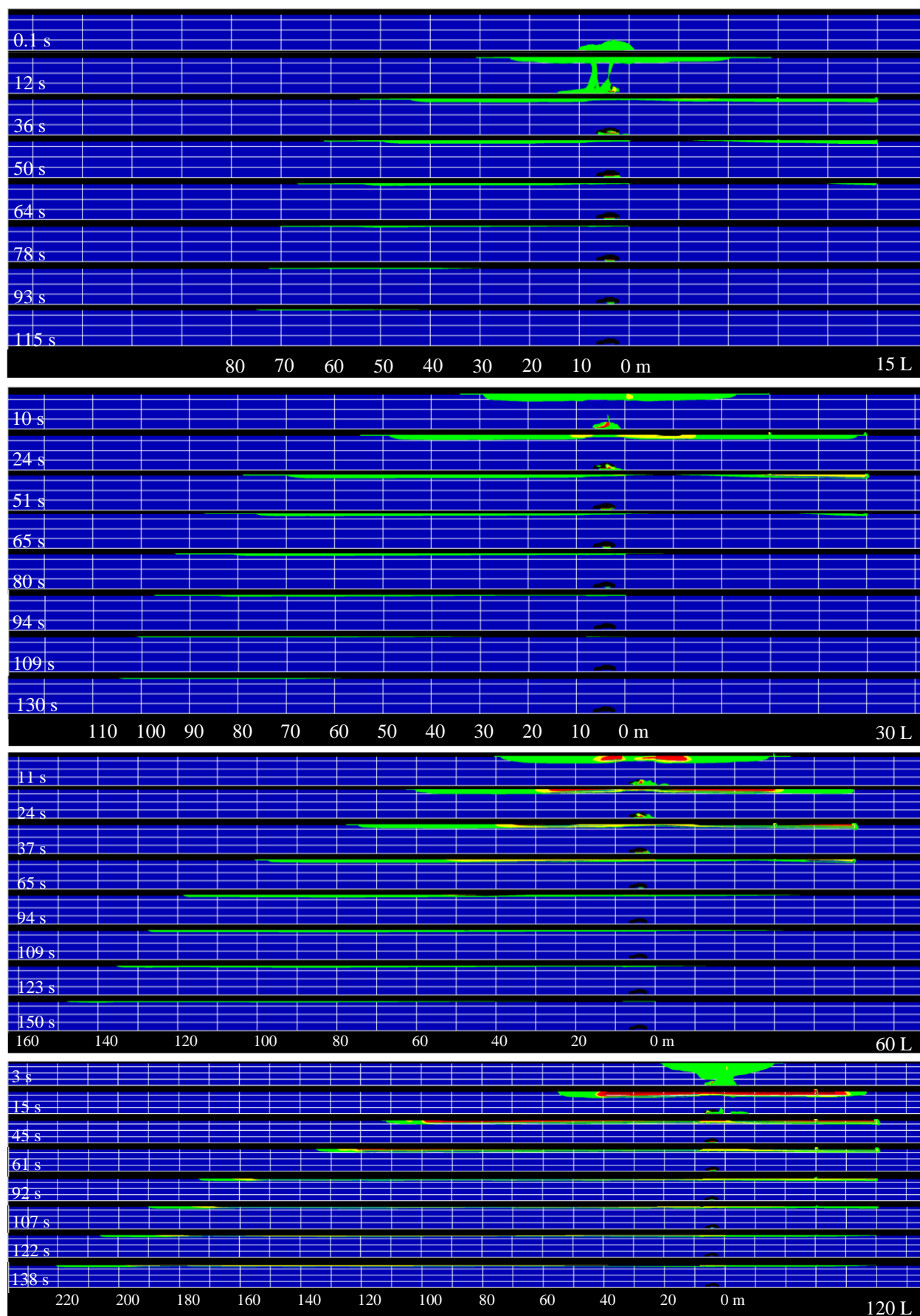
Figure 147: Snapshots of hazard distance defined by temperature distribution in a five lane tunnel.

The propagation of the hazard distance with time for various tunnels and inventories is presented in Figure 148 below.
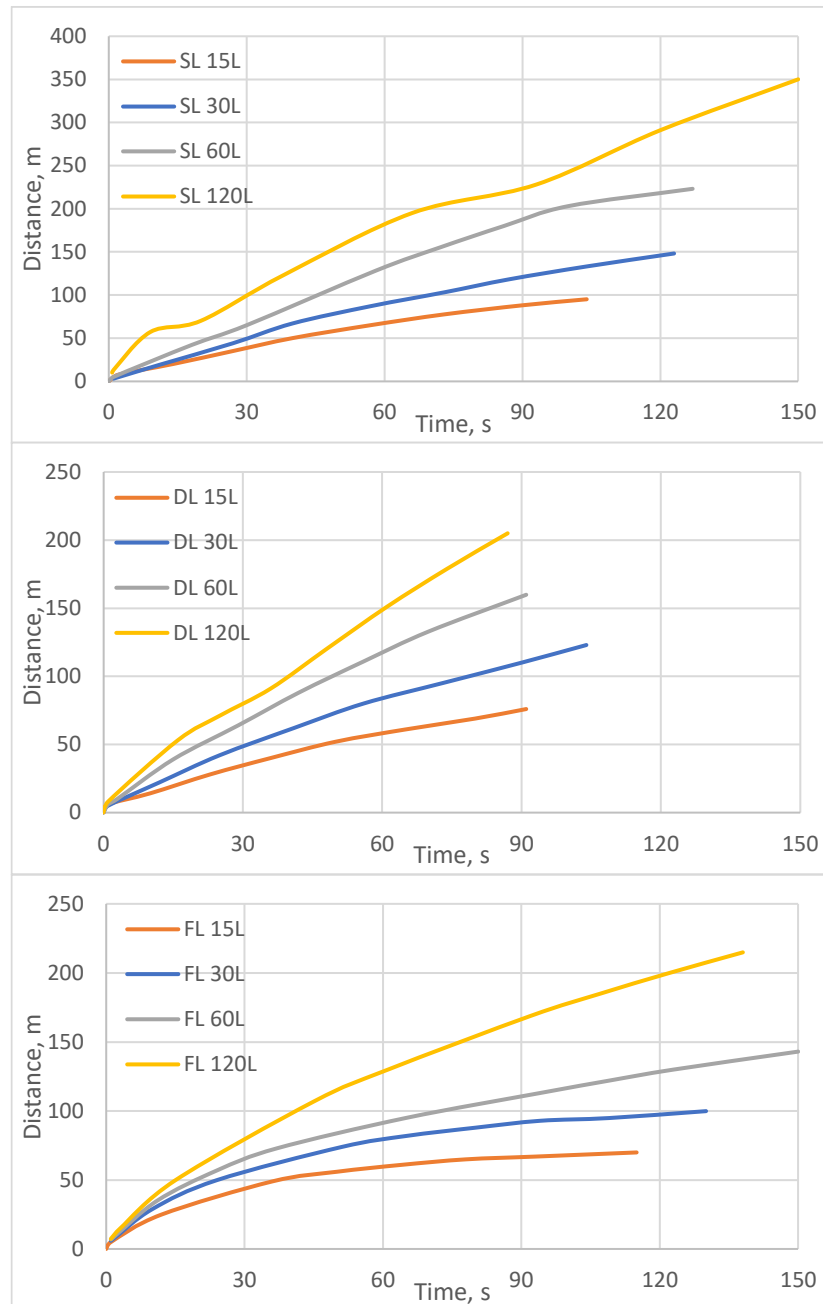
Figure 148: Fireball distance with time in a single (top), double (middle) and five (bottom) lane tunnels.

As can be seen, the distance is clearly dependent on the area of the tunnel. The extent of fireball propagation is decreasing with the increase of the tunnel area and increases with the increase of hydrogen inventory.

Figure 149 shows the velocity of the fireball with time, and it is clear that at the beginning it is higher due to the momentum of the expansion of the hydrogen gas followed by the combustion. The velocity decreases with time regardless of the inventory and tunnel area but still, the maximum is higher for larger inventories. Therefore, having this data it is possible to derive a

correlation to predict the velocity and location of the fireball hazard distance for any inventory and tunnel parameters.
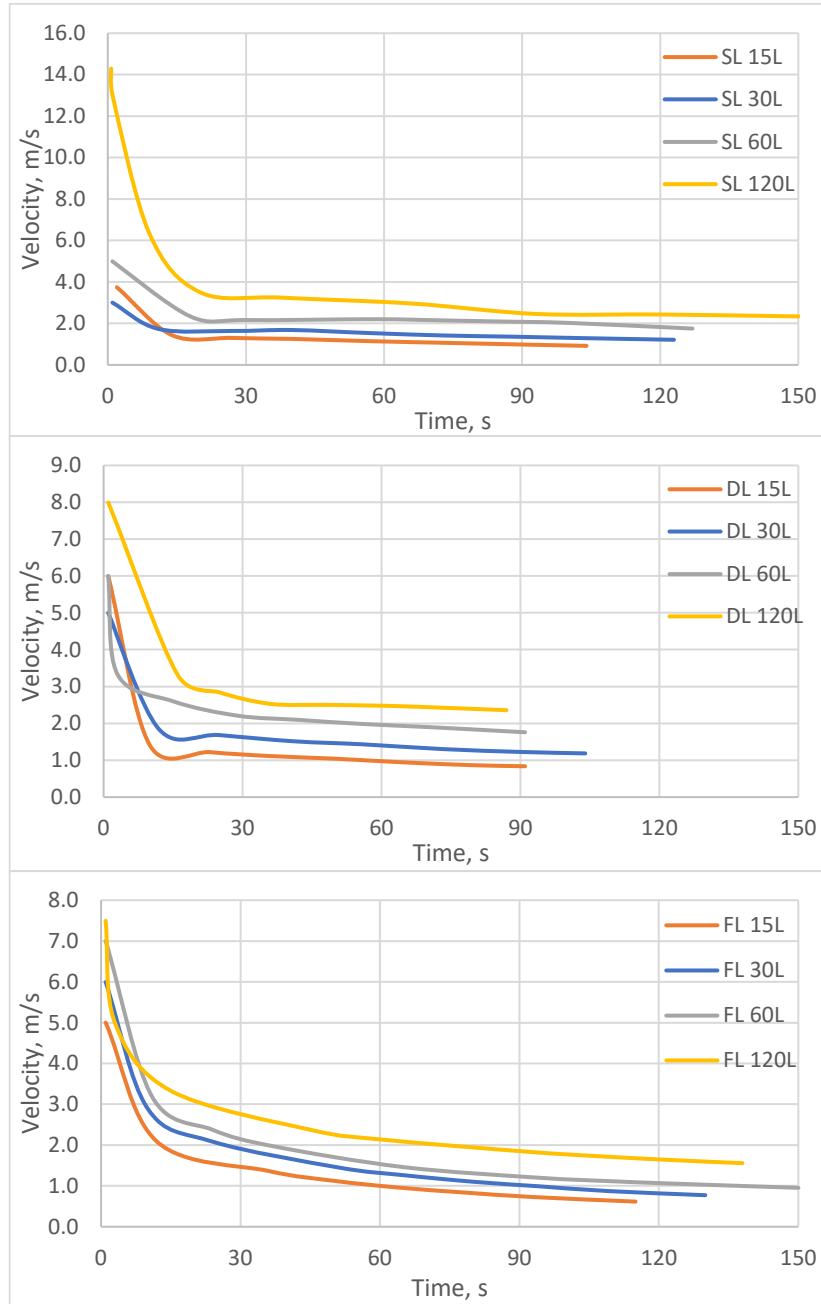
Figure 149: Fireball velocity decay with time in a single (top), double (middle) and five (bottom) lane tunnels.

7.1.1.2.2 Dimensionless correlation

Following similitude analysis of the data from Figure 148 and Figure 149 the dimensionless distance for the fireball propagation was expressed as:

$$\overline{L_T} = \frac{LA_T}{E \cdot AR^n} \left(\frac{fL}{D_T}\right)^m$$

where L is the location of the no-harm hazard distance (m), A_T is a area of the tunnel (m^2), E total energy of the hydrogen contributed energy (J), AR – aspect ratio of the tunnel, f – friction

losses, D_T – is hydraulic diameter represents an equivalent diameter of the non-circular tunnel, $D_T=(4A_T)/P$, where P – is perimeter (m). D_T is 4.95, 6 and 10.5 m for the single-lane, double-lane and five-lane tunnels respectively, $n=0.5$, $m=1$.

The dimensionless parameter is defined as

$$\bar{t} = \frac{\overline{L_T}}{U}$$

where U is the velocity of the fireball propagation (m/s) (L/t) with time along the distance L.

Therefore, the best-fit correlation for the hazard distance time can be expressed as:

$$\bar{t} = 0.2\overline{L_T}^{-0.82}$$
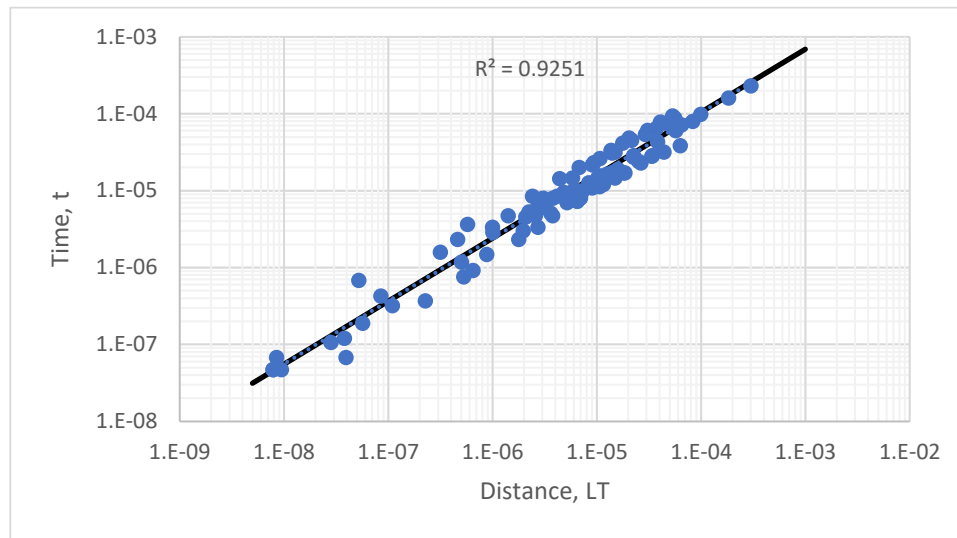
Figure 150: The correlation in dimensionless parameters $\overline{L_T}$ - $\bar{t}$.

The proposed correlation reproduces the model prediction and is in good agreement with experimental data.

7.1.1.3 Conclusions

The correlations to assess the blast wave and fireball size after high-pressure hydrogen tank rupture in a tunnel are proposed on compressed hydrogen tank rupture in a fire. The correlations have been compared with the numerical simulation to assess the dynamics of blast wave and the size of the fireball. It could be stated that none of simple correlations can be applied for the fireball hazard distance in a tunnel due to dynamics of its propagation.

7.2 Numerical studies (Task 4.3, NCSRD)

7.2.1 CFD analysis of blast wave and fireball in a split tunnel (UU)

The simulation to account for the presence of the congestion in the tunnel and the split of the two-lane single tunnel into two tunnels of single lane each has been considered in this study. This aims to answer the question of the blast wave and fireball behaviour at the accident zone and along the tunnel at both ends, investigating which side of the traffic lane of the tunnel will be affected more in terms of thermal and pressure hazards. Having traffic congested on one side of the accident creates an additional blockage of the tunnel cross-section which could result in non-uniform blast wave distribution on both sides and act as a mitigation measure to further disperse the energy of the blast by reflecting it to the opposite side. Apart from that the hazards and associated risks could be investigated following this study to inform first responders on the potential actions and ways to tackle them.

7.2.1.1 Numerical model

Simulations are performed using ANSYS Fluent V2021R2 as a CFD engine. The density-based solver is coupled with LES for turbulence with the Smagorinsky-Lilly model for simulation of sub-grid scale turbulence and the Finite rate Eddy Dissipation combustion employing one-step reaction. The governing equations are based on the filtered conservation equations for mass, momentum, and energy in their compressible form with Redlich-Kwong real gas EoS. The tunnel walls and floor are specified as non-adiabatic to allow heat transfer from the combustion no-slip wall conditions applied. The external non-reflecting boundary is defined as a pressure outlet with zero-gauge pressure. The Least Square Cell-Based and second-order upwind scheme were used for convective terms. The time step adapting technique was employed to maintain a constant Courant-Friedrichs-Lewy (CFL) number at the value of 0.2 until the blast wave left the tunnel at 1 s and gradually increased up to the value of 2 during 100 time seps to speed up the simulation of a fireball.

7.2.1.2 Model validation

Two fire tests were conducted in Japan (Tamura et al., 2006) on NWP=70 MPa tanks. The blast wave pressure was recorded at 5 m and 10 m perpendicular to the tank axis. In the test used for validation (Figure 151), the type 3 tank of 36 L ruptured 11 min after fire exposure (burst pressure 99.47 MPa). The maximum overpressure was 74.3 kPa at 5 m and 23.4 kPa at 10 m. In Test 2, the maximum overpressure at the 5 m sensor was 30% less than in Test 1, despite the slightly bigger volume of the tank and the burst pressure.
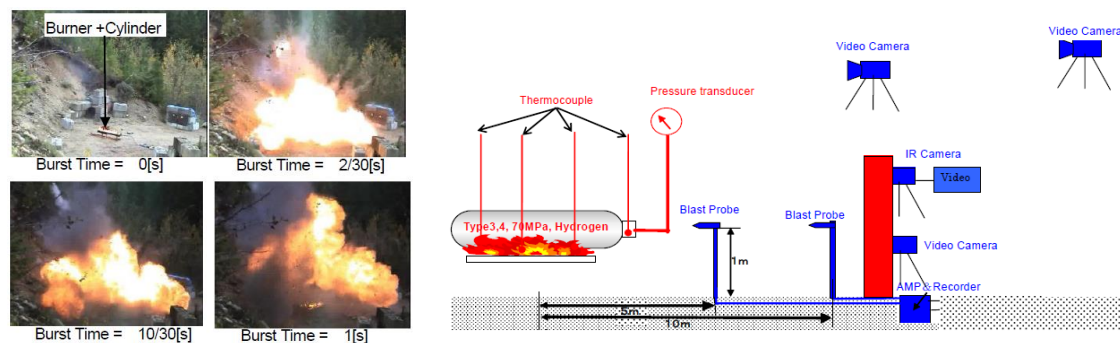
Figure 151: Validation test setup (Tamura et al., 2006).

The given model has been validated against (Tamura et al., 2006) experiments and the results of the comparison are presented in Figure 152 below. As can be seen, the peaks and dynamics reproduced with high accuracy for both sensors at 5 and 10 m and therefore the model can be applied for the simulations on the tunnel.
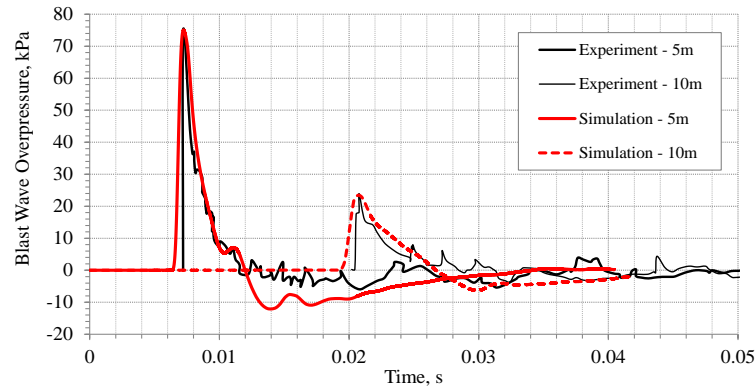
Figure 152: Model validation against Japanese experiments by (Tamura et al., 2006).

The parametric study on the initial turbulence has been performed to allow for the correct initial conditions at the vicinity of the tank rupture and bring it closer to realistic conditions when the car body ruptures and creates turbulence conditions under and around the vehicle.

Before going into the series of final simulations the zone of initial turbulence were assessed to conclude to which extent the initial conditions affect the pressure wave.

Figure 153 shows schematic zones for parametric study of initial turbulence. Four simulations with different sizes of turbulence initialisation were performed: zone 0 is just under the vehicle and zones 1-3 with 1-3 m respectively from the vehicle in each horizontal direction.
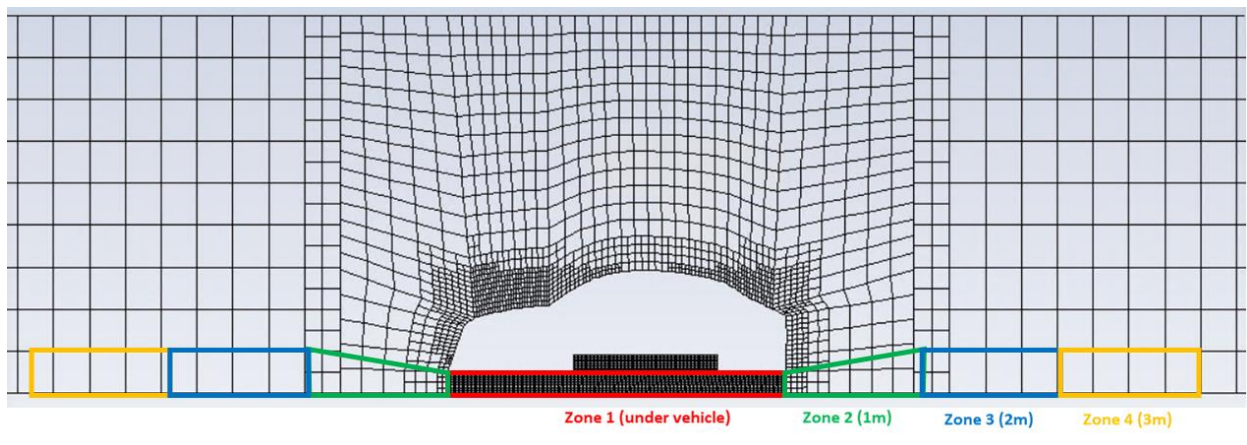
Figure 153: Schematic zones for parametric study of initial turbulence.

Four patch zones of isentropic velocity field were tested as shown in Figure 154.
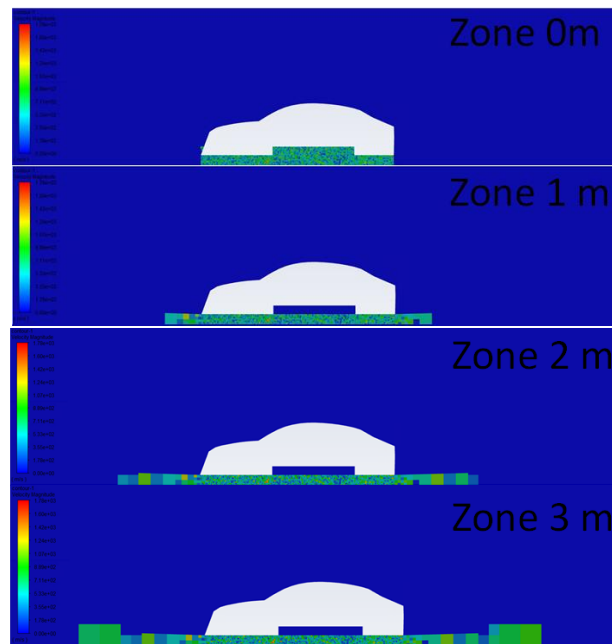
Figure 154: Turbulence initialisation for parametric study.

The graph shows the overpressure along the middle of the tunnel at the same time of 56.4-56.5 ms (within 0.1ms). As can be seen the maximum pressure in the shock front is nearly the same for zones 0-2 but a significant increase is observed for zone 3. There is some difference in overpressure at the vehicle location which is thought due to the difference in reflections caused by turbulence patch but apart from that, they are pretty much the same. In general, it can be concluded that 2 m patch is sufficient to start simulations.
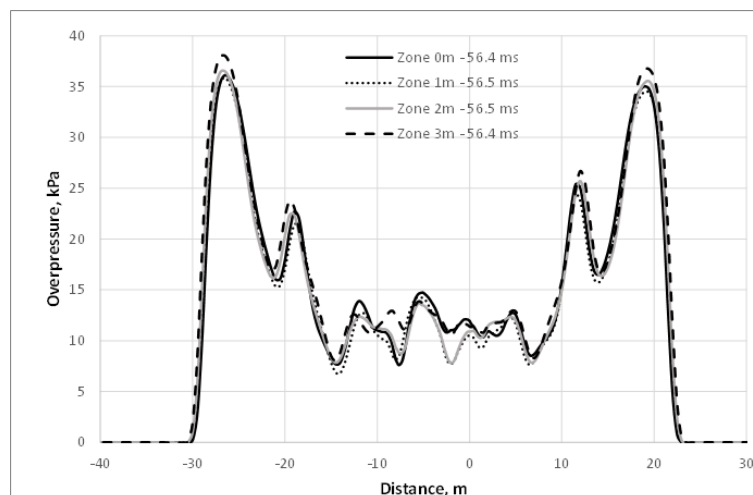
Figure 155: Pressure decay difference for each turbulence zone.

7.2.1.3 Considered scenario and problem formulation

The two-lane tunnel was considered for the simulation which splits into two single-lane branches 250 m on each side from the accident. The two-lane tunnel has a width of 9 m and a height of 4.5 m, each single lane is 5.5 m in width and 4.5 m in height resulting in a cross-section area of 40.5 m^2 (single two-lane) and 49.5 m^2 (double single-lane) respectively. The two-lane section of 250 m long is filled with traffic congestion of 8 busses, 16 vans and 32 cars occupying both lanes as shown in Figure 156. For the considered case the tank has a volume

of 120 L under 945 bar and an initial temperature of 375°C located beneath the vehicle. This is done to take into account the presence of the car to provide as realistic as possible scenarios of fireball formation and blast wave propagation.

The biggest vehicle standing in a tunnel is a bus with the size of 2.8 x 2.1 m, standing on each lane and resulting in the 29% blockage of the cross-section area i.e. (2.8x2.1x2)/(4.5x9)x100=29%. Having that in mind and that the cross-section area of two single-lanes is 18% larger than one double lane, the effective area for empty tunnels is 42% larger than the congested one.
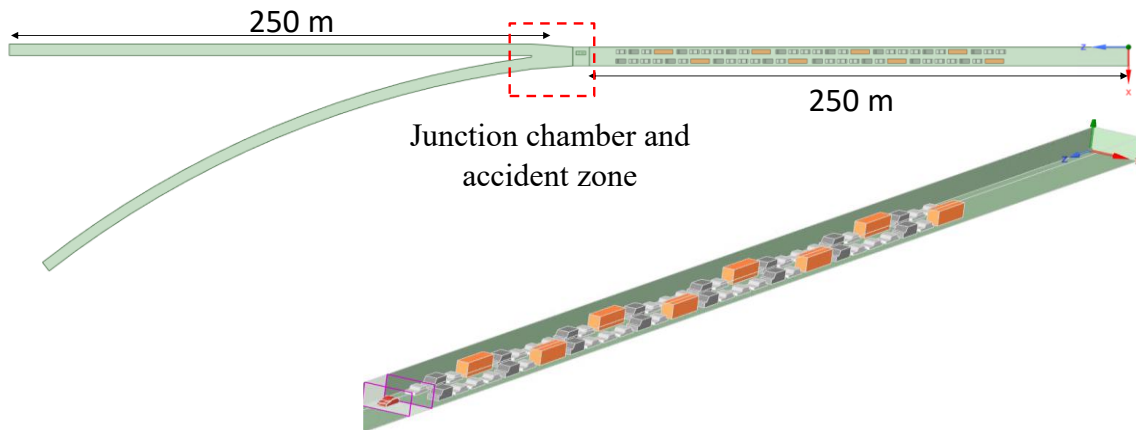
Figure 156: Split tunnel outline with traffic.

7.2.1.4 Results

7.2.1.4.1 Blast wave dynamics

The maximum pressure along the tunnel length at any point is shown in Figure 157. As can be seen, the absence of the obstacles provides lower oscillation amplitude and higher overpressure even for the larger total cross-section of two single-lane tunnels. The higher peaks observed for the congested side are due to reflection from the vehicles. The presence of the vehicles helped in the reduction of the blast wave decay at the exit by nearly 2 times at 250 m 26 kPa vs 14 kPa respectively.
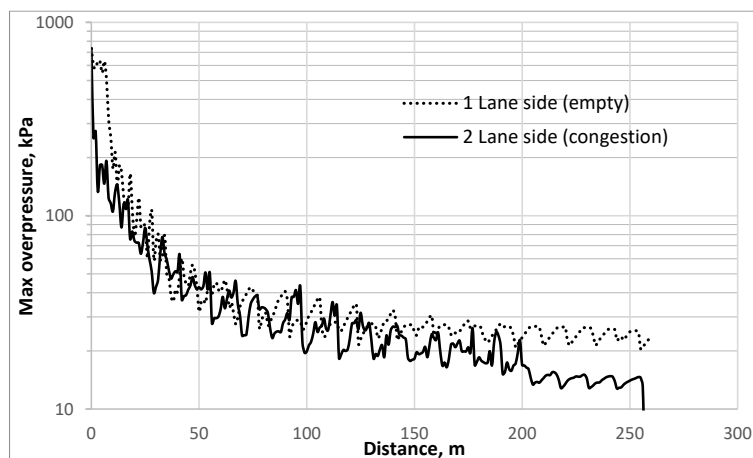
Figure 157: Maximum overpressure (negative) versus distance.

Figure 158 shows the dynamics of the blast wave overpressure from the top view cross-section at 1 m height. The total time for the blast to propagate on both sides takes under 1 s. The figure shows the pressure limited by 16.5 kPa, which is the limit for serious injury (Molkov and Kashkarov, 2015) and it is seen that the whole tunnel is subject to higher overpressure except for a small part after the congestion zone just before the tunnel exit.
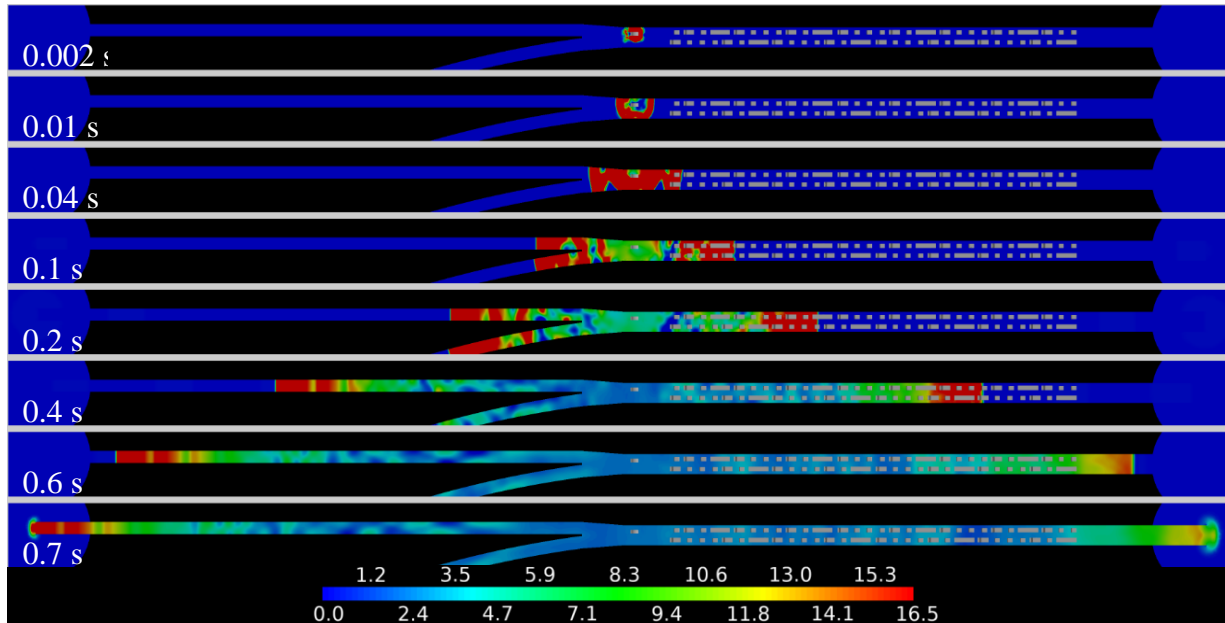
Figure 158: Dynamics of the blast wave overpressure (kPa), top view cross-section at 1 m height.

Multiple oscillations and reflections can be seen between vehicles, which disperse the single shock into a series of smaller ones reducing the leading blast for the congested side of the tunnel, see Figure 158 and Figure 159. On the other hand, for the empty tunnel part there is no obstacles and the shock formed is planar at a distance of around 70 m from the tank rupture at 0.17 s (Figure 159).
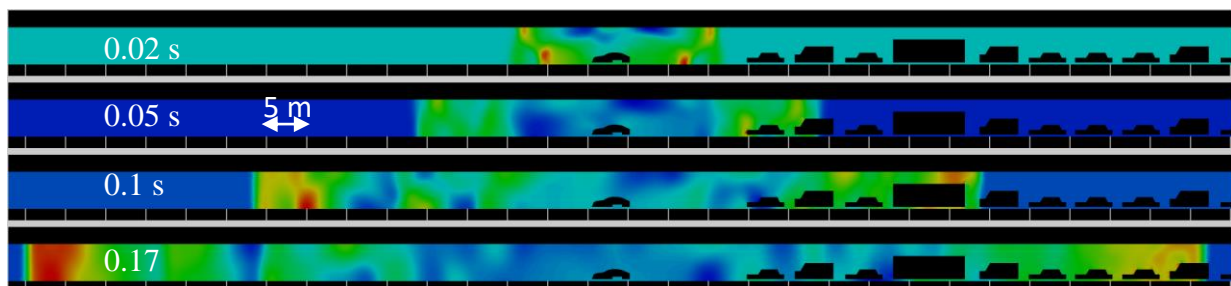
Figure 159: Non-uniformity of the shock in the empty and congested tunnel sections.

Another observation and hazard which could cause harm to people is the underpressure after the leading blast wave front left the tunnel. The refraction wave starts to travel back into the tunnel creating a wave of negative pressure of around -15 kPa along the whole length of the tunnel. As can be seen from Figure 160 the maximum underpressure for both sides of the tunnel is shown with its high peaks at the accident zone of tank rupture. Contrary to the overpressure the underpressure does not decay and stays at the same value throughout the whole length of the empty tunnel, while for the congested lane we see oscillations created by the presence of

obstacles. Again the presence of vehicles also reduces the underpressure at the end of the tunnel twice.
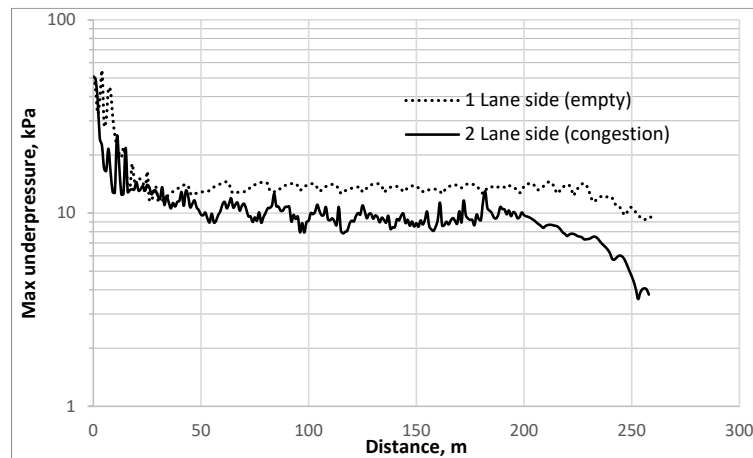
Figure 160: Maximum underpressure versus distance.

The visual dynamics of the underpressure rarefaction wave is shown in Figure 161 where the legend is inverted to show the lowest pressure by red colour. The rarefaction wave travels back into the tunnel from both sides collapse in the middle and goes back. These rarefaction waves continue until the pressure inside the tunnel fully stabilizes. The figure below confirms the graph and shows how the presence of obstacles help to dissipate the blast.
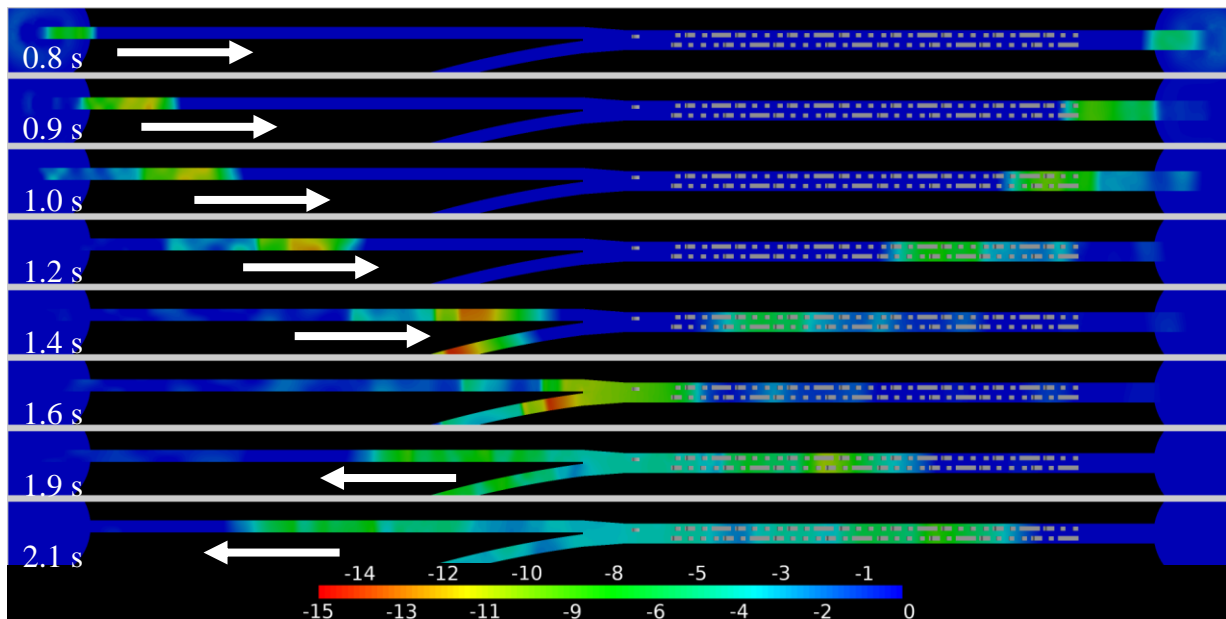
Figure 161: Dynamics of the blast wave underpressure (kPa), top view cross-section at 1 m height.

7.2.1.4.2 Fireball dynamics

The thermal hazards are from the fireball. Figure 162 shows the dynamic of the hydrogen combustion with time. Compared to open space when it takes 2 s to burn 100% of hydrogen (Molkov et al., 2021) in confined space this takes longer, while only 80% of hydrogen burns within 2 s and the rest 20% takes up to 24 s due to confinement and absence of air entrainment from all sides.
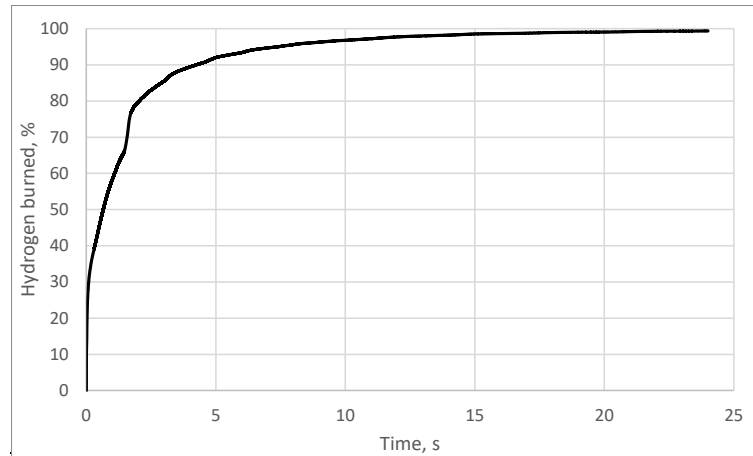
Figure 162: The amount of burned hydrogen in the domain as a function of time.

At the end of the combustion stage when the fireball spread in the tunnel distance of around 110 m, propagating 40 m towards the congested part and 70 m to the empty single-lane tunnels. Figure 163 shows the dynamics of fireball formation in form of temperature iso-surfaces of hazard distance based on the temperature limits i.e. "no-harm" - green 70 °C, "pain" - yellow 115 °C, "fatality" - red 309 °C (LaChance, 2010). The speed of fireball propagation can be assessed. During the first two seconds, it has the highest speed of propagation and spreads up to 50 m which correlates with the combustion speed shown in Figure 162. The rest of the time up until 24 s the fireball was governed mainly by the buoyancy and driven to the ceiling of the tunnel and spreading to both sides at a total distance of 120 m. At a distance of 15 m to the nearest car, the fireball didn't affect or engulf it.

The direction of the fireball extent is also correlated and governed by the highest overpressure propagation direction which is the single-lane tunnel branch.
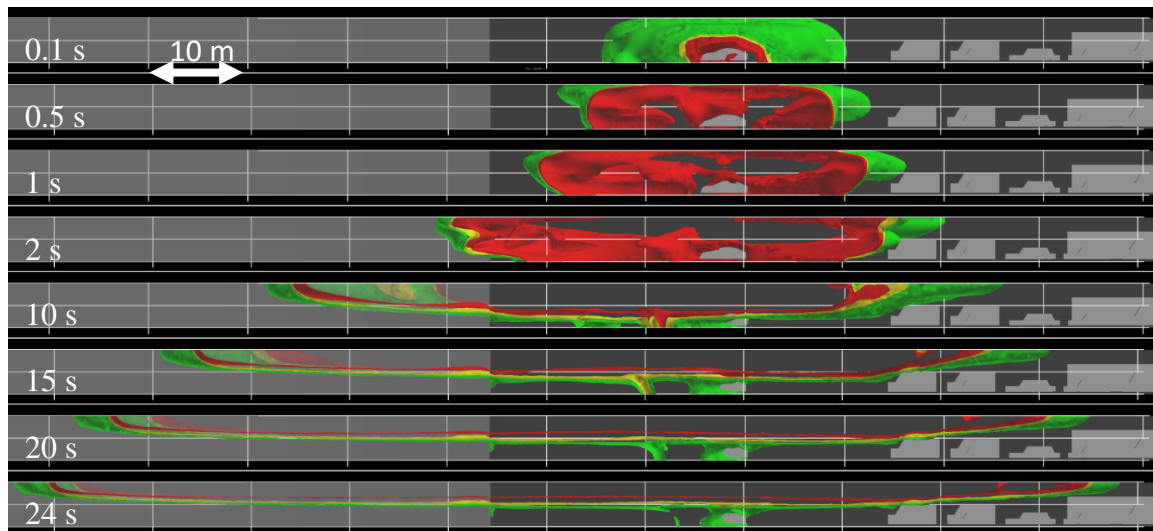
Figure 163: Dynamics of the fireball hazard distances, No-harm (green, 70 °C), pain (yellow, 115 °C), fatality (red, 309 °C).

7.2.1.4.3   Thermal dose

Even though the person is not affected by the direct flame, the probability of exposure to high radiation heat flux still exists. If the exposure time is extensive it could result in third-degree

burns and even death. To express the harm from the radiation heat flux the thermal dose term was introduced by LaChance, (2010) in the following equation $Thermal\ doze = q_R^{4/3}t$

In Table 40 (LaChance, 2010) a range of thermal doses is outlined for the ultraviolet and infrared spectrum that can result in first, second, or third-degree burns. Using Table 40 it is possible to calculate the time required whereby the level of certain skin damage is not exceeded.

Table 40: Radiation burn data (LaChance, 2010).

Burn Severity	Threshold Burn Severity dose $(kW/m^2)^{4/3}s$	
	Ultraviolet	Infrared (mean)
First Degree	260-440	80-130 (105)
Second Degree	670-1100	240-730 (290)
Third Degree	1220-3100	870-2640 (1000)

Figure 164 shows the radiation heat flux at the height of the person's head of 1.8 m at a time of 24 s. This can be used to calculate and identify the thermal hazards from flame radiation.
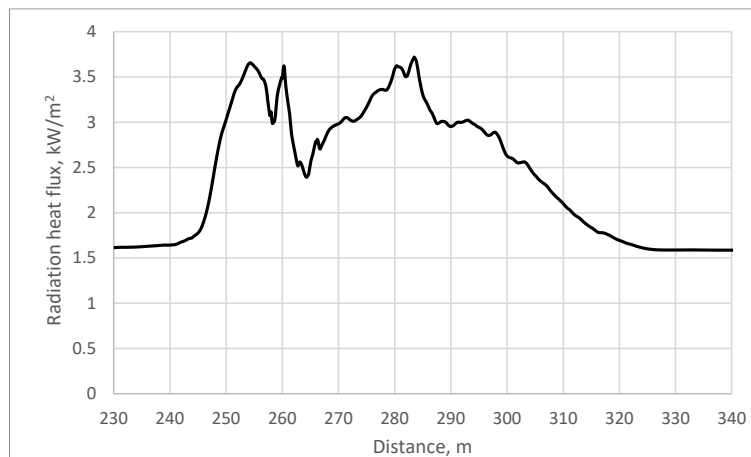
Figure 164: Radiation heat flux along the tunnel length at 1.8 m height.

Figure 165 shows the thermal dose as a function of distance along the tunnel at 1.8 m height and it can be seen that according to (LaChance, 2010) the 1st degree burn threshold is exceeded at the fireball spread distance.
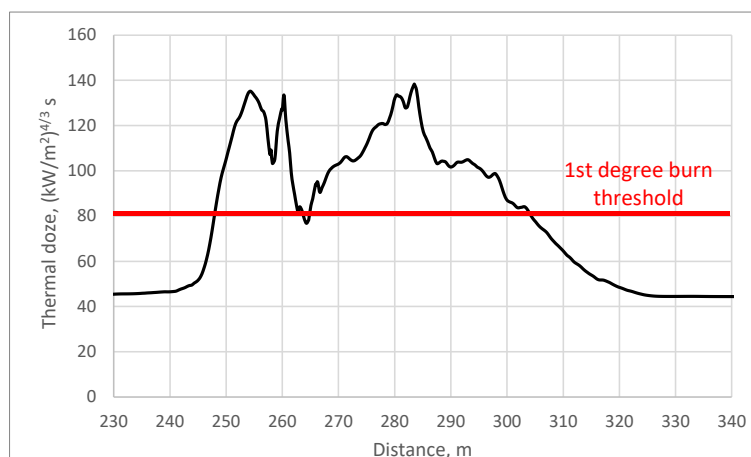
Figure 165: Thermal dose as a function of distance along the tunnel.

7.2.1.4.4   Comparison of fireball size in the tunnel and the open space for the same tank rupture

Calculation of the fireball (FB) on the open space gives the radius of the hemisphere equal to 16.65 m which is equivalent to the FB volume of 1206 m^3. Having this in mind and applying it to the tunnel tank rupture with the cross-section area equal to HxW=9x4.5=40.5 m^2 will result in 1206/40.5= 29.7 m of the tunnel fully occupied by the fireball. In fact, the fireball occupies not the whole cross-section but only the upper part of it due to the buoyancy of hot combustion products. At 24 s after the tank rupture, the volume of combustion products with a temperature higher than the fatality limit, i.e. 309 °C, is 1537 m^3. Which is 301 m^3 larger than that received by theoretical calculation. In open space, the fireball rises up quickly and disperses in the open air in around 4 s, but in the confined space, there is no way to go further than the ceiling and it spreads along the tunnel mixing with air and diluting combustion products. This results in a higher volume of hot gas by the fatality temperature due to the mixing of hot FB with cold air.

7.2.1.5   Concluding remarks

It was observed that the blast wave increases in direction of the tunnel split even though the cross-section area is larger, this is thought due to the presence of traffic congestion which mitigates the blast strength. The overpressure at the tunnel exit is twice lower on the congestion side compared to the empty. The strong influence of underpressure was observed with a potential hazard to pedestrians, the pressure does not decay through the tunnel length. Having traffic congested on one side of the accident creates an additional blockage of the tunnel cross-section which results in non-uniform blast wave distribution on both sides and acts as a "mitigation measure" to disperse the energy of the blast by multiple reflections.

The fireball propagates towards to side with higher pressure for the 120 L tank and occupies 110 m of tunnel length in 24 s. Comparison with the open space tank rupture in terms of combustion products correlates with the model prediction but the distance is 7 times longer inside the tunnel. Thermal hazards from radiation heat flux result in a 1st-degree burn threshold that does not exceed the fireball spread distance.

The hazards following this study can be used to inform first responders on the potential actions and ways to tackle them.

7.2.2   Deflagration of non-uniform hydrogen-air cloud created by release in HSE tunnel experiments in Task 4.4 (NCSRD)

7.2.2.1   Introduction

Deflagration simulations of hydrogen released from a train inside the HSE tunnel were conducted in order to validate our CFD model. The experimental test number 25 was chosen to be studied which involves hydrogen release that is characteristic of a release from a train. The train obstacle is not included in this test (empty tunnel case). The hydrogen mass is equal to 5.55 kg stored at 580 bars. The release diameter is equal to 4.7 mm and the release direction is upwards. The length of the tunnel is equal to 70 m and the maximum height from the floor equal to 3.25 m. Ventilation equal to 1.25 m/s from the one opening of the tunnel was considered. Initially, dispersion simulation was performed in order to define the initial conditions for the deflagration simulations.

7.2.2.2   Simulations details

For the simulations the ADREA-HF CFD code (Venetsanos et al., 2010) was used. For turbulence, the Kato-Launder modification (Kato et al., 1993) of k-e model was utilized. The equations were discretized using the second order upwind bounded numerical scheme for the convection terms and a first order upwind discretization for time. For the release the experimental release rate was used which was calculated based on the measured tank conditions (tank temperature, pressure and volume). Figure 166 shows the blowdown experimental results. A moving average trend line is also shown. As input mass flow rate for the simulation a smooth curve of the moving average trend line was used. The Birch 84 notional approach was applied to calculate the notional diameter evolution in time based on the smoothed flow rate. The ignition occurs 12 s after the start of the release.
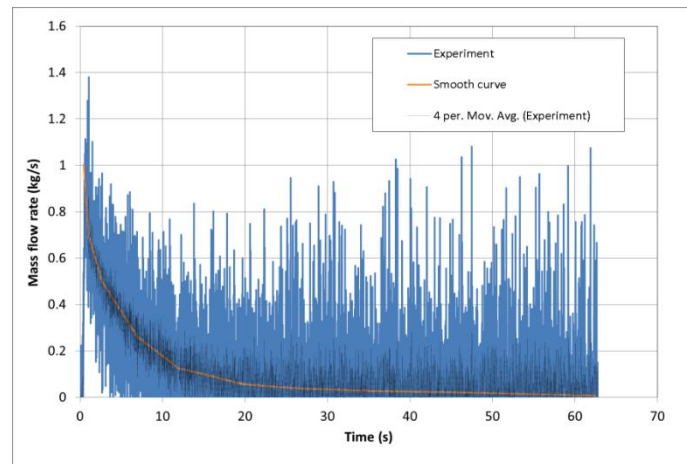
Figure 166: The blowdown experimental results and the smoothed curve used in the release simulation.

For deflagration simulation a recently developed model was used. The model utilized the Schmid's formula for turbulent flame speed and several wrinkling factors to account for flame instabilities. Model details and validation can be found in (Tolias et al. 2018), (Tolias et al. 2020) and (Momferatos et al. 2021). The parameters of the model were the same as the one used for the pre-test simulations.

The release area was discretized using 4 cells. For the deflagration simulations two numerical grids were used, Grid 1 and Grid 2. The total number of (active) cells was equal to 495,968 in Grid 1 and 1,234,360 in Grid 2. The grids were extended outside the tunnel in all vertical directions. The main difference between Grid 1 and 2 was the larger number of cells that were used in Grid 2 downwind the x=40 m position. Grid 2 is also more refined along y- and z-direction. Images of the grids are presented in Figure 167. These two grids were also used to perform the dispersion simulations to obtain the initial hydrogen concentration profiles for the two deflagration simulations.
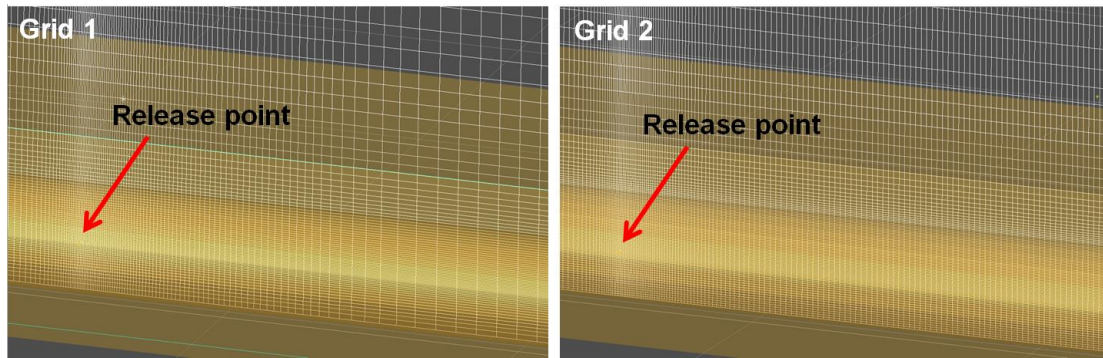
Figure 167: Grid 1 (left) and Grid 2 (right) at a xz-plane passing through the release point.

7.2.2.3   *Hydrogen dispersion simulation results*

Hydrogen dispersion was simulated first in order to estimate the initial conditions for the deflagration simulation (see also Section 5.2.1). In Figure 168 the comparison between the experimental and the simulation results of hydrogen volume concentration (%) are presented at various sensors. The release area is located at x=35 m, y=0.61 m, z=1.54 m (coordinates are relative to the entrance of the tunnel, the tunnel symmetry plane and the bottom of the tunnel cylinder). Regarding deflagration simulations, the comparison should be focused at the time of ignition, i.e. at 12 s. At sensor 8, 9, 10 the agreement between simulation and experimental results is satisfactory at 12 s. Moreover the two grids give similar results. On the other hand at sensor 2 the two grids have significant differences indicating that grid independence is not achieved. Grid 2 is, in general, in better agreement with the experiment at this sensor. At sensor 5 both grids underpredict the measurements at 12 s. Simulations also underpredict the experiment at sensor 3. The underprediction of Grid 2 is smaller in this sensor.
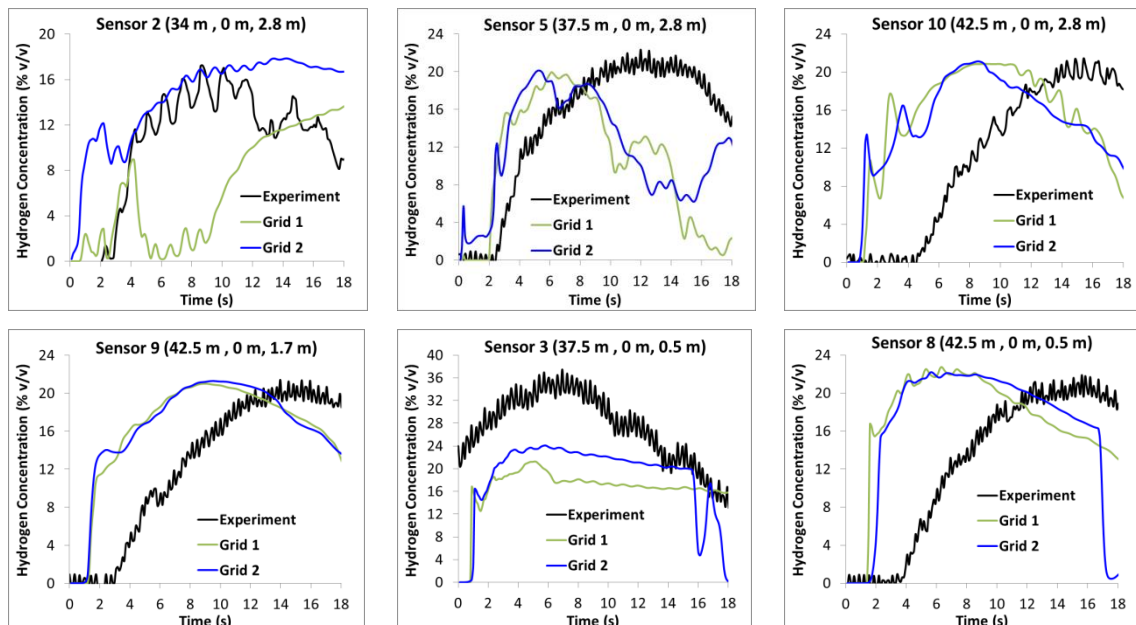
Figure 168: Hydrogen volume concentration time series. Comparison between experimental and simulation results (using Grid 1 and 2).

In Figure 169 the predicted hydrogen volume fraction contours are presented at the y-plane passing through the release point for Grid 1 (top) and Grid 2 (bottom) at 12 s from the start of

the release. The ignition point is set at x=38 m, y=0.61 m and z=3.4 m for the deflagration simulation. We observe that hydrogen concentrations above 25% occur only above the release area. The main volume of hydrogen occupies the area downstream the release from x=35 m to x=65 m. The maximum concentration at this area is approximately 20-22% v/v. Comparing the results from the two grids some differences are observed. Firstly, at the ceiling area upwind the release (x=30-35 m) the predicted hydrogen concentration is higher in Grid 2 compared to Grid 1. Moreover, Grid 2 predicts also higher concentrations at the floor area around x=38 m. Finally, differences in hydrogen distribution are observed at the area between x=40 and x=55 m. In Grid 1 concentration of 20-22% occupies only the upper layers of the tunnel whereas in Grid 2 these concentrations extend to the ground and are closer to the release.
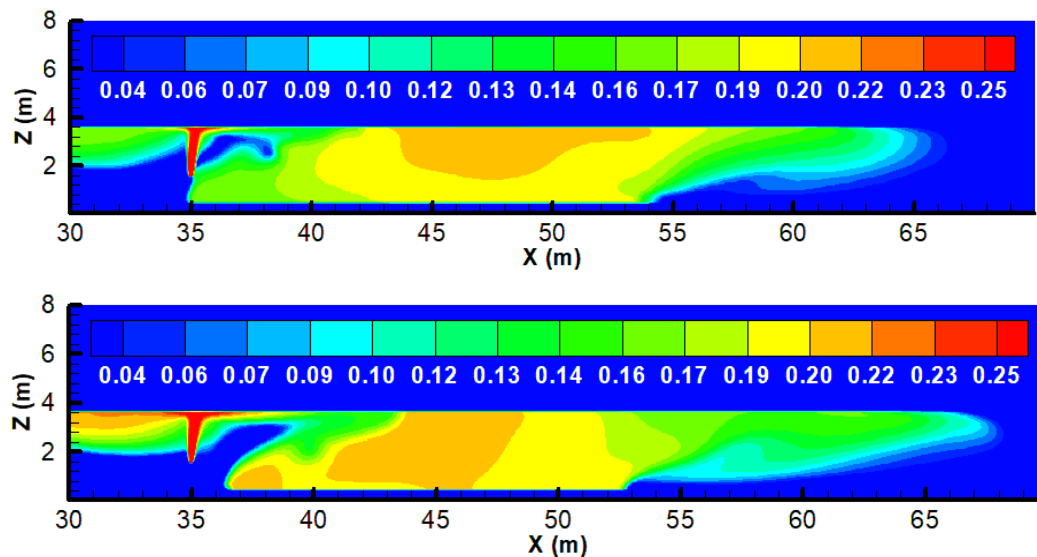
Figure 169: Predicted hydrogen volume fraction contours at the y-plane passing through the release point for Grid 1 (top) and Grid 2 (bottom) at 12 s from the release start.

In Figure 170 the hydrogen flammable volume and hydrogen volume in the range of 25-35% v/v for the two grids are presented. We observe that the hydrogen flammable volume is almost the same until 20 s. After that time Grid 1 predicts slightly higher values. Regarding the 25-35% cloud which is considered the most important for overpressure generation in case of deflagration, Grid 2 predicts higher values. At the time of ignition (12 s), the 25-35% volume in Grid 2 is approximately twice the volume in Grid 1.
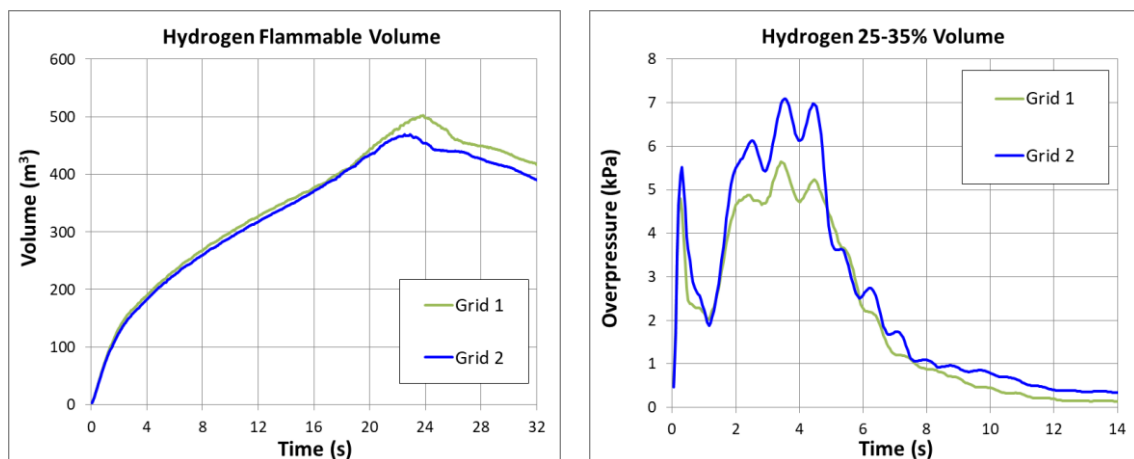
Figure 170: Predicted hydrogen flammable volume and hydrogen overpressure in the range of 25-35% using Grid 1 and 2.

7.2.2.4 Hydrogen deflagration simulation results

In Figure 171 the experimental overpressure time-series are presented at the measurements points. We observe that all sensors give very similar results. Only sensor P3, which is placed in the furthest distance from the release, has noticeable smaller values of overpressure. Sensor P5 exhibits a sharp increase in pressure at about 0.38 s. This pressure peak does not appear on his neighbour sensors and probably can be ignored. Given that fact the maximum overpressure is approximately equal to 32 kPa.
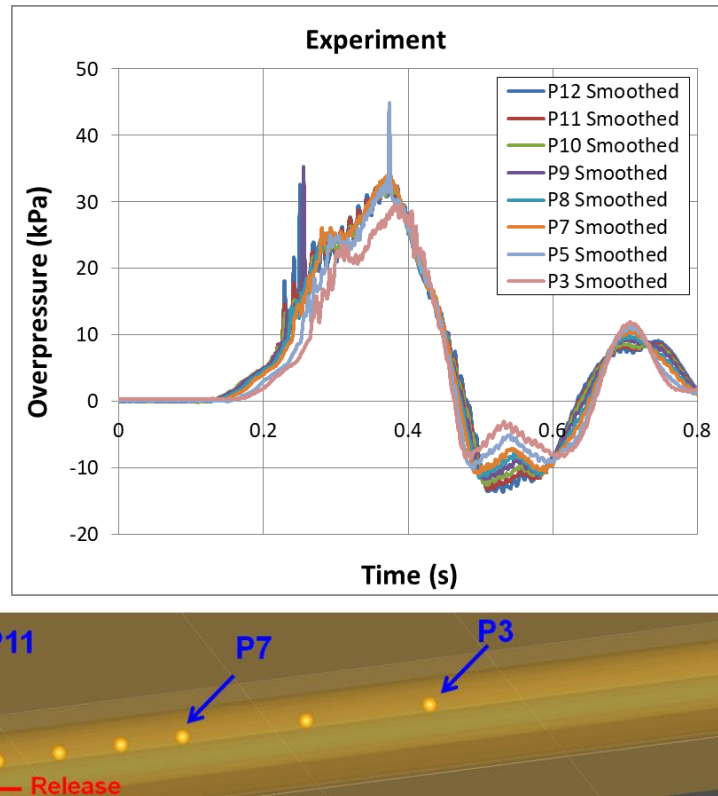
Figure 171: Experimental pressure time-series at various sensors. Sensor positions are indicated in the photo.

In Figure 172 the comparison between the experimental and the computational overpressure are presented at 4 sensors. We observe that the computational results with Grid 1 have an excellent agreement with the experiment. Both maximum overpressure and the general shape of the curves are predicted very accurately. However, the results with the refined Grid 2 are different and the maximum overpressure is now overpredicted by approximately 12 kPa. On the other hand, the denser grid is able to reproduce some of the oscillation that appears in the experiment at 0.22 s at sensors P12 and P11. Moreover, the steadiness of the overpressure that occurs in the experiment at the sensors P7 and P3 at around 0.3 s is reproduced in Grid 2.
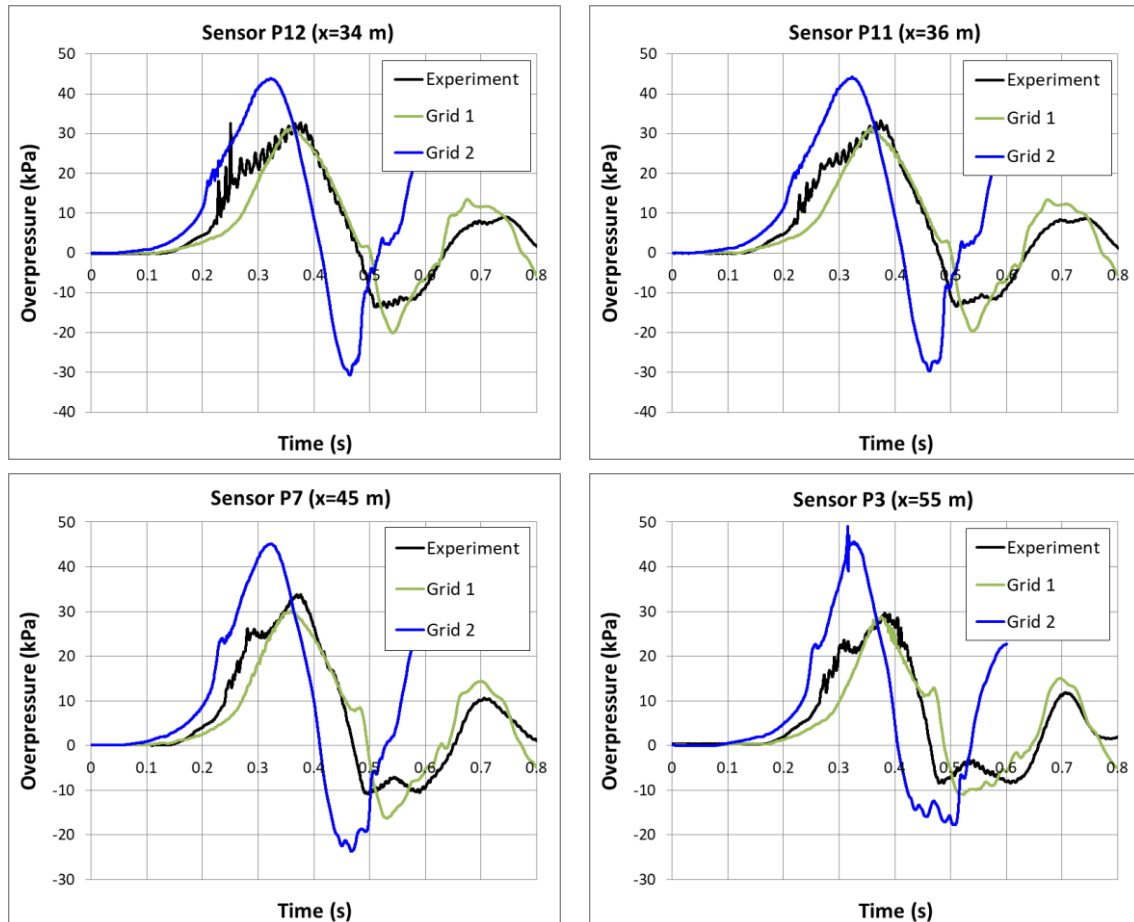
Figure 172: Hydrogen deflagration: Overpressure time-series. Comparison between experimental and computational results (using Grid 1 and 2).

In order to verify that the deflagration results are grid independent, another deflagration simulation was conducted using Grid 2 and using as initial conditions the results from Grid 1 of the dispersion simulation. The predicted overpressure time-series was similar to the Grid 1 results shown in the previous Figure. This indicates that the deflagration results are grid independent and that the reason for the disagreement between Grid 1 and Grid 2 is the different initial hydrogen concentrations that were predicted in the dispersion simulations. Thus, denser grids should be examined in the dispersion simulations in order to predict the initial concentrations with higher accuracy.

In Figure 173 the predicted flame front using Grid 2 is indicated through the hydrogen volume concentrations contours at 0.20, 0.22, 0.28 and 0.32 s from the ignition. Time 0.20 s corresponds to the time when the rate of pressure rise increases (Figure 172). At 0.22 s pressure oscillations appears at sensor P12. We observe that at this time the flame has passed through the hydrogen jet which is probably the reason for the oscillations. At 0.28 s the flame front reaches the x=50 m position and the pressure still increases. Finally, at 0.32 s which is the time when maximum overpressure occurs, the flame front touches the floor of the tunnel. We observe that at this time a significant amount of hydrogen is still unburned with concentrations around 19%. As a result this amount of hydrogen does not contribute to overpressure increase. The reason for this is probably the high velocity field that has been developed from the explosion pushing the mixture towards the exit of the tunnel.
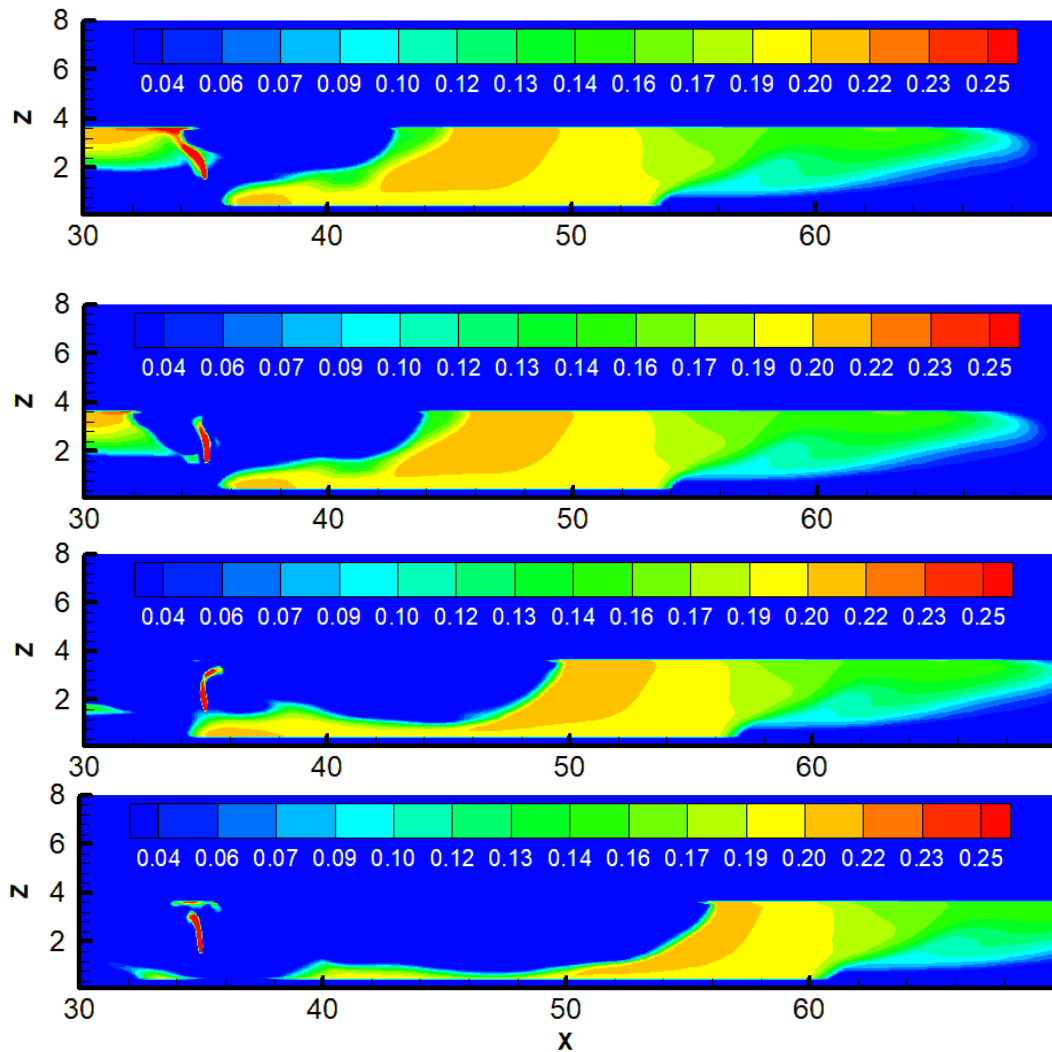
Figure 173: Predicted hydrogen volume fraction contours at the y-plane passing through the release point for Grid 2 at 0.20, 0.22, 0.28 and 0.32 s from the ignition. The flame front is indicated by the missing hydrogen.

7.2.2.5 Conclusions

The experimental test number 25 of HSE experiments was used in order to validate our CFD model. Two computational grids were used, a coarse and a fine one. The course grid achieved excellent agreement with the experiment predicting accurately enough the maximum overpressure and the general shape of the overpressure curved. The fine grid predicted higher overpressures, overpredicting the experimental maximum by 12 kPa. The reason for this seems to be the differences in the initial conditions (hydrogen concentration) that were predicted by the two grids in the dispersion simulations. The results of denser grids in the dispersion simulations need to be tested as initial conditions in the deflagration simulations in order to use a more accurate initial hydrogen distribution. In the case that the final deflagration results using the proper initial concentrations overpredict the experimental overpressure, the combustion model parameters will be calibrated in order to achieve a better agreement with the experiment.

7.2.3 Analysis of the interaction between absorbing materials and systems and shock wave attenuation (KIT)

7.2.3.1 Background

Shockwaves can be mitigated by means of attenuation by water mist or absorbing materials, soft bulkheads or sacrificial pre-evacuated volumes etc. This subtask focuses on the analysis of effect of different absorbing materials of varying thickness on shockwaves. The mitigation capacity of different absorbing materials is discussed.

7.2.3.2 Objectives

The scope of this work is to study the efficiency of different absorbing materials with different thickness to attenuate the strength of a blast or shock wave generated by an explosion.

7.2.3.3 Methodology

The hydrogen explosion tests are performed in the HYKA A2 vessel of 220 m^3 volume (6 m diameter, 9 m height). As shown in Figure 174, hydrogen detonation is initiated in a combustion unit containing 4 g H_2 located at the centre of the A2 vessel. Absorbing materials are put on the solid wall of the vessel. The interaction of the absorbing materials to the incident shockwave is measured, with focus on the amplitudes of the reflected shock pressures by the soft layer.

The tested different absorbing materials are:

- polystyrene,
- polyurethane foam and
- acoustic glass wool

with different thickness of 2 cm, 12 cm or 20 cm.
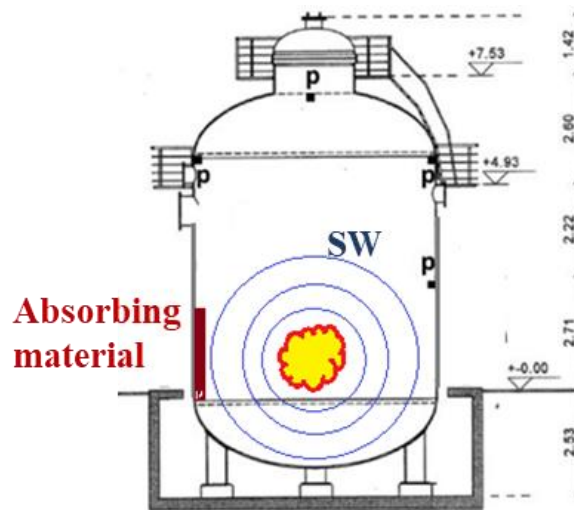
Figure 174: Experiment of hydrogen explosion shockwave attenuation by absorbing materials with different thickness in the HYKA A2 vessel.

7.2.3.4 Models

The hydrogen detonation and shockwave propagation are simulated by using COM3D code with a moving boundary at the surface of the absorbing material block. The soft material

surface deforms due to the incoming shock pressure wave, which forms a moving boundary for the COM3D calculations.

The deformation of the soft materials is computed by using the ABAQUS code with the crushable foam plasticity model. The computed pressure by the COM3D code acts as a pressure boundary at the surface of the absorbing material block for the ABAQUS simulations. On the contrary, the computed deformation of the material surface by the ABAQUS supplies a moving boundary condition for the gas dynamics simulations of the COM3D.

Therefore, the COM3D and the ABAQUS calculations have to be coupled at each time step for simulation.

The geometry model of the A2 vessel is shown in Figure 175 for COM3D simulation. The hydrogen combustion unit is located at the centre of the vessel. The computational cell size is 1 cm.
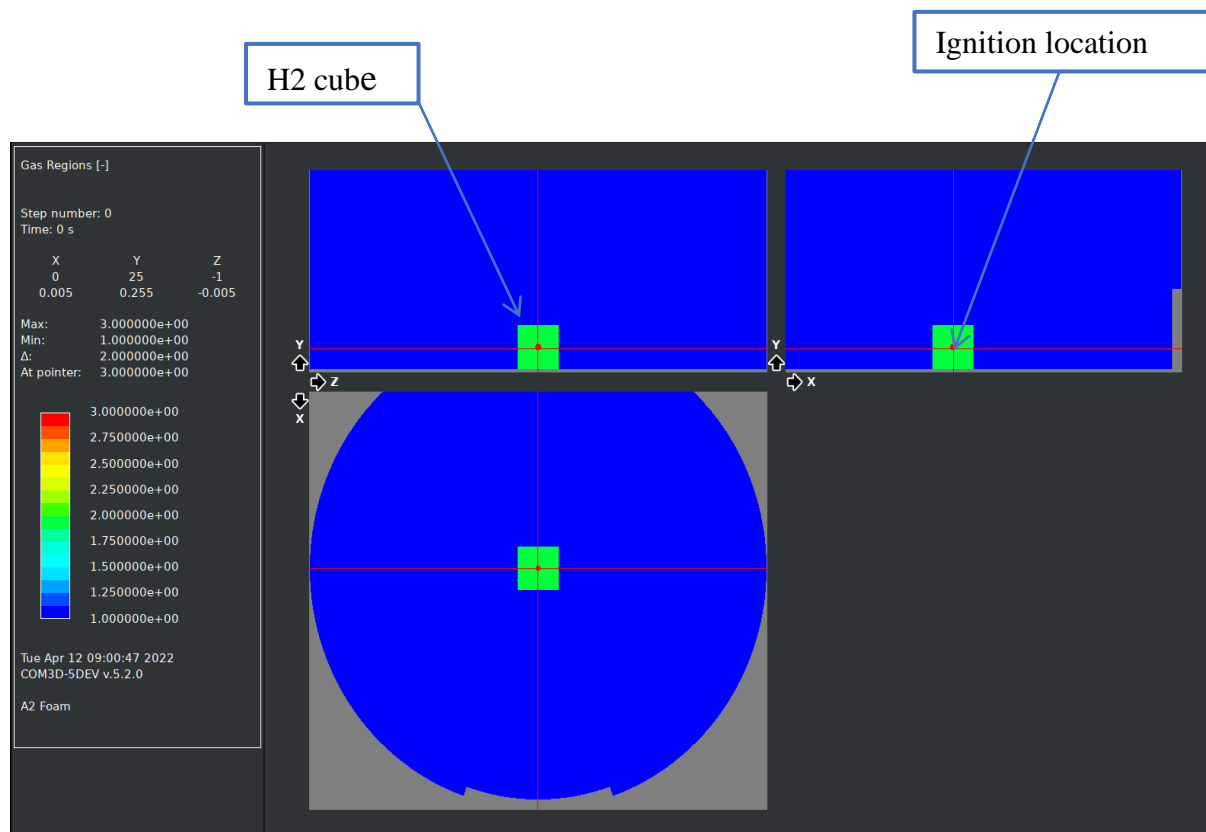
Figure 175: Geometry model of the A2 vessel with the hydrogen combustion unit at the centre.

A series of pressure sensors are aligned between the combustion unit and the centre of the absorbing materials, as shown in Figure 176 and Figure 177.

7.2.3.5 Boundary conditions and initial conditions

The hydrogen combustion unit is designed for the strongest possible (unconfined) combustion with low H_2 amount. The unit is a cube of 0.55 x 0.55 x 0.55 m^3, with 4 g H_2.

Non-reflecting boundary conditions are specified on the back wall facing the wall covered by foam layer and on the ceiling of the A2 vessel, as indicated in Figure 177.

The surface of the foam layer is modelled as the data exchange interface between COM3D and ABAQUS, as shown in Figure 178, where the pressure and displacement of the soft materials (moving boundary condition) are exchanged between the two codes.
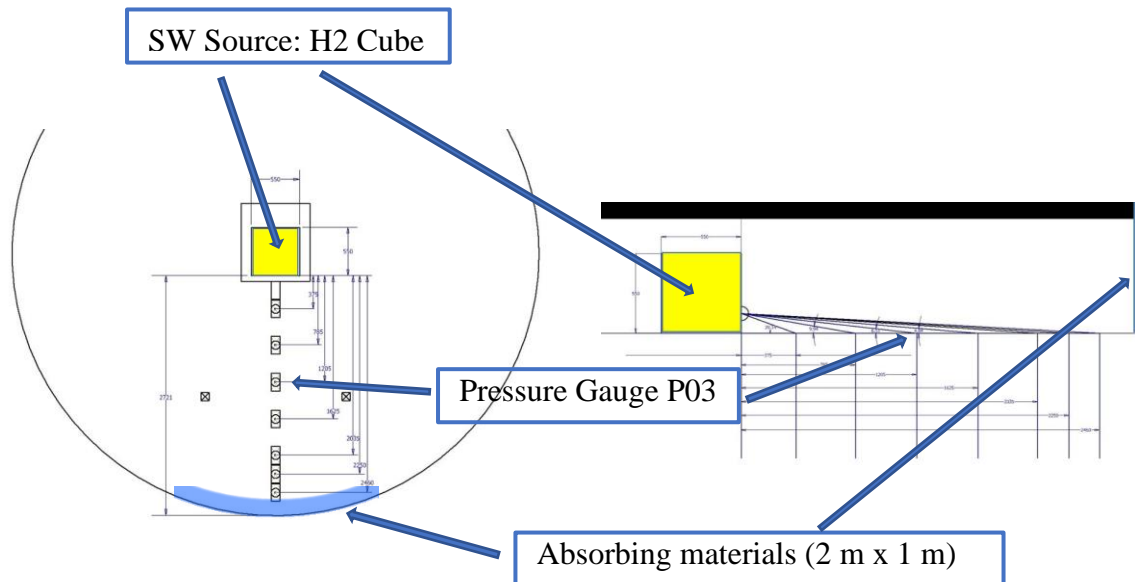
Figure 176: Pressure sensor arrangement for recording the shockwave evolution process.
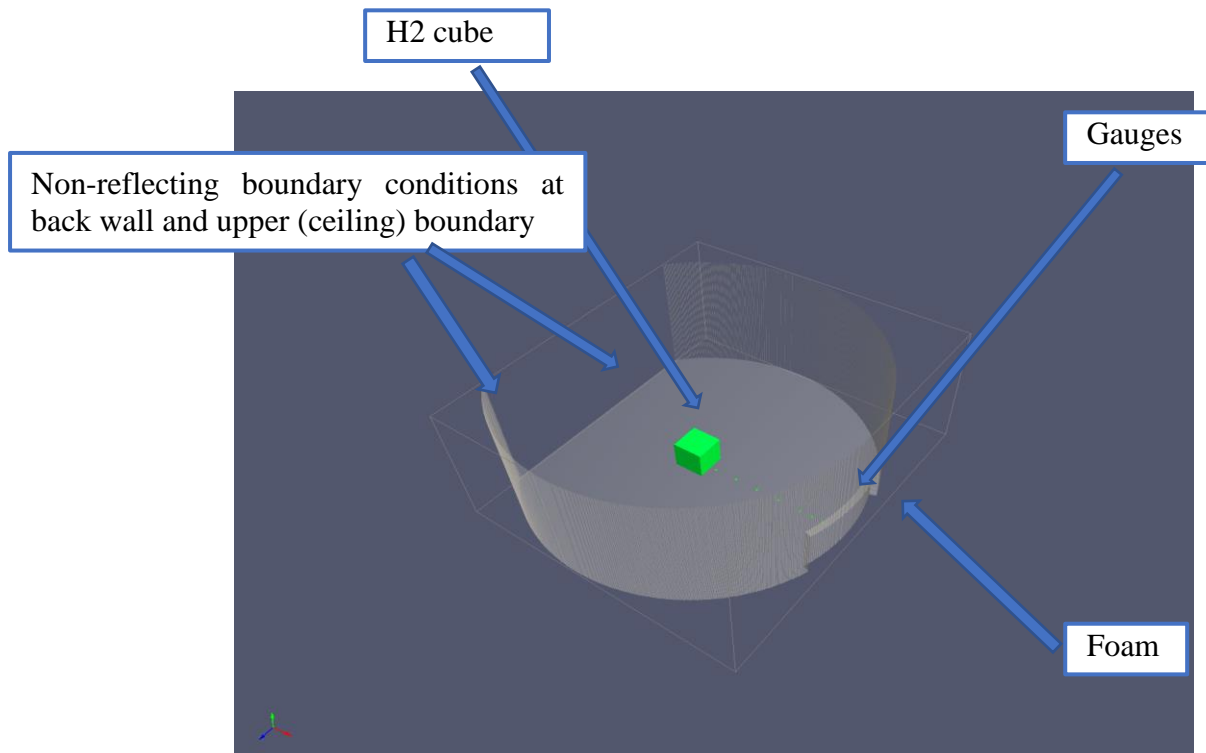
Figure 177: Boundary conditions for simulations, showing the location of H_2 cube, soft foam layer, and pressure gauges.
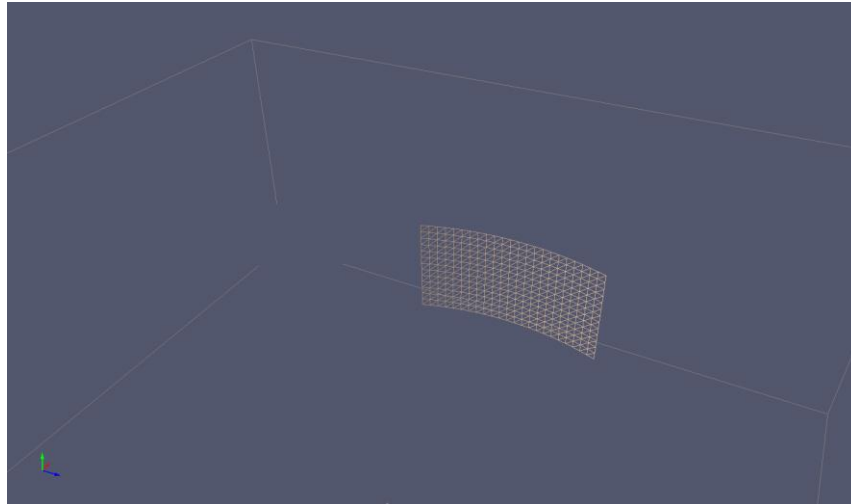
Figure 178: The curved foam layer surface modelled as interface for data exchange between COM3D and ABAQUS simulations.

Due to the limited availability of the mechanical properties of the absorbing materials, only the test case with the polyurethane foam is simulated. The mechanical properties of the foam for the crushable foam model in the ABAQUS code are listed as follows.

```
**
*SECTION CONTROLS,NAME=FOAM,HOURGLASS=ENHANCED
*SOLID SECTION,ELSET=FOAM,MATERIAL=FOAM,CONTROLS=FOAM
0.180,
*MATERIAL,NAME=FOAM
*ELASTIC
7.5E6, 0.0
*CRUSHABLE FOAM,HARDENING=ISOTROPIC
1.0, 0.0
*CRUSHABLE FOAM HARDENING
0.2000E6, 0.0000
0.2577E6, 0.0094
0.2760E6, 0.0258
0.3053E6, 0.0452
0.3267E6, 0.0655
0.3623E6, 0.1084
```

(Source: https://abaqus-docs.mit.edu/2017/English/SIMAINPRefResources/cyl_isoexp_fin.inp)

7.2.3.6 Simulation results

1. The hydrogen detonation is simulated by using COM3D code. The evolution of the pressure shock front is shown in Figure 179 by the iso-surface pressure contours at different moments. Figure 179 (b) presents the moment that the shock front hits on the concerned foam covered wall region. Figure 179 (c) presents a reflected pressure contour by the vessel walls.

(a)

(b)

(c)
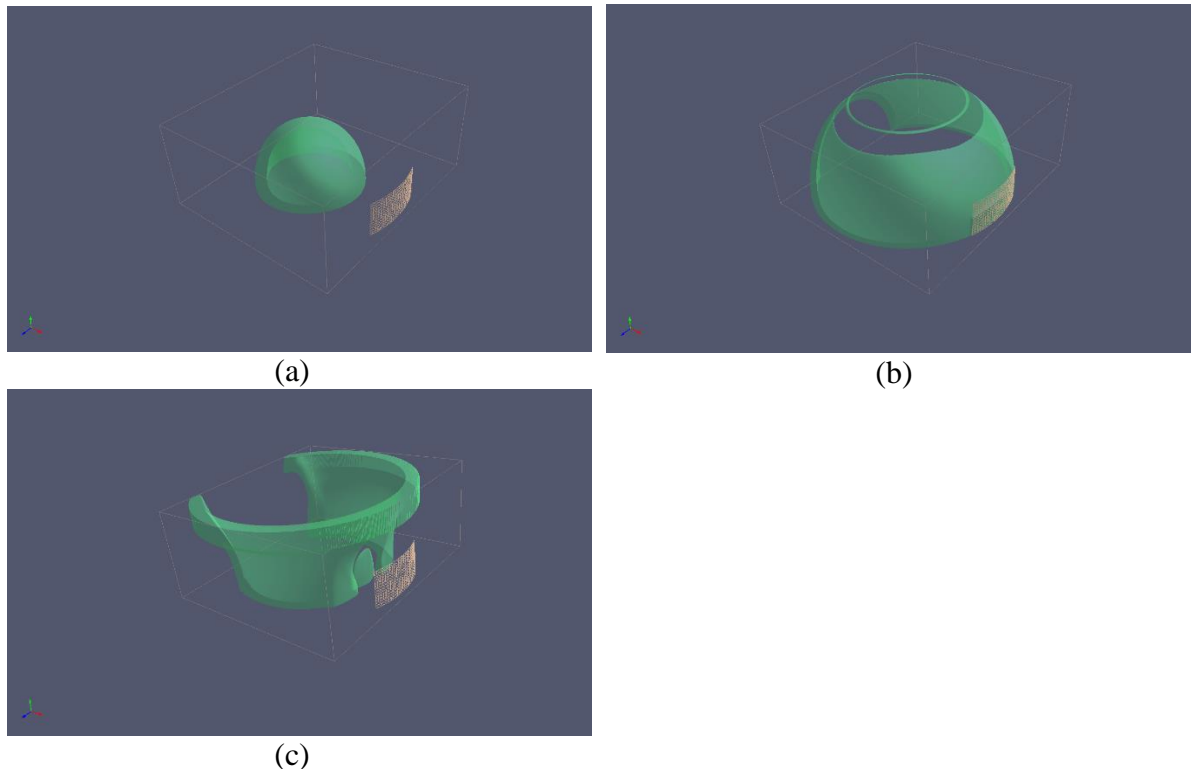
Figure 179: Simulated pressure evolution of hydrogen detonation, iso-surfaces of (a) 1.2 bar at 2.3 ms, (b) 1.2 bar at 5.5 ms, and (c) 1.1 bar at 8.7 ms.

2. The incident shock wave and reflected pressure shock by the bare steel wall is plotted as functions of time at different pressure gauge locations in Figure 180 for (a) experiment and (b) simulation, respectively. The slopes of the dotted line (left wing in (a)) and the dashed line (left wing in (b)) stand for the travelling speed of the incident shockwave in test and in simulation, respectively. The figure shows that the computed shockwave speed is consistent to the measured one. Likewise, the slopes of the right wings of (a) and (b) manifest a good agreement about the reflected shockwave speed between test and simulation. However, at most pressure gauges, the computed shock impulse is not as sharp as the measured. The primary reason might be that the resolution of the computational grid (1 cm cell size in the case) is not fine enough.

One can in principle make a judgement that the dynamics of the hydrogen detonation shockwave is computed properly by the code. Especially the pressure time-history records at the gauge P3 are further analysed in later sections.

3. The computed time histories of the reflected shockwaves by steel or by foam are compared in Figure 181. The figure shows that the incident pressure shocks are identical to each other.

Nevertheless, the reflected pressure shocks are different between the steel reflection and the foam reflection, especially with concern on the pressure amplitudes of the reflected wave.

4. The computed pressure amplitudes of the reflected shockwave by steel or by foam are compared in Figure 182 (c), which clearly indicates a decrease of the pressure amplitude by the foam layer. For reference, the measured pressure amplitudes of the reflected waves by steel and by foam are shown in Figure 182 (a) and (b), in different time scale, respectively. It shows that, the computed pressure amplitudes have still deviations from the measured amplitude. The main reason might be that the used mechanical property of the polyurethane foam in the crushable foam model in ABAQUS simulation may not represent the real properties of the selected foam in experiments, which is unfortunately unavailable.

(a) Experiment   (b) Simulation
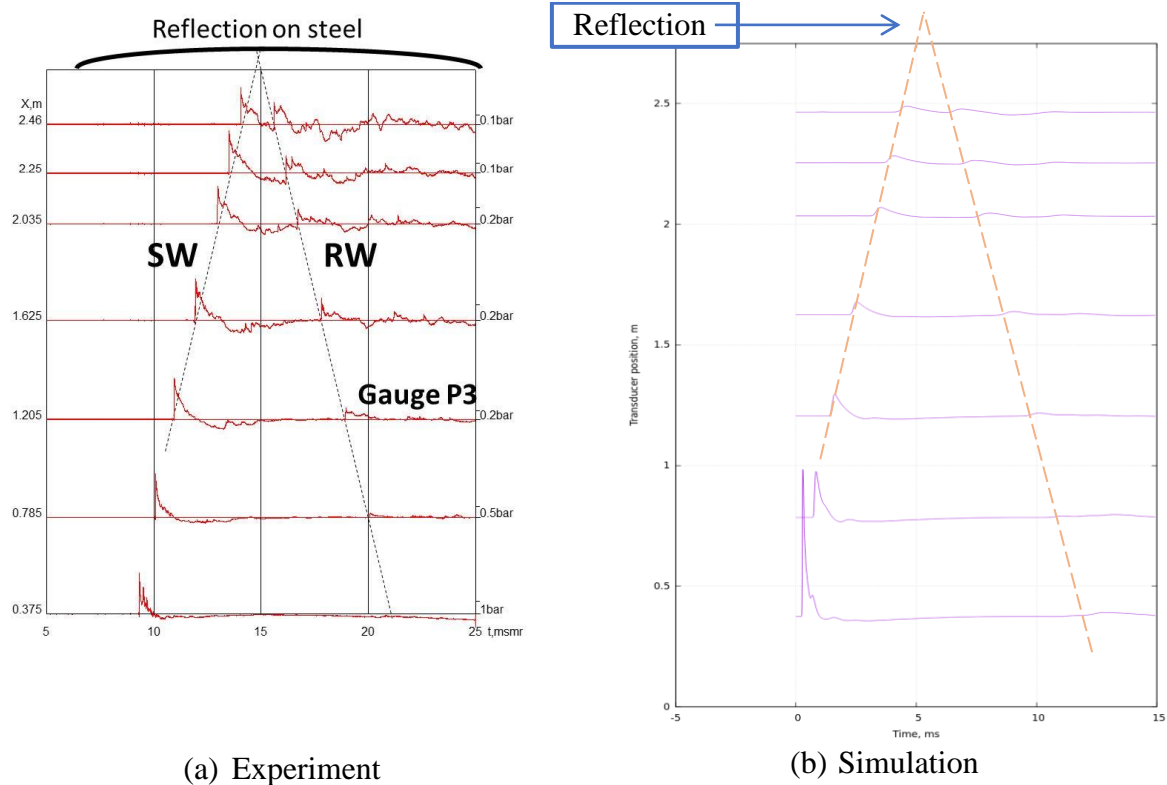
Figure 180: Comparison between test and simulation of incident shock wave and reflected wave at the pressure gauge P3 by bare steel wall without foam layer.

(a) Reflected by steel wall

(b) Reflected by polyurethane foam layer
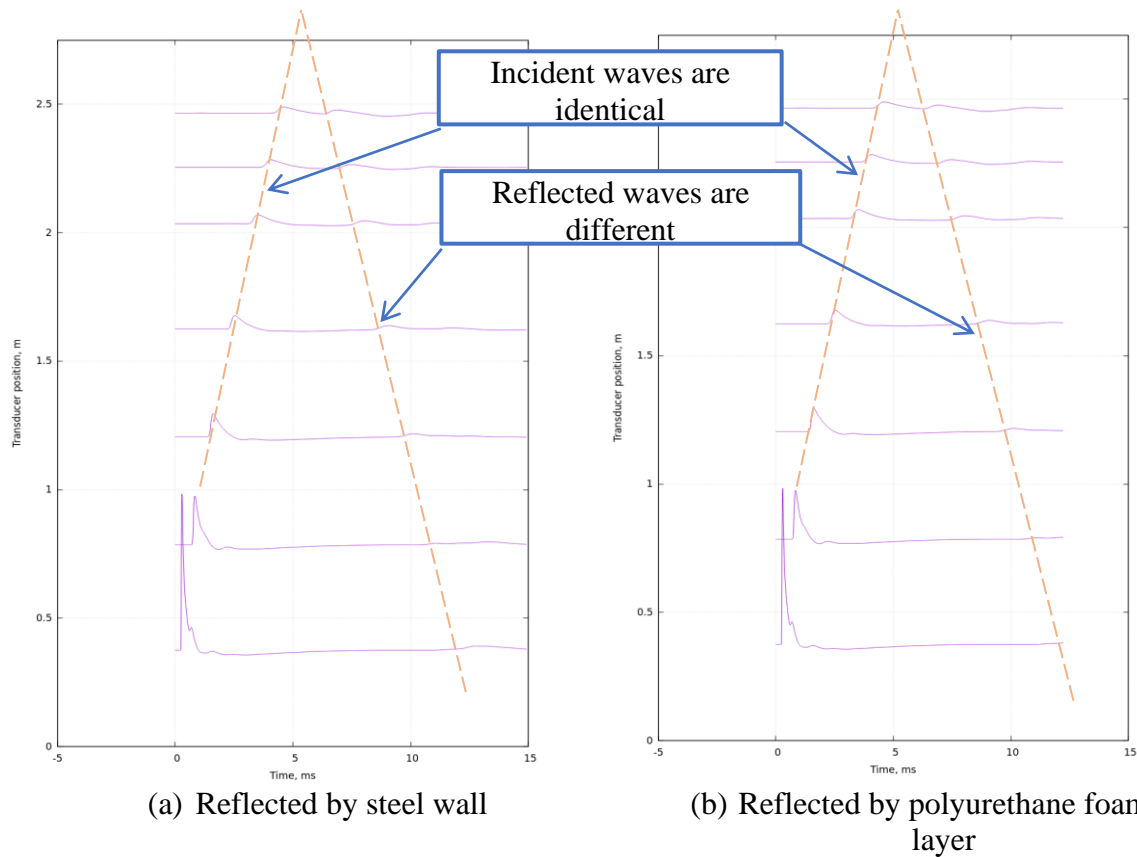
Figure 181: Comparison of the two simulation cases of reflected shock wave (a) by bare steel wall, (b) by polyurethane foam layer, at the pressure gauge P3.

(a) Experimental data in 1.5 ms

(b) Experimental data in 0.27 ms
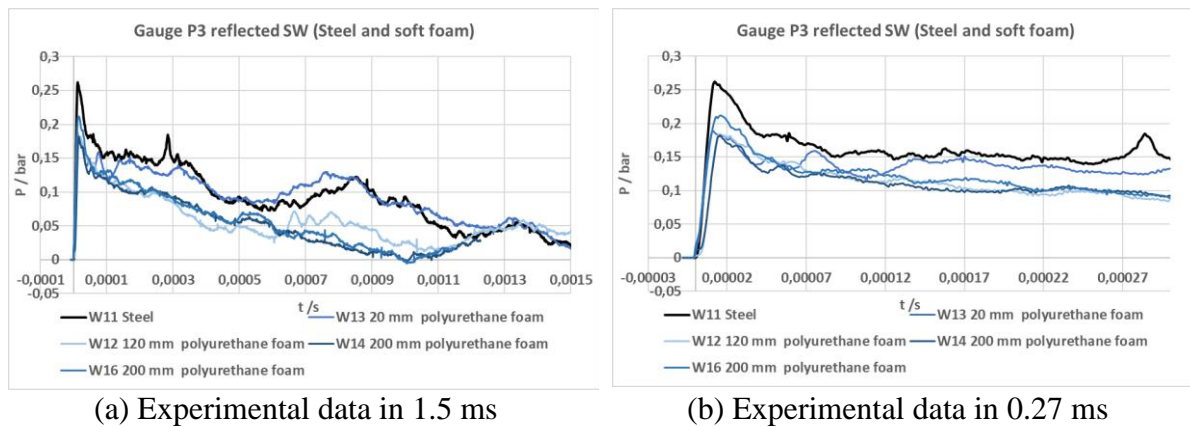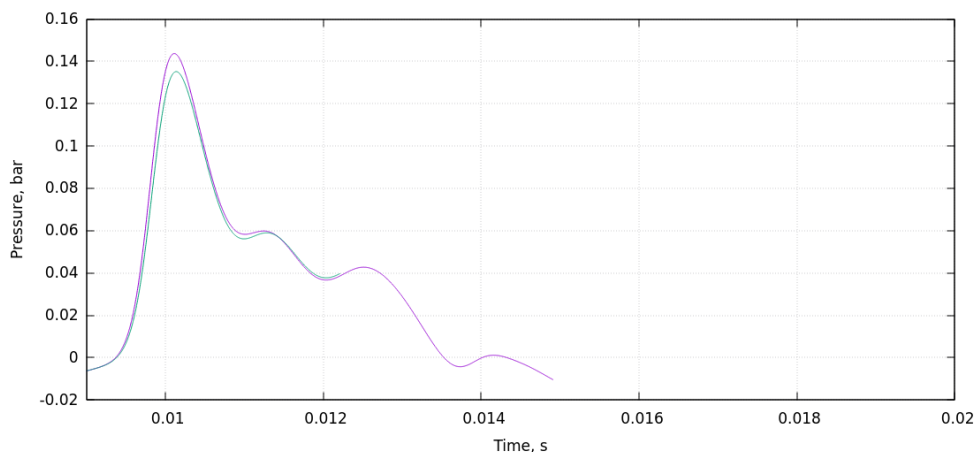
(c) Simulation

Figure 182: Comparison of measured and computed amplitudes of the reflected shock waves by bare steel wall or by soft foam in experiment (a, b) and in simulation (c), respectively.

7.2.3.7 Simulation results

The preliminary simulation results by using the coupled COM3D-ABAQUS codes manifest that the soft materials e.g. polyurethane foam can mitigate the pressure amplitude of the reflected shockwave. Based on currently available data, a clear agreement between tests and simulations is observed both qualitatively and quantitatively. The simulation conclusion of the attenuation effect of soft materials on shockwaves is an additional proof of the experimental results.

7.3 Experiments (Task 4.4, HSE)

7.3.1 Blast wave and fireball of hydrogen tank rupture in a tunnel (ST4.4.1, HSE)

7.3.1.1 Background

This section outlines a series of experiments undertaken at the HSE Science and Research Centre investigating the catastrophic failure of hydrogen cylinders within a tunnel. These experiments have taken place within HSE's 70 m long, 3.7 m diameter steel tunnel and are scaled to be representative of cylinder failures in larger real-world tunnels.

7.3.1.2 Objectives

Since one of the pressurised vessel failure scenarios, which must be considered, is that of catastrophic failure at hydrogen pressures up to 700 bar, then a suitable experimental arrangement to represent this event needed to be found. In the extreme case, the vessel was considered to split around a circumference resulting in the rapid separation of the two halves of a containment sphere or cylinder.

A review of typical failure behaviour of pressurised vessels (Zheng et al. (2008), Zalosh et al. (2005)) led to the conclusion that end cap failure or wall splitting failure was a more likely scenario, and further, that the timescale for a circumferential separation event was judged to be several miliseconds.

In view of these observations and the need to be able to re-use the storage vessel for longer discharge tests, the decision was made to use a 100 mm diameter bursting disc system and carry out the necessary observations on its behaviour during failure.

A double diaphragm bursting disc system is tried and tested and known to have an opening time of a small fraction of 1 ms. It was also considered that a representative expanding spherical shock wave would emerge from this system in a similar way to that expected from an end cap failure. An image of the sudden release vessel and the double bursting disc arrangement can be seen in Figure 183.

Figure 183: Image of the sudden release vessel in position at the mid-point of the HSE 70 m steel tunnel. Also visible are the vertical thermocouple arrays.

The phase of the program being described here relates to the behaviour of the release within the first milisecond of the vessel rupture and in the immediate vicinity of the bursting disc.

Of particular interest are 1) the development phase of the shock system as it emerges from the burst disc location, 2) the magnitude of the shock velocities and shock pressures for different release conditions and 3) the observation of any early onset combustion following disc rupture.

The experimental arrangement used to reveal this detail is described in the following section (7.3.1.3).

7.3.1.3   Experimental arrangement

The facility was largely unchanged from the configuration used for the hydrogen release and dispersion experiments described in detail in section 5.3.1.3. The notable difference being the sudden release vessel itself and its associated pipework. A P&ID of the modified pipework is shown in Figure 184.

Whilst the observation of any combustion behaviour associated with the bursting disc event is straightforward and relies on the availability of a sufficiently high speed and sensitive camera system, the observation of the emerging blast wave (shock wave) is more challenging. It is important to be able to make such an observation however, since the impact and behaviour of the event is strongly related to the dynamics of this shock system.

The most obvious property by which the emergent shock may be identified is the density discontinuity across the shock, and since we are dealing with high pressure it was anticipated that the optical distortion available via this density step could be used for its monitoring on a short timescale.

Schlieren photography is a long established technique for the observation of fluid density gradients and has been used routinely for small scale measurements. The traditional method involves two spherical mirrors and a knife edge, which acts as an edge filter in the absence of any density anomaly. Transient density fluctuations allow the light rays to diverge from their undisturbed path and pass the knife edge revealing the location of the fluctuations of interest.

The difficulty with the traditional method is that it requires mirror dimensions similar to the field of interest and this becomes problematic when these are of several meters in size.

Several variants of the traditional schlieren exist and one of these, background oriented schlieren (BOS), has become more widely used to reveal much larger density structures, sometimes of several km in size. Descriptions of the method can be found, for example in the following references (Goldhahn et al., 2007 and Raffel et al., 2015)

A typical geometry used is shown in Figure 185.
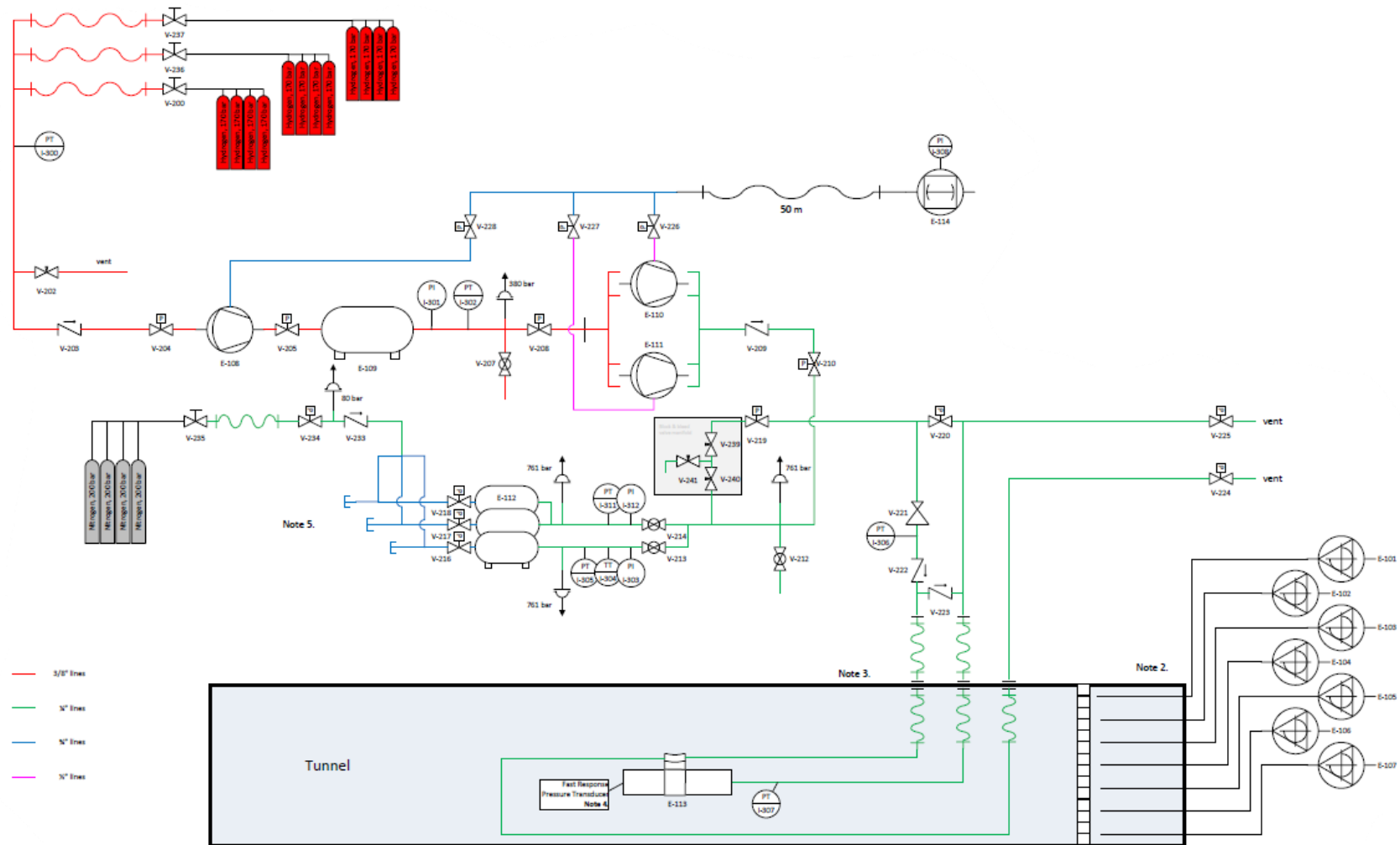
Figure 184: P&ID of gas delivery system with attached sudden release vessel inside the tunnel.
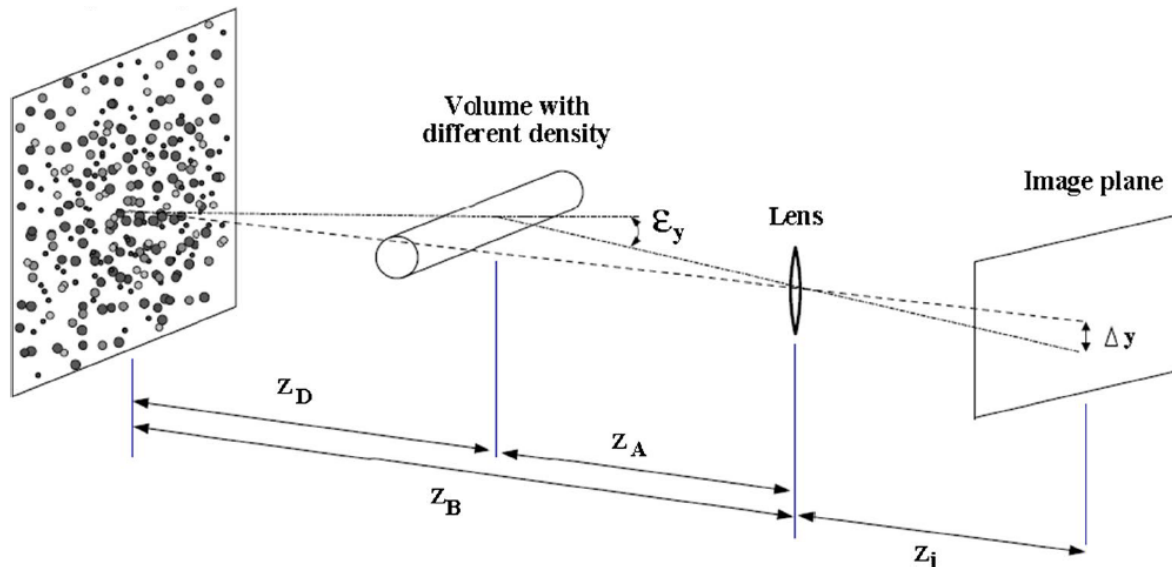
Figure 185: Basic Background oriented schlieren geometry (Raffel, 2015). The object plane carrying a chosen pattern is focused on the camera image plane and is undistorted in the absence of any density fluctuations within the test space. Density gradients in the test space produce angular deviations in the light rays (ey as shown) giving rise to pattern distortions in the image plane (Dy).

The bursting disc tests will give rise to a spherical shock field, and as the vessel exit is upward pointing, the vertical direction will be a known direction of density discontinuity associated with the emergent shock. A useful background pattern to investigate this shock structure is therefore a simple black/white grid oriented horizontally and illuminated sufficiently strongly to allow for short exposure time using a high speed camera.

For this purpose a black background plane of 2 x 1.5 m in size was covered with a white grid pattern 10 mm in width with 20 mm grid spacing. This was located against one wall of the tunnel, within which the vessel was located on the tunnel axis and pointing vertically upwards. The grid was illuminated with a 65000 lm constant light source inside the tunnel and imaged using a high speed CCD camera, which was located outside the tunnel and using an 80mm diameter viewing window. This is shown schematically in Figure 186.

The received image of the grid used is shown in Figure 187.
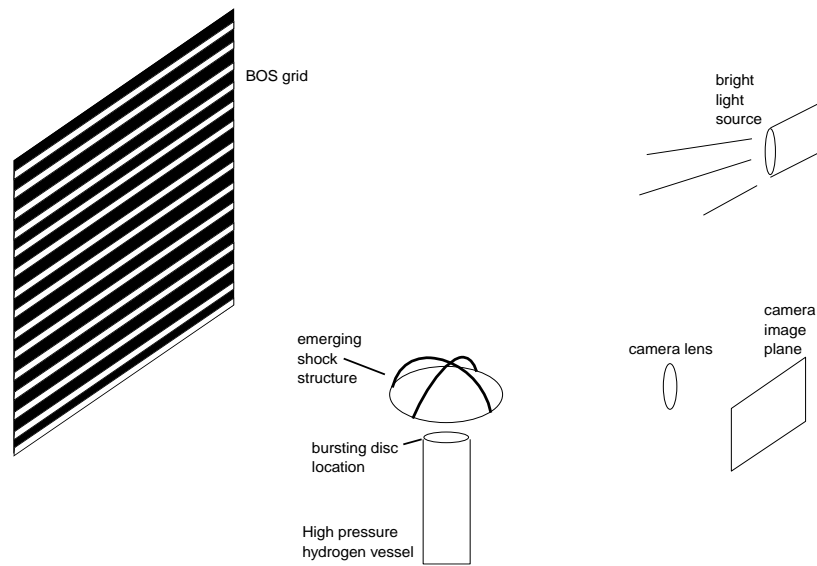
Figure 186: Schematic of background oriented schlieren used to observe the shock emerging from the bursting disc system.
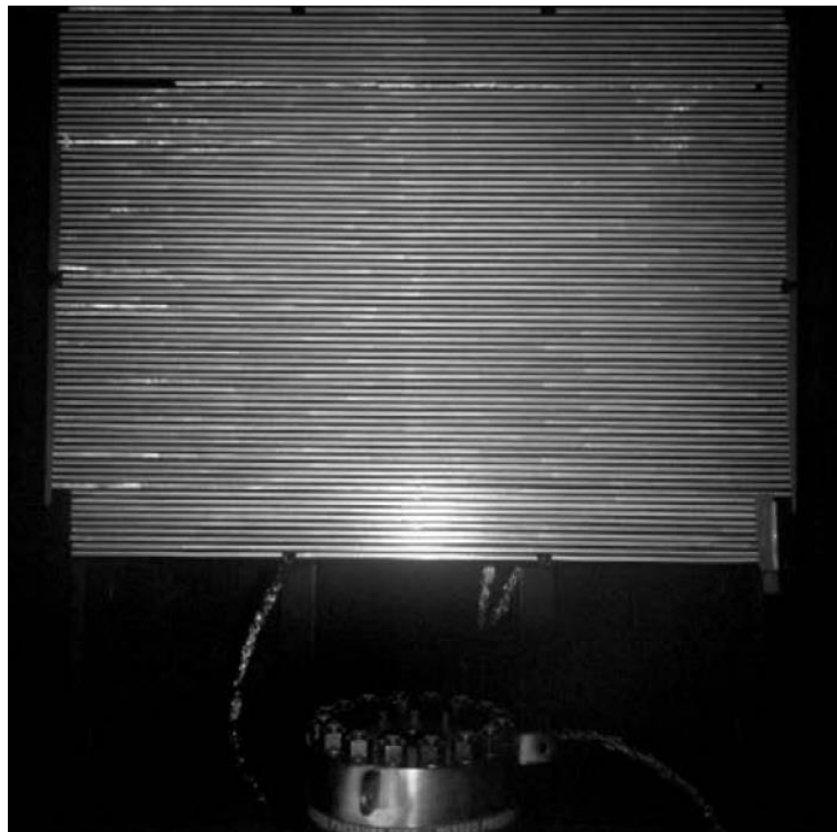
Figure 187: Received image of the BOS grid system using the 65000 lm light source and an exposure time of 4 μs.

Catastrophic discharge tests have been carried out for a number of vessel volumes and pressures. Vessel volumes were able to be changed by the insertion of 'dummy' tubular blocks into the vessel as required. Table 41 details the test conditions investigated.

Table 41: Test parameters for catastrophic release tests.

Test number	Vessel volume (liters)	Starting reservoir pressure (barg)
26	5	637
27	5	636
28	5	630
30	12	658
31	12	554
32	12	602
33	12	503
34	18	609

7.3.1.4 Results

All of the tests show closely similar behaviour. In particular the emerging shock shows well developed hemi-spherical growth behaviour and this is shown in Figure 188 as the shock approaches the top area of the grid at 924 µs following disc rupture. This provides confirmation that the geometry used is an appropriate substitute for a circumferentially sheared rupture configuration.
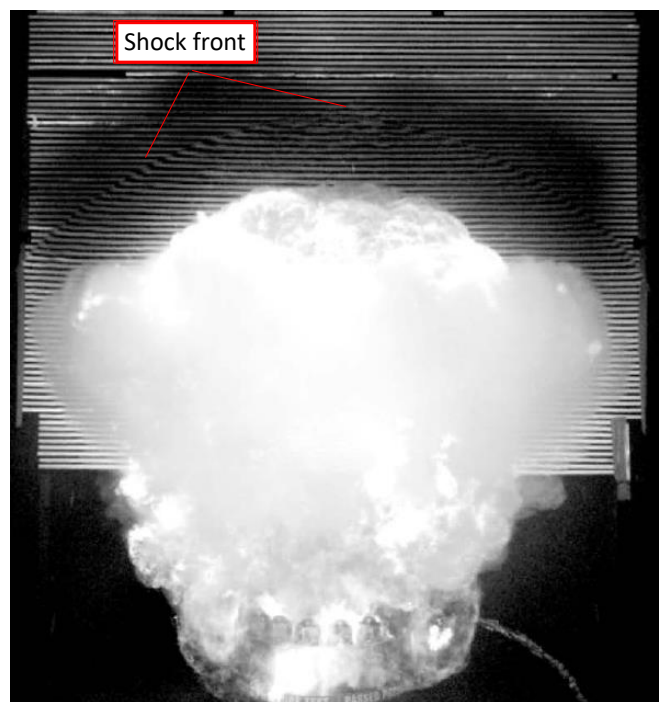
Figure 188: Schlieren image at 924 µs after disc rupture showing spherical shock front ahead of flame plume.

It can be seen from Figure 188 that combustion accompanies the disc rupture event. The progress of the discharge is closely similar for all cases studied and the images below in Figure 189 relate to Test 26. The post-shock gas temperature can be deduced from the information extracted from the schlieren images and is discussed below.
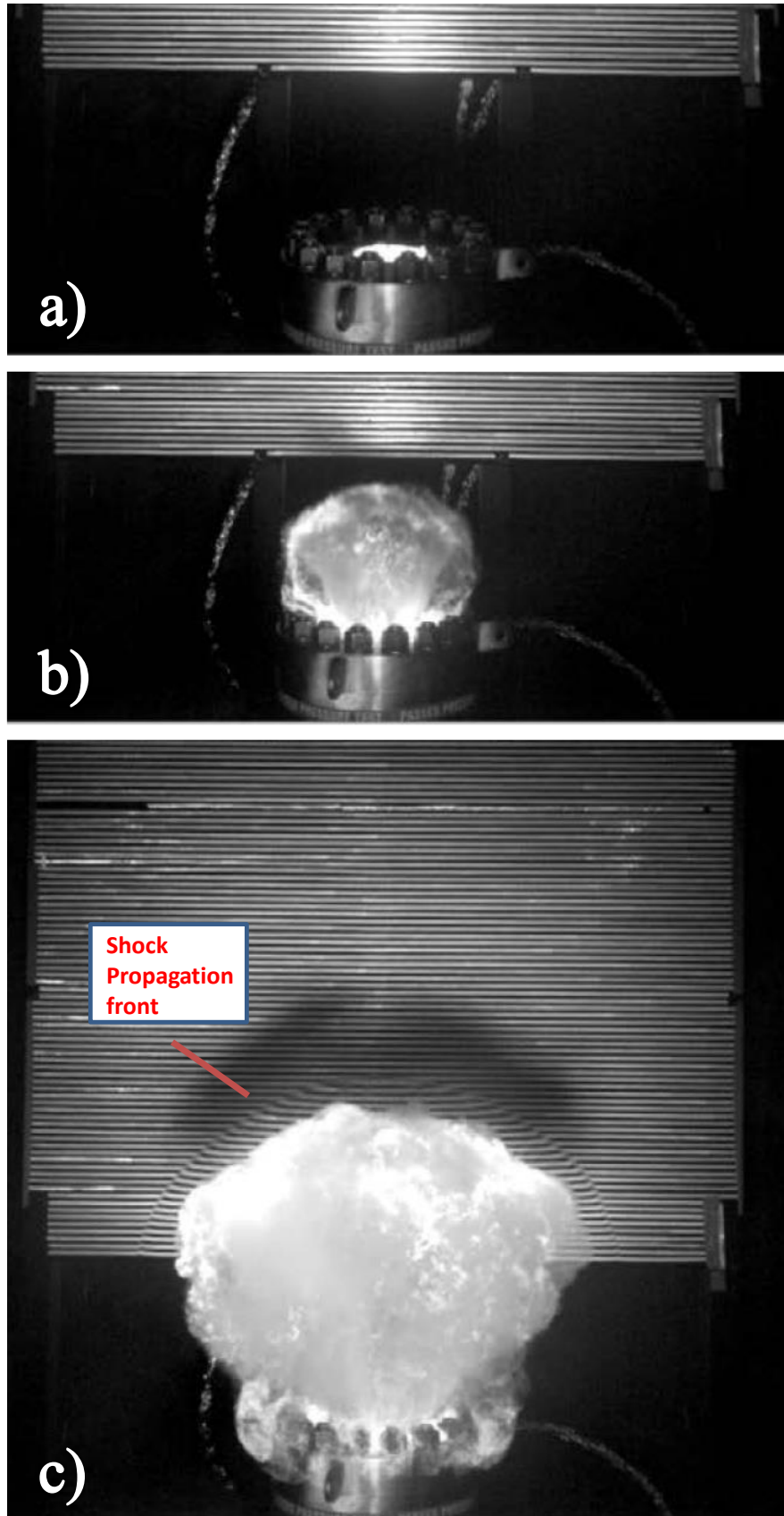
Figure 189: Sequence of shock front development following disc rupture for Test 26. (a) at t=0, (b) at 178 μs and (c) at 480 μs

The sequence of images such as those shown in Figure 189(c) have been recorded at 53kHz and for each test, the position of the shock front has been plotted using the BOS grid as a calibrated background. This provides a semi-quantitative means of establishing the shock velocity as a function of distance from the disc position.

Figure 190 (a) & (b) show the resulting variation of shock Mach number for Test 26 over the distance monitored based on the measured shock position and camera frame timing.

Normal shock relations provide a means of relating the shock Mach number (M_1) to the gas temperature and pressure behind the shock as described in the NACA report 1135 (Ames Research Staff, 1951). For a shock moving into a stationary gas at pressure P1, the pressure behind the shock at P2 is then given by the following, based on ideal gas behaviour:

$$\frac{P_2}{P_1} = \frac{2\gamma M_1^2}{\gamma + 1} - \frac{\gamma - 1}{\gamma + 1}$$

Since P_1 = 1 atm, this allows the calculation of the pressure behind the shock and this is shown as a function of distance in Figure 190 (b) for Test 26.

a)

b)
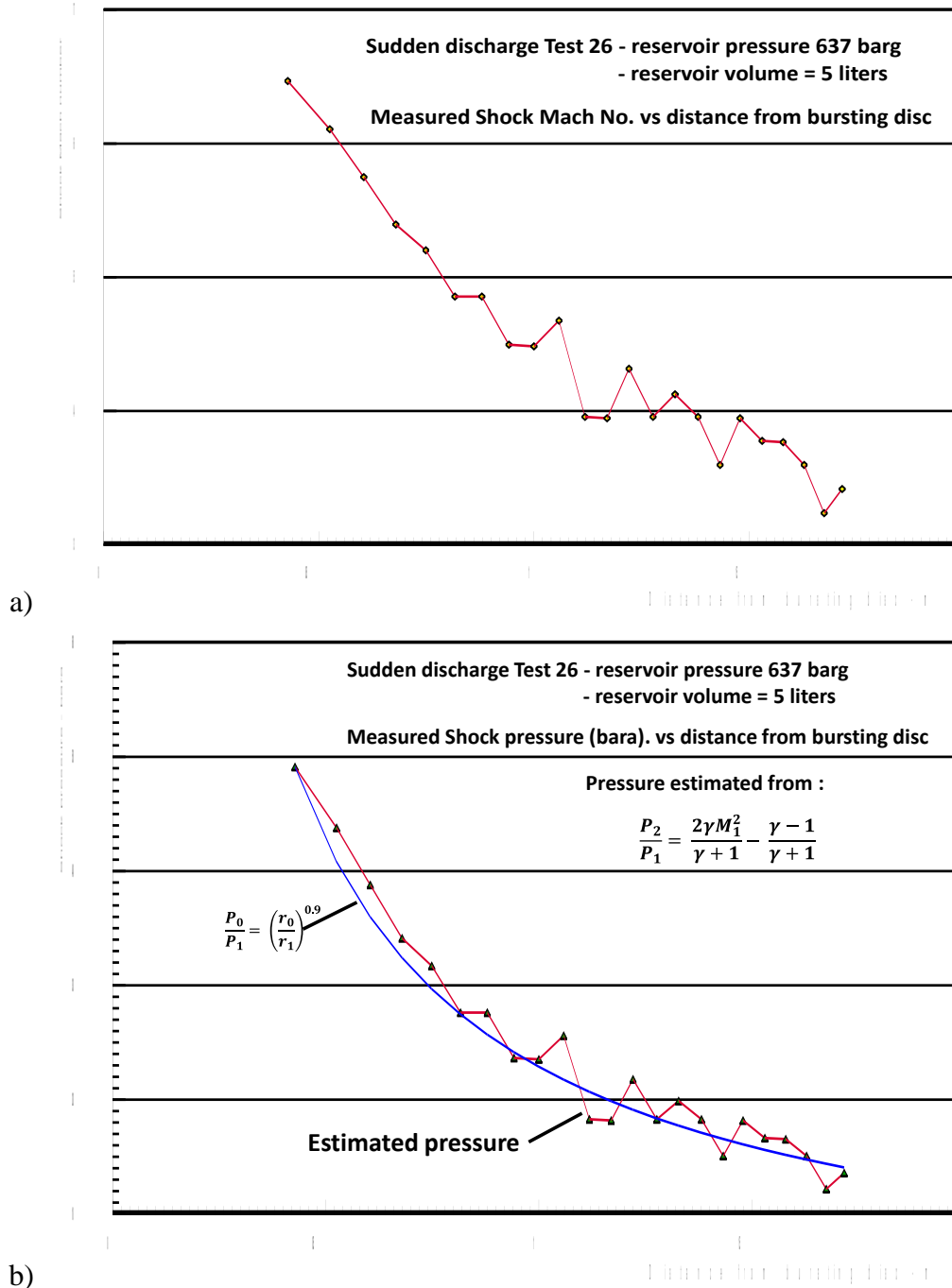
Figure 190: (a) Variation of shock Mach number with distance from the disc rupture position for Test 26. (b) Estimated 'shock processed' gas pressure behind the shock front versus distance based on normal shock relations for an ideal gas and $\gamma = 1.4$.

An estimated best-fit curve is drawn through the data of Figure 190 (b), taking the first data point as the reference P_o and radius r_o. For the pressure P at radius r, the curve is taken to be of the form $P = P_o(r_o/r)^n$. Reported blast tests using small explosive charges (Kandula et al., 2008) observe that the near field pressure decay can be represented in this form and where n was found to be 1.06. As can be seen the curve for Figure 190 (b) is better represented using an n value of 0.9.

Appendix A1.2 shows the results for all of the tests indicated in Table 41, and includes the variation of shock Mach number and the estimated pressure decay. As can be seen from these, the n values for the estimated curve fit against pressure, range from 0.7 - 1.0.

Figure 189 (a) shows that combustion exists before the flame plume exits from the rupture disc housing and immediately following rupture. Within a few miliseconds of disc rupture, the flow conditions for shock propagation will have been established, i.e. the shock will have begun to propagate outward and the contact surface between high pressure hydrogen and external air will have established.

The temperature of gas mixture (T_2) immediately behind the shock can be estimated assuming ideal gas behaviour based on the following (Ames Research Staff, 1951):

$$\frac{T_2}{T_1} = \frac{[2\gamma M_1^2 - (\gamma - 1)]\,[(\gamma - 1)M_1^2 + 2]}{(\gamma + 1)^2 M_1^2}$$

where M_1 is the shock Mach number and T_1 is the temperature of stationary gas ahead of the shock. Taking $\gamma=1.4$ and T_1 as 283K gives the following values in Table 42 for the gas temperature in the region of the contact surface following disc rupture for each of the discharge tests.

Table 42: Mach number and associated gas temperature at the shock front

Test No	Measured exit Mach No.	Shock heated gas temperature T_2 (°C) (Estimated for ideal gas, $\gamma=1.4$)
26	6.7	2464
27	6.2	2133
28	6.9	2613
30	6.3	2205
31	6.2	2114
32	6.6	2428
33	6.5	2311
34	6.9	2662

Given that the autoignition temperature of hydrogen in air is 585 °C, then the immediate ignition observed in Figure 189 (a) is to be fully expected since the entrainment of the relatively small quantities of hydrogen required to reach flammable concentrations will not markedly reduce the temperature of the resulting mixtures.

7.3.1.5   Conclusions

The discharge tests have provided supporting data for the events immediately following vessel rupture and can be summarised as follows.

1. A hemi-spherical shock wave will emerge from the rupture site and this can be represented using a rupture disc of a dimension representative of the expected rupture size.

2. Ignition of the hydrogen will occur at the instant of disc rupture and this will propagate as a plume on a timescale very similar to that of the propagating shock front filling the immediate area of discharge region.

3. The shock Mach number will be around a value of 6.5 and give rise to initial shock pressures of around 45 - 50 bar.

4. Decay of the shock pressure toward the tunnel walls follows an $\sim r^{-n}$ law, where, for the present work, n has been found to be in the range 0.7-1.0, and enabling an estimate of the shock impact on the structures in the immediate vicinity of the rupture.

7.3.1.6   Comparison of sudden discharge releases with and without tunnel vehicles

As part of the series of release tests in which a sudden release is initiated, comparisons have been made of the consequences when tunnel vehicles are present or absent. The sudden release was that used for the schlieren tests using a 4" bursting disc, with the chamber exit facing vertically upward. Comparisons have been made for the specific cases involving 12 L of hydrogen, and cases with and without vehicles have been similarly matched for initial reservoir pressures.

In most cases photographic records have also been made, and an example of the sequence of events following disc rupture is shown in Figure 191.

1 ms after rupture	8 ms after rupture
90 μs after rupture	328 μs after rupture
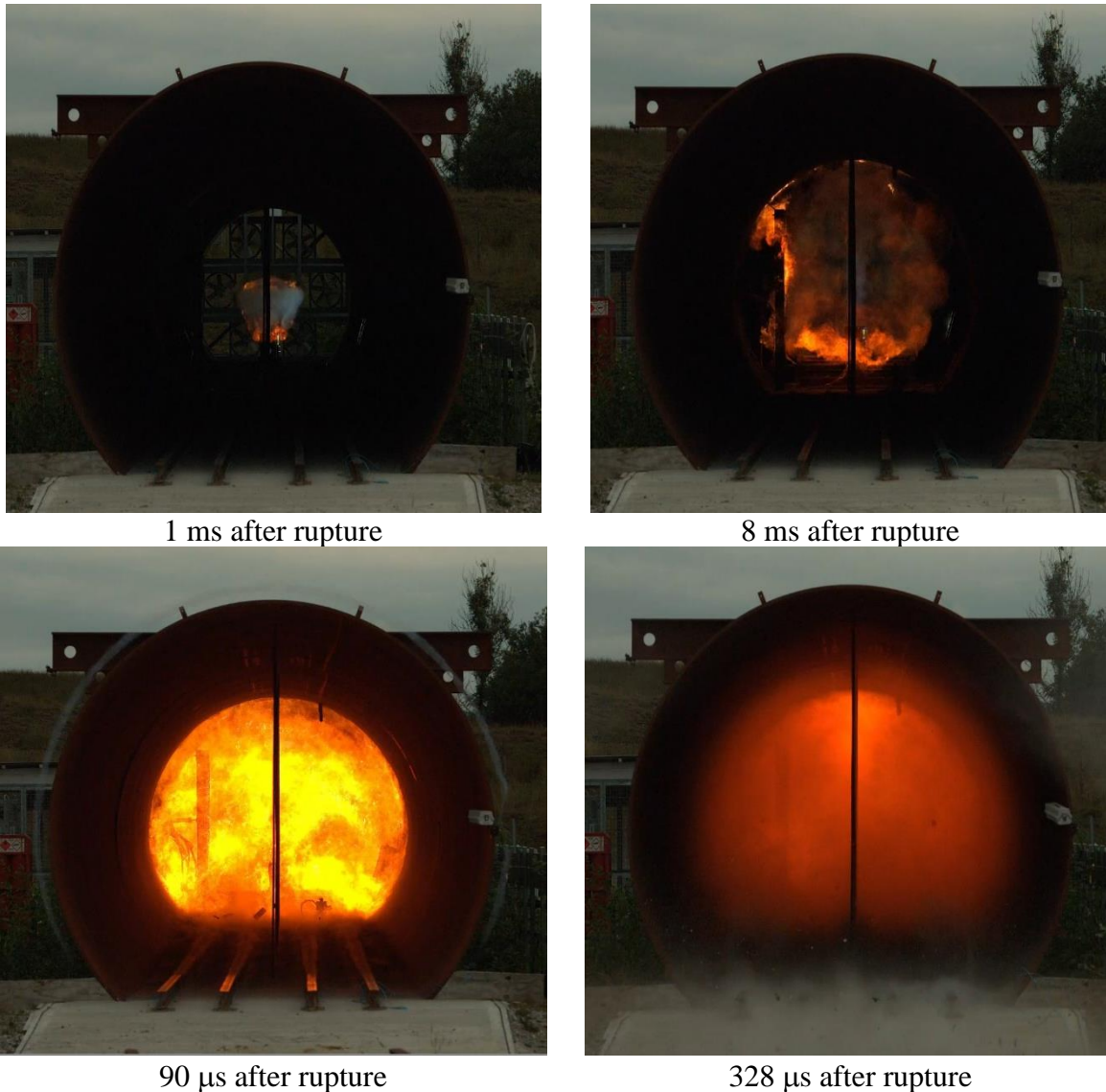
Figure 191: Development of body of flame following sudden rupture of 4" disc. Reservoir volume is 12 L and pressure is 658 barg.

It has already been noted in the high speed schlieren recordings that shock heating on disc rupture will always result in ignition. For the 12 L cases compared, pressures were in the 500 to 600 bar range, which means that stored hydrogen masses are in the 0.5-0.6 kg range. The oxygen demand for full combustion would then correspond to around 4 kg, and an air volume of 20 m^3 at ambient conditions. The cross section of the tunnel is 10 m^2, which indicates that, within a tunnel length of 2 m, there is sufficient air to fully burn the discharged hydrogen, suggesting that combustion will be a local event. The pictures in Figure 191 provide confirmation of this expectation and suggest that locations further downstream are likely to experience exhaust gas temperatures and exhaust flow conditions rather than full combustion temperatures.

The initial events connected with a strong shock emerging and propagating down the tunnel. This weakens as it emerges from the ruptured disc and moves toward the tunnel walls and subsequently travels towards the exit. This can be seen emerging from the tunnel in Figure 191 at 90 μs revealing a condensation ring at the tunnel walls.

The vehicles introduced into the tunnel for the comparison corresponded to the Bus scaled dimensions. These are shown in Figure 193 indicating their position relative to the discharge point. The vehicles extend for a length of 26.35 m down the tunnel from the discharge point.

Nine tests have been used in the comparison and further four tests are included to indicate behaviour for different stored volumes and pressures. Table 43 shows the test conditions used.

Table 43. Sudden release tests investigated.

Test with vehicles	Comparison tests without vehicles	
35 (12 L, 642 barg)	30 (12 L, 658 barg)	29 (12 L, 660 barg)
36 (12 L, 654 barg)	30 (12 L, 658 barg)	
37 (12 L, 460 barg)	33 (12 L, 503 barg)	31 (12 L, 549 barg)
38 (12 L, 605 barg)	32 (12 L, 602 barg)	
	26 (5 L, 634 barg)	
	27 (5 L, 634 barg)	
	28 (5 L, 625 barg)	
	34 (18 L, 338barg)	

The tunnel is instrumented with vertical flame sensor arrays at nine axial locations and wall mounted pressure sensors at eight axial positions. The flame sensors are type-K thermocouples of 0.25 mm with good response time. The co-ordinates of the pressure transducers inside the tunnel is shown in

Table 44. A 3D layout and the co-ordinates of the thermocouple arrays are given in Figure 192 and Table 45 respectively.

Table 44. Location of pressure sensors inside the tunnel

Sensor ID	Co-ordinate (m)		
	x	y	z
P12	34.0	1.85	1.85
P11	36.0	1.85	1.85
P10	37.5	1.85	1.85
P9	40.0	1.85	1.85
P8	42.5	1.85	1.85
P7	45.0	1.85	1.85
P5	50.0	1.85	1.85
P3	55.0	1.85	1.85

For each test certain data has been extracted and tabulated for comparison. The hot gas or flame propagating down the tunnel impinges progressively on the sensor arrays, and at each axial

array station, a range of times are observed for the deviation of the sensor off its base position. This is due to the sensors being arranged vertically within the array and hot gas arriving at slightly different times at the top and floor of the tunnel. For the purpose of flame arrival identification, only the lift-off time of the flame sensor is noted.

The eight axial flame positions downstream of the release are tabulated and hot gas arrival is identified by a range of times corresponding to a first and a last flame response at that axial station. Due to the good response time of the thermocouples, the maximum flame temperature recorded at each axial station is considered useful and this is also tabulated.
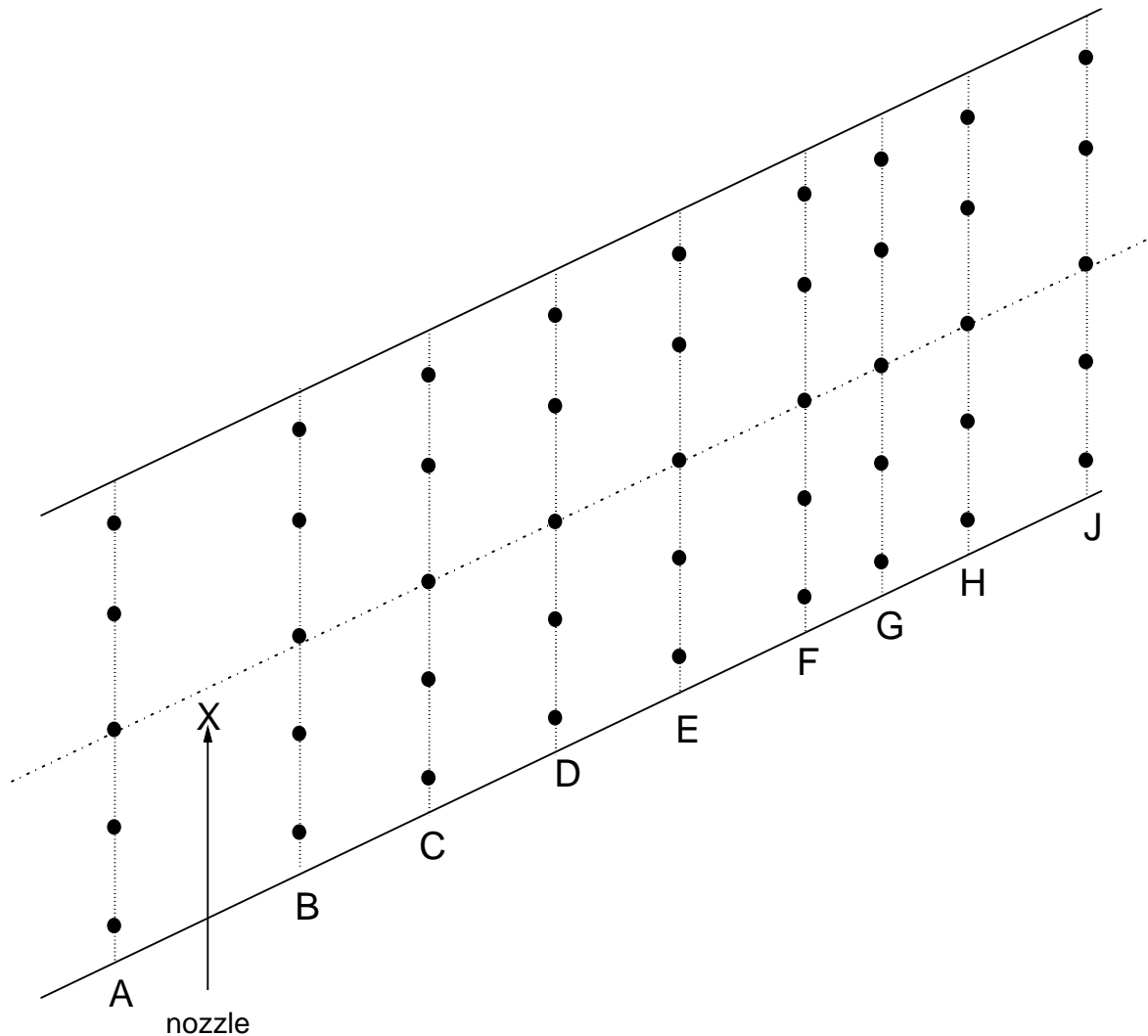
Figure 192. 3D representation of thermocouple flame sensor locations relative to release point

In order to provide an indication of the timescale of hot gas progress down the tunnel, an estimate of 'flame progress' is also provided by dividing the distance between adjacent axial stations by the difference in average arrival times at each of the two stations.

For each test case, the shock behaviour on disc rupture is also tabulated. Four pressure measurement stations are reported, including the shock arrival time, the peak shock pressure and the calculated shock speed between adjacent measurement stations.

Due to the randomness associated with disc rupture, the event timings for both flame and shock arrival are referenced to the arrival of the upstream shock closest to the rupture vessel i.e. P11.

Table 45. Location of thermocouple sensor arrays inside tunnel

Array	Sensor ID	Co-ordinate (m)		
		x	**y**	**z**
J	T45, T44, T43, T42, T41	34.0	0	3.25, 2.75, 2.15, 1.65, 0.95
H	T40, T39, T38, T37, T36	37.5	1.85	3.25, 2.75, 2.15, 1.65, 0.95
G	T35, T34, T33, T32, T31	40.0	1.85	3.25, 2.75, 2.15, 1.65, 0.95
F	T30, T29, T28, T27, T26	42.5	1.85	3.25, 2.75, 2.15, 1.65, 0.95
E	T25, T24, T23, T22, T21	45.0	1.85	3.25, 2.75, 2.15, 1.65, 0.95
D	T20, T19, T18, T17, T16	50.0	1.85	3.25, 2.75, 2.15, 1.65, 0.95
C	T15, T14, T13, T12, T11	55.0	1.85	3.25, 2.75, 2.15, 1.65, 0.95
B	T10, T09, T08, T07, T06	60.0	1.85	3.25, 2.75, 2.15, 1.65, 0.95
A	T05, T04, T03, T02, T01	65.0	1.85	3.25, 2.75, 2.15, 1.65, 0.95

7.3.1.7 Summary of sudden discharge results

Results are tabulated in Table 46 to Table 73.

For the four 12 L comparison tests, the shock propagation behaviour is closely similar and is characterised by a shock strength of around 1 barg from the first measurement station (P11) to the 45 m point (P7) and a weakening of the shock toward the exit at 55 m (P3) to a value around 0.5 barg.

The slightly lower pressure tests of 37, 33 and 31 show slightly lower initial and exit peak amplitudes.

Overall the presence of vehicles in the tunnel have no significant effect on the shock amplitudes, and propagation speeds are consistent with ambient temperatures, with the exception of the initial shock between P11 and P9 which shows evidence of propagation through a higher temperature environment in the vicinity of the ruptured vessel. This behaviour is true in all cases, with and without vehicles.

The additional test cases 26, 27, 28 and 34 shown in Table 66 to Table 73 employ reduced volumes of 5 L at similar pressures of around 600 barg and one case of increased volume (18 L) but at a lower pressure of 338 barg. For the 5 L cases, the peak initial shock pressure is around 0.8 barg with the exit shock amplitude being around half of this. For the 18 L case, there is a higher initial shock pressure of 1.36 barg, which has been mitigated by the lower reservoir pressure but this also shows a 50% decrease in amplitude at the tunnel exit.

Turning to the flame behaviour following disc rupture the tables show the progression of hot gas along the tunnel. For a fast deflagration of around 100 m/s one would expect that flame would arrive at exit in around 300 ms. This is not what one sees in the tables.

Flame progress speeds in the immediate vicinity of the vessel are in the range of 10 – 20 m/s to the 40 m distance. By the 50 m distance these have dropped to 1 – 3 m/s and continue at this level up to the tunnel exit. Total times for hot gases to be observed at the exit are typically 12 seconds. This confirms that the combustion event is localised around the rupture vessel and the subsequent expansion and convection of hot gas accounts for its transport at low velocities to the tunnel exit. Observed maximum temperatures are consistent with this as these are typically around 150 – 200 °C at the exit and often well below this figure.

No significant difference is observed in these behaviours between cases with and without obstacles.
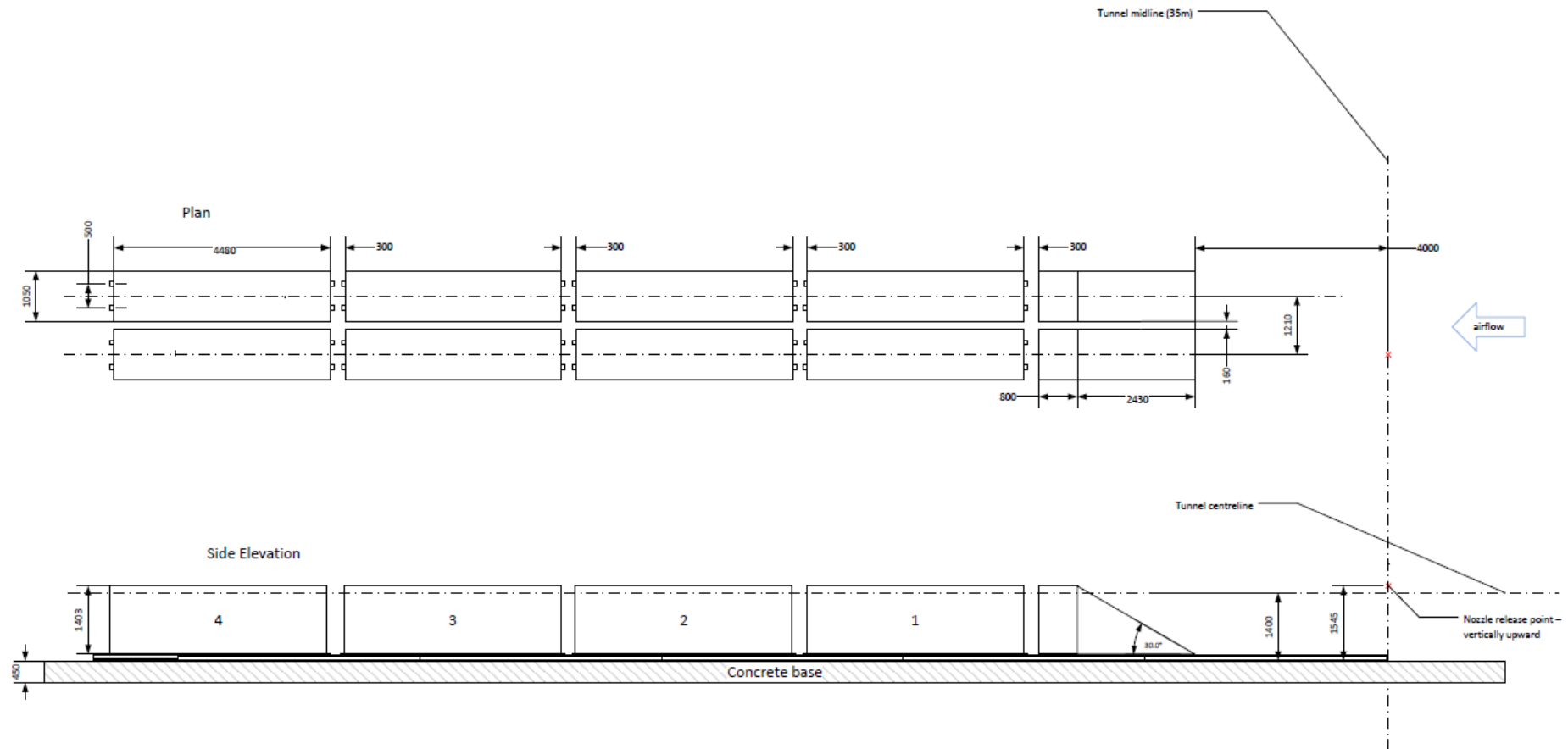
Figure 193. Geometry within the tunnel corresponding to the Bus and Train obstacles.

Table 46: TEST 29, 12 L, 660 bar. Flame arrival time range at each station and maximum indicated flame temperature (°C). Time referenced to shock arrival at P11. Discharge nozzle at 35 m. No Obstacles present

Axial position (m)	37.5	40	42.5	45	50	55	60	65
Arrival time range (s)	0.0142	0.0672-0.210	0.206-0.295	0.623	5.392-5.762	8.246	10.261-10.581	12.388
Max. flame T (°C)	905 (T9)	725 (T12)	435 (T16)	270 (T22)	324 (T26)	213 (T32)	221 (T36)	68 (T41)
Flame progress speed (m/s)		20.1	22.3	6.7	1.0	1.9	2.3	2.5	

Table 47: TEST 29, 12 L, 660 bar. Shock arrival times (s)(referenced to shock arrival at P11), peak pressures and intermediate shock velocities. Discharge nozzle at 35 m. No Obstacles present.

Axial position (m)	P11 (36 m)	P9 (40 m)	P7 (45 m)	P3 (55 m)
Shock arrival time (s)	0	0.009	0.022	0.047
Peak pressure (barg)	1.015	1.017	0.990	0.497
intermediate velocity (m/s)		444	384	395	

Table 48: TEST 30, 12 L, 658 bar. Flame arrival time range at each station and maximum indicated flame temperature (°C). Time referenced to shock arrival at P11. Discharge nozzle at 35 m. No Obstacles present.

Axial position (m)	37.5	40	42.5	45	50	55	60	65
Arrival time range (s)	0.0181	0.078 - 0.248	0.188-0.318	0.628-2.798	5.078-5.378	7.908- 8.478	10.01- 13.01	12.03-13.11
Max. flame T (°C)	892 (T8)	596 (T12)	352 (T16)	255 (T22)	348 (T26)	231(T32)	243(T36)	217(T41)
Flame progress speed (m/s)		17	28	1.7	1.4	0.77	1.5	2.5	

Table 49: TEST 30, 12 L, 658 bar. Shock arrival times(s)(referenced to shock arrival at P11), peak pressures and intermediate shock velocities. Discharge nozzle at 35 m. No Obstacles present.

Axial position (m)	P11 (36 m)	P9 (40 m)	P7 (45 m)	P3 (55 m)
Shock arrival time (s)	0	0.0088	0.0217	0.0471
Peak pressure (barg)	0.997	1.128	0.887	0.507
intermediate velocity (m/s)		454	387	393	

Table 50: TEST 35, 12 L, 642 bar. Flame arrival time range at each station and maximum indicated flame temperature (°C). Time referenced to shock arrival at P11.Discharge nozzle at 35 m. Obstacles present.

Axial position (m)	37.5	40	42.5	45	50	55	60	65
Arrival time range (s)	0.034	0.134 - 0.334	0.024-2.634	2.874-3.314	5.194-5.634		No Data	
Max. flame T (°C)	990 (T7)	580(T12)	338(T16)	227(T22)	163(T26)			
Flame progress speed (m/s)		12.5	2.3	1.4	2.1			

Table 51: TEST 35, 12 L, 642 bar. Shock arrival times(s)(referenced to shock arrival at P11), peak pressures and intermediate shock velocities. Discharge nozzle at 35m. Obstacles present.

Axial position (m)	P11 (36 m)	P9 (40 m)	P7 (45 m)	P3 (55 m)
Shock arrival time (s)	0	0.0089	0.0221	0.0482
Peak pressure (barg)	1.057	0.805	1.010	0.479
intermediate velocity (m/s)		449	378	383

Table 52: TEST 30, 12 L, 658 bar. Flame arrival time range at each station and maximum indicated flame temperature (°C). Time referenced to shock arrival at P11.Discharge nozzle at 35 m. No Obstacles present.

Axial position (m)	37.5	40	42.5	45	50	55	60	65
Arrival time range (s)	0.0181	0.078 - 0.248	0.188-0.318	0.628-2.798	5.078-5.378	7.908- 8.478	10.01- 13.01	12.03-13.11
Max. flame T (°C)	892 (T8)	596 (T12)	352 (T16)	255 (T22)	348 (T26)	231(T32)	243(T36)	217(T41)
Flame progress speed (m/s)		17	28	1.7	1.4	0.77	1.5	2.5

Table 53: TEST 30, 12 L, 658 bar. Shock arrival times (s)(referenced to shock arrival at P11), peak pressures and intermediate shock velocities. Discharge nozzle at 35 m. No Obstacles present.

Axial position (m)	P11 (36 m)	P9 (40 m)	P7 (45 m)	P3 (55 m)
Shock arrival time (s)	0	0.0088	0.0217	0.0471
Peak pressure (barg)	0.997	1.128	0.887	0.507
intermediate velocity (m/s)		454	387	393

Table 54: TEST 36, 12 L, 654 bar. Flame arrival time range at each station and maximum indicated flame temperature (°C). Time referenced to shock arrival at P11.Discharge nozzle at 35 m. Obstacles present.

Axial position (m)	37.5	40	42.5	45	50	55	60	65
Arrival time range (s)	5.96	6.11-6.32	6.26-6.59	6.6	9.73-10.13	No Data		
Max. flame T (°C)	531(T9)	550(T12)	252(T18)	285(T22)	180(T26)			
Flame progress speed (m/s)		10	12	13.8	1.5			

Table 55: TEST 36, 12 L, 654 bar. Shock arrival times(s)(referenced to shock arrival at P11), peak pressures and intermediate shock velocities. Discharge nozzle at 35 m. Obstacles present.

Axial position (m)	P11 (36 m)	P9 (40 m)	P7 (45 m)	P3 (55 m)
Shock arrival time (s)	0	0.0087	0.022	0.0482
Peak pressure (barg)	0.926	0.853	0.911	0.440
intermediate velocity (m/s)		459	376	382

Table 56: TEST 31, 12 L, 549 bar. Flame arrival time range at each station and maximum indicated flame temperature (°C). Time referenced to shock arrival at P11.Discharge nozzle at 35 m. No Obstacles present.

Axial position (m)	37.5	40	42.5	45	50	55	60	65
Arrival time range (s)	0.006	0.178-0.260	0.494-0.635	2.842-4.208	6.164-6.735	9.693	12.260-12.669	14.898-16.454
Max. flame T (°C)	991(T10)	667(T14)	110(T16)	224(T22)	300(T26)	173(T32)	194(T36)	167(T41)
Flame progress speed (m/s)		11.7	7.2	0.84	1.7	1.5	1.8	1.6

Table 57: TEST 31, 12 L, 549 bar. Shock arrival times(s)(referenced to shock arrival at P11), peak pressures and intermediate shock velocities. Discharge nozzle at 35m. No Obstacles present.

Axial position (m)	P11 (36 m)	P9 (40 m)	P7 (45 m)	P3 (55 m)
Shock arrival time (s)	0	0.0089	0.022	0.0481
Peak pressure (barg)	0.939	0.804	0.769	0.435
intermediate velocity (m/s)		449	381	383

*Table 58: **TEST 33**, 12 L, 503 bar. Flame arrival time range at each station and maximum indicated flame temperature (°C). Time referenced to shock arrival at P11.Discharge nozzle at 35 m. No Obstacles present.*

Axial position (m)	37.5	40	42.5	45	50	55	60	65
Arrival time range (s)	0.012	0.202-0.352	0.512-1.022	2.832-3.652	6.072-6.222	9.222-10.162	11.932-12.442	14.752
Max. flame T (°C)	731(T9)	429(T11)	277(T16)	233(T22)	281(T26)	171(T32)	177(T36)	163(T41)
Flame progress speed (m/s)		9.6	5.1	1.0	1.7	1.4	2.0	1.9	

*Table 59: **TEST 33**, 12 L, 503 bar. Shock arrival times(s)(referenced to shock arrival at P11), peak pressures and intermediate shock velocities. Discharge nozzle at 35m. No Obstacles present.*

Axial position (m)	P11 (36 m)	P9 (40 m)	P7 (45 m)	P3 (55 m)
Shock arrival time (s)	0	0.0087	0.022	0.048
Peak pressure (barg)	0.906	0.911	0.737	0.455
intermediate velocity (m/s)		460	391	377	

*Table 60: **TEST 37**, 12 L, 460 bar. Flame arrival time range at each station and maximum indicated flame temperature (°C). Time referenced to shock arrival at P11.Discharge nozzle at 35 m. Obstacles present.*

Axial position (m)	37.5	40	42.5	45	50	55	60	65
Arrival time range (s)	0.016	0.166-0.356	0.556-0.766	1.996-2.416	4.556-4.696		No Data	
Max. flame T (°C)	404(T9)	440(T12)	194(T16)	23(T22)	279(T26)			
Flame progress speed (m/s)		10.2	6.3	1.6	2.1				

*Table 61: **TEST 37**, 12 L, 460 bar. Shock arrival times(s)(referenced to shock arrival at P11), peak pressures and intermediate shock velocities. Discharge nozzle at 35 m. Obstacles present.*

Axial position (m)	P11 (36 m)	P9 (40 m)	P7 (45 m)	P3 (55 m)
Shock arrival time (s)	0	0.0088	0.022	0.049
Peak pressure (barg)	0.902	1.003	0.894	0.396
intermediate velocity (m/s)		454	376	369	

Table 62: TEST 32, 12 L, 602 bar. Flame arrival time range at each station and maximum indicated flame temperature (°C). Time referenced to shock arrival at P11.Discharge nozzle at 35 m. No Obstacles present.

Axial position (m)	37.5	40	42.5	45	50	55	60	65
Arrival time range (s)	0.020	0.190-0.300	0.310-0.340	1.970-2.410	4.970-5.340	7.750-8.480	9.920-10.250	12.020
Max. flame T (°C)	913(T9)	527(T12)	364(T16)	269(T22)	329(T26)	220(T33)	230(T36)	204(T41)
Flame progress speed (m/s)		11.4	29.4	1.3	1.7	1.7	2.5	2.6	

Table 63: TEST 32. 12 L, 602 bar. Shock arrival times(s)(referenced to shock arrival at P11), peak pressures and intermediate shock velocities. Discharge nozzle at 35 m. No Obstacles present.

Axial position (m)	P11 (36 m)	P9 (40 m)	P7 (45 m)	P3 (55 m)
Shock arrival time (s)	0	0.0088	0.022	0.048
Peak pressure (barg)	1.168	0.968	0.623	0.461
intermediate velocity (m/s)		454	382	386	

Table 64: TEST 38, 12 L, 605 bar. Flame arrival time range at each station and maximum indicated flame temperature (°C). Time referenced to shock arrival at P11.Discharge nozzle at 35 m. Obstacles present.

Axial position (m)	37.5	40	42.5	45	50	55	60	65
Arrival time range (s)	0.018	0.128-0.328	0.320-0.644	0.338-3.108	2.938	5.43	6.768-6.858	
Max. flame T (°C)	686(T9)	599(T11)	316(T16)	298(T22)	332(T26)	61(T33)	278(T36)	
Flame progress speed (m/s)		11.9	9.8	2.0	4.1	2.0	3.6	

Table 65: TEST 38, 12 L, 605 bar. Shock arrival times(s)(referenced to shock arrival at P11), peak pressures and intermediate shock velocities. Discharge nozzle at 35 m. Obstacles present.

Axial position (m)	P11 (36 m)	P9 (40 m)	P7 (45 m)	P3 (55 m)
Shock arrival time (s)	0	0.0086	0.021	0.048
Peak pressure (barg)	0.975	0.812	0.937	0.420
intermediate velocity (m/s)		465	394	383	

*Table 66.: **TEST 26**, 5 L, 634 bar. Flame arrival time range at each station and maximum indicated flame temperature (°C). Time referenced to shock arrival at P11.Discharge nozzle at 35 m. No Obstacles present.*

Axial position (m)	37.5	40	42.5	45	50	55	60	65
Arrival time range (s)	0.0221	0.199-0.3712	1.5189-2.3024	3.144-3.670	5.816-6.132	8.306-9.069	10.727-10.846	12.939-14.018
Max. flame T (°C)	578(T9)	269(T11)	341(T17)	201(T22)	220(T27)	217(T31)	176(T36)	162(T41)
Flame progress speed (m/s)		9.5	1.5	1.7	1.9	1.8	2.4	1.8	

*Table 67.: **TEST 26**, 5 L, 634 bar. Shock arrival times(s)(referenced to shock arrival at P11), peak pressures and intermediate shock velocities. Discharge nozzle at 35 m. No Obstacles present.*

Axial position (m)	P11 (36 m)	P9 (40 m)	P7 (45 m)	P3 (55 m)
Shock arrival time (s)	0	0.0089	0.0224	0.0502
Peak pressure (barg)	0.897	0.707	0.597	0.421
intermediate velocity (m/s)		449	370	359	

*Table 68.: **TEST 27**, 5 L, 634 bar. Flame arrival time range at each station and maximum indicated flame temperature (°C). Time referenced to shock arrival at P11.Discharge nozzle at 35 m. No Obstacles present.*

Axial position (m)	37.5	40	42.5	45	50	55	60	65
Arrival time range (s)	0.0448	0.201-0.4956	1.610-1.875	3.176-3.5632	5.696			
Max. flame T (°C)	643(T9)	436(T14)	264(T16)	231(T22)	207(T27)	No Data		
Flame progress speed (m/s)		8.1	1.8	1.5	1.3			

*Table 69.: **TEST 27**, 5 L, 634 bar. Shock arrival times(s)(referenced to shock arrival at P11), peak pressures and intermediate shock velocities. Discharge nozzle at 35 m. No Obstacles present.*

Axial position (m)	P11 (36 m)	P9 (40 m)	P7 (45 m)	P3 (55 m)
Shock arrival time (s)	0	0.0088	0.022	0.050
Peak pressure (barg)	0.858	0.689	0.561	0.411
intermediate velocity (m/s)		454	446	357	

*Table 70.: **TEST 28, 5 L, 625 bar**. Flame arrival time range at each station and maximum indicated flame temperature (°C). Time referenced to shock arrival at P11.Discharge nozzle at 35 m. No Obstacles present.*

Axial position (m)	37.5	40	42.5	45	50	55	60	65
Arrival time range (s)	0.0025-0.0535	0.999-1.793	3.086-3.472	4.564-4.800	No Data			
Max. flame T (°C)	989(T10)	267(T11)	228(T16)	119(T21)				
Flame progress speed (m/s)		1.8	1.3	1.8				

*Table 71.: **TEST 28, 5 L, 625 bar**. Shock arrival times(s)(referenced to shock arrival at P11), peak pressures and intermediate shock velocities. Discharge nozzle at 35 m. No Obstacles present.*

Axial position (m)	P11 (36 m)	P9 (40 m)	P7 (45 m)	P3 (55 m)
Shock arrival time (s)	0	0.0087	0.0219	0.0489
Peak pressure (barg)	0.845	0.619	0.671	0.343
intermediate velocity (m/s)		459	388	370

*Table 72.: **TEST 34, 18 L, 338 bar**. Flame arrival time range at each station and maximum indicated flame temperature (°C). Time referenced to shock arrival at P11.Discharge nozzle at 35 m. No Obstacles present.*

Axial position (m)	37.5	40	42.5	45	50	55	60	65
Arrival time range (s)	0.0094	0.0595-0.188	0.216-0.276	0.282-0.363	5.340-5.713	No Data		
Max. flame T (°C)	944(T8)	757(T12)	492(T18)	154(T25)	349(T26)			
Flame progress speed (m/s)		21.8	19.9	32.7	0.96			

*Table 73.: **TEST 34, 18 L, 338 bar**. Shock arrival times(s)(referenced to shock arrival at P11), peak pressures and intermediate shock velocities. Discharge nozzle at 35 m. No Obstacles present.*

Axial position (m)	P11 (36 m)	P9 (40 m)	P7 (45 m)	P3 (55 m)
Shock arrival time (s)	0	0.0086	0.021	0.0456
Peak pressure (barg)	1.365	1.21	1.004	0.565
intermediate velocity (m/s)		465	403	406

7.3.2   Overpressure during spurious operation of TPRD (ST4.4.2, HSE)

HSE has performed several hydrogen release experiments simulating the spurious release of hydrogen inside a tunnel at storage pressure up to 700 bar.

7.3.2.1   Background

Ignition tests have been carried out in the tunnel employing hydrogen reservoir volumes scaled to represent both Bus and Train scenarios. The reservoir volumes have been kept constant throughout these tests at 159 L but the pressures have been varied to represent the different scenarios. The experimental setup is precisely the same as that for the unignited releases described in 5.3.1.3. with the addition of an electrical spark igniter.

The geometry has already been indicated for the inclusion of vehicles and the additional relevant parameters are the location of the igniter, the discharge nozzle diameter and the timing of the ignition following the discharge valve opening. The igniter was located at 38 m from the tunnel entry, which was therefore 3 m downstream of the discharge nozzle, which was oriented vertically upwards and on the centreline of the tunnel.

The sequence of events can be described by the following :

1. discharge valve is opened
2. a variable delay is introduced before ignition
3. the igniter is activated and allowed to continuously spark
4. combustion begins with subsequent pressure development and gas expansion
5. flame propagates through the hydrogen/air mixture towards the tunnel exit
6. flame burns back to the discharge nozzle giving rise to a steady burning jet
7. the tunnel pressure peaks when the flame has progressed some distance down the tunnel
8. gas continues to flow from the tunnel exit, reducing the pressure to below ambient pressure
9. the negative pressure stops the exit flow and gas returns into the tunnel raising the pressure once again
10. the cycle of gas outflow and inflow continues in a diminishing cycle.

The peak pressure developed in the tunnel through flame propagation will depend on the amount of hydrogen discharged into the tunnel before ignition and also on the burning velocity arising from the turbulence generated in the tunnel by obstacles, in particular the vehicles introduced.

The concentration of hydrogen prior to ignition will be influenced by the delay introduced between valve opening and ignition and this has been used as a variable to investigate the sensitivity of the peak pressure to overall concentration levels.

The dispersion tests carried out and described in Section 5.3 are particularly useful in understanding the hydrogen concentration profile in the tunnel at the moment of ignition. The

dispersion tests most relevant to the ignition tests can be taken from Table 17 and denoted by test numbers 4 and 6, and relating to Bus and Train2 scenarios respectively. The time dependent concentration profiles shown in Figure 49 show the evolution of the profile over a 25 m distance and a 51 second interval following release. These profiles can be used to predict the differences in concentration environment which a propagating flame will experience depending on the moment of ignition relative to the moment of valve opening.

The ignition cases examined are summarised in Table 74. Except for cases 55 - 57, all cases include tunnel vehicles.

The volume of tunnel downstream of the discharge nozzle is 430 m^3 and Table 74 gives the masses discharged before ignition in each case. These range from 1.77 - 3.1 kg, which if fully mixed with the downstream tunnel air would result in concentrations in the range 4.5% - 8% by volume. However Figure 49 indicates full mixing in this suggested manner is never achieved and that there is a growth and decay of concentration at each tunnel location.

Table 74: Tunnel operating conditions for ignition tests.

Test case	Tunnel contents	Discharge nozzle diameter (mm)	Ignition delay (s)	Tank starting pressure (barg)	Tank pressure at ignition (barg)	Tank starting mass (kg)	Discharged mass (kg)
40	Vehicles present	4.0	20.15	316	77	3.50	2.32
43	Vehicles present	4.0	24.14	317	62	3.52	2.54
44	Vehicles present	4.7	4.46	583	531	5.67	1.80
45	Vehicles present	4.7	6.12	583	381	5.67	2.27
46	Vehicles present	4.7	8.13	580	284	5.64	2.73
55	No vehicles	4.7	4.32	591	553	5.72	1.77
56	No vehicles	4.7	5.02	584	425	5.67	1.95
57	No vehicles	4.7	10.0	584	222	5.67	3.10

The result is that maximum concentrations of over 20% are observed at certain times at each location. However, if ignition is initiated at times which are well shifted from the times of maximum concentration at each location, then the concentration field which the flame experiences may be very much lower resulting in weak combustion events.

7.3.2.2 *Ignition results discussion*

The results are presented in a similar way as for the sudden discharge tests in which hot gas arrival time ranges are tabulated for each of the 9 axial measurement stations. Also reported at each axial station is the first and last flame sensor to indicate flame arrival. Where possible, flame progress speeds are calculated between adjacent axial stations by using only the first flame arrival time at each station. This is often the sensor closest to the ceiling.

Also in this table the temperature is recorded on the most downstream flame sensor. This gives an indication of the intensity of the combustion event and also whether a flame was likely to have emerged from the tunnel exit.

A second table is presented for each case which details the pressure parameters at four measurement locations. This includes peak pressure, giving an indication of the magnitude of the generated pressure wave and the time location of the peak amplitude.

For ease of interpretation, both the flame arrival times and peak pressure times are referenced to the ignition timing for each case. The tabulated data is presented in Table 75 to Table 90.

Table 75. TEST 40. 159 L, 316 bar. Ignition at 38 m, discharge nozzle at 35 m. Flame arrival time range at each station. Time referenced to spark at 20.15 s. Vehicles present.

Axial position (m)	34	37.5	40	42.5	45	50	55	60	65
Arrival time range (s)	0.21-9.38	0.29	0.17-0.49	0.26-0.45	0.33-0.52	0.42-0.64	0.51-0.70	0.58-3.11	0.89
First/Last	T1/T4	T9	T11/T15	T17/T20	T21/T25	T26/T30	T33/T35	T36/T40	T43/T44
Flame progress speed (m/s)				27	35	55	55	71	16	
Flame peak exit temperature (°C)									223

Table 76: TEST 40. 159 L, 316 bar. Ignition at 38 m, discharge nozzle at 35 m. Pressure wave arrival times (s) and amplitudes. Time referenced to spark at 20.15 s. Vehicles present.

Axial position	P11 (36 m)	P9 (40 m)	P7 (45 m)	P3 (55 m)
Peak pressure (barg)	0.095	0.095	0.114	0.071
Peak pressure timing (s)	0.29	0.29	0.29	0.32

Table 77: TEST 43. 159 L, 317 bar. Ignition at 38 m, discharge nozzle at 35 m. Flame arrival time range at each station. Time referenced to spark at 24.135 s. Vehicles present.

Axial position (m)	34	37.5	40	42.5	45	50	55	60	65
Arrival time range (s)	0.146-0.223	0.136-0.211	0.108-0.182	0.172-0.203	0.201-0.225	0.250-0.298	0.287-0.345	0.311-0.497	0.332-0.355
First/Last	T1/T4	T9/T10	T11/T15	T16/T20	T21/T25	T26/T30	T33/T35	T36/T40	T43/T42
Flame progress speed (m/s)				39	86	102	135	208	238	
Flame peak exit temperature (°C)									438

Table 78: TEST 43. 159 L, 317 bar. Ignition at 38 m, discharge nozzle at 35 m. Pressure wave arrival times (s) and amplitudes. Time referenced to spark at 24.135 s. Vehicles present.

Axial position	P11 (36 m)	P9 (40 m)	P7 (45 m)	P3 (55 m)
Peak pressure (barg)	0.31	0.31	0.39	0.28
Peak pressure timing (s)	0.275	0.275	0.265	0.285

Table 79: **TEST 44.** *159 L, 583 bar. Ignition at 38 m, discharge nozzle at 35 m. Flame arrival time range at each station. Time referenced to spark at 4.462 s. Vehicles present.*

Axial position (m)	34	37.5	40	42.5	45	50	55	60	65
Arrival time range (s)	0.092-0.269	0.383	0.107-0.471	0.216-0.663	0.287-1.088	0.776-1.056	No Data		
First/Last	T1/T4	T9	T12/T15	T16/T20	T23/T25	T27/T26			
Flame progress speed (m/s)				22	35	10			
Flame peak exit temperature (°C)						162			

Table 80: **TEST 44.** *159 L, 583 bar. Ignition at 38 m, discharge nozzle at 35 m. Pressure wave arrival times (s) and amplitudes. Time referenced to spark at 4.462 s. Vehicles present.*

Axial position	P11 (36 m)	P9 (40 m)	P7 (45 m)	P3 (55 m)
Peak pressure (barg)	0.180	0.131	0.148	0.096
Peak pressure timing (s)	0.139	0.139	0.146	0.155

Table 81: **TEST 45.** *159 L, 583 bar. Ignition at 38m, discharge nozzle at 35m. Flame arrival time range at each station. Time referenced to spark at 6.12s. Vehicles present.*

Axial position (m)	34	37.5	40	42.5	45	50	55	60	65
Arrival time range (s)	0.062	0.077	0.047-0.147	0.103-0.153	0.134-0.233	0.184-0.197	0.230-0.437	0.251-0.417	No Data
First/Last	T1	T9	T11/T15	T16/T20	T21/T25	T29/T26	T33/T35	T36/T40	
Flame progress speed (m/s)				45	81	100	108	238	
Flame peak exit temperature (°C)								502	

Table 82: **TEST 45.** *159 L, 583 bar. Ignition at 38 m, discharge nozzle at 35 m. Pressure wave arrival times (s) and amplitudes. Time referenced to spark at 6.12 s. Vehicles present.*

Axial position	P11 (36 m)	P9 (40 m)	P7 (45 m)	P3 (55 m)
Peak pressure (barg)	0.30	0.297	0.363	0.257
Peak pressure timing (s)	0.136	0.136	0.143	0.150

*Table 83: **TEST 46.** 159 L, 580 bar. Ignition at 38 m, discharge nozzle at 35 m. Flame arrival time range at each station. Time referenced to spark at 8.125 s. Vehicles present.*

Axial position (m)	34	37.5	40	42.5	45	50	55	60	65
Arrival time range (s)	0.050-0.067	0.037	0.034-0.084	0.067-0.105	0.082-0.088	0.113-0.159	0.152	0.176-0.200	No Data
First/Last	T1/T4	T9	T11/T15	T17/T20	T22/T25	T26/T30	T33	T36/T39	
Flame progress speed (m/s)				76	166	161	128	208	
Flame peak exit temperature °C								535	

*Table 84: **TEST 46.** 159 L, 580 bar. Ignition at 38 m, discharge nozzle at 35 m. Pressure wave arrival times (s) and amplitudes. Time referenced to spark at 8.125 s. Vehicles present.*

Axial position	P11 (36 m)	P9 (40 m)	P7 (45 m)	P3 (55 m)
Peak pressure (barg)	0.695	0.695	0.798	0.641
Peak pressure timing (s)	0.103	0.103	0.106	0.118

*Table 85: **TEST 55.** 159 L, 591 bar. Ignition at 38 m, discharge nozzle at 35 m. Flame arrival time range at each station. Time referenced to spark at 4.32 s. No vehicles present.*

Axial position (m)	34	37.5	40	42.5	45	50	55	60	65
Arrival time range (s)	0.18-4.0.62	0.37	0.16-0.31	0.26-0.45	0.37-0.70	1.23-1.58	No Data		
First/Last	T1/T3	T9	T11/T14	T16/T20	T21/T25	T27/T30			
Flame progress speed (m/s)				23.8	5.8				
Flame peak exit temperature (°C)						232			

*Table 86: **TEST 55.** 159 L, 591 bar. Ignition at 38 m, discharge nozzle at 35 m. Time referenced to spark at 4.32 s. No vehicles present.*

Axial position	P11 (36 m)	P9 (40 m)	P7 (45 m)	P3 (55 m)
Peak pressure (barg)	0.074	0.083	0.090	0.075
Peak pressure timing (s)	0.21	0.21	0.22	0.24

Table 87: TEST 56. 159 L, 584 bar. Ignition at 38 m, discharge nozzle at 35 m. Flame arrival time range at each station. Time referenced to spark at 5.02 s. No vehicles present.

Axial position (m)	34	37.5	40	42.5	45	50	55	60	65
Arrival time range (s)	0.08-0.12	0.28-1.07	0.06-0.17	0.11-0.18	0.14-0.22	0.24-0.32	0.3-0.69	No Data	
First/Last	T1/T3	T9/T8	T11/T15	T17/T20	T21/T25	T27/T30	T33/35		
Flame progress speed (m/s)				62					
Flame peak exit temperature (°C)							140		

Table 88: TEST 56. 159 L, 584 bar. Ignition at 38m, discharge nozzle at 35 m. Time referenced to spark at 5.02 s. No vehicles present.

Axial position	P11 (36 m)	P9 (40 m)	P7 (45 m)	P3 (55 m)
Peak pressure (barg)	0.200	0.191	0.242	0.209
Peak pressure timing (s)	0.14	0.15	0.15	0.16

Table 89: TEST 57. 159 L, 584 bar. Ignition at 38 m, discharge nozzle at 35 m. Flame arrival time range at each station. Time referenced to spark at 10.00 s. No obstacles.

Axial position (m)	34	37.5	40	42.5	45	50	55	60	65
Arrival time range (s)	0.08-0.11	0.05-0.11	0.05-0.12	0.09-0.12	0.11-0.13	0.15-0.16	0.17-0.20	0.22	No Data
First/Last	T1/T4	T9/T8	T11/T15	T16/T20	T22/T25	T27/T30	T30/T35	T40	
Flame progress speed (m/s)				160					
Flame peak exit temperature (°C)							467		

Table 90: TEST 57. 159 L, 584 bar. Ignition at 38m, discharge nozzle at 35 m. Time referenced to spark at 10.0 0s. Discharge nozzle at 35 m. No vehicles present.

Axial position	P11 (36 m)	P9 (40 m)	P7 (45 m)	P3 (55 m)
Peak pressure (barg)	0.497	0.554	0.624	0.528
Peak pressure timing (s)	0.016	0.016	0.016	0.017

Table 75 to Table 78 show the results for the two tests numbers 40 and 43. These relate to the Bus conditions using a 4 mm discharge nozzle and tank pressures of 316/317 barg. The ignition delay time for Test 40 is 20.15 s and for 43 it is 24.14 s. Table 79 indicates that the masses discharged are 2.32 kg and 2.54 kg respectively. The behaviour for each test is significantly different with Test 40 yielding a peak pressure of 0.114 barg and flame progress speeds reaching only 71 m/s whereas Test 43 yields a pressure peak at 0.39 barg and flame progress speed of 238 m/s at the exit. The exit flame sensor for Test 40 shows a modest temperature of 223 °C, whereas for Test 43 this is 438 °C. Both cases show some signs of the flame speeding up towards the exit but this is more pronounced for Test 43. Understanding the difference in behaviour for these two cases may lie in the graph of Figure 49 and relate to the concentration/time profile in the presence of tunnel vehicles.

Comparing tests 44 (with vehicles) and 55 (without vehicles) is particularly interesting in revealing the consequence of an early ignition. Figure 49 shows that, for the Train1 scenario studied, the peak concentration observed occurred at 8.6 seconds. At this time the concentrations downstream were well below their subsequent peaks, and at 25 m the concentration was still zero. For tests 44 and 55, the ignitions were initiated at 4.46s and 4.32 s respectively. Referring to Figure 49 shows that only down to 7.5 m is there likely to be any significant hydrogen for combustion. Table 79 and Table 80 show the data for Test 44 and Table 85 and Table 86 for Test 55. In both cases no flame signature is observed below the 50 m distance and flame progress speeds are low and more consistent with hot exhaust flows rather than passage of a flame front. These cases are therefore consistent with the observations from the dispersion tests.

Of particular relevance to the discussion on combustion intensity is the relation of the developed pressure amplitude to the flame propagation behaviour.

The rise and fall of the first pressure peak carries this intensity information and it will be observed that in all cases the peak amplitude falls within a narrow time range for each case, e.g. for Test 40 the peak pressure ranges from 0.29 - 0.32 s. The sound speed for gas in the tunnel ranges from 350 - 700 m/s, meaning the pressure increments are transmitted over the 20 m from P11 to P3 in around 25 - 50 ms. This is short compared to the duration of the flame progress along the tunnel, which is more than 250 ms. This means that an examination of the pressure development on the upstream pressure sensor P11 in relation to flame progress will provide an insight into the relative intensity of the test cases and the role of tunnel vehicles in exacerbating the combustion.

The pairs of tests 56/45 and 57/46 provide a good indication of the magnitude of the effect of tunnel vehicles in influencing the combustion intensity.

Test 56, with no vehicles present has an ignition delay of 5.02 s and a discharged mass of 1.95 kg, whilst for Test 45 with vehicles, the mass discharged is 2.27 kg and the delay is 6.12 s. Both of these tests use an early ignition delay where it might be expected that the concentration profile is weak along the tunnel.

Figure 194 has an expanded view of the first pressure wave from Test 56, where the time axis has been referenced to the ignition spark at t=0. Superimposed on this curve is a series of flame arrival events at various locations along the tunnel based on the extracted data from Table 87.

This shows that the flame arrival events are contained within the envelop of the first pressure peak and also reveals the decay in pressure as the flame reaches the 50 m position. For Test 56 the tunnel pressure crosses the 0.0 barg point at 0.28 s after ignition and its peak amplitude is 0.242 barg. No flame indication is shown beyond the 55 m distance and the final indicated flame sensor records a weak 140 °C.

Comparing this behaviour with Test 45 containing vehicles, shown in Figure 195, reveals a very similar qualitative behaviour, with a 0.0 barg crossing at 0.27 seconds and a peak amplitude of 0.363 barg. The higher peak pressure means that positive pressure is still being recorded by the 60 m distance at the end of the vehicle group, and the final recorded peak temperature is 502 °C, indicating that a flame front is still active in this region. This result could be due to a combination of the slightly higher mass discharged, the slightly later ignition delay and the presence of vehicles in generating additional turbulence, but airflow velocity would need to be considered to make this assertion. An important difference in this regard with Test 56 is the flame progress speed at the end of the tunnel, which is 140 m/s for Test 56 but 238 m/s for the more intense Test 45. It should also be noted in this regard that the presence of vehicles restricts the available free volume in the tunnel and will lead to a natural acceleration in the exhaust flow.

A comparison in the same way has been made for tests 57 (no vehicles) and 46 (with vehicles). The delays for 46 and 57 are 8.125 s and 10 s and discharged masses are 2.73 kg and 3.1 kg, respectively. This places the ignition delay into the maximum concentration region for tunnel positions from the igniter down to 50 m according to Figure 49 and one would expect a more intense combustion event.

Figure 196 has an expanded view of the first pressure wave from Test 57, with the time axis again referenced to the ignition spark at t=0. The superimposed flame arrival events at various locations along the tunnel have been extracted from Table 89. As before this shows that the flame arrival events are contained within the envelop of the first pressure peak and also reveals the decay in pressure as the flame nears the exit. For Test 57 the tunnel pressure crosses the 0.0 barg point at 0.27 s after ignition and its peak amplitude is 0.45 barg.

Comparing this behaviour with Test 46 containing vehicles, shown in Figure 197, reveals a very similar qualitative behaviour but with a 0.0 barg crossing at 0.22 s and a peak amplitude of 0.695 barg.

It is noted that the exit flame sensor temperatures for Tests 57 and 46 are 465 °C and 535 °C respectively indicating that a combustion front has likely passed the 60 m measurement station.
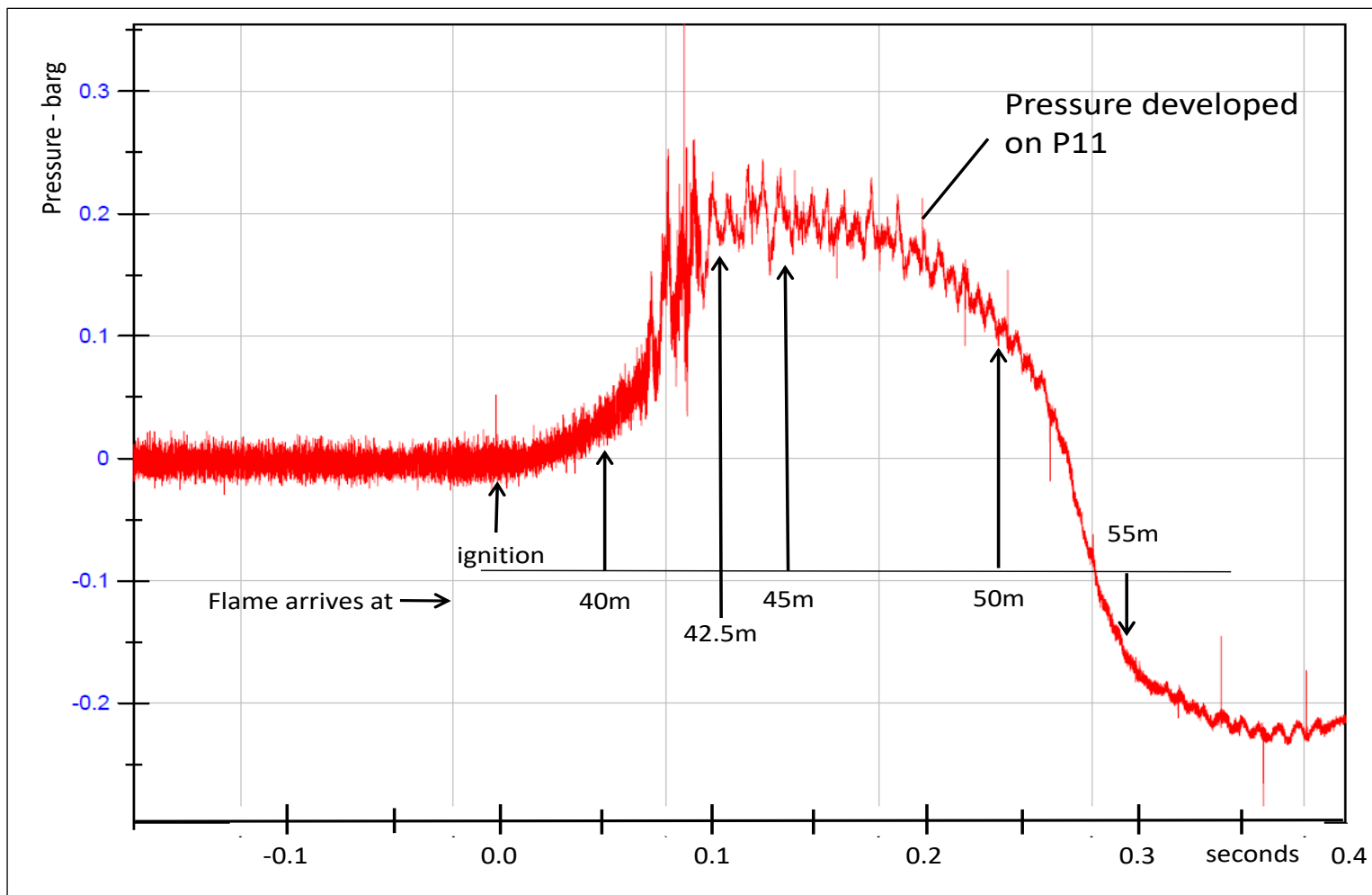
Figure 194: Observed initial pressure development on P11 for Test 56 - No vehicles present. Inset shows position of flame front at various times during pressure development phase. Timings have been referenced to ignition event.
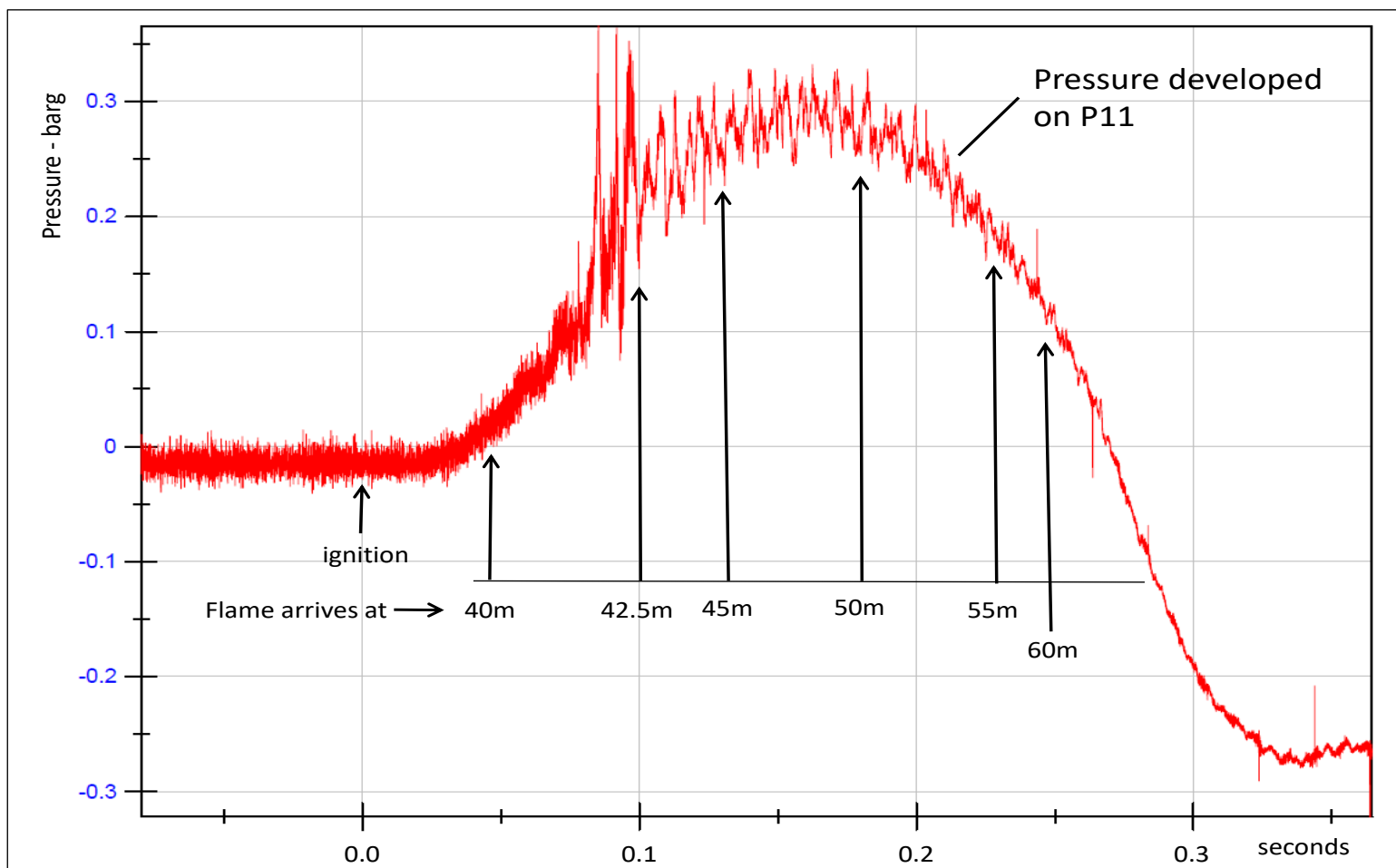
Figure 195: Observed initial pressure development on P11 for Test 45 - Vehicles present. Inset shows position of flame front at various times during pressure development phase. Timings have been referenced to ignition event.
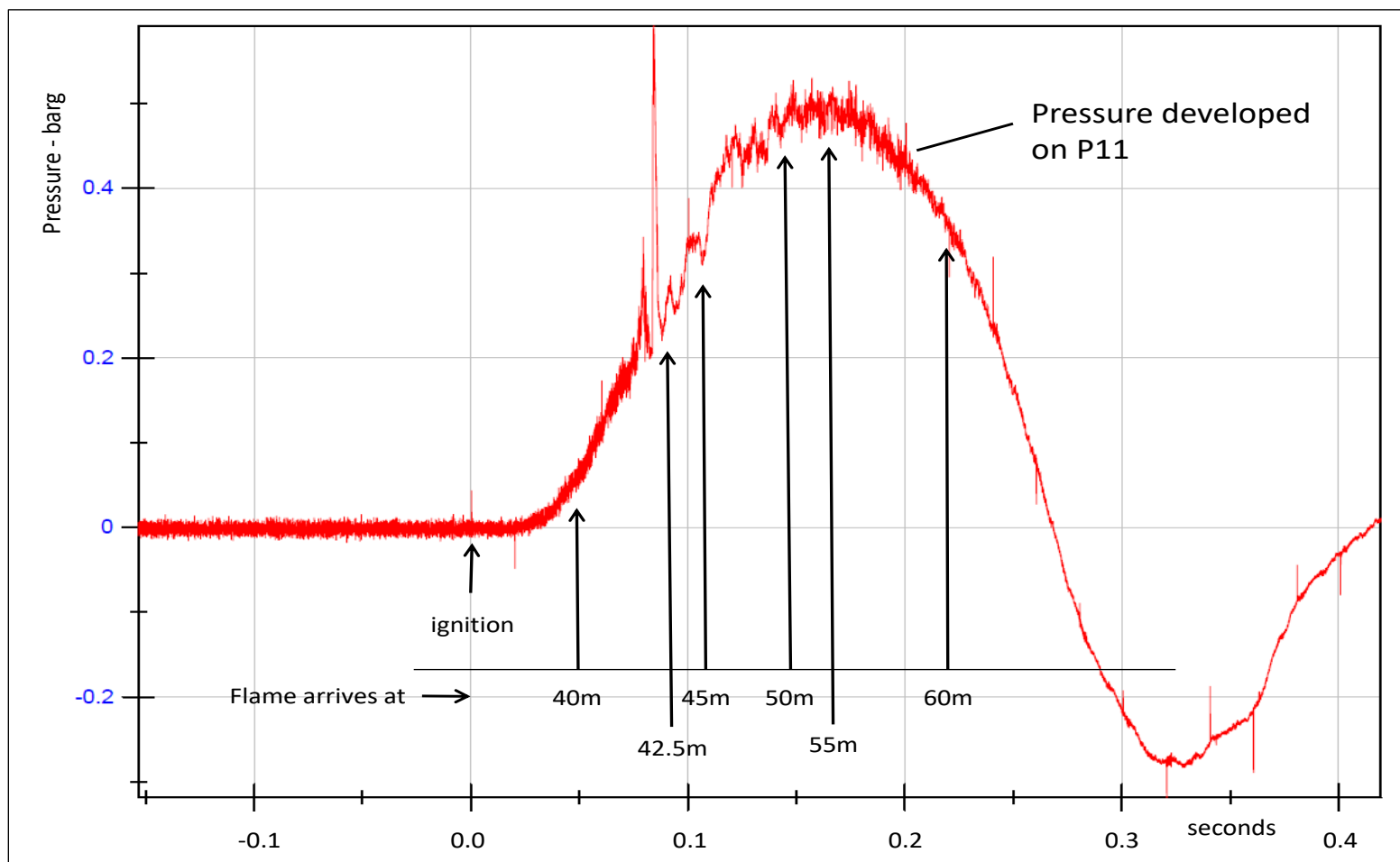
Figure 196: Observed initial pressure development on P11 for Test 57 - NO vehicles present. Inset shows position of flame front at various times during pressure development phase. Timings have been referenced to ignition event.
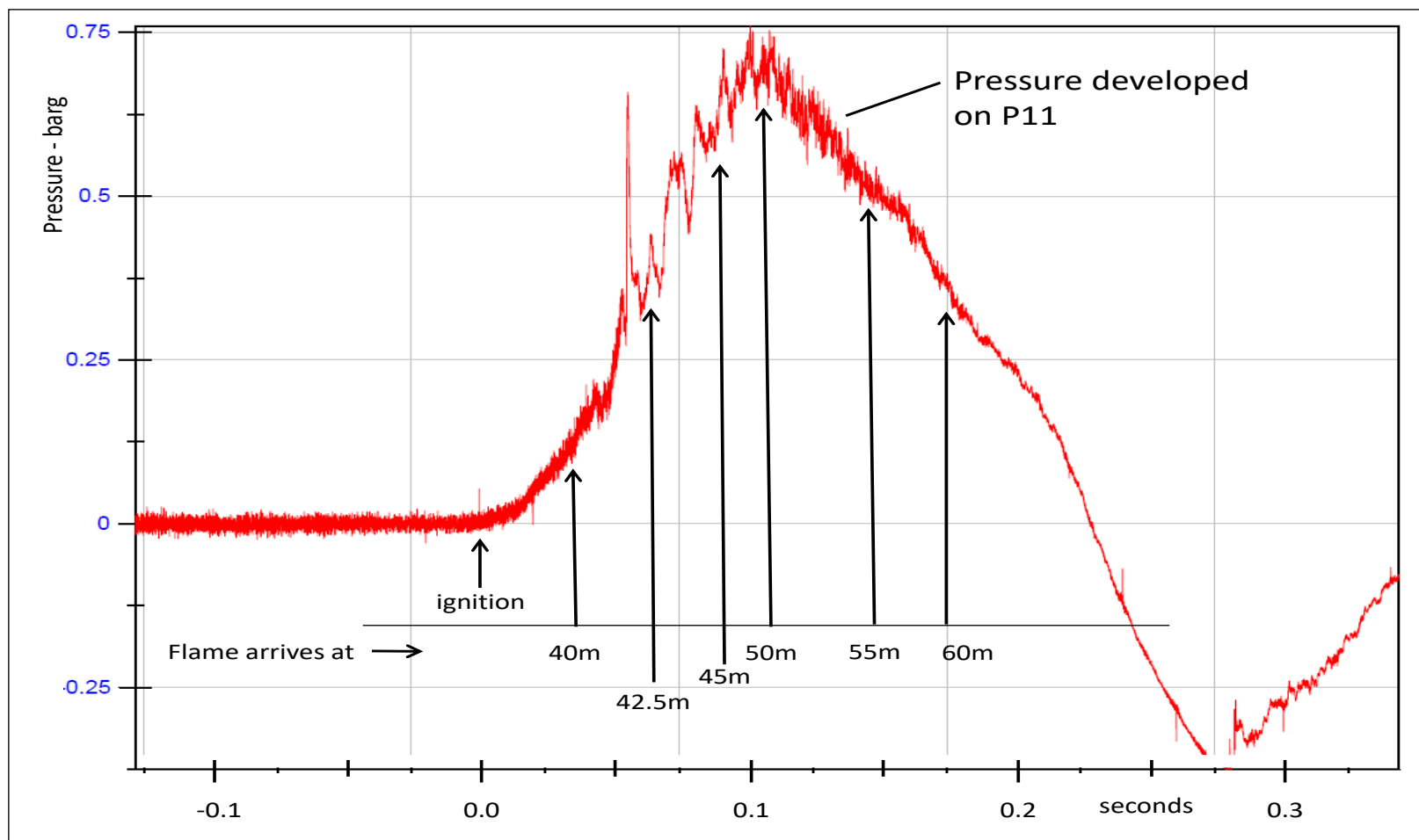
Figure 197: Observed initial pressure development on P11 for Test 46 - Vehicles present. Inset shows position of flame front at various times during pressure development phase. Timings have been referenced to ignition event.

7.3.2.3   Conclusions

Following an ignition, the pressure within the tunnel decayed at a relatively moderate rate. This would indicate that the hazard distances associated with such an event in a real world tunnel would be large.

The ignition behaviour has shown a subtle interplay between the total mass of hydrogen discharged before ignition and hence the ignition delay, the distribution of hydrogen along the tunnel at the moment of ignition and the likely role of vehicles in promoting combustion once ignited.

The generally aerodynamic nature of train geometries do not necessarily generate the level of turbulence which can be found within industrial structure and hence their effect on flame acceleration is not likely to be as great.

7.3.3   Deflagration of non-uniform cloud in a tunnel: Experiments on deflagration of non-uniform hydrogen-air cloud created by release in mock-up tunnel sections (ST4.4.3, PS)

7.3.3.1   Background

Accidentally released H_2 can accumulate below the ceiling of a tunnel or a garage or other roofs. Such scenarios can create semi-confined local pockets of reactive H_2/air-mixtures with concentration gradient. The combustion of such mixtures can lead to flame acceleration even detonation, thus, strong pressure loads causing structural damage.

7.3.3.2   Objectives

The aim of the experiment is to investigate the deflagration of hydrogen-air mixture in tunnel-like structure with a rectangular cross section. The combustion behaviour of stratified hydrogen-air mixture will be compared with the combustion behaviour of uniform hydrogen-air mixtures.

7.3.3.3   Knowledge gaps and accident scenarios assessed

There is a lack of experimental data for flame acceleration of H_2/air mixture with concentration gradient in semi-confined unobstructed tunnel-like geometries.

7.3.3.4   Description

The tests were performed inside the H110 (A1) vessel of HYKA, as shown in Figure 198. The safety vessel H110 has main dimensions of 3.3 m id and 12 m length with a volume of 100 m^3 and a design pressure of 100 bar. The vessel was used as a safety vessel. A rectangular sub-compartment of 9 x 3 x 0.6 m^3 was constructed in the vessel to study the combustion and detonation of stratified H_2/air mixture in a horizontal semi-confined chamber, as shown in Figure 198, right. The safety vessel is equipped with measuring ports and windows for visual observations. A special gas-filling system allows to creating a layer of hydrogen-air mixtures with a linear vertical concentration gradient from 0.1 to 1.1 vol.% H_2/cm. The measuring system for combustion detection consists of an array of fast thermocouples (flame arrival time) and fast pressure gauges (combustion pressure and shock wave). The data acquisition system is based on multi-channel (64) ADC with a sampling rate of 1 MHz.
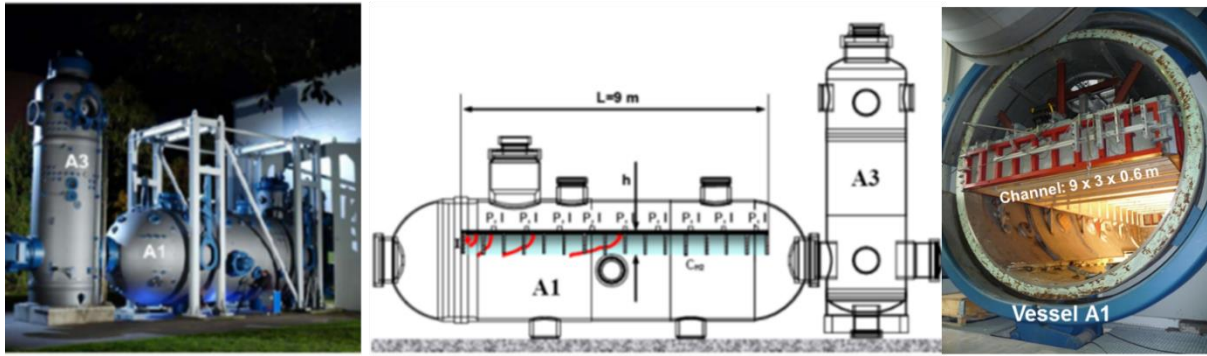
Figure 198: Test facility H110 (A1) of HYKA with large scale rectangular combustion channel 9 x 3 x 0.6 m³, open from below.

The mixture with concentration gradient was created as a thin layer under the ceiling by a special gas injection system. A detailed description of the procedure presented in (Grune et al., 2013). The non-uniform H_2-layer is quantified with a specific maximum H_2-concentration on the top (right below the ceiling) and a nearly linear concentration gradient of 0.3 - 0.6 vol.% H_2/cm.

Technically, the hydrogen concentration gradient in the layer is controlled by injection of different air diluted uniform hydrogen mixtures of 70 – 100 vol.% H_2 inside the channel via a grid with many release points directed under the ceiling (Figure 200 (B)). The maximum initial injection pressure is 1.2 to 2 bar from a fixed 4 m³ reservoir, which controls the maximal hydrogen concentration on the top of the layer. By this way, the total hydrogen inventory is controlled, accordingly.

Figure 199 presents the hydrogen layers with different concentration gradients and peak concentrations for various cases. The plots show average values from many measurement points. A higher hydrogen concentration of the injected gas leads to a stronger concentration gradient in the 0.6 m height channel. Therefore, the maximum possible concentration gradient in this setup is limited to ~0.6 c/cm (c = vol.% H_2). The minimum concentration gradient of the setup is limited to 0.28 c/cm due to safety reasons regarding the mixture reactivity inside the 4 m³ reservoir. All concentration gradients show nearly linear dependences from the maximum concentration down to the LFL of 4 vol.% H_2.
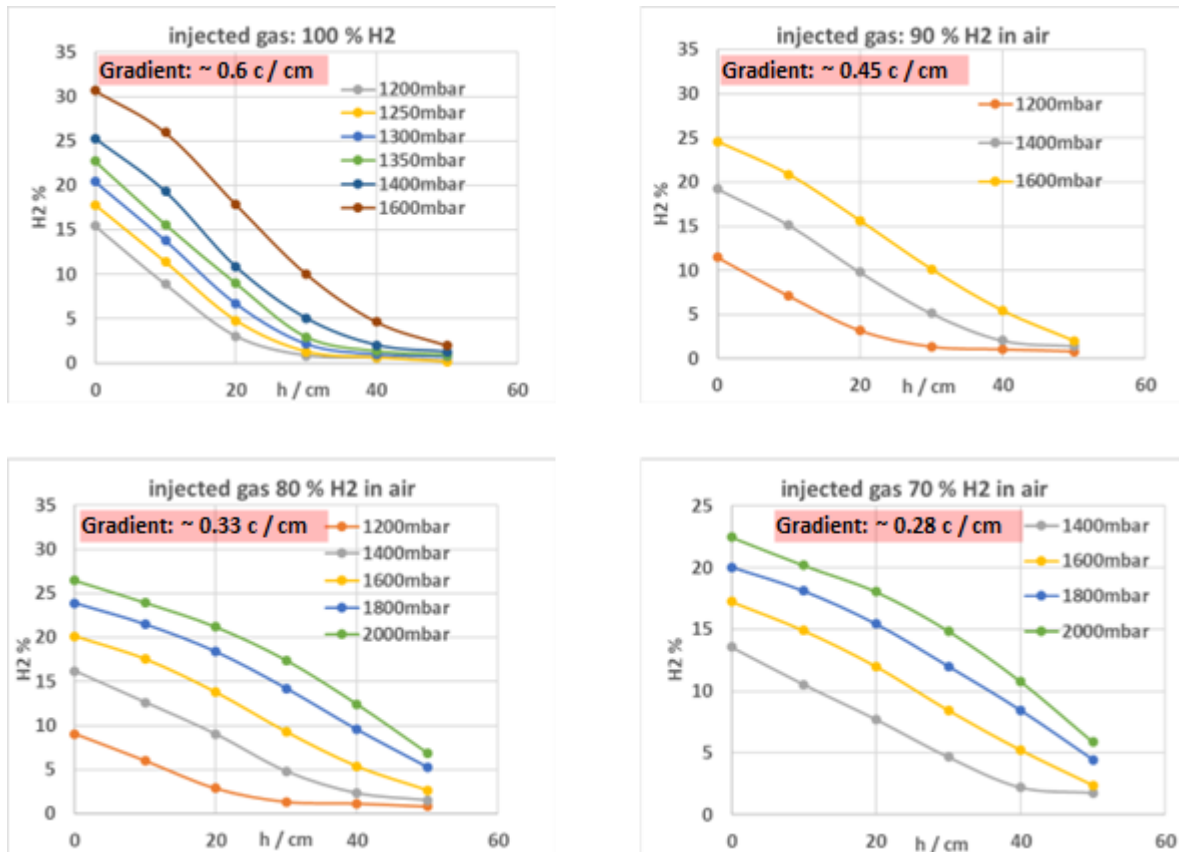
Figure 199: Various hydrogen layers are produced by injection of different air diluted hydrogen mixtures at different injection pressures.

In case of a uniform H_2 layer, a thin foil on the bottom side of the 0.6 m height channel separates the combustion channel filled with uniform hydrogen-air mixture. The separating film is cut just shortly before ignition. In the configurations with H_2 gradients no separation film was used. Figure 200 shows a view inside the combustion channel from the ignition side. The hot wire ignition was realized in a special perforated tube, acting as a line igniter in all configurations. In all configurations, only a thin plastic film at the channel end (right side) acts as the open end "wall" (A).
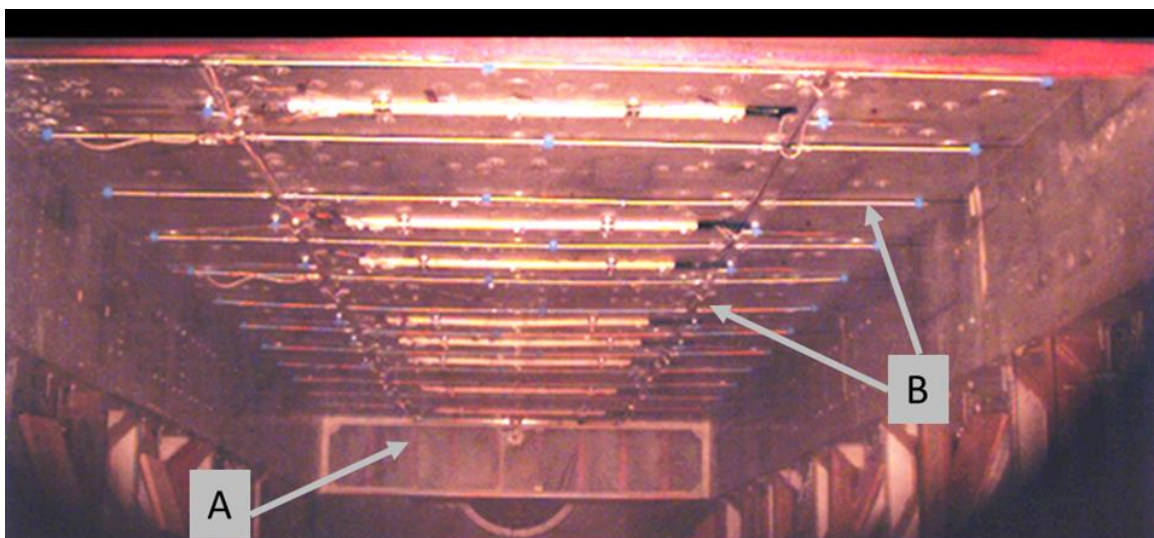
Figure 200: View inside the combustion channel from the ignition side. Gradient configuration; without separating film.

To measure the flame propagation in 2D geometry, the rectangular combustion channel is equipped with fast pressure gauges (PCBs) for combustion overpressure measurement and an array of ion probes and fast thermocouples for detection of the flame speed, respectively. Figure 201 shows the positions of the sensors in a top view of the channel. The signals from the ion probes are not included in this work, since they work for fast flame measurements. The sketched line igniter is visible on the left side of the channel.
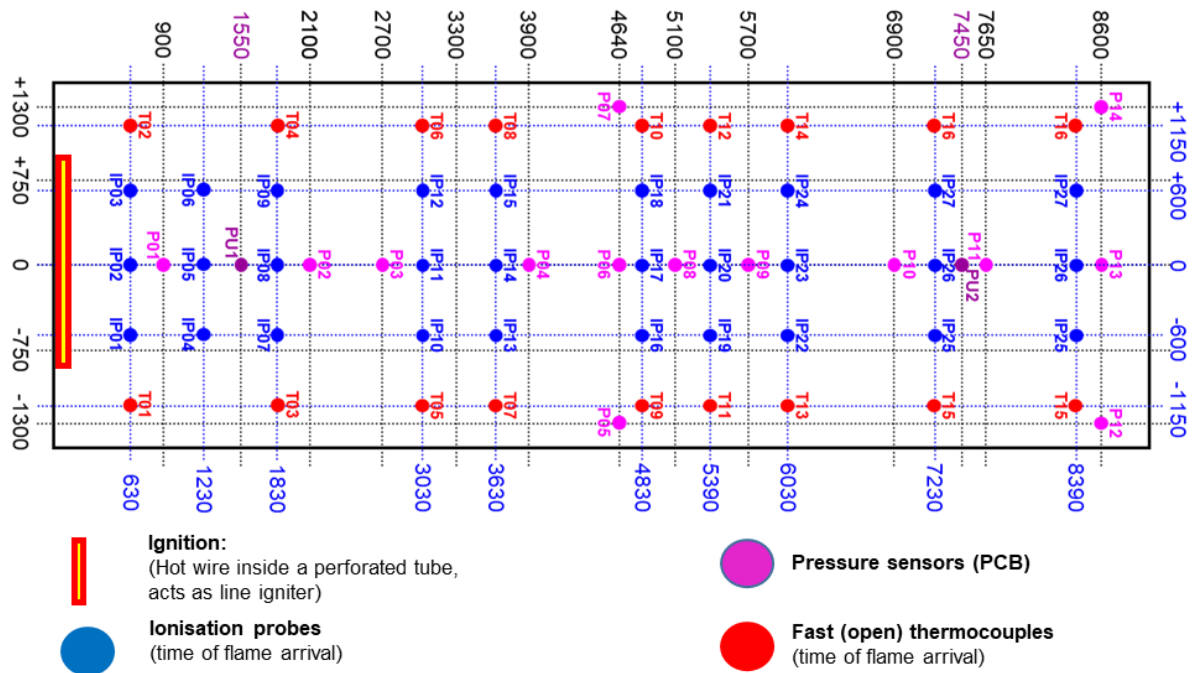
Figure 201: Positions of the sensors and igniters in a top view of the channel.

The designed test cases are summarized in Table 91, as the test matrix. The table lists the nominal H_2-concentration gradient, the maximum H_2-concentration under the ceiling and the calculated volume of burnable H_2-inventory in the combustion channel. In cases of uniform mixtures, the nominal H_2-concentration gradient is zero.

Table 91: Test matrix of non-uniform and uniform hydrogen-air cloud in a tunnel.

Test Case	Injected H_2 in Air, vol.%	Nominal H_2 Concentration Gradient, vol.% /cm	H_2 Conc. on the Ceiling, vol.%	H_2-Inventory/ m³
HyT240	100	0.6	25.30	1,366
HyT241	100	0.6	22.74	1,077
HyT242	100	0.6	20.43	0,882
HyT243	100	0.6	17.79	0,720
HyT244	100	0.6	15.45	0,584

HyT245	100	0.6	30.67	2,070
HyT246	70	0.28	24.45	2,740
HyT247	70	0.28	22.47	2,246
HyT248	70	0.28	20.04	1,987
HyT249	70	0.28	17.26	1,474
HyT250	70	0.28	13.55	0,691
HyT251	90	0.45	24.59	1,587
HyT252	90	0.45	19.22	1,147
HyT253	90	0.45	11.49	0,291
HyT254	80	0.33	26.47	2,970
HyT255	80	0.33	23.89	2,386
HyT256	80	0.33	20.14	1,474
HyT257	80	0.33	16.19	1,004
HyT258	80	0.33	9.04	0,283
1	Uniform mixture	0	10	1,62
2	Uniform mixture	0	15	2,428
3	Uniform mixture	0	15	2,428
4	Uniform mixture	0	20	3,24
5	Uniform mixture	0	25	4,05
6	Uniform mixture	0	30	4,86

7.3.3.5   Results

Flame speed and combustion overpressure

Due to the large scale and the limited optical access, a quantitative optical flame front observation is not possible due to the separating film in case of uniform mixture configuration. Nevertheless, in the gradient configuration optical flame observation demonstrates the combustion process in the 2D plane. As shown in Figure 202, the picture series taken from high-speed movie (500 f/s) present as an example the flame propagation from the ignition end up to the open-end (plastic film) wall. The first picture is a low-light snapshot of the view in the channel. The horizontal lines of the main luminescence in the following pictures indicate the evolution process of the nearly planar 2-D combustion in the main part of the channel.
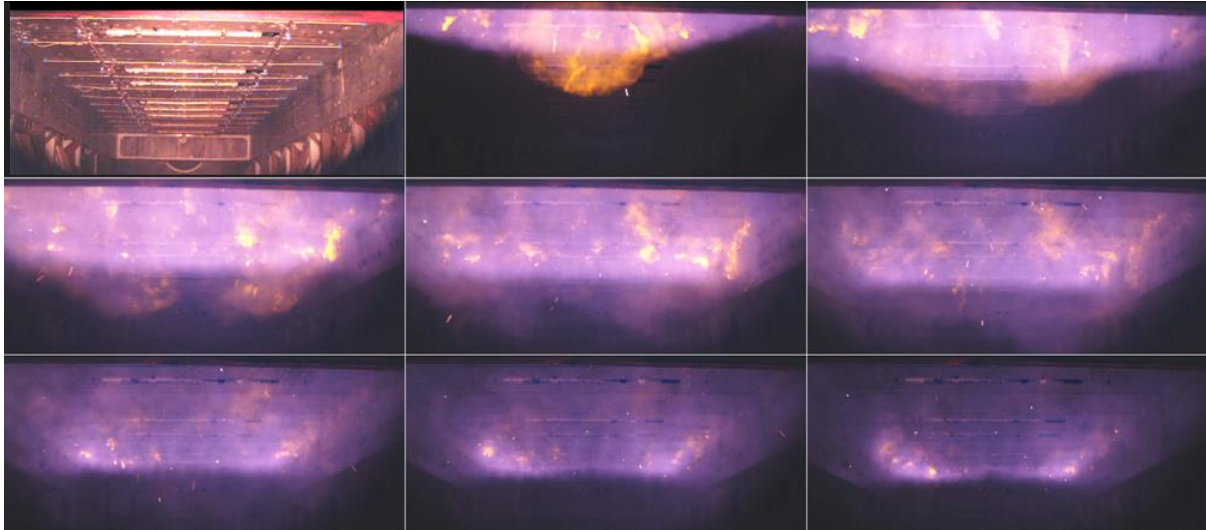
Figure 202: Flame propagation from the ignition end up to the open-end (plastic film) wall 1.2.5.1 (Gradient configuration (HYT242); time interval 0.03 s).

Flame speed and combustion overpressure were measured via point sensors. The flame speed was calculated as average, based on the arrival times of the flame front at the fast thermocouples positioned along the flame propagation passage. An example of arrival times of the flames in test cases HyT242 and HyT256 is shown in Figure 203 top. The corresponding calculated flame speeds are plotted (Figure 203 centre). The values of the data are separated for the two columns, corresponding to the left and right line of fast thermocouples as shown in Figure 201. According to Figure 203, the both flame speed are subsonic, about 40 m/s and the agreement of both measurement lines is good.

The combustion overpressures were recorded by fast dynamic PCB gauges. Figure 203 below, shows the maximum measured overpressure along the channel for the test case HyT242 and HyT256. The figure manifests that the top overpressure in Case HyT242 is about 0.13 bar, and Case HyT256 0.28 bar, respectively. With increasing flame propagation-distance, the measured overpressure increases. In contrast to this, the flame speed decreases with increasing flame propagation-distance. This behaviour is typical for a slow deflagration combustion regime in the semi-confined channel. Due to the solid wall on the ignition side the flame front was pushed a little by this additional enclosure. Nevertheless, after a flame running distance of 4 to 5 m the flame propagation is undisturbed and the flame velocity becomes constant. To compare the flame speed and combustion overpressure from non-uniform and uniform hydrogen-air mixtures, the average flame velocity and overpressures were measured in a distance greater than 4 m from the ignition location.
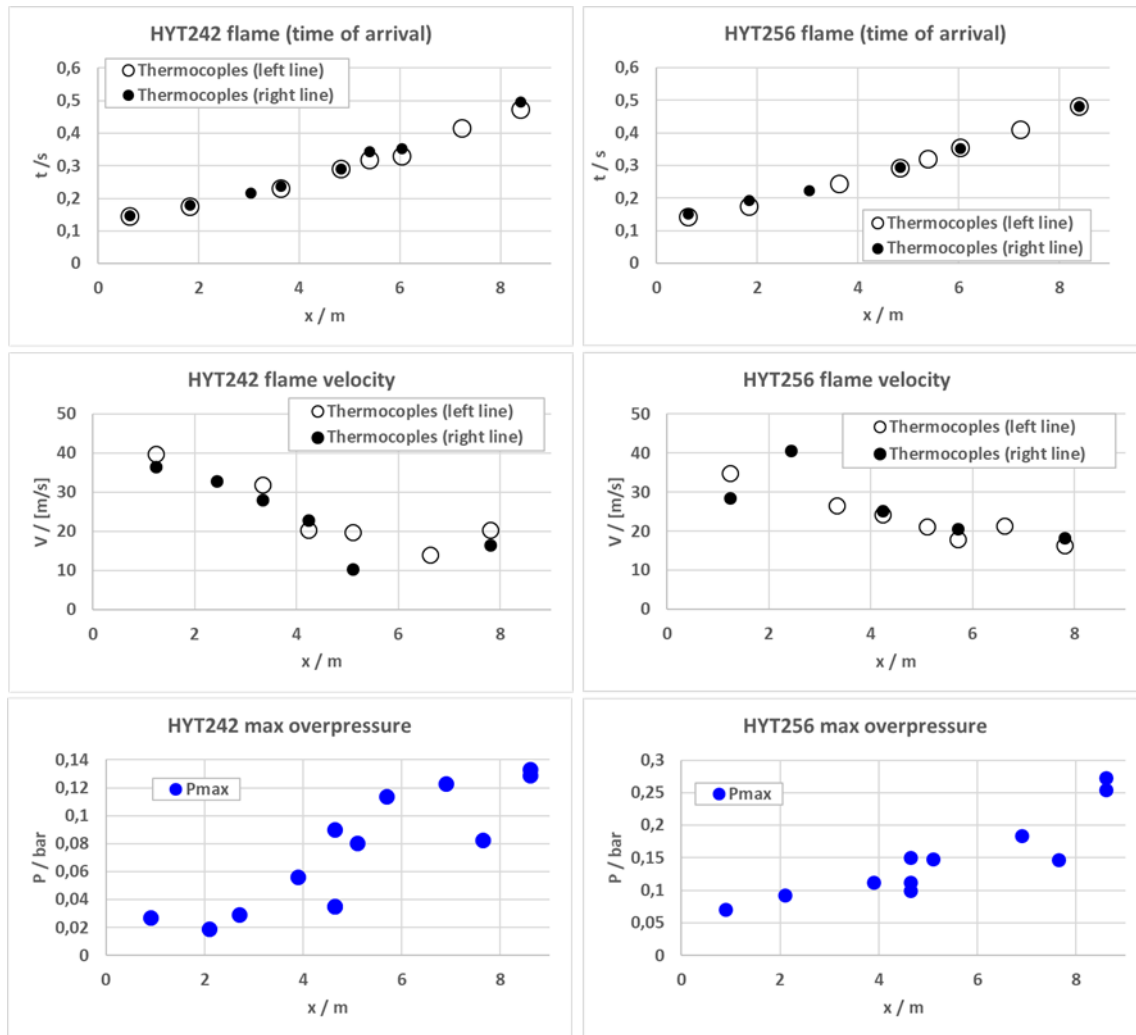
Figure 203: Example of measured arrival times (top), calculated flame speed (center) and measured maximum overpressure (below) for test cases HyT242 (0.6 vol.% H_2/cm and max. H_2 concentration of 20 vol.% H_2) and test case HyT256 (0.33 vol.% H_2/cm and max. H_2 concentration of 20 vol.% H_2).

7.3.3.6 *Comparison of flame speed and combustion overpressure in non-uniform und uniform hydrogen-air mixtures*

The average flame velocities and overpressures measured in a distance > 4 m are compared between non-uniform and uniform hydrogen-air mixtures. For safety analysis the main parameters are the burnable inventory and the reactivity of the mixture given as H_2-concentration (Table 91).

Figure 204 shows average flame speeds (left) and combustion overpressures (right) of uniform and non-uniform mixtures with different hydrogen concentration gradients (slopes), scaled with the burnable hydrogen inventory under the ceiling. With increasing burnable H_2-inventory the overpressures increase, this behaviour looks completely independent of the H_2-concentration distribution of the mixture. All the pressure curves collapse in a good agreement (Figure 204 Right). However, the curves of flame speeds (Figure 204 Left) behave differently. The concentration gradient influences the flame speed significantly. For example, if the burnable inventory is given as 2 m³, the highest flame speed occurs in the case with the highest concentration gradient (0.6 c/cm); the lowest speed occurs in the uniform mixture. In other

view, e.g., if the flame speed is given as 40 m/s, an inventory of as much as ~5 m³ is necessary in the case of uniform mixture to generate the flame speed; meanwhile, an inventory of less than 2 m³ is sufficient in all stratified mixtures to produce the same flame speed. It manifests that the dominant factor influencing flame speed is the H_2 concentration gradient, instead of the H_2-inventory.
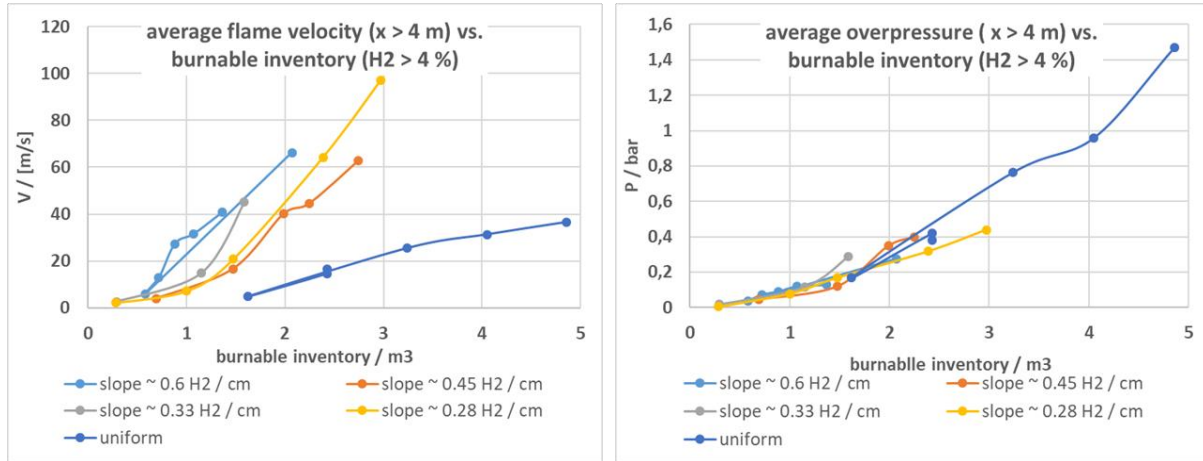
Figure 204: Flame speed (left) and combustion overpressure (right) comparisons between uniform and non-uniform mixtures with different hydrogen concentration gradients (slopes), scaled with the burnable hydrogen inventory under the ceiling.

The data of flame velocity and combustion overpressure are analysed as functions the maximum H_2-concentration of the mixture as shown in Figure 205 with the flame speeds (left) and combustion overpressures (right), respectively.
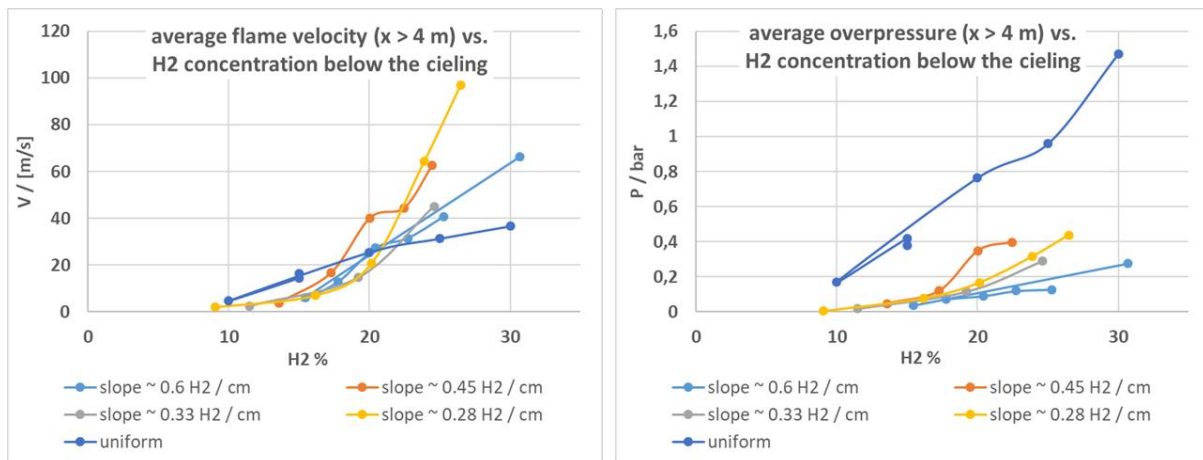
Figure 205: Flame speed (left) and combustion overpressure (right) comparisons between uniform and non-uniform mixtures with different hydrogen concentration gradients (slopes), scaled with the maximum hydrogen concentration under the ceiling.

Figure 205 (left) shows that the flame speed increases as hydrogen concentration increases in both uniform and non-uniform mixtures. On the other hand, the flame speed curves of uniform and non-uniform mixtures cross over each other in the vicinity of the point of 20 vol.% H_2. It is noticeable that, the flame velocity of the uniform mixture is higher than those of all the investigated gradient mixtures when the maximum H_2-concentration is less than ~20 vol.%. However, the flame speeds of non-uniform mixtures are higher than that of uniform mixture when the maximum H_2-concentration is greater than ~21 vol.%. Therefore, the flame speed is

influenced by both the hydrogen concentration and inhomogeneity of the mixture. Figure 205 (right) presents the rising overpressure of combustion as long as the hydrogen concentration increases. It is in the same logic that a larger hydrogen inventory produces a higher overpressure, as drawn on Figure 204 right.

The main conclusion of this work is that a mixture with concentration gradient is more reactive than a uniform mixture with the same H_2-inventory. Only slow deflagrations were observed in the work. The reason is due to the unobstructed character of the combustion channel. The fact is that the design of some obstacles in the channel can lead to a catastrophic detonation with unacceptably high flame speed and overpressure, see next section.

7.3.3.7 Influence of obstacles on stratified mixture combustion

The combustion behaviour of layered H_2/air mixtures (uniform and concentration gradients) in semi-confined geometry was studied extensively in the past, referring to the selected references. The combustion process in this work is very sensitive to the presence of obstacles inside the flame channel. Flames can easily accelerate and result in fast deflagration or even detonation with its corresponding high pressure loads.

Figure 206 shows as an example of the influence of obstacles on the combustion regime. The plot shows flame velocities (left) and overpressures (right) along the channel in case of HyT256 with H_2 concentration gradient of 0.33 vol. % H_2/cm and max. H_2 concentration of 20 vol. % H_2 without obstacles (this work) in comparison with an experiment with the same mixture conditions with an obstacle set-up. Inside the smooth channel geometry (HYT 256) the flame does not accelerate (slow deflagration) and the pressure loads are moderate (details in Figure 203). The flames of the same mixture, in the configuration with obstacles, accelerate rapidly and reach a supersonic velocity of ~700 m/s, above the sound speed of the mixture. Such fast deflagration shows a top overpressure of 6 bar. It can be assumed that the event of DDT may occur.
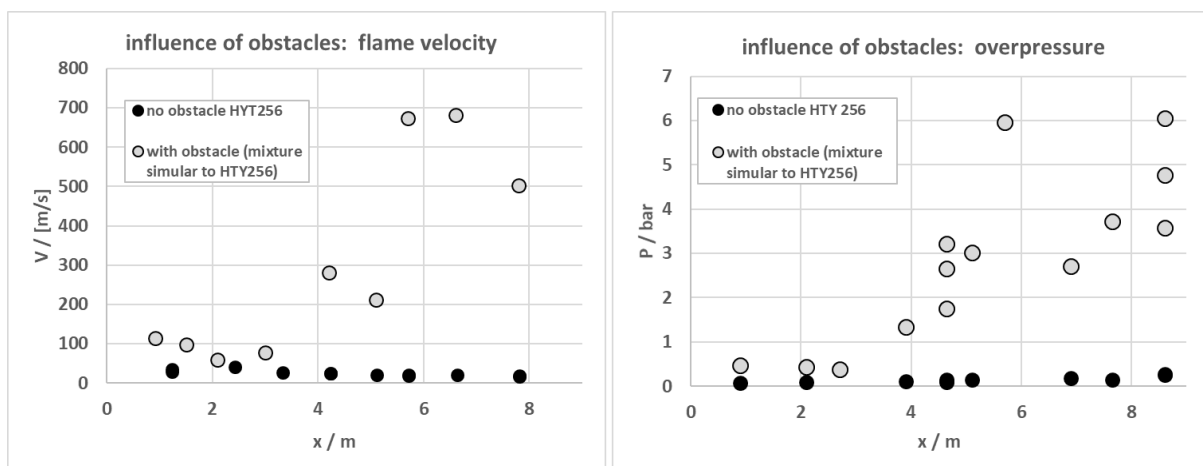
Figure 206: Influence of obstacles on flame velocity (left) and overpressure (right) in case of HyT256 with H_2 concentration gradient of 0.33 vol.%H_2/cm and max. H_2 concentration of 20 vol. %H_2.

7.3.4 Tests on flame propagation through a layer of fire extinguishing foam filled with flammable hydrogen-air mixtures (ST4.4.4, PS)

7.3.4.1 Background

An important element of modern firefighting is sometimes the use of foam. After a usage of extinguishing foam on vehicles or machinery operated by compressed gases, it is conceivable that masses of foam can be enriched by escaping fuel gas. Furthermore, generation of new foam filled with a high level of fuel gas, from the deposed foam solution becomes theoretically possible.

7.3.4.2 Objectives

The aim of the experiment is to testify the interaction of fire extinguishing foam with H_2, to clarify if the foam can be enriched with H_2 and become burnable, and what is the behaviour of flame propagation in the foam.

7.3.4.3 Knowledge gaps and accident scenarios assessed

Very little data of combustible aquatic foams are published. No experiences or data regarding "combustible" fire-extinguishing foam are available.

7.3.4.4 Description

The use of foam in firefighting technology is on a very high professional level. Many different foam agents and foam generator for different applications are available on the market. Foam itself is not a uniform medium. Foam is commonly defined as a dispersion of gas bubbles in a liquid. In general, it contains water, gas, foaming agent and mechanical energy necessary to create aquatic foam. In this work deionized water and a defined H2/air mixture flow, provided by mass-flow-controller, were used. Two different foaming agents were investigated. A professional firefighter extinguisher foam concentrate (STHAMEX®-class A Classic 1% F-15) especially designed for extinguishing solid material (class A) fires was used with compressed air-foam technology (CAFS). The STHAMEX® class A agent (Figure 207, right) can also be used for non-polar class B fuels (e.g. diesel or petrol) as low- and medium-expansion foam and is suitable to extinguish car fires. The extinguishing foam STHAMEX® class A is described as fluorine-free, physiologically harmless, and fully, very easily biodegradable, but, on the other hand, a special wastewater treatment is required on the test side using firefighter extinguisher foams. To reduce the waste production to a minimum, a second, completely harmless, commercial standard family bubble bath concentrate was used in this work (Figure 207, left).

Figure 207: Investigated foaming agents. Left, commercial standard family bubble bath concentrate. Right, professional firefighter extinguisher foam concentrate (STHAMEX®-class A Classic 1% F-15).

The used foam generators were directly integrated inside the combustion facility. The sketches in Figure 208 show the different combustion ducts and their periphery. The horizontal pool geometry (Figure 208, left) consists of a steel pool (0.30 m x 1 m x 2 m) with an adapted foam generator on the bottom side. The reservoir of the foam generator can hold up to 15 dm^3 water foam concentrate mixture (foam solution). Several small porous stones are mounted on the bottom of the foam generator, see Figure 209 (d). A constant, premixed H_2/air mass flow (100 STP dm^3/min) passes through the porous stones into the solution and creates foam above the liquid level. The pre-foams are squished through the sintered plate for more uniformity, Figure 209 (e).
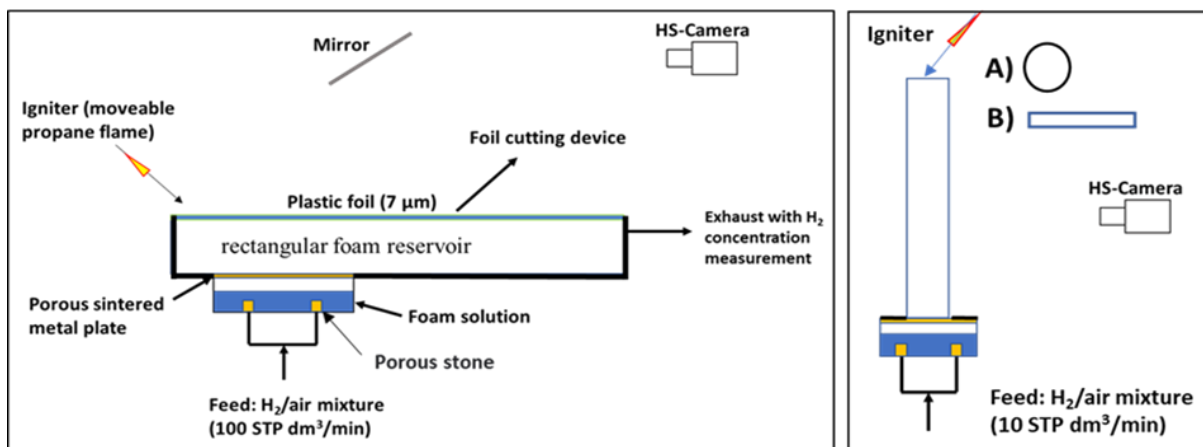
Figure 208: Scheme of the ducts. (a) Lange scale pool; (b) Small scale tubes: (circular A; rectangular B).

In order to fill the pool completely with foam it is necessary to direct the foam flow horizontally. For this reason, a thin foil (7 µm) covers the pool. The foam filling procedure with 100 STP dm^3/min gas-flow takes 5 minutes. During this time the H_2-concentration in the squished out atmosphere is measured continuously. The very low measured H_2-concentration is remarkably below 1 % in all cases. Figure 209 (a) shows the foam filled pool covered with the thin plastic foil. Short before the ignition the foil was removed via a foil cutting device, Figure 209 (b). The ignition source is a 2 cm long laminar propane diffusion flame, which is immersed in the foam mass at the front end. The snapshot Figure 209 (c) shows the ignited foam, which is fully open at the top. To observe and measure the combustion behaviour, the foam surface of the pool was recorded via a mirror above the pool with a high-speed camera.

Figure 209 (f) shows a picture from a high-speed movie (2000 f/s) of the foam surface short before the ignition. Most experiments were performed in an unobstructed pool. To investigate the influence of obstacles in the flame path, the pool can be equipped with 50 % blockage ratio, see Figure 209 (e). The principle of the foam formation is exactly the same as in the pool facility. The foam generator is smaller. The reservoir can hold up to 5 dm^3 foam solution and the feed gas flow of the pre-mixed H_2/air flow is fixed at 10 STP dm^3/min. Two different transparent combustion channels made from Plexiglas can be adapted above the sintered plate of the foam generator. Small channel experiments were also performed in a rectangular thin layer open-end channel with dimensions of 0.02 m x 0.2 m x 2 m, and in a circular tube with an inner diameter of 0.09 m and a length of 1.5 m. The tests in small channels are not part of the HyTunnel-CS project, therefore the description is spare. However, the unpublished data supports the understanding of the results from the larger horizontal channel and will be provided.
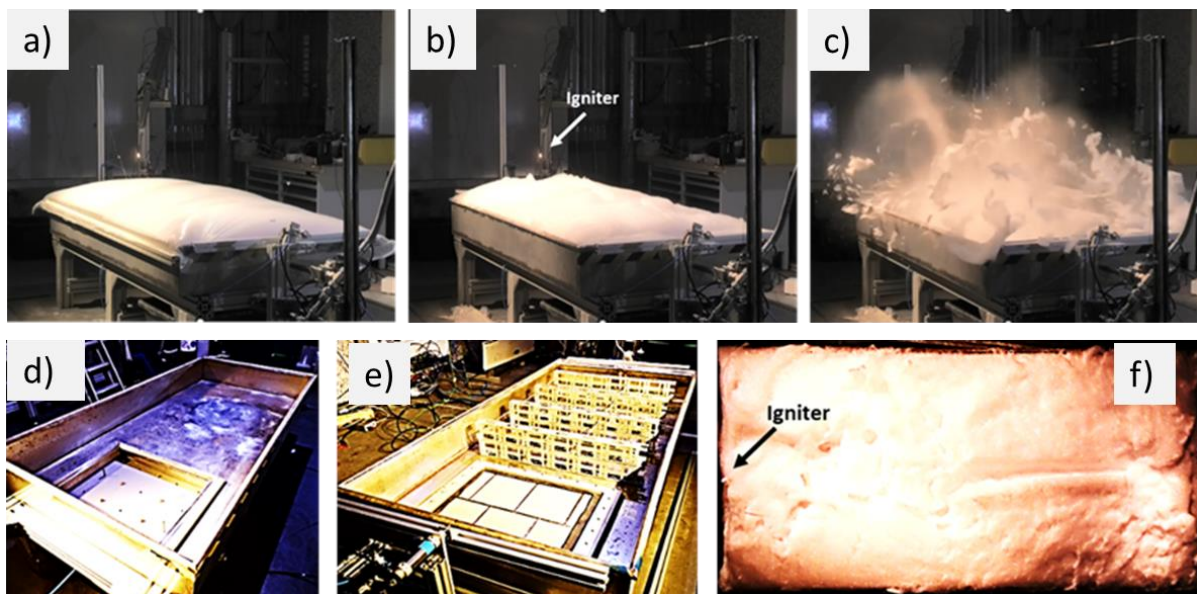
Figure 209: Large-scale pool. (a) Pool filled with foam and covered with foil; (b) Pool filled with foam and removed foil; (c) Snapshot after ignition. (d) Empty pool with open foam generator. (e) Empty pool with sinter plate covered foam generator and obstacle lines. (f) Snapshot from high speed video (2000 f/s).

Several properties are important to the characterization of foam e.g. bubble size distribution, foam stability, and foam density. The used foaming agents were speciality professional products. It was found that the method of foam generation could influence the foam properties significantly. Fortunately, due to the fixed method of foam formation, the variation of the foam properties is limited. All measurements of the foam properties were directly performed in the combustion facilities. Foam itself is not a uniform medium; additionally a rapid start of foam aging takes place. Due to the drainage of liquid with time, the foam density decreases with time. Visually the best foam uniformity was observed for a gas-flow rate of 10 dm^3/min in the small-scale facility and 100 dm^3/min in the larger pool facility.
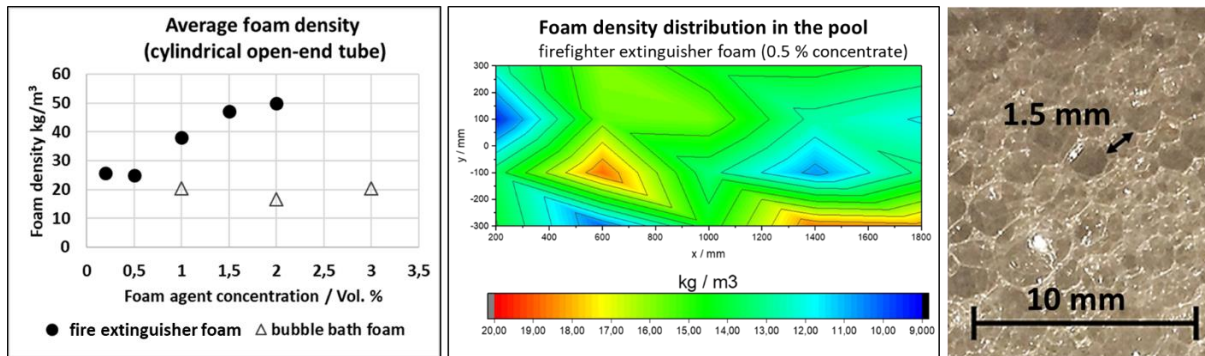
Figure 210: Left, average foam density vs. foam agent concentration. Centre, example of foam density distribution in large-scale pool. Right, extinguisher foam (0.5 % concentrate).

The foam densities were measured at the time of ignition gravimetrically by probes. According to Figure 210 left, the measured foam density of ~ 20 kg/m³ for the bubble bath foam is independent of the foam agent concentration. In contrast, the fire extinguisher foam density increases with increasing foam agent concentration. Figure 210 centre shows the foam density distribution in the large-scale pool for the extinguisher foam with 0.5 % concentrate. The measured density distribution is quite uniform and in average 15 kg/m³. Due to the long filling duration of 5 min for the pool, the drainage effect in the pool is stronger as in the small tubes, where the average foam density for extinguisher foam with 0.5 % concentrate is 25 kg/m³. In summary all experiments were performed with medium expansion foam (foam expansion ratio is between 20 to 200). The foam generator produces serviceable foams using solution concentration between 0.5 % and 2 % for extinguisher agent and 1 % and 3 % for bubble bath agent, respectively. The visible differences of the foam variations are limited; Figure 210 right shows the exemplary foam structure. Most bubbles have a size in the range of 1.5 mm but sometimes the bubble size is much larger.

Table 92 lists the test matrix for the larger scale pool experiments. The used foam concentrates were fixed to 0.5 % for professional firefighter extinguisher foam and 1 % for family bubble bath, respectively.

Table 92: Test matrix for the larger scale pool experiments.

	Family bubble bath 1 %	Firefighter extinguisher foam 0.5 %
15 % vol H_2	X	X
18 % vol H_2	X	
20 % vol H_2	X	X
25 % vol H_2	X	X
30 % vol H_2	X	X
20 % vol H_2 Channel with obstacles	X (obstacles)	

7.3.4.5　Results

The foams created with H_2/air-mixtures burn very well. A typical combustion behaviour is shown exemplary in Figure 211 with a 25 vol.% H_2 in air for firefighter extinguisher foam. The

left side shows the picture from the high-speed movie (1000 f/s) at the time of ignition. The right side shows the combustion process in x-direction (1D centre-line) as a stack montage from the movie. The montage visualizes the flame front propagation as a distance-time diagram. After the ignition, the flame velocity is low. Up some point (Hot spot), the flame velocity changes rapidly the flame front propagates nearly constant with a faster velocity till the channel end.
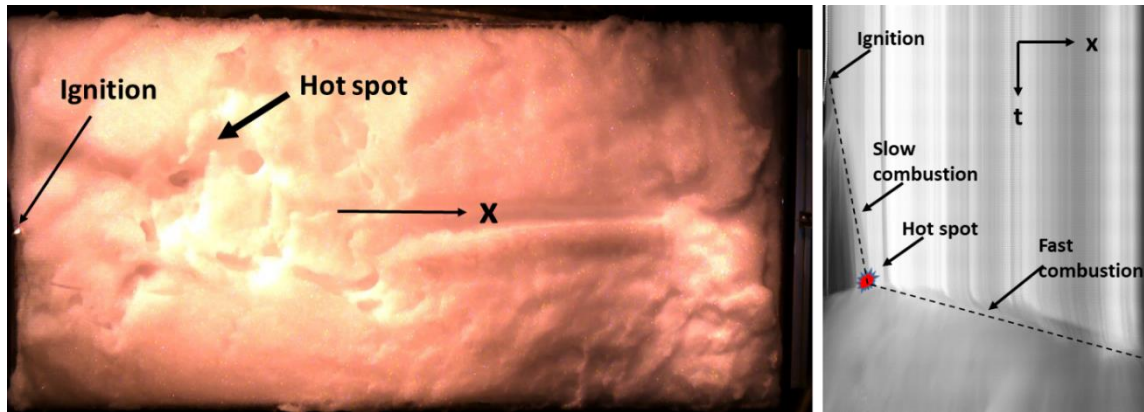
Figure 211: Left, snapshot from the high-speed movie (1000 f/s) at the time of ignition. Right, stack montage from the high-speed movie as distance-time diagram (25 vol.% H_2 firefighter extinguisher foam).

The stack montage from the high-speed movie as distance-time diagram (Figure 211, right) shows the combustion process in 1D. The picture series in Figure 212 taken from high-speed movie show the combustion process in 2D inside the horizontal pool as a top view. The position of the hot spot is visible, indicated by red arrow.
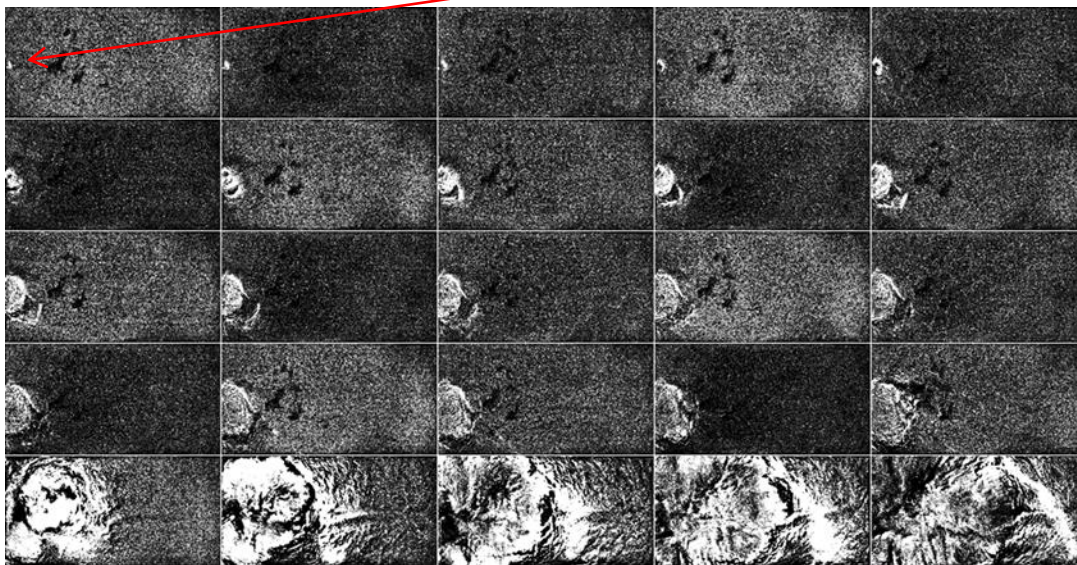
Figure 212: The picture series high-speed movie (25% vol. H2 firefighter extinguisher foam; time step between frames = 6 ms).

For a lower H_2-concentration 20 vol.% H_2 inside the foams, the effect of rapid flame acceleration was not observed, independent of an obstacle setup in the pool. Figure 213 shows the comparison of flame front propagation in an unobstructed (A) and obstructed pool (B) for a 20 vol.% H_2 foam, corresponding to a family bubble bath 1 % for foam generation. The plot in Figure 213 shows the distance vs. time of flame evolutions for the two lines sketched in

Figure 213 (A). The plot shows nearly straight slopes that collapse together for all configurations, the average flame velocity is 16.6 m/s for both. This indicates that the combustion inside the foam is not sensitive to obstruction.
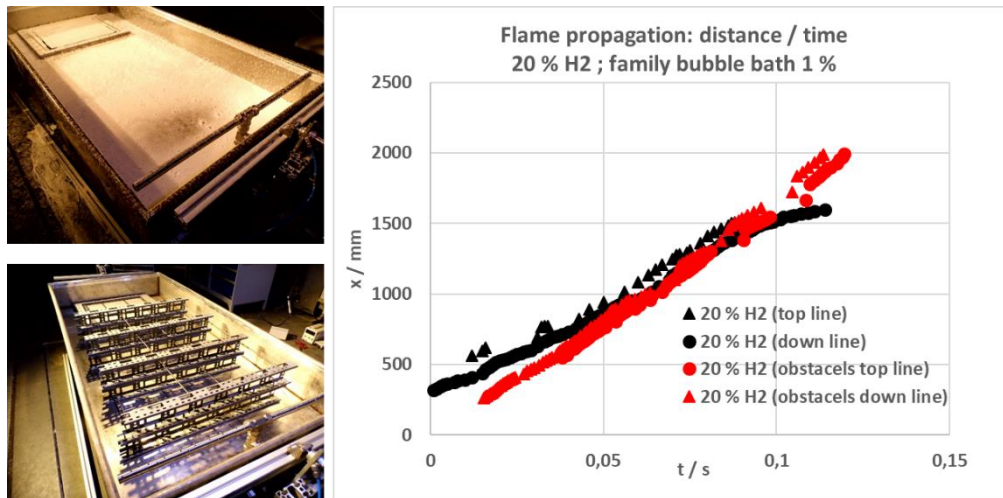
Figure 213: (A) Unobstructed pool. (B) Obstructed pool, four lines with blockage ratio 50 %. Distance vs. time-Diagram: unobstructed and obstructed pool; 20 vol.% H_2 (family bubble bath 1 %) foam.

The observation of the flame front propagation in foam is made inside the transparent small-scale tubes substantial superior as in the larger pool. Examples are shown in Figure 214, where the ignition is on the top (x = 0) and the flame propagates downwards. Three different combustion behaviours were observed in the experiments. 1) For lean mixture (< ~20 vol.% H_2) and rich mixtures (> ~60 vol.% H_2) the flame velocity is constant and low. 2) For high reactive mixtures (> ~28 vol.% to < ~40 vol.% H_2) the flame velocity is in a fast mode directly initiated by the ignition, referring to Figure 214 right. For the other mixtures, the flame velocity starts first slow and accelerates rapidly, referring to Figure 214 left and Figure 211 left.

On the point of rapid velocity changes (hot spot) a shock wave (SW) is generated and propagates through the unburned foam. During the fast flame propagation, the shock waves were generated continuously in a nearly constant frequency (see Figure 214 right).
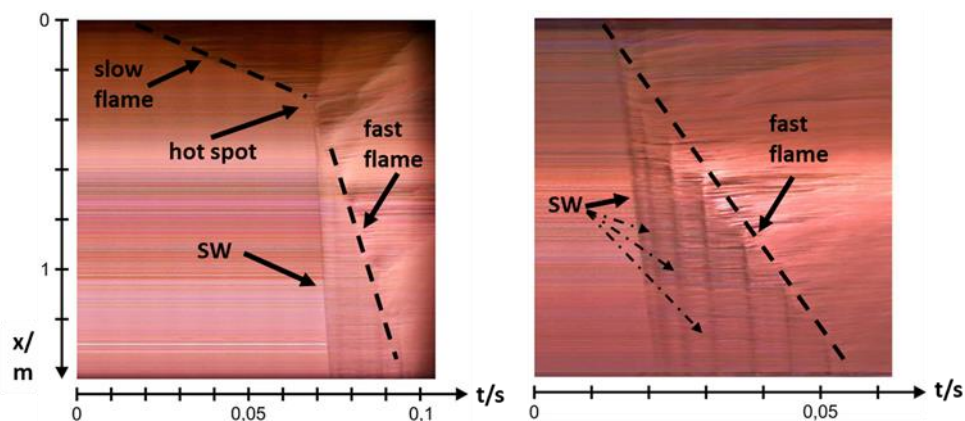
Figure 214: Stack montage from the high-speed movie (4000 f/s) as distance-time diagram. Vertical small transparent channel (d = 90 mm); family bubble bath 1 %. Left, 23 vol.% H_2;Right, 40 vol.% H_2.

Figure 215 summarises the results for the burning velocities in family bubble bath (1 %) and the fire extinguisher foam (0.5 %), respectively. The measured flame velocities in the

horizontal larger pool experiments (red triangles) are in good agreement with the values measured in the vertical smaller tube (black points). Additionally the measured speed of sound in the foams is plotted as grey points. The speed of sound inside the foams is nearly constant. It manifests that the speed of sound is nearly independent of the gas mixture in the foam. However, the speed of sound in the normal gas mixtures increases noticeable with increasing H_2-concentration. The flammability limit of the foam (family bubble bath (1 %)) was found to be LFL =< 9 vol.% H_2 and UFL => 65 vol.% H2. It indicates that, under consideration of downwards propagation, the flammability limit in foam is close to the flammability limit of the H_2/air gas mixture, but with a narrowed flammability range.
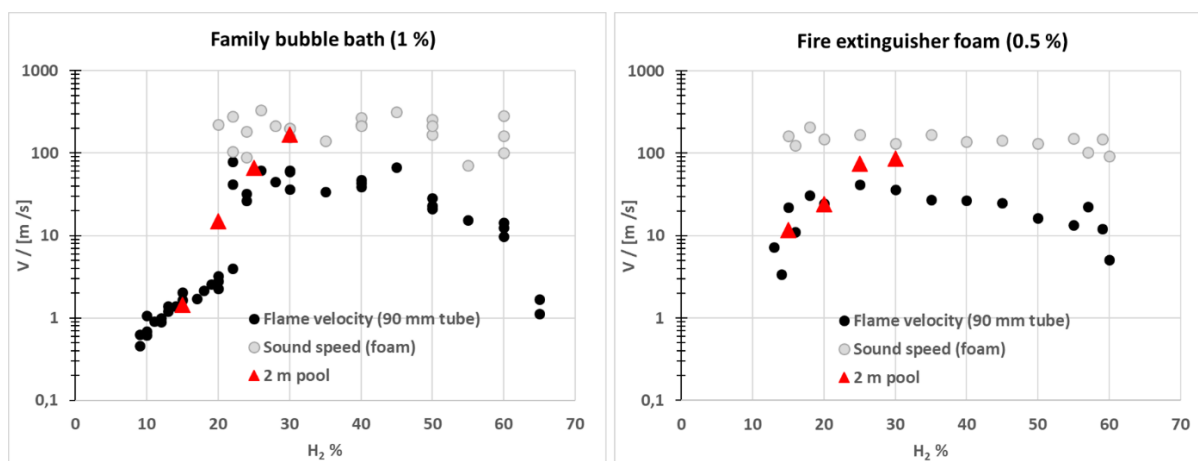
Figure 215: Burning velocities in family bubble bath (1 %)(Left) and the fire extinguisher foam (0.5 %) (Right).

The differences between the two investigated types of foam were surprisingly low. In general, the burning velocity increases slowly, starting from the LFL (~ 9 vol.% H_2), up to the H_2-concentration ~ 20 vol.% H_2. The rapid transition of flame velocity occurs at the hot spot. The maximums of flame velocities (~ < 100 m/s) were observed at near stoichiometric conditions. With further increase of H_2-concentration the flame velocities decrease continuously.

An onset of detonation was not observed in all cases by using H_2/air-mixture. Nevertheless, by using higher reactive H_2/O_2-mixture the burnable foam mixture easily detonates. Figure 216 shows exemplary the combustion of a family bubble bath (2 %) foam filled with 50 vol.% H_2 in O_2. The picture series show the flame propagation inside the rectangular (cross section of 0.02 m x 0.2 m) vertical 2 m high channel with a frame rate of 10000 f/s. The combustion starts first in a fast mode, DDT occurs between frame 4 and 5 in Figure 216. The measured detonation velocity is 1180 m/s, which is less than the half of the theoretical detonation velocity (CJ = 2324.5 m/s) of the pure H_2/O_2-mixture.
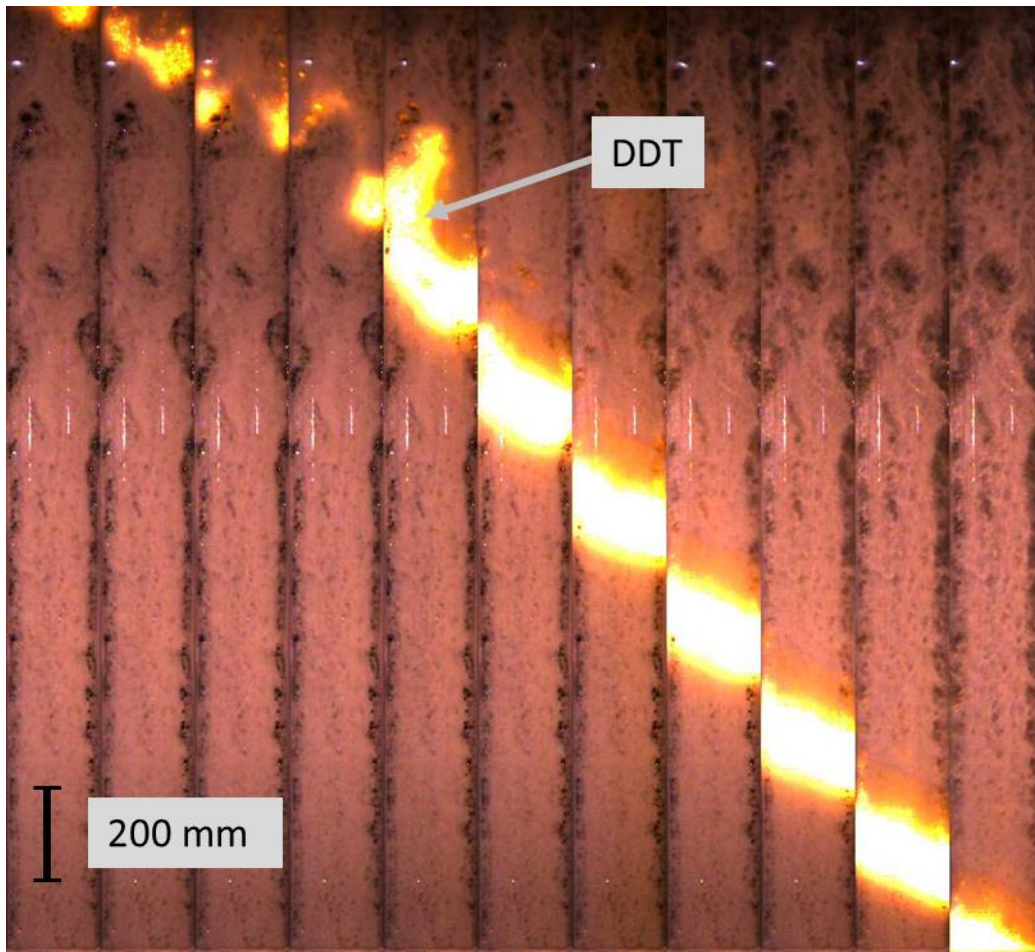
Figure 216: Picture series of the combustion of a family bubble bath (2 %) foam inside the rectangular (cross section of 0.02 m x 0.2 m) vertical 2 m high channel (50 vol.% H_2 in O_2; 10000 f/s).

Burnable or explosive fire extinguisher foam is a curio itself. The main conclusion of this work is that foam built with H_2/air-mixture become burnable. H_2 gas can be confined for several hours inside foams. There is no buoyancy effect and rapid dilution. The flammability limit in foam is comparable with the flammability limit in pure gas. For reactive mixtures of $\sim >20$ vol.% H_2, a special sudden flame acceleration due to hot spots was observed. The maximums of flame velocities of $\sim < 100$ m/s were observed near stoichiometric conditions. Detonation of foam enriched with H_2/air-mixture were not observed, however foams enriched with H_2/O_2-mixture easily detonate.

7.3.5   Tests on effect of water sprays and mist systems on combustion and DDT (ST4.4.4, PS)

7.3.5.1   Background

Water injections like spray or mist generation systems are traditionally applied to extinguish fires in conventional accident scenarios. However, it might be a challenge for conventional fire protection systems, when hydrogen vehicles are involved in a fire due to hydrogen release in confined spaces like traffic tunnels, parking garages, storehouses. It is still a question whether a water spray is able to effectively extinguish or suppress a hydrogen fire. Nuclear containment

safety studies for water reactors have shown that water spray is not a sufficiently good extinguisher of hydrogen fires in some circumstances, but the injected water droplets and vaporised steam can change the composition of the atmosphere in the containment and the chemical sensitivities of the gas mixtures.

In case of hydrogen deflagration or detonation in confined spaces like tunnels or garages, injected water mist interacts with the reacting zone. The pressure waves caused by explosion are supposed to be attenuated by the interaction. The attenuation effect is still unclear.

7.3.5.2   Objectives

The aim of the experiment is to test the suppression effect of water injection on the combustion of premixed hydrogen-air mixture in unobstructed semi-confined tunnel like geometry. The influence of water mist on the combustion behaviour of layered hydrogen-air mixture will be linked by the comparison of experiments with mist injected and dry experiments.

7.3.5.3   Knowledge gaps and accident scenarios assessed

There is sparse data available regarding the dynamics of flame propagation in semi confined hydrogen-air mixture in presence of water spray or mist. The presence of water droplets maybe acts as turbulence source and is able to accelerate flames or it acts as energy sink and suppresses the combustion process.

7.3.5.4   Description

The tests were performed inside the H110 (A1) vessel of HYKA, as shown in Figure 217. The safety vessel H110 has main dimensions of 3.3 m id and 12 m length with a volume of 100 m^3 and a design pressure of 100 bar. The vessel is used as a safety vessel. A rectangular sub-compartment of 9 x 3 x 0.6 m^3 was used to study a combustion and detonation in a horizontal semi-confined layer of hydrogen air mixture, as shown in Figure 217 left. The safety vessel is equipped with measuring ports and windows for visual observations. A gas-filling system allows to creating layer of uniform hydrogen-air mixtures. The measuring system for combustion detection consists of an array of fast thermocouples (flame arrival time) and fast pressure gauges (combustion pressure and shock wave). The data acquisition system is based on multi-channel (64) ADC with a sampling rate of 1 MHz. The longitudinal mid-point of the rectangular combustion channel 9 x 3 x 0.6 m^3 is equipped with a water spray system, as shown in Figure 217 right. The test was performed with uniform H_2 layers. The open from below side of combustion channel is separated with a thin foil. The layer height is 60 cm in all tests. The ignition was performed in a perforated tube which acts as a line igniter. The flame propagates through the first half of the channel without spray nozzles and enters the water spray section after 4.5 m.
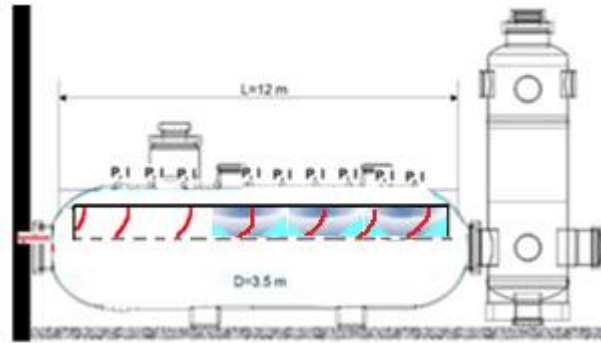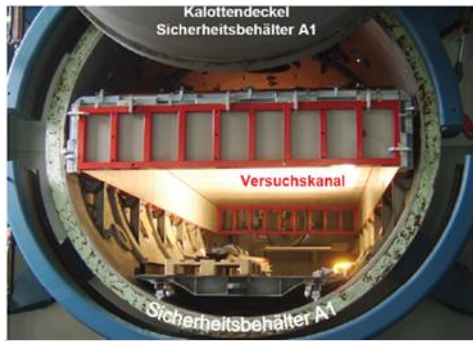
Figure 217: Test facility H110 (A1) of HYKA with large scale rectangular combustion channel 9 x 3 x 0.6 m³ and section with water spray.

The professional high-pressure water mist system (Callies GmbH) used, with four mist nozzle heads (Danfoss SEM-SAFE® Type: HNMP-5-10-1.19-00) is described in detail in Subtask 3.4.6 (Hytunnel-CS D3.3) and Subtask 4.4.5 (HyTunnel-CS D4.3). In the used four nozzle head configuration the mist output (droplet size: 10 – 80 µm) is 32 kg/min corresponding to 1-1.8 kg/min/m². Figure 218 right shows one Danfoss nozzle head with five single nozzles. The left side of Figure 218 shows the section of the combustion channel with the installed four nozzle heads. The bottom and the end wall of the 0.6 m high layer is covered with a 7 µm thin foil. The nozzle heads pass from below the foil. To protect the foil from defection and rupturing, special drainage holes were placed on the foil. The drainage pipes are compressed foil tubes, which allow the escape of liquid water without gas mixing, referring to Figure 221 top.
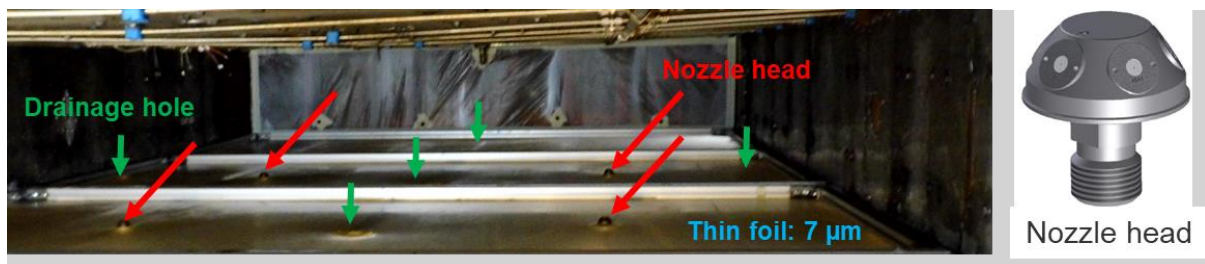
Figure 218: Right, Danfoss nozzle head with five single nozzles. Left, section of the combustion channel with the four installed nozzle heads.

The premixed hydrogen-air mixture fills in a rectangular domain H x W x L = 0.6 x 3 x 9 m³. The water spray system operates 2 min before the ignition and during the ignition. The spray zone is 4.5 m long. It was observed that, after 15 s mist injection time, the whole channel was filled with mist fog up to the ignition end. Figure 219 shows the mist cloud in the channel after 12.5 s mist release time. The view point of the snapshot is at the ignition position.

Figure 219: Snapshot viewed from ignition position in the channel after 12.5 s mist release time.

To measure the flame propagation in 2D geometry an array of sensors is necessary. The rectangular combustion channel is equipped with 14 fast pressure (P) gauges (PCB) for combustion pressure and 10 fast thermocouples (TC) to detect the arrival time of the flame front. Figure 220 shows the positions of the sensors and spray nozzle as a top view of the open-end channel.
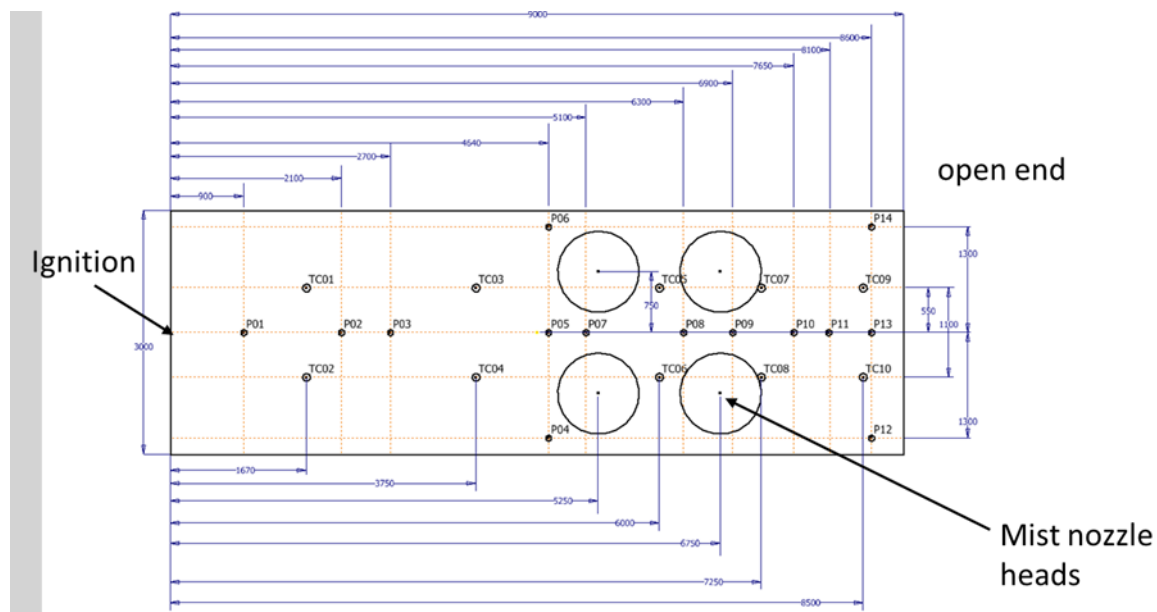
Figure 220: Scheme of sensor and spray nozzle positions.

Combustions experiments with different hydrogen concentrations up to stoichiometric mixtures were performed with or without spray. The test matrix is shown in Table 93.

Table 93: Test matrix of water injection effect on hydrogen combustion.

Water spray	Mist	Dry
10 % vol. H_2	**1**	**7**
12 % vol. H_2	**2**	
15 % vol. H_2	**3**	8 / 9
20 % vol. H_2	**4**	10
25 % vol. H_2	**5**	11
30 % vol. H_2	**6**	12

7.3.5.5 Results

The picture series in Figure 221 shows the comparison of deflagration of 25 %vol. H2 in mist atmosphere (line A) and dry atmosphere (line B). The pictures taken from a video camera show the film-covered underside of the combustion channel. The first picture A1, taken short before ignition, shows the high-pressure water supply for the mist nozzles and the water drainage pipes and the basins to collect the flowing water. In the dry experiments the picture B1 shows only the drainage pipes installed to reach equal conditions for both configurations. The second pictures (A2 and B2) show snapshots of the combustion with high luminescence. The high luminescence is mostly a result of the reacting carbon from the foil material and its fixing tape. It is visible that the wet conditions suppress this effect. The cooling and fire suppressing effect of the water mist is clearly visible in the third pictures A3 and B3 after the H2-combustion. In contrast, the burning of the foil and tape is visible in the dry experiment (B3), but no fire and only fog are visible in the wet experiment (A3).
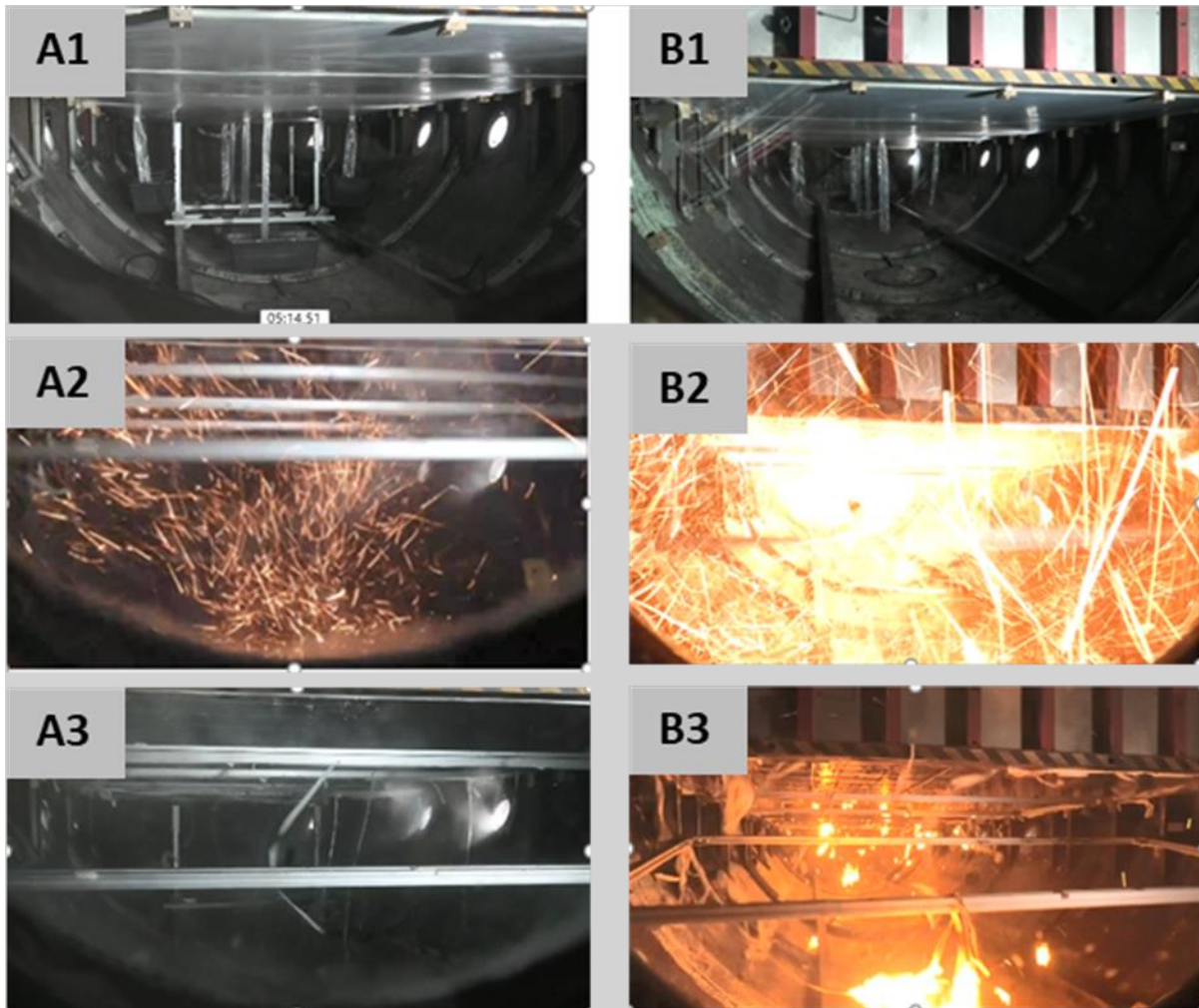
Figure 221: Comparison of 25 %vol. H_2 deflagration in mist (line A) and dry atmosphere (line B).

The impact of the H_2 deflagration on the environment was measured by the array of sensors. Figure 222 shows histories of pressure signals and thermocouple signals (green/blue) in distance-time-diagram. The left graph is a 30 %vol. H_2 experiment with mist injection while the right graph is an experiment with the same H_2-concentration in dry conditions. The comparison of flame propagation along the channel shows no significant differences between mist atmosphere and dry atmosphere. The main difference is faster pressure decay in the mist atmosphere than in dry conditions due to the cooling effect of the liquid water. The pressure amplitudes (curves in red) look similar as well as the arrival times of the flame fronts (green/blue).
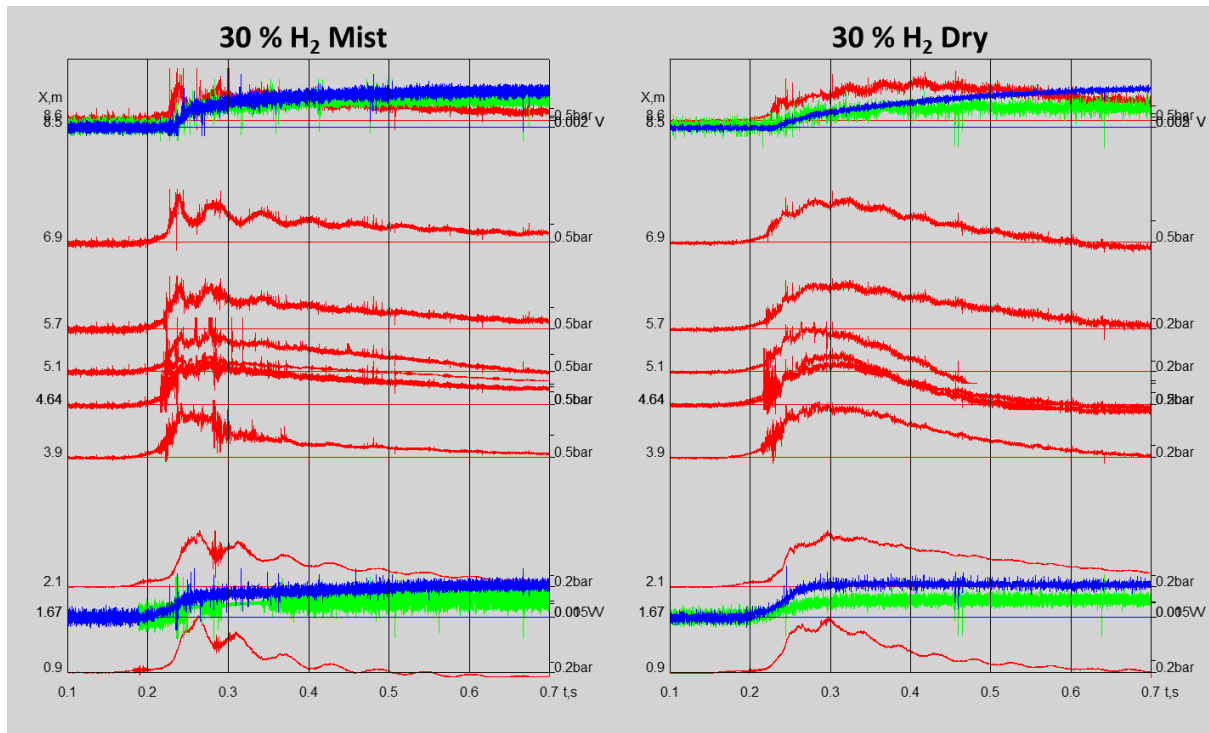
Figure 222: Comparison of flame propagation with distance-time-diagrams 30 %vol. H₂ in mist (left) and dry atmosphere (right).

Figure 223 shows the measured flame velocities (left) and overpressure amplitudes (right) along the channel for the whole test matrix. Only slow deflagrations were observed, the maximum flame velocity on the end of the channel lies below 40 m/s (30 %vol. H_2 dry). Nevertheless, flame acceleration along the channel is visible for H_2-concentrations up to 15 %vol. H_2 in dry cases and 20 %vol. H_2 in misted cases, respectively. This indicates that, higher flame speeds can be expected with a transition to fast flames or even detonation, if the channel is long enough. The measured overpressure amplitudes along the channel reflected that only slow deflagrations occurred in the experiments. The maximum overpressure looks volumetric, it is nearly independent of the sensor position in the channel. Only for H_2 concentrations up to 15 %vol. in dry cases, and 20 %vol. in misted cases, is a slight increase of pressure visible in the second half of the channel length.
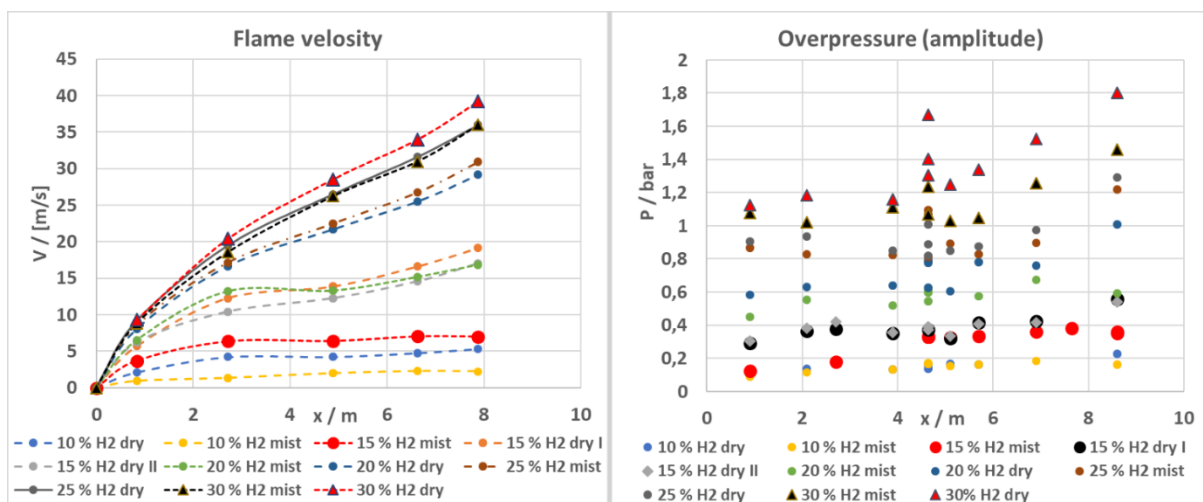
Figure 223: Flame velocities (left) and overpressure amplitudes (right) along the channel for the whole test matrix.

Figure 224 summarizes the suppression efficiency of water injection on hydrogen deflagration as comparison of the results between the dry and wet (mist) experiments. Therefore, the average values in the second half of the passage length (x > 4.5 m) are compared. The left plot shows the averaged overpressure as a function of H_2-concentration. With increasing H_2-concentrations the overpressure increases, the slopes look linear for dry and wet (mist) atmosphere, respectively. The slope in the dry conditions is a little greater than that in the mist atmosphere. The averaged flame velocity shown in Figure 224 right presents a linear character of function of H_2-concentrations for dry and wet (mist) atmosphere, respectively. However, the flame velocities in the dry cases are clearly greater than the wet cases at the corresponding hydrogen concentration. Both lines look parallel for concentrations > 15 %vol. H_2. The parallel shift corresponds approximately to a concentration value of 5 %vol. H_2. For example, the flame velocity of a 15 %vol. H_2 mixture in dry conditions is equal to the flame velocity of a 20 %vol. H_2 mixture in mist atmosphere.
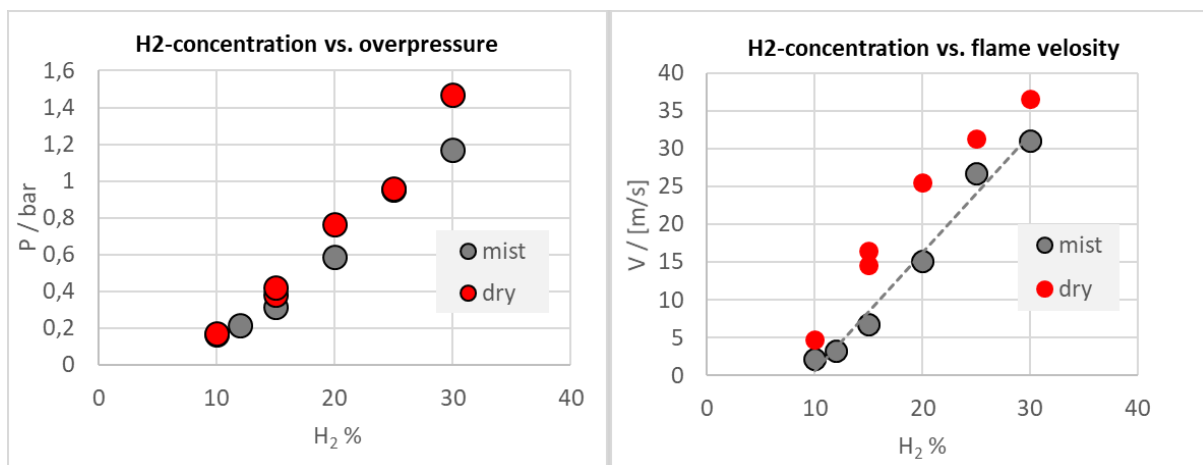
Figure 224: Suppression efficiency of water injection on hydrogen deflagration.

The main conclusion of this work is that, the mitigation effect of a mist sprinkler system on the deflagration process of a H_2/air-mixture is low in the semi-confined channel. An initial 10 %vol. H_2 mixture burns without problems in the semi-confined geometry in a highly mist enriched atmosphere. Flame acceleration along the channel for H_2-concentrations up to 15 % for dry cases and 20 % for misted cases was observed. In principle, the combustion of H_2/air-mixture in the mist-enriched atmosphere leads to lower overpressure and lower flame velocities than in dry atmosphere. However, the tests shows that the mitigation effect is quite limited, and that the difference between the dry and wet cases is smaller than expected. Another observation is that, the rapid cooling effect due to liquid water phase has remarkable positive effects. The decay of the overpressure in wet cases is faster than in dry atmosphere and the H_2-deflagration is not able to ignite highly combustible solids.

The test results show that only slow deflagrations were observed in the semi-confined unobstructed geometry in the work. The key point is due to the unobstructed character of the combustion channel. The fact is that the design of some obstacles in the channel can lead to a catastrophic detonation with an unacceptably high flame speed and overpressure independent of dry or wet atmosphere, referring to the last section in Sub-task 4.4.3 (Influence of obstacles on stratified mixture combustion).

7.3.6 Shock wave attenuation: Experiments on effect of water spray / mist system on shock wave attenuation (ST4.4.5, PS)

7.3.6.1 Background

Water injections like spray or mist generation systems are traditionally applied to extinguish fires in conventional accident scenarios. However, it might be a challenge for the conventional fire protection systems when hydrogen vehicles are involved in fire, due to hydrogen release in confined spaces like traffic tunnels or other confined spaces. The review of literature shows that that high-density water sprays are able to attenuate shock or blast waves. The interaction mechanism of shockwaves with water sprays in common density-based fire extinguisher system needs to be studied.

7.3.6.2 Objectives

The aim of the experiment is to investigate the attenuation effect of water spray injection of a common fire extinguisher spray system on the shock wave of hydrogen detonation. A droplet and mist dominated sprinkler system will be investigated and compared with the shock wave propagation without sprinkler.

7.3.6.3 Knowledge gaps and accident scenarios assessed

Pressurised H_2-tank rupture and fast hydrogen deflagration or detonation leads to an emission of a shockwave. Pressure loads due to shockwaves are the major hazard potential in hydrogen applications. A shockwave has a rapid increase of peak-overpressure (amplitude) in a positive phase followed by a negative phase (Figure 225, left).The shockwave propagates with a supersonic high velocity in air over long distances. In free field, the area of the shock front increases continuously due to the spatial expansion, which leads to a relative good attenuation of the amplitude with distance. In tube geometries like tunnels, the shock front propagates in all time with the same tunnel cross section area. Mainly friction and reflection on the tunnel walls were responsible to reduce the amplitude with distances (Figure 225, right).
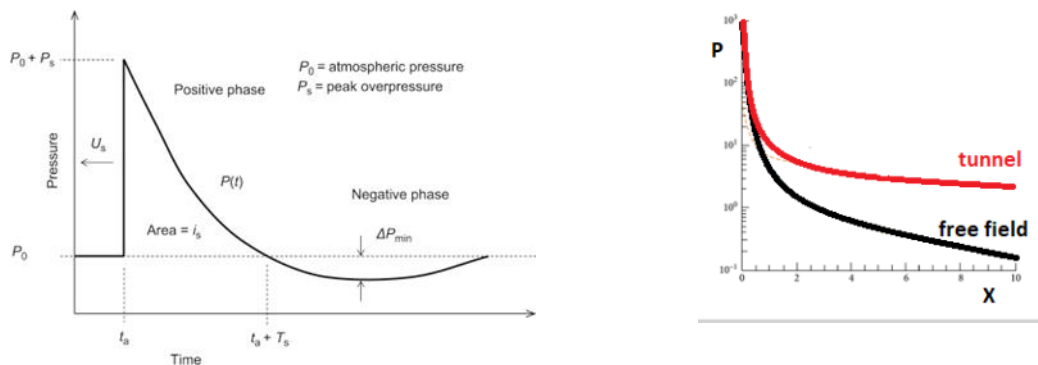
Figure 225: Left, idealized shockwave. Right, decaying of the amplitude of a shockwave with distance, in free field and tunnel geometry.

Due to the attenuation effect of sprays on shockwaves, common fire extinguisher sprinkler systems can be used simply as a counteraction to improve tunnel safety. However, no data are available whether a common fire extinguisher mist or droplet dominated sprinkler system is able to attenuate shockwaves effectively.

7.3.6.4 Description

The experiments were performed inside the safety vessel V220 (A2), as shown in Figure 226, left. The safety vessel, with an inner diameter ~ 6 m and a height ~ 8 m provides a volume of 220 m^3. It is designed for a static overpressure of 11 bar and temperatures up to 150 °C. The vessel is equipped with a number of vents and ports and windows for optical access. The largest two flanges with an inner diameter 1.890 m are parallel and located near the ground. Inside the safety vessel a defined H_2 detonation will be initiated. Figure 226 shows a sketch of the experimental set-up. The basic principle is sketched in Figure 226, right. A local H_2-detonation takes place inside the safety vessel. An incident shock wave (SW) runs from the source to the vessel wall and the shock wave propagations are recorded by pressure sensors placed on the floor.
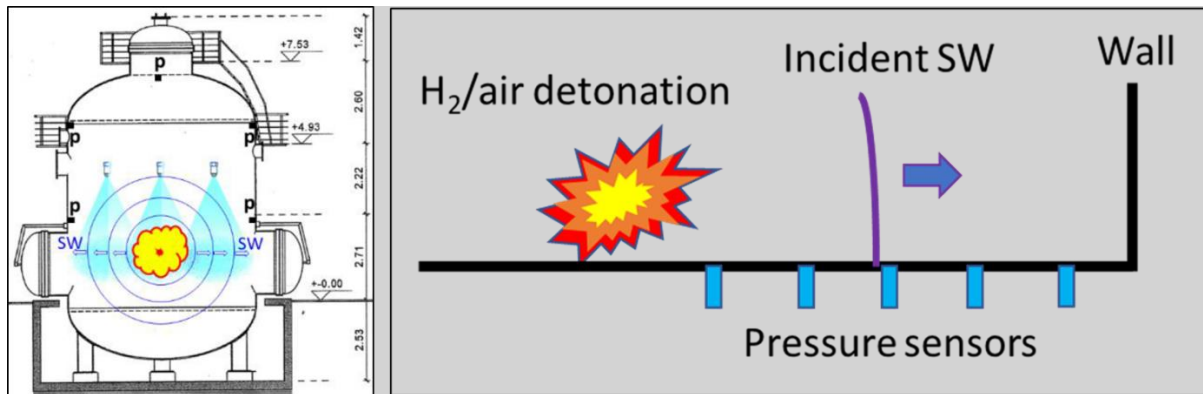
Figure 226: Left, test facility V220 (A2) of HYKA for attenuation of water spray on hydrogen detonation shock waves. Right, sketch of the principle set-up for suppression tests of water spray on shock waves.

As a detonation source, a combustion unit with 4 g H_2 was used to provide stoichiometric H_2/air mixture. The cube-shaped 4 g H_2-combustion unit (0.5 x 0.5 x 0.5 m) is covered with thin plastic film (7µm) and produces, after ignition in its centre, an unconfined H_2-detonation. The picture series in Figure 227, left shows the detonation of the 4 g H_2-cube. Figure 227, right shows the dimensionless pressure in air blast wave, versus distance in free field tests for the 4 g H_2-cube and other cubes with higher H_2-inventory. The combustion unit was initially developed to test buildings and laboratories against worst-case combustion of a limited amount of H_2. Its description is given in (Grune et. al., 2003). Due to the film cover, the combustion unit is usable in wet sprinkler atmosphere.
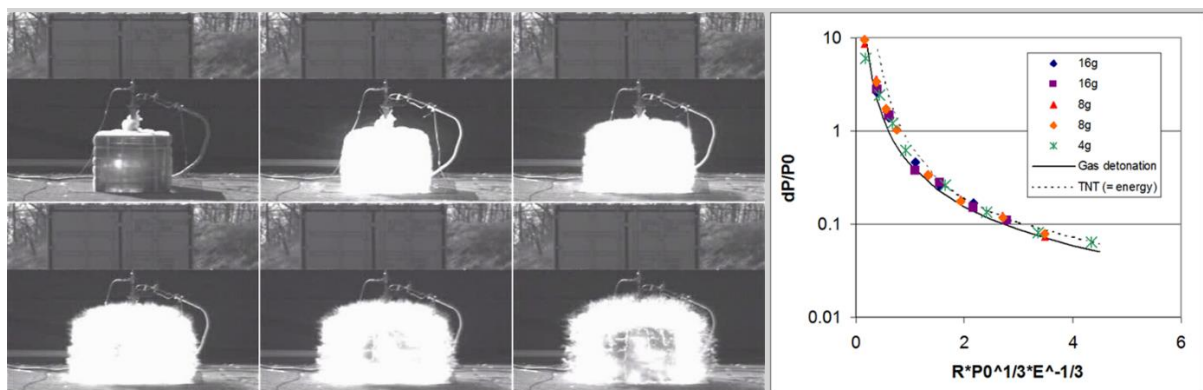
Figure 227: Left, detonation of the combustion unit with 4 g H_2 provided as stoichiometric H_2/air mixture (time-step between pictures 1 ms). Right, dimensionless pressure in air blast wave, versus distance in free field tests for the 4 g H_2-cube and larger cubes with higher H_2-inventory.

Fast pressure sensors type PCB placed on the ground in heavy lead bricks are used for precisely measuring the shock wave history. A high-speed camera was used to record the uniformity of the combustion unit in dry conditions (see 7.2.3). Figure 228 shows the traverse of the seven pressure sensors and the combustion cube inside the safety vessel as top and side view.
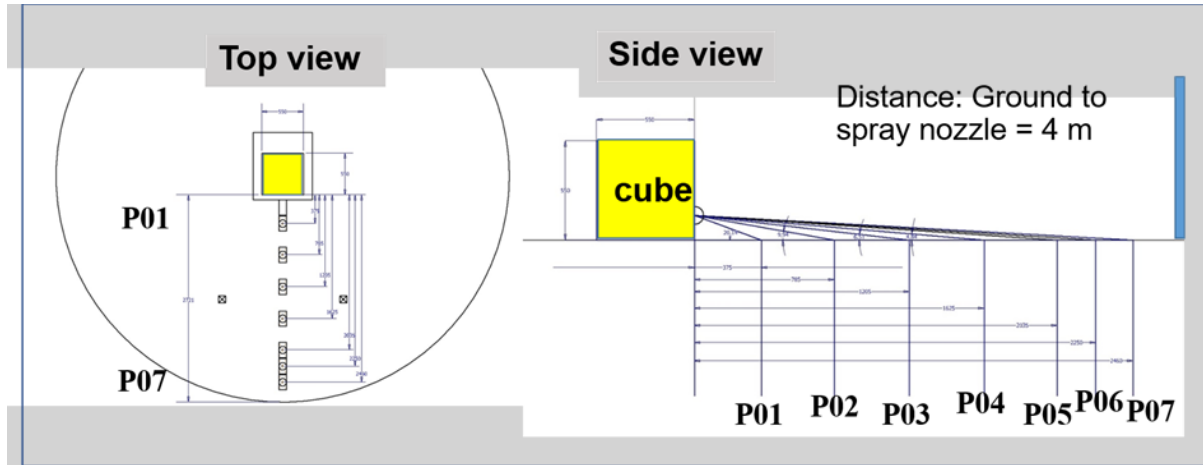
Figure 228: Pressure sensors and combustion cube inside the safety vessel as top and side view.

The used sprinkler systems are placed in a distance of 4 m above the ground. The nozzles are placed under a partial roof, regarding the guidelines. A droplet dominated spray system with one full cone nozzle (Figure 229 left) and a mist dominated multi nozzle sprinkler system are used as two-nozzle or three-nozzle head configuration (Figure 229 right). The used sprinkler set-up is described in detail in D3.1, sub-task 3.4.6.

Figure 229: Left, droplet dominated spray system with one full cone nozzle. Right, mist dominated sprinkler system in three-nozzle head configuration.

The sprinkler nozzles are placed in a position to achieve a high uniformity of water charge in the test section with the pressure gauges. On the other hand, the spray should not directly hit the vessel wall because a water film on the steel wall should not influence the shock wave reflection. Figure 230 shows the water charge values in the concerned section between the cube-shaped H_2-combustion unit and the vessel wall for all investigated configurations. The water charge was measured gravimetrically by using 80 small pools in the concerned area. The droplet dominated spray system with one full cone nozzle shows a high water charge of ~ 6 mm/min in its centre, which placed under the position of the combustion unit. In the concerned area the water charge is highly uniform and lies in a range of 4 +/- 0.5 mm/min. Nearby, the vessel wall the water charge decays in 0.5 m to almost zero. The water charge of the mist system with three-nozzle head configuration shows in the concerned area nearly the

same figure as the droplet full cone nozzle. In this configuration, the water charge in a range of 3.5 +/- 0.5 mm/min is very high for a mist fires extinguish application. Due to the use of two-nozzle head configuration, the water mist charge is in a realistic range of 1.5 +/- 0.5 mm/min in the completely concerned area.
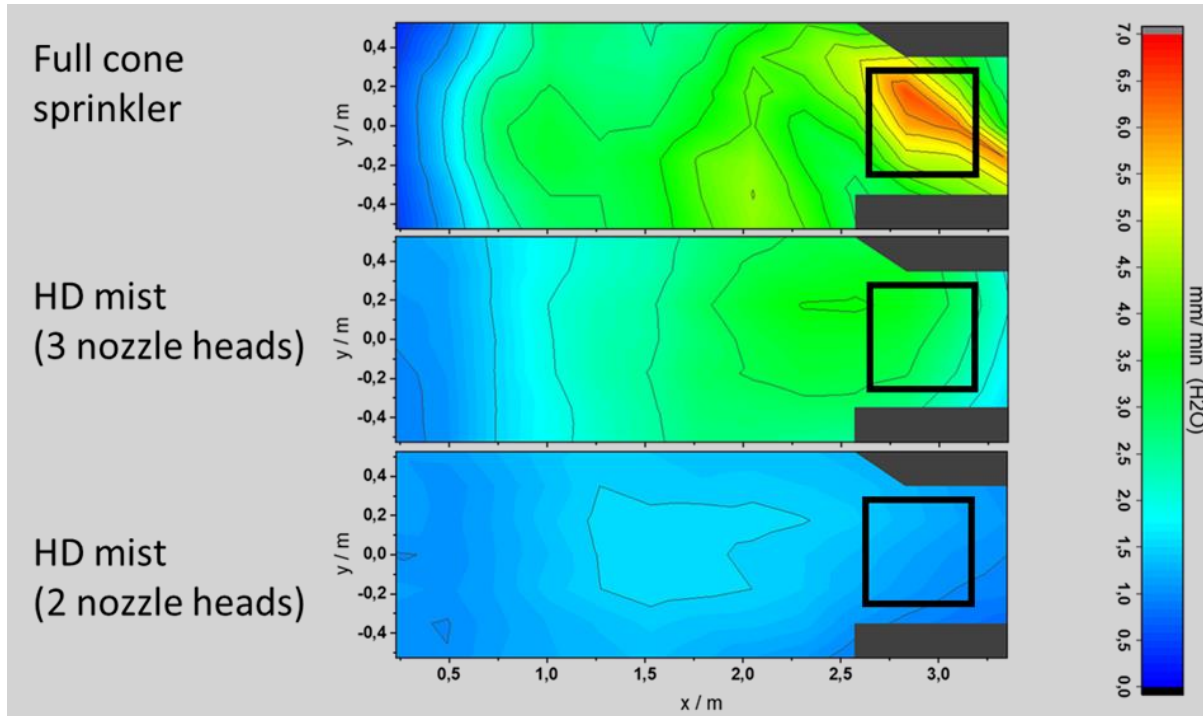
Figure 230: Water charge values in the concerned section between the cube-shaped H_2-combustion unit and the vessel wall for all investigated configurations.

To investigate the attenuation effect of the sprinkler system on shock waves, tests of shock wave propagations are compared between with running sprinkler system and without sprinkler influence. Table 94 lists the test numbers in a chronological style.

Table 94: Test matrix of attenuation of water injection on shock wave of hydrogen detonation.

Test No. /Water charge	none	droplet	mist low	mist high
Test 01	X			
Test 02		X		
Test 03		X		
Test 04	X			
Test 05				X
Test 06	X			
Test 07				X
Test 08			X	
Test 09	X			
Test 10			X	

7.3.6.5   Results

The proper measurement of shock waves is challenging itself even in dry conditions. In wet atmosphere the sensor surface, which captures the fast pressure transition, can be blocked by water droplets, as shown in Figure 231. Droplets can fully cover or partially cover the shock wave sensor membrane. This circumstance requires a carefully interpretation of the measured shock wave pressure histories.

Figure 231: Left, water droplet fully covered the shock-wave sensor membrane. Right, partially covered sensor membrane of the shock-wave sensor membrane.

Figure 232 shows exemplarily an example of a failed measured pressure history on pressure gauge P3. The plot in the left diagram shows the pressure histories in dry conditions (black) and with droplet-dominated spray (red), visible are the incident shock and later in time the wall vessel reflected shock wave. The plot in the centre diagram amplifies the incident shock; it is visible that the main difference between the shock waves is only the peak value of the amplitude. Therefore, the amplitude with spray is 20 % less than in dry conditions. However, according to the amplification of the reflected shock waves, as shown in right diagram, the behaviour is opposite: the amplitude with spray is higher than in dry conditions. It can be assumed that a droplet on the sensor membrane is responsible for the discount of the measured amplitude by P3 sensor in the case with spray. Sensor signals with such a discount in the amplitude are separated in this work and are not considered.
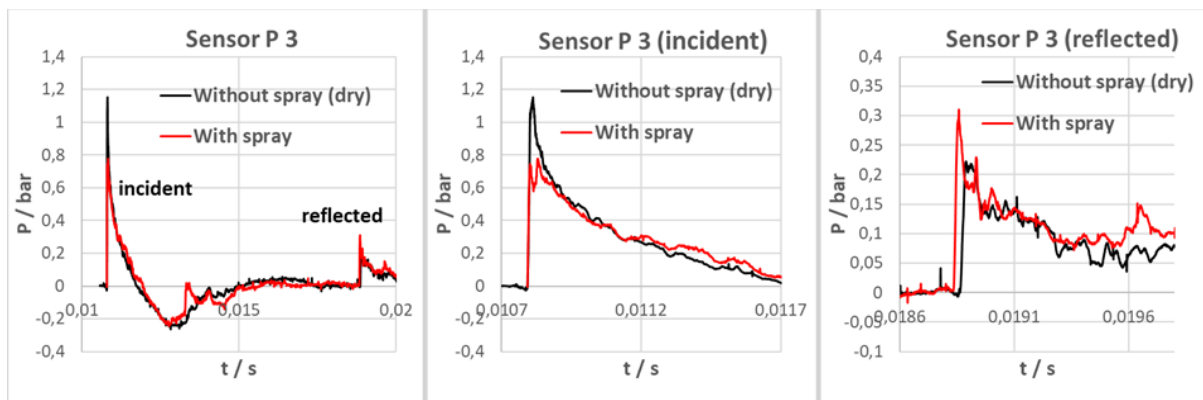
Figure 232: Example of a failed measured pressure history on pressure gauge P3.

The measured shock waves in all tests reflect that the used combustion unit is highly repeatable. Figure 233 shows examples of the pressure histories from gauge P1, P3 and P7. The sensor P1 is placed in a short distance to the detonation source, after a short, strong peak amplitude of around 3 bar, the decaying part of the wave shows instability. Nevertheless, the pressure histories from all tests, independent of sprinkler or no sprinkler, collapse in a good agreement. The pressure histories from sensor P3, which is placed in the middle of the test section, show nearly the idealized shockwave shape (Figure 225) with a positive and negative phase. The shape here is relatively smooth and the pressure histories from all tests collapse in a very good agreement including the wall reflected pressure waves at $t = 0.008$ s. Near the vessel wall, the time difference between the incident and reflected shock wave is very small. For the pressure sensor P7, this timespan lies at 1.55 ms for all tests and the amplitudes of the incident and reflected shock wave are nearly identical. It is amazing that the amplitude of the reflected wave arrives at the sensor almost simultaneously with the negative phase of the incident wave. However, the pressure histories P7 from all tests collapse in a good agreement.
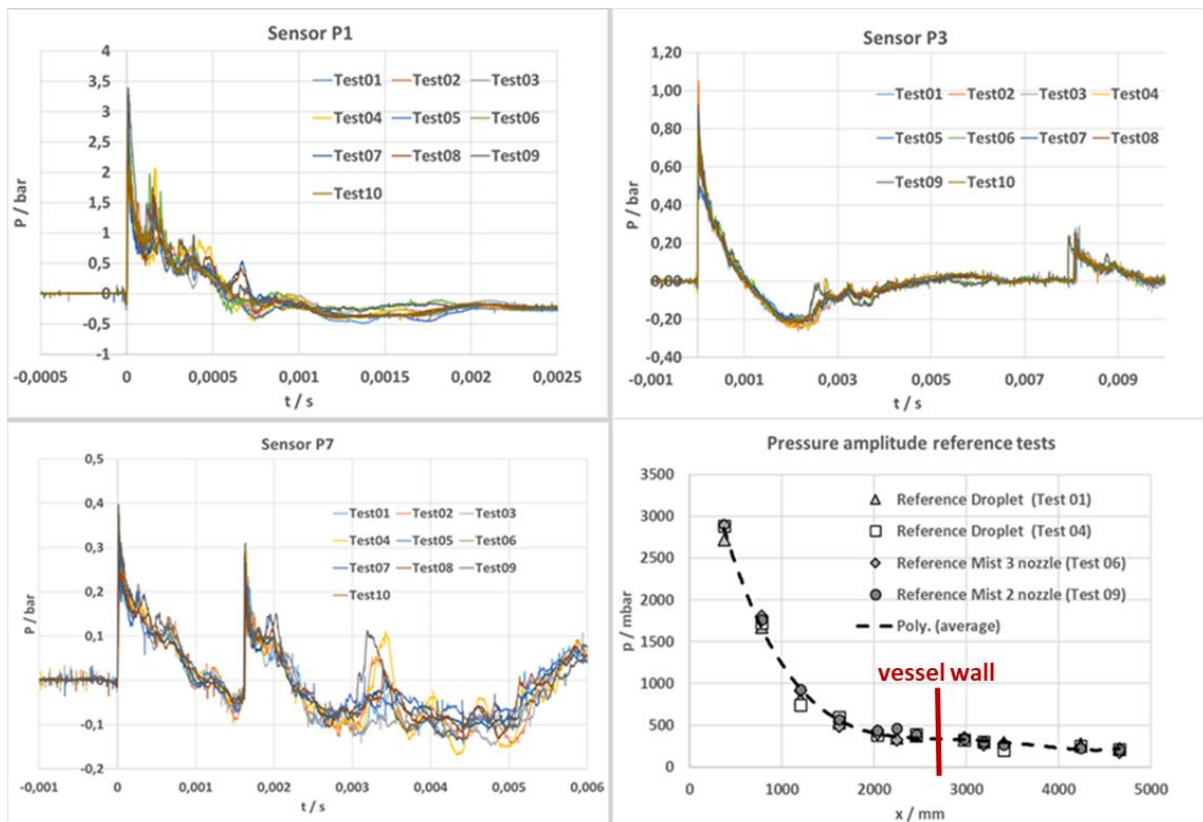
Figure 233: Pressure histories from gauge P1, P3 and P7 from all tests. Comparison of amplitudes vs. distance from all reference tests without sprinkler influence.

A comparison of the amplitudes versus the propagation distance from all reference tests without sprinkler influence is shown in Figure 233 bottom-right. The distance is plotted from the border of the combustion unit and is scaled as total propagation distance for the shock wave. The incident amplitudes are plotted on the left side from the sketched vessel wall, while the reflected amplitudes on the right side. The amplitude shows a rapid decaying near the combustion unit, after a propagation distance of 2 m, where the amplitude lies below 0.5 bar. From this point the amplitude decays slowly and the reduction of the amplitude due to the

reflection on the steel wall is negligible. The scattering from all reference tests without water spray is low, but present.

To identify the shock wave attenuation due to the presence of water or mist spray, the pressure amplitude and the impulse of the wet and dry tests are compared. The values of the specific reference tests are normalised to one and the values of the tests with spray are plotted in this normalised form. Figure 234 presents the shock wave attenuation from the droplet dominated full cone spray. The normalized value (unit) from the specific reference tests are plotted along the propagation distance of the shock wave (red line). The values of the corresponding two tests with spray are normalised in the same way and plotted as dark points. Droplet dominated water spray in the atmosphere leads to lower shock wave amplitudes. Only few points lies slightly above the normalised line. Nevertheless, the amplitudes of droplet test 02 (grey points) are all near by the reference line. As for the positive impulse, the normalized values from the droplet tests lie partially above or below the reference line.
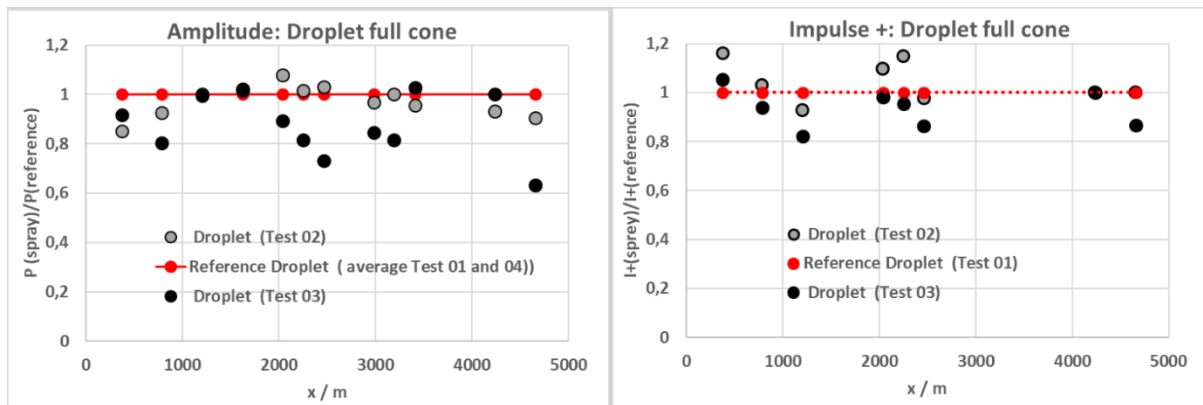
Figure 234: Normalised visualisation of the shock wave attenuation due to the droplet dominated full cone spray. (Left, amplitude; Right, impulse+)

In contrast to the slight shock wave attenuation due to the droplet dominated spray, a clear shock wave attenuation effect was identified in the cases of mist dominated spray.
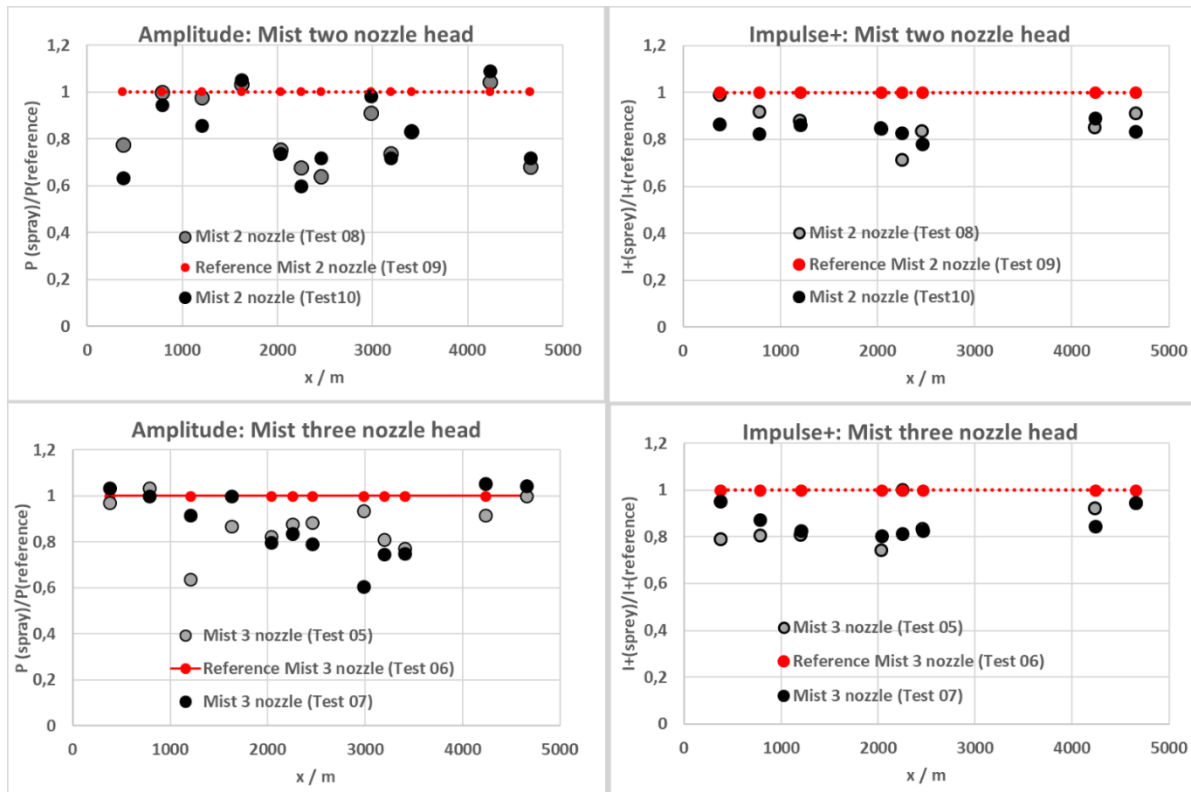
Figure 235: Normalised visualisation of the shock wave attenuation due to the mist dominated spray with two and three nozzle heads (Left, amplitude. Right, impulse+).

Figure 235 shows the normalised visualisation of the shock wave attenuation due to the mist-dominated spray for both investigated nozzle set-ups. For the two and three nozzle head configuration only few amplitude points lies slightly above the reference line. The maximal shock wave attenuation can reach values up to 40 % of the amplitude. An average of ~ 20 % of shock wave attenuation is observed. The attenuation is independent of the mist charge from two or three nozzle configuration. Regarding the positive impulse, all mist-dominated points lies below the reference line. The reduction of the positive shock wave impulse can reach up to 20 %. This value is also close to the average attenuation for the two and three nozzle head configuration. Remarkable is that, no increasing shock wave attenuation with increasing runtime was observed for all configurations.

7.3.6.6   Conclusions

The investigated water spray used in fire extinguisher systems shows a moderate effect on shock wave attenuation. For the droplet-dominated spray, no robust clear attenuation trend is visible, but some suppression of pressure amplitudes. The amplitude attenuations are obtained as 0~15 % for droplet water spray and 10~30 % for mist spray, respectively. Only slight attenuation on positive impulse of the shock wave is found for droplet water spray; while the mist water spray shows an clear impulse attenuation of 10~20 %.

The general conclusion is that water spray has a positive effect on shock wave attenuation. It is expected that high-density water sprays, like a curtain or waterfall, show higher effect on shock wave attenuation.

7.3.7 Safety technology to prevent tank rupture: tests on prototypes of leak no burst composite type 4 tanks at USN (ST4.4.6, UU/USN)

In total 10 LNB tank prototypes were designed and manufacture in HyTunnel-CS project. The volumetric capacity of all tanks is V=7.5 L and the nominal working pressure is 70 MPa. The prototypes designs were built based on the original Type IV composite overwrapped tanks with minimum burst pressure ratio 2.25 and with two kinds of high density polyethylene (HDPE) liner. The description of LNB tank prototype designs, including components and objectives of testing are given in Table 95.

Table 95: List of LNB prototypes designed and manufactured in Hy-Tunnel-CS project: materials and objectives.

COPV#	Liner	FRP/TPL	Wall+	Objectives of fire testing series	Partn.
1	L2	C1/B	+2 mm	Burst test: definition of burst pressure ratio	N/A *
2	L2	C1/B	+2 mm	Effect: fibre+resin in protection layer on leak/flame size and P dynamics in the same laboratory (#2 vs #3)	USN
3	L2	C1/C2	+2 mm	Effect: same as in #2	USN
4	L1	C1/C2	+2 mm	Effect: liner type on leak (flame size) and pressure dynamics (#3 vs #4)	USN
5	L1	C1/C2	+2 mm	Effect: burner/laboratory and repetition of experiment (#4 vs #5)	CEA
6	L2	C1/B	0	Effect: liner type on leak (flame size) and pressure dynamics for original thickness (#6 vs #7)	USN
7	L1	C1/B	0	Effect: same as in #6	USN
8	L1	C1/B	+2 mm	Effect: fibre+resin in protection layer on leak/flame size and P dynamics in the same laboratory (#5 vs #8)	CEA
9	L1	C1-B	+2 mm	Performance in a "new" fire scenario - jet fire impingement from nearby storage	HSE
10	L1	C1/B	+2 mm	Same as #10, experiment repetition (#9 vs #10)	HSE

Notes:
*   - test performed by the tank manufacturer,
L1   - liner polymer 1 (HDPE cross-linked),
L2   - liner polymer 2 (HDPE not cross-linked),
C1   - carbon fibre reinforced polymer 1,
C2   - carbon fibre reinforced polymer 2,
B   - basalt fibre reinforced polymer.

7.3.7.1 Requirements to the testing conditions

The testing planned for USN was initially suggested to be conducted with the fire source $HRR/A=1$ MW/m^2 (for localised and engulfing burner portions). The reason behind this is that the tank fire resistance rating was previously found by the authors (Kashkarov et al., 2021, 2018) to saturate at this HRR/A. The fire test stages and timing is presented in the picture below, as per (UNECE, 2015; United Nations Economic Commission for Europe, 2013).

Temperature profile of fire test
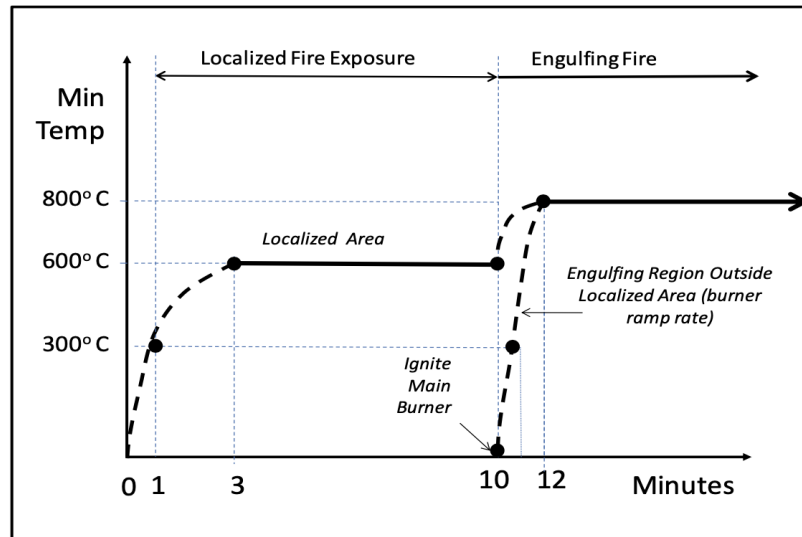
Figure 236: Test portions durations (UNECE, 2015; United Nations Economic Commission for Europe, 2013).

Table 96 below shows the total HRRs and flow rates necessary to achieve the specific $HRR/A=1$ MW/m^2.

Table 96: Propane flow rates for the burner to achieve $HRR/A=1$ MW/m^2.

Fire portion	W, m	L, m	A, m^2	HRR, kW	HRR/A, kW/m^2	Propane flow rates (at NTP)	
						g/s	l/min
Localised	0.5	0.24	0.12	120	1000	2.6	84.7
Engulfing*	0.84	1.29	1.084	1084	1000	23.4	765.2

Note: * - obsolete.

As noted above, it was decided to exclude the engulfing fire stage from the testing procedure, hence the engulfing part of the burner was not used. The flow rate and the total HRR for engulfing portion are given in Table 96 for demonstration purpose.

The burner used in the fire tests at USN was designed at Ulster University and USN. The burner, fuel supply, control and measurement system was produced at USN.

Figure 237: Localised burner portion performance at HRR/A=1 MW/m².

The tests started with burner ignition, localised portion only, the HRR/A was 1 MW/m². There was constant pressure and temperature monitoring inside the tank. After there is a pronounced pressure drop (leak start), the propane supply to the burner was stopped and the water sprinkler was initiated. The aim was to extinguish the combusting resin and hydrogen on the tank until no visual flames appear.

7.3.7.2 Testing of prototype (COPV#6)

Figure 238 demonstrates the positioning of the COPV#6 over the burner prior the test.
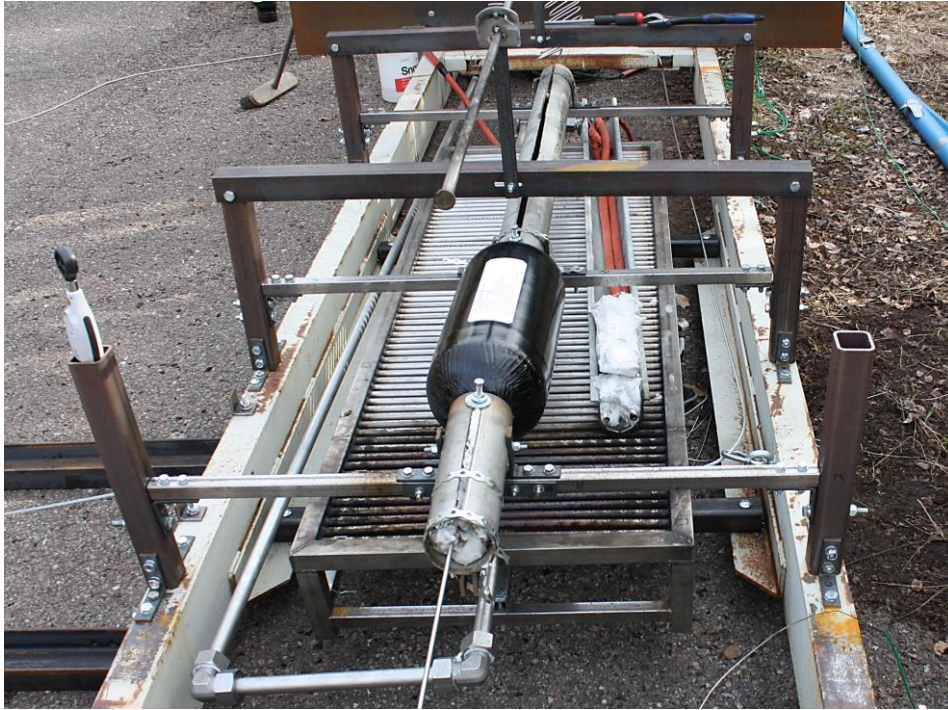
Figure 238: COPV#6 positioning above the localised burner portion prior to the test.

COPV#6 has leaked in a fire, as expected. One of the purposes of this test was to quench the fire source and the combusting resin and hydrogen on the tank after hydrogen leak is initiated, to demonstrate the technology operation (tank blow-down) even if there is no fire source. Another purpose was to measure hydrogen concentration in the vicinity of the tank surface, after the flames had been put out. The water sprinkler which was installed above the tank for this purpose, could not extinguish the leaking hydrogen and the burning resin completely and hydrogen concentration was not measured. Figure 239 demonstrates several snapshots from the experimental video.
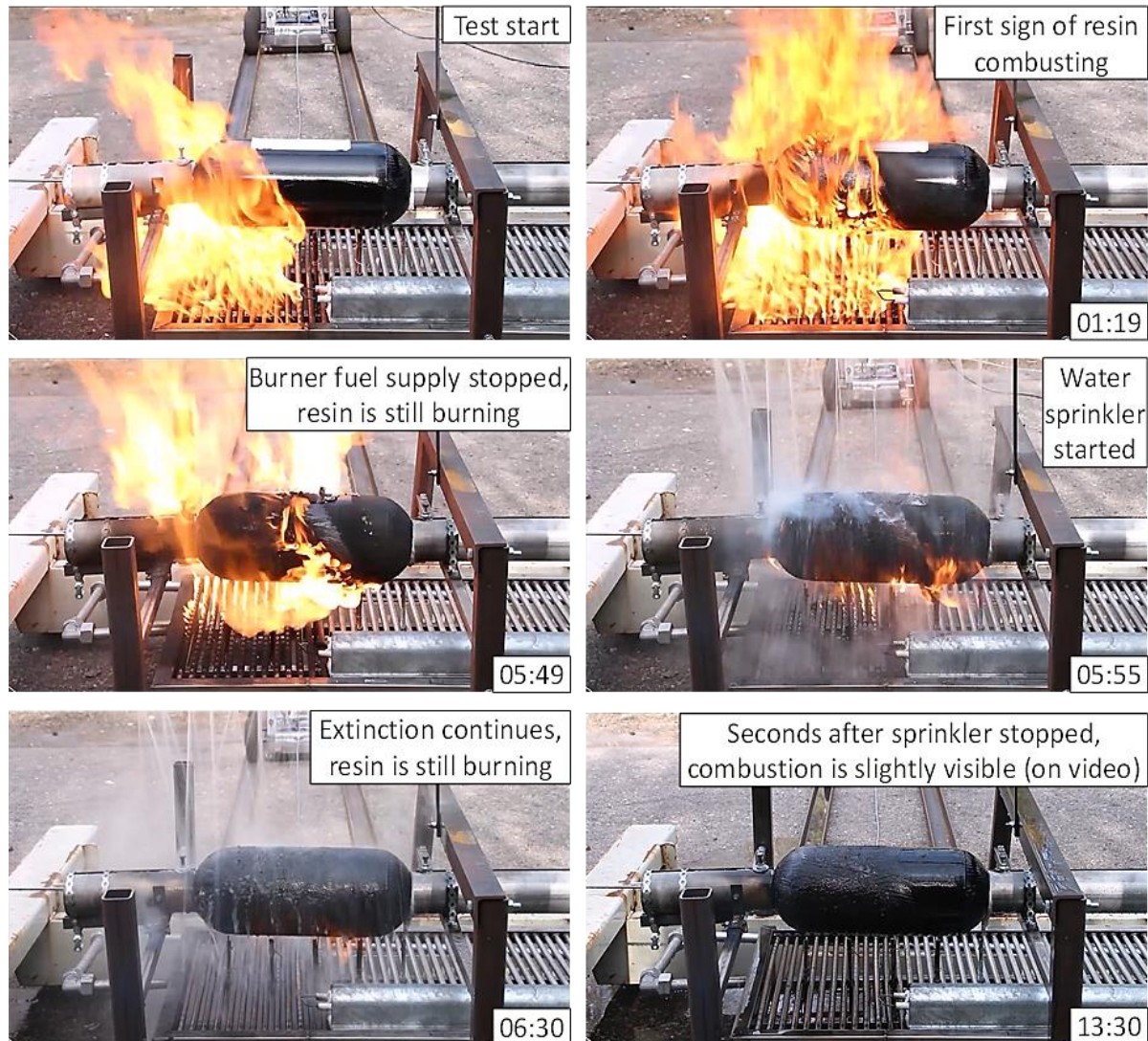
Figure 239: Experiment - COPV#6 in a localised fire of $HRR/A=1$ MW/m²: events captured from the video of the experiment.

The time to COPV#6 prototype leak was 332 s (5 min 32 s), the inside pressure and temperature are presented in Figure 240 below.
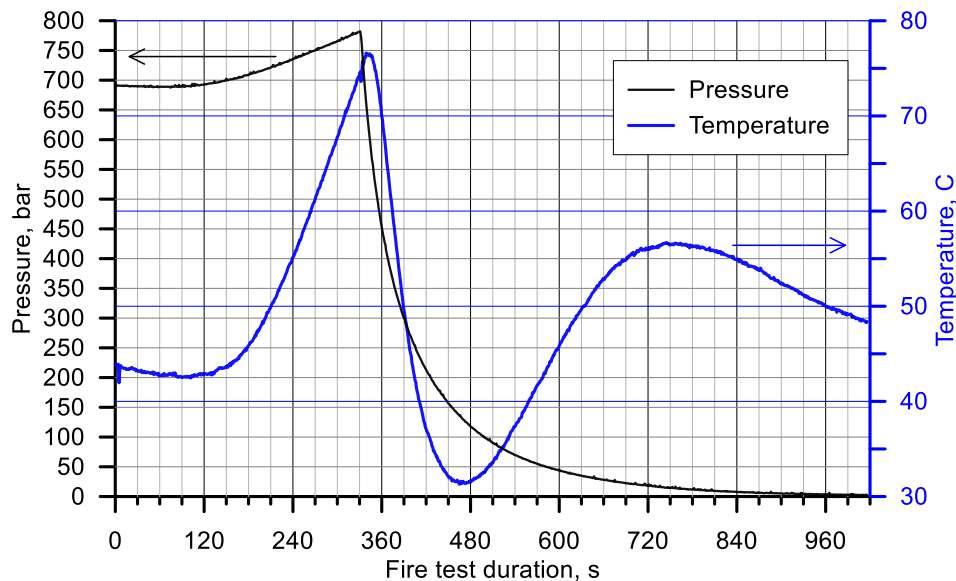
Figure 240: Experiment - COPV#6 in a localised fire of $HRR/A=1$ MW/m² – readings of pressure and temperature inside the tank.

The experiment confirmed that the LNB technology worked in the case of a localized fire of 1MW/m².

7.3.8 Safety technology to prevent tank rupture: tests on prototypes of leak no burst composite type 4 tanks at HSE (ST4.4.6, UU/HSE)

HSE successfully performed ignited hydrogen jet impingement tests on 2 type IV, 7.5 litre, prototype tanks, COPV1 and COPV2. The prototype tanks were charged to 70 MPa with hydrogen and then impinged with an ignited hydrogen jet, positioned 1.0 m from the tank, blowing down from 70 MPa through a 0.6 mm nozzle. This storage pressure and nozzle size would allow a total jet impingement time on the tank for longer than 30 minutes. The pressure and temperature inside the prototype tanks were monitored during the impingement, as well as the blowdown pressure of the jet. Two HD video cameras recorded video from the tests.

The first tank was impinged for around 23 minutes, with data and video recorded successfully, see Figure 241 and Figure 242.

The plan was to undertake a repeat test on the second prototype tanks. However, this test was terminated by the safety control software, due to a leak from the rear of the nozzle, after only 30 seconds of jet impingement. The tank still fully held hydrogen at 70 MPa, without leaks. The opportunity was used to retest the tank with a storage pressure of 70 MPa and a blowdown starting pressure of 70 MPa. Data and video were recorded successfully for both tests.

The main findings are as follows:

- The first tank, COPV1, reached a peak pressure of around 790 bar in 260 seconds from the start of jet impingement, before releasing its hydrogen content via surface leakage over a period of around 3 minutes.
- Tank COPV1 did not experience any catastrophic rupture.

- Tank COPV2 was exposed to an extreme test condition beyond GTR#13 requirements and failed suddenly from a storage pressure of 70 MPa, during the second impingement from an ignited hydrogen jet. The total impingement time was around 5 minutes.

The tests showed encouraging behaviour for the tank under ignited hydrogen jet impingement conditions. Extreme conditions and heat cycling altered the behaviour of the second tank leading to sudden failure of the pressure envelope.
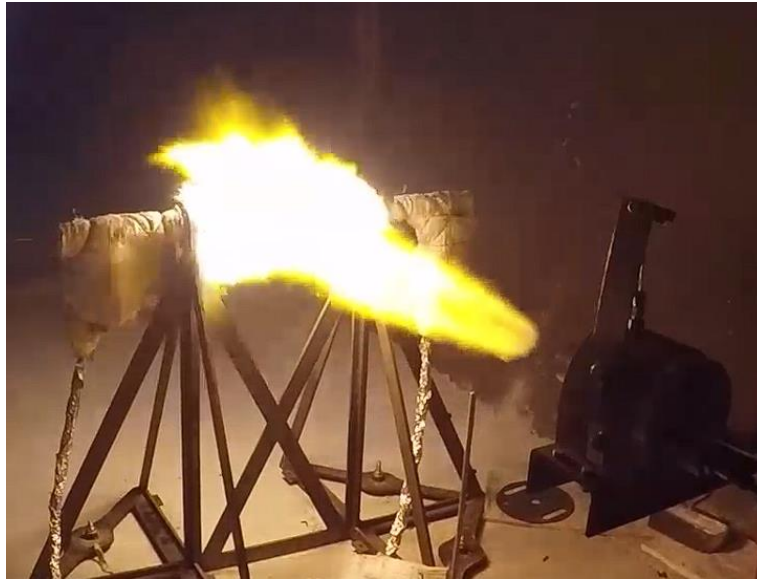
Figure 241: Experiment - COPV#1 prototype in a jet fire impinging test: event captured from the video of the experiment.

Figure 242: Experiment - COPV#1 prototype after the jet fire impinging test.

7.3.9 Shock wave attenuation: tests on shock wave attenuation by using shock absorbing materials, soft bulkheads and sacrificial pre-evacuated volumes (ST4.4.5, PS)

7.3.9.1 Background

Pressurised hydrogen tank rupture, and fast hydrogen deflagration or detonation, leads to an emission of a shockwave. Pressure loads due to shockwaves are the major hazard potential in hydrogen applications. In free field, the area of the shock front increases continuously due to the spatial expansion, which leads to a relatively good attenuation of the amplitude with distance. In tube geometries like tunnels, the shock front propagates in all time with the same tunnel cross section area. Mainly friction and reflection on the tunnel walls are responsible to reduce the amplitude with distances. There is still a question how additional shock-absorbing material can attenuate shockwaves.

7.3.9.2 Objectives

The aim of the experiment is to investigate the attenuation effect of absorbing materials on the shock wave of hydrogen detonation.

7.3.9.3 Knowledge gaps and accident scenarios assessed

Only sparse data is available regarding the dynamics and attenuation of shock waves on absorbing materials.

7.3.9.4 Description

The experiments were performed in the safety vessel V220 (A2). The experimental set-up is mainly the same as described in section Shock wave attenuation: [Experiments on effect of water spray / mist system on shock wave attenuation (Section 7.3.6, PS)]. The emitted shock wave from a cube-shaped 4 g H_2 combustion unit is applied to investigate the shock wave attenuation by different absorbing materials. Probes of selected absorbing materials with an area of 2 m^2 are fixed, at the same height of the combustion tube, on the wall of the safety vessel. A traverse of fast pressure sensors are placed in front of the test probes to measure precisely the incident shock wave history and the waves reflected from the absorbing materials. The reference case is defined as the shock wave reflected from the steel body of the vessel, as shown in Figure 243. In selected cases a high-speed shadow imaging setup was used to record the shock wave reflection behaviour of the tested material.
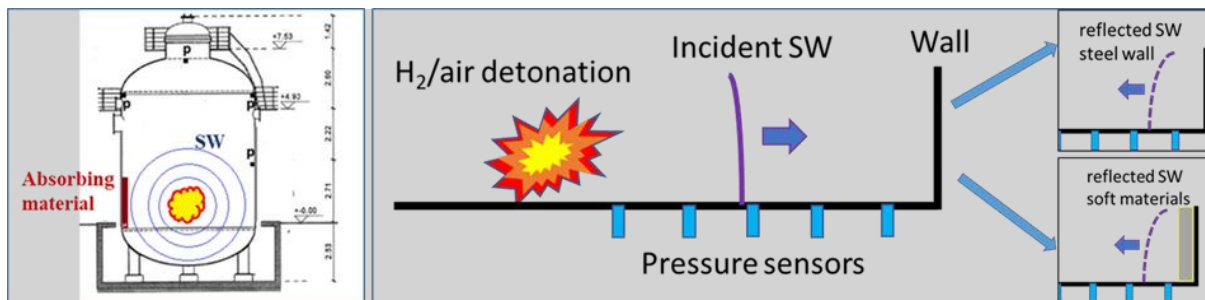
Figure 243: Left, test facility V220 (A2) of HYKA for shock waves attenuation on absorbing material. Right, a sketch showing the principal set-up for the suppression tests of absorbing materials on shock waves.

Different absorbing materials with different thickness are applied to test their attenuation effect of shock wave of hydrogen detonation. Therefore, probes of absorbing material with an area of

~2 m^2 were form-fit mounted on the steel wall of the safety vessel. Figure 244 shows the traverse of the seven pressure sensors and the combustion cube inside the safety vessel.
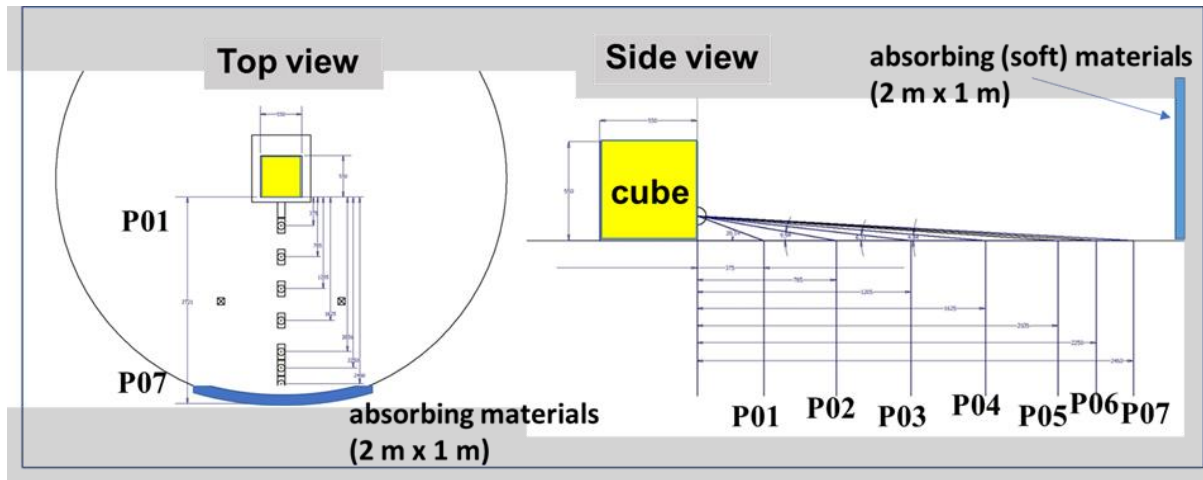
Figure 244: Pressure sensors and combustion cube inside the safety vessel as top and side view.

Figure 245 gives an impression of the experimental setup inside the safety vessel. The combustion unit is covered with a thin (7 µm) plastic film and stabilised with paper tape. The base of the combustion unit is separated from the pressure sensor floor to avoid any disturbing vibration on the sensor signals. The pressure sensor is mounted with special adapters and placed on lead bricks. In this example, a 1 m x 2 m polystyrene plate with a thickness of 120 mm is mounted as test probe form-fit on the vessel wall.
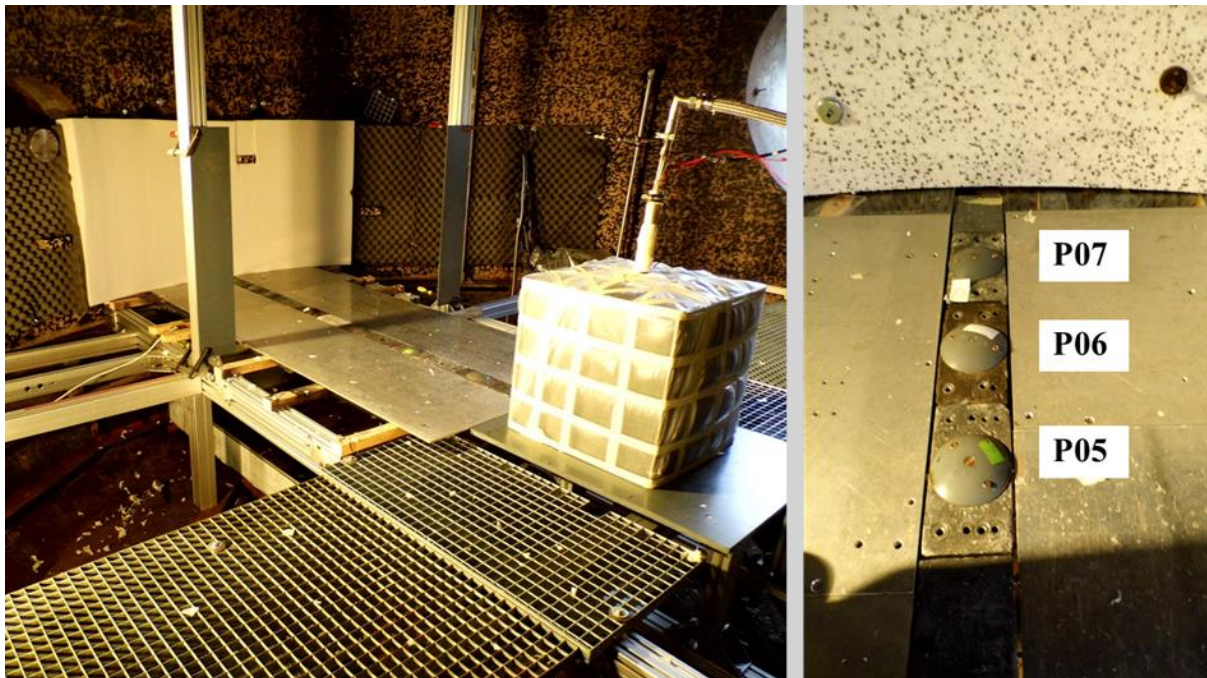
Figure 245: Left, experimental setup inside the safety vessel. Right, pressure sensors (P05, P06; P07) in front of the absorbing material (Polystyrene).

Different absorbing materials with different thicknesses are applied to test their attenuation effect of shock wave of hydrogen detonation. Expanded polystyrene plates are selected as soft

material with closed surface structure. Plates with thickness of 20 mm and 40 mm are used to fix the plates on the steel wall. Figure 246 shows an arrangement of a thickness of 120 mm and the closed surface structure of the material. The used polystyrene has a static resistance to pressure of 100 kPa for 10 % deformation.
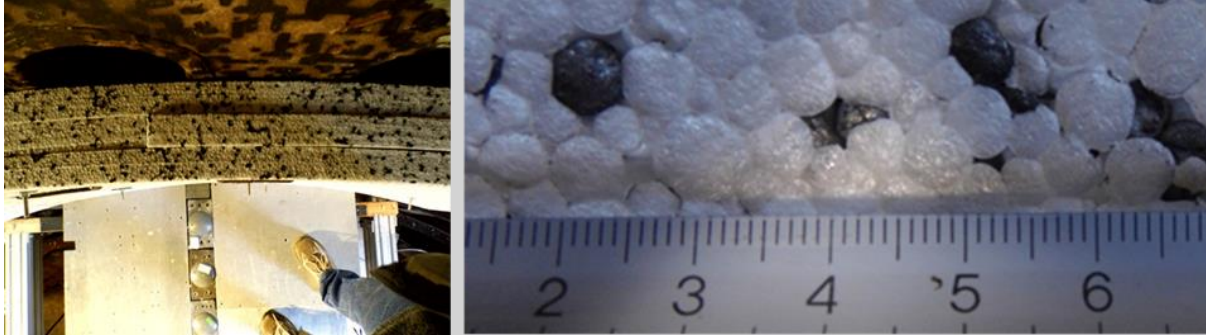
Figure 246: Left, polystyrene plates with thickness of 120 mm (3 x 40 mm) on wall of the safety vessel. Right, the surface structure of the polystyrene plate.

As a testing material with an open surface structure, glass wool plates with 80 mm and 120 mm are selected. The material is advertised as acoustic glass wool with a density of 12.8 kg/m³. Figure 247 shows the installation on the reflected wall (120 mm) and the open glass fibre surface of the material.

Figure 247: Installation of a 120 mm glass wool plates on the reflected wall and macroscopic open glass fibre surface.

As a further target for the shock wave attenuation, polyurethane soft foam plats with thickness of 20 mm and 100 mm are used. This soft material has a density of 25 kg/m³ and its compression hardness is 4 kPa for 40 % deformation. Figure 248 left shows the open surface structure of the polyurethane soft foam plats. The bubble size of the fixed foam lies at ~0.33 mm.
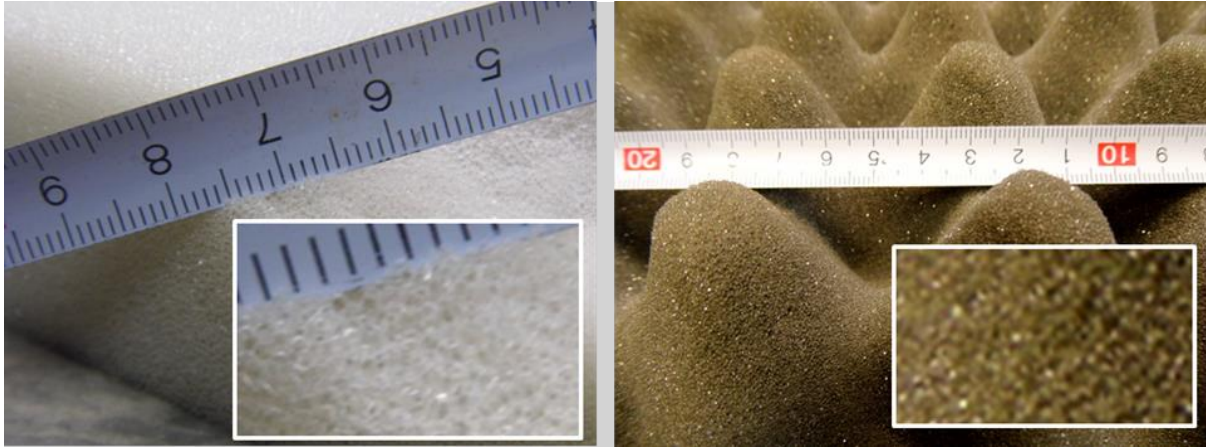
Figure 248: Left, open surface structure of the polyurethane soft foam plats. Right, special structured acoustic polyurethane foam plates.

Additional to this planar polyurethane soft foam plate, a special structured acoustic foam polyurethane plate is designed for acoustic wave attenuation. Figure 248 right shows a black acoustic polyurethane plate. The waveform structure of the surface can impinge acoustic wave to diffuse. Due to reflection in different direction, an attenuation of the level of sound takes place. This material has a density of 28 kg/m³ with a compression hardness of 4 kPa for 40 % deformation. The thickness of the investigated acoustic polyurethane plates was 50 mm. The test matrix with materials and thicknesses is shown in Table 97. To investigate the attenuation effect of the absorbing materials on shock wave, three tests with reflection from the steel body of the vessel were performed as a reference.

Table 97: Test matrix of absorbing materials.

Absorbing material	Polystyrene	Foam polyurethane	Acoustic glass wool	Others
Thickness, **20 mm**	X	X		Steel; XXX
Thickness, **120 mm**	X	X	X	**Acoustic foam** Thickness,50 mm X
Thickness, **200 mm**	X	XX	X	

7.3.9.5 *Results*

The used combustion unit generates a highly repeatable H_2-detonation with 4 g H_2. The picture series in Figure 249 left taken from a high-speed movie (5000 f/s) shows the high uniformity of the detonation in cube geometry. For the visualisation of the emitted shock wave, a large-scale shadow setup with a frame rate of 40000 f/s was used, as shown in Figure 249 right.
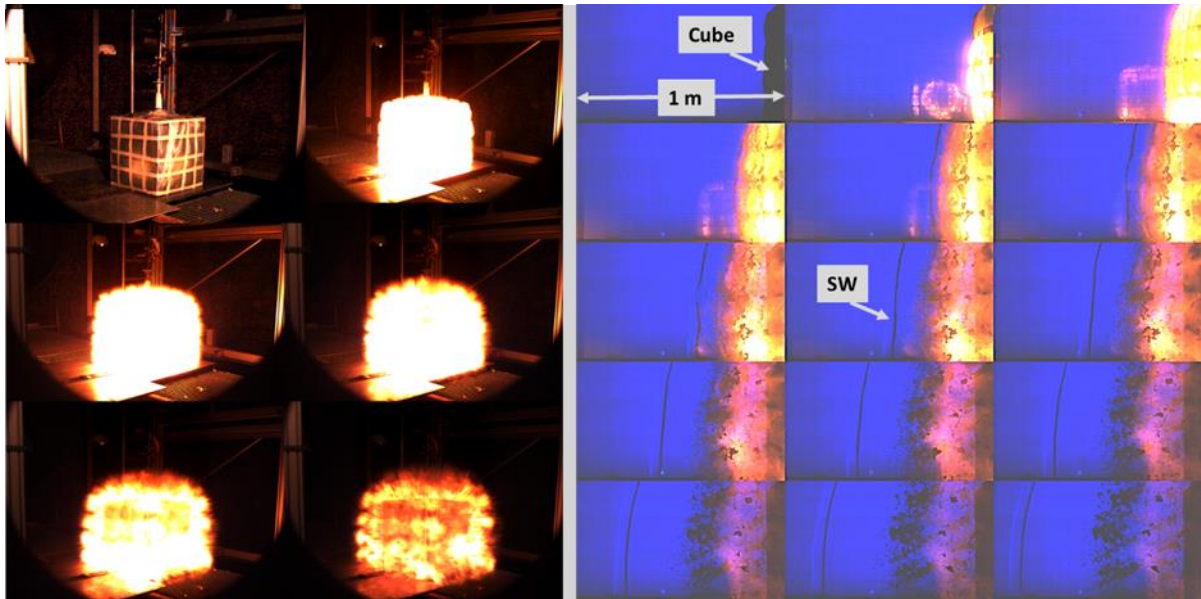
Figure 249: Left, picture series taken from a high-speed movie (5000 f/s). Right: visualisation of the emitted shock wave via large-scale shadow setup with a frame rate of 40000 f/s.

The first picture shows one cube side. In the second picture, the detonation inside the cube is present and the thin plastic film blows slightly up. The emitted shock wave is visible in the fifth picture as a black line. The shock wave looks planar and propagates undisturbed from the combustion products inside the test area in the direction towards the reflection wall. The shock wave was measured quantitatively with the gauges (P1 to P7) in side on configuration. Figure 250 show the shock wave propagation and its reflection on the wall by using the pressure history of the gauges (P1 to P7). The left side shows the shock wave propagation from the combustion unit and its reflection from the steel wall; the right side visualises the shock wave reflection from the acoustic foam material (50 mm). It is directly visible that reflected shock wave from the steel wall has a clear identified shock front in contrast to the reflected shock wave from the acoustic foam material, which is not very clear.
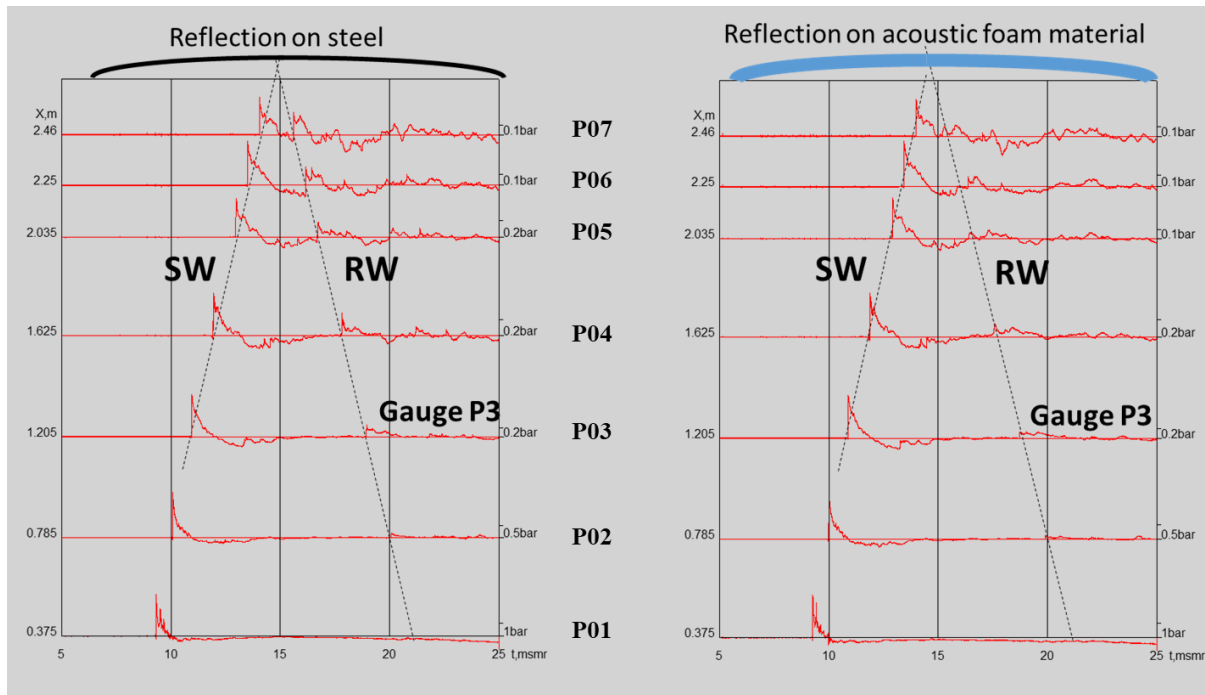
Figure 250: Shock wave propagation and its reflection on the wall using the pressure history is of the gauges. Left: reflection on the steel wall. Right: reflection on acoustic foam material (50 mm).

The incident shock wave shows a negative phase with a duration of several milliseconds after the positive shock front. The reflected positive shock front overlaps with the negative phase of the incident shock wave for the gauges near wall. For the gauge P3, the incident shock wave and its reflection is separated (Figure 251). The pressure histories from gauge P3 for all tests are compared in Figure 252. It is obvious that all curves from the incidence shocks collapse together in a very good agreement, including all small uncertainties from an ideal shape of a shock wave pressure history. By contrast, the reflected shock waves arrive with time shifts. It is caused by the different propagation distances due to the different thickness of the test materials. This effect leads itself to a difference in the magnitude of the reflected shock wave. However, this slight attenuation effect in a distance of 2.5 m is not dominant in this application and is not considered in the data interpretation either.
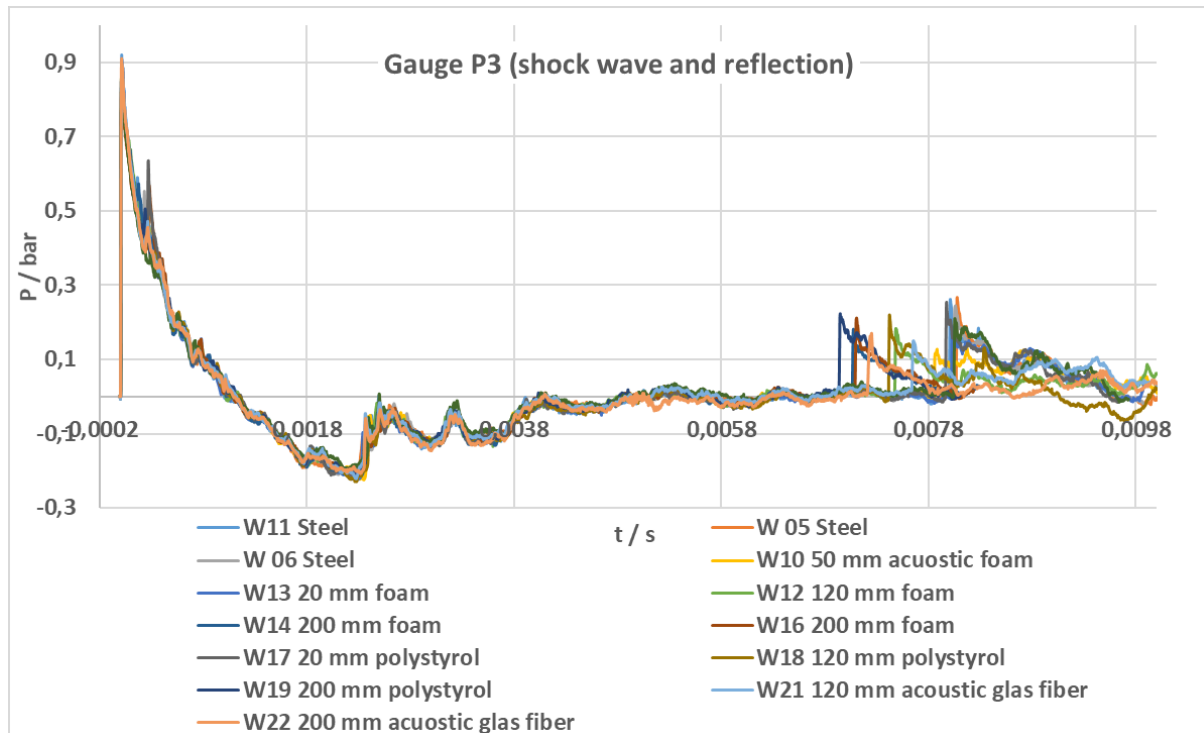
Figure 251: Comparison of the pressure histories from gauge P3 for all tests.

All arrival times of the reflected shockwaves were set to zero to highlight the differences of amplitudes and impulse. Figure 252 and Figure 253 show the comparison of the reflected shock wave (gauge P3) from tests with reflection on absorbing material with the reference test with a reflection on the steel wall.
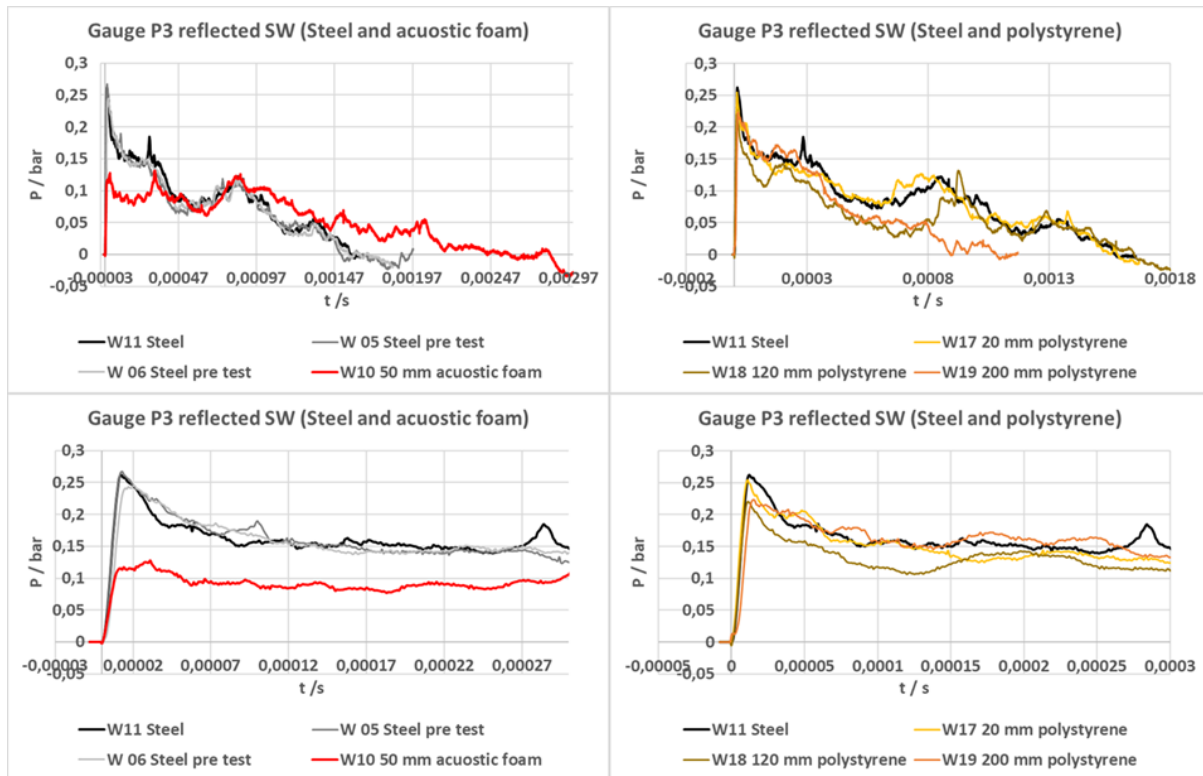
Figure 252: Comparison of the reflected shock wave (gauge P3) from tests with reflection on absorbing material with the reference test with a reflection on the steel wall.

The left side of Figure 252 shows the pressure histories of the reflection (gauge 3) for the three reference tests (steel wall) and the test with the acoustic polyurethane structured plates (50 mm). The top diagram shows the complete positive shock wave, while the below is the zoomed amplitude in a shorter time range. It is visible that all reference tests (reflection on steel) shows a nicely identical shape. The shape of the pressure history of the reflection on acoustic polyurethane plate (red line) looks different. The magnitude of the amplitude reaches 50 % of that in reference test. On the other hand, the duration of the positive amplitude is roughly two times longer than that of all steel tests. In the right side of Figure 252, the shock reflection on polystyrene plates with different thickness is compared with the steel reference case. The pressure history of the 20 mm plate looks very close to the steel reference. The reflection on the 120 mm and 200 mm polystyrene plates shows only a slight attenuation effect. It can be seen from the zoomed plot in Figure 252 bottom right.
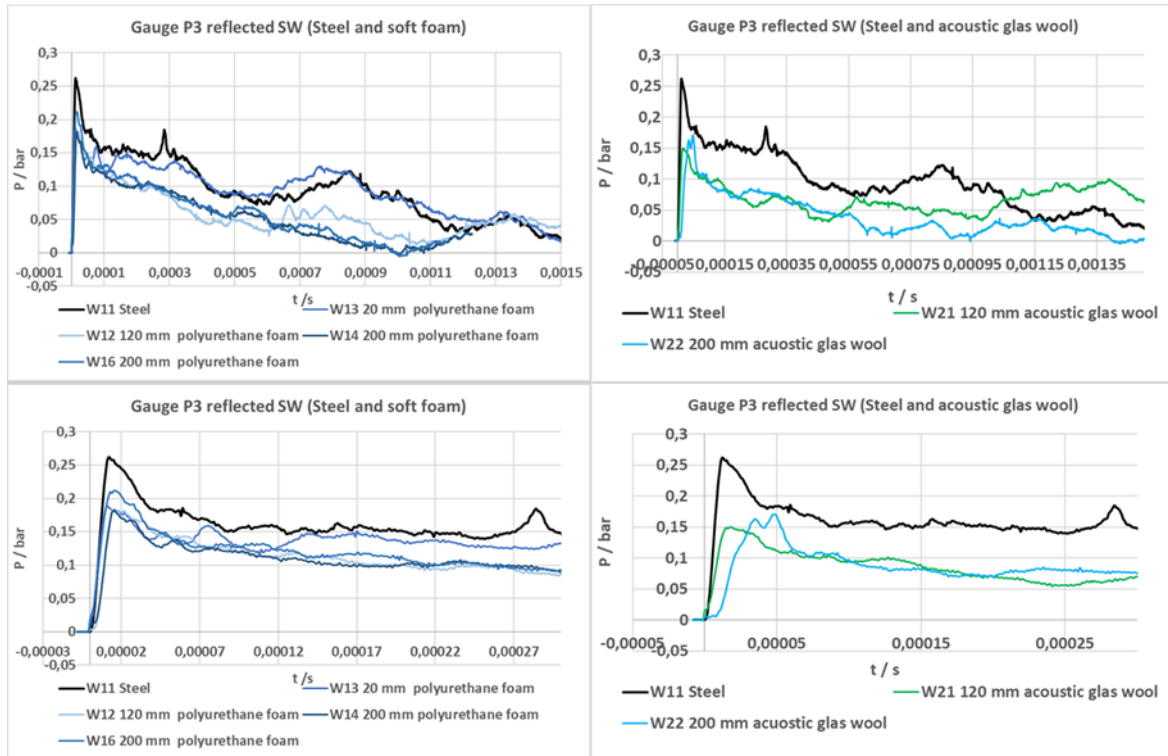
Figure 253: Comparison of the reflected shock wave (gauge P3) from tests with reflection on absorbing material with the reference test with a reflection on the steel wall.

The left side of Figure 253 shows the pressure histories of the reflection (gauge 3) from polyurethane soft foam (thickness 20 mm, 120 mm and 200 mm) and the reference test (steel wall). The top diagram shows the complete positive shock wave, while the below is the amplitude in a reduced time scale. The reflection on the polyurethane soft foam shows a clear attenuation effect regarding the amplitude. The difference between the plate with 20 mm and the both tests with 200 mm thickness is very low. In the right side of Figure 253, the shock reflection on glass wool plates with different thickness is compared with the steel reference. There is a clear reduction of the shock amplitude due to the absorbing material. However, the attenuation effect is almost the same for both investigated thicknesses (120 mm; 200 mm).

The top left plot in Figure 254 shows the amplitudes from all pressure gauges and all tests in the distance of the reflected wall (x = 0). The amplitude of the incidence shock wave decays fast at earlier stage, then decays moderately near the reflection. The red curve represents the measured maximum value from the three reference tests with reflection on steel. This value is taken as the reference value and is normalized to 100 %. To visualize the attenuation effect due to the shock absorbing material, the values of all amplitudes are expressed in this normalized way. In Figure 254 top right, the normalized amplitudes from the maximum values of the reference steel wall tests are compared with the normalized data from the acoustic polyurethane structured plates (50 mm) and the acoustic glass wool. All incident shock amplitudes are nearly equal and close to 100 %. The results of the reflected amplitudes are 100 % for the reference test. The top-right plot shows a reduction of the shock wave amplitude due to the reflection on the absorbing material of ~50 % in average. Remarkable is that the observed attenuation effect decreases with increasing propagation distance of the wave. The observed attenuation effect of the soft polyurethane foam looks constantly in a range of ~40 % and is independent of the

thickness of the probes, as shown in Figure 254 bottom left. The investigated polystyrene plates show a value of ~ 20 % attenuation. It is the lowest effect in the test series. In the case, the thickness of the test plates looks negligible too.
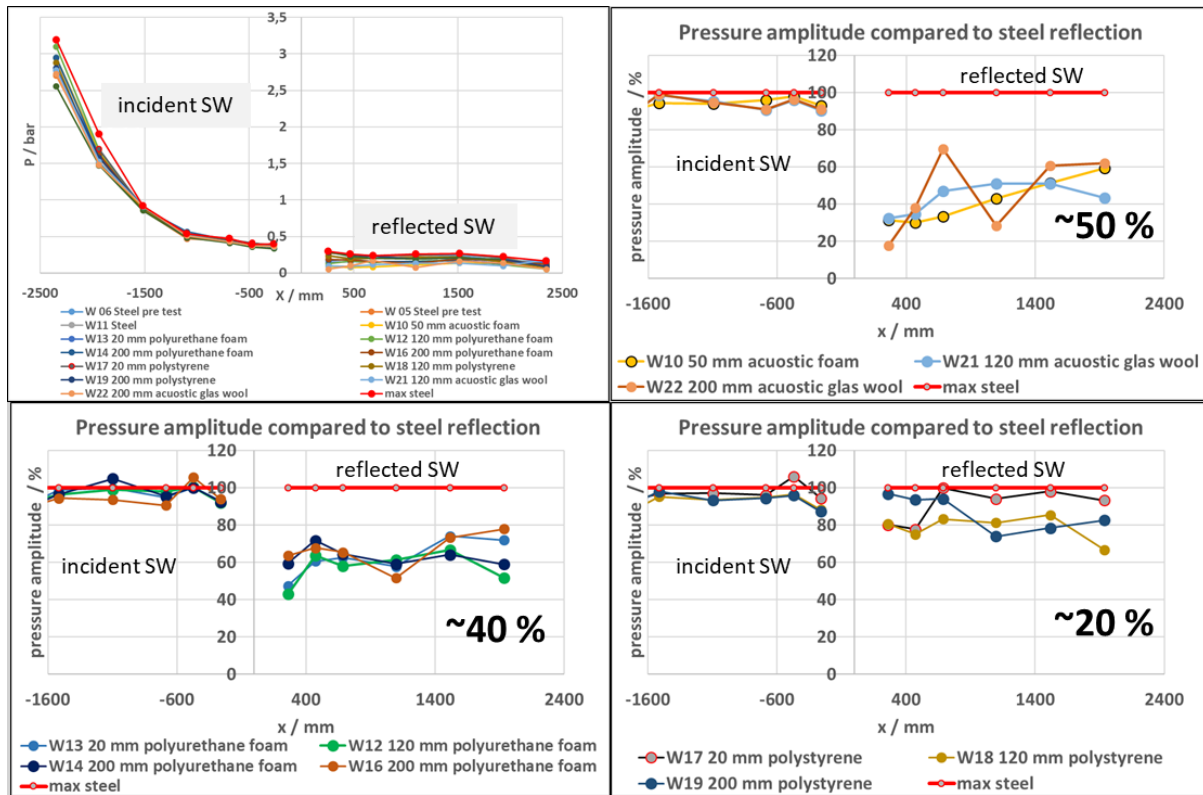
Figure 254: Top left, amplitudes from all pressure gauges and all tests in the distance of the reflected wall (x = 0). Comparison of the pressure amplitudes with normalized steel wall reflection.

A proper evaluation of the positive impulse of the reflected shock wave is possible only for pressure gauge P2 and P3. Figure 255 shows the impulse values plotted against the thickness of the investigated absorbing material. For the reference tests (reflection on the steel wall), the thickness is zero, denoted as red points. Remarkable is that the measured positive impulse for the structured acoustic polyurethane plate with a thickness of 50 mm (black points) is higher than that of the steel reference (referring to Figure 252). All other plates including the polyurethane present a decreasing positive impulse with increasing thickness of the tested material. The all test material with a thickness of 200 mm shows an attenuation of the positive impulse of ~50 % compared to the reference value (steel wall). In contrast to the amplitude analysis, a clear influence of the absorbing material thickness is observed to the attenuation of the positive impulse.
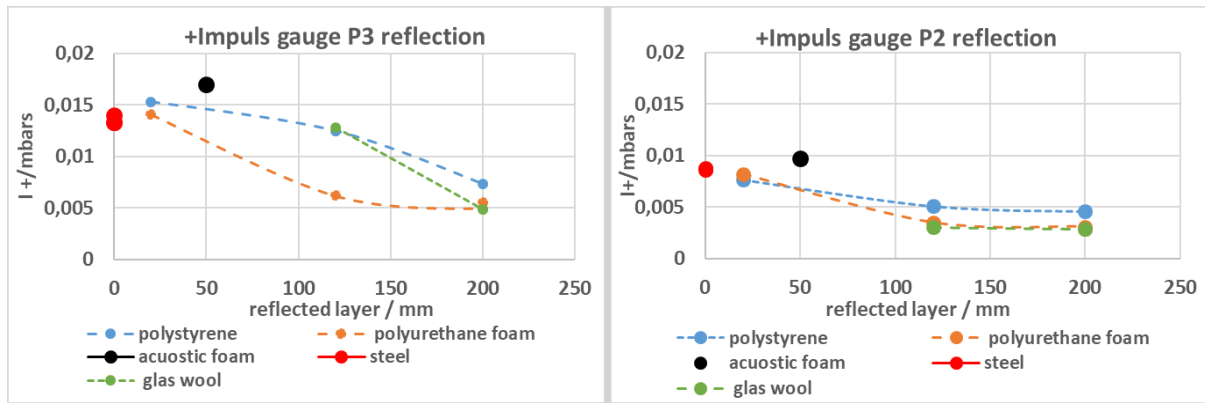
Figure 255: Positive impulse values plotted against the thickness of the investigated absorbing material for pressure gauge P2 and P3.

7.3.9.6   Conclusions

The shock wave attenuation due to reflection on soft materials was investigated inside a vessel of 220 m³ volume. A cube sized (0.55 m) combustion unit filled with 4 g H_2 was used to provide reproducible shock wave from an unconfined H_2/air detonation.

A shock wave amplitude attenuation, expressed as difference of the reflected shock wave amplitude from the steel wall to the reflected shock wave amplitude from absorbing (soft) materials was found:

> ~50 % Glass wool (fibre) and structured acoustic polyurethane
>
> ~40 % Polyurethane foam (soft foam)
>
> ~20 % Polystyrene

Regarding the shock wave amplitude attenuation, clear influence of the thickness of the absorbing material was not observed.

For the shock wave positive impulse attenuation, an influence of the thickness of the absorbing material was observed. The positive impulse attenuation increases with increasing thickness of the absorbing material. An exception is the structured acoustic polyurethane foam. Its' reflected positive impulse is higher than the reflected positive impulse from the steel wall.

8. References

Ames Research Staff, 'Equations Tables and Charts for Compressible Flow', NACA Report 1135, 1951.

BS EN 12390-1:2021 British Standards Institution. (2021). BS EN 12390-1:2021 - Testing hardened concrete. BSI Standards Publication.

BS EN 12504‑4:2021 British Standards Institution. (2021). BS EN 12504‑4:2021 Testing concrete in structures Part 4: Determination of ultrasonic pulse velocity. In BSI Standards Publication (pp. 6, 19.).

BS EN 12664:2001 British Standards Institution. (2001). BS EN 12664:2001. Thermal performance of building materials and products. Determination of thermal resistance by means of guarded hot plate and heat flow meter methods. Thick products of high and medium thermal resistance. British Standards Publications, 3(1).

Cirrone, D., Shentsov, V., Kashkarov, S., Dadashzadeh, M., Makarov, D., & Molkov, V. (2019). Deliverable 1.2 Report on hydrogen hazards and risks in tunnels and similar confined spaces (Issue Hytunnel-CS).

Coolprop, https://github.com/CoolProp/CoolProp/blob/master/dev/fluids/Helium.json

Coughlan, D., Diez, R., Comins, J., & Stärk, A. (2017). Crossrail project: Use of sprayed concrete tunnel linings on London's elizabeth line. Proceedings of the Institution of Civil Engineers: Civil Engineering, 170(5), 39–46. https://doi.org/10.1680/jcien.16.00026.

Curran, D.R. (1966). Underground storage of ammunition: experiments concerning accidental detonation in an underground chamber. Norwegian Defence Construction Service.

Fang, Y., Zou, Y.-L., Zhou, J., Yao, Z., Lei, S., Yang, W. (2019). Field Tests on the Attenuation Characteristics of the Blast Air Waves in a Long Road Tunnel: A Case Study. Shock Vib. 2019, 1–11. https://doi.org/10.1155/2019/9693524

Dadashzadeh, M., Makarov, D., & Molkov, V. (2017). Non-adiabatic blowdown model: a complimentary tool for the safety design of tank-TPRD system. International Conference on Hydrogen Safety, September 11-13, 2018, Hamburg, Germany, 1–18.

Dadashzadeh M., Makarov D., Kashkarov S. and Molkov V. (2019), Non-adiabatic under-expanded jet theory for blowdown and fire resistance rating of hydrogen tank, 8th Int. Conf. on Hydrogen Safety, Adelaide, Australia, 24-26 Sept. 2019.

E-laboratory. (2020). FCH2 education. FCH2 Education. https://fch2edu.eu/home/e-laboratory/

European Committee for Standardization. (1992). CEN - EN 1992-1-2 Eurocode 2: Design of concrete structures - Part 1-2: General rules - Structural fire design.

Goldhahn, E., & Seume, J. (2007). The background oriented schlieren technique: sensitivity, accuracy, resolution and application to a three-dimensional density field. Experiments in fluids, 43(2), 241-249.Grune J, et al., Experimental investigation of hydrogen air deflagrations

and detonations in semi-confined flat layers, Journal of Loss Prevention in the Process Industries, 26 (2013) 317-326

Grune J, et al., Experimental investigation of fast flame propagation in stratified hydrogen air mixtures in semi-confined flat layers; Journal of Loss Prevention in the Process Industries, 26 (2013) 1442-1451

Grune, J., Sempert, K., Friedrich, A., Kuznetsov, M., Jordan, T., Detonation wave propagation in semi-confined layers of hydrogen–air and hydrogen–oxygen mixtures, International Journal of Hydrogen Energy, 16 March 2017, Vol.42(11), pp.7589-7599

Hall, David. J. and S. Walker. "Scaling rules for reduced-scale field releases of hydrogen fluoride." Journal of Hazardous Materials 54 (1997): 89-111.

Hertz K.D. & Sørensen L.S. (2005): Test method for spalling of fire exposed concrete, Fire Safety Journal, 40, pp. 466-476

Hertz, K. D. (2019) Design of Fire-resistant Concrete Structures. 1st edition. ICE Publishing; Thomas Telford limited; London (UK); ISBN 978-0-7277-6444-7; Available at: www.icebookshop.com. Last accessed: 10.07.2022

Hertz, K. D. (2003). Limits of spalling of fire-exposed concrete. Fire Safety Journal, 38(2), 103–116. https://doi.org/10.1016/S0379-7112(02)00051-6

HyTunnel-D111 (2009) Internal project on investigating the use of hydrogen vehicles in road tunnels, Deliverable D111, 15 April 2009. Accessible from: http://www.hysafe.net/download/1763/Hyunnel_Final%20ReportDraft_20Feb09_final.pdf

HyTunnel-CS D1.3, 'Deliverable D1.3 Report on selection and prioritisation of scenarios', November 2019.

HyTunnel-CS D2.2. 'Deliverable D2.2 Intermediate report on analytical, numerical and experimental studies', August 2020.

HyTunnel-CS D2.3. 'Deliverable D2.3 Final report on analytical, numerical and experimental studies on hydrogen dispersion in tunnels, including innovative prevention and mitigation strategies, February 2022.

HyTunnel-CS D3.3. 'Deliverable D3.3 Final report on analytical, numerical and experimental studies on fires, including innovative prevention and mitigation strategies', February 2022.

HyTunnel-CS D4.3. 'Deliverable D4.3 Final report on analytical, numerical and experimental studies on explosions, including innovative prevention and mitigation strategies', February 2022.

International Organization for Standardization. (1999). ISO 834-1:1999 Fire-resistance tests — Elements of building construction — Part 1: General requirements. In ISO.org.

Kandula, M., Freeman, R. (2008), 'On the Interaction and coalescence of Spherical Blast Waves', Shock Waves 18, 21–33.

Kashkarov, S., Makarov, D., Molkov, V. (2021). Performance of hydrogen storage tanks of Type IV in a fire: effect of the state of charge. Hydrogen - SUBMITTED.

Kashkarov, S., Makarov, D., Molkov, V. (2018). Effect of a heat release rate on reproducibility of fire test for hydrogen storage cylinders. Int. J. Hydrog. Energy 43, 10185–10192. https://doi.org/10.1016/j.ijhydene.2018.04.047

Kato, M. & Launder, B.E. (1993). The modeling of turbulent flow around stationary and vibrating square cylinders. In Ninth Symposium on Turbulent Shear Flows. Kyoto, Japan, August 16-18

Kuznetsov, M., Pariset, S., Friedrich, A., Stern, G., Travis, J., & Jordan, T. (2015). Experimental investigation of non-ideality and non-adiabatic effects under high pressure releases. International Journal of Hydrogen Energy, 40(46), 16398–16407. https://doi.org/10.1016/j.ijhydene.2015.10.037

Kuzentsov, M. J. Grune, A. Friedrich, K. Sempert, W. Breitung and T. Jordan, Hydrogen-Air Deflagrations and Detonations in a Semi-Confined Flat Layer, In: Fire and Explosion Hazards, Proceedings of the Sixth International Seminar (Edited by D. Bradley, G. Makhviladze and V. Molkov), 2011, pp 125-136, ISBN: 978-981-08-7724-8, doi:10.3850/978-981-08-7724-8_02-05.

Kuzentsov, M. Jorge Yanez, Joachim Grune, Andreas Friedrich, Thomas Jordan, Hydrogen Combustion in a Flat Semi-Confined Layer with Respect to the Fukushima Daiichi Accident, Proceedings of ICAPP '12, Chicago, USA, June 24-28, 2012, Paper 12419, pp. 1-10.

LaChance, J. (2010). Analyses to support development of risk-informed separation distances for hydrogen codes and standards, in: 6th ISCARW. Belfast.

Leachman J. W., Jacobsen R. T., Penoncello S. G., and Lemmon E. W., Fundamental Equations of State for Parahydrogen, Normal Hydrogen, and Orthohydrogen, J. Phys. Chem. Ref. Data, 38 (2009) 721-748.

Lundberg J., Sikka R., Vaagsaether K. Bjerketvedt D., "Water Mist Characteristics for Explosion Mitigation", to be presented at 10th Int. Seminar on Fire and Explosion Hazards, 22-27 May 2022, Oslo, Norway.

Machalek D.M., Anleu G.B., Hecht E.S., Influence of non-equilibrium conditions on liquid hydrogen storage tank behavior, 9th Int. Conf. on Hydrogen Safety, 21-23 Sept. 2021, Edinburgh, UK.

Mcnamee, R. J., & Jansson, R. (2015). Fire Spalling of Concrete : Theoretical and Experimental Studies Fire Spalling of Concrete Theoretical and Experimental Studies. October 2013.

Mindeguia, J.-C., Pimienta, P., Carre, H., & La Borderue, C. (2009). Experimental study on the Contribution of Pore Vapour Pressure to the Thermal Instability Risk of Concrete. 1st International Workshop of Concrete Spalling Due to Fire Exposure, Leipzig.

Mogi, T.; Nishida, H.; Horiguchi, S. (2005). Flame Characteristics of high-pressure hydrogen gas jet. First International Conference on Hydrogen Safety.

Mohammed, H., Ahmed, H., Kurda, R., Alyousef, R., & Deifalla, A. F. (2022). Heat-Induced Spalling of Concrete: A Review of the Influencing Factors and Their Importance to the Phenomenon. Materials, 15(5). https://doi.org/10.3390/ma15051693

Molkov, V., Makarov, D., & Bragin, M. (2009). Physics and modelling of underexpanded jets and hydrogen dispersion in atmosphere. In Russian Academy of Sciences: Vol. Physics of (pp. 146–149).

Molkov, V, & Saffers, J. (2012). Introduction to hydrogen safety engineering. In International Conference on Hydrogen Safety (ICHS2011). http://www.hysafe.org/IAHySafe

Molkov, Vladimir, & Saffers, J.-B. (2013). Hydrogen jet flames. International Journal of Hydrogen Energy, 38, 8141–8158. https://doi.org/10.1016/j.ijhydene.2012.08.106

Molkov, V., Dery, W. (2020). The blast wave decay correlation for hydrogen tank rupture in a tunnel fire. Int. J. Hydrog. Energy 45, 31289–31302. https://doi.org/10.1016/j.ijhydene.2020.08.062

Molkov, V., Kashkarov, S. (2015). Blast wave from a high-pressure gas tank rupture in a fire: Stand-alone and under-vehicle hydrogen tanks. Int. J. Hydrog. Energy 40, 12581–12603. https://doi.org/10.1016/j.ijhydene.2015.07.001

Molkov, V.V., Cirrone, D.M.C., Shentsov, V.V., Dery, W., Kim, W., Makarov, D.V. (2021). Dynamics of blast wave and fireball after hydrogen tank rupture in a fire in the open atmosphere. Int. J. Hydrog. Energy 46, 4644–4665. https://doi.org/10.1016/j.ijhydene.2020.10.211

Molkov V., Dadashzadeh M., Kashkarov S., Makarov D., Performance of hydrogen storage tank with TPRD in an engulfing fire, Int. J of Hydrogen Energy, 46 (2021) 36581-36597

Momferatos, G., Giannissi, S.G., Tolias, I.C., Venetsanos, A.G., Vlyssides, A. & Markatos, N. (2021). Vapor cloud explosions in various types of confined environments: CFD analysis and model validation. Loss Prevention and Safety Promotion in the Process Industries, accepted

Mróz, K. (2016). Assessment of spalling risk - Dissertation outline. October 2016, 52. https://doi.org/10.13140/RG.2.2.34074.85447

Petitpas, G., Simulation of boil-off losses during transfer at a LH2 based hydrogen refueling station. International Journal of Hydrogen Energy, 43 (2018) 21451-21463.

Phan, L. T. (2008). Pore pressure and explosive spalling in concrete. Materials and Structures, 41, 1623–1632.

Proust, C., Jamois, D., & Studer, E. (2011). High pressure hydrogen fires. International Journal of Hydrogen Energy, 36(3), 2367–2373. https://doi.org/10.1016/j.ijhydene.2010.04.055

Pursell, M., & Garcia, M. (2019). Deliverable 1.3 Report on Selection and Prioritisation of Scenarios.

Raffel, M. (2015). Background-oriented schlieren (BOS) techniques. Experiments in Fluids, 56(3), 1-17.

Roberts, I. L., Coney, J. E. R., & Gibbs, B. M. (2011). Estimation of radiation losses from sheathed thermocouples. Applied Thermal Engineering, 31(14–15), 2262–2270. https://doi.org/10.1016/j.applthermaleng.2011.03.020

Saleheen, Z., Krishnamoorthy, R. R., & Nadjai, A. (2022). A review on behavior, material properties and finite element simulation of concrete tunnel linings under fire. Tunnelling and Underground Space Technology, 126(May), 104534. https://doi.org/10.1016/j.tust.2022.104534

Schefer, R. W., Houf, W. G., Bourne, B., & Colton, J. (2006). Spatial and radiative properties of an open-flame hydrogen plume. International Journal of Hydrogen Energy, 31(10), 1332–1340. https://doi.org/https://doi.org/10.1016/j.ijhydene.2005.11.020

Shuttleworth, P. (2001). Fire Protection of Concrete Tunnel Linings. Third International Conference on Tunnel Fires, 157–165.

Smith, A.C., Sapko, M.J. (2005). Detonation wave propagation in underground mine entries. J. Mine Vent. Soc. South Afr. 58, 20–25.

Sørensen L.S. Concrete types – proposals. Note, September 2019, Department of Civil Engineering, Technical University of Denmark

Sørensen, L.S. Spalling tests – Exposure of concrete walls with gas flame. Subtask 3.4.3 Fire effect on structure integrity and concrete spalling. Presented on HyTunnel-CS project, 6th Project Meeting, held on 15-17 September 2021

Tamura, Y., Takahashi, M., Maeda, Y., Mitsuishi, H., Suzuki, J., Watanabe, S. (2006). Fire Exposure Burst Test of 70MPa Automobile High-pressure Hydrogen Cylinders, in: Society of Automotive Engineers of Japan Annual Autum Congress 2006. Presented at the Society of Automotive Engineers of Japan Annual Autum Congress 2006, Sapporo.

Tolias, I. C ., & Venetsanos, A. G. (2016). Comparison of Convective Schemes in Hydrogen. Conference: 6th International Conference on Hydrogen Safety (ICHS2015), 1–12

Tolias, I.C. & Venetsanos, A.G. (2018). An improved CFD model for vented deflagration simulations – Analysis of a medium-scale hydrogen experiment. International Journal of Hydrogen Energy, 43(52), pp.23568–23584

Tolias, I.C., Venetsanos, A.G., Kuznetsov, M. & Koutsoukos, S. (2020). Evaluation of an improved CFD model against nine vented deflagration experiments. International Journal of Hydrogen Energy, 46(23), pp.12407–12419

UNECE, 2015. Addendum 133 – Regulation No. 134. Uniform provisions concerning the approval of motor vehicles and their components with regard to the safety-related performance of hydrogen fuelled vehicles (HFCV) (No. E/ECE/324/Rev.2/Add.133)

United Nations Economic Commission for Europe, 2013. Global technical regulation on hydrogen and fuel cell vehicles. Addendum 13: Global technical regulation No. 13. Global Registry. UNECE, Global Registry.

Venetsanos, A.G., Papanikolaou, E.A. & Bartzis, J.G. (2010). The ADREA-HF CFD code for consequence assessment of hydrogen applications. International Journal of Hydrogen Energy, 35(8), pp.3908–3918.

Venetsanos A.G. and Giannissi S.G., Release and dispersion modeling of cryogenic under-expanded hydrogen jets, Int. J of Hydrogen Energy, 42, (2017) 7672-7682.

Venetsanos A.G., Homogeneous non-equilibrium two-phase choked flow modelling, Int. J. of Hydrogen Energy, 43 (2018) 22715-22726.

Venetsanos A.G., Choked two-phase flow with account of discharge line effects, 8th International Conference on Hydrogen Safety, Adelaide, Australia, 24-26 Sept. 2019

Venetsanos A.G., e-Lab HFE based tools, https://www.youtube.com/watch?v=3iTAt3HdAWI, 2020.

Venetsanos A., An engineering tool for discharge calculations, PRESLHY project dissemination conference, 5-6 May 2021 (virtual event). https://hysafe.info/wp-content/uploads/sites/3/2021/05/4_5_Venetsanos_engineering_tool_discharge.pdf

Venetsanos, A.G., Giannissi, S.G., Tolias, I.C., Friedrich, A., Kuznetsov, M. (2021a). Cryogenic and ambient gaseous hydrogen blowdown with discharge line effects, in: International Conference on Hydrogen Safety, Edinburgh, UK.

Venetsanos, A.G., Ustolin, F., Tolias, I.C., Giannissi, S.G., Momferatos, G., Coldrick, S., Atkinson, G., Lyons, K., Jallais, S. (2021b). Discharge modeling of large scale LH2 experiments with an engineering tool, in: International Conference on Hydrogen Safety, Edinburgh, UK.

Visser J.H. Maria, Extensile hydraulic fracturing of (saturated) porous materials, Civil Eng. Geosci. 44 (1998) S13–S14.

Xu, Z., Jordan, T., & Kuznetsov, M. (2019). Deliverable 1.1 Report on assessment of effectiveness of conventional safety measures in underground transportation systems and similar confined spaces (Issue Hytunnel-CS)

Zalosh, R. Weyandt, N. Hydrogen fuel tank, fire exposure burst test. SAE Technical Paper 2005-01-1886, 2005

Zaineb, T. Experimental and numerical study of concrete exposed to rapid fire. Master Thesis, August 2020. Department of Civil Engineering, Technical University of Denmark.

Zheng, J.Y. and Lui, P.F. Elasto-plastic stress analysis and burst strength evaluation of AL-carbon fibre/epoxy composite cylindrical laminates. Comp. Mai. Sci. 42 (2008). p.453-461.

A1. Appendices

A1.1 Additional jet release for modelling validation, 5 mm nozzle

The test parameters for this release were 350 bar, 98 L, 5 mm nozzle (Test 12 in Table 30). The experiment was set up as a horizontal, impinging jet, where the instrumented temperature sensing plate was placed at a standoff distance of 3.3 m, as shown in Figure 256. Temperature measurements at each location are plotted in Figure 257.

Figure 256: Jet blowdown, 350 bar, 3.3 m standoff distance, 5 mm nozzle. Still of visible recording (5 secs approx. into release).
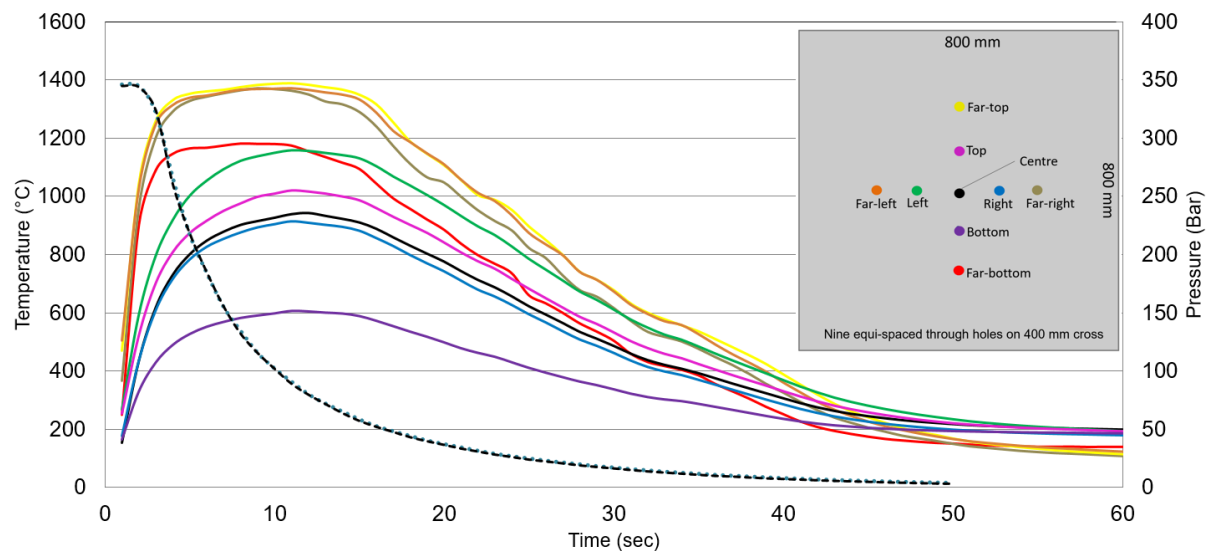

Figure 257: Jet blowdown, 350 bar, 3.3 m standoff distance, 5 mm nozzle. Plot of thermocouple measurements on temperature sensing plate. (Black dashed line represents pressure decay in cylinder during blowdown).

A1.2 Mach number and pressure decay for all sudden release tests

This appendix shows the results from all the tests described in 7.3.1.4.

a)

Sudden discharge Test 26 - reservoir pressure 637 barg - reservoir volume = 5 liters

Measured Shock Mach No. vs distance from bursting disc

b)

Sudden discharge Test 26 - reservoir pressure 637 barg - reservoir volume = 5 liters

Measured Shock pressure (bara). vs distance from bursting disc

Pressure estimated from :

$$\frac{P_2}{P_1} = \frac{2\gamma M_1^2}{\gamma + 1} - \frac{\gamma - 1}{\gamma + 1}$$

$$\frac{P_0}{P_1} = \left(\frac{r_0}{r_1}\right)^{0.75}$$
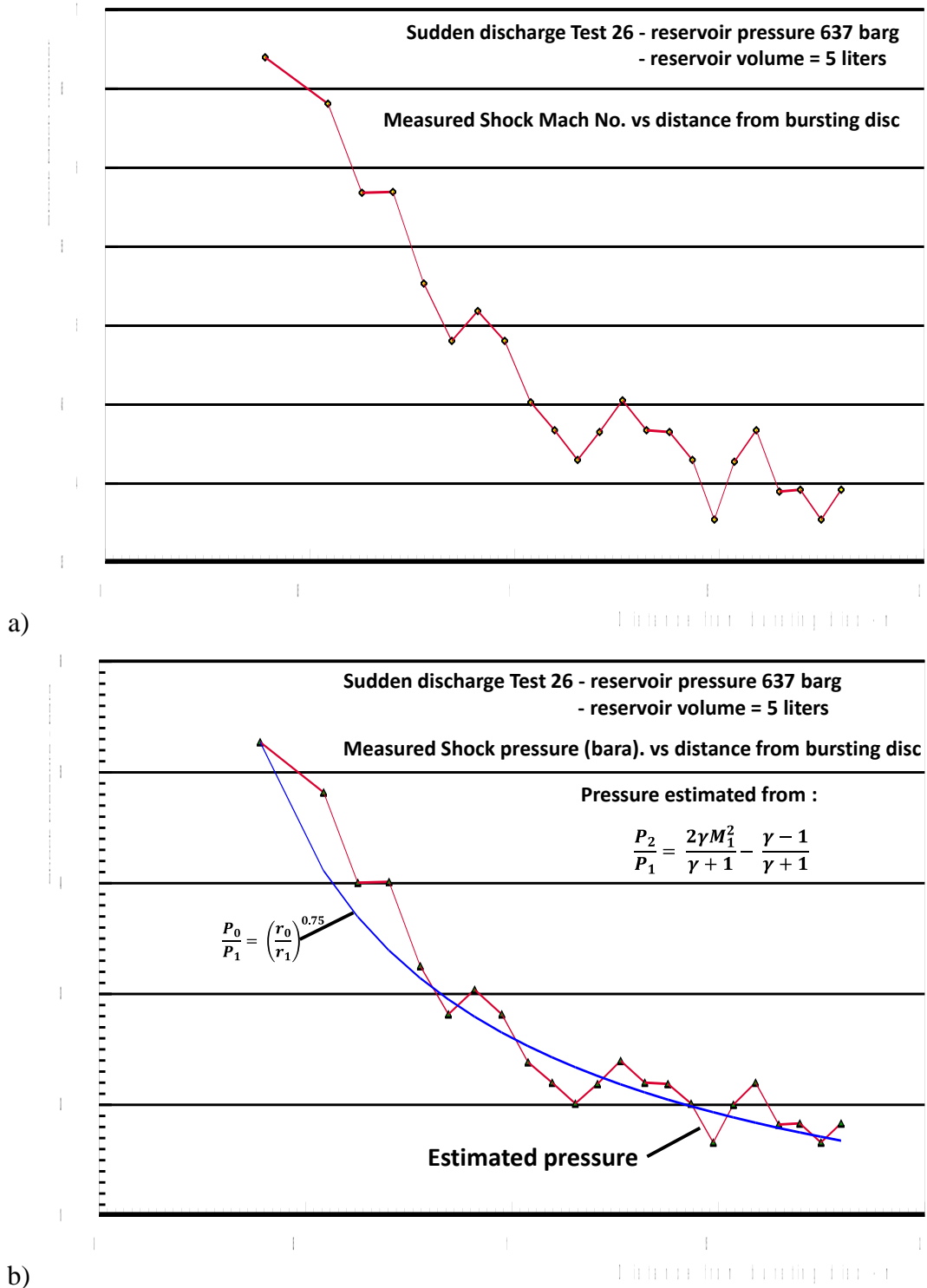
Estimated pressure

Figure 258: (a) Variation of shock Mach number with distance from the disc rupture position for Test 26. (b) Estimated 'shock processed' gas pressure behind the shock front versus distance based on normal shock relations for an ideal gas and $\gamma = 1.4$.

a)

b)

Figure 259: (a) Variation of shock Mach number with distance from the disc rupture position for Test 27. (b) Estimated 'shock processed' gas pressure behind the shock front versus distance based on normal shock relations for an ideal gas and γ=1.4.
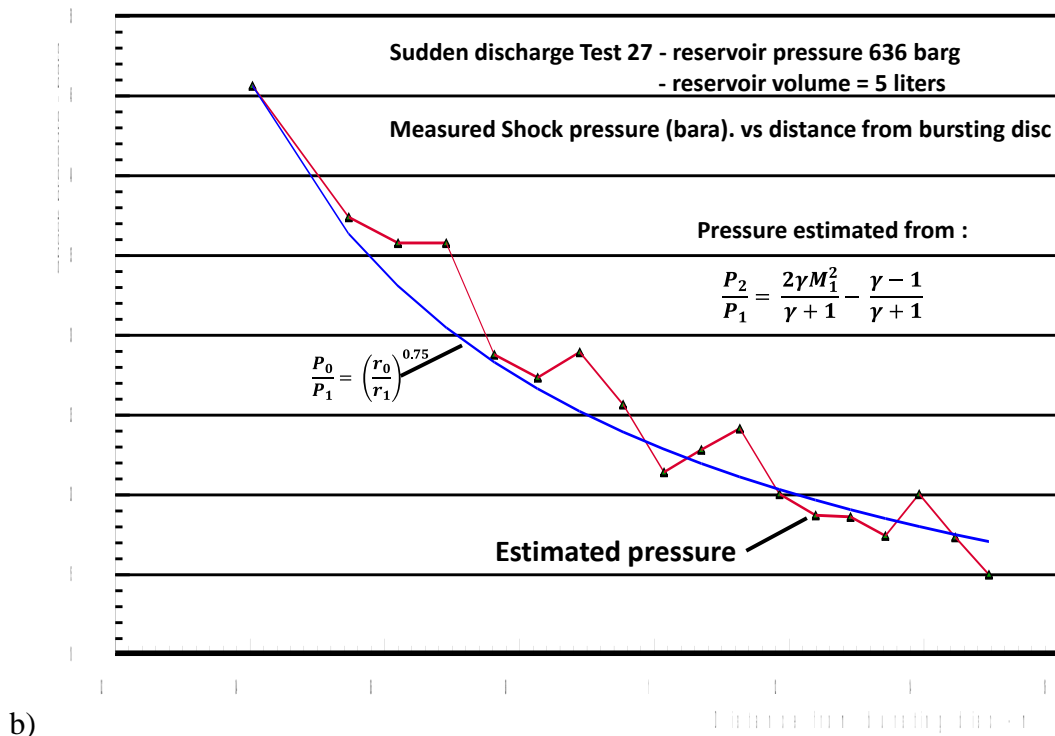
a)

b)

Figure 260: (a) Variation of shock Mach number with distance from the disc rupture position for Test 28. (b) Estimated shock processed' gas pressure behind the shock front versus distance based on normal shock relations for an ideal gas and γ=1.4.
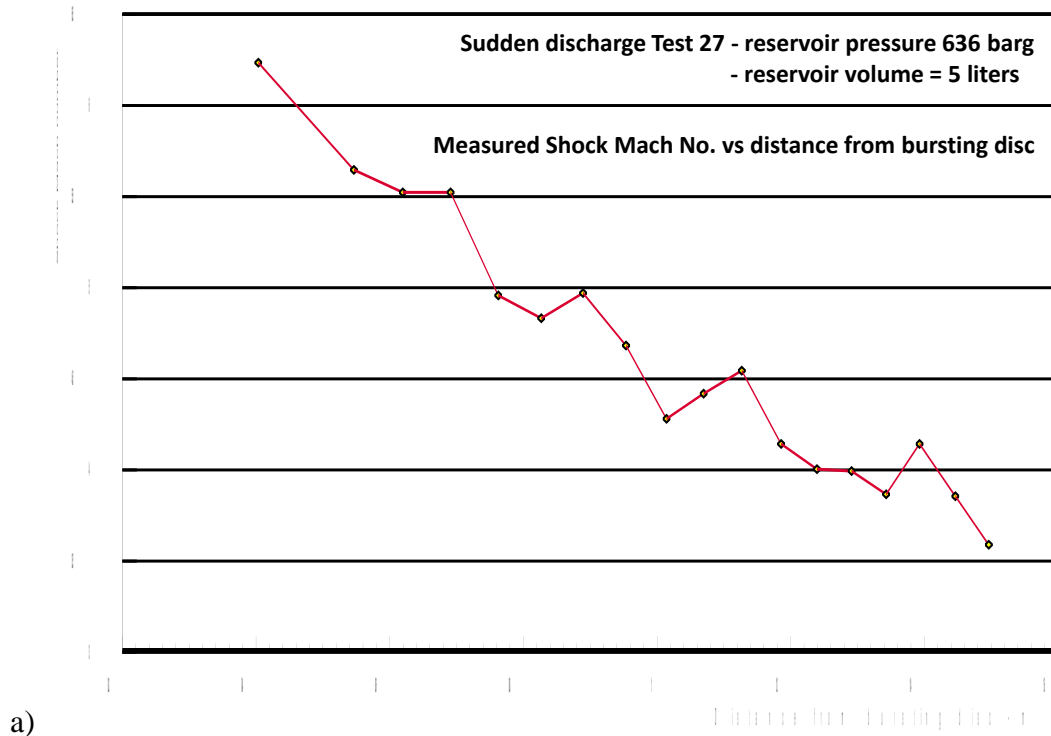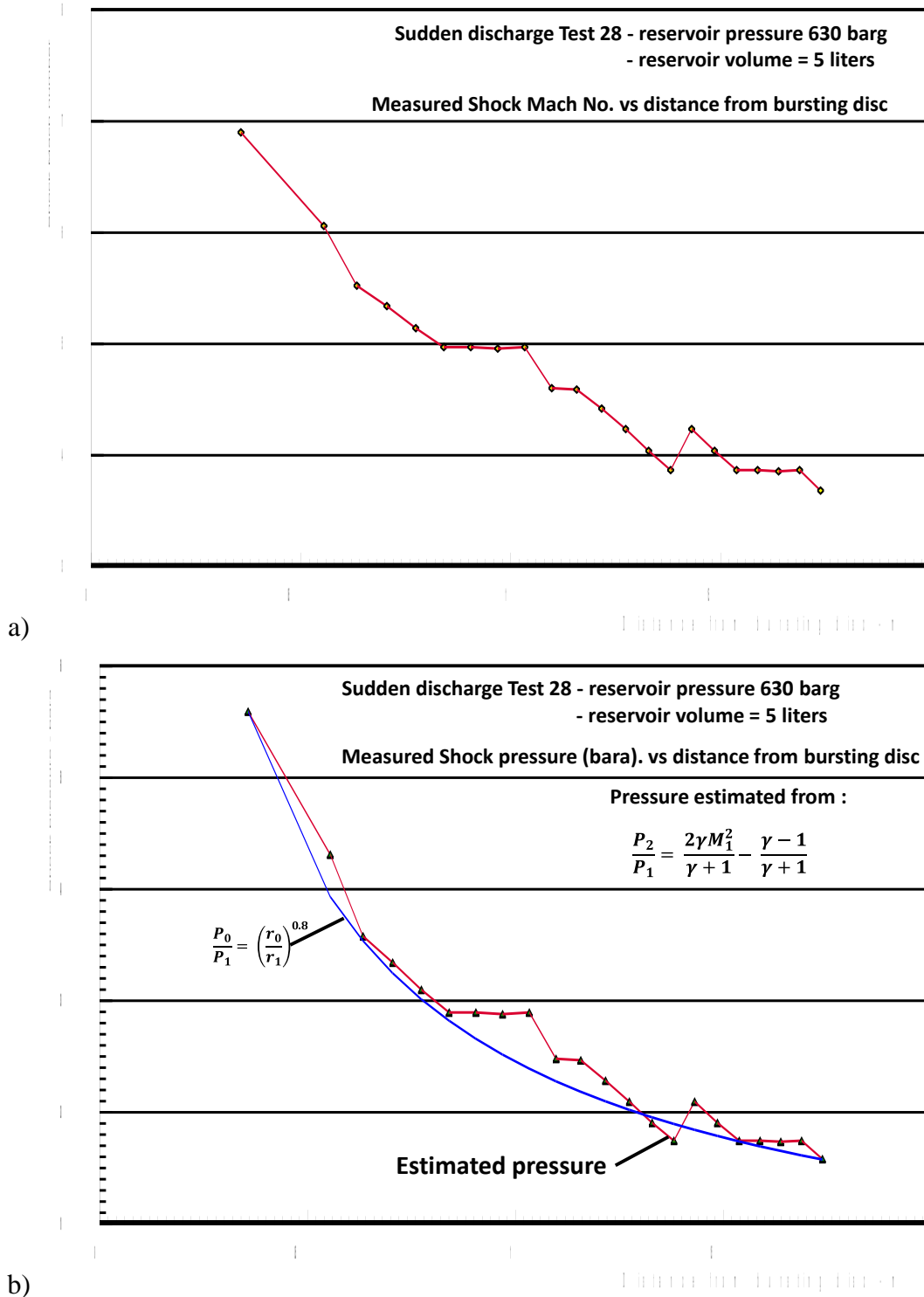
a)

b)

Figure 261: (a) Variation of shock Mach number with distance from the disc rupture position for Test 30. (b) Estimated 'shock processed' gas pressure behind the shock front versus distance based on normal shock relations for an ideal gas and γ=1.4.

Sudden discharge Test 31 - reservoir pressure 554 barg
- reservoir volume = 12 liters

Measured Shock Mach No. vs distance from bursting disc

a)

Sudden discharge Test 31 - reservoir pressure 554 barg
- reservoir volume = 12 liters

Measured Shock pressure (bara). vs distance from bursting disc

Pressure estimated from :

$$\frac{P_2}{P_1} = \frac{2\gamma M_1^2}{\gamma+1} - \frac{\gamma-1}{\gamma+1}$$

$$\frac{P_0}{P_1} = \left(\frac{r_0}{r_1}\right)^{0.7}$$
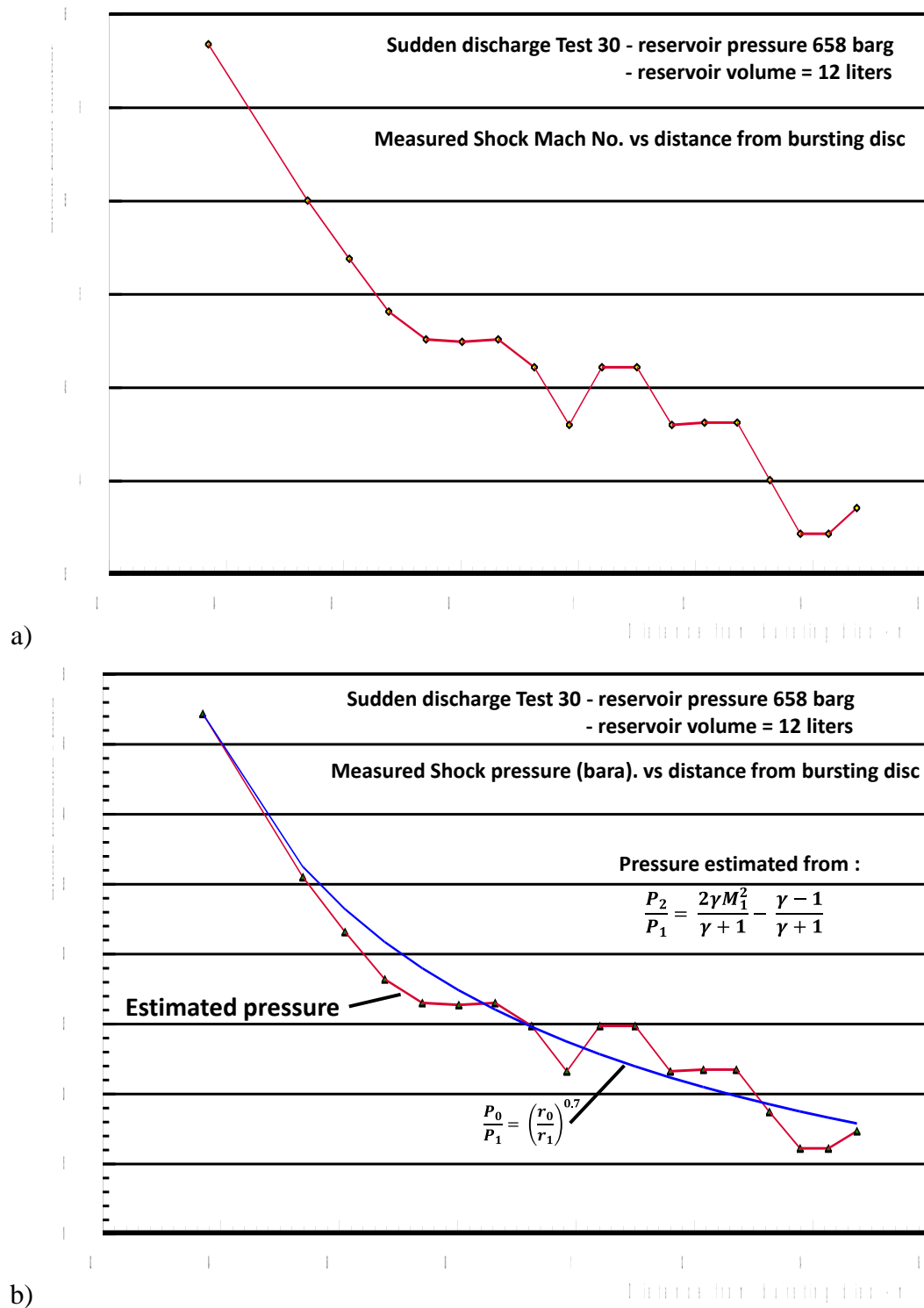
Estimated pressure

b)

Figure 262: (a) Variation of shock Mach number with distance from the disc rupture position for Test 31. (b) Estimated 'shock processed' gas pressure behind the shock front versus distance based on normal shock relations for an ideal gas and γ=1.4.
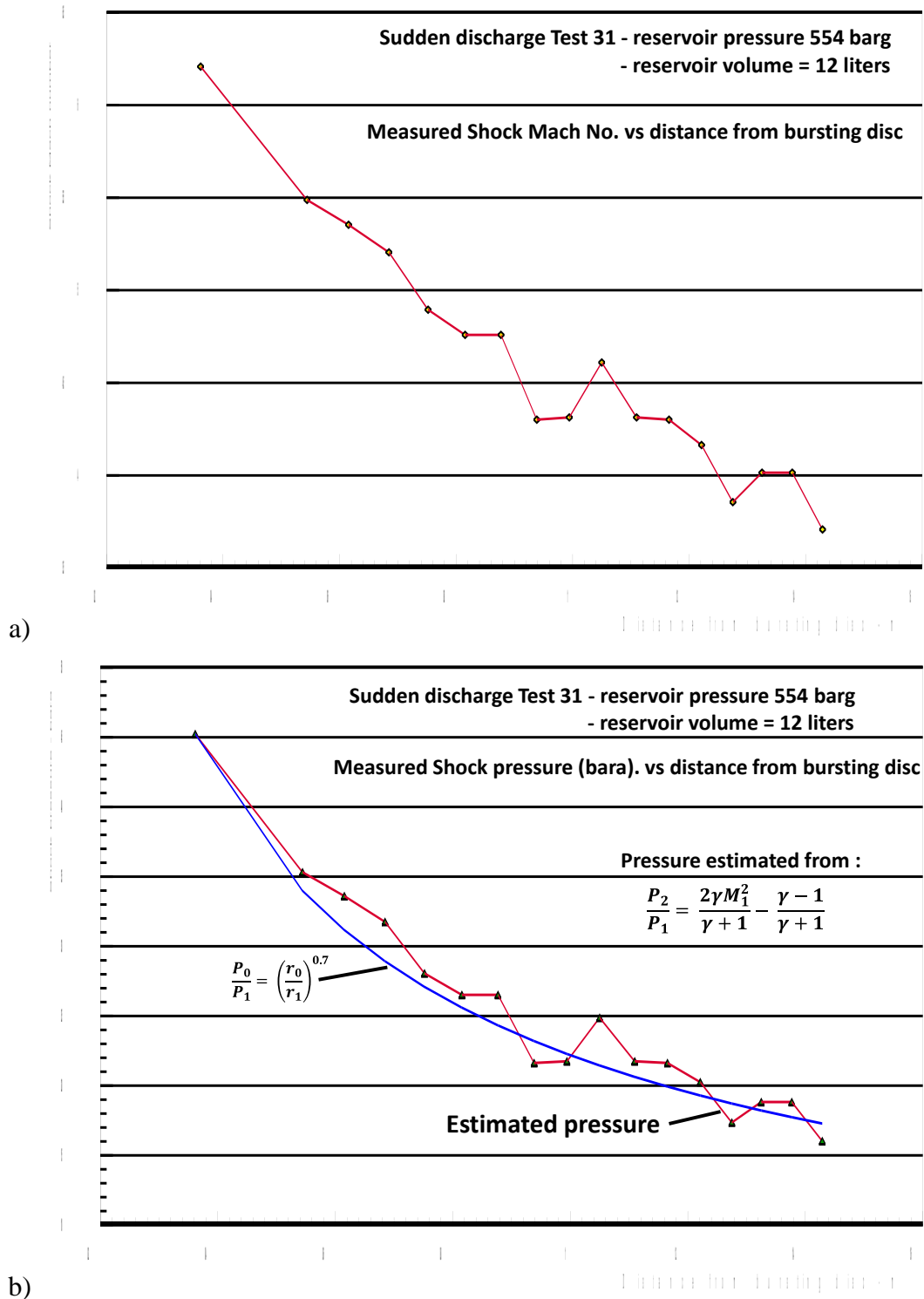
a)

b)

Figure 263: (a) Variation of shock Mach number with distance from the disc rupture position for Test 32. (b) Estimated 'shock processed' gas pressure behind the shock front versus distance based on normal shock relations for an ideal gas and $\gamma=1.4$.

a)

Sudden discharge Test 33 - reservoir pressure 503 barg - reservoir volume = 12 liters

Measured Shock Mach No. vs distance from bursting disc

b)

Sudden discharge Test 33 - reservoir pressure 503 barg - reservoir volume = 12 liters

Measured Shock pressure (bara). vs distance from bursting disc

Pressure estimated from :

$$\frac{P_2}{P_1} = \frac{2\gamma M_1^2}{\gamma + 1} - \frac{\gamma - 1}{\gamma + 1}$$

$$\frac{P_0}{P_1} = \left(\frac{r_0}{r_1}\right)^1$$
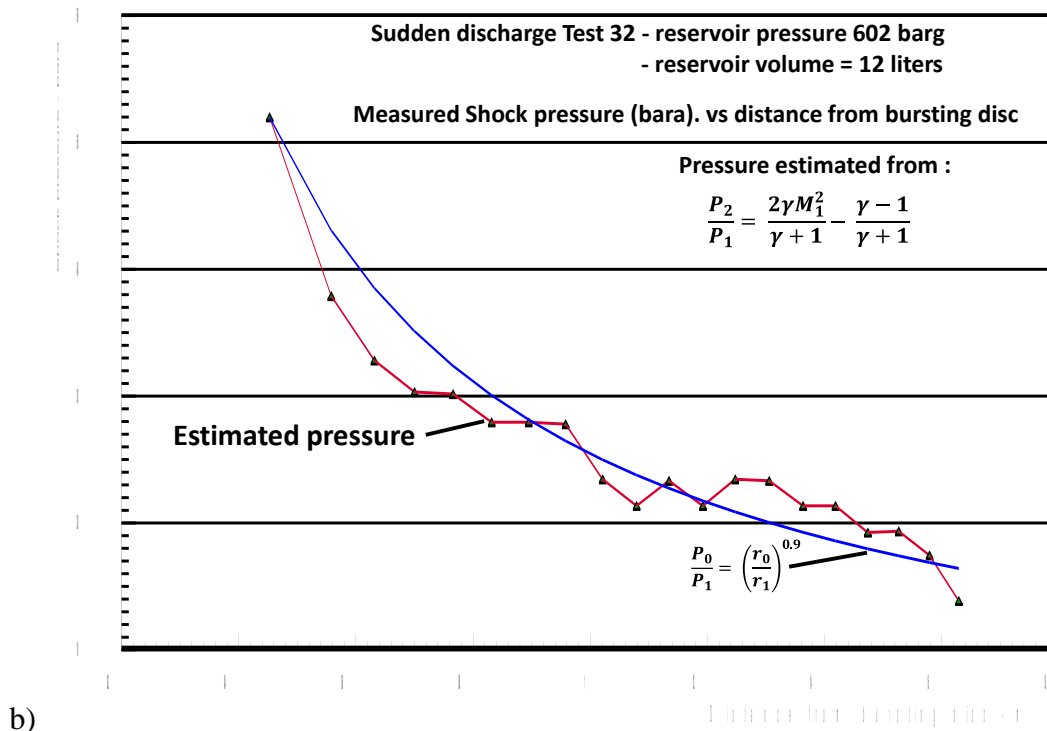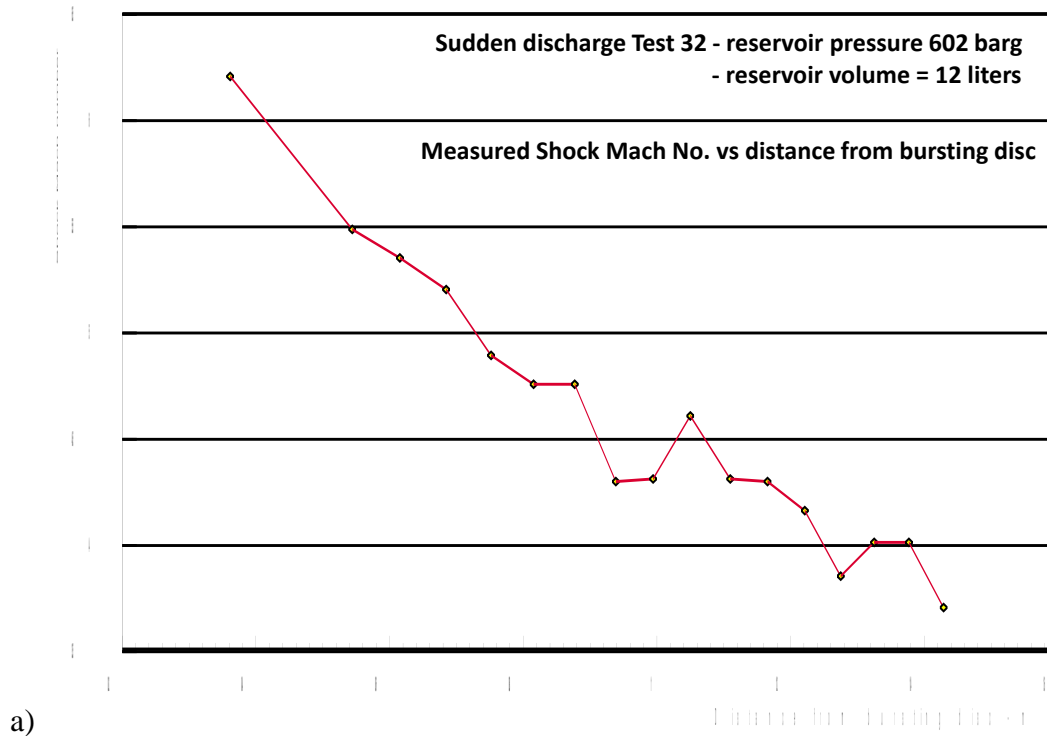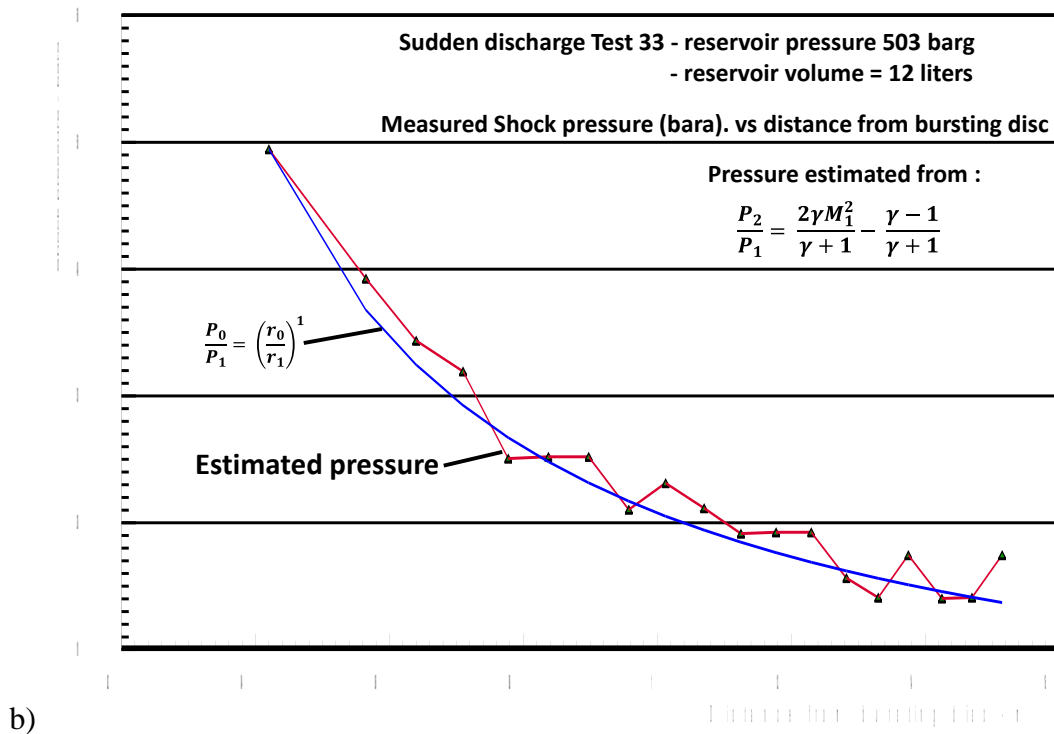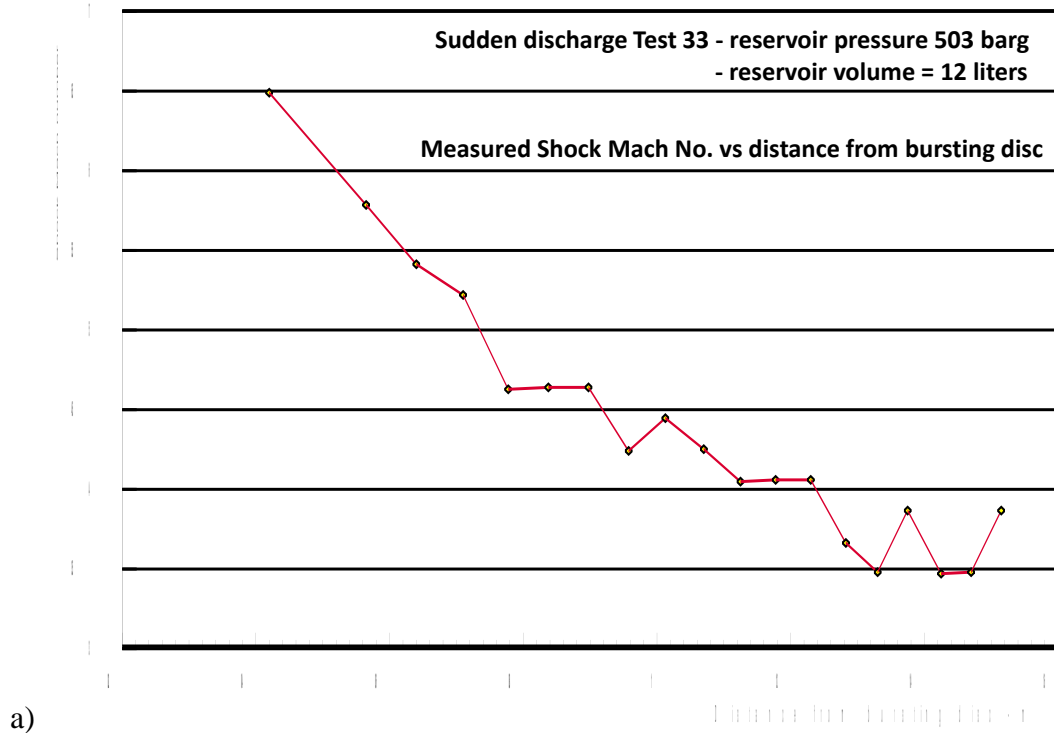
Estimated pressure

Figure 264: (a) Variation of shock Mach number with distance from the disc rupture position for Test 33. (b) Estimated 'shock processed' gas pressure behind the shock front versus distance based on normal shock relations for an ideal gas and γ=1.4.

tu∩∩el

a)

Sudden discharge Test 34 - reservoir pressure 609 barg - reservoir volume = 18 liters

Measured Shock Mach No. vs distance from bursting disc

b)

Sudden discharge Test 34 - reservoir pressure 609 barg - reservoir volume = 18 liters

Measured Shock pressure (bara). vs distance from bursting disc

Pressure estimated from :

$$\frac{P_2}{P_1} = \frac{2\gamma M_1^2}{\gamma + 1} - \frac{\gamma - 1}{\gamma + 1}$$

$$\frac{P_0}{P_1} = \left(\frac{r_0}{r_1}\right)^{0.85}$$
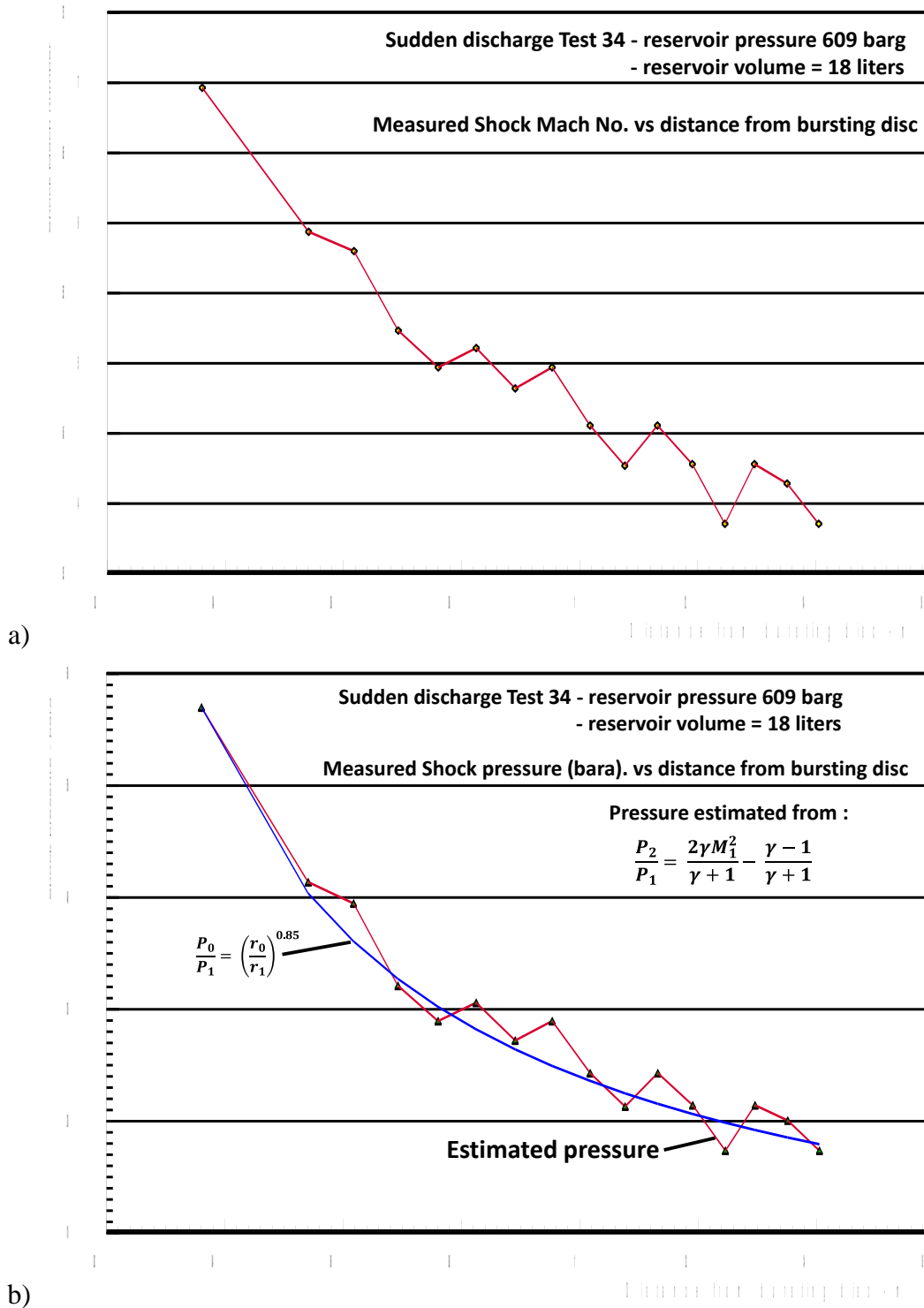
Estimated pressure

Figure 265: (a) Variation of shock Mach number with distance from the disc rupture position for Test 34. (b) Estimated 'shock processed' gas pressure behind the shock front versus distance based on normal shock relations for an ideal gas and γ=1.4.